

ADA 042805

12

014521

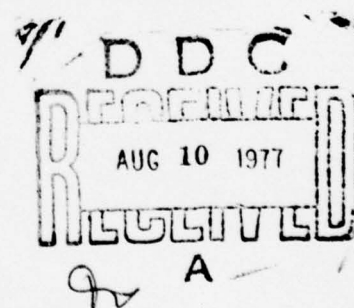
*Preliminary Reports, Memoranda
and Technical Notes of the
Materials Research Council
Summer Conference*

La Jolla, California

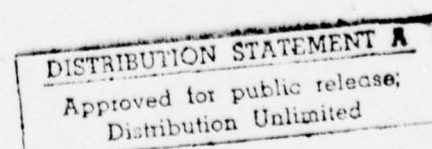
July 1976

AD No. _____
DDC FILE COPY

Sponsored by
Advanced Research Projects Agency
ARPA Order No. 2341/3



Department of Materials and Metallurgical Engineering



6
PRELIMINARY REPORTS, MEMORANDA AND TECHNICAL NOTES
of the
MATERIALS RESEARCH COUNCIL SUMMER CONFERENCE
La Jolla, California,

11 July 1976

10 Maurice J. Sinnott

12/665p.

DARPA Order Number: 2341/3

Program Code Number: 6D10

Contractor: The Regents of The University of Michigan

Effective Date of Contract: 1 July 76

Contract Expiration Date: 30 June 77

Amount of Contract: \$265,000

Contract Number: MDA903-76C-0250

Principal Investigator: Associate Dean Maurice J. Sinnott

15 College of Engineering

The University of Michigan

Ann Arbor, Michigan 48109

(313) 763-0242

DARPA Order - 2341

DISTRIBUTION STATEMENT A

Approved for public release
Distribution Unlimited

407222

Y/B

The views and conclusions contained in this document are those of the authors and should not be interpreted as necessarily representing the official policies, either expressed or implied, of the Defense Advanced Research Projects Agency or the U.S. Government.

| | |
|---------------------------------|---|
| ACCESSION TAG | |
| NTIS | White Section <input checked="" type="checkbox"/> |
| DDC | Buff Section <input type="checkbox"/> |
| UNANNOUNCED | <input type="checkbox"/> |
| JUSTIFICATION | |
| <i>Letter on file</i> | |
| BY | |
| DISTRIBUTION/AVAILABILITY CODES | |
| Dist. | AVAIL. and/or SPECIAL |
| <i>A</i> | |

TABLE OF CONTENTS

- I. Foreword
- II. Steering Committee
- III. Participants
- IV. Guest Consultants
- V. Preliminary Reports, Memoranda and Technical Notes

The following papers fall into two categories; (1) papers in a state ready for publication, and (2) reports and memoranda for limited distribution representing work in progress. The former category is available for general distribution and in some cases are in the process of publication in the appropriate technical journals. The limited distribution reports and memoranda represent initial ideas, problem suggestions, position papers, and status reports and are aimed primarily to stimulate discussion with the Council. However, they are available subject to the author's release by request to the Project Director.

| <u>TITLE</u> | <u>PAGE</u> |
|---|-------------|
| Summary of Meeting on Pyroelectric and Piezoelectric Materials G. S. Kino. | 1 |
| Fundamental Limitations on Performance of Pyroelectric Vidicon Detectors M. Tinkham and A. Yariv | 36 |
| Heating Effects in High-Frequency Metallic Josephson Devices: Voltage Limit, Bolometric Mixing and Noise M. Tinkham. | 49 |
| Molecular Dipolar Pyroelectricity W. H. Flygare | 87 |
| Summary of the MRC Workshop on NDE M. Buckley and R. M. Thomson. | 101 |
| Workshop on the Theory of Ultrasonic Scattering with Application to Adaptive Computerized NDE R. M. Thomson | 122 |

cont

TITLE

PAGE

Interpretation of Elastic Wave Scattering Theory,
for Analysis and Design of Flaw Characterization
Experiments: I. Long Wavelength Limit

J. E. Gubernatis, J. A. Krumhansl, R. M. Thomson. . . . 129

Perturbation Theory for Scattering of Acoustic
Waves by Flaws

G. S. Kino. 147

Variational Formulae for Scattering of Acoustic
Waves by Flaws, and for Acoustic Wave Propagation

G. S. Kino. 171

Variational Principle for Sound Scattering from a
Localized Defect (One Dimension)

W. Kohn 190

Experimental Characterization of Defects with
Elastic Waves

L. Adler, G. S. Kino, R. B. Thompson, B. R. Tittman . . 199

Report of a Meeting on Fatigue Crack Growth

B. Budiansky, D. C. Drucker, J. W. Hutchinson and
J. R. Rice. 211

Fatigue Crack Growth

P. C. Paris 231

Summary of the Meeting on Epitaxy

A. Yariv. 240

A Mechanism for Liquid Phase Epitaxial Growth of
Nonequilibrium Compositions Producing a Coherent
Interface

J. P. Hirth and G. B. Stringfellow. 247

Summary of Meeting on Rapidly Solidified Powders
and Related Technology

E. E. Hücke, J. P. Hirth and M. Cohen 255

Advanced Powder-Making Processes - Fundamentals of
Droplet Formation

Alan Lawley 269

Theory of Dendrite Solidification During Very
Rapid Cooling

M. C. Flemings. 306

| <u>TITLE</u> | <u>PAGE</u> |
|---|-------------|
| Methods of Achieving Rapid Solidification in Fine Particles N. J. Grant | 316 |
| High Performance Materials by Crucible's P/M Processes J. N. Fleck and E. J. Dulis | 325 |
| Superplasticity in Metals and Alloys O. D. Sherby. | 338 |
| Prospects for Superplasticity in Ceramics: A Preliminary Appraisal A. G. Evans, R. L. Coble and R. M. Cannon | 372 |
| Systems for Storage and Retrieval of Thermochemical Data and Calculation of Phase Diagrams L. Kaufman and H. Nesor | 390 |
| Undercooling During Atomization of Complex Alloy Powders R. Mehrabian. | 392 |
| Surface Treatment of Superalloys by Laser Skin Melting E. M. Breinan, B. H. Kear, C. M. Banas and L. E. Greenwald | 399 |
| Rapid Solidification Processing (RSP) of Thermoelastic Alloys M. Cohen. | 401 |
| Small Particle Technology R. L. Coble | 403 |
| Progress in Making PM Shapes from Ti_3Al and $TiAl$ H. A. Lipsitt and A. M. Adair | 407 |
| Shock Waves as a Means of Producing Very Rapid Cooling E. E. Huckle and G. H. Vineyard. | 408 |
| Very Rapid Quenching with Thermal Spikes G. H. Vineyard. | 411 |
| Some Recent Developments of Powder Processing in Electronic Devices G. Y. Chin. | 418 |
| Electronic Materials Applications Suggestions: Small-Particle Phenomena and Technologies J. H. Wernick | 421 |

| <u>TITLE</u> | <u>PAGE</u> |
|--|-------------|
| Amorphous Alloy Powders P. E. Duwez | 423 |
| Curvature Effects in the Thermodynamics of Multicomponent Systems: Possible Effect on Dendrite Spacing in Rapidly Cooled Small Liquid Metal Drops H. Reiss. | 425 |
| Prospects for NDE of Powdered Metals G. S. Kino. | 440 |
| Nucleation, Undercooling and Homogeneous Structures in Rapidly Solidified Powders J. P. Hirth | 443 |
| Suggested New Alloys with Promise for Small-Particle Alloy Development E. E. Huccke, J. P. Hirth and M. Cohen | 456 |
| Comments on RSP M. C. Flemings. | 459 |
| A Key Bottleneck in the Exploitation of Rapid Solidification Processing (RSP) M. Cohen. | 461 |
| Highlights of Sessions on Rapidly Solidified Powders and Related Technology E. E. Huccke, J. P. Hirth and M. Cohen | 462 |
| Metallic Glasses H. Ehrenreich, J. J. Gilman, J. P. Hirth and G. H. Vineyard. | 467 |
| Metallic Glass Structures J. J. Gilman. | 480 |
| Electrical Properties and Metastability of Metallic Glasses H. Ehrenreich | 491 |
| On the Mechanism of Shear of an Amorphous Metal J. P. Hirth | 496 |
| Structural Reliability of Optical Fibers A. G. Evans and F. A. McClintock. | 504 |
| Chlorofluorocarbon Update, 1976 J. L. Margrave. | 539 |

| <u>TITLE</u> | <u>PAGE</u> |
|---|-------------|
| Thermal Decomposition of CFX in Fluorine and in Other Atmospheres P. Kamarchik and J. L. Margrave | 554 |
| Tight Binding Theory of Metallic Adhesion W. Kohn and R. Gomer. | 572 |
| The Use of Bubble Domain Materials for Submillimeter Wave Magnetic Devices P. L. Richards. | 595 |
| Mechanistic Limitations on the Speed of Response of Electrochromic Optical Devices R. A. Huggins | 607 |
| Aluminum-Carbon Composites Developed for Sliding Seal Members E. E. Hucke | 632 |
| A Fluid Thermal Switch H. Reiss. | 634 |

END

Foreword

This collection of papers does not constitute a formal reporting of the activities of the DARPA Materials Research Council Summer Conference. Each report, memoranda or technical note is a draft of the author or authors and is their work alone. The Steering Committee, in conjunction with the authors, will decide how this material can best be presented as a formal report to DARPA.

Steering Committee

Professor Willis H. Flygare
Secretary of the Steering Committee
Department of Chemistry
University of Illinois
Urbana, Illinois 61801

Professor Nico Bloembergen
Division of Engineering & Applied Physics
Harvard University
Cambridge, Massachusetts 02138

Professor Bernard Budiansky
Division of Engineering and Applied Science
Harvard University
Cambridge, Massachusetts 02138

Professor Morris Cohen
Department of Materials Science & Engineering
Massachusetts Institute of Technology
Cambridge, Massachusetts 02139

Dr. John J. Gilman, Director
Materials Research Center
Allied Chemical Corporation
Morristown, New Jersey 07960

Professor Paul L. Richards
Department of Physics
University of California
Berkeley, California 94720

Dr. Robb M. Thomson
National Bureau of Standards
Office of Programs
Washington, D.C. 20234

Project Director

Associate Dean Maurice J. Sinnott
College of Engineering
The University of Michigan
Ann Arbor, Michigan 48109

Participants

Professor Robert Coble
Materials Science Department
Massachusetts Institute of Technology
Cambridge, Massachusetts 02139

Dean Daniel C. Drucker
Engineering College
University of Illinois
Urbana, Illinois 61801

Professor Henry Ehrenreich
Pierce Hall
Harvard University
Cambridge, Massachusetts 02138

Dr. Anthony G. Evans
Mechanical Ceramics
Rockwell International Science Center
Thousand Oaks, California 91360

Professor Robert Gomer
James Franck Institute
University of Chicago
Chicago, Illinois 60637

Professor M. Fred Hawthorne
Chemistry Department
University of California
Los Angeles, California 90024

Professor John P. Hirth
Metallurgical Engineering Department
Ohio State University
Columbus, Ohio 43201

Professor Robert A. Huggins
Center for Materials Research
Stanford University
Stanford, California 94305

Professor Gordon S. Kino
Microwave Laboratory
Stanford University
Stanford, California 94305

Professor Walter Kohn
Department of Physics
University of California
La Jolla, California 92037

Professor John L. Margrave
Department of Chemistry
Rice University
Houston, Texas 77001

Professor Frank A. McClintock
Department of Mechanical Engineering
Massachusetts Institute of Technology
Cambridge, Massachusetts 02139

Professor Elliott W. Montroll
Department of Physics & Astronomy
University of Rochester
Rochester, New York 14534

Professor Howard Reiss
Department of Chemistry
University of California
Los Angeles, California 90024

Professor James R. Rice
Division of Engineering
Brown University
Providence, Rhode Island 02912

Professor Michael Tinkham
Department of Physics
Harvard University
Cambridge, Massachusetts 02138

Dr. George H. Vineyard
Brookhaven National Laboratory
Upton, Long Island, New York 11973

Professor Amnon Yariv
Electrical Engineering Department
California Institute of Technology
Pasadena, California 91125

GUEST CONSULTANTS

A. M. Adair
AFML/LLM
Wright Patterson AFB
Ohio 45433

L. Adler
Dept. of Physics
University of Tennessee
Knoxville, Tennessee

D. J. Albares
NELC
Code 2500
San Diego, California 92152

M. F. Amateau
Aerospace Corporation
2300 El Segundo Blvd.
El Segundo, California

R. T. Anderson
ASNT
3200 Riverside Drive
Columbus, Ohio 43220

D. B. Arnold
General Electric Company
M-87
Cincinnati, Ohio 45215

B. A. Auld
Ginzton Laboratory
Stanford University
Stanford, California 94305

D. W. Ballard
Sandia Laboratories
P.O. Box 5500
Albuquerque, New Mexico 87115

T. W. Barbee, Jr.
Center for Materials Research
Stanford University
Stanford, California 94305

W. J. Baxter
General Motors Research Labs.
12 Mile & Mound Roads
Warren, Michigan 48090

M. I. Bell
Physics Department
Yeshiva University
New York, New York 10033

A. L. Bement
Material Sciences Office
DARPA
1400 Wilson Boulevard
Arlington, Virginia 22209

B. Bendow
RADC/ETSS
Hanscom AFB
Massachusetts 01731

D. Berlincourt
Channel Products Inc.
Chagrin Falls, Ohio 44022

J. R. Biard
Spectronics, Inc.
830 East Arapaho Road
Richardson, Texas 75080

J. G. Bjeletich
Lockheed Missile & Space Co.
Bldg. 204
Palo Alto, California 94304

H. K. Bowen
M.I.T.
Room 13-4066
Cambridge, Massachusetts 02139

J. Brinkman
U.S. Army Armament Command
Rock Island, Illinois 61201

G. A. Bruggeman
AMMRC
Metals Research Division
Watertown, Massachusetts 02172

O. Buck
Rockwell International
Science Center
Thousand Oaks, California 91360

M. J. Buckley
AFML/LLP
Wright Patterson AFB
Dayton, Ohio 45433

R. A. Burmeister
Hewlett-Packard Laboratories
Palo Alto, California 94304

J. C. Bushnell
Sandia Laboratories
Albuquerque, New Mexico 87115

N. E. Byer
Martin Marietta Laboratories
1450 S. Rolling Road
Baltimore, Maryland 21227

G. R. Chanani
Northrup Corporation
ORG. 3771/62
Hawthorne, California 90250

G. Y. Chin
Bell Laboratories
Murray Hill, New Jersey 07974

A. Y. Cho
Bell Laboratories
Murray Hill, New Jersey 07974

W. J. Coleman
Battelle North West
Richland, Washington 99352

T. H. Conklin
Amperex Electronic Corp.
EOD Division
Slatersville, Rhode Island 02876

R. J. Considine
3600 E. Foothill Blvd.
Pasadena, California 91109

D. M. Corbly, Jr.
AFML/LLN
Wright Patterson AFB
Ohio 45433

S. Cowen
Naval Undersea Center
Code 6513
San Diego, California 92132

A. R. Cox
Pratt & Whitney Aircraft
West Palm Beach, Florida

E. L. Criscuolo
Naval Surface Weapons Center
Bldg. 70
Silver Spring, Maryland 20910

L. E. Cross
Electrical Engineering Dept.
Pennsylvania State University
State College, Pennsylvania 16802

L. A. Davis
Allied Chemical Corporation
Materials Research Center
Morristown, New Jersey 07960

H. D. Dill
McDonnell Douglas
Bldg. 32, P.O. Box 516
St. Louis, Missouri 63166

R. H. Doremus
Materials Department
Rensselaer Polytechnic Inst.
Troy, New York 12309

N. E. Dowling
Westinghouse Research
Beulah Road
Pittsburgh, Pennsylvania 15235

E. J. Dulis
Crucible Inc./Colt Ind.
Box 88
Pittsburgh, Pennsylvania 15230

P. Duwez
Applied Physics & Materials
Science Department
California Inst. of Technology
Pasadena, California 91125

W. Elber
NASA
MS 188E
Hampton, Virginia 23665

N. B. Elsner
General Atomic
L-340, Box 81608
San Diego California 92138

G. Epstein
Aerospace Corporation
P.O. Box 92957
Los Angeles, California 90009

E. A. Fisher
Ford Motor Company
20000 Rotunda
Dearborn, Michigan 48121

M. C. Flemings
M.I.T.
Room 8-407
Cambridge, Massachusetts 02139

J. M. Florence
AFFDL/FBA
Wright-Patterson AFB
Ohio 45433

D. S. Fox
Hughes Aircraft Company
Bldg. 802, Room 507
Tucson, Arizona 85713

R. M. Fulrath
266 Hearst Mining Bldg.
University of California
Berkeley, California 94720

J. P. Gallagher
AFFDL/FBE
Wright-Patterson AFB
Ohio 45433

A. F. Garito
Department of Physics
University of Pennsylvania
Philadelphia, Pennsylvania 19174

A. M. Glass
Bell Laboratories
Murray Hill, New Jersey 07974

A. C. Gossard
Bell Laboratories
Murray Hill, New Jersey 07974

C. D. Graham, Jr.
LRSM/K1
University of Pennsylvania
Philadelphia, Pennsylvania 19174

N. J. Grant
M.I.T.
Room 13-2090
Cambridge, Massachusetts 02139

J. E. Gubernatis
Los Alamos Scientific Lab.
T-11, MS-457
Los Alamos, New Mexico 87545

J. P. Gudas
Naval Ship R&D Center
Code 2813
Annapolis, Maryland 21402

D. J. Hagemaiier
Douglas Aircraft Company
C1-253 (1-18)
Long Beach, California

J. S. Haggerty
A. D. Little Company
15 Acorn Park
Cambridge, Massachusetts 02140

R. Hasegawa
Allied Chemical Corporation
Morristown, New Jersey 07960

C. N. Helmick, Jr.
Naval Weapons Center
Code 6014
China Lake, California 93555

L. R. Hettche
Naval Research Laboratory
Washington, D.C. 20375

W. B. Hillig
General Electric R&D Center
Box 8
Schenectady, New York 12301

A. Hurlich
Convair Division
General Dynamics Corporation
P.O. Box 80841
San Diego, California 92138

J. W. Hutchinson
Applied Mechanics Dept.
Harvard University
Cambridge, Massachusetts 02138

R. E. Johnson
U.S. Airforce Materials Lab.
AFML/LLN
Dayton, Ohio 45433

D. H. Kaelble
Rockwell International
Science Center
Thousand Oaks, California 91360

G. S. Kamath
Hughes Research Laboratories
Malibu, California 90265

C. Kao
ITT
EOPD Plantation Road
Roanoke, Virginia 24019

G. Kaposhilin
Hewlett-Packard Laboratories
1501 Page Mill Road
Palo Alto, California 94304

R. Katz
Naval Avionics Facility
D-810, 6000 E. 21st Street
Indianapolis, Indiana 46218

L. Kaufman
ManLabs Inc.
21 Erie Street
Cambridge, Massachusetts 02139

B. H. Kear
Pratt & Whitney Aircraft
Middletown, Connecticut 06443

E. G. Kendall
Aerospace Corporation
P.O. Box 92957
Los Angeles, California 90009

M. A. Kinna
Naval Sea Systems Command
Code 03521
Washington, D.C. 20362

G. Kosmos
Naval Electronics Laboratory
Code 4400
San Diego, California 92152

E. A. Kraut
Rockwell International
Science Center
Thousand Oaks, California 91360

J. A. Krumhansl
Physics Department
Cornell University
Ithaca, New York 14850

C. E. Land
Sandia Laboratories
Division 5133
Albuquerque, New Mexico 87115

J. B. Lando
Olin Building
Case Western Reserve University
Cleveland, Ohio 44106

F. R. Larson
U.S. AMMRC
Watertown, Massachusetts 02172

A. Lawley
Materials Engineering
Drexel University
Philadelphia, Pennsylvania 19104

R. L. Lebduska
Naval Electronics Laboratory
271 Catalina Blvd.
San Diego, California 92152

I. Lefkowitz
Army Research Office
Durham, North Carolina

E. M. Lenoe
Army Research Center
Watertown, Massachusetts 02172

H. A. Lipsitt
Air Force Materials Laboratory
Wright-Patterson AFB
Ohio 45433

S. T. Liu
Honeywell Corp. Research Center
10701 Lyndale Avenue S.
Bloomington, Minnesota 55420

M. H. Loew
Adaptronics, Inc.
West Gate Research Park
McLean, Virginia 22101

G. M. Loiacono
Philips Laboratories
Briarcliff Manor, New York 10510

P. Macedo
Catholic University
B-10 Keane
Washington, D.C. 20017

M. S. Maklad
ITT-EOPD
7635 Plantation Road
Roanoke, Virginia 24019

H. Marcus
University of Texas
TAY 167
Austin, Texas 78759

R. E. Maringer
Battelle Memorial Institute
505 King Avenue
Columbus, Ohio 43201

O. Marsh
Hughes Research Laboratories
Malibu, California 30265

R. D. Maurer
Corning Glass Works
Sullivan Park
Corning, New York 14830

A. McEvily
Metallurgy Department
University of Connecticut
Storrs, Connecticut 06268

M. McLandrich
NELC
Bldg. 4, Code 2500
San Diego, California 92152

A. F. McLean
Ford Motor Company
Turbine Development Dept.
Dearborn, Michigan 48121

R. Mehrabian
Metallurgical & Mining Eng.
University of Illinois
Urbana, Illinois 61820

A. G. Metcalfe
Solar Division
International Harvester Co.
2200 Pacific Highway
San Diego, California 92138

J. B. Moore
Materials Laboratories
Pratt & Whitney Aircraft
West Palm Beach, Florida

A. N. Mucciardi
Adaptronics, Inc.
7700 Old Springhouse Road
McLean, Virginia 22101

P. Packman
Vanderbilt University
Box 3245
Nashville, Tennessee

A. Paluszny
Ford Motor Company
Scientific Laboratory
Dearborn, Michigan 48121

M. B. Panish
Bell Telephone Laboratories
Murray Hill, New Jersey 07974

S. Paprocki
Material Concepts Inc.
2747 Harrison Road
Columbus, Ohio 43204

P. C. Paris
Brown University
Providence, Rhode Island 02912

R. M. Pelloux
Room 8-237
M.I.T.
Cambridge, Massachusetts 02139

J. Persh
ODDR & E
Room 3D1089, Pentagon
Washington, D.C. 20301

W. H. Pfeifer
METCO
110 Pine Avenue
Long Beach, California

D. Pinnow
Hughes Research Laboratories
Room 2270
Malibu, California 90265

R. C. Pohanka
U.S. Naval Research Laboratory
Code 6361
Washington, D.C. 20375

M. Pomerantz
U.S. Army Electronics Command
Attn: DRSEL-TL-ME
Fort Monmouth, New Jersey 07703

H. Rast
Naval Electronics Lab. Center
Code 2500
San Diego, California 92150

C. Rau
Failure Analysis Associates
Palo Alto, California 94304

W. H. Reimann
USAF/AFML
Dayton, Ohio 45433

R. Reynolds
Materials Science Office
DARPA
1400 Wilson Boulevard
Arlington, Virginia 22209

R. W. Rice
Naval Research Laboratory
Code 6360
Washington, D.C. 20375

W. C. Riley
Aerospace Corporation
El Segundo, California

R. O. Ritchie
University of California
Room 139, LBL Bldg. 62
Berkeley, California 94720

J. E. Ritter, Jr.
Mechanical Engineering
University of Massachusetts
Amherst, Massachusetts 01002

C. Roundy
Electrical Engineering Dept.
Utah State University
Logan, Utah 84322

S. Ruby
Materials Science Office
DARPA
1400 Wilson Boulevard
Arlington, Virginia 22209

W. D. Scott
Ceramic Engineering FB-10
University of Washington
Seattle, Washington 98195

W. R. Scott
NADC
Code 30233
Warminster, Pennsylvania 18974

E. J. Sharp
U.S. Army Night Vision Lab.
Room 307
Ft. Belvoir, Virginia 22060

H. J. Shaw
Ginzton Laboratory
Stanford University
Stanford, California 94305

O. D. Sherby
Materials Science & Engineering
Stanford University
Stanford, California 94305

B. Singer
Philips Laboratories
345 Scarborough Road
Briarcliff Manor, New York 10510

R. M. Spriggs
Alumni Memorial Bldg.
Lehigh University
Bethlehem, Pennsylvania 18015

R. W. Staehle
Materials Engineering
Ohio State University
Columbus, Ohio

H. L. Staubs
SAMSO/YAPC
Los Angeles AFS
World Way Postal Center
Los Angeles, California 90009

K. M. Stiles
Air Logistics Corporation
Pasadena, California 91107

A. J. Strauss
M.I.T. Lincoln Laboratory
Lexington, Massachusetts 02173

G. B. Stringfellow
Hewlett Packard Laboratories
1501 Page Mill Road
Palo Alto, California 94304

A. Thompson
Rockwell International
Science Center
Thousand Oaks, California 91360

D. O. Thompson
Rockwell International
Science Center
Thousand Oaks, California 91360

R. B. Thompson
Rockwell International
Science Center
Thousand Oaks, California 91360

D. M. Tracey
Army Materials & Mechanics
Research Center
Bldg. 39
Watertown, Massachusetts 02912

D. Turnbull
Pierce Hall
Harvard University
Cambridge, Massachusetts 02138

J. C. Uy
Ford Motor Company
Scientific Research Laboratory
Dearborn, Michigan 48121

E. C. van Reuth
Materials Science Office
DARPA
1400 Wilson Boulevard
Arlington, Virginia 22209

P. Vohl
M.I.T. Lincoln Laboratories
Lexington, Massachusetts 02173

D. L. Waidelich
Dept. of Electrical Engineering
University of Missouri
Columbia, Missouri 65201

J. N. Walpole
M.I.T. Lincoln Laboratories
Lexington, Massachusetts 02173

B. A. Webb
DWA Composite Specialties, Inc.
17321 Lahey Street
Granada Hills, California 91344

R. P. Wei
327 Sinclair Lab. Bldg. 7
Lehigh University
Bethlehem, Pennsylvania 18015

C. H. Wells
Southwest Research Institute
Materials Sciences
San Antonio, Texas 78230

J. H. Wernick
Bell Laboratories
Murray Hill, New Jersey 07974

P. White
Owens-Illinois, Inc.
Technical Center, P.O. Box 1035
Toledo, Ohio 43666

G. A. Wilkins
Naval Undersea Center
Box 997
Kailua, Hawaii 96734

H. Winsor
Materials Sciences Office
DARPA
1400 Wilson Boulevard
Arlington, Virginia 22209

W. H. Woodworth
Naval Weapons Center
Code 3951
China Lake, California 93555

G. W. Yee
General Dynamics
P.O. Box 718
Ft. Worth, Texas 76101

SUMMARY OF MEETING ON PYROELECTRIC
AND PIEZOELECTRIC MATERIALS

G. S. Kino

INTRODUCTION

A meeting was held between members of the MRC, university and industry groups to discuss the present status and future possibilities for the development of pyroelectric and piezoelectric materials.

A complete program of the formal papers, presented at the meeting, with abstracts, is given as an appendix to the report. There were also some unscheduled papers which we summarize here. A list of participants at the meeting is given. Members of the Council participating throughout the meeting included N. Bloembergen, G. S. Kino and A. Yariv, while numerous other members attended one or more of the individual presentations.

Because of the broad range of this subject, and ARPA's interests, the main emphasis, as far as pyroelectric materials were concerned, was placed on materials for use in vidicon and other imaging devices suitable for infrared imaging.

As far as piezoelectric materials were concerned, the emphasis was placed on piezoelectric ceramics which are used in a wide variety of applications varying from rf filters to

acoustic transducers for non-destructive testing. Particular attention was paid to the interesting new organic polymers, polyvinyl fluoride (PVF) and polyvinylidene fluoride (PVF₂). These are both pyroelectric and piezoelectric; they appear to have a wide range of possible applications because of their very low cost, ease of fabrication, and reasonably high piezoelectric and pyroelectric coupling coefficients.

Pyroelectric materials have the property that a polarization field proportional to the temperature is generated within them. Because of inevitable dielectric losses, this implies that at a given temperature the polarization gradually decreases to zero, but a current is generated at the terminals which is proportional to the rate of change of polarization and hence temperature. The devices therefore give an output current which is proportional to the rate of change of temperature but does not depend on the ambient temperature. They, therefore, have the great advantage that they can be operated at room temperature rather than at cryogenic temperatures.

Pyroelectric detectors are constructed by evaporating metal on both surfaces of a thin layer of pyroelectric material, which is typically bonded to a supporting substrate which is a good thermal insulator. Ideally for optimum sensitivity the pyroelectric material is chosen to have a low dielectric constant, and a high piezoelectric coupling coefficient defined by the relation

$$p = dP/dT$$

where P is the polarization and T the temperature.

It is usually best to make the material as thin as possible so as to lower its heat capacity and hence increase the temperature for a given heat flux. This puts a premium on the use of materials and technological methods for constructing layers a few microns thick.

As these materials are insulators rather than the fairly good conductors which have to be used in cryogenic infrared detectors, they are suitable for use as a detector array in a vidicon. Such vidicons have been constructed, with minor changes from standard optical vidicons, the main difference being that provision must be made for discharging the insulating layer between frames. Otherwise, the electron beam would charge up the insulator continuously and eventually cut itself off.

REVIEW OF THE MEETING

The meeting started with a short review of pyroelectric properties by A. Glass (Bell Labs.). He described a new type of pyroelectric effect associated with the displacement of electronic charge along the polar axis of a pyroelectric material, in distinction to the more well known effect associated with the displacement of charged ions. He described possible applications of this ultrafast effect to detection, optical imaging and high voltage energy conversion. However, because the effect rests on the presence of traps which can only be

optically excited, it is more interesting for study in the optical range rather than the infrared range.

Two closely related papers on pyroelectric vidicons were given by C. N. Helmick, Jr. and W. H. Woodworth (Naval Weapons Center) and by B. Singer (North American Philips). Both groups gave TV presentations of their images. These authors describe the present state of development of room temperature operated pyroelectric vidicons indicating that the present Philips array has a definition of 5-7 lines mm, determined by thermal diffusion. The pyroelectric material employed is TGS usually of the order of 30 μ m thick with 1.8 cm active diameter and a ge faceplate for transmission at 8-14 μ m. Commercial devices are available from Thomson CSF in France, English Electric Valve Co. in England, and Philips Laboratories in the U.S. The sensitivity of these devices is 0.3°C-0.5°C at the target with 100-200 TV lines. Philips use a change in the electron beam voltage to give a 2:1 secondary emission factor between frames to recharge the pyroelectric material positively.

Scene modulation or motion is required to give a finite output current. This is commonly done by chopping the input, as shown by Singer. Helmick and Woodworth by taking the difference signal between two frames, one with no radiation reaching the sensor, and one fully illuminated were able to enhance the sensitivity and quality of the image. Both groups showed pictures of cars, people, and various objects in day-

light and in the dark, taken with a 1976 Philips tube with 170 TV lines and $f=0.75$ optics. Very clearly recognizable pictures were obtained, deteriorating in quality when taken with an outside temperature of 20°C in the dark. Streaking of fast moving images was observed due to the slow thermal response of the system. Singer described chemical techniques for making a reticulated target supported on a 1000\AA thick organic polymer which seem to be well in hand. This should eliminate thermal diffusion and losses for all practical purposes, thus making it possible to obtain better resolution. Both sets of authors predicted that within the next 2-3 years we could expect better resolution, perhaps 300 TV lines or more with a thermal sensitivity of 0.3°C at the target.

A study of sensitivity limits due to thermal fluctuations in these devices is given in an accompanying paper by M. Tinkham and A. Yariv.

The next two papers discussed the theoretical limitations of pyroelectric detectors. S. T. Liu (Honeywell) gave a thorough exposition of the limitations of single detectors, taking account of the problem of matching to an input circuit. He defined a material figure of merit $M_1 = p/c\sqrt{\kappa\tan\delta}$, where p is the pyroelectric coefficient, c the specific heat, κ the relative permittivity and $\tan\delta$ the loss tangent. He showed that $p/\sqrt{\kappa}$ and c are approximately constant for most pyroelectric materials, so that the loss limits the performance. For this reason, relatively low loss materials like LiTaO_3

are desirable in pyroelectric detectors. M. I. Bell (Yeshiva Univ.) gave a theory suitable for vidicon arrays. This was derived from elementary thermodynamics and simple microscopic models. With this model he was able to define a figure of merit, and to show that it is unlikely that this figure of merit could be increased by more than a factor of 2 or 3 over that obtained with the normal ferroelectric materials presently used. These materials exhibit interesting universal property relating p/κ . A class of materials relatively little studied in this country, the improper ferroelectrics, might provide an improvement in performance by a factor of 10. This is basically because as temperature is changed p goes through a maximum, but κ does not increase in the same way as it does in normal ferroelectrics. In later discussions the chances for such an improvement did not appear to be very strong. A short review of the properties of such materials is given by L. E. Cross in an accompanying paper.

We then heard two papers on the relatively new pyroelectric polymers, cheap plastic materials which are normally available in the form of thin flexible sheets with a similar toughness to polythene sheet, so they are easily cut and handled. A review talk on this subject was to be given by M. G. Broadhurst (NBS) who had been chairman of a recent conference on this subject¹. Unfortunately, at the last minute,

¹"Proceedings of Piezoelectric and Pyroelectric Symposium Workshop," M. G. Broadhurst Coordinator, Institute for Materials Research, National Bureau of Standards, Washington, D.C. 20234, September 1975.

Dr. Broadhurst could not come to the meeting. A. Glass (BTL) and J. Lando (Case Western Reserve), between them, kindly gave impromptu review talks on the subject. An additional review of these materials is given in an accompanying paper by A. Garrito (Univ. of Pennsylvania).

The materials which have been used up to the present time are PVF and PVF_2 . PVF_2 has the highest piezoelectric and pyroelectric coupling coefficients and appears to behave like a proper ferroelectric. The best quality PVF_2 is made in Japan, and is used in Pioneer headphones. This quality material is unavailable in base form commercially. The material is stretched to align the polymer chains along the sheet and becomes partially crystalline; it is then poled at a temperature of the order of 100°C with poling fields of the order of 10^6 volt/cm for several hours. The piezoelectric behavior could be due to trapped, but not uniformly distributed charge, or it could be due to the orientation of polar crystal domains, as suggested by Broadhurst. The problem with this latter explanation is that it is difficult to account fully for the polarization coefficient observed, $4 \text{ nc}/^\circ\text{C cm}^2$. Thus, no complete explanation of the behavior of this material yet known. As a pyroelectric material, its pyroelectric coefficient is 10-20 times less than materials like TGS and SBN, but the figure of merit for the material is 2-5 times worse than these other materials. It does offer the possible advantage of being very easy to make in sheets a few microns thick.

Lando discussed new techniques for making this material and a wide class of related materials. He has made small samples of this material in crystalline form, without stretching. He suggests that incorporation of different molecules in the polymer should give rise to much higher dipole moments, and should be pursued.

H. J. Shaw (Stanford) reviewed his work on PVF_2 piezoelectric transducers made of material obtained from Japan. With 25 μm thick PVF_2 , he was able to obtain an essentially flat response to a water load from zero frequency to 20 MHz. The efficiency, because of the good impedance match to water was as good as a typical commercial PZT transducer, but with a much wider bandwidth. The measured piezoelectric coupling coefficient ($k_T = 0.11$) is better than quartz. The acoustic Q is B at 50 MHz. The material lends itself easily to the construction of two dimensional arrays of transducers which can be laid down on curved surfaces. Shaw showed some results of this kind.

The rest of the formal papers at the meeting were devoted to piezoelectric ceramics. L. E. Cross (Penn. State) gave a review of the properties of piezoelectric ceramics. He suggested that radical changes in processing methods and materials with deliberately engineered macroscopic heterogeneities could give major improvements in the properties of ceramic piezoelectrics.

D. Berlincourt (Channel) reviewed the device appli-

cations of piezoelectric ceramics. These materials are widely used, because of their low cost and flexibility as filters in FM and AM radios, for phonograph cartridges, ignition devices for lighters and gas burners, and for HF speakers, as well as in sonar NDE and medical acoustic transducers. The materials have not, so far, proved suitable for mass produced TV IF filters because of their variability from batch to batch (1% velocity variation is typical). In bulk wave filters, some technique for trimming such as grinding away part of the material is employed.

R. Fulrath (U.C. Berkeley) discussed the effect of processing on the properties of PZT materials. He demonstrated how pores in controlled numbers and sizes could be introduced artificially into such ceramics. This technique is employed to determine the effects of such defects on the properties of the ceramic, and compare with theories which have been difficult to check in the past.

B. A. Auld (Stanford) showed how excellent Fresnel lens piezoelectric transducers could be made with PZT ceramics by reverse poling the ceramic along cylindrical rings. He suggested that the same techniques could be employed to make new types of acoustic waveguides.

C. A. Land (Sandia) gave an impressive review of his work on optical memory devices, based on PLZT materials. The information is stored as a spatial variation either of birefringence or light scattering centers. This is induced by

changes in poling due to the fields near a photoconductor on one surface when a dc field is applied to the device, and it is illuminated. More recently, the effect has been obtained with no photoconductor present, and is due to electrons generated near the surface of the piezoelectric material and trapped there after the illumination is removed. Good grey scale stored pictures were demonstrated. The storage time can be several hours, but the read in time is fairly long at present, at least several seconds.

Two further unscheduled papers were given. One by N. Byer (Martin Marietta) described work on sensitive photo-detectors in which neighboring detectors were reverse poled to eliminate microphony problems, with only one illuminated from the infrared source. He described ion etching procedures to produce high quality devices only a few microns thick, a parameter needed to obtain good sensitivity.

C. Roundy (Molelectron) proposed new techniques for making a solid state scanned imaging device using CCD sensors. He suggested methods for eliminating the thermal loss in the connections. The basic problem is the technology for connecting the imaging device elements to the CCD's. This is extremely difficult, and would require a major effort to develop a suitable technology.

RECOMMENDATIONS AND CONCLUSIONS

The results of the discussions at this meeting, and with members of the MRC in particular Bloembergen, Yariv and Tinkham are summarized in the following conclusions and recommendations.

Pyroelectric Devices

1. Proper (intrinsic) ferroelectric materials have thoroughly been investigated, both experimentally and theoretically. The best materials are within a factor of of the theoretical performance limit (figure of merit for sensitivity). The pay-off for further materials research here appears to be small.

2. In an accompanying paper M. Tinkham and A. Yariv discuss the fundamental limitations on performance of pyroelectric vidicons. It is concluded that the present vidicons are close to the limits set by thermal fluctuations. By thinning the retina to 1- or 2 μ m a 5-fold reduction in minimum detectable temperature might be achievable. Then better methods of readout, which deposit less energy from the electron beam on the retina would be required as well as a smaller velocity spread than is obtained with the present beams used in these vidicons. Reticulation techniques, which appear to be perfectly feasible would provide some improvement in definition. Such thin retinas might be achievable by the use of organic polymers, although some improvement in their present characteristics would be needed. At the same time, the problem of

microphony must be tackled, and improvements made in these devices.

3. The electron beam scanning method should be compared with an all solid state design, in which the polarization changes are probed by photoelectric or photoconductive devices. An analysis of the signal to noise ratio in the latter configurations is needed.

4. The field of improper pyroelectrics in which the large polarization near the transition temperature is not necessarily accompanied by a large change in dielectric constant, deserves some closer scrutiny. The considerable amount of data collected by workers in Czechoslovakia should be analyzed. Although the possibility for improved performance with these materials exists in principle, the realistic prospects, based on past experimental efforts, does not appear very promising.

5. The situation is quite different in the pyroelectric polymers. The potential of this class of materials has not yet been assessed. First, the basic physical mechanism of the pyroelectric response in these materials must be understood. When the critical factors are known, it is likely that improved polymeric thin film pyroelectric detectors may be constructed. An increased support by ARPA for this purpose is highly recommended.

6. The introduction of transition metal ions in pyroelectric crystals (introduced by A. Glass) provides an

additional degree of freedom which has led to some novel applications, such as the detection and measurement of picosecond optical pulses and far infrared difference frequency generation without critical phase matching condition. It does not appear feasible, however, to utilize this technique to improve infrared detection capabilities.

Piezoelectric Devices

6. The use of piezoelectric polymers appears extremely promising because of their many possible applications, as acoustic transducers for NDE and sonar, fast strain gauges, artillery shell fuses, external and implanted body sensors, etc. They are low in cost, easy to make, and flexible. Among other desirable properties, they have a good acoustic impedance match to the body, are very low in weight, are chemically inert, and can be cut with a pair of scissors. Considerable improvements are likely to be made in these types of materials. Increased support by ARPA to develop and understand a range of high quality materials is recommended. At the same time, work on the device applications of this materials for acoustic transducers, and other sensors should be encouraged. The use of this material may well make many new applications of acoustic technology feasible which were not feasible before.

7. The development of piezoelectric ceramics is at a fairly mature stage. No further development for specialized purposes is likely to take place by the manufacturers because of much larger market for low cost, relatively uncritical

consumer items. Some improvement in characteristics, such as better uniformity from sample to sample appears to be possible by better control over processing. Special materials for particular purposes are often required in small quantities for research devices. These could be made but are unavailable.

A small scale effort to see what improvements could be made, particularly if done in collaboration with device researchers would be worthwhile.

8. The Sandia work on optical memories is impressive and original. The work should be continued and encouraged.

ACKNOWLEDGEMENT

This research was supported by the Advanced Research Projects Agency of the Department of Defense under Contract No. MDA903-76C-0250 with The University of Michigan.

ELECTRONIC PROCESSES IN PYROELECTRIC CRYSTALS

A. M. Glass

ABSTRACT

Thermal excitation of pyroelectric crystals results in a small displacement of charged ions associated with the polar optic modes. This is the conventional pyroelectric effect. Electronic (optical) excitation of pyroelectrics, on the other hand gives rise to displacement of electronic charge along the polar axis, together with some ionic displacement due to electron-phonon coupling, which is quite distinct in origin and magnitude from the pyroelectric effect. The electronic displacement may give rise to a steady state bulk photovoltaic current, or else to a transient current impulse depending on the nature of the electronic states involved. Effects of this kind can be used for such applications as ultrafast detection, optical mixing, holography and high voltage energy conversion.

These effects and their ultimate limitations will be discussed.

RECENT DEVELOPMENTS IN PYROELECTRIC VIDICON SYSTEMS

W. H. Woodworth and C. N. Helmick, Jr.

ABSTRACT

The pyroelectric vidicon, being insensitive to steady-state or non-changing thermal radiation, requires modulation of the image in order to produce a useable output. Commonly the camera head is panned or orbited to produce this effect. In our system we use synchronous frame or field rate focal plane chopping at 15 or 30 Hz to modulate the image. The resulting open and closed fields are subtracted from each other by means of a delay device of $1/30$ or $1/60$ seconds, depending on the chopper frequency, so that the only remaining signal components are those affected by the chopper. Using this system called "Image Difference Processing" and chopping at 15 Hz, we achieve a spatial resolution of 200 TV lines at 0.5 degrees C differential temperature.

Image difference processing has been accomplished by both analog and digital methods and realizations of each are shown. In addition, the mechanical design of a compact, synchronous focal plane shutter is described.

STATE OF THE ART PEV AND PROSPECTS
FOR IMPROVED PERFORMANCE

B. Singer, T. Conklin, G. Loiacono

ABSTRACT

A review of the operation and operating principles of the secondary emission pedestal mode (SEMP) will be given. Data on performance, life, and performance-limiting parameters such as dielectric constant, and thermal diffusivity will be discussed. Improved performance PEV using non-crossover electron guns and new materials TGFB and DTGFB will be given, and recent advances in reticulation of pyroelectric material to reduce thermal diffusion will be shown. DTGFB material preparation and growth will be discussed and shown. A video tape of a PEV made with DTGFB material will be shown.

PERFORMANCE LIMITATIONS OF PYROELECTRIC DETECTORS

S. T. Liu

ABSTRACT

The pyroelectric detectors are thermal transducers of radiation based on the pyroelectric effect. They are sensitive across a wide optical spectrum, especially in the far infrared region. They can be used advantageously at room temperature in many applications as infrared detectors.

The performance of pyroelectric detectors is generally described by a signal to noise ratio. For a pyroelectric detector of area A and thickness b , receiving uniformly a sinusoidally modulated radiation with rms power density P_1/A , the signal current is given by

$$i_{\text{rms}} = R_i \eta P_1, \quad (1)$$

where η is the emissivity of the detector front surface and R_i is the current responsivity (amps/watt) of the detector. The current responsivity is given by

$$R_i = \left(\frac{p}{c^E b_1} \right) T_R, \quad (2)$$

where p and c^E are the pyroelectric coefficient and the heat capacity per unit volume of the pyroelectric material respec-

tively. The factor T_R describes the frequency characteristics of the detector response, which is a function of the thermal circuit involving the pyroelectric material, substrate and surroundings. In addition to the useful signal current, various noise currents are also present at the pyroelectric detector. The noise sources are the temperature noise, the detector noise, thermal noise of the input circuit, the open-circuit noise of the amplifier, and the short-circuit noise of the amplifier. The total noise $\overline{i_n^2}$ can be described by

$$\overline{i_n^2} = F \overline{i_{dz}^2} \quad (3)$$

where F is the degradation factor and $\overline{i_d^2} = 4kT\omega C_d \tan\delta$ is the detector thermal noise. The factor F depends on the frequency characteristics of electrical circuits consisting of the amplifier, the detector, and the biasing resistors. The performance of the detector thus can be described by the signal to noise ratio given by

$$i_{rms} / \sqrt{\overline{i_n^2}} = M \eta P_1 / \sqrt{4kT\omega \epsilon_0 (b,A) B} \quad , \quad (4)$$

where $M = M_1 \cdot T_R \cdot \frac{1}{\sqrt{F}}$ and $M_1 = p/c^E \sqrt{\kappa \tan\delta}$ is the material figure of merit.

The performance limitations of pyroelectric detectors are discussed in this paper from three important factors; namely, M_1 , T_R , and F . The frequency characteristics are limited by the two dimensionless factors, T_R and F . The temperature characteristics are limited by M_1 , the material

parameters involving the pyroelectric coefficient p , the dielectric constant κ , dielectric loss factor $\tan\delta$, and the heat capacity per unit volume c^E . For practical pyroelectric detectors using ferroelectrics as detector materials, $p/\sqrt{\kappa}$ and c^E in the factor M_1 have been found to be nearly constant among various ferroelectrics so that $\tan\delta$ often plays an important role, limiting the performance. The fact that $p/\sqrt{\kappa}$ is nearly constant will be discussed. Because of the inability of complete penetration of the thermal wave into the detector causing partial clamping of the detector, the pyroelectric coefficient may be reduced. Other limitations will also be discussed. Finally, a comparison of pyroelectric materials of current interest and the high performance pyroelectric detectors will be made.

THEORY OF PYROELECTRIC MATERIALS

M. I. Bell

ABSTRACT

Elementary thermodynamics and simple microscopic models are used to examine the properties of pyroelectric materials which determine their performance as infrared detectors and vidicon targets. It is shown that for small-area detectors the signal-to-noise ratio is subject to a theoretical limit dictated entirely by thermodynamic considerations. In a large class of simple microscopic models for intrinsic (proper) ferroelectrics, the ratio of the pyroelectric coefficient and dielectric constant (which is a figure of merit for vidicon target performance) is found to exhibit an interesting universal behavior. This behavior can be exploited to yield estimates of the figure of merit which suggest that improvements of more than a factor of three are most unlikely using intrinsic ferroelectrics. An examination of extrinsic (improper) ferroelectrics using phenomenological models for the free energy shows that the vidicon figure of merit is not subject to the limitations found for intrinsic ferroelectrics, so that these materials offer the possibility of substantially improved vidicon performance.

THE BASIS OF PYROELECTRICITY IN POLYMERS AND
THE PROPERTIES OF POLYMERIC RADIATION DETECTORS

M. C. Broadhurst

ABSTRACT

Polyvinylidene fluoride (PVDF) is a semicrystalline material which can be polarized to give a stable room temperature pyroelectric coefficient of up to $4\text{nC K}^{-1}\text{cm}^{-2}$. Peterson et al¹ have reported room temperature detectivities of about $1 \times 10^9 \text{ cm Hz}^{1/2}\text{W}^{-1}$ at a modulation frequency of 4 Hz, and responsivities of about $3 \times 10^{-6} \text{ AW}^{-1}$ in $6\mu\text{m}$ thick PVDF films. A molecular model based on the known chemical and crystal structures of PVDF has been analyzed. This model identifies the polarization with orientation of polar crystal domains and the temperature dependence of the polarization with combined effects of thermal expansion and librational fluctuations of the molecular dipoles. From crystal structures, molecular dipole moments and reaction field calculations, the maximum single crystal polarization of PVDF in the polar β phase is 22 nC cm^{-2} , and the pyroelectric coefficient of this crystal, calculated using the above model, is $16 \text{ nC K}^{-1}\text{cm}^{-2}$. An actual film of PVDF contains crystalline domains dispersed in the supercooled liquid phase of the polymer. Real charges, whether electronic or ionic, will tend to respond to the internal

fields of the polar crystals by accumulating on the crystal-liquid interfaces and producing a moment equal in magnitude and opposite in direction to that due to the crystal. Thus the film will become neutral and non-polar after storage for about one day. The moment due to crystal dipoles and that due to real charges will respond differently to a temperature change however, and the above model predicts that the expected response of an actual 2/3-crystalline sample will be about $6 \text{ nC K}^{-1} \text{ cm}^{-2}$ or less than twice presently realizable values.

Many other polar polymers are pyroelectric but one more sensitive than PVDF has not been identified. The advantages of PVDF for radiation detectors are that they are cheap, fast and rugged having a toughness similar to polyethylene commonly used in sandwich bags. Already, commercial PVDF radiation detectors are being produced in the U.S. Nanosecond rise times using nickel as an absorber are possible according to Peterson et al.

¹R. L. Peterson, G. W. Day, P. M. Gruzensky and R. J. Phelan, Jr., J. Appl. Phys. 45, 3296 (1974).

Note: This talk was not delivered, and replaced by informal talks by J. Lando and A. Glass. The abstract is included for reference.

STUDY OF ULTRASONIC RESONANCE AND BROADBAND
TRANSDUCTION IN PVF₂ PIEZOELECTRIC FILM

H. J. Shaw

ABSTRACT

Measurements have been made of the acoustic loss factor and piezoelectric coupling coefficient of poled PVF₂ plastic polymer films which are of interest for high frequency ultrasonic applications. A theory for piezoelectric resonance in unsupported films was developed for interpretation of the measurements. Unloaded acoustic Q of approximately 14 has been observed at frequencies of 41 and 21.5 MHz for films of 25 and 50 μ thickness, respectively.

Broadband ultrasonic transducers using PVF₂ piezoelectric plastic films, combining efficient transduction with extremely wide and uniform pass bands, have been fabricated using very simple procedures without any critical tolerances. Frequency spectra of impulsed transducers using films of 25 μ and 50 μ thickness, centered at 10 MHz and 5 MHz, respectively, are shown.

PEIZOELECTRIC MATERIALS

L. E. Cross

ABSTRACT

This talk will concentrate primarily upon piezoelectric materials with high coupling coefficients which are derived from ferroelectric or other ferroic crystals. Important basic limitations upon the realizable piezoelectric applicability of different ferroelectric crystal systems arise through the symmetry constraints upon the orientation of the polar domains, and from the large 'spontaneous' strains which accompany the onset of the ferroelastic phase, and exert a profound influence upon the nature, orientation and switching characteristics of the ferroelectric domain walls. The symmetry restrictions upon polarization orientation will be examined using Aizu¹ and Shuvalov² classifications, and the simple phenomenological description of the strain effects in proper ferroelectrics developed to separate those ferroelectric systems which have full, partial or no ferroelasticity. This development will be used to examine the nature of the elastic constraints upon domain wall orientations through the Fousek-Janovec³ criterion.

For the fully ferroelectric:fully ferroelastic systems, the piezoelectric properties in paraelectric and ferroelectric

phases will be briefly reviewed. In this group the unique nature of the response in lithium thallium tartrate monohydrate will be considered.

Conditions which are required for the generation of strong piezoelectric response in a randomly axed polycrystal (ceramic) material will be discussed, and the need to use a fully ferroelectric-partially ferroelastic system for these applications underscored. Techniques which have been used to enhance electrical poling in ceramics will be considered and some of the many advantageous features of the lead zirconate: lead titanate based composition systems examined. From these considerations, it is intended to develop the thesis that for major improvement in the properties of ceramic piezoelectrics, either (a) new families of ferroelectric crystals with high Curie temperature and high prototypic symmetry must be developed, or that (b) by radical changes in processing methods, grain oriented ceramics, or ceramic materials with deliberately engineered macroscopic heterogeneity must be explored.

If time permits, some of the intriguing possibilities for generating complex domain structures in piezoelectrically active secondary ferroic crystals will be discussed, and the development of a randomly axed but non-ferroelectric polycrystal piezoelectrics by a secondary poling process described.

References:

1. K. Aizu, J. Phys. Soc. Japan 27, 387 (1969).
2. L. A. Shuvalov, J. Phys. Soc. Japan 28, 38 (1970).
3. J. Fousek, V. Janovec, J. Appl. Phys. 40, 135 (1969).

PIEZOELECTRIC CERAMIC MATERIALS AND
THEIR APPLICATION IN DEVICES

D. Berlincourt

ABSTRACT

The characteristics of piezoelectric ceramics are reviewed with emphasis on device applications. These applications are described in order to identify the important material requirements. These applications include high quantity applications such as filters in consumer FM and AM radios, phonograph cartridges, ignition devices for gas burners, ignition devices for flashbulbs and drivers for high frequency speakers. Reasons for the displacement of magnetostrictive devices and piezoelectric single crystals by ceramics in ultrasonic and sonar applications are given as well as reasons for failure of ceramics to displace quartz in narrow band filtering and frequency control.

Proposed and marginal applications of ceramics as power supplies, transformers, displacement generators and pumps are also discussed. This leads to future requirements for materials and a discussion of likelihood of developing such materials.

PROCESSING OF POLYCRYSTALLINE PIEZOELECTRIC
CERAMICS IN THE PZT SYSTEM

R. M. Fulrath

ABSTRACT

The ferroelectric and piezoelectric properties of ceramics in the lead zirconate-lead titanate system are determined by the composition, including dopants and impurities, and the processing sequence including the final poling step. Examples are given showing the affect of processing on properties and the result of cation substitution on the B site in the ABO_3 structure. Mechanical properties are also strongly influenced by grain size, porosity, and secondary phases present. Recent studies on the porosity-pore size relation give indications that piezoelectric properties may be strongly influenced by these parameters.

ACOUSTIC WAVE GUIDING ALONG FERROELECTRIC
DOMAIN WALL BOUNDARIES

B. A. Auld

ABSTRACT

Naturally and artificially created domain wall patterns have many interesting applications to acoustic wave devices, where the relationship between the ferroelectric poling direction and the sign of the piezoelectric coupling permits one to control the excitation and distribution of the acoustic wave fields. One may consider either standing wave geometries such as a transducer or resonator, or traveling wave geometries, such as a waveguide transmission system.

In the first category (standing wave devices), use of tailored domain patterns has been demonstrated experimentally in phase plate transducers for radiating focused ultrasonic beams into water. These phase plate transducers are poled in a domain pattern having the form of a set of Fresnel zones. The counter poling of alternate zones reverses the sign of the piezoelectric excitation from one zone to the next, and, thereby, as in optics, produces a radiation field that is spherically focused at a point. Results of imaging experiments demonstrating the characteristics and capabilities of these devices will be discussed. Materials properties relative to

improved devices of this kind will be considered.

With regard to traveling wave devices, it has been known for several years that an elastic surface wave can be guided along the interface between media having different piezoelectric properties, or along a ferroelectric domain wall in an infinite medium. The fact that elastic waves can be guided along infinite domain walls suggests that finite wall structures will also exhibit waveguiding, and, therefore, constitute a new kind of acoustic waveguide configuration. Measurements on the domain wall patterns in the phase plate transducers referred to above show that the thickness of the walls is comparable to the thickness of the transducer plate. This, indeed, provides a basic argument for the existence of a guided wave in this case. Within the domain wall, where the material is unpoled, the piezoelectric stiffening is reduced essentially to zero and the wall, therefore, constitutes a slow velocity region. As in optics, this permits trapping of a guided wave within the domain wall. An approximate calculation of waveguiding in PZT will be illustrated, including an assessment of the material and excitation problems.

PLZT MATERIAL PROPERTIES OF IMPORTANCE TO INFORMATION
STORAGE AND DISPLAY APPLICATIONS*

C. E. Land

ABSTRACT

Electrooptic and photosensitive properties of PLZT ceramics are being considered for a number of information storage and display device applications. Information storage, including image storage with gray scale, has been achieved in PLZT-photoconductor devices in which the information is stored as a spatial variation either of birefringence or of light scattering centers. These devices also store image information in the form of variable surface deformation. Very recently it has been found that high resolution, high contrast images can also be stored in PLZT ceramics without a photoconductive film by simultaneously exposing the image on a surface of a ceramic plate and switching the ferroelectric polarization through a portion of the hysteresis loop. Effective image storage is achieved only if the light source contains spectral components at or near the band gap energy (about 3.35 eV or 0.37 μ m). This paper discusses our present understanding of the electro-optic and photosensitive properties of PLZT ceramics relating to a variety of information storage and display applications.

*This work was supported by the United States Energy Research and Development Administration (ERDA) under Contract AT(29-1)-789.

IMPROPER FERROELECTRICS

L. E. Cross

ABSTRACT

DEFINITIONS

The terms proper and improper refer strictly to the phase transitions in a ferroelectric crystal. In a proper ferroelectric the electric polarization P is the phase transition parameter (PTP) which characterizes the onset of the spontaneously polarized phase. In the improper ferroelectric, conversely, the electric polarization is not the proper phase transition parameter, but arises through a 'coupling' between P and the true PTP.

Thus P_s in an improper material is in some sense like the spontaneous elastic strain in BaTiO_3 which arises through electrostrictive coupling to the PTP.

EXAMPLES OF IMPROPER FERROELECTRICS

- (a) Gadolinium molybdate family $(\text{Gd}_2(\text{MoO}_4)_3)$
- (b) Lanbeinite family $\text{Cd}_2(\text{NH}_4)_2(\text{SO}_4)_3$
- (c) Boracite family $\text{Fe}_3\text{B}_7\text{O}_{13}\text{I}$
- (d) Rubidium trihydrogen selenite $\text{RbH}_3(\text{SeO}_3)_2$
- (e) Ammonium Rochelle Salt
- (f) Ammonium Fluoberyllate $(\text{NH}_4)_2\text{BeF}_4$

SIMPLIFIED THERMODYNAMICS

(a) Proper Ferroelectric

$$\Delta G_1 = \frac{1}{2} \chi P^2 + \frac{1}{4} B P^4 + \frac{1}{6} C P^6 + b P X + Q P^2 X$$

χ is a linearly decreasing function of T going through zero in the vicinity of T_c ,

b piezoelectric constants

Q electrostrictive constants

(b) Improper Ferroelectric

$$\Delta G_1 = \frac{1}{2} \alpha q^2 + \frac{1}{4} \beta q^4 + \frac{1}{6} \kappa q^6 + \frac{1}{2} \chi_0 P^2 + \gamma q^n P$$

α is a linearly decreasing function of T going through zero near T_c and leading to spontaneous values q_s for the order parameter q below T_c , and through the coupling parameter γ non-zero values of P also.

For values of $n > 2$ the order parameter does not have the same symmetry as P and if χ_0 is not a function of T , the permittivity ϵ is independent of T in the paraelectric (orthoelectric) phase above T_c . If $n = 1$ the order parameter has the same symmetry as P . Such cases are now termed pseudo-proper, e.g., $(\text{NH}_4)_2\text{SO}_4$.

REASON FOR EXPLORING IMPROPER AND PSEUDO-PROPER FERROELECTRIC FOR THERMAL IMAGING

Several figures of merit have been proposed for use in materials for thermal imaging, all involve a ratio of the pyroelectric coefficient and the dielectric permittivity ϵ in the direction of P_s , i.e.,

$$F = \frac{\pi}{\epsilon} \cdot K \quad n = 1 \text{ (or } n = \frac{1}{2} \text{ for point detectors)}$$

In proper ferroelectrics the large values of π which occur close to T_c cannot be exploited because of correspondingly large values of ϵ which are an automatic consequence of the polarization being the order parameter for the ferroelectric phase.

For improper and pseudo-proper ferroelectrics the direct relations are broken and there is a possibility to exploit the very large values of π occurring near weak first order phase changes, e.g., in $\text{Gd}_2(\text{MoO}_4)_3$ ϵ_{33}^x does not change at T_c but π goes through a maximum.

Data are available in the literature to calculate $\pi/\epsilon(T)$ for $\text{Gd}_2(\text{MoO}_4)_3$, $\text{Fe}_3\text{B}_7\text{O}_{13}\text{I}$, and $(\text{NH}_4)_2\text{SO}_4$.

It is possible that none of these crystals will be advantageous over existing materials and there is considerable need to expand the base of known improper ferroelectrics.

LITERATURE ON IMPROPER FERROELECTRICS

A rather complete review of 'impropriety' was given at the September 1973 IMF in Edinburgh, Scotland by V. Dvorak.

There was also a complete session on this topic at the meeting.
V. Dvorak, Improper Ferroelectrics, *Ferroelectrics* 7, 1-9, 1974.
Other papers on this subject are given in the same issue.

More recent work not included in the review by Dvorak includes:

- (1) J. F. Scott, Soft Mode Spectroscopy: Experimental Studies of Structural Phase Transitions, *Rev. Mod. Phys.* 46, 1, 83 (1974).
- (2) K. Aizu, Phenomenological Lattice-Dynamical Theory of Ferroelectricity, *J. Phys. Chem. Solids* 32, 1959-1969 (1971).
- (3) K. Aizu, Ferroelectric and Ferroelastic Phase Transformations in Which the Soft Waves Have a Wave Length Equal to a General Rational Number Times the Lattice Constants, *J. Phys. Soc. Japan* 34, 6, 1567 (1973).
- (4) K. Aizu, Hard Vibrational Modes Which Are or Are Not Induced to Condense by the Condensation of Soft Modes: Extension of the Concept of Faintness Index to Ferroelectricity and Ferroelasticity, *J. Phys. Soc. Japan* 37, 885 (1974).
- (5) K. Aizu, The Condensation of Hard Modes Induced by the Condensation of Soft Modes When Both the Soft and Hard Modes are of Non-Zero Wavenumber, *J. Phys. Soc. Japan* 37, 1485 (1974).
- (6) K. Aizu, General Considerations of Homophone Sequences of Phase Transitions, *J. Phys. Soc. Japan* 38, 1592 (1975).
- (7) J. Kobayashi, Peculiar Physical Properties of Improper Ferroelectrics, *Ferroelectrics* 10, 277 (1976).

FUNDAMENTAL LIMITATIONS ON PERFORMANCE OF PYROELECTRIC VIDICON DETECTORS

M. Tinkham and A. Yariv

Even if one were given a pyroelectric material with arbitrarily large pyroelectric coefficient and a noiseless readout system, the sensitivity of a pyroelectric vidicon system would be limited by thermodynamic fluctuations. In this paper we first treat this ideal limit, then consider the degree to which practical systems approach it, and finally analyze the potential for improvements.

ULTIMATE LIMIT FOR IDEALIZED DETECTOR

For an initial orientation, consider a single detector element of heat capacity C connected to a thermal bath by a thermal conductance K so that its thermal time constant is

$$\tau = C/K \quad (1)$$

For incident radiation P chopped at frequency $\omega < 1/\tau$, the response is

$$\Delta T = P/K \quad (2)$$

while it is well-known that thermodynamic fluctuations give

$$(\delta T)_{\text{rms}} = (k/C)^{1/2} T \quad (3)$$

where the frequency spectrum of the fluctuation is concentrated in $\omega\tau \leq 1$. Accordingly, the minimum detectable power will be of the order of

$$P_{\min} = K(\delta T)_{\text{rms}} = (kC)^{\frac{1}{2}}T/\tau = (kK/\tau)^{\frac{1}{2}}T \quad (4)$$

Thus, for given τ (as dictated by the frame rate in this application) and ambient temperature T , the minimum detectable power scales with $K^{\frac{1}{2}}$ or $C^{\frac{1}{2}}$, which must scale together to retain the desired response time τ .

If one could scale the detector element down to atomic size, then C would be $\sim k$, and one would recover the familiar limit $P_{\min} \approx kT/\tau \approx kT\Delta\nu$; but we are interested in a macroscopic detector element. In that case, the limit is set by how small one can make K . The irreducible limit to K is the radiant conductance to the surroundings via the black-body radiation. If we assume there is a reflective coating on the back side, the conductance per unit area is $4\sigma T^3$, of which a fraction $\sim 1/8F^2$ (F = f-number of optics) is to the desired source and the great majority ($1-1/8F^2$) is to the ambient within the detector. Thus, for an isolated detector of area $(\Delta x)^2$ and time constant τ , the absolute minimum detectable power (in Watts) is

$$P_{\min} = 2(\Delta x)T^2 \left(\frac{k\sigma T}{\tau} \right)^{\frac{1}{2}} = 2.8 \times 10^{-11} (\Delta x) \tau^{-\frac{1}{2}} \quad (5)$$

for $T = 300^\circ\text{K}$, with (Δx) in cm. Since the incremental incident power from the source is

$$\Delta P = \frac{4\sigma T^3}{8F^2} (\Delta x)^2 \Delta T \quad (6)$$

the minimum detectable temperature change is

$$\Delta T_{\min} = 4(k/\sigma T)^{\frac{1}{2}} \frac{F^2}{(\Delta x) \tau^{\frac{1}{2}}} = 3.6 \times 10^{-7} \frac{F^2}{(\Delta x) \tau^{\frac{1}{2}}} \quad (7)$$

As a numerical example, for $F \approx 1$, $\Delta x = 3 \times 10^{-3} \text{ cm } (\geq \lambda)$, $\tau = 5 \times 10^{-3}$ ($1/\tau = 2\pi$ times a frame rate of 30/sec), we find

$$\Delta T_{\min} \approx 0.002^\circ \text{C} \quad (8)$$

which is about two orders of magnitude better than actual reported performance.

The existence of this large difference is explained by noting that an extremely thin detector would be needed to give this value of τ with only the radiant thermal conductance. In fact, the required thickness is

$$d = \frac{4\sigma T^3 \tau}{C} \quad (9)$$

which is about 10^{-6} cm for our numerical example, C being the heat capacity per unit volume. Evidently, such a thickness is not practicable for a self-supporting film of pyroelectric material capable of absorbing IR radiation with high efficiency and of tolerating electron-beam readout. This number does dramatize, however, the goal toward which development should be directed if performance approaching this absolute theoretical limit is to be obtained.

MODEL OF REALISTIC SYSTEMS

Now let us turn to consideration of a model of current practical devices, in which retinas of thickness 10-50 μ m are used. In this case, the dominant heat transfer is by conduction across the retina rather than by radiation, and the thickness of the retina is constrained by the readout system as well as the desire to have high sensitivity.

In our model, we consider a sensing retina of thickness d ($\sim 30\mu$ m), conceptually divided into square elements Δx on a side ($\Delta x \sim 30\mu$ m) in an $N \times N$ array ($N \sim 300$), illuminated through a lens of diameter D (~ 1 cm) and F-number F (~ 1), and readout by an electron beam which sweeps over the entire raster ~ 30 times per second, ($\omega = 2\pi \times 30$).

The dimension Δx can not be less than the diffraction-limited resolution of the optics $\sim \lambda F \sim 10\mu$ m, for thermal radiation. It is also limited by the thermal diffusion length $\sim \sqrt{D_T t}$ between scans. A representative value of the thermal diffusion constant is $D_T = 3 \times 10^{-3} \text{ cm}^2/\text{sec}$ for TGS. [For numerical examples we also take $C = 2 \text{ J/cm}^3\text{-}^\circ\text{K}$ and $K = 6 \times 10^{-3} \text{ W/cm}^\circ\text{K}$, such that $D_T = K/C$.] Thus, in the 1/30 second between scans, heat diffuses $\sim 100\mu$ m, and spatial structures on a smaller scale in the image are detected with reduced sensitivity. This loss of sensitivity can be prevented by using a larger Δx and hence a larger overall retina and optical system for a given number of lines in the raster, but this becomes inconvenient if the retina exceeds one or two centimeters in diameter. Alterna-

tively, one can seek a pyroelectric material with lower D_T , or effectively lower D_T by reticulation, but, as we shall see, these approaches are limited by the need to remove heat generated by the readout process. Finally, one can always reduce thermal diffusion by using a higher scan or chopping frequency, but this would reduce the overall sensitivity. Rather than deal in detail with these tradeoffs, in our numerical estimates, we shall take $\Delta x = 30\mu\text{m}$. This is a geometric-mean compromise between the diffraction limited resolution and estimated thermal diffusion length between frames, and corresponds to a 1.3 cm diameter for a 300×300 raster. It also corresponds to the center-to-center distance in an experimental articulated retina reported at this conference by Dr. Singer of North American Philips.

Some comments should also be made about the thermal response time. Given high vacuum conditions in the tube and only a very thin metallic film for electrical contact, the heat flow in the retina will be a two-dimensional diffusive one. Thus, the thermal relaxation time will increase as the square of the linear dimension of the relaxing area. If our $30\mu\text{m} \times 30\mu\text{m}$ square relaxes in $(\Delta x)^2/D \sim 3 \times 10^{-3}$ sec, then an area $(10\Delta x) \times (10\Delta x)$ will relax in ~ 0.3 sec, and so forth. Thus, there is a spectrum of relaxation times depending on the spatial frequency of the pattern, and the significance of any single quoted relaxation time is limited. For simplicity, we shall continue to use τ to refer to the relaxation time of a

single raster element to its surroundings in the retina. In contrast to τ , however, the static thermal conductance K of a region of the retina to its surroundings does not scale with size because the increased periphery cancels the decreased thermal gradient in the larger area, leaving a value of the order of Kd in all cases.

For this model, in which the conductance from an element to its surroundings in the retina is much greater than the radiant conductance, we can again use (4), but now $K = Kd$ rather than the radiant conductance used earlier. Using (6) to refer the sensitivity to a minimum detectable temperature difference, we have the general result

$$\Delta T_{\min} = 2 \frac{F^2}{(\Delta x)^2} \frac{1}{\sigma T^2} \left(\frac{kK}{\tau} \right)^{\frac{1}{2}} = \frac{2}{D^2 (\Delta \theta)^2 \sigma T^2} \left(\frac{kK}{\tau} \right)^{\frac{1}{2}} \quad (10)$$

where now $K = Kd$, and in the second form we have re-expressed $F/(\Delta x)$ in terms of the diameter D of the lens and the angular resolving power of the system in the absence of diffraction, $\Delta \theta$. Taking $\Delta x = 3 \times 10^{-3} \text{ cm}$, $F = 1$, $T = 300^\circ \text{ K}$, $K = 6 \times 10^{-3} \text{ W/cm-}^\circ \text{ K}$, $d = 3 \times 10^{-3} \text{ cm}$ and $\tau = 5 \times 10^{-3} \text{ sec}$, this yields

$$\Delta T_{\min} = 0.1^\circ \text{ C} \quad (11)$$

compared to a best observed value of $\sim 0.2^\circ \text{ C}$. Since a factor of two could easily be lost by reflection and absorption in the optical system, this suggests that current devices are operating close to the limit set by thermal fluctuations in

retina. Of course, precise comparisons would have to take more careful account of spatial and temporal resolving power, especially the former since it enters as a squared factor, but the order of magnitude agreement should hold. If that is true, amplifier and beam noise relative to retina response have apparently been reduced to the point that in favorable cases they are not adding much noise to the signal.

SCOPE FOR IMPROVEMENT

The fact that present systems are operating close to their thermodynamic limit does not preclude substantial improvement toward the ultimate thermodynamic limit (7), (8), which is almost two orders of magnitude better. From (10) we see that the key to improved performance for given lens size D , angular resolution $\Delta\theta$, and response time τ is the reduction of the thermal conductance $K = Kd$. This can be done by reducing d , by using a material with lower K , or by using some form of reticulated retina. But this approach can not be carried too far without running into limitations in performance as well as difficulties in fabrication.

In a real system, the smallness of d is limited by two requirements of beam readout; capacitance and dissipation. The capacitance of an element (in pF) is approximately

$$C = \frac{\epsilon(\Delta x)^2}{4\pi d} \quad (12)$$

(if Δx and d are in cm). The effective beam resistance R is

given by

$$R = \frac{V_o}{I_{ped}} \quad (13)$$

where $V_o \approx 0.2$ volts $\approx kT_{cathode}/e$ is a measure of the energetic spread of the beam, and I_{ped} is the "pedestal current" ($\sim 10^{-7}$ Amps) required to override the alternating positive and negative potentials to allow readout by a beam of negative electrons. For efficient readout, the resulting time constant RC must be less than the dwell time of the beam, which will be $\sqrt{\frac{2\pi}{\omega}} \times \frac{1}{N^2} \sim 0.4 \times 10^{-6}$ sec. Thus, we have a constraint $RC \leq 0.4 \times 10^{-6}$ sec, or

$$d \geq 5 \times 10^{-8} \epsilon (\Delta x)^2 / I_{ped} \quad (14)$$

The limit (14) is eased by large I_{ped} , but this leads to dissipation and heating. If we estimate that V_1 (~ 10) electron volts of energy are deposited for each secondary electron in I_{ped} , then the temperature rise is given by $\Delta T = V_1 I_{ped} / K = V_1 I_{ped} / Kd$. For a typical material, the tolerable ΔT is limited to a few degrees. This constrains d by

$$d \geq \frac{V_1 I_{ped}}{K \Delta T} \approx 5 \frac{I_{ped}}{K} \quad (15)$$

The most favorable choice of I_{ped} in terms of the conflicting requirements (14) and (15) is that for which the constraints are equal, that is,

$$I_{ped} = 10^{-4} (\Delta x) (\epsilon K)^{\frac{1}{2}} \approx 1.6 \times 10^{-7} \text{ Amps} \quad (16)$$

where we have taken the values $\epsilon = 50$, $K = 6 \times 10^{-3}$ W/cm-°K, and $\Delta x = 30 \mu\text{m}$. This estimated optimum seems to be close to the values used in practice. For the optimum I_{ped} , we find

$$d \geq 5 \times 10^{-4} \Delta x (\epsilon/K)^{1/2} \quad (17)$$

which in this case is

$$d \geq 1.4 \mu\text{m} \quad (17a)$$

and $K = Kd \geq 8 \times 10^{-7}$ W/°K. For this minimum value of d , (10) yields

$$\Delta T_{\text{min}} = 0.02^\circ\text{C} \quad (18)$$

using the same values of the other system parameters which gave an estimate of 0.1°C for the $30 \mu\text{m}$ thickness characterizing present practice. The result (18) can also be compared with our estimate (8) of 0.002°C for the absolute thermodynamic limit for a detector of this area and response time.

From these considerations we conclude that there appears to be scope for improvement by about a factor of 5 in the sensitivity of current pyroelectric vidicons before the combined capacitance-heating constraint sets a limit. Since the minimum value of d allowed by (17) varies as $(V_O V_I \epsilon / K \Delta T)^{1/2}$, it follows from (10) that

$$\Delta T_{\text{min}} \propto (Kd)^{1/2} \propto (K V_O V_I \epsilon / \Delta T)^{1/4} \quad (19)$$

Because the optimized sensitivity depends only on the 4th root of these parameters, our estimate (18) is relatively

insensitive to the numbers assumed for illustrative purposes.

To gain this factor of 5, the retina conductance K must be decreased by a factor of $5^2 = 25$, and the heat capacity C must be reduced by a similar factor to retain the proper value of τ . This will not be easy to do. One can certainly reduce d from $30\mu\text{m}$ to $\sim 10\mu\text{m}$ with sufficient care in fabrication, but a further reduction to $\sim 1\mu\text{m}$ for a 1 cm diameter self-supported pyroelectric retina is more problematic in a tube robust enough for field use.

Another proposed approach to reducing transverse thermal conductance is reticulation, in which discrete sensitive elements are connected only by a thinner substrate of thermally less conductive material, such as a polymeric film. But to maintain the correct thermal response time, it would be necessary to reduce C in proportion to K . Thus, for the 5-fold sensitivity gain, the pyroelectric material would still need to be only $1\text{-}2\mu\text{m}$ thick, and reticulation does not really avoid the need to go to a very thin retina to gain sensitivity. Put another way, unless the thickness is reduced overall, reticulation only improves spatial resolution at the expense of temporal resolution.

Even if one were willing to sacrifice response speed, the constraint (15) limits the degree to which K can be reduced by reticulation or any other means, so long as a pedestal current must be generated, with its associated heating of the retina. This heating constraint could be eased

by use of a pyroelectric operating further from its Curie point T_c , where small temperature changes would have less effect on sensitivity. But, on the other hand, the high responsivity near T_c helps lift the initial signal strength above other noise sources in the system.

Another approach to higher sensitivity is to reduce the beam temperature parameter V_o . By suitable tube design, V_o could be reduced to $\sim kT/e$ for room temperature. This would be an 8-fold reduction from our assumed value of 0.2 volts, which would reduce our theoretical limit by a factor of $8^{1/4} = 1.7$. But to realize this gain, recall that the effective retina thickness would need to be reduced by another factor of $\sqrt{8}$, i.e., from $\sim 1.4\mu\text{m}$ to $\sim 0.5\mu\text{m}$, which would be very difficult indeed.

In this connection, we note that an n -fold reduction of K and C , as by simply an n -fold thinning of the retina, should cause an n -fold increase of the signal amplitude for a given ΔT , while increasing the fluctuation amplitude by \sqrt{n} . This causes only a \sqrt{n} -fold gain in signal relative to thermodynamic fluctuations of the retina, but it should give the full n -fold improvement relative to extrinsic amplifier noise, etc. Thus, if these noise sources have already been reduced to the point that they are comparable with fluctuations in a $30\mu\text{m}$ retina, as we inferred above, they would need no further improvement for use with a thinner, more sensitive retina. However, if a new scheme for readout that involved less energy

deposition in the retina could be devised, it would open the way to the use of still lower K retinas (if they could be developed) with still higher sensitivities. Of course, the fundamental black-body results (7), (8) form the ultimate limit, even if one could fabricate and use a retina only $\sim 100\text{\AA}$ thick.

CONCLUSIONS

From the foregoing analysis we conclude that:

1) The best present pyroelectric vidicons already have sensitivities that are close to the limit set by thermodynamic fluctuations in their retinas. Thus, there is probably only limited scope for improved performance by further reduction of amplifier and electron beam noise, although an improved pyroelectric material might reduce the stringency of the amplifier requirements.

2) The only direct route toward better performance is by lowering both the thermal conductance and heat capacity of the retina, essentially by making it thinner. If fabrication can be managed, it appears in principle possible to operate with a retina as thin as $\sim 1.4\mu\text{m}$, with a ~ 25 -fold increase in signal and 5-fold increase in fluctuation noise relative to a $30\mu\text{m}$ retina. A 5-fold reduction in minimum detectable temperature difference would result if such a thin retina could be used. The increased responsivity would actually make amplifier requirements less stringent than in present devices.

3) Reticulation of the retina can increase spatial resolution at the expense of temporal resolution, but only a proportionate reduction of both heat capacity and thermal conductance can improve sensitivity without change of response time.

4) If much thinner retinas can be developed, it will be important to devise improved readout schemes which involve less energy deposition in the retina, in order that the full potential benefit of reducing the thermal conductance of the retina can be realized.

ACKNOWLEDGEMENT

This research was supported by the Advanced Research Projects Agency of the Department of Defense under Contract No. MDA903-76C-0250 with The University of Michigan.

HEATING EFFECTS IN HIGH-FREQUENCY METALLIC JOSEPHSON DEVICES:
VOLTAGE LIMIT, BOLOMETRIC MIXING AND NOISE

M. Tinkham

INTRODUCTION

In the usual resistively-shunted Josephson junction (RSJ) model, one considers an ideal Josephson element with critical current I_c shunted by a normal resistance R and a capacitance C . Thus the total current is given by

$$I = I_c \sin \phi + V/R + C \, dV/dt \quad (1)$$

where ϕ is the phase difference of the superconducting wavefunction across the link, which increases with time as

$$d\phi/dt = 2eV/\hbar \quad (2)$$

(For simplicity, we ignore the $\cos \phi$ term and the frequency dependence of I_c , since these matters have been discussed extensively by others and are not crucial for our discussion.) For ideal junctions, either tunnel¹ or constriction,² I_c and R are not independent, but are related by³

$$I_c R = \frac{\pi \Delta(T)}{2e} \tanh \frac{\Delta(T)}{2kT} \quad (3)$$

which is proportional near T_c to $(1-T/T_c)$, and approaches the limit $\pi \Delta(0)/2e$ or $0.24 T_c$ (mV) at $T=0$, assuming the BCS result

$\Delta(0) = 1.76 kT_C$. Since the Josephson coupling energy is only $-(\hbar I_C/2e) \cos\phi$, in practice I_C must be greater than about $1 \mu A$ to avoid partial loss of coherence due to noise. For junctions showing the ideal $I_C R$ product, this corresponds to requiring $R < 1000\Omega$. On the other hand, R should be greater than 1Ω for efficient matching to circuits and radiation.

It is now generally recognized⁴ that the usefulness of Josephson devices at high frequencies is limited by three distinct considerations: 1) The $I_C R$ product defines a characteristic frequency $\omega = 2eI_C R/\hbar$ of order the energy gap frequency ω_g , above which resistive shunting of the ideal nonlinear inductive Josephson element increasingly degrades performance, 2) the RC time constant defines a characteristic frequency $\omega = (RC)^{-1}$ above which capacitive shunting becomes more serious than resistive shunting, and 3) heating effects due to the power dissipated tend to increase as $(\hbar\omega/2e)^2/R$ since the ac voltage level V_1 must increase roughly as $\hbar\omega/2e$ to give a useful nonlinear response. While 1) and 2) give power-law rolloffs, in this paper we show that 3) leads to an exponential cutoff at high voltage levels.

Since the $I_C R$ product (3) scales with T_C , the first consideration favors high T_C materials, independent of junction type. The RC limit, on the other hand, depends critically on the junction type: in tunnel junctions, one can achieve $\omega_g RC \leq 1$ (essentially the Stewart-McCumber⁵ criterion) only by going to extremely small area junctions ($\leq 1 \mu m^2$) and extremely high

tunnel current densities ($J_c \geq 10^5 \text{ amp/cm}^2$), parameters at the limit of current research. (Of course tunnel junctions can operate in resonant modes beyond $\omega = 1/RC$, but $1/RC$ still gives the bandwidth.) By contrast, in a well-shaped point contact or microbridge, one can have $\omega_g RC \ll 1$, so that capacitive limits are not serious until well above the gap frequency. This makes metallic weak links appear attractive for broad-band high-frequency applications. But the heating limit also depends critically on junction type. It can be minimized in tunnel junctions by keeping the tunnel resistance large relative to the resistance of the film, but in constriction weak links (point contacts and microbridges) this degree of freedom is missing since the electrical and thermal conductances are proportional. This leads to a fundamental limitation on the achievable performance of metallic Josephson devices which is explored in this paper.

A useful measure of the high-frequency performance of Josephson devices is the observability of microwave-induced constant-voltage steps in the dc I-V characteristic. In the presence of an applied voltage $V_1 \cos \omega_1 t$, steps occur at $V_n = n\hbar\omega_1/2e$, and, according to the RSJ model, they have amplitudes $I_c J_n(2eV_1/\hbar\omega_1)$ for ideal voltage-biased conditions. For current-biased junctions at $\hbar\omega \lesssim eI_c R$, these are distorted into "quasi-Bessel-functions". At the gap frequency and above, however, the voltage-biased approximation is reasonably good. The characteristic dependence on $(2eV_1/\hbar\omega_1)$ originates from the

inductive nature of the supercurrent; to obtain non-linear response, the phase ϕ must be driven to excursions

$$\delta\phi = \frac{2e}{\hbar} \int V_1 \cos \omega_1 t \, dt = \frac{2eV_1}{\hbar\omega_1} \sin \omega_1 t$$

which are at least of order unity. Since $J_n(x)$ is small for $x \lesssim n$, the Bessel function dependence implies that the amplitude V_1 must be of order V_n to get a strong step at V_n , at which voltage the internal Josephson frequency is $2eV_n/\hbar = n\omega_1$. Similarly, if one is operating a square-law detector or heterodyne mixer based on reducing the height of the zero-voltage step, as given by $J_0(2eV_1/\hbar\omega_1) \approx 1 - (eV_1/\hbar\omega_1)^2$, one clearly needs $V_1 \approx \hbar\omega_1/2e$ for efficient non-linear operation.

As a result of these finite voltage levels, the power dissipated will be

$$P = \frac{V_{\text{rms}}^2}{R} = \frac{V_{\text{dc}}^2 + \frac{1}{2}V_1^2}{R} = 0 \left(\frac{\hbar\omega}{2e} \right)^2 \frac{1}{R} \quad (4)$$

where the last form presumes that efficient non-linear operation is required at ω . For example, if $R = 10\Omega$, (4) implies $P \sim 30$ nW at 1 mm wavelength, ~ 3 μ W at 100 μ m, and ~ 300 μ W at 10 μ m.

These increasing levels of power dissipation imply increasing disequilibrium of the electrons in the tiny weak link in which the dissipation occurs. One can at least crudely describe this disequilibrium by defining a local temperature of the hot electrons in terms of the increase in average excitation energy, even though the gradients are so great that local equilibrium described by an ideal Fermi distribution does not exist. Work-

ing in this way, Skocpol, Beasley, and Tinkham⁶ showed that planar microbridges would be limited to $V \leq 2\Delta/e$, whereas geometries with 3-dimensional metallic cooling should be useable up to $V \sim (2\Delta/e) (\bar{\xi}/a)^{1/2}$, where $\bar{\xi}$ is some averaged coherence length and a is the neck radius.

In this paper, we explore in more detail the implications of this heating model of the local disequilibrium, restricting our attention to the especially favorable case of 3-dimensional metallic cooling, as in a point contact or a short high-performance variable-thickness bridge. We find that:

1) The temperature in the center of the junction may be far above T_c , as high as 70K in Nb point contacts, when high Josephson steps are observed; accordingly, the noise temperature may be far above ambient.

2) The critical current falls approximately as e^{-P/P_0} , where P is the power dissipated in the junction and P_0 ($\sim 10 \mu W$) depends on material parameters and junction geometry. This result accounts well for the limited number of microwave steps observed experimentally by Octavio et al⁷ in a tin variable thickness bridge and by McDonald et al⁸ in a Nb point contact. For a junction of optimized resistance, the maximum voltage step is found to scale as $T_c [\Omega \xi(0)/\rho_0]^{2/7} (v_1/T_c)^{1/7}$, where Ω is the solid angle for 3-dimensional cooling, $\xi(0)$ is the coherence length extrapolated to $T = 0$, ρ_0 is the residual resistivity, and v_1 is the microwave frequency.

3) Thermal or "bolometric" mixing will dominate

Josephson mixing for carrier frequencies above ~ 3 THz, as in the mixing experiments of McDonald⁹ using CO₂ lasers; this bolometric mixing should work for beat frequencies up to the order of the energy gap frequency.

THE HEATING MODEL

Although the local heating model outlined above should apply semiquantitatively to any geometry with 3-dimensional metallic cooling extending far enough from the neck for the temperature to have dropped to near the bath temperature T_b , it is convenient to consider a specific geometry. An appropriate choice is that defined by a hyperboloid of revolution with neck radius a and apex angle 2θ , for which the normal resistance is

$$R = \frac{\rho}{2a} \cotn \frac{\theta}{2} \quad (5)$$

so long as the mean free path $\ell \ll a$. The cooling solid angle on each side is

$$\Omega = 2\pi(1 - \cos\theta) = 4\pi \sin^2\theta/2 \quad (6)$$

To simplify calculation further, we replace this configuration by an artificial one defined by two collinear intersecting cones with the same apex angle 2θ and solid angle Ω , which intersect at a radius r_1 from the apexes, as illustrated in Fig. 1. This r_1 is chosen so that the resistance of the purely radial current flow from r_1 to ∞ , namely

$$R = \frac{2\rho}{\Omega r_1} \quad (7)$$

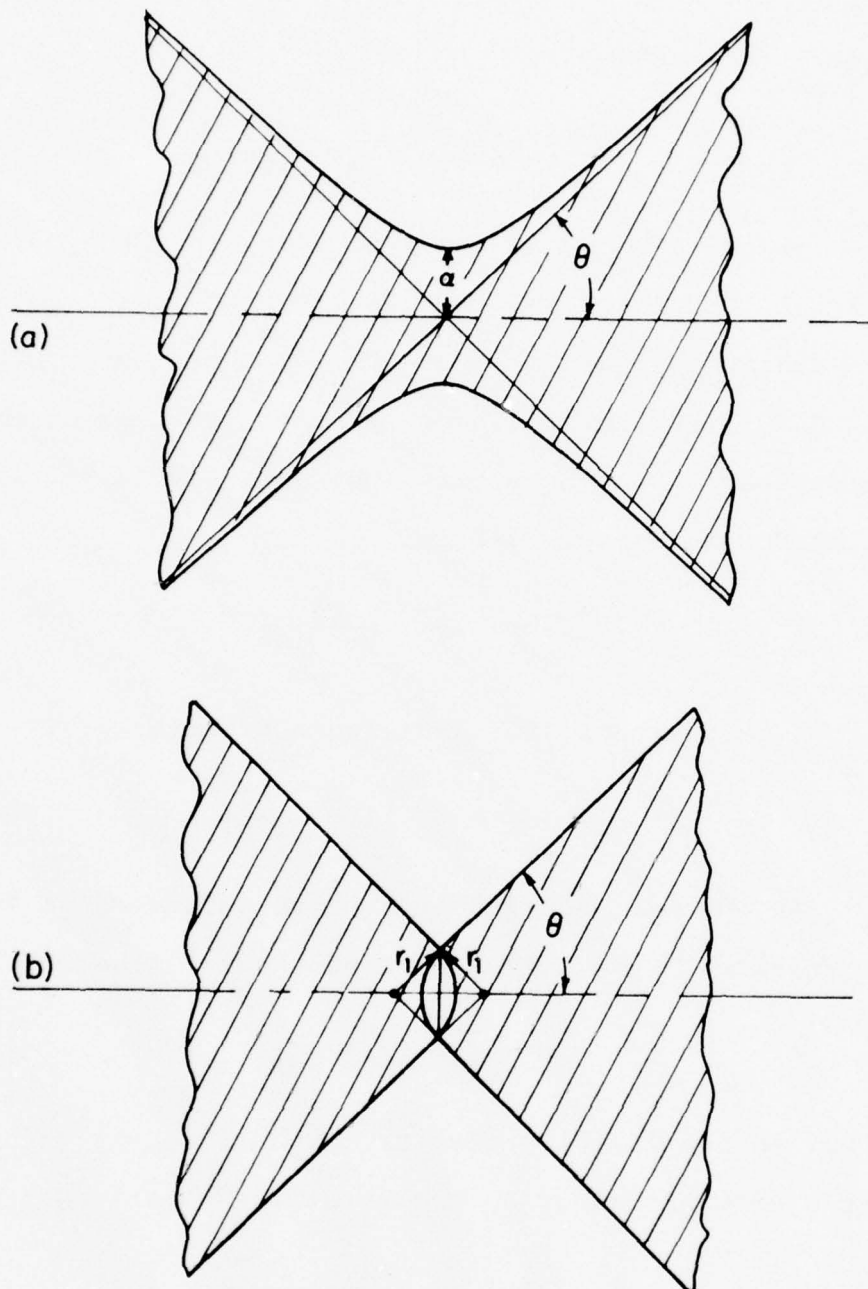


Figure 1. (a) Longitudinal section of hyperbolic neck of radius a and apex angle 2θ .
 (b) Section of artificial collinear cone neck having same apex angle and same electrical resistance. The unshaded space inside the radii r_1 is non-physical.

reproduces (5). Thus

$$r_1 = \frac{2a}{\pi \sin \theta} = \frac{4a}{[\Omega(4\pi - \Omega)]^{1/2}} \quad (8)$$

By this construction we define a geometry in which calculations are trivial, but which should have electrical, thermal, and superconductive properties close to those of the hyperbolic neck.

Our first step in generalization is to relax the requirement that $\ell \ll a$ by putting boundary scattering in explicitly, if approximately, by setting

$$\frac{1}{\ell_{\text{eff}}} = \frac{1}{\ell} + \frac{1}{2r \sin \theta} \quad (9)$$

so that ℓ_{eff} reduces to the local cone diameter if $\ell \rightarrow \infty$. Then

$$\rho_{\text{eff}}(r) = \rho_0 \left[1 + \frac{\ell}{2r \sin \theta} \right] \quad (10)$$

where ρ_0 is the bulk resistivity, which we assume is independent of temperature. Using (10), we find the resistance to be

$$R = \frac{2\rho_0}{\Omega r_1} \left(1 + \frac{\pi \ell}{8a} \right) \quad (11)$$

Note that in the limiting case of two half spaces connected through a hole or radius a , $\Omega = 2\pi$ and $r_1 = 2a/\pi$, so that

$$R = \frac{\rho_0}{2a} \left(1 + \frac{\pi \ell}{8a} \right) + \frac{\pi}{16} \frac{\rho_0 \ell}{a^2} \quad (12)$$

where the latter form applies for very small contacts, where $a \ll \ell$. It is obviously important to use (11) or (12) rather than (5) to infer contact areas from measured resistances in high resistance (i.e., small area) contacts.¹⁰ For example,

using (11) and taking the typical parameters $\rho_0 = 10^{-6}$ ohm-cm, $\ell = 10^{-5}$ cm, and $\Omega = \pi$, we find $a = 63\text{\AA}$ for $r = 10\Omega$ (typical of a Nb point contact) and $a = 478\text{\AA}$ for $R = 0.33\Omega$ (typical of a Sn microbridge). If we had used (5) instead, the corresponding values would have been 9\AA and 260\AA . Thus, at least in high resistance junctions, the size effect corrections can increase the local resistivity near the neck by almost a factor of 10. For our model (and that of Ref. 2) to be entirely applicable, it is necessary that a be distinctly less than the coherence length. These typical neck radii fulfill this requirement.

When a current I flows through this link, the total power dissipated is $I^2 R$. The amount dissipated per unit radius is $I^2 \rho_{\text{eff}} / \Omega r^2$, which falls very rapidly as r increases from r_1 , so that to a first approximation, one could treat it as all occurring at r_1 . More precisely, however, the power dissipated inside radius r (on each side) is

$$P(r) = \frac{I^2 \rho_0}{\Omega} \int_{r_1}^r \left(1 + \frac{\ell}{2r \sin \theta} \right) \frac{dr}{r^2} = \frac{I^2 \rho_0}{\Omega} \left[\left(\frac{1}{r_1} - \frac{1}{r} \right) + \frac{\ell}{4 \sin \theta} \left(\frac{1}{r_1^2} - \frac{1}{r^2} \right) \right] \quad (13)$$

The temperature gradient required to carry this power away is

$$\frac{dT}{dr} = \frac{P(r)}{\Omega K_{\text{eff}} r^2} \quad (14)$$

where, by the Wiedemann-Franz law

$$K_{\text{eff}} = \frac{\pi^2}{3} \left(\frac{k}{e} \right)^2 \frac{T}{\rho_{\text{eff}}} \quad (15)$$

ρ_{eff} being the position-dependent value defined by (10).

Integrating in from $r = \infty$ where $T = T_b$ and using (11), we obtain

$$T^2(r) - T_b^2 = \frac{3}{\pi^2} \frac{e}{k^2} \frac{\rho_0}{\Omega} \frac{I^2 R}{r} \left(1 + \frac{\ell}{4r \sin \theta} \right) \left[1 - \frac{r_1}{2r} \frac{(1 + \frac{\ell}{4r \sin \theta})}{(1 + \frac{\ell}{4r_1 \sin \theta})} \right] \quad (16)$$

When $\ell \ll r_1 \sin \theta$ so that boundary scattering is unimportant, this simplifies to

$$T^2(r) - T_b^2 = \frac{3}{2} \left(\frac{eV}{\pi} \right)^2 \frac{r_1}{r} \left(1 - \frac{r_1}{2r} \right) \quad (16a)$$

where $V = IR$. Another important special case of (16) is to determine the maximum temperature T_m , which is given (for all ℓ/r_1) by

$$T_m \equiv T(r_1) = \left[T_b^2 + 3 \left(\frac{eV}{2\pi k} \right)^2 \right]^{1/2} \quad (17)$$

This result is not really new; it has long been known that such an expression for T_m holds for quite general geometries.¹¹ In fact, Iwanyshyn and Smith¹² have applied similar considerations specifically to heating effects at a superconducting point contact, but our analysis is applied to different phenomena. Numerically, the second term in (17) is $(3.2 \text{ V})^2$ if V is in millivolts. From this, we will estimate center temperatures of $\sim 15\text{K}$ in Octavio's variable thickness tin bridge and $\sim 70\text{K}$ in the Nb point contact of McDonald et al. at the highest voltage at which steps are observed. These examples show that we are indeed concerned with major departures from equilibrium at the bath temperature.

In assessing (17), it is important to note that all properties of the junction have dropped out, including its

resistivity and size except the underlying requirement of the 3-dimensional geometry and the assumption of the Wiedemann-Franz law. The latter holds if the electronic mean free path is the same for electrical and thermal conductivity, which it should be for impurity and boundary scattering as is implicit in our assumed temperature-independent ρ_0 . Thus it should apply quite generally, including in the dissipative superconductive state, where the quasiparticle density is nearly normal.

In more microscopic terms, (16) and (17) can be interpreted as follows: eV is the extra energy given to electrons on being accelerated through the neck, corresponding to a rise in temperature; the hot electrons then diffuse out radially, being "diluted" by cool electrons so that the average excess energy falls as $1/r$, even without individual electrons losing energy by inelastic scattering from phonons; finally, the excess energy is shared with phonons and becomes equilibrium "heat" in a quasiparticle diffusion length¹⁵ $\Lambda = \sqrt{D\tau_2}$. Because $\tau_2 \propto E^{-3}$ or T^{-3} the appropriate value of Λ here is that corresponding to T_m , which will be much shorter than that measured near T_c . For example, in Sn, $\Lambda(T_c) \sim 5 \mu\text{m}$; hence at 15K, $\Lambda \sim 0.6 \mu\text{m}$. Thus the departures from an equilibrium distribution for a local temperature actually may not be too large. Since the electronic thermal conductivity usually dominates the phonon contribution, the details of this thermalization are not critical to the argument.

Another point that should be underlined is the impor-

tance of the size-effect increase of the local resistivity near the neck. While not upsetting the Wiedemann-Franz relation, this position-dependent resistivity in high-resistance junctions confines the spatial extent of the very high temperatures given by (17), which itself is independent of resistivity. Thus, even within a nominally homogeneous material, one gets some of the reduction in heating effects noted earlier for tunnel junctions, where one has a high-resistance tunnel barrier between two good conductors.

One effect of these high temperatures will be additional electronic noise because of the hot electrons described by (16). If one can treat the link as a series of Johnson noise sources at different temperatures, the appropriate noise temperature will be given by

$$T_N = \frac{1}{R} \int T(r) \frac{dR}{dr} dr \quad (18)$$

Insofar as (16) can be approximated by $\Delta T \propto 1/r$, and $dR/dr \propto 1/r^2$, it is easy to see that this reduces to

$$T_N = \frac{1}{2} (T_b + T_m) \quad (19)$$

Because of the oversimplification involved in using the Johnson noise approximation for a highly non-equilibrium situation, it is probably not worth going beyond (19) without a more careful examination of the nature of the noise to be expected. Qualitatively, however, one must expect substantial additional noise if $(eV/2\pi kT_b)$ is greater than unity.

REDUCTION IN I_c

The dominant effect of the heating-induced disequilibrium is to reduce the superconducting critical current of the weak link. We treat this effect by generalizing the Aslamazov-Larkin² calculation of the equilibrium Josephson effect I_c of a constriction weak link. Their calculation takes advantage of the fact that if the neck radius a (as well as its length) is small compared to the coherence length ξ , the gradient terms dominate the free energy density in the neck region. Minimizing this energy implies that ψ satisfies Laplace's equation, $\nabla^2 \psi = 0$, subject to suitable boundary conditions. They consider a particular solution $f(\vec{r})$ which tends asymptotically to unity when the distance from the contact increases to one side of the contact, and to zero with increasing distance on the other side, and which has zero normal surface derivative. They then write the (approximate) solution to the Ginzburg-Landau (GL) equation as

$$\psi = \psi_0 \{ f(\vec{r}) e^{i\chi_1} + [1-f(\vec{r})] e^{i\chi_2} \} \quad (20)$$

where ψ_0 is the equilibrium value of $|\psi|$, deep in the metal away from the contact, and the phase factors depend on time but not on position. Since the supercurrent density is given by

$$\vec{J}_s = \frac{e^* \hbar}{2m^*} (\psi^* \vec{\nabla} \psi - \psi \vec{\nabla} \psi^*) = \frac{e^* \hbar}{m^*} |\psi_0|^2 \vec{\nabla} f \sin \phi \quad (21)$$

(neglecting the vector potential term, as is legitimate for small diameters) where $\phi = \chi_2 - \chi_1$, it follows that the critical

current of the link is

$$I_c = \pi a^2 \frac{e^* \hbar}{m^*} |\psi_0|^2 \nabla f \quad (22)$$

where ∇f is averaged over the cross section at the center of the link. For the hyperbolic neck geometry, its value is

$$\nabla f = \frac{2}{\pi a} \tan \frac{\theta}{2} \lesssim \frac{2}{\pi a} \quad (23)$$

In our collinear cone model, $\nabla f|_{r_1} = \frac{1}{2r_1} = \frac{\pi \sin \theta}{4a}$, and the area is Ωr_1^2 rather than πa^2 . More generally, $\nabla f \approx 1/a$. It follows that the critical current density in the neck of the link is larger than the bulk value by a ratio of order ξ/a , which exceeds unity since this Laplace equation approach is only valid for $a \ll \xi$, so that I_c falls off as \underline{a} rather than a^2 , as one goes to smaller and smaller contact areas.

Since the electrical potential in a uniform resistive medium also satisfies Laplace's equation, it can be written in terms of the same $f(\vec{r})$ as

$$V(\vec{r}) = V_1 + \nabla f(\vec{r}) \quad (24)$$

where V is the total potential difference, $V_2 - V_1$. We can then write the normal resistance of the link in terms of ∇f , by noting that the current through the neck is

$$I = \pi a^2 \sigma \nabla f = V/R \quad (25)$$

so that

$$R = (\pi a^2 \sigma \nabla f)^{-1} \quad (26)$$

Comparing (22) and (26), we see that all junction-dependent quantities cancel and one has

$$I_c R = \frac{e^* \hbar}{m^*} \frac{|\psi_0|^2}{\sigma} \quad (27)$$

Using standard normalization conventions¹⁴ for the dirty limit case, this reduces directly to (3), at least near T_c where the conventions are clearly defined. Some caution is needed when the mean free path ℓ is comparable with or larger than the neck radius a , since then the conductivity in (25)-(27) is position dependent, as we noted in the previous section. However, the effective superconducting density $|\psi_0|^2$ is also proportional to ℓ when the effective mean free path is below ξ_0 , and these two effects tend to cancel, leaving the $I_c R$ product unchanged. Further detailed attention to this question when ℓ , ξ_0 and $\xi(T)$ are of similar magnitudes might provide a consistent explanation of the minor increase of the $I_c R$ product with decreasing R (or increasing neck radius) found in the data of Zimmerman,¹⁵ of Octavio et al.,⁷ and of Yanson¹⁰ for low resistance ($\leq 1\Omega$) contacts, where a may be approaching ξ_0 , causing our approximations to break down.

Before discussing the reduction of I_c by heating, it is interesting to note that a result for T_m similar to (17) can be obtained using the same technique used above to derive the invariant $I_c R$ product. If one approximates the problem by having all the heat deposited in the midplane of the neck, and if one considers only small changes in T so that K can be treated as

constant, then the temperature on either side of the midplane satisfies Laplace's equation. The solution is symmetrical about the midplane, being given on one side by $(T-T_b) = (T_m-T_b)2f$, and the boundary condition at the midplane is

$$\frac{P}{2\pi a^2} = K\nabla T = 2K(T_m-T_b)\nabla f \quad (28)$$

Since $P = V^2/R$, R being given by (26), and K is related to σ by the Wiedemann-Franz law (15), we find

$$(T_m-T_b)T_b = 3(eV/2\pi k)^2$$

Apart from a factor of 2 excess resulting from the approximation of putting all the heat load on the midplane, rather than distributed properly over a volume, this confirms (17) in its small heating limit without restriction to a particular geometry.¹¹

To take heating into account in the framework of the AL model, the form (20) must be generalized to take account of the reduction in the superconducting electron density. As it stands, (20) describes a $|\psi|^2$ which oscillates in time between $|\psi_0|^2$ and 0 at the center of the contact, where by symmetry $f = 1-f = \frac{1}{2}$. In the presence of heating, we expect $|\psi|^2$ to oscillate between some lower value and zero. This can be incorporated in (20) by writing it more generally, but still with inversion symmetry as

$$\psi = \psi_0 \{f(\vec{r})e^{i\chi_1} + f(-\vec{r})e^{i\chi_2}\} \quad (29)$$

In the absence of heating, $f(-\vec{r}) = 1-f(\vec{r})$, and we recover (20). But in the presence of heating, $f(0)$ is depressed below $\frac{1}{2}$, so

that $|\psi|^2$ oscillates between $|2f(0)\psi_0|^2$ and zero. With the generalization (29), J_s is proportional to $[f(-\vec{r})\nabla f(\vec{r}) - f(\vec{r})\nabla f(-\vec{r})]$ instead of simply to ∇f . In particular, at the midplane ∇f is replaced by $2f(0)\nabla f(0)$. So long as $a \ll \xi$, we expect $\nabla f(0)/f(0) \approx (4/\pi a)\tan\theta/2$ as given by (23), for example, to remain essentially unchanged. In that case, I_c will simply be reduced in proportion to $|f(0)|^2$ by the heating.

We consider two simple limits: a) small heating ($T_b < T_m \ll T_c$), in which case $f(0)$ decreases linearly with P , and b) large heating ($T_m > T_c$), in which case $f(0)$ falls exponentially.

Small Heating

Since $f(\vec{r})$ can only respond to heating over a length scale of order ξ without excessive gradient energy, we expect $f(0)$ to reflect the average temperature rise over a volume extending from the contact out to $\sim \xi(T_b)$. This average will be approximately the temperature rise at $r = \xi/2$. Then, we crudely expect

$$\frac{I_c(P)}{I_c(0)} = |2f(0)|^2 \approx \left| \frac{\psi_0 \left[T\left(\frac{\xi}{2}\right) \right]}{\psi_0(T_b)} \right|^2 \quad (30)$$

Returning to (16) for $T(r)$, for small heating we can linearize the left member, writing it as $2T_b[T(r) - T_b]$. Also, in the right member, it will usually be justified to drop terms of order $2r_1/\xi$ and $\ell/2\xi\sin\theta$ compared to unity. This causes (16) to simplify to

$$T\left(\frac{\xi}{2}\right) - T_b = \frac{3}{\pi^2} \frac{e^2 \rho_0 P}{k^2 T_b \Omega \xi} \quad (31)$$

$$= \frac{P}{\Omega K \xi} \quad (31a)$$

where in (31a) we have reexpressed the result in terms of the thermal conductivity. This result could essentially have been written down by inspection. Nonetheless, our discussion illuminates the fact that one should use a value of K close to the purely electronic part, since the excess energy is only shared with phonons over a distance Λ , which is typically greater than ξ .

Given (30) and (31), we see that for small power dissipations we expect

$$\begin{aligned} I_c(P) &\approx I_c(0) \left[1 + \frac{1}{\psi_0^2} \frac{\partial \psi_0^2}{\partial T} \frac{P}{\Omega K \xi(T_b)} \right] \\ &\approx I_c(0) \left[1 - \frac{4t_b^2}{(1+t_b^2)^{3/2} (1-t_b^2)^{1/2}} \frac{P}{\Omega K(T_c) \xi(0) T_c} \right] \end{aligned} \quad (32)$$

In obtaining the final form, we have used the two-fluid approximation that $\psi_0^2 \propto (1-t^4)$, and we have used the fact that $K \propto T$, to allow replacing $K(T_b)$ by $t_b K(T_c)$. We conclude that one expects an initial linear decrease in I_c , with a characteristic power level $\sim t_b^{-2} (1-t_b^2)^{1/2} K(T_c) T_c \xi(0) \Omega$, apart from slowly varying factors.

Large Heating

When the power level is so large that the temperature at the center of the contact $T_m \gg T_c$, we can use the WKB approximation to estimate the penetration of the pairs as measured by $f(0)$. We start with the GL equation, with neglect of vector

potential:

$$-\frac{\hbar^2}{2m^*} \nabla^2 \psi + \alpha \psi + \beta |\psi|^2 \psi = 0 \quad (33)$$

Specializing to radial solutions without angular dependence, and dropping the non-linear term since ψ is small in the region above T_c , we have

$$\frac{d^2}{dr^2} (r\psi) = \frac{2m^* \alpha [T(r)]}{\hbar^2} (r\psi) \equiv \frac{1}{\xi^2(r)} (r\psi) \quad (34)$$

To simplify as much as possible, we take the simple linear variation of α (or $\frac{1}{\xi^2}$) with $(T-T_c)$, so that

$$\frac{1}{\xi^2(r)} = \frac{1}{\xi^2(0)} [t(r)-1] \quad (35)$$

for the "forbidden" region where $T > T_c$, or $t(r) > 1$. Then, neglecting all but the dominant exponential dependence of the WKB approximation, we expect $r\psi$ to be attenuated by a factor

$$2f(0) = e^{-W} \quad (36)$$

where

$$W = \frac{1}{\xi(0)} \int_{r_1}^{r(T_c)} [t(r)-1]^{\frac{1}{2}} dr \quad (37)$$

We have evaluated this integral numerically using (16) for representative situations, but the result is similar to that obtained using a simple analytic approximation. We can write (37) as

$$W = \frac{r(T_c) - r_1}{\xi(0)} \langle [t(r)-1]^{\frac{1}{2}} \rangle_{av}. \quad (38)$$

If we then drop r_1 compared to $r(T_c)$ and approximate the average of $(t-1)^{\frac{1}{2}}$ by its value in the middle of the range of r , we have

$$W \approx \frac{r(T_c)}{\xi(0)} \{t[\frac{1}{2}r(T_c)]-1\}^{\frac{1}{2}} \quad (39)$$

Since $r(T_c)$ will typically be large compared to ξ when the power level is high, and $\xi > a \approx r_1$ for our model to be applicable, it is a good approximation in (16) to drop terms in $r_1/r(T_c)$ and $\ell/4r(T_c)\sin\theta$, so that it reduces to

$$T^2(r) - T_b^2 = \frac{3}{\pi^2} \frac{e^2}{k^2} \frac{\rho_0}{\Omega} \frac{P}{r} \quad (40)$$

from which we find

$$r(T_c) = \frac{3}{\pi^2} \frac{e^2}{k^2} \frac{\rho_0}{\Omega} \frac{P}{T_c^2 (1-t_b^2)} \quad (41)$$

It then follows from (40) that

$$t[\frac{1}{2}r(T_c)] = (2-t_b^2)^{\frac{1}{2}} \quad (42)$$

so that

$$\begin{aligned} \{t[\frac{1}{2}r(T_c)]-1\}^{\frac{1}{2}} &\approx (\sqrt{2}-1)^{\frac{1}{2}} = .64 & (t_b \ll 1) \\ &\approx \left\{ \frac{1-t_b^2}{2} \right\} & (t_b \approx 1) \end{aligned}$$

Since the second form agrees with the first to within 10% even at $t_b = 0$, we use it for all t_b . Combining these factors, (39) becomes

$$W \approx \frac{1}{\sqrt{2}(1-t_b^2)^{\frac{1}{2}}} \frac{3}{\pi^2} \frac{e^2}{k^2} \frac{\rho_0 P}{T_c^2 \xi(0) \Omega} \quad (43)$$

Finally, since we expect I_c to vary as $[2f(0)]^2 = e^{-2W}$, we expect

$$I_c(P) = I_c(0) e^{-P/P_0} \quad (44)$$

where

$$P_0 = \frac{(1-t_b^2)^{1/2}}{\sqrt{2}} \frac{\pi^2}{3} \frac{k^2 T_c^2 \xi(0) \Omega}{e^2 \rho_0} \quad (45)$$

$$= \frac{1}{\sqrt{2}} (1-t_b^2)^{1/2} K(T_c) T_c \xi(0) \Omega \quad (45a)$$

Again, we expect $K(T_c)$ should be taken to include only the electronic contribution [as given by (45)] but if $\Lambda(T_m) \lesssim r(T_c)$, an appreciable part of the phonon conductivity should be included; this is usually a rather small correction. It is reassuring that this result involves the same characteristic power level as we found for the case of small heating in (32), apart from the factor t_b^{-2} which reflects the weak temperature dependence of $|\psi_0|^2$ at low temperatures. Thus, for qualitative and semi-quantitative considerations, we can use the exponential form (44) for all power levels, but we should recall that at $t_b \ll 1$ the initial decrease will be slower than predicted by this simple form.

Our primary conclusion is that P_0 forms a figure of merit for avoiding heating limits. It can be maximized for a given material by reducing t_b toward zero and increasing the cooling solid angle Ω toward its limiting value 2π . In comparing materials, one wants to maximize $T_c K(T_c) \xi(0)$ or $T_c^2 \xi(0) / \rho_0$. Evidently there is a tendency toward cancellation, since materials with high T_c tend to have short $\xi(0)$ and high ρ_0 . In fact,

assuming a residual resistance ratio of ~ 10 in all cases, $\xi(0)T_C^2/\rho_0$ turns out to be about the same ($\pm 20\%$) for Al, Sn, Pb, and Nb, but much smaller for Nb₃Sn because its very short coherence length and poor conductivity outweigh the high T_C .

Taking $t_b = 0$ and $\Omega = \pi$, (45) becomes

$$P_O = \frac{\pi^3}{\sqrt{2}} \frac{k^2}{3 e^2} \frac{T_C^2 \xi(0)}{\rho_0} \approx 10 \mu W \quad (46)$$

for the typical simple metallic superconductors. Because of the many approximations, and the varying values of Ω and ℓ in actual contacts, this numerical value is certainly open to variation by factors of 2 or more, but it does establish a definite order of magnitude at which I_C should be reduced by $1/e$. To reduce I_C by a factor of 100, as might be required to reduce Josephson steps below detectability, would require $4.6 P_O$, about 50 μW .

VOLTAGE LIMIT FOR MICROWAVE-INDUCED STEPS

Since this predicted decrease in amplitude of the observed Josephson steps on the I-V curve depends on the total power dissipated in the junction, it will manifest itself in many ways. For example, it will tend to cut off the oscillatory quasi-Bessel function dependence of the amplitude of a given step on the rf power level. It will also alter the frequency dependence of the maximum amplitude of the first Josephson step because of the higher rf voltage levels required at higher frequencies. Finally, it will limit the maximum dc voltage at which any Josephson effect steps can be observed. We have been

primarily interested in the latter overall limit, which has the feature of allowing a straightforward comparison with experimental data.

The predictions of our model can be compared with the data of McDonald et al⁸ in which steps were seen up to 17mV in a Nb point contact detector. Although the resistance was not stated, a typical value in such experiments is 10 Ω . If we assume the peak value of the applied high frequency voltage was equal to the step height, the power dissipated would be $P = (17)^2 \times (1 + \frac{1}{2}) / 10 = 43 \mu W$, which is in excellent agreement with our expectations. It is of interest also that in this case, using (17), we estimate $T_m \approx 70^\circ K$, so that the noise temperature might be $\sim 35K$. This linearly increasing noise temperature with higher steps together with the exponentially falling value of I_c combine to give quite a decisive limit to the number of observable steps.

As a second comparison, we consider the experimental data on variable thickness tin microbridges reported by Octavio, Skocpol, and Tinkham.⁷ They observed some 180 X-band microwave steps, extending up to $\sim 3.7mV$ in a 0.33 Ω bridge. Again assuming $V_1 \sim V_{dc}$, we find $P = 62 \mu W$, again in satisfactory order of magnitude agreement with our expectations. In this case, we estimate $T_m \approx 15^\circ K$, and a noise temperature of $\sim 8K$.

A more complete illustration of the comparison of our model with the data of Octavio et al is shown in Fig. 2. Here the experimental step heights are compared with the theoretical

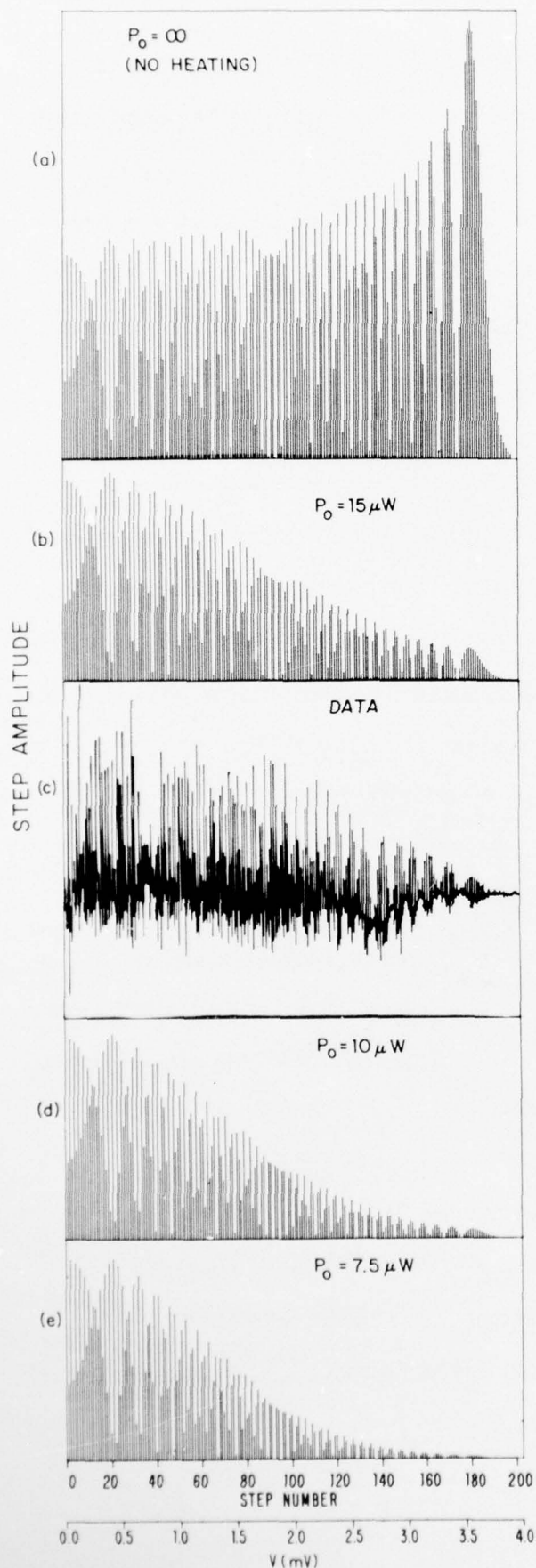


Figure 2. Step amplitudes at 10GHz for different values of P_0 compared with experimental step amplitudes for a variable thickness tin bridge with $R = 0.33\Omega$.

step heights $J_n(2eV_1/\hbar\omega_1)e^{-P/P_0}$ for several values of P_0 . The plot for $P_0 = \infty$ corresponds to no heating, and simply shows the Bessel function dependence. It appears that the best fit occurs for P_0 between 10 and 15 μW , in good agreement with our expectations. Other of our bridges giving poorer performance could be fit by P_0 values in the range 1-3 μW . Blaney¹⁶ has published data on a Nb point contact which also suggest $P_0 \sim 3 \mu\text{W}$.

Since these comparisons appear to support the validity of our analysis, we are led to attribute the superior performance of the Nb point contact over the Sn variable thickness bridge primarily to its higher resistance giving less dissipation per millivolt. In other words, it might appear that the mechanical hardness of Nb, which allows a smaller area contact, is a more decisive parameter than its higher T_c .

Of course, V_{max} can not be increased indefinitely by going to higher resistance junctions because the critical current must remain large enough to maintain phase coherence even in the presence of the thermal noise at the higher noise temperature, and $I_c(P=0)$ varies as T_c/R . Thus, it is useful to consider a criterion based on the relation of the step height to the noise, rather than its reduction relative to its value at $P = 0$. Based on the work of Ambegaokar and Halperin¹⁷ on the noise rounding of the dc I-V curve, as extended by Stephen¹⁸ to the case of rf-induced steps, a reasonable criterion for observable steps is that the width of the n^{th} step in the absence of noise $I_n = I_c J_n(2eV_1/\hbar\omega_1)$ should exceed ekT_N/\hbar . Of course

one could introduce a numerical factor depending on how clearly observable the steps should be, but we eschew that refinement. Since $J_n(x)$ oscillates with an amplitude of $\sim x^{-1/2}$ until it rises to a maximum and dies out for $n \geq x$, as illustrated by Fig. 2(a), the most favorable amplitude V_1 is that for which $x \approx n$, (i.e., $V_1 \approx V_{dc}$, so that $V^2 \equiv V_{rms}^2 = \frac{3}{2} V_{dc}^2$, as anticipated above) in which case $J_n(x)$ reaches a maximum of approximately $\pi/2n^{1/2} = (\pi/2)(\hbar\omega_1/2eV_{dc})^{1/2}$ before dying off. Also, according to (19), we expect $T_N \approx \frac{1}{2}(T_b + T_m)$, with T_m given by (17). Thus, we require

$$I_C \geq \frac{ekT_N}{\hbar J_n} \geq \frac{ek}{\pi \hbar} \left(\frac{2eV_{dc}}{\hbar\omega_1} \right)^{1/2} \{T_b + [T_b^2 + 3(eV/2\pi k)^2]\}^{1/2} \quad (47)$$

where the curly bracket reduces to $\sqrt{3} eV/2\pi k$ for $eV \gg \pi kT_b$. But combining (3) and (44), we have

$$I_C \leq I_C(0)e^{-P/P_0} \approx \frac{\pi \Delta}{2eR} \tanh \frac{\Delta}{2kT} e^{-V^2/RP_0} \quad (48)$$

where the latter form presumes a junction showing the full theoretical $I_C R$ product. These two constraints on I_C are compatible only when

$$\left(\frac{eV}{kT_C} \right) \left(\frac{eV_{dc}}{\hbar\omega_1} \right)^{1/2} e^{V^2/RP_0} < \frac{9.2 \times 10^4}{R} \quad (T_b \approx 0) \quad (49a)$$

$$\left(\frac{eV_{dc}}{\hbar\omega_1} \right)^{1/2} e^{V^2/RP_0} < \frac{(1-t_b)}{R} \times 3.4 \times 10^4 \quad (T_b \approx T_C) \quad (49b)$$

with R in ohms.

For given values of R , P_0 , T_C , and ω_1 , (49a) can be solved numerically to find the maximum value of V compatible

with the constraint, recalling that $V \equiv V_{\text{rms}} \approx (3/2)^{1/2} V_{\text{dc}}$. Taking $P_0 = 10 \mu\text{W}$, the result for the 0.33 ohm tin microbridge studied at X-band by Octavio et al.⁷ is $V_{\text{dc}} \leq 4.1 \text{ mV}$. This should be compared with the maximum observed experimentally of 3.7 mV, bearing in mind that not enough microwave power was available to reach the ultimate limit, and that $t_b \approx 0.4 > 0$. Taking as estimated resistance of 10 ± 5 ohms for the N_b point contact studied at 70 GHz by McDonald et al.⁸ we calculate a limit of $16 \pm 3 \text{ mV}$ compared to the reported experimental limit of 17 mV. This level of agreement is highly satisfactory considering our limited knowledge about the microscopic configurations of these links, the resistance of the point contact, the rather arbitrary condition for observability we have taken, and other major approximations.

Returning to the general condition (49), we see that for any given V , the value of R minimizing the left member is $R = V^2/P_0 \approx 1.5 V_{\text{dc}}^2/P_0$. Inserting this optimum value in (49), and again taking $V_1 = V_{\text{dc}}$ so that $V \equiv V_{\text{rms}} = \sqrt{3/2} V_{\text{dc}}$, we have

$$V_{\text{dc}} \lesssim 10 T_c^{2/7} v_1^{1/7} P_0^{2/7} \quad (50a)$$

and

$$R_{\text{opt}} = 152 T_c^{4/7} v_1^{2/7} P_0^{-3/7} \quad (50b)$$

where V_{dc} is in mV, v_1 in THz, P_0 in μW , and R_{opt} in Ω . For our two examples, taking $P_0 = 10 \mu\text{W}$, this gives $V_{\text{dc}} \lesssim 15 \text{ mV}$ for Sn at X-band with $R_{\text{opt}} \approx 32 \Omega$, and $V_{\text{dc}} \lesssim 25 \text{ mV}$ for Nb at 70 GHz, with $R_{\text{opt}} \approx 94 \Omega$.

Finally, we may reexpress (50) in terms of more basic quantities by using (45) for P_0 , obtaining with $e_n = 2.718\dots$

$$V_{dc} \approx \left[\frac{10\sqrt{2} \pi^5 1.76}{9e_n (e^2/\hbar c)} \right]^{2/7} (\hbar v_1)^{1/7} (kT_c)^{6/7} [\xi(0)\Omega/\rho_0]^{2/7} \quad (51a)$$

$$\approx 3.2 T_c (v_1/T_c)^{1/7} [\Omega\xi(0)/\rho_0]^{2/7}$$

and

$$R_{opt} \approx 870 \left(\frac{v_1}{T_c} \right)^{2/7} \left[\frac{\rho_0}{\Omega\xi(0)} \right]^{3/7} \quad (51b)$$

in the same units as used in (50). The form (51a) shows particularly clearly how the basic proportionality of V_{max} to T_c is modified by the transport properties embodied in $[\xi(0)/\rho_0]$, which favor materials with high electronic conductivity. For example, in dirty superconductors this ratio varies as $\ell^{3/2}$. Equation (51) also shows the importance of a large solid angle Ω for cooling, and the relatively weak frequency dependence.

THERMAL RESPONSE TIME: BOLOMETRIC MIXING

Our analysis above has considered only time-averaged effects. We now extend it to consider situations in which the dissipated power is time-dependent. To be concrete, let us consider the important example in which two carriers $V_1(\omega_1)$ and $V_2(\omega_2)$ simultaneously drive the junction. The instantaneous dissipation is proportional to

$$\begin{aligned} V^2(t) &= (V_1 \cos \omega_1 t + V_2 \cos \omega_2 t) \\ &= V_1^2 \cos^2 \omega_1 t + V_2^2 \cos^2 \omega_2 t + V_1 V_2 \cos(\omega_1 - \omega_2)t + V_1 V_2 \cos(\omega_1 + \omega_2)t \end{aligned} \quad (52)$$

Averaged over the period at the carrier frequencies, one has

$$P = \frac{V^2}{R} = \frac{V_1^2 + V_2^2}{2R} + \frac{V_1 V_2}{R} \cos \omega_b t \quad (53)$$

where $\omega_b = \omega_2 - \omega_1$ is the beat frequency, which we take to be small compared to ω_1 and ω_2 . The first term will give the time-average depression of I_c , while the second term gives a modulation of I_c at ω_b which can be converted to a current or voltage signal at ω_b .

Two questions must be answered: (a) how efficient is this bolometric mixing relative to the Josephson effect mixing for ω_b very small? and (b) at what beat frequency $1/\tau$ will the thermal response fall off?

a) The reduction in height of the zero-voltage current step by Josephson effect is given by

$$\frac{I_c}{I_{c0}} = J_0 \left(\frac{2eV_1}{\hbar\omega_1} \right) \approx 1 - \left(\frac{eV_1}{\hbar\omega_1} \right)^2 \quad (54)$$

Thus

$$\left. \frac{d(I_c/I_{c0})}{dV_1^2} \right|_{\text{Jos.}} = - \left(\frac{e}{\hbar\omega_1} \right)^2 \quad (55)$$

By comparison, from the heating effect, using (44), we have

$$\left. \frac{d(I_c/I_{c0})}{dV_1^2} \right|_{\text{therm.}} = - \frac{1}{P_0} \frac{dP}{dV_1^2} = - \frac{1}{2RP_0} \quad (56)$$

Taking the ratio, we find

$$\frac{\delta I_c|_{\text{therm.}}}{\delta I_c|_{\text{Jos.}}} = \frac{1}{2RP_0} \left(\frac{\hbar\omega_1}{e} \right)^2 \quad (57)$$

so that the crossover occurs for

$$\hbar\omega_1 \approx e(2RP_0)^{1/2} \quad (58)$$

Neglecting local variations of ρ due to size effect, this $\hbar\omega_1$ scales with $kT_c [\xi(0)/\Omega r_1]^{1/2}$. Taking our characteristic value of $P_0 = 10 \mu\text{W}$ and $R = 10 \Omega$, one finds the crossover at $\frac{\omega}{2\pi} = \nu \approx 3\text{THz}$, or $\lambda \approx 100 \mu\text{m}$. That is, for $\nu > 3\text{THz}$ or $\lambda < 100 \mu\text{m}$, we expect the bolometric mixing of two carriers to produce a low frequency beat to be more efficient than the mixing by the intrinsic non-linearity of the Josephson effect. For the specific case of $10 \mu\text{m CO}_2$ laser radiation in a 10Ω junction, we expect the bolometric effect to be $\sim 10^2$ times as important. Of course the bolometric mixing does not have the capability for high-order mixing that is provided by the extraordinarily complex non-linearity of the Josephson effect.

b) We now address the question of the thermal response time τ which will limit the beat frequency for which the thermal mixing is effective. As noted above, most of the power is dissipated between r_1 and $2r_1$, which, for the small contacts of interest here, is typically a distance small compared to $\xi(T_b)$ or to $r(T_c)$. Thus, we can think of the temperature modulation as arising by thermal diffusion outward from a localized source at the center which is supplying heat modulated at ω_b . Since $P = 0$ except at the center, the heat flow is governed by

$$D\nabla^2 T = \frac{\partial T}{\partial t} \quad (59)$$

where $D = K/C = \frac{1}{3} v_F \ell$ is the electronic thermal diffusion coefficient. (We presume as above that energy conversion to phonons does not occur fast enough to be very important.) Taking an $e^{i\omega t}$ time-dependence, and considering only radial flow, (59) becomes

$$\frac{d^2}{dr^2} (rT_\omega) = \frac{i\omega}{D} (rT_\omega) \quad (60)$$

so that

$$T_\omega \propto \frac{1}{r} e^{-r/\delta} e^{i(\omega t - r/\delta)} \quad (61)$$

where

$$\delta = (2D/\omega)^{1/2} \quad (62)$$

In other words, the rolloff frequency for temperature modulation to a distance δ is

$$\omega_{b, \text{rolloff}} = \frac{2D}{\delta^2} \approx \omega_g(0) \frac{\xi^2(0)}{\delta^2} \quad (63)$$

where in the second form we have used the fact that in dirty superconductors, $\xi^2(T) = D\tau_{GL} \approx 2D/(1-t)\omega_g(0)$. For thermal mixing to be fully effective, δ must at least exceed $\xi(T_b)$, and in the case of strong heating, it must exceed $r(T_c) \approx (P/P_0)\xi(T)$. Thus, $\omega_{b, \text{rolloff}}$ should be highest if the local oscillator power is kept low enough ($\leq P_0$) to reduce I_c only moderately, and it should fall roughly as $(P_0/P)^2$ for $P > P_0$. For $P < P_0$, we can take $\delta \approx \xi(T_b)$ and (63) becomes

$$\omega_{b, \text{rolloff}} \approx \omega_g(0)(1-t) \approx 2/\tau_{GL} \quad (64)$$

Thus we reach the somewhat surprising conclusion that the energy

gap sets the scale for the maximum beat frequency in this bolometric mixing mode. The observations of beat signals of two CO_2 lasers by McDonald et al⁹ confirm the observability of beats up to at least $106 \text{ GHz} \approx v_g(0)/6$, but these measurements were not sufficiently extensive or systematic¹⁹ to set quantitative limits on the attainable performance. However, since the zero-voltage step was said to be nearly suppressed, the power level presumably exceeded P_0 by a considerable margin, so that a reduced rolloff frequency would be expected, as explained above. These very high rolloff frequencies of order the gap frequency make experimental tests difficult, but they suggest that one could make an extremely wide-band IR superheterodyne receiver using this bolometric mixing to obtain a wideband IF frequency, and using the true Josephson effect only for harmonic generation and frequency mixing in this microwave IF range.

CONVENTIONAL VTB GEOMETRY

Although our collinear-cone model of a hyperbolic neck should be quite appropriate for a point contact or a very short variable thickness bridge (VTB), it is important to consider also the case of the conventional VTB geometry in which a thin narrow bridge of cross sectional area $A = wd$ and length L connects two very thick banks. At low power levels, the whole structure is below T_c . At intermediate power levels, more and more of the bridge is above T_c . And at the high power levels of most interest to us here, the entire bridge is above T_c , and the region above T_c expands radially outward into the banks from

the ends of the bridge. In this latter case, the situation is close to the 3-dimensional problem treated in detail in the earlier part of this paper, with $\Omega \approx \pi$ fixed by the vertical bank at the end of the bridge. (It would be $\Omega = 2\pi$, giving better performance, if the bank went below the bridge as well as above.) The effect of the non-zero length of the bridge is essentially to add another contribution to the WKB integral W defined in (37). We can get an upper bound by taking the whole length of the bridge to have the maximum temperature T_m , which actually occurs only at the center of the bridge. Then, setting $T_m/T_c = t_m$,

$$W_{\text{bridge}} \lesssim \frac{L}{2\xi(0)} (t_m - 1)^{\frac{1}{2}} \quad (65)$$

and I_c is reduced by an additional factor $e^{-2W_{\text{bridge}}}$.

To compute T_m accurately for a given power dissipation, one must take account of the spatial distribution of the dissipated power. Because of the excess quasiparticle population generated by the dissipation, we treat the material in and near the bridge as having normal resistive properties, as we did in Section II. In that case, one finds in the bridge a parabolic profile of T^2 with a maximum in the center identical to (17), except that T_b is replaced by T_b' , the bank temperature at the end of the bridge, and V is the voltage across the bridge. Combining this result with the temperature gradient due to the radial heat flow into the banks, one finds that (17) is recovered. That is

$$T_m = \left[T_b^2 + 3 \left(\frac{eV}{2\pi k} \right)^2 \right]^{1/2} \quad (66)$$

still holds, with V now the total voltage across bridge plus spreading resistance. This example illustrates the generality of (17), so long as one can neglect surface heat transfer.

Inserting (66) in (65), and taking the limiting form for $eV \gg kT_c$, we find

$$2W_{\text{bridge}} \leq \frac{L}{\xi(0)} \frac{3^{1/4}}{\sqrt{2}} \left(\frac{eV}{\pi k T_c} \right)^{1/2} \quad (67)$$

For comparison, the radial contribution (43) can be written in terms of $r_1/\xi(0)$ as

$$2W_{\text{radial}} = \frac{P}{P_0} \approx \frac{r_1}{\xi(0)} \frac{3}{\sqrt{2}} \left(\frac{eV}{\pi k T_c} \right)^2 \quad (68)$$

specializing for simplicity to $t_b = 0$. The physical reason for these differing forms is quite evident: the bridge contribution comes from a fixed length L , the weak dependence on V coming from the increasing temperature making the bridge harder for the pairs to penetrate. The radial contribution comes from a normal length which scales up from r_1 in proportion to the power dissipated $\propto V^2$. Since the ratio of the two terms is

$$\frac{W_{\text{radial}}}{W_{\text{bridge}}} \approx \frac{3^{3/4} r_1}{L} \left(\frac{eV}{\pi k T_c} \right)^{3/2} \quad (69)$$

we see that W_{rad} will dominate for $eV > \pi k T_c \sqrt{2\Delta(0)}$, unless $L \geq 2r_1$. For the voltage limits discussed earlier, $(eV/\pi k T_c) \sim 5-10$, so the radial part dominates unless $L \geq 20 r_1$. (In these

expressions, it is a reasonable approximation to determine r_1 by setting $\pi r_1^2 = wd$, the cross sectional area of the bridge, at least if w and d are not too different. If $d \ll w$, the initial spreading into the banks is 2-dimensional, and a different analysis is required.) Thus, the voltage limits found earlier should apply quite well for the conventional VTB geometry as well as for the purely radial geometry treated above in more detail. However, the initial heating effects at lower voltages will be modified significantly unless $L \ll \xi(0)$.

CONCLUSIONS

In this paper we have treated the non-equilibrium effects limiting the performance of metallic Josephson devices in a simple electronic heating approximation. The calculations have been carried out in detail for the case of 3-dimensional metallic cooling in solid angle Ω , but the extension to the conventional VTB geometry is sketched also. We found that the temperature in the center of the junction with voltage V applied is $T_m \approx [T_b^2 + 3(eV/2\pi k)^2]^{1/2}$, which can be as high as 70K in a Nb point contact showing microwave-induced steps to 17mV. Although T_m is independent of details, the spatial extent of the hot region is reduced if the neck is small, which favors tiny high resistance links. The device noise temperature is expected to be $T_N \approx \frac{1}{2}(T_b + T_m)$, which can greatly exceed T_b .

The major effect of this increased temperature, however, is the reduction of I_c . At high power levels, we find I_c to fall as e^{-P/P_0} , where P is the power dissipated and P_0 [given by

(45)] scales with $T_C^2 \xi(0) \Omega / \rho_0$, and turns out to be $\sim 10 \mu W$ for Al, Sn, Pb, and Nb, but much smaller for Nb_3Sn . This prediction of the model gives a good account of the reduction in amplitude of high-order microwave-induced steps observed by Octavio et al. in tin microbridges, with a limit of 3.7mV as shown in Fig. 2. Coupled with the extra noise associated with the increased T_N , the reduction of I_C leads to a determination of the maximum voltage (51a) at which steps can be observed for a given material if the junction resistance has its optimum value (51b). In particular, the simple proportionality of V_{max} to T_C is modified by transport properties so as to favor materials with high electronic conductivity, and there is also a weak frequency dependence.

Finally, we have estimated that for low beat frequencies the bolometric mixing due to temperature modulation of the junction should be more effective than true Josephson mixing for carrier frequencies greater than $\sim 3 THz$. Moreover, the characteristic relaxation time should be of order τ_{GL} , so this response should be available for beat frequencies up to the order of the gap frequency.

ACKNOWLEDGEMENT

This research was supported by the Advanced Research Projects Agency of the Department of Defense under Contract No. MDA903-76C-0250 with The University of Michigan.

References

1. V. Ambegaokar and A. Baratoff, Phys. Rev. Letters 10, 486 (1963); 11, 104 (1963).
2. L. G. Aslamasov and A. I. Larkin, JETP Letters 9, 87 (1969).
3. The form quoted here is that for a tunnel junction between two identical superconductors. The AL result (Ref. 2) for constrictions is exactly the same near T_C , and is derived under the assumption that $\ell \ll a \ll \xi$, where ℓ is the mean free path, a is the neck radius, and ξ is the coherence length. If these assumptions are not satisfied, the result may not be exact. Also, the temperature dependence may not be exactly the same at lower temperatures.

P. L. Richards, Semiconductors and Semimetals, Vol. 12, Infrared Detectors (II), Willardson and Beer, Eds. McGraw-Hill, New York (1976).
5. W. C. Stewart, Appl. Phys. Lett. 12, 277 (1968); D. C. McCumber, J. Appl. Phys. 39, 3113 (1968).
6. W. J. Skocpol, M. R. Beasley, and M. Tinkham, Rev. Phys. Appl. 9, 19 (1974); J. Appl. Phys. 45, 4054 (1974).
7. M. Octavio, W. J. Skocpol, and M. Tinkham, Proc. 1976 Applied Superconductivity Conference, Stanford University, to appear.
8. D. G. McDonald, V. E. Kose, and K. M. Evenson, Appl. Phys. Letters 15, 121 (1969).
9. D. G. McDonald, F. R. Peterson, J. D. Cupp, B. L. Danielson, and E. G. Johnson, Appl. Phys. Letters 24, 335 (1974).
10. A similar comment has been made by I. K. Yanson, Sov. J. Low Temp. Phys. 1, 67 (1975).
11. R. Holm, Electric Contacts, Springer-Verlag, Berlin, 1967, p. 31; F. Kohlrusch, Ann. Physik Leipzig 1, 132 (1900).
12. O. Iwanyshyn and H. J. T. Smith, Phys. Rev. B6, 120 (1972).
13. W. J. Skocpol, M. R. Beasley, and M. Tinkham, J. Low Temp. Phys. 16, 145 (1974).
14. M. Tinkham, Introduction to Superconductivity, McGraw-Hill, New York, 1975, p. 109.

15. J. E. Zimmerman, Proc. 1972 Appl. Supercond. Conf., IEEE Conf. Rec. No. CHO 682-5-TABSC, 544 (1972).
16. T. G. Blaney and C. C. Bradley, J. Phys. D. 5, 180 (1972).
17. V. Ambegaokar and B. I. Halperin, Phys. Rev. Lett. 22, 1364 (1969).
18. M. J. Stephen, Phys. Rev. 182, 531 (1969); 186, 393 (1969).
19. D. G. McDonald, private communication.

MOLECULAR DIPOLAR PYROELECTRICITY

W. H. Flygare

INTRODUCTION

Pyroelectricity is associated with the temperature dependence of the polarization in a permanently polarized material. Of course, the most convenient material is a solid but pyroelectric behavior can certainly be associated with liquids or gases as well. Normally, pyroelectric behavior is associated with solids where the polarization is frozen in and persists in the absence of the field. Pyroelectric materials are often associated with ferroelectric and piezoelectric materials. A ferroelectric material is composed of permanently polarized domains; if the domains are aligned the system will then be pyroelectric. In a piezoelectric material the polarization is changed by application of strain in the material. If the material is permanently polarized it can exhibit both piezoelectric and pyroelectric behavior.

In the case of ionic crystals which are pyroelectric, there are normally several near-equal energy positions for a particular ion (usually positive ions are more mobile). One of these positions which can be induced in the presence of an electric field (or some other poling effect) will lead to a permanent polarization by lowering the temperature in the

presence of the electric field. Pyroelectric coefficients range as high as $(dE/dT)_{E=0} = 2$ (barium titanate, BaTiO_3 (ceramic)) in units of 10^{-4} (coulomb/m²°K) where E is the electric depolarizing field due to the increase in temperature. Early theories of pyroelectricity were described by Adams in terms of the permanent orientated dipole moments called electrets² by analogy to permanent magnets.

More recently, several polymeric systems have been studied which show a spontaneous polarization when poled in an electric field. The most often studied system is polyvinylidene fluoride which apparently crystallizes in two forms, the lower temperature phase having orientated dipole moments and a resultant pyroelectric effect³ with a temperature stable coefficient in the range of 10^{-4} coulomb/m²°K.

In this paper we suggest that pyroelectric materials may be made by fast cooling of a viscous liquid (or solution) of dipolar molecules under the influence of an orientating electric field. Other possible techniques of fixing the molecular dipolar polarization might include some polymeric matrix such as epoxy where the solidification takes place under the influence of the external field. In the absence of the field, the polarization remains and the temperature dependence gives the pyroelectric effect.

In the next section we review Onsager's theory of electric moments of molecules in liquids in order to apply the theory to the pyroelectric effect. Following that we develop a

quantum mechanical model for the temperature dependence of the polarization of a system of cylindrically symmetric molecules in the liquid state which depends on the thermal excitation of librational energy levels of the molecule trapped in a cylindrically symmetric potential. The dipole moment along the directing axis will be different in the different librational states leading to the pyroelectric effect.

THE ELECTRIC POLARIZATION OF DIPOLAR MOLECULES IN LIQUIDS

We start by defining a few basic equations governing polarization and internal fields. Let \underline{E}_0 be the applied external field and \underline{E} be the field in the uniform medium which we are examining. Now, according to Maxwell's equation we can write

$$\begin{aligned}\epsilon \underline{E} &= \underline{E} + 4\pi \underline{P} \\ \underline{P} &= \frac{\epsilon - 1}{4\pi} \underline{E} \quad , \quad (1)\end{aligned}$$

where ϵ is the low frequency dielectric constant and \underline{P} is the polarization of the medium. The relationship between \underline{P} and measured depolarizing field, \underline{E}_p , depends on the geometry of the experiment". For a thin slab of material where \underline{P} is perpendicular to the flat surface of the slab, we have

$$\underline{E}_p = 4\pi \underline{P} \quad (2)$$

Similarly, we note that for the same geometry, if an applied field is \underline{E}_0 , the field in the slab is reduced according to

$$\underline{E} = \frac{1}{\epsilon} \underline{E}_0 \quad (3)$$

The field tending to orientate a dipolar molecule in the medium is called the local field. We will now examine the nature of the local field. Now, the uniformity of the dielectric is broken by the presence of a dipolar molecule which creates a cavity in the medium. The field at the center of a spherical cavity, \underline{E}_{sc} , is given by⁴

$$\underline{E}_{sc} = \frac{4\pi}{3} \underline{P} \quad (4)$$

Debye⁵ assumed that the local field, \underline{F} , was the sum of \underline{E} with \underline{E}_{sc} to give

$$\underline{F} = \underline{E} + \frac{4\pi}{3} \underline{P} = \underline{E} + \left(\frac{\epsilon - 1}{4\pi} \right) \frac{4\pi}{3} \underline{E} = \left(\frac{\epsilon + 2}{3} \right) \underline{E} \quad (5)$$

which is called the Debye-Lorentz spherical cavity local field.

Onsager's theory of electric moments of molecules in liquids is a more complete theory.⁶ Onsager writes the local field as a sum of a cavity field, \underline{G} , which tends to orientate the dipole in the cavity and a reaction field, \underline{R} , which is parallel to the dipole moment. \underline{R} is the field acting on the dipole moment as a result of the electric displacements due to its own presence.

$$\underline{F} = \underline{G} + \underline{R} \quad (6)$$

In the case of a spherical cavity, Onsager has shown that

$$\underline{F} = \frac{3\varepsilon}{2\varepsilon+1} \underline{E} + \frac{2(\varepsilon-1)}{(2\varepsilon+1)r^3} \underline{m} \quad (7)$$

where r is the radius of the cavity and the total molecular dipole moment, \underline{m} , is then given by

$$\underline{m} = \underline{\mu}_0 \underline{U} + \alpha \underline{F} \quad (8)$$

where $\underline{\mu}_0$ is the permanent moment of the cylindrically symmetric dipolar molecule, \underline{U} is the unit vector in the dipole direction, and α is the scalar polarizability of the molecule. Substituting Eq. (7) into Eq. (8) gives

$$\underline{m} = \underline{U} \underline{\mu}_0^* + \frac{3\varepsilon\alpha \underline{E}}{(2\varepsilon+1) - 2(\varepsilon-1)\alpha/r^3}$$

$$\underline{\mu}_0^* = \underline{\mu}_0 \left[\frac{(2\varepsilon+1)r^3}{(2\varepsilon+1)r^3 - 2(\varepsilon-1)\alpha} \right] \quad (9)$$

The force couple and resultant potential energy, ω , is used to calculate the average value of \underline{m} :

$$\langle \underline{m} \rangle = \frac{\int_0^{2\pi} \int_0^\pi \underline{m} e^{-\omega/kt} \sin\theta \, d\theta d\phi}{\int_0^{2\pi} \int_0^\pi e^{-\omega/kt} \sin\theta \, d\theta d\phi} \quad (10)$$

Consider the force couple:

$$\underline{\tau} = \underline{F} \times \underline{m} = \underline{G} \times \underline{m} = \underline{\mu}_0^* \underline{G} \times \underline{U}$$

$$\tau = \underline{\mu}_0^* G \sin\theta \quad (11)$$

where we have recognized that \tilde{G} is parallel to \tilde{E} . Remembering that the torque is given by $\tau = d\omega/d\theta$, where ω is the orientational energy, leads to

$$\omega = -\mu_0^* \tilde{G} \cos\theta = -\left(\frac{3\epsilon}{2\epsilon+1}\right) \mu_0^* \tilde{E} \cos\theta \quad (12)$$

Substituting Eqs. (9) and (12) into Eq. (10) gives

$$\begin{aligned} \langle m \rangle &= \mu_0^* L(x) + \frac{3\epsilon\alpha\tilde{E}}{(2\epsilon+1)-2(\epsilon-1)\alpha/r^3} \\ L(x) &= \frac{d}{dx} \log(e^x - e^{-x}) - \frac{d}{dx} \log x = \coth x - \frac{1}{x} \\ x &= \left(\frac{3\epsilon}{2\epsilon+1}\right) \mu_0^* \tilde{E}/kt \end{aligned} \quad (13)$$

where $L(x)$ is the Langevin function. Now normally we can use

$$\begin{aligned} \lim L(x) &= \left(\frac{3\epsilon}{2\epsilon+1}\right) \frac{\mu_0^* \tilde{E}}{3kT} \\ \left(\frac{3\epsilon}{2\epsilon+1}\right) \frac{\mu_0^* \tilde{E}}{kt} &\ll 1 \end{aligned} \quad (14)$$

which gives

$$\langle m \rangle = \left(\frac{3\epsilon}{2\epsilon+1}\right) \frac{(\mu_0^*)^2}{3kt} \tilde{E} + \frac{3\epsilon\alpha\tilde{E}}{(2\epsilon+1)-2(\epsilon-1)\alpha/r^3}, \quad (15)$$

and the polarization is given by

$$\begin{aligned} \tilde{P} &= \rho_0 \langle m \rangle = \left[\left(\frac{3\epsilon\rho_0}{2\epsilon+1}\right) \frac{(\mu_0^*)^2}{3kt} + \frac{3\epsilon\rho_0\alpha}{(2\epsilon+1)-2(\epsilon-1)\alpha/r^3} \right] \tilde{E} \\ &= \rho_0 \tilde{E} \left[\frac{3\epsilon}{(2\epsilon+1)-2(\epsilon-1)\alpha/r^3} \left[\frac{\mu_0 \mu_0^*}{3kt} + \alpha \right] \right] \end{aligned} \quad (16)$$

Now if we also use Onsager's estimate for

$$r^3 = \frac{n^2+2}{n^2-1} \alpha \quad (17)$$

where n is the optical refractive index, we have

$$P = \rho_0 E \epsilon \left(\frac{n^2+2}{n^2+2} \right) \left[\frac{\mu_0 \mu_0^*}{3kt} + \alpha \right] = \frac{3\rho_0 E \epsilon}{(2\epsilon+1)} \left[\frac{(\mu_0^*)}{3kt} + \alpha^* \right]$$

$$\frac{\mu_0^*}{\mu_0} = \frac{(2\epsilon+1)(n^2+2)}{3(n^2+2\epsilon)} = \frac{\alpha^*}{\alpha} \quad (18)$$

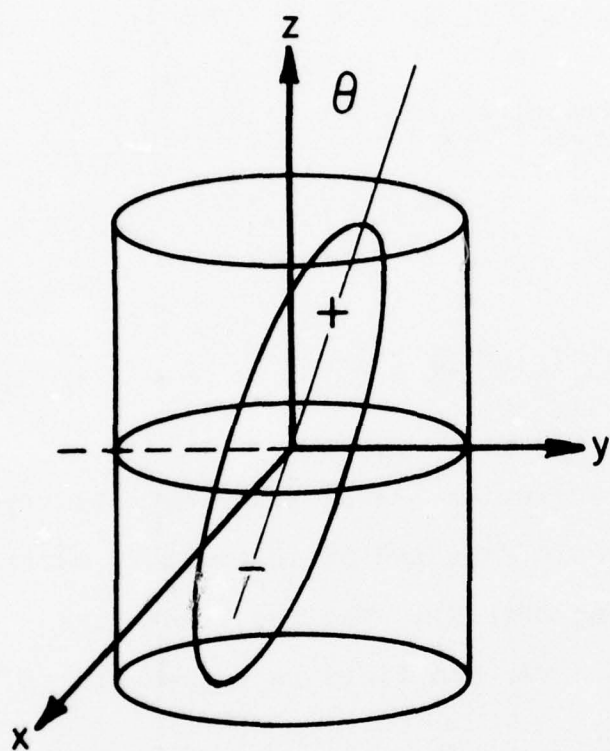
We now assume that the polarization can be fixed by solidifying the liquid either by rapid freezing or in an epoxy matrix (or other suitable hardening matrix). The resultant fixed polarization which remains after the field is turned off is given by

$$P_f = \rho_0 E_f \epsilon \left(\frac{n^2+2}{n^2+2\epsilon} \right) \left[\frac{\mu_0 \mu_0^*}{3kt_f} + \alpha \right] \quad (19)$$

where E_f is the field present when the dipoles were hardened (or fixed) and T_f is the temperature at which the fixing took place.

FLUCTUATING DIPOLES AND THE TEMPERATURE DEPENDENCE

Consider now the dipole moment of the frozen dipole in the polarized medium. Consider the cylindrically symmetric molecule with a cylindrical axis dipole in a cylindrical potential.



$$V(\theta) = \frac{V_2}{2} (1 - \cos 2\theta)$$

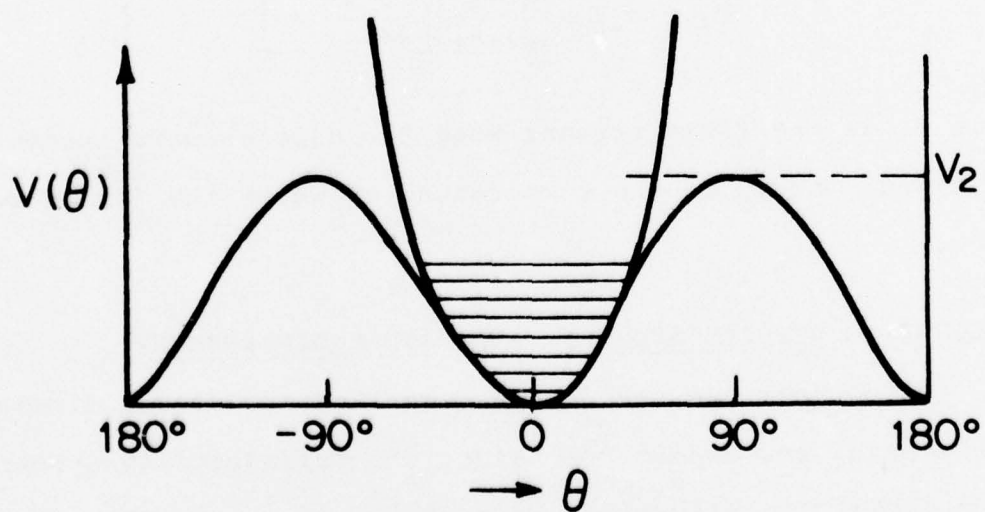


Figure 1.

The potential function can be expanded about $\theta=0$ if the barrier height is high to give

$$V(\theta) = \frac{V_2}{2}(1-\cos 2\theta) = \frac{V_2}{2} 1 - (1 - \frac{(2\theta)^2}{2} + \dots) \\ \approx \theta^2 V_2 \quad (20)$$

For small angles we can also see from Fig. 1 that

$$\sin \theta \approx \theta = 2y/r \quad (21)$$

where r is the length of the cylindrical molecule. Substituting Eq. (21) into Eq. (20) gives

$$V(\theta) = \frac{4y^2}{r^2} V_2 = \frac{1}{2} \left(\frac{8V_2}{r^2} \right) y^2 = \frac{1}{2} k y^2 \quad (22)$$

where $k = 8V_2/r^2$ is the effective harmonic force constant. The resultant energy spacings of a harmonic oscillator are

$$E_n = \hbar \sqrt{\frac{k}{\mu}} (n + \frac{1}{2}) \\ = \hbar \sqrt{\frac{8V_2}{\mu r^2}} (n + \frac{1}{2}) = \hbar \sqrt{\frac{8V_2}{I}} (n + \frac{1}{2}) \quad (23) \\ n = 0, 1, 2, \dots$$

where n is the harmonic oscillator state and $\mu r^2 = I$ is the molecular moment of inertia perpendicular to the molecular symmetry axis.

We now refer again to Fig. 1 and note that the average alignment of the dipole moment along the z axis will depend on the vibrational state according to

$$(\mu_z)_n = \mu_0 \cos \left(\frac{\langle 4Y^2 \rangle_n}{r^2} \right)^{\frac{1}{2}} \quad (24)$$

where $\langle Y^2 \rangle_n$ is the average value of the displacement, y , in the n^{th} vibrational state.

$\langle Y^2 \rangle_n$ can be evaluated according to the virial theorem:

$$\begin{aligned} H &= \frac{1}{2\mu} p^2 + \frac{1}{2} k y^2 = T + V \\ T_{nn} &= V_{nn} \\ E_n &= T_{nn} + V_{nn} = \hbar \sqrt{\frac{8V_2}{I}} (n + \frac{1}{2}) \\ \frac{1}{2\mu} \langle p^2 \rangle_n &= \frac{1}{2} k \langle Y^2 \rangle_n \end{aligned} \quad (25)$$

Thus,

$$4 \frac{\langle Y^2 \rangle_n}{r^2} = 4 E_n / k r^2 = \frac{E_n}{2V_2} = \hbar \left(\frac{2}{V_2 I} \right)^{\frac{1}{2}} (n + \frac{1}{2}) \quad (26)$$

Substituting into Eq. (24) gives

$$(\mu_z)_n = \mu_0 \cos \left\{ \hbar \left(\frac{2}{V_2 I} \right)^{\frac{1}{2}} (n + \frac{1}{2}) \right\}^{\frac{1}{2}} \quad (27)$$

Substituting this expression into Eq. (19) gives the polarization for the n^{th} librational state. The total polarization involves a Boltzmann weighted sum over all thermally occupied librational states:

$$\begin{aligned} P_f &= \rho_0 E_f \epsilon \left(\frac{n^2 + 2}{n^2 + 2\epsilon} \right) \left[\alpha + \frac{\mu_0 \mu_0^*}{3kT_f} \Gamma \right] \\ \Gamma &= \frac{1}{Q} \sum_{j=0}^{\infty} e^{-j h \nu / kT} \cos^2 \left[\hbar \left(\frac{2}{V_2 I} \right)^{\frac{1}{2}} (n + \frac{1}{2}) \right]^{\frac{1}{2}} \end{aligned}$$

$$= \left(\frac{1}{1-e^{-B}} \right) \sum_{j=0}^{\infty} e^{-jB} \cos^2 [\gamma(j+\frac{1}{2})]^{\frac{1}{2}}$$

$$B = \hbar\omega/kT = \frac{\hbar}{kT} \sqrt{\frac{8V_2}{I}}$$

$$\gamma = \hbar \left(\frac{2}{V-I} \right)^{\frac{1}{2}} \quad (28)$$

where Q is the vibrational partition function. The temperature dependence in P_f will be completely described by Γ .

$$\frac{dP_f}{dT} = \rho_0 E_f \epsilon \left(\frac{n^2+2}{n^2+2\epsilon} \right) \left[\frac{\mu_0 \mu_0^*}{3kT_f} \frac{d\Gamma}{dT} \right]$$

$$\frac{d\Gamma}{dT} = \frac{B}{T} \left(\frac{1}{1-e^{-B}} \right) \sum_{j=0}^{\infty} \left(\frac{1}{1-e^{-B}} + j \right) e^{-jB} \cos^2 [\gamma(j+\frac{1}{2})]^{\frac{1}{2}} \quad (29)$$

Calculated values of Γ for reasonable sets of parameters are shown in Table 1. All numbers shown under $d\Gamma/dT$ converge to three significant figures well below n_B .

We will now estimate dP_f/dT in Eq. (29) for a typical high dipole liquid such as nitrobenzene or cyanoacetylene which have

$$\begin{aligned} \epsilon &\approx 35 \\ n &= 1.5 \\ \rho_0 &\approx 6 \times 10^{21} \text{ molecules/cm}^3 \text{ (in pure liquid)} \\ \mu_0 &\approx 3.8 \times 10^{-18} \text{ esu cm} \end{aligned} \quad (30)$$

Now we also assume

$$E_f = \frac{E_0}{\epsilon} = \frac{1}{\epsilon} 60,000 \text{ v/cm} \approx \frac{1}{\epsilon} \times 200 \text{ esu/cm}^2 \approx 5.7 \text{ esu/cm}^2$$

Table 1. Calculated values of $d\Gamma/dT$ from Eqs. (29) and (28) for $T=300K$ as a function of I and V_2 . We also list the number of librational levels below the barrier given by $n_B \approx (V_2 I / 8\hbar^2)^{1/2}$.

| | | $I (\times 10^{-38} \text{ gr cm}^2)$ | | | | |
|------------------------|---------------------|---------------------------------------|--------|--------|--------|--------|
| $V_2 (\text{cm}^{-1})$ | | 1 | 2 | 4 | 8 | 16 |
| 5,000 | $n_B \approx 35$ | | 50 | 71 | 100 | 141 |
| | $B=0.7071$ | | 0.5000 | 0.3536 | 0.2500 | 0.1768 |
| | $\gamma=0.1414$ | | 0.1000 | 0.0707 | 0.0500 | 0.0354 |
| | $d\Gamma/dT=0.0202$ | | 0.0329 | 0.0568 | 0.1025 | 0.1904 |
| 10,000 | | 50 | 71 | 100 | 141 | 200 |
| | | 1.000 | 0.7071 | 0.5000 | 0.3536 | 0.2500 |
| | | 0.1000 | 0.0707 | 0.0500 | 0.0354 | 0.025 |
| | | 0.0156 | 0.0233 | 0.0379 | 0.0655 | 0.1182 |
| 20,000 | | 71 | 100 | 141 | 200 | 282 |
| | | 1.414 | 1.000 | 0.7071 | 0.500 | 0.3536 |
| | | 0.0707 | 0.0500 | 0.0354 | 0.0250 | 0.0177 |
| | | 0.0125 | 0.0167 | 0.0251 | 0.0408 | 0.0705 |
| 40,000 | | 100 | 141 | 200 | 282 | 400 |
| | | 2.000 | 1.414 | 1.000 | 0.7071 | 0.5000 |
| | | 0.0500 | 0.0354 | 0.0250 | 0.0177 | 0.0125 |
| | | 0.0113 | 0.0130 | 0.0174 | 0.0260 | 0.0423 |
| 80,000 | | 141 | 200 | 282 | 400 | 565 |
| | | 2.828 | 2.000 | 1.414 | 1.000 | 0.7071 |
| | | 0.0354 | 0.0250 | 0.0177 | 0.0125 | 0.0098 |
| | | 0.0117 | 0.0115 | 0.0132 | 0.0177 | 0.0265 |
| 100,000 | | 200 | 282 | 400 | 565 | 800 |
| | | 4.000 | 2.828 | 2.000 | 1.4142 | 1.0000 |
| | | 0.0250 | 0.0177 | 0.0125 | 0.0088 | 0.0063 |
| | | 0.0142 | 0.0119 | 0.0116 | 0.0134 | 0.0179 |

$$T_f = 300K \quad (31)$$

which gives

$$\mu_0^* = \frac{(2\epsilon+1)(n^2+2)}{3(n^2+2\epsilon)} \mu_0 \approx 1.4 \mu_0 \quad (32)$$

$$\frac{dP_f}{dT} = 11.9 \frac{d\Gamma}{dT} \frac{\text{esu}}{\text{cm}^2 \circ K} = \frac{11.9 \times 10^5}{c} \frac{d\Gamma}{dT} \frac{\text{coulomb}}{\text{m}^2 \circ K} = 4.0 \times 10^{-5} \frac{d\Gamma}{dT} \frac{\text{coulomb}}{\text{m}^2 \circ K} \quad (33)$$

Now the observable depolarizing field perpendicular to a thin slab is given by

$$\frac{dE_p}{dT} = 4\pi \frac{dP_f}{dT} = 5.0 \times 10^{-4} \frac{d\Gamma}{dT} \frac{\text{coulomb}}{\text{m}^2 \circ K} \quad (34)$$

Combining this estimate with the values of $d\Gamma/dT$ in Table 1 shows typical values for the pyroelectric effect. It is evident that low barrier (V_2) and high moments (I) will lead to the largest pyroelectric behavior.

Substituting Eq. (3) into Eq. (29) shows that dP_f/dT goes approximately as μ_0^2/ϵ (assuming $\epsilon > n^2$). Thus, systems with large μ_0 and small ϵ are good candidates for large dP_f/dT .

ACKNOWLEDGEMENT

This research was supported by the Advanced Research Projects Agency of the Department of Defense under Contract No. MDA903-76C-0250 with The University of Michigan.

REFERENCES

1. Am. Inst. Phys. Handbook, ed. D. E. Gray (McGraw-Hill Book Co., New York, 1963), p. 9-102.
2. E. P. Adams, J. Franklin Inst. 204, 469(1927).
3. G. Pfister, M. Abkowitz and R. G. Crystal, J. Appl. Phys. 44, 2064(1973). See previous reference on this material in this paper.
4. C. Kittel, Introduction to Solid State Physics, 3rd ed. (John Wiley and Sons, New York, 1967).
5. P. Debye, F. Physik 13, 97(1912).
6. L. Onsager, J. Am. Chem. Soc. 58, 1486(1936).

SUMMARY OF THE MRC WORKSHOP ON NDE

M. Buckley and R. M. Thomson

A workshop was held at the 1976 MRC meeting in La Jolla to explore NDE issues of possible interest to ARPA. Since ARPA already funds a program at the Rockwell Science Center in NDE, our aim was to determine if other NDE areas outside the present project existed which demanded additional attention at this time. After prior discussion, the organizers determined to focus the attention of the workshop on four specific areas, but also to give the participants ample opportunity to bring up additional topics, if it seemed appropriate. The four areas were adhesive bonding and composites, automation in NDE, fatigue life determination of individual parts, and the institutional structure within which NDE activities now exist. We shall review briefly in turn each of these topics as they were addressed by the workshop.

Since the style of the workshop was informal, no written material was developed by the individual participants, so the views stated in the current summary must be considered the responsibility of the authors, though they are intended to represent the general discussion as closely as possible. The material labeled "Conclusions" comprises our own conclusions based on the general discussion at the meeting. The speakers

in each of the sessions are listed in the accompanying program and the total list of non-MRC participants is also included.

NDE FOR ADHESIVE BONDING AND COMPOSITES

Florence and Hagemaiier reviewed the Air Force program to demonstrate the limits of adhesive bonding as a possible replacement for bolts and rivets in primary aircraft archives (PABST). The program is funded at about \$18M per year currently, and is restricted to current NDE techniques. In the course of this work, a number of important areas have been turned up for which no adequate NDE techniques yet exist. These are:

1. Anodized thickness and characterization (2 μ m)
2. Adhesive primer thickness immediately after application (3-10 μ m)
3. Adhesive thickness after bonding (100-400 μ m)
4. Adhesive quality
5. Cohesive bond strength for multi-laminates
6. Moisture intrusion during service
7. Interfacial bond joint corrosion of aluminum in service

NDI R&D Areas - Graphite Epoxy Laminates

Thousands of graphite epoxy laminates have been non-destructively tested by ultrasonic c-scan, low Kv X-ray, thermal neutron, sonic, and liquid penetrant methods. R&D should be performed in the following areas:

- Relate NDT measured void content to mechanical properties such as interlaminar shear strength
- Develop a fabrication inspection technique for quantitative measurement of void content by ultrasonic attenuation
- Develop a fabrication inspection technique for quantitative measurement of resin content by ultrasonic velocity, low Kv X-ray or thermal neutron absorption
- Determine optimum time for application of pressure during cure cycle. Develop feed-back device for controlling temperature or pressure during cure cycle
- Develop a fabrication technique for monitoring degree of cure by electromagnetic capacitance, electrical resistance (ion graphing), or other methods
- Determine effect of cure variables (pressure, temperature, time) on free state resin properties such as viscosity, degree of polymerization, activation energy, etc.
- Develop dye penetrant which can be used to find cracks, delaminations, and porosity but does not contaminate part for repair procedures
- Develop accurate destructive method for measuring void and resin content
- Develop method to measure resin cure state of prepreg material prior to use

- Develop in-service inspection method for measurement of moisture content in laminate structure
- Develop in-service inspection method for measuring extent of aging
- Develop method for measuring fatigue damage
- Develop method for measuring localized stress concentrations
- Determine micromechanical properties of fiber/matrix interface during slow and fast cycle fatigue tests
- Determine frequency for in-service inspection of composites
- Determine NDI methods for evaluating in-service damage to composites
- Determine repair procedures and NDI methods for quality evaluation of repairs.

We were not briefed regarding coordinated R&D programs to pursue new NDE capability in the needed areas for adhesive bonding, but apparently such programs are small in number and not closely coupled to the PABST program. Nevertheless, some of the research areas listed are crucial if adhesive bonding is ever to be an extensively used alternative to mechanical fasteners. In our opinion, substantial NDE applied research and development programs should be organized to explore the technical solutions to these problems, or the true potential of adhesive bonding as visualized in the PABST program probably will not be realized. The Rockwell NDE program contains some overlap with

the PABST program, but there appears to be an excluded middle ground between current practice and advanced research which address the specific Air Force needs.

The composites NDE area is an even more complex problem. However, Kaelbe reported some general results for detection of moisture degradation in composites by means of ultrasonic velocity and attenuation measurements. He then proposed a general approach toward characterizing these materials. Obviously, much research is needed before such a scheme will yield a practical NDE for composites. His outline is included below:

Short Outline for Composite Durability Characterization

Part 1: Analysis of Separated Fiber and Matrix

- a. Obtain and separate uncured prepreg components,
- b. Analyze fiber and matrix surface energies,
- c. Analyze resin chemistry and curing mechanism,
- d. Define curing kinetics and network structure,
- e. Analyze hydrothermal aging effects on network structure.

Part 2: Analysis of Composite Laminate Aging

- a. Obtain composite laminates for aging studies,
- b. Measure kinetics of water diffusion into composite,
- c. Determine interlaminar shear strength versus moisture content,
- d. Determine fracture energy versus moisture content,
- e. Measure dynamic mechanical (NDT) response versus moisture content.

Part 3: Data Analysis and NDT Methodology

- a. Determine relation between strength degradation mechanisms and NDT methodology,
- b. Design NDT experiments and statistical analysis for tracking strength degradation,
- c. Define improved matrix and interface chemistries.

Yee presented results of studies of fracture toughness in composites, an area which has been difficult to define because the failure of a composite is usually much more complex than that in a macroscopically homogeneous material such as a metal or ceramic. Nevertheless, he is able to obtain both rough crack growth thresholds in static tests and fatigue limits. By using acoustic emission, it is possible to obtain relatively smooth curves of damage which integrates both fiber separation and crack growth. However, the general problem of characterizing the failure modes remains wide open still.

Conclusions

We believe that the area of adhesive bonding and composites remains an area where the ultimate forms of useable NDE techniques are yet to be demonstrated. The adhesive bond problem is inherently much simpler than that for entire composites.

For adhesive bonding, from a research point of view, progress is being made in finding methods for characterizing the cohesive strength of a bond layer through tests which detect the state of cure, void content, etc., but the adhesive

strength problem is mostly unknown territory. Hence research being carried out in the Rockwell program in a limited way could well be augmented elsewhere. However, the most crying need appears to be in the middle ground between research and the final application. Attempts should be made in satellite NDE applied research and development programs to solve the specific problems uncovered by the Air Force PABST program. Methods should be found to inject the competence generated in the ARPA-AF program into the PABST program for this purpose.

Currently, quality control in the composites field is primarily a matter of controlling the manufacturing processes, without much reliance on NDE to check the manufactured part. This is to say that NDE for composites is still in a very primitive stage. The cause of the problem is that a quantitative delineation of the failure modes of the material itself is not available, and when one realizes that the general fracture mechanics approach is no longer applicable in a straightforward way to composites, then the magnitude of the problem becomes apparent. This is a problem for the basic research community, at least in part, and a revisit of the basics of the modes of composite failure is badly needed. By and large, the Air Force has turned its attention away from basics to the engineering problems associated with getting composites into flying airplanes, but some of the most fundamental problems remain, and ultimately the reliable and widespread use of composites will require solution of these fundamentals. It may be that a brute

force numerical approach to the stress analysis of flaws will be required, but we should hope that a theoretical model of failure in composites can be developed which will be less arduous in application. In this situation, fundamental NDE developments must go hand in glove with the materials characterization development. For the time being, quality control of the manufacturing processes will remain the central focus, and NDE will have to content itself with such things as checks on the interfacial moisture content, and matrix and fiber quality, without being able to relate these parameters in a quantitative way to the stresses which can be sustained by the part. Furthermore, even these limited NDE accomplishments are still in a rudimentary stage. Thus, NDE for composites is very primitive overall, when compared with the structure mechanics-NDE picture for metals.

AUTOMATION

Ballard listed eight constraints and ten driving forces for automation of NDE. They were:

- Basic NDE equipment constraints variability
- Imprecise NDE standards/calibration
- Inadequate NDE fixturing equipment
- Scarcity of trained NDE and computer-oriented test personnel
- Poor signal-to-noise ratios for some NDE test methods
- High costs of computerized systems

- Cost and difficulty of programming computer for variety of NDE tasks
- Lack of understanding of physics of that method required for automated/computerized NDE

Ten Driving Forces for Automated/Computerized Nondestructive Evaluation

- Switch to 100% testing
- Minimizing human errors
- Assuring total coverage of extended structures
- Matching test/production rates
- Testing in unfavorable environments
- Computer analysis of test data and records keeping
- Enhanced sensitivity and repeatability
- Quantitative rather than qualitative
- Trends, pattern recognition, feedback control
- Correlations with DT/fracture mechanics

Bushnell at Sandia illustrated a sophisticated computerized NDE laboratory arrangement where three PDP 11's were used interchangeably with a range of NDE equipment. Bushnell emphasized the need for a high level computer language capability and for modular peripheral instrumentation in such applications. The Sandia arrangement also featured a hook-up to their central large computer. (With such equipment, they were able to test a block of ATJ graphite, and by computer decide how to cut multiple heat shield shapes from the blank so as to minimize flaw content in the finished parts.) The costs for computerization

were estimated at about \$50K per set up, including the peripherals. According to Bushnell, the guiding principles in computerization of NDE were flexibility, real time data analysis and graphical display of results.

Coleman described an elaborate assembly line quality control center for automated small arms ammunition manufacture in which the entire operation was automated. The overall inspection rate was 20/sec., and during this time a number of specific tests were performed and evaluated.

A similar on-line computerized automatic NDE operation was described by Criscuolo for medium caliber ammunition fuse manufacture. In this case, the sensor was X-rays, and by careful positioning of the part, a number of critical tests of the internal component position and content could be made.

Conclusions

Applications of computers to automate NDE procedures and in overall quality control evaluation represent, in our opinion, probably the major new opportunity for ARPA in this area at the present time. The workshop adequately demonstrated the vastly increased power and speed which computer automation gives to the whole NDE process as it is applied most clearly in manufacturing, but undoubtedly in service applications as well. Computerization solves several limiting problems at once: 1) It provides methods for graphical display and image enhancement, 2) it is fast, 3) it is able to correlate a vast amount of data from several NDE processes

simultaneously, 4) it is able to provide a standardized evaluation based on numerous parallel inputs which is more reliable than the human operator, 5) it can be very cheap for high-volume operations, and 6) it offers the capability of developing certain kinds of "judgement" through the use of adaptive techniques. Thus, computerization is the final key to widespread use of a mature NDE capability, once the research goals of quantifying the physical basis of NDE have borne fruit through the current Rockwell effort.

However, the current institutional structure of NDE (to be further discussed in the next section) is the major roadblock to progress in this direction. By and large, the current NDE industry is equipment manufacture oriented, and does not possess the requisite in house computer and electronics capability. Further, the integration of such vastly disparate fields as the current NDE community and the computer and electronics communities is well beyond the typical NDE company.

Such a situation seems made to order for ARPA intervention, since ARPA has relevant programs in all the requisite technologies and because of the ultimate pay-off to DoD as a whole.

Technically, some of the challenges are pattern recognition by computer, development of small smart instruments for flexible field use, development of modular units for flexibility, development of adaptive techniques based on theoretical

models of flaw criteria, and development of correlative judgments based on a variety of parallel NDE inputs. In the adaptive mode statistical correlations of fracture mechanics criteria for NDE have yet to be explored in the NDE connection. Limitations of computerization should be studied, so that optimum combinations of automated judgement-supplied-by-operator alternatives are understood. Both hardware and software issues are posed and should be integrated into the overall program. A part of this issue is also the stimulation of an integrated private industrial base for NDE.

FATIGUE

The challenge for NDE in the fatigue area is to enable one to move away from relying on statistically determined fatigue life, and instead detect specific flaws in particular parts. If this goal can be accomplished, the average life of fatigue sensitive engine parts can be extended from 2-10 times. One important element in the problem is the moving target on the materials side. The current engine disks being retired are Ni based alloys designed in the 1960's, which form fatigue cracks on the surface, especially near bolt holes, etc. Also, the critical crack size is large, so that NDE must merely be capable of detecting .3cm length flaws, where current penetrants are useful. Thus, in these cases, current NDE technology appears to be adequate to solve the problem. However, current engines (e.g., Pratt & Whitney 101) are already

operating in a more critical engine environment with critical crack sizes in the 300 μ m range, though the cracks are still on the surface. Reliable detection of such cracks is not yet feasible. In addition, future engines are planned to operate in the lower portion of the high temperature creep regime, where grain boundary voids will be nucleated, and internal flaws generated. Also, critical flaw sizes are expected to decrease into the 100 μ m or less range, where flaw detection becomes even more severe. In a programmatic sense, however, the gains to be obtained from a "retirement for cause" philosophy will put tremendous pressure on the NDE community to develop adequate tools.

The NDE technical problem revolves around reliable detection of fatigue cracks. In this case the issue of quantitative NDE becomes crucial. An additional factor is the character of the fatigue cracks themselves, because residual stresses due to both crack growth and cooling close up the faces of the crack and form a contact which is partially transparent to ultrasonic waves. Hence, a quantitative tool must include the specific characteristics of fatigue in the given material.

Conclusions

The application of NDE to the problem of monitoring fatigue in current and future jet engine discs, as well as fatigue generated cracks in other high performance materials, represent probably the most severe challenge to NDE ultra-

sonics science. It follows that the Rockwell program serves as the appropriate foundation for the development of the appropriate background capability and knowledge. Although the main action is likely to be in ultrasonics, in those cases where surface flaws are concerned, other techniques (e.g., eddy current) should be explored for augmentation of ultrasonic testing.

NDE INSTITUTIONAL QUESTIONS

NDE should be considered as a very broad group of activities which cover the whole gamut of physical monitoring of the state of materials in all stages of manufacture and in maintenance. It is also closely allied to monitoring the condition of whole systems and to quality control in general because the techniques in use are often similar, and NDE is in fact a subset of that larger problem. As such, NDE is an area of enormous importance and leverage to DoD. The Air Force alone spent 6½% of the total expenditures for F-111 airplanes on NDE (this ratio is growing for later purchases) and currently spends 15% of its total budget on maintenance. In addition, there are certain areas where NDE is the crucial limiting element in important Air Force goals, as for example in detection of fatigue cracks in high time air frames, and in the attempt to go over to a massive use of adhesive bonding in primary air frame structures. Hence, the health and viability of the ongoing scientific base which serves NDE must be considered as a

long term and significant DoD wide concern. Likewise, the institutional framework which supports and interconnects the diverse activities of NDE is a major concern, especially as the whole field of NDE is now in a state of fast development and flux. It thus seemed appropriate to explore institutional needs and roadblocks at this workshop.

A number of topics were discussed, including the desirability for an, or several, centers dedicated to NDE. As stated by D. Thompson, the reasons for establishing a center are:

- Nature of R&D for NDE is highly thrust oriented,
- Many if not most of the problems require an interdisciplinary involvement,
- R&D can be more efficiently applied.

He sees the requirements for such a center to be as follows:

Requirements of an NDE Center

- Input Function - Should develop and maintain contact with DoD systems planners, systems contractors, field installations for problem definition and prioritization.
- Vertical Integration - Should be capable of performing the necessary RD&E in an integrated, interdisciplinary way along project lines. Appropriate admixtures of RD&E must be defined by the project area - some will be more basic and heavily materials related, and some will be more developmental and engineering related.

- Output Function - Should develop and maintain close coordination and planning with various service manufacturing technologies for effective transfer of results to practice.
- "Core" R&D should be primarily funded by ARPA, product engineering should be primarily funded by manufacturing technology groups.

Much discussion of various types of center followed with various advocates speaking for private corporation, government contract center, university, Not-for-profit, and civil service laboratory. Each mode would serve a different constituency and somewhat different function. Some opinion was expressed that NDE would be better served by a dispersed base because the future applications of NDE will far transcend DoD, and that all the sectors (universities, private industry, etc.) have legitimate roles to play.

Since the current NDE industry is fragmented, with 200 companies in the field with sales of about \$200M in hardware, little industrial support of research is to be expected. Hence, at least for the time being, government, and DoD in particular, will remain the primary source of research support.

A second major theme of the discussion was introduced by Brinkman with the observation that NDE is not in essence a discipline, but a service. That is, NDE is the satisfaction of some kind of quality assurance question, either during manufacture or in use.

From this point of view, the NDE industry is not organized properly, because very few companies offer a complete NDE service. With a few important exceptions, private companies in NDE are primarily organized to sell hardware of various types instead of the total service. The inference from this argument is that if the industry were organized on a service basis, and the users were accustomed to purchase a total NDE service, then the focus would shift from the present fragmented NDE picture to a more integrated one. In the latter case, the provider of an NDE service would have to integrate a non-destructive test procedure into a total evaluation, and would at the same time be highly motivated to optimize his instrumentation, including computerization as discussed earlier, for a wide range of applications. Such an operation would also have the advantage of consolidating NDE know-how so that tricks used in one application would quickly be transferred to others.

The nuclear industry is now moving in this direction. Nuclear power reactors are serviced by specialized NDE companies who are brought in during the construction phase, and remain responsible for continuing in-service monitoring. Current DoD practice is not oriented in this direction, but rather leaves the NDE entirely in the hands of the prime contractor, once specifications are set. We note again that the proposed type of NDE industrial base would have every incentive to automate and computerize its operations in the interest of overall efficiency, and with the economic drives in this di-

rection should waste no time in bringing together the necessary interdisciplinary teams to do so.

CONCLUSION

We take no specific position on the desirability of a centralized NDE center. In our opinion, there are several ways of serving the functions intended for such a center. We do take a strong position, however, on the need to stabilize the research base in this field. We believe that ARPA and the Air Force have demonstrated remarkable leadership in establishing the AF/ARPA Rockwell project. The Rockwell project shows every evidence of serving as a model for future research ventures in NDE, and it should be allowed to achieve a reasonable maturity. In our opinion the Rockwell project has had excellent success in upgrading the level of basic research in this field by colonizing research in allied fields, which in turn has begun to make NDE a respectable field of research in such areas as physics, mechanics, metallurgy, and electrical engineering. We believe ARPA should remain active in the funding picture until other agencies, especially other DoD funding agencies, have responded with adequate programs of their own.

We are intrigued with the advantages that a fully integrated service oriented NDE industry would offer. Although we were not able to consider fully all the important impacts such a development would have on DoD, the apparent advantages appear sufficiently attractive, and possibly important, that

the subject should be studied further.

ACKNOWLEDGEMENT

This research was supported by the Advanced Research Projects Agency of the Department of Defense under Contract No. MDA903-76C-0250 with The University of Michigan.

CONFERENCE ON NON-DESTRUCTIVE EVALUATION

PROGRAM SCHEDULE

July 8, 9, 1976

Introductory Remarks - R. Thomson

Current ARPA-AF Program in NDE
M. Buckley and D. Thomson

NDE for Adhesive Bonding and Composites
W. Yee, J. Florence, D. Hagemaiier

Automation in NDE
D. Ballard, J. Bushnell, W. Coleman, D. Green

Fatigue Detection
W. Reimann, C. Wells, R. Johnson, R. B. Thompson

Institutional Issues in NDE
R. Thomson, D. Thompson, R. Anderson, D. Ballard,
E. Criscuolo, G. Darcy, P. Packman, D. Waidelich,
M. Buckley

PARTICIPANTS AND GUESTS

Robert T. Anderson
ASNT
3200 Riverside Dr.
Columbus, Ohio 43220

D. W. Ballard
Sandia Laboratories
Albuquerque, New Mexico 87115

John Brinkman
U.S. Army Armament Command
Rock Island, Illinois 61201

Michael J. Buckley
AFML/LLP
Wright-Patterson AFB
Dayton, Ohio 45433

J. D. Bushnell
Sandia Laboratories
Albuquerque, New Mexico 87115

Edward L. Criscuolo
Naval Surface Weapons Ctr.
Building 70
Silver Spring, Maryland 20910

W. J. Coleman
Battelle-Northwest
Richland, Washington 99352

Jamie M. Florence
AFFDL/FBA
Wright-Patterson AFB
Dayton, Ohio 45433

Donald J. Hagemaiier
Douglas Aircraft Co.
3855 Lakewood Blvd.
Long Beach, California

Richard E. Johnson
U.S. Air Force Materials Lab.
AFML/LLN
Dayton, Ohio 45433

David H. Kaelble
Rockwell International
Science Center
1049 Camino Dos Rios
Thousand Oaks, California 91360

Paul Packman
Vanderbilt University
Box 3245
Nashville, Tennessee

Charles Rau
Failure Analysis Associates
Palo Alto, California 94304

Walter H. Reimann
USAF/AFML
Dayton, Ohio 45433

William R. Scott
Naval Air Development Ctr.
Warminster, Pennsylvania 18974

R. Bruce Thompson
Rockwell International
Science Center
1049 Camino Dos Rios
Thousand Oaks, California 91360

D. O. Thompson
Rockwell International
Science Center
1049 Camino Dos Rios
Thousand Oaks, California 91360

D. L. Waidelich
University of Missouri
Dept. of Electrical Engineering
Columbia, Missouri 65201

Clifford H. Wells
Southwest Research Institute
Materials Sciences
San Antonio, Texas 78230

Bill G. W. Yee
General Dynamics
P.O. Box 718
Ft. Worth Texas 76101

WORKSHOP ON THE THEORY OF ULTRASONIC SCATTERING
WITH APPLICATION TO ADAPTIVE COMPUTERIZED NDE

R. M. Thomson

This workshop was organized at the suggestion of J. Krumhansl to explore the current prospects for quantitative ultrasonic characterization of defects in solids by combining the most advanced features of elastic wave scattering theory, current experimental capability, and computer adaptive techniques.

The underlying assumption is that recent success in applying adaptive computer techniques to the fatigue crack problem make it worthwhile to explore systematically which measurable parameters will form a complete set with respect to flaw characterization. Needless to say, the task was not completed, but a much deeper insight was generated during the workshop regarding the types of theories which could be developed in the various ranges of ka (k is the wave vector and a is the size of the scattering object), and the types of information such theories give in relation to the "inverse problem". (The inverse problem is to infer the character of a flaw from scattered wave data.)

The workshop featured a number of tutorial review talks including recent developments by participants to provide back-

ground for the collaborative work.

Bruce Thomson discussed recent work at the Science center comparing detailed comparisons between theory and experiment for scattering of ultrasonic waves from simple standardized scattering shapes embedded in solids. The experimental precision in this work was gratifyingly good with excellent verification of the predicted results. This work shows that not only is the ultrasonic apparatus excellent, but the materials variables of the standard samples is under control. In addition to work with the standard transducers, the people of the Science Center have developed an electromagnetic transducer which has the advantages that physical contact between transducer and sample is not necessary, and that surface waves can be generated directly.

Gordon Kino described some remarkable success in his laboratory on controlling the variables in the manufacture of ultrasonic transducers which approach the theoretical predicted performance of perfect transducers, i.e., that the transducer act as a simple piston. The general secret in this success is the great care taken in coupling the backing and face plates to the piezoelectric crystal. He also reported on the construction of arrayed transducers, which opens possibilities for electronic beam control and lens formation. Of particular interest are new piezoelectric polymers (polyvinyl fluoride) which can be used in thin sheets to generate frequencies in the range up to 50 MHz. On the theoretical side, Kino emphasized the usefulness

of the use of nonlinear effects in the study and characterization of flaws.

Mucciardi reported on recent work at Adaptronics in using the computer to sort out which parameters in a signal trace are correlated with flaw shape and size for fatigue cracks at rivets in aluminum plates, e.g., like those in an aircraft skin. In this work, the computer calculates the cepstrum defined by

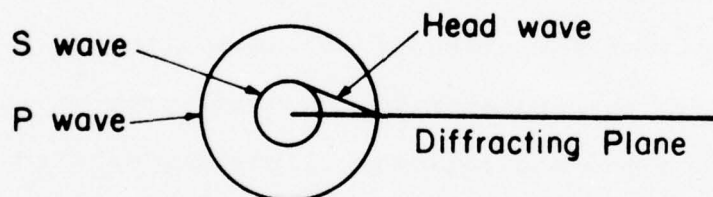
$$C = F^{-1}(\log|F(y(t))|)$$

where F is the Fourier transform and $y(t)$ is the signal. The frequency content of the cepstrum will contain information about repeated signals from various reflected portions of the main signal, and certain frequency ranges of C are found to be highly correlated with cracks. All of this work is entirely empirical, and one of the goals of the workshop was to provide a set of theoretically based parameters which could be computerized in some such scheme for flaw characterization.

The theoretical background was reviewed by Adler, Kraut and Gubernatis. Kraut reviewed the exact solutions which have been worked out in the most generality by Filipczynski, but only for a simple shape. Since the elastic field is a tensor field with three polarization directions, the equations are very complex, and the major task is to derive useful expressions or algorithms for analysis of the practical cases. Some important work has already been done and applied to the flaw problem.

Keller¹ has published work on the scalar field in the Kirchhoff regime, ($ka \gg 1$) for scattering by sharp edged shapes which has been applied by Adler to scattering by discs in water. One of the important results of this work is the prediction that the diffracted wave is defined by constructive interference from opposite edges of the shape which have extremum path difference values.

From such results, one can infer the size of the scattering object. Another predicted result for the sharp edge case for the full 3-wave elastic field (not contained in Keller's results) and reported by Kraut is appearance of a "head wave" transient shear wave when a pulse is diffracted from a straight edge, illustrated below.



In a general way, such effects led Kraut to recommend a careful look at pulse shape effects in the time domain for unravelling the inverse problem.

The analysis of the inverse problem for scattering of elastic waves in the $ka \gg 1$ regime has been exhaustively studied by the geophysical community over a 20 year period in a project sponsored through UCLA by the American Petroleum Institute. The work of this project has not been openly published, but is

now available at UCLA in report form. This literature will be carefully reviewed for results which can be applied to the NDE case.

Gubernatis reported on the extensive theoretical work by himself and Krumhansl on the integral equation formulation of the scattering problem. Results have been obtained for scattering for volume scattering in two expansions. In one of these the zero frequency limit is obtained in all orders of the perturbation, and in the second, the Born approximation has been obtained. One of the limitations of the Born approximation is its poor prediction of forward scattering, but it can be a very useful tool because it is not restricted to a simple shape.

The review of present status led to a number of general conclusions and suggestions for future work. In particular, present theoretical formulations of the scattering problem are not yet adequate to parameterize the crack problem. At the workshop, work along the following lines was carried out and reports are included in the proceedings.

1. The Gubernatis-Krumhansl integral equation formulation ultimately is expressed in the form

$$U_i^S = \hat{r}_i \hat{r}_j f_j(\alpha) \frac{e^{i\alpha r}}{r} + (\delta_{ij} - \hat{r}_i \hat{r}_j) f_j(\beta) \frac{e^{i\beta r}}{r}$$

$$f_i(k) = \frac{k^2}{4\pi\rho\omega^2} \left[\delta\rho\omega^2 \int_R dv' u_i e^{-ik \cdot \underline{r}'} + ik\hat{r}_j \delta c_{ijkl} \int_R dv' \epsilon_{kl} e^{-ik \cdot \underline{r}'} \right]$$

$$\epsilon_{ij} = \frac{1}{2}(U_{i,j} + U_{j,i})$$

where U^S is the far field scattered wave, \hat{r} is the unit vector in the scattered direction, r is the radius to the observation point, and R is the region of integration containing a perturbation ($\delta\rho$ is a perturbed density and δc_{ijkl} is a perturbed elastic constant). This formulation will be systematized for both long and short wave limits for both volume and surface scatterers. One significant result already apparent is that the long wave length limit contains significant information about the shape of the scatterer not present for scalar fields.

2. Scattering problems can be formulated in a variational format. W. Kohn presented the background theory for this approach, and with Kino, will attempt a formulation for the elastic problem.

3. Montroll has developed a very general scattering theory in which the entire formalism is discretized. In this case, an exact solution in terms of lattice Green's functions can be obtained in which the number of perturbed scattering points is finite. Since the discretized problem is suitable for immediate computer formulation, the theory should be a powerful practical technique.

4. McClintock and Kino have written a short note on the possibility that acoustic emission from fatigue cracks could be used to distinguish various features of the crack such as growth and friction during crack closure through discrimination between P and S waves.

5. Finally, a general review of the current state of

the experimental art is made by Adler, Kino, Thompson and Tittman. In this review, the needs are formulated for theoretical guidance.

6. For the future, these various lines of investigation will be pursued, and a special point will be made to review the UCLA seismic report literature for the short wave case.

The general impact of the conference was considerable because of the focus it brought to the attempt to combine theory and experiment for the practical problem of unravelling the flaw characterization problem. In our opinion, the attempt of the ARPA program to develop a feasible quantitative NDE is close to a practical form of realization through the means of the type of effort begun at this workshop. Every effort should be made to continue the momentum of the work started here, and to apply it to the appropriate areas for further applied development. ARPA should also be aware of the effectiveness of the format provided by the combined Rockwell project/MRC operations in germinating this type of progress.

ACKNOWLEDGEMENT

This research was supported by the Advanced Research Projects Agency of the Department of Defense under Contract No. MDA903-76C-0250 with The University of Michigan.

INTERPRETATION OF ELASTIC WAVE SCATTERING THEORY
FOR ANALYSIS AND DESIGN OF FLAW CHARACTERIZATION
EXPERIMENTS: I. LONG WAVELENGTH LIMIT

J. E. Gubernatis, J. A. Krumhansl,
R. M. Thomson

FAR FIELD RESULTS

We are concerned with the experimental situation depicted in Fig. 1. In general we must consider:

1. Different scattering modes and mode conversion
T→L, T→T, L→L, L→T, (L-longitudinal; T-transverse)
2. Orientation of the flaw
Euler Angles (ζ, η, γ)
3. Scattering angles
 θ, ϕ with $\cos \theta = \frac{\mathbf{k} \cdot \mathbf{k}_0}{kk_0} = \hat{\mathbf{r}}_0 \cdot \hat{\mathbf{r}}$
4. Flaw shape and size
5. Changes in material parameters
 $\delta \rho$, change in density
 δC_{ijkl} , change in elastic stiffness

It was shown in Ref. (1) that for a flaw embedded in an isotropic medium the far field scattered displacement field has the components

$$A_i(\theta, \phi) = \hat{r}_i \hat{r}_j f_j(\underline{\alpha}) \quad (1a)$$

$$B_i(\theta, \phi) = (\delta_{ij} - \hat{r}_i \hat{r}_j) f_j(\underline{\beta}) \quad (1b)$$

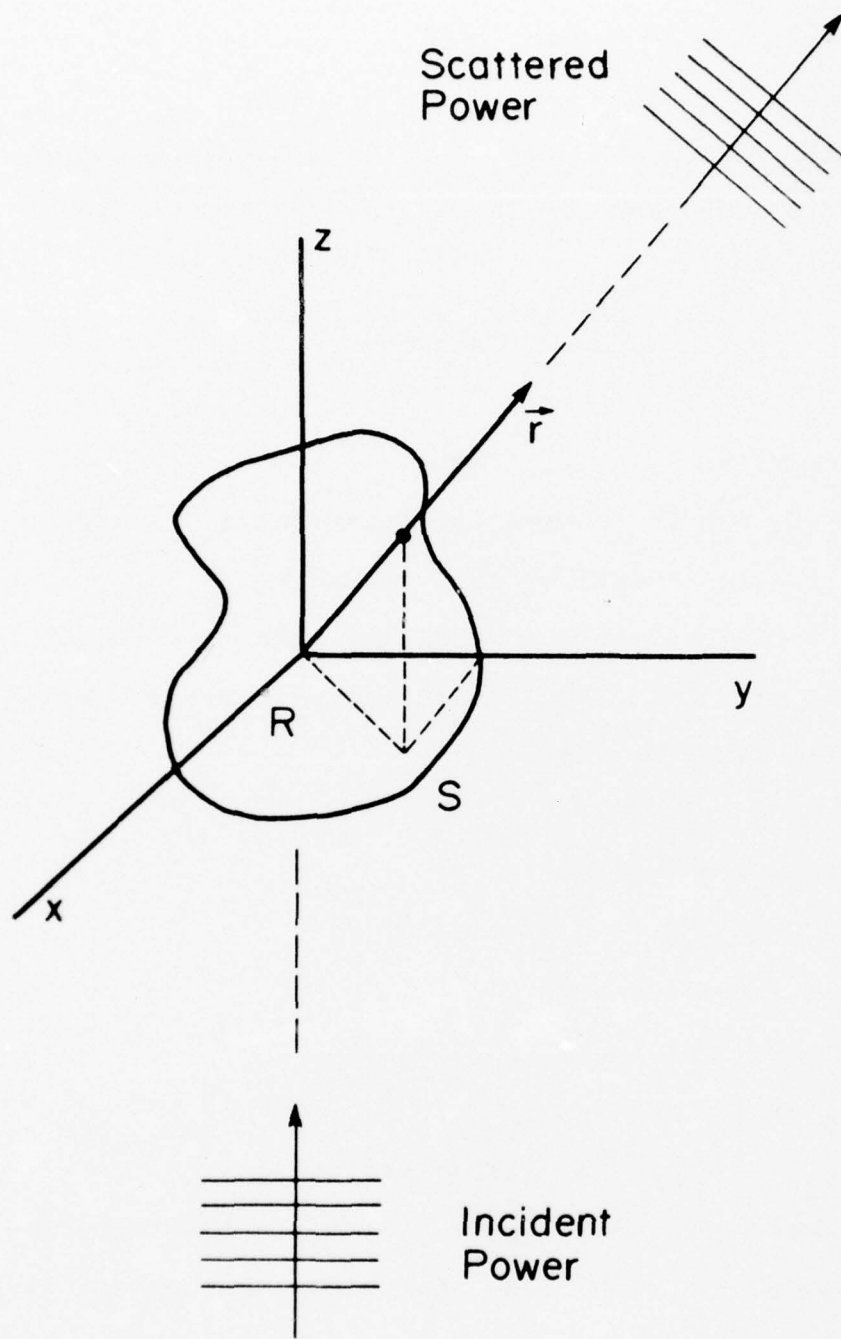


Figure 1. The experimental situation. Incident power scatters from a flaw into a receiver in the direction \underline{r} .

where A_i is the longitudinal component and $\underline{\alpha}$ is the associated wave vector, and B_i is the transverse component and $\underline{\beta}$ is the associated wave vector. Subscripts denote Cartesian components; repeated subscripts denote summation. Components of the f-vector for a volume flaw are given by

$$f_i(\underline{k}) = \frac{k^2}{4\pi\rho\omega^2} \left[\delta\rho\omega^2 \int_R dV' u_i(\underline{r}') e^{-i\underline{k}\cdot\underline{r}'} + i k \hat{r}_j \delta C_{ijkl} \int_R dV' \epsilon_{kl}(\underline{r}') e^{-i\underline{k}\cdot\underline{r}'} \right] \quad (2)$$

where u_i and ϵ_{kl} are the displacement and strain fields inside the volume R of the flaw. In Eq. (2) the material constitution is assumed to have different constant values inside and outside the flaw. When extended material gradients are present, modification of Eq. (2) is possible.

For an idealized crack in an isotropic medium, the components of the f-vector are⁶

$$f_i(\underline{k}) = \frac{k^2}{4\pi\rho\omega^2} C_{ijkl} \left[\int_{S^+} ds' n_j^+ \Delta u_{k,l} e^{-i\underline{k}\cdot\underline{r}'} + i k \hat{r}_j \int_{S^+} ds' n_k^+ \Delta u_l e^{-i\underline{k}\cdot\underline{r}'} \right] \quad (3)$$

where $C_{ijkl} = \lambda \delta_{ij} \delta_{kl} + \mu (\delta_{kl} \delta_{jk} + \delta_{ik} \delta_{jl})$, S^+ is the surface on one side of the crack, n_i^+ is the outward unit normal to S^+ , and Δu_l and $\Delta u_{k,l}$ are the discontinuities in u_l and $u_{k,l}$ measured relative to the surface of the crack complementary to S^+ . The scattered amplitudes A_i and B_i are defined as for the volume flaw.

Examining Eqs. (2) and (3), we note:

1. Material property changes enter via $\delta\rho, \delta C_{ijkl}$ or assumptions about crack properties.
2. Incident wave polarization, direction, frequency and flaw orientation, shape and volume all may play a role in determining u_i and ϵ_{kl} inside the flaw, in the most general case.
3. The shape and size enters via the integrations.
4. Phase variation arises from both the $e^{-ik \cdot r'}$ in the integrals and the incident wave.
5. Explicit angle dependence enters through the unit vector \hat{r}_j . (\hat{r}_j is the direction to the receiver.)

We now proceed to discuss a few simple examples, chosen to simplify the general expression for the f-vector. In this way we may illustrate the laying out and analysis of an experiment. More general cases need to be worked out in detail.

THE LONG WAVELENGTH LIMIT

In the long wavelength limit, $ka \ll 1$ where a is some characteristic length of the flaw. Thus, within the flaw

$$e^{ik_0 \cdot r'} \approx 1, \quad e^{-ik \cdot r'} \approx 1.$$

This implies the non-zero strains associated with an incident wave $u_i^0 e^{ik_0 z}$ are

$$\begin{aligned} \epsilon_{33}^0 &= ik_0 u_3^0, \text{ for incident longitudinal wave} \\ \epsilon_{13}^0 &= ik_0 j_1^0 / 2 \text{ for incident transverse wave polarized} \\ &\text{in the x-direction.} \end{aligned}$$

Thus, the applied strains are locally uniform for small k_0 .

In this quase-static limit the displacement field $u_i^0(\underline{r}) \approx u_i^0$, over the volume of the flaw. Also, in this limit, the strain field within a general ellipsoid of uniform material was shown by Eshelby⁷ to be a constant tensor contracted with the applied uniform strain. Thus, for insertion into the f-vector we have

$$u_i(\underline{r}') = u_i^0$$

$$\epsilon_{k\ell}(\underline{r}') = \Gamma_{k\ell mn} \epsilon_{mn}^0$$

where we denote the "strain proportionality tensor" by Γ . Consequently, the integrations in the f-vector reduce to the multiplication of the above displacement and strain fields by the volume of the flaw:

$$f_i(\underline{k}) = \frac{V k^2}{4\pi} \left[\frac{\delta \rho}{\rho} u_i^0 + \frac{i k}{\rho \omega^2} \hat{r}_j \delta C_{ijkl} \Gamma_{k\ell mn} \epsilon_{mn}^0 \right] . \quad (4)$$

Justification of this quasi-static approximation as well as the evaluation of $\Gamma_{k\ell mn}$ for the general ellipsoid shape and orientation will be presented in another paper.² We can now, however, find interesting results for a sphere.

For an elastically isotropic sphere Γ can be evaluated using the results of Eshelby. We find

$$\Gamma_{ijkl} = \frac{1}{3}(X-Y) \delta_{ij} \delta_{kl} + \frac{1}{2}Y(\delta_{il} \delta_{jk} + \delta_{ik} \delta_{jl}) \quad (5)$$

with

$$X = \left(1 + \frac{\delta \lambda}{\lambda + \frac{2}{3}\delta \mu} \right)^{-1} \quad (6a)$$

$$Y = \left(1 + \frac{2}{15} \frac{\delta\mu}{\mu} \frac{3\lambda + 8\mu}{(\lambda + 2\mu)} \right)^{-1} \quad (6b)$$

We note that Γ_{ijkl} is an isotropic fourth rank tensor. This is true only for an elastically isotropic sphere which by its symmetry cannot be preferentially oriented.

Incident Longitudinal Wave

If the incident displacement field is longitudinally polarized, we find

$$u_1^O = 0, u_2^O = 0, u_3^O = u^O$$

$$\epsilon_{ij} = ik_O u^O \delta_{i3} \delta_{j3}.$$

Since $\epsilon_{ij} = \Gamma_{ijkl} \epsilon_{kl}$, we may write

$$\epsilon_{11} = \epsilon_{22} = ik_O u^O (X-Y)/3$$

$$\epsilon_{33} = ik_O u^O (X+2Y)/3,$$

indicating that a compressional wave incident in one direction induces in the sphere strains associated with the transverse directions in addition to a strain associated with the incident direction.

The f-vector is

$$f_i(\underline{k}) = \frac{vk^2 u^O}{4\pi} \left[\frac{\delta\rho}{\rho} \delta_{i3} - \frac{kk_O}{\rho\omega^2} (\delta L \hat{r}_i + 2\delta M \hat{r}_3 \delta_{i3}) \right] \quad (7)$$

where

$$\delta L = \frac{1}{3} [(3\delta\lambda + 2\delta\mu) X - 2\delta\mu Y]$$

$$\delta M = \delta\mu Y$$

Writing the incident wave number as $\alpha = k_O = \rho\omega^2 (\lambda + 2\mu)^{-1}$ we find that the longitudinal scattered amplitude is

$$A_i = \frac{\alpha^2 u^0 V}{4\pi} \left[\frac{\delta \rho}{\rho} \cos \theta - \frac{\delta L + 2\delta M \cos^2 \theta}{\lambda + 2\mu} \right] \hat{r}_i \quad (8)$$

This expression may be compared to the Born approximation for $ka \ll 1$:

$$A_i = \frac{\alpha^2 u^0 V}{4\pi} \left[\frac{\delta \rho}{\rho} \cos \theta - \frac{\delta \lambda + 2\delta \mu \cos^2 \theta}{\lambda + 2\mu} \right] \hat{r}_i \quad (9)$$

The difference between the Born approximation and the exact quasi-static result is the "renormalization" of $\delta \lambda$ and $\delta \mu$ into the quantities δL and δM . There are several points to be made:

1. In the limit of small perturbations of elastic stiffness, $\frac{\delta \lambda}{\lambda} \ll 1$ and $\frac{\delta \mu}{\mu} \ll 1$, $\delta L = \delta \lambda$ and $\delta M = \delta \mu$. This limit is equivalent to approximating X by 0 and Y by $\frac{1}{2}$ and thus resulting in the replacement of Γ_{ijkl} by $I_{ijkl} = \frac{1}{2}(\delta_{ik} \delta_{jl} + \delta_{il} \delta_{jk})$, the idempotent fourth rank tensor.
2. For the strain fields, the Born approximation takes $\epsilon_{ij} = \epsilon_{kl}^0$ and thus ignores the induced transverse strains in addition to giving an incorrect magnitude for the longitudinal strain.
3. The usual Born approximation failure for scalar waves in the long wavelength limit is simply one of magnitude. For elastic waves the problem is much more serious because of the interplay between the angular factors in the expressions for the scattered amplitudes.

Our remarks have only been for $L \rightarrow L$ scattering; similar comments apply for $L \rightarrow T$, $T \rightarrow L$, $T \rightarrow T$. We will not discuss these scattering cases here.

Interpretive Comments

The following remarks apply to the scattering of elastic waves from a sphere for $ka \ll 1$ irrespective of whether one speaks of the Born approximation or the exact result:

(a) The size of the flaw enters the scattering only through the volume V . To determine this volume an absolute measurement of the magnitude of the scattering is necessary. The implications are that in the absence of such measurements and in the long wavelength limit so size information can be found from directional or frequency measurements.

(b) On the other hand, for a given incident direction there is significant information on material parameter changes. For example, we present the ratios of the scattering cross-sections at 90° to 180° for the following flaws in Ti-6Al-4V:

| | Ratios | $\delta\rho/\rho$ | $\delta\lambda/\lambda$ | $\delta\mu/\mu$ |
|-----------------|--------|-------------------|-------------------------|-----------------|
| Void | 0.89 | -1.00 | -1.00 | -1.00 |
| Aluminum | 2.12 | -0.39 | -0.35 | -0.34 |
| Stainless Steel | 0.77 | 0.79 | 0.09 | 0.87 |

Similar remarks can be developed for incident transverse waves. There seems to be many ways of extracting $\delta\rho$, $\delta\lambda$, and $\delta\mu$ from a few well-chosen measurements. We also note in passing that phase information is present, as a + or - sign depending on the change in material parameters.

Our remarks have been addressed to the very long wavelength limit. The extent to which this limit is experimentally

accessible is not perfectly clear. We estimate for Ti-6Al-4V the need of frequencies of the order of 0.1 MHz. For frequencies above this, one can use the full expression for the Born approximation in which the V in Eq. (9) is replaced by the shape factor:^{3,4}

$$\int_R dV' e^{i(\underline{k}_s - \underline{k}_o) \cdot \underline{r}'}$$

where R is the region of space occupied by the flaw, and \underline{k}_s and \underline{k}_o are the scattered and incoming wave vectors. A similar replacement has been motivated for the V in Eq. (8).² Since the shape factor contains explicit information about the radius of the sphere, the radius can be determined even in the absence of absolute measurements if the relative measurement is precise. Equations (8) and (9) with the shape factor inserted are expected to yield accurate predictions for the scattered wave from a spherical void in Ti-6Al-4V for frequencies in the 2.25 MHz range, although the use of the Born approximation must be restricted to $135^\circ \leq \theta \leq 180^\circ$.

SCATTERING BY A CRACK

We assume in this section that the scattering center is a "penny-shaped" crack. Mathematically, we apply Eq. (3) to a circular cut in the material, and assume that the displacements, Δu_k , and strains, $\Delta u_{k,\ell}$, are obtained from the solutions for a penny-shaped crack under a static externally applied stress. Since we are in the long wavelength limit, this procedure is allowed². The displacements on the crack surface, Δu_i , near the

crack line are given by

$$\begin{aligned}\Delta u_z &\approx \frac{2}{\mu} K_I \sqrt{\frac{r}{2\pi}} (1-\nu) \\ \Delta u_n &\approx \frac{2}{\mu} K_{II} \sqrt{\frac{r}{2\pi}} (1-\nu) \\ \Delta u_t &\approx \frac{2}{\mu} K_{III} \sqrt{\frac{r}{2\pi}}\end{aligned}\quad (10)$$

where the local coordinate system at the crack line is shown in Fig. 2, with \hat{z} perpendicular to the crack plane, \hat{t} the oscillating tangent, and \hat{n} the normal to the crack line in the plane of the crack. r is the distance along the cut surface from the crack line, ν is Poisson's ratio, and K_i are the various stress intensity factors for stresses causing the displacements indicated. For a penny-shaped crack, solutions are known for mode I opening stresses, and in this case

$$K_I = 2\sigma \sqrt{\frac{a}{\pi}} \quad (11)$$

where a is the radius of the penny-shaped crack, and σ is the normal stress on the crack surface. In order to make our algebraic manipulations not too onerous, we shall make some important assumptions. We first assume that K_{II} , and K_{III} are also related to the radius and to the relevant stresses on the crack plane in the same way as if K_I , and we shall assume that the terms $(1-\nu)$ in Eq. (10) can be set equal to 1. Then we can write a simple vector equation combining Eqs. (10) and (11) as

$$\Delta u_i = \frac{2}{\mu\pi} \sqrt{2ra} \sigma_{ij} \hat{n}_j \quad (12)$$

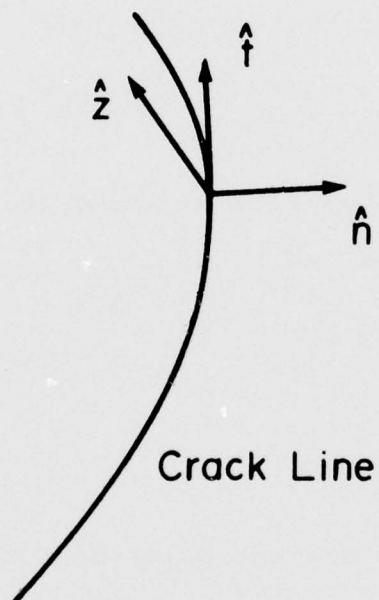


Figure 2. Tangent, normal and z-directions for a curved crack.
 \hat{z} is normal to the plane of the crack.

where σ_{ij} is the stress tensor evaluated on the crack plane and \hat{n}_j is the normal to the crack plane. With this simplification, we can derive relatively simple analytic expressions for the f -vectors.

In applying these ideas to the general expression for f , Eq. (3), we first note that the term $\Delta u_{k,\ell}$ when integrated over the surface is strictly zero. This result follows from the fact that $\Delta u_k \rightarrow 0$ at all points along the line of the crack which bounds the surface, S . Thus f_i takes the form

$$f_i(\underline{k}) = \frac{ik^3}{4\pi\rho\omega^2} \hat{r}_j C_{ijk\ell} \int dS'_k \Delta u_\ell \quad (13)$$

Using Eq. (12) for the surface integrations over the entire crack surface, we have

$$\begin{aligned} \int dS_k \Delta u_\ell &= \frac{2}{\mu\pi} \sqrt{2a} \sigma_{ij} \hat{n}_j \int_0^{2\pi} d\phi \int_0^a d\rho \rho \sqrt{a-\rho} \\ &\approx \frac{2\sqrt{2}}{\mu} \sigma_{ij} \hat{n}_j a^3 \end{aligned} \quad (14)$$

In this expression, ρ and ϕ are the solar coordinates in the plane of the crack. The error made when we assume that the \sqrt{r} solution near the crack tip is extended over the entire crack surface is a small numerical factor which multiplies all amplitude expressions, and is not significant.

With these substitutions into the expression for f_i , Eq. (13), we finally have

$$f_i(\underline{k}) = \frac{ik^3 a^3}{\sqrt{2}\pi\rho\omega^2} \left\{ \hat{r}_i \frac{\lambda}{\mu} \sigma_{33} + \delta_{i3} \sigma_{3j} \hat{r}_j + \hat{r}_3 \sigma_{3i} \right\} \quad (15)$$

In writing this equation, we make use of the coordinate equation shown in Fig. 3. σ_{ij} are the stresses on the crack plane caused by the incoming wave. In working out these stresses, we have three cases, corresponding to the three independent polarization possibilities for the incoming wave.

Case I. Incoming Longitudinal Wave

$$\begin{aligned} f_1 &= \frac{\sqrt{2} \alpha^2 u^0 a^3}{\pi (\frac{\lambda}{\mu} + 2)} \left[\frac{\lambda}{\mu} g(\theta_i) \sin \theta_s \cos \phi_s \right] \\ f_2 &= \frac{\sqrt{2} \alpha^2 u^0 a^3}{\pi (\frac{\lambda}{\mu} + 2)} \left[\frac{\lambda}{\mu} g(\theta_i) \sin \theta_s \sin \phi_s - h(\theta_i) \cos \theta_s \right] \\ f_3 &= \frac{\sqrt{2} \alpha^2 u^0 a^3}{\pi (\frac{\lambda}{\mu} + 2)} \left[(\frac{\lambda}{\mu} + 2) g(\theta_i) \cos \theta_s - h(\theta_i) \sin \theta_s \sin \phi_s \right] \end{aligned}$$

$$g(\theta) = \frac{\lambda}{\mu} + 2 \cos^2 \theta; \quad h(\theta) = \sin 2\theta \quad (16)$$

In this case the scattered longitudinal wave is proportional to the relatively simple expression

$$f_j \hat{r}_j = \frac{\sqrt{2} \alpha^2 u^0 a^3}{\pi (\frac{\lambda}{\mu} + 2)} \left[g(\theta_i) g(\theta_s) - h(\theta_i) h(\theta_s) \sin \phi_s \right] \quad (17)$$

For the mode converted shear wave, the angular dependence is quite complex, and is not written explicitly.

Case II. T_1 wave (polarization of incoming wave is in the plane of the crack)

$$f_1 = \frac{\beta^2 a^3 u^0}{\sqrt{2} \pi} \cos \theta_i \cos \theta_s$$

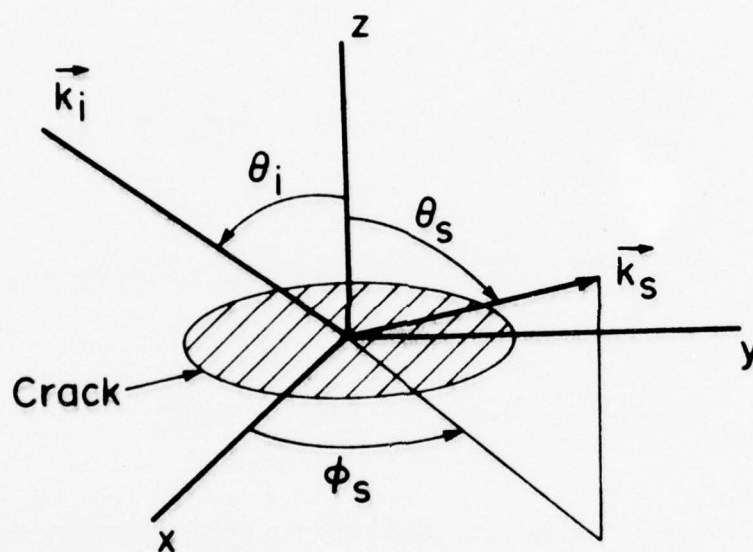


Figure 3. Coordinate system for a penny-shaped crack. The incoming wave vector \underline{k}_i is in the ZY plane, and the outgoing wave vector \underline{k}_s is specified by the spherical angles θ_s and ϕ_s .

$$f_2 = 0$$

$$f_3 = \frac{\beta a^3 u^0}{\sqrt{2} \pi} \cos \theta_i \sin \theta_s \cos \phi_s \quad (18)$$

from which we obtain for the scattered L-wave

$$f_j \hat{r}_j = \frac{\beta^2 a^3 u^0}{\sqrt{2} \pi} \cos \theta_i \sin 2\theta_s \cos \phi_s \quad (19)$$

The square of the magnitude of the scattered T-wave is

$$u_j u_j = f_j f_j - (f_j \hat{r}_j)^2 = \frac{\beta^4 a^6 u^{02}}{2\pi^2} \{ \cos^2 \theta_i \cos^2 \theta_s - \cos^2 \theta_i \cos 2\theta_s \\ \times \sin^2 \theta_s \cos^2 \phi_s \} \quad (20)$$

Case III. T_2 wave (incident wave polarized in the YZ plane)

When the polarization of the incident wave is in the XY plane, the f-vector becomes more complex, and the results are

$$f_1 = \frac{\beta^2 a^3 u^0}{\sqrt{2} \pi} \left\{ \frac{\lambda}{\mu} \sin 2\theta_i \sin \theta_s \cos \phi_s \right\} \\ f_2 = \frac{\beta^2 a^3 u^0}{\sqrt{2} \pi} \left\{ \frac{\lambda}{\mu} \sin 2\theta_i \sin \theta_s \sin \phi_s + \cos 2\theta_i \cos \theta_s \right\} \\ f_3 = \frac{\beta^2 a^3 u^0}{\sqrt{2} \pi} \left\{ \frac{\lambda}{\mu} \sin 2\theta_i \cos \theta_s + \sin 2\theta_i \cos \theta_s + \cos 2\theta_i \right. \\ \left. \times \sin \theta_s \sin \phi_s \right\} \quad (21)$$

For mode conversion to an L-wave, we have

$$f_j \hat{r}_j = \frac{\beta^2 a^3 u^0}{\sqrt{2} \pi} \{ g(\theta_s) h(\theta_i) + \frac{1}{2} \cos 2\theta_i [h(\theta_s) \sin \phi_s + h(\phi_s) \sin \theta_s] \}$$

and the shear scattering is quite complicated.

In summary, the incident shear mode, T_1 , leads to the simplest crack signature results. For an incident T_1 mode, the only reflected waves are the L-mode and the T_1 -mode. The $T_1 \rightarrow T_1$ scattering is maximum for normal incidence and back reflection or forward scattering, i.e., $\theta_s = 0, \pi$. Mode conversion to the L-mode ($T_1 \rightarrow L$) occurs over most of the range, but is zero for incident angle $\theta = \pi/2$, and for scattered waves in back reflection and in-plane scattering, i.e., for $\theta_s = 0, \pi/2, \pi$. Thus, experimentally, a crack signature is obtained by locating the normal incidence direction (maximum back reflection in T_1), and then checking that the mode converted L-wave disappears in back reflection and in all in-plane directions. The T_1 mode has the characteristic that after scattering, for all forward directions ($\phi_s = 0$), the plane of polarization is unchanged. In the T_2 mode, the polarization is rotated for these angles. Of course, when the incident wave is normal to the crack plane, T_1 is the only shear mode possible.

Because pure shear modes are not always easy to produce in a solid with arbitrary polarization, crack signatures for L-modes are important. Again, the back scatter (single transducer) arrangement is maximum for normal incidence on the crack. For a two-transducer arrangement, in which the incident wave is normal to the crack, then only a T_1 wave is scattered by mode conversion for in-plane scattering ($\theta_s = \pi/2$). This crack signature again involves distinguishing the various polarization directions of the scattered waves.

SUMMARY AND CONCLUSIONS

Although we examined only two flaw geometries, a sphere and an idealized crack, we believe the following statements are generally true in the quasi-static ($ka \ll 1$) limit:

1. Various parameters characteristic of the flaw's size, shape, orientation, and material properties are present in scattered fields and, in precision experiments, are measurable.
2. Mode converted scattering contains useful and important information.
3. Certain features of the flaw are accentuated by changing the polarization of the incident wave, for example, from longitudinal to transverse.

We remark that the scattering region discussed here is diametrically opposite the region appropriate for acoustic imaging ($ka \gg 1$, the high frequency limit). Furthermore, acoustic imaging principally analyzes the phases of the scattered fields; we are discussing amplitude (power) measurements. Consequently, in this report our flaw characterization philosophy is quite distinct from standard imaging techniques.

We conclude that theoretical studies of the scattering of elastic waves can aid the design and the analysis of flaw characterization experimental studies in a frequency regime where the wavelength is larger than the characteristic size of the flaw, and imaging is not possible.

ACKNOWLEDGEMENT

We thank Walter Kohn and other members of the Materials Research Council for their suggestions and critical commentary on the topics in this report.

References

1. J. E. Gubernatis, E. Domany, and J. A. Krumhansl, to be published.
2. J. E. Gubernatis, to be published.
3. J. E. Gubernatis, E. Domany, J. A. Krumhansl and M. Huberman, Report 2654, Materials Science Center, Cornell University. Also listed as ERDA technical Report #C00-3161-42.
4. J. E. Gubernatis, E. Domany, J. A. Krumhansl and M. Huberman, to be published.
5. B. R. Tittman, E. R. Cohen and J. M. Richardson, J. Acoust. Soc. of Amer., in press.
6. J. E. Gubernatis, unpublished.
7. J. D. Eshelby, Proc. Roy. Soc. London, Ser. A271, 376 (1957).

I. PERTURBATION THEORY FOR SCATTERING OF ACOUSTIC WAVES BY FLAWS

G. S. Kino

INTRODUCTION

The theory of acoustic wave scattering from flaws is normally carried out by using an exact solution for scattering from simple shapes such as spheres or ellipsoids. More generally, a Green's function approach can be employed and has recently been demonstrated in the Born approximation by Gubernatis et al.¹ In this paper, our purpose is to introduce the reader to a formal technique originally developed by Rumsey in electromagnetic scattering problems, "the reaction principle".² This was applied by Rumsey and others to the derivation of variational theories for scattering and the determination of eigenvalues of propagating waves.³ We have adapted this method to acoustic wave scattering problems. We derive our results in terms of scattering matrices, a formalism much used in EM theory.^{3,4} This makes it possible to directly calculate the power scattered by a flaw from a transmitting transducer to a receiving transducer. The method has the advantages that a complicated Green's function formalism is not required, and the results obtained are expressed in a physically meaningful form, so that one can determine which parameters are most important in their contribution to scattering.

Furthermore, it is very easy to adapt the technique to use with waveguide modes or surface acoustic waves, for it need not be restricted to use with plane waves.

In this paper we first derive the reaction principle, and the associated scattering matrix. We then determine a number of formulae for scattering from flaws, and demonstrate their use in determining the scattering of a plane wave from a flaw, and the scattering of a Rayleigh wave from a cylindrical vacancy, perpendicular to the surface of the substrate. We compare this latter result to experimental results obtained by Viktorov; the agreement is quite good.⁴

In the second paper, which accompanies this one, we use the same procedures to derive variational theories akin to those of Kohn and Krumhansl and of Nemat-Nasser, to determine the eigenvalues for propagating waves. We then go on to derive variational scattering theories.

DERIVATION OF THE REACTION PRINCIPLE

In EM theory and network theory, a very useful relation, the reciprocity theorem can be obtained between two sets of fields; \underline{E}^a , \underline{H}^a and \underline{E}^b , and \underline{H}^b and their current sources \underline{J}^a , \underline{J}^b which exist in a given region of volume V , with a bounding surface S . This can be stated in the form

$$\int_S \left[\left(\underline{E}^a \times \underline{H}^b \right) - \left(\underline{E}^b \times \underline{H}^a \right) \right] \cdot \underline{n} dS = \int_V \left(\underline{J}^a \cdot \underline{E}^b - \underline{J}^b \cdot \underline{E}^a \right) dV \quad (1)$$

where \underline{n} is the outward normal to the surface S . When there are

no sources present within the volume V , the left hand side of Eq. (1) is zero.

The equivalent relation for acoustic fields in a given volume V enclosed by a surface S , when there are no internal sources present, and the stress tensor and displacement vector are σ_{ij}, u_i , respectively, is

$$I = \int \left(\sigma_{ij}^a u_j^b - \sigma_{ij}^b u_j^a \right) n_i dS = 0 \quad (2)$$

where n_i is the outward normal to the surface. Thus, in this simplified case, the reciprocity relation is a relation between two given sets of forces $n_i \sigma_{ij}^a, n_i \sigma_{ij}^b$ and displacements u_i^a, u_i^b at the bounding surfaces.

We now suppose that all rf quantities vary as $e^{j\omega t}$, and first derive the general form of the reciprocity relation for acoustic waves. We take the displacement, stress, and strain, in the medium to be u_i, σ_{ij} , and ϵ_{ij} , respectively. These obey the relations:

$$\sigma_{ij,j} = -\omega^2 \rho u_j + f_j \quad (3)$$

$$\epsilon_{ij} = \frac{1}{2}(u_{i,j} + u_{j,i}) + g_{ij} \quad (4)$$

$$\sigma_{ij} = C_{ijkl} \epsilon_{kl} + h_{ij} \quad (5)$$

where a comma denoted differentiation in the standard way and the term f_j is a source term (force). We also find it mathematically convenient to introduce artificial source terms or inhomogeneous terms g_{ij}, h_{ij} into Eqs. (4) and (5), respectively.

These terms are zero for the true fields in the medium. However, f_j, g_{ij}, h_{ij} can be the errors between the quantities of interest when trial fields not obeying the true equations in the medium are used. They can also be used as source terms which represent the "polarization" of a perturbing medium.

We now derive the general form of the reciprocity relation for acoustic fields. Equation (3) for the (a) and (b) fields can be written in the form

$$\sigma_{ij,j}^a = -\omega^2 \rho u_j^a + f_j^a \quad (6)$$

$$\sigma_{ij,j}^b = -\omega^2 \rho u_j^b + f_j^b \quad (7)$$

respectively.

Multiplying Eq. (6) by u_i^b and Eq. (7) by u_i^a and subtracting and then integrating over the volume V , we find that

$$\int (\sigma_{ij,j}^a u_i^b - \sigma_{ij,j}^b u_i^a) dv = \int (f_i^a u_i^b - f_i^b u_i^a) dv \quad (8)$$

This yields the relation

$$\int_V (\sigma_{ij}^a u_j^b - \sigma_{ij}^b u_j^a)_{,i} dv = \int_V (\sigma_{ij}^a u_{i,j}^b - u_{ij}^b u_{i,j}^a) dv + \int_V f_i^a u_i^b - f_i^b u_i^a dv \quad (9)$$

After substituting from Eqs. (4) and (5), and using Gauss's theorem on the left hand side of Eq. (9), we obtain the following form of the reciprocity theorems

$$\begin{aligned} \int_S (\sigma_{ij}^a u_j^b - \sigma_{ij}^b u_j^a) n_i dS + \int_V (f_i^a u_i^b + g_{ij}^a \sigma_{ij}^b + h_{ij}^a \epsilon_{ij}^b) dv \\ - \int_V (f_i^b u_i^a + g_{ij}^b \sigma_{ij}^a + h_{ij}^b \epsilon_{ij}^a) dv = 0 \end{aligned} \quad (10)$$

where n_i is the outward normal to the enclosing surface.

We note that the surface integrals should, in general, be taken over surfaces of discontinuity, as well as over the enclosing surface of the volume V .

Equation (10), the reciprocity theorem, can be written in the compact notational form first used by Rumsey in EM theory

$$\langle a, b \rangle = \langle b, a \rangle \quad (11)$$

Here the comma is just a comma! The first letter in a bracket is associated with the volume source terms f_i, g_{ij}, h_{ij} and surface sources $f_j^S = \sigma_{ij} n_j$. The second term in the bracket is associated with the field quantities in the volume $u_i, \sigma_{ij}, \epsilon_{ij}$ and the displacement at the surface u_i . We call the quantity

$$\langle a, b \rangle = \int_S (\sigma_{ij}^a u_j^b) n_i dS + \int_V (f_i^a u_i^b + g_{ij}^a \sigma_{ij}^b + h_{ij}^a u_j^b) dV \quad (12)$$

the reaction between the (a) sources and the (b) fields. We note that the reaction $\langle a, b \rangle$ is closely related to the work done by the sources. We will find that the reaction is a very useful conceptual tool in the logical derivation of scattering relations and variational principles, both physically and because of its compact notation.

SCATTERING THEORY

The Scattering Matrix

In order to obtain some physical insight into the significance of the reciprocity theorem and make it possible to use the concept of reaction in scattering theory, we shall

consider two transducers of areas S_1 , S_2 , respectively, immersed in a volume V of material, as shown in Fig. 1.

We shall assume that the transducers, when used as receivers, sample the power incident upon them, and do not perturb the fields, i.e., they are like open circuited antennas in EM theory, or weakly coupled transducers for acoustic surface waves. Put another way, when the transducers are used as receivers, we ignore the reflected waves due to their presence. We can regard them as thin discs transparent to the acoustic wave which sample the power incident in the wave, by measuring the displacement fields associated with the wave.

Because we shall be concerned with scattering of a wave from a perturbation, it is convenient to relate the fields to the power in the transmitted and received waves. For this reason, we shall set up the theory in terms of the so-called Scattering Matrix used in EM theory; this makes a very convenient formulation which can be generalized fairly simply.

An acoustic beam can be excited by one of the transducers. The displacement fields and stresses normal to the surface of the transducer are

$$u_i^+ = A^+ u_i^0 \quad (13)$$

$$n_i \sigma_{ij}^+ = A^+ n_i \sigma_{ij}^0 \quad (14)$$

where n_i is taken to be the outward normal to the surface, i.e., the inward normal to the transducer, as shown in Fig. 1. The

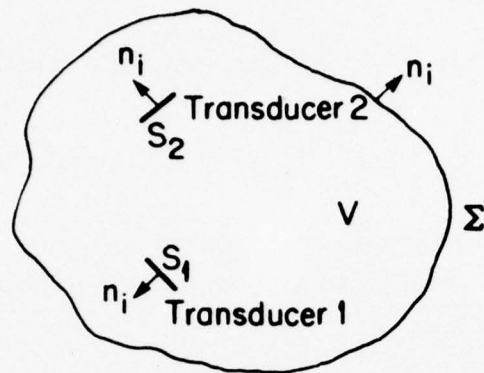


Figure 1. An illustration of the system considered in the derivation of the scattering matrix.

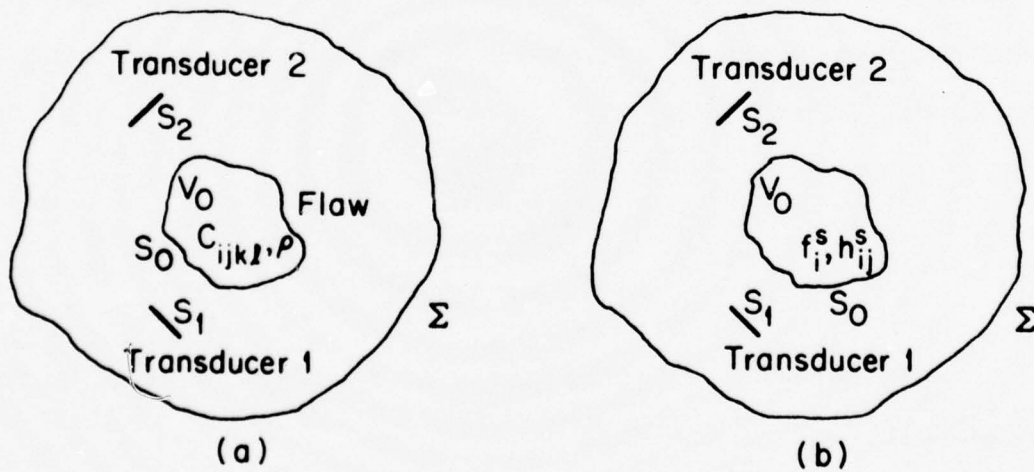


Figure 2. An illustration of equivalent configurations used in the theory of scattering from a flaw.

amplitudes u_i^0 , σ_{ij}^0 are chosen to correspond to unit power emitted by the transducer.

Thus, we define u_i^0 , σ_{ij}^0 to satisfy the relation

$$\frac{j\omega}{2} \int_S (\sigma_{ij}^0 u_j^{0*}) n_i dS = 1 \quad . \quad (15)$$

The power emitted by the transducer is, therefore,

$$P = \frac{1}{2} \operatorname{Re} \frac{j\omega}{2} A^{+*} \int_S (\sigma_{ij}^0 u_j^{0*}) n_i dS = A^+ A^{+*} \quad (16)$$

where S is the area of the transducer.

The transducer can also respond to an acoustic beam traveling in the opposite direction. If we suppose that the component of this beam to which the transducer responds is exactly the same in form, we can write an expression for the incident components of this wave which excites a receiving transducer in the form

$$u_i^- = A^- u_i^0 \quad (17)$$

$$n_i \sigma_{ij}^- = -A^- n_i \sigma_{ij}^0 \quad . \quad (18)$$

In general, the components of the wave, normal to the transducer, are of the form

$$u_i = (A^+ + A^-) u_i^0 \quad (19)$$

$$n_i \sigma_{ij} = (A^+ - A^-) n_i \sigma_{ij}^0 \quad . \quad (20)$$

The power emitted by the transducer is, therefore,

$$P = A^+ A^{+\star} - A^- A^{-\star} \quad (21)$$

Suppose now there are two transducers, 1 and 2, present in the system. Then we can determine, by linear superposition, the amplitude of the waves incident on the transducers in terms of the amplitudes of the waves emitted by the transducers.

Thus, we write

$$\begin{bmatrix} A_1^- \\ A_2^- \end{bmatrix} = \begin{bmatrix} S_{11} & S_{12} \\ S_{21} & S_{22} \end{bmatrix} \begin{bmatrix} A_1^+ \\ A_2^+ \end{bmatrix} \quad (22)$$

The matrix S is known as the scattering matrix of the system.

We now consider two situations; (a) transducer 1 is the transmitter, and transducer 2 is the receiver; (b) transducer 1 is the receiver, and transducer 2 is the transmitter. In case (a) $(A_1^+)^a$ is finite, $(A_1^-)^a = 0$, and $(A_2^+)^a = 0$, with $(A_2^-)^a$ finite.

It follows from the scattering matrix formulation that

$$(A_2^-)^a = S_{21} (A_1^+)^a \quad (23)$$

Similarly, it will be seen that

$$(A_1^-)^b = S_{12} (A_2^+)^b \quad (24)$$

Now we consider the reactions $\langle a, b \rangle$, $\langle b, a \rangle$, respectively. When the transducer is used as a transmitter, we regard it as a surface source $(f_i)_S = n_i \sigma_{ij}$ inside the volume V with, for convenience, $\sigma_{ij} = 0$ on one side of the transducer. More generally, a transducer such as a surface wave transducer with σ_{ij} finite

on both sides of the transducer can be taken into account by defining $(f_i)_S$ in terms of the discontinuity in stress at the transducer. When the transducer is used as a receiver, we regard it as not perturbing the field; so $(f_i)_S = 0$ in this case, and $n_i \sigma_{ij}$ is continuous through it. Thus there is no contribution to the reaction by the transducer in this case.

It, therefore, follows from Eq. (12) that the reaction due to the transducer alone, not including the enclosing surfaces at infinity, are $\langle a, b \rangle_t$, $\langle b, a \rangle_t$ respectively, where

$$\langle a, b \rangle_t = \int_{S_1} (f_i^a)_S u_i^b dS = (A_1^+)^a (A_1^-)^b = S_{12} (A_1^+)^a (A_2^+)^b \quad (25)$$

$$\langle b, a \rangle_t = \int_{S_2} (f_i^b)_S u_i^a dS = (A_2^+)^b (A_2^-)^a = S_{21} (A_1^+)^a (A_2^+)^b \quad (26)$$

Thus, the subscript t is used to denote the contributions to the reaction from the transducers alone. Here we have assumed that there is no source term associated with the receiving transducer, i.e., it is an open circuited antenna, and the power incident on it passes through it.

If we take account of the contributions from the enclosing surface Σ of the volume V , it will be seen that

$$\langle a, b \rangle_t = \langle a, b \rangle - \int_{\Sigma} (\sigma_{ij}^a u_j^b) n_i dS \quad (27)$$

It follows that, as $\langle a, b \rangle - \langle b, a \rangle = 0$, then

$$\langle a, b \rangle_t - \langle b, a \rangle_t = \int_{\Sigma} (\sigma_{ij}^b u_j^a - \sigma_{ij}^a u_j^b) n_i dS \quad (28)$$

But when Σ is a large sphere, we can write $n_i \sigma_{ij} = Z_0 u_j / j\omega$ where Z_0 is the impedance of the medium. Hence the integral in Eq. (28) is zero, and

$$(S_{21} - S_{12}) (A_1^+)^a (A_2^+)^b = \langle b, a \rangle_t - \langle a, b \rangle_t = 0 \quad (29)$$

Thus, it will be seen that $S_{12} = S_{21}$. This is a general reciprocity condition which holds under much less restrictive conditions than those given here. Furthermore, it will be seen that, when the transducers are excited by unit power, the scattering term S_{21} is given by the relation

$$S_{21} = \langle b, a \rangle_t \quad (30)$$

This concept can be generalized and taken all the way to the electrical terminals of the transducers by using the more general normal mode theory given by Auld and Kino.⁵

Perturbation Theory

We shall consider the scattering of acoustic waves from a flaw "s". We shall use two transducers "1" and "2" as detectors and transmitters. We will apply unit power to transducer 1 to excite an acoustic wave, and measure the amplitude S_{21} of the signal arriving at transducer 2. As we are interested only in the scattering of the incident wave from flaw, we will be interested in that component of S_{21} which we call S_{21}^s . The component of S_{21} when there is no flaw present we call S_{21}^i (i for incident). So we can write the relation

$$S_{21} = S_{21}^i + S_{21}^s \quad (31)$$

It is convenient to represent the scattering object in terms of effective volume sources $(f_i^S)_1$, $(h_{ij}^S)_1$ in the original unperturbed medium, which are due to the scattering object being irradiated by transducer 1 which is itself excited by unit power.

Now consider the reaction $\langle b^i, a \rangle_t$ in the following situation: (b^i) corresponds to using transducer 2 as the transmitter, with unit input power and no perturbing object present, thus setting up fields $(u_i^i)_2$, $(\sigma_{ij}^i)_2$ in the volume; (a) corresponds to using transducer 1 as the transmitter in the presence of the perturbing object, which behaves like an effective volume source $(f_i^S)_1$, $(h_{ij}^S)_1$. Following the procedure used in deriving Eq. (35) from Eq. (12), we see that

$$S_{21} = \langle a, b^i \rangle_t = \int_{S_2} (f_i^{b^i})_S u_i^a dS + \int_{V_0} \left[(f_i^S)_1 (u_i^i)_2 + (h_{ij}^S)_1 (\epsilon_{ij}^i)_2 \right] dv \quad (32)$$

where $(f_i^{b^i})_S$ is the effective surface source of transducer 2.

But, it follows from Eq. (35) that

$$S_{21}^i = \int_{S_2} (f_i^{b^i})_S u_i^a dS \quad (33)$$

Hence it will be seen that the scattered amplitude is

$$S_{21}^S = S_{21} - S_{21}^i = \int_{V_0} \left[(f_i^S)_1 (u_i^i)_2 + (h_{ij}^S)_1 (\epsilon_{ij}^i)_2 \right] dv \quad (34)$$

This is the basic expression for S_{21}^S that we require.

It is an exact result. The problem is to evaluate $(f_i^S)_1$, $(h_{ij}^S)_1$. These source terms can be evaluated in terms of the total field

within the scattering object.

It follows from Eq. (31) that

$$(\sigma_{ij,j})_1 = -\omega^2 \rho (u_j)_1 + (f_j^S)_1 \quad (35)$$

But within the scattering object, it is also apparent that

$$(\sigma_{ij,j})_1 = -\omega^2 \rho' (u_j)_1 \quad (36)$$

where ρ' is the density of the perturbing object.

It follows by subtracting Eq. (35) from Eq. (36) that

$$(f_j^S)_1 = -\omega^2 (\rho' - \rho) (u_j)_1 \quad (37)$$

Similarly, it will be seen that

$$(h_{ij}^S)_1 = (C'_{ijkl} - C_{ijkl}) (\epsilon_{kl})_1 \quad (37)$$

Hence the scattering formula can be written in the form

$$S_{21}^S = \int_{V_0} \left[-\omega^2 \delta \rho (u_i)_1 (u_i^1)_2 + (\epsilon_{ij}^1)_2 \delta C_{ijkl} (\epsilon_{kl})_1 \right] dv \quad (39)$$

where

$$\delta C_{ijkl} = C'_{ijkl} - C_{ijkl} \quad (40a)$$

$$\delta \rho = \rho' - \rho \quad (40b)$$

and the fields $(u_i)_1$, $(u_i)_2$, $(\epsilon_{ij}^1)_2$, $(\epsilon_{kl})_1$ correspond to unit powers exciting the transducers.

A very similar scattering formula can also be derived for scattering from a cavity or rigid body. In this case, we use the reciprocity theorem of Eq. (9) to derive the equivalent

of Eq. (39). Now, however, the only contributions are from surface integrals around the scattering region. So we find that

$$S_{21}^S = \int_{S_0} \left[(\sigma_{ij})_1 (u_j^i)_2 - (\sigma_{ij}^i)_2 (u_j)_1 \right] n_i dS \quad (41)$$

where now n_i is defined as the inward normal to the body of surface area S_0 . This is a general surface scattering formula.

We note that the normal stress at the surface of a cavity is zero. Hence $(\sigma_{ij})_1 n_i = 0$. So the formula for surface scattering from a cavity becomes

$$S_{21}^S(\text{cavity}) = - \int_{S_0} (\sigma_{ij}^i)_2 (u_j)_1 n_i dS \quad (42)$$

This is, again, an exact result for the scattered field, provided we know $(u_j)_1$, a difficult task to determine exactly.

Very similarly, the scattering formula for scattering from a rigid body is obtained by putting $u_i = 0$ on the surface of the body in Eq. (41). This yields the relation

$$S_{21}^S(\text{rigid body}) = \int_{S_0} (\sigma_{ij})_1 (u_j^i)_2 n_i dS \quad (43)$$

The Born Approximation

The Born approximation, which is often used in scattering theory, can considerably simplify the application of these formulae. In this approximation, the assumption is made that the perturbed fields in the vicinity of the flaw $(\sigma_{ij})_1$, $(u_i)_1$ in Eq. (39), $(u_j)_1$ in Eq. (42), and $(\sigma_{ij})_1$ in Eq. (43), respectively, can be replaced by the unperturbed incident fields

from transducer 1. Equations (39) and (42) then become, in the Born approximation, respectively

$$S_{21}^S = \int \left[-\omega^2 \delta \rho (u_i^i)_1 (u_i^i)_2 + (\epsilon_{ij}^i)_2 \delta C_{ijkl} (\epsilon_{ij}^i)_1 \right] dv \quad (44)$$

and

$$S_{21}^S(\text{cavity}) = - \int_{S_0} (\sigma_{ij}^i)_2 (u_j^i)_1 n_i dS \quad (45)$$

where now we assume the displacement is not much changed by the presence of a flaw. The surface scattering Born approximation can be further simplified by using Gauss's theorem to write it as a volume integral in the form

$$\begin{aligned} S_{21}^S(\text{cavity}) &= - \int_{V_0} \left[(\sigma_{ij}^i)_2 (u_j^i)_1 \right]_{,i} dv \\ &= - \int_{V_0} (\sigma_{ij,i}^i)_2 (u_j^i)_1 + (\sigma_{ij}^i)_2 (u_{j,i}^i)_1 dv \end{aligned} \quad (46)$$

or

$$S_{21}^S(\text{cavity}) = \int_{V_0} \left[\omega^2 \rho (u_i^i)_1 (u_i^i)_2 - (\epsilon_{ij}^i)_2 C_{ijkl} (\epsilon_{kl}^i)_1 \right] dv. \quad (47)$$

Hence, it follows that the scattering due to a vacancy may be obtained by replacing $\delta \rho$ by $-\rho$ and δC_{ijkl} by $-C_{ijkl}$ in the volume integral for scattering, as might be expected.

When a similar analysis is followed through for a rigid body, we find that $\delta \rho$ must be replaced by 2ρ and δC_{ijkl} by $2C_{ijkl}$, a result that would not necessarily be expected intuitively.

Example 1. Plane Wave Scattering

We can gain considerable physical insight into the nature of the scattering from flaws by examining the Born approximation and the more exact solutions given by Eqs. (39), (40) and (43). Consider first what occurs for longitudinal plane wave scattering into a longitudinal wave propagating at an angle θ to the incident wave, as illustrated in Fig. 3.

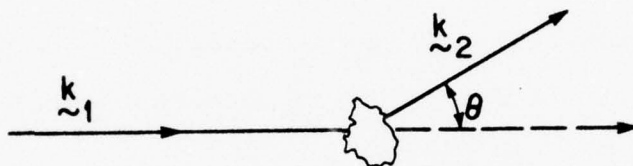


Figure 3. An illustration of scattering at an angle θ .

In this case, if the medium is isotropic $k_1^i = k_2^i = k$ and for quasi plane waves at the object, we can write $(u^i)_1$ in terms of a scalar potential:

$$(u^i)_1 = -jk_{1i}(\phi^i)_1 e^{-jk_1 \cdot r} \quad (48)$$

with

$$(u^i)_2 = -jk_{1i}(\phi^i)_2 e^{-jk_2 \cdot r} \quad (49)$$

Hence

$$(u^i)_1 (u^i)_2 = B \cos\theta e^{-jk(1-\cos\theta)x} \quad (50)$$

where $B = k^2(\phi^i)_1(\phi^i)_2$ is a constant. B can be evaluated for unit power emitted from each transducer, by writing

$$S\omega^2 u_i^2 / 2Z_\ell = 1 \quad (51)$$

where S is the area of the transducer. It is assumed that the transducer emits a plane wave, and the flaw is in the near field of the transducer, and Z_ℓ is the longitudinal wave impedance. Following this argument, we see that

$$B = 2Z_\ell/\omega^2 (S_1 S_2)^{\frac{1}{2}} . \quad (52)$$

A similar relation can be found for B when the flaw is in the Fraunhofer zone of the transducers. In this case, if the transducers are pointed at the flaw, at distances r_1, r_2 , respectively from the flaw, and emit beams of solid angles Ω_1, Ω_2 , respectively, we find that

$$B = 2Z_\ell/\omega^2 r_1 r_2 (\Omega_1 \Omega_2)^{\frac{1}{2}} . \quad (53)$$

Again, if the medium is isotropic and \underline{k}_1 is directed along the x axis, we write $C_{1111} = \mu + 2\lambda$, $C_{1122} = \lambda$, $C_{1212} = \mu$, and

$$(\epsilon_{ij}^i)_2 \delta C_{ijkl} (\epsilon_{kl}^i)_1 = -k^2 B \left[\delta C_{1111} \cos^2 \theta + \delta C_{1122} \sin^2 \theta \right] \quad (54)$$

Thus, it follows that in the Born approximation for longitudinal to longitudinal wave scattering, with $k^2 = \omega^2 \rho / C_{1111}$,

$$S_{21}^S = \omega^2 \rho B \int_{V_0} e^{-ikz(1-\cos\theta)} \left[\frac{\delta \rho}{\rho} \cos\theta - \frac{\delta C_{1111}}{C_{1111}} \cos^2 \theta - \frac{\delta C_{1212}}{C_{1111}} \sin^2 \theta \right] dV . \quad (55)$$

We note that the scattered fields have a peak value where $\theta = 0$ and $\theta = \pi$. When there is a vacancy present, the Born approxi-

mation with $\delta C_{1111} = -C_{1111}$, $\delta \rho = -\rho$, gives a result which is exactly zero at $\theta = 0$. This does not occur, however, if the flaw has a finite density or elastic constant, unless it is completely rigid. But in the exact solution, the density terms and the elastic terms would not cancel. In this case, because the term $\exp -jkz(1-\cos\theta)$ at $\theta = 0$ would have a very small argument; if the Born approximation were relaxed, we would expect the integral to become large if kz could become large within the volume of the flaw. So, in fact one would expect the forward scattering to increase monotonically with frequency or size, and become very large at high frequencies, because of the cumulative contribution to the integral when the exponential term does not change in sign. On the other hand, we would expect the backward scattering ($\theta = \pi$) to exhibit peaks and valleys of roughly the same magnitude as the frequency is increased. We note also that in the Born approximation, the scattering at $\theta = \pi/2$ is zero.

Now consider the situation when the flaw is small in size so that its largest dimension a is such that $ka \ll 1$. In this case, the scattered field, as far as the Born approximation is concerned, becomes

$$S_{21}^S(\text{longitudinal} - \text{longitudinal}) = \omega^2 \rho B V_0 \left[\frac{\delta \rho}{\rho} \cos \theta - \frac{\delta C_{1111}}{C_{1111}} \cos^2 \theta - \frac{\delta C_{1212}}{C_{1111}} \sin^2 \theta \right] \quad (56)$$

It follows that as far as the Born approximation is concerned the shape of the flaw has no effect on the longitudinal-to-

longitudinal wave scattering as a function of angle in the Rayleigh limit. However, the nature of the material in the flaw certainly will affect the scattering as a function of angle. If the Born approximation is not used, but instead a more correct static approximation to find the fields within the flaw is employed, the situation changes. Now the shape of the flaw affects the direction of the fields within it. So there should, in practice, be some, but probably a small effect of scatterer shape, on scattering as a function of angle.

We now consider scattering from a longitudinal wave to a shear wave in the Born approximation. In this case, if the unperturbed material is isotropic, there can be no coupling between longitudinal and shear strain terms, i.e., from the last term in the integrand of Eq. (44). It follows that the longitudinal to shear wave coupling from a longitudinal wave propagating along the axis to a shear wave in the θ direction, taking the propagation constants to be k_L, k_T , respectively, we find that

$$S_{21}^S(\text{longitudinal-shear}) = -\omega^2 \rho A \int_{S_0} \delta \rho e^{-j(k_L - k_T \cos \theta)z} \sin \theta \, dV \quad (57)$$

where A is a constant. We see that now we would expect zero scattering from a longitudinal wave to a shear wave at $\theta = 0$, $\theta = \pi$. However, we would expect the scattering to reach a maximum, at least in the Rayleigh limit, when $\theta = \pm \pi/2$. Furthermore, as the frequency or size of the object becomes large we would also expect strong scattering near where $k_L = k_T \cos \theta$ provided

$\sin\theta$ is sufficiently large in this region. This implies that

$$\cos\theta \approx \frac{v_T}{v_L} . \quad (58)$$

We note that as $v_T/v_L \approx 0.4$ in most metals, the implication is that the shear wave scattering is still strong near $\theta = \pi/2$. Again, in the Rayleigh limit, the Born approximation would not indicate that the scattering as a function of angle would depend on the specimen shape or size.

The conclusions we have reached here appear to be in reasonable qualitative agreement with the numerical calculations of Gubernatis, et al, and yield some physical explanations of the behavior of their plotted curves.

Example 2. Scattering of Rayleigh Waves from a Small Hole

We now consider scattering of a straight crested Rayleigh wave from a hole of length h and radius a , whose axis is normal to the surface of the substrate. We only consider the back scattering ($\theta = \pi$) of the Rayleigh wave from the hole, although the same techniques can be used to determine the scattering at any angle. We have carried out the integration of Eq. (42) over the cylindrical surface of the hole. We neglect the contribution from the bottom of the hole, and use potentials

$$\phi^i = A e^{\gamma Y} e^{-j\beta z} \quad (59)$$

$$\psi_x^i = - \frac{2jA\gamma_L^\beta}{\beta^2 + \gamma_T^2} e^{\gamma_T Y} e^{-j\beta z} \quad (60)$$

where the propagation constant of the Rayleigh wave is β , and

$$\gamma_L^2 = \beta^2 - k_L^2, \quad (61)$$

$$\gamma_T^2 = \beta^2 - k_T^2 \quad (62)$$

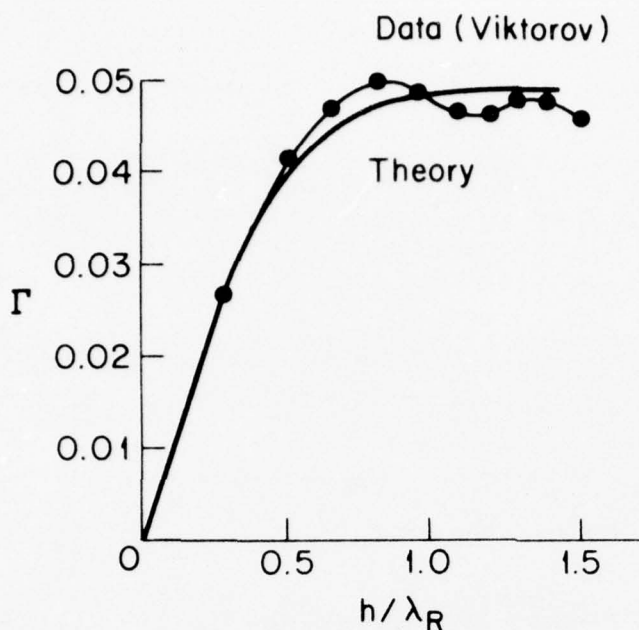
and k_L , k_T are the propagation constants of longitudinal and shear plane waves, respectively. Following through this analysis, we find that for a hole of radius a and a length h , the scattered amplitude is of the form

$$S_{21}^S = C\beta a J_1(2\beta a) \left\{ \frac{\beta^2 - \gamma_T^2}{2\beta\gamma_L} \left[1 - e^{-2\gamma_L h} \right] + \frac{\gamma_L(\beta^2 + 3\gamma_T^2)}{2\gamma_T^2\beta} \left[1 - e^{-2\gamma_T h} \right] \right. \\ \left. + \frac{2(3\beta^2 + \gamma_T^2) - 2\gamma_L^2\gamma_T}{\beta(\gamma_L + \gamma_T)(\beta^2 + \gamma_T^2)} \gamma_L \left[1 - e^{-(\gamma_L + \gamma_T)h} \right] \right\} \quad (63)$$

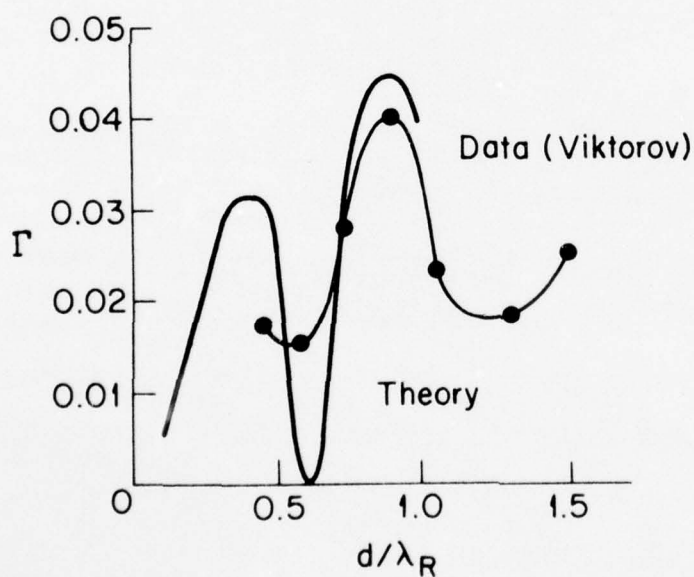
where C is a constant and $J_1(x)$ is a Bessel function of the first kind and first order.

We would expect this formula to give its best results for $\beta a < 1$, and $h < \lambda$; for creeping waves on the cylinder can influence the scattering. In addition, large perturbations of the incident field are to be expected when the hole is large in size.

We have calculated Eq. (36) for aluminum and compared the results to measurements made by Viktorov,⁴ normalizing our results to the maximum value of the experimental curves. It will be seen from Fig. 4, that the theory and experiment appear to agree fairly well. Whether this result is fortuitous or an



(a) Normalized reflection amplitude Γ vs hole depth h for small (0.9λ) flat bottom holes.



(b) Data for through drilled holes of varying diameters.

Figure 4. Comparison of the theory of Eq. (63) with data from Viktorov with the theoretical results normalized to a maximum value of 0.048.

accurate one remains to be seen after further experimental results are obtained.

CONCLUSIONS

The use of the reaction principle and of scattering matrices provides a convenient formalism from which to obtain scattering formulae. The method does not require the use of elaborate Green's function formulae, and gives physically meaningful results which can provide a great deal of insight into the interactions which occur. In this paper the method has been applied to obtain the Born approximation for scattering of plane waves and Rayleigh waves. It should be easily adaptable to derive the Keller⁶ formulation for scattering from cracks large comparable to the wavelength, and to the use of elastostatic formulae to give a better estimate of the fields in the neighborhood of a small flaw. Thus, it should be possible to obtain a fairly good insight into the nature of the scattering from nonspherical defects over the complete size range.

ACKNOWLEDGEMENT

This research was initially supported by the Advanced Research Projects Agency of the Department of Defense under Contract No. MDA903-76C-0250 with The University of Michigan and completed under Rockwell International Contract No. 74-20773 for the Advanced Research Projects Agency and the Air Force Materials Laboratory under Contract F33615-74-C-5180.

REFERENCES

1. J. E. Gubernatis, E. Domany, J. A. Krumhansl and M. Huberman, "The Fundamental Theory of Elastic Wave Scattering by Defects in Elastic Materials - Integral Equation Method for Application to Ultrasonic Flaw Detection," Report No. 2654, Materials Science Center, Cornell University.

See also, J. E. Gubernatis, E. Domany, M. Huberman and J. A. Krumhansl, "Theory of the Scattering of Ultrasound by Flaws," Ultrasonics Symposium Proceedings, September 22-24, 1975, pp. 107-110.

2. V. H. Rumsey, "The Reaction Concept in Electromagnetic Theory," Phys. Rev. Ser. 2, Vol. 94, No. 6, June 15, 1954, pp. 1483-1491.
3. R. F. Harrington, Tome Harmonic Electromagnetic Fields, McGraw-Hill, New York, 1961.
4. I. A. Viktorov, Rayleigh and Lamb Waves, Plenum Press, New York, 1967, pp. 57-65.

See also, I. A. Viktorov and T. M. Kaekina, "The Scattering of Ultrasonic Rayleigh Waves at Models of Surface Defects," Akust. Zh. 10(1): 30-33 (1964).

5. B. A. Auld and G. S. Kino, "Normal Mode Theory for Acoustic Waves and its Application to the Interdigital Transducer," IEEE Trans. on Electron Devices, Vol. ED-18, No. 10, October, 1971, pp. 898-908.
6. J. B. Keller, "Diffraction by an Aperture," J. Appl. Phys. Vol. 28, (1967), pp. 426-443.

II. VARIATIONAL FORMULAE FOR SCATTERING OF ACOUSTIC WAVES BY FLAWS, AND FOR ACOUSTIC WAVE PROPAGATION

G. S. Kino

INTRODUCTION

We shall derive here a set of variational formulae which can be used both to determine the eigenvalues of a propagating mode, and also to determine the scattering of an incident wave from a small region where the elastic properties or mass density is different from that of the surrounding medium. The eigenvalue results we obtain are similar to those of Nemat-Nasser, and in fact, our formulae can be shown to reduce to his. We shall use a logical formalism based on the reaction principle first applied to EM theory by Rumsey. This enables us to derive different classes of variational formulae in which we can use trial functions for either stress, strain, or displacement, or more than one of these parameters.

In general, the variational formulae can be used when the trial functions do not obey all the boundary conditions at the surface between two different elastic media. However, such variational formulae are always most accurate when the trial fields form as close an approximation as possible to the true fields. For eigenvalue problems, it is necessary to use a trial function which is, at least, an approximation to the true eigenfunction.

We first illustrate the use of the reaction principle in variational theory by deriving the variational formulae for the eigenvalues of a propagating wave. After deriving a general formula, we show how it may be specialized to obtain a variational theorem equivalent to that of Kohn, Krumhansl, and Lee,¹ and a second formula equivalent to that of Nemat-Nasser.²

We derive the variational scattering formulae from the perturbation theory, which is itself based on the use of the reaction principle, as discussed in paper I. In this case the true fields due to excitation of waves by either one of the transducers, are replaced by trial fields. Then by use of the reaction principle, it is possible to find a variational formula which gives a scattering amplitude accurate to second order when the trial fields are only accurate to first order.

We find that we can obtain Green's function variational formulae for scattering, as well as different types of formulae involving differentials of the trial functions. We have not used these formulae, at the present time, to obtain numerical results for scattering. However, we believe they should form a basis for such types of analyses, and for application to Rayleigh-Ritz procedures.

VARIATIONAL FORMULAE FOR THE EIGENVALUES OF A PROPAGATING WAVE

We follow the methods and notation given in paper I, and consider the form of the reaction and the reciprocity relation when the fields in the medium are not exact solutions, but trial fields. We obtain a variational principle by requiring the trial

fields to obey the reciprocity theorem to at least first order.

We assume that within the volume, the trial fields obey Eqs. (3) and (5) of paper I. The source terms f_i , g_{ij} , h_{ij} may then be regarded as accounting for errors in the trial field. Furthermore, if we regarded the trial fields as having first-order errors, f_i , g_{ij} , h_{ij} , can be regarded as first-order terms. These source terms are zero for the true field.

Following Rumsey's^{3,4} notation, we denote the trial fields and sources by the symbol a , and the true fields and sources by the symbol c_a (c stands for correct, so c_a is the correct value of a). We consider the difference of the reactions $\langle a, c_a \rangle - \langle c_a, a \rangle$. As all contributions to the right hand side of Eq. (13) of paper I from within the volume must be zero, because there are no internal sources associated with the true fields, it follows that we can write the reaction principle in the form

$$\langle a, c_a \rangle - \langle c_a, a \rangle = \int (\sigma_{ij}^a u_j^c - \sigma_{ij}^c u_j^a) n_i dS - \int (f_i^a u_i^c + g_{ij}^a \sigma_{ij}^c + h_{ij}^a \epsilon_{ij}^c) dV = 0 \quad (1)$$

We require $\langle a, c_a \rangle - \langle c_a, a \rangle$ to be zero only to second order. Therefore, it will be seen that, because the source terms are themselves first-order error terms, the true fields can be replaced by trial fields in the volume integral. In addition, if the true and trial fields obey the boundary conditions of zero stress or displacement, the surface integral is zero, and we can write our variational principle as

$$\langle a, a \rangle = 0 \quad (2)$$

a statement correct to second order.

More generally, the variational principle in its most general form can be obtained by replacing the fields in the volume integral by trial fields, and writing Eq. (1) in the form

$$\int_V (f_i^a u_i^a + g_{ij}^a \sigma_{ij}^a + h_{ij}^a \epsilon_{ij}^a) dV - \int_S (\sigma_{ij}^a u_j^c - \sigma_{ij}^c u_j^a) n_i dS = 0 \quad (3)$$

where the surface integral, in general, includes integrals taken over the boundary surface between two elastic regions. This statement has, at most, second-order errors.

Before proceeding further, it is also worth noting that it is often convenient to work with the complex conjugate fields which vary as $\exp-j\omega t$. These also obey the same governing equations, Eqs. (3), (4) and (5) of paper I, and the reciprocity theorem. So, it is possible to state that

$$\langle a c_a^* \rangle = \langle c_a^* a \rangle \quad (4)$$

Following the same reasoning as before, the variational principle becomes

$$\int_V (f_i^a u_i^{a*} + g_{ij}^a \sigma_{ij}^{a*} + h_{ij}^a \epsilon_{ij}^{a*}) dV - \int_S (\sigma_{ij}^a u_j^{c*} - \sigma_{ij}^{c*} u_j^a) n_i dS \quad (5)$$

Example 1. The Kohn, Krumhansl, Lee Variational Principle¹

Suppose we use trial displacement fields $u_i^a = u_i^{a*}$, where $*$ denotes the complex conjugate field. We derive ϵ_{ij} from u_i , using Eq. (4) of paper I with $g_{ij} \equiv 0$; and determine σ_{ij} in any region, by using Eq. (5) of paper I with $h_{ij} \equiv 0$.

In this case

$$\int (\sigma_{ij}^a u_j^{c*} - \sigma_{ij}^{c*} u_j^a) n_i dS - \int u_i^{a*} (\sigma_{ij,i}^a + \omega^2 \rho u_i^a) dV = 0 \quad (6)$$

becomes the variational principle.

Now the exact fields u_i^c , σ_{ij}^c , u_i^{c*} and σ_{ij}^{c*} obey the boundary conditions. So u_i^c , u_i^{c*} , and the normal components of σ_{ij}^c , σ_{ij}^{c*} are continuous through the surface between different media.

Suppose we choose a trial function for which u_i^a is continuous through these surfaces. Then we can write the variational principle in the form

$$\underbrace{\int (\sigma_{ij}^a u_j^{c*} - \sigma_{ij}^{c*} u_j^a) n_i}_{\text{outer boundary surface}} + \underbrace{\int (\sigma_{ij}^{a+} - \sigma_{ij}^{a-}) u_j^{a*} n_i dS}_{\text{surface of discontinuity}} - \int u_i^{a*} (\sigma_{ij,i}^a + \omega^2 \rho u_i^a) dV = 0 \quad (7)$$

where + and - superscripts denote quantity just outside and just inside the surface of discontinuity respectively.

We have replaced u_j^c with u_j^a in the surface integral at the surface of discontinuity, as this only introduces a second-order error.

It will be noted that there are equivalent forms for this variational principle. We can write in the volume integral

$$\begin{aligned} u_i^{a*} \sigma_{ij,i}^a &= (u_i^{a*} \sigma_{ij}^a)_{i,j} - \sigma_{ij}^a u_{i,j}^{a*} \\ &= (u_i^{a*} \sigma_{ij})_{,j} - \sigma_{ij}^a \epsilon_{ij}^{a*} \end{aligned} \quad (8)$$

So it follows that the integrals over the surfaces of discontinuity cancel out and

$$\int (\sigma_{ij}^a \epsilon_{ij}^{a*} - \omega^2 \rho u_i^a u_i^{a*}) dV + \int_{\text{outer surface}} \left[\sigma_{ij}^a (u_j^{c*} - u_j^{a*}) - \sigma_{ij}^{c*} u_j^a \right] n_i dS = 0 \quad (9)$$

In this case, $\sigma_{ij}^a, \epsilon_{ij}^a$ are derived from u_i^a by use of Eqs. (4) and (5) of paper I with $g_{ij} = h_{ij} = 0$. Note, however, we do not need to evaluate surface integrals over the surface of discontinuity when using the variational principle in this form; nor do the trial fields have to obey the boundary conditions at the surface. So, in some situations, the analysis can be considerably simplified in this form, when u_i^a is continuous through the surface between two elastic media. We note that this is the Variational Principle first used by Kohn, Krumhansl and Lee.¹

Example 2. Stress and Displacement as Independent Trial Functions

(Nemat-Nasser Theory²)

Suppose we define trial displacement fields and trial stresses independently. We use Eq. (5) of paper I with $h_{ij} = 0$ to define the strain. Thus, we write $h_{ij}^a = 0$ in Eq. (5). We put $\epsilon_{ij}^a = S_{ijkl} \sigma_{kl}^a$, $\epsilon_{ij}^{a*} = S_{ijkl} \sigma_{kl}^{a*}$; with $S_{ijkl} = (C_{ijkl})^{-1}$.

In this case, Eq. (5) becomes

$$\begin{aligned} \int_S (\sigma_{ij}^a u_{ij}^{c*} u_j^a) n_i dS - \int_V u_i^{a*} (\sigma_{ij,i}^a + \omega^2 \rho u_i^a) dV \\ + \int_V \sigma_{ij}^{a*} (S_{ijkl} \sigma_{kl}^a - u_{i,j}^a) dV = 0 \quad (10) \end{aligned}$$

If we choose u_i^a and σ_{ij}^a to satisfy the boundary conditions, as we could do in certain cases, i.e., to be continuous

like the true values of these fields, the variational principle becomes

$$\int_V \sigma_{ij}^{a*} (s_{ijkl} \sigma_{kl}^a - u_{i,j}^a) dV - \int_V u_i^{a*} (\sigma_{ij,i}^a + \omega^2 \rho u_i^a) dV = 0 \quad (11)$$

This is identical to Nemat-Nasser's Eq. (3.13), if the integrands are taken to be real, as they normally are.²

VARIATIONAL SCATTERING THEORY

In paper I we have derived a scattering theory which is based on the use of exact fields. Approximations such as the Born approximation are not variational in form. Suppose, now, we try and determine a variational form of the scattering theory where we replace the true fields with trial fields. As a first step we must express all parameters in the scattering theory in terms of the fields within the system which we are intending to replace with trial fields. Then we can write the scattered amplitude in terms of the reaction of the sources at the obstacle with the fields at the obstacle.

We start with the exact scattering formula of Eq. (34) of paper I and use the notation given in that paper. Thus we put

$$s_{21}^s = \int_{V_0} \left[(f_i^s)_1 (u_i^i)_2 + (h_{ij}^s)_1 (\epsilon_{ij}^i)_2 \right] dV \quad (12)$$

We note that it follows from the reciprocity theorem that we can exchange sources and fields and write an equivalent formula:

$$S_{21}^S = S_{12}^S = \int \left[(f_i^S)_2 (u_i^i)_1 + (h_{ij}^S)_2 (\epsilon_{ij}^i)_1 \right] dv \quad (13)$$

The incident fields u_i^i , ϵ_{ij}^i can be written in terms of the total and scattered fields at the obstacle as follows:

$$u_i^i = u_i - u_i^S \quad (14)$$

and

$$\epsilon_{ij}^i = \epsilon_{ij} - \epsilon_{ij}^S \quad (15)$$

But it follows from Eqs. (37) and (38) of paper I that there are direct relations between the total fields u_i , ϵ_{ij} and their sources. These are

$$\omega^2 (\rho' - \rho) (u_i)_2 = \omega^2 \delta \rho (u_i)_2 = -(f_i^S)_1 \quad (16)$$

or

$$(u_i)_2 = -(f_i^S)_2 / \omega^2 \delta \rho \quad (17)$$

$$(C'_{ijkl} - C_{ijkl}) (\epsilon_{kl})_2 = \delta C_{ijkl} (\epsilon_{kl})_2 = (h_{ij}^S)_2 \quad (18)$$

or

$$(\epsilon_{kl})_1 = (\delta C_{ijkl})^{-1} (h_{ij}^S)_1 \quad (19)$$

Hence it will be seen that after substitution of Eqs. (14), (15), (17) and (19) in Eq. (13), that the scattering formula can be written in the form

$$S_{21}^S = \int_{V_0} \left[- \frac{(f_i^S)_2 (f_i^S)_1}{\omega^2 \delta \rho} + (h_{ij}^S)_1 (\delta C_{ijkl})^{-1} (h_{ij}^S)_2 - (u_i^S)_2 (f_i^S)_1 - (\epsilon_{ij}^S)_2 (h_{ij}^S)_1 \right] dv \quad (20)$$

The fields $(u_i^s)_1$ and $(\epsilon_{ij}^s)_1$ can be expressed in terms of some combination of the $(f_i^s)_1$ and $(h_{ij}^s)_1$ by means of a Green's function; and vice versa, if required. As an example $(u_i^s)_1 = G(f_i^s)_1$ where G is a linear operator. This is also true of $(u_i^s)_2$ and $(\epsilon_{ij}^s)_2$.

Hence we can write S_{21}^s in terms of the reaction theory formalism, as follows:

$$S_{21}^s = K \langle c_1, c_2 \rangle \quad (21)$$

where K is a constant, and c_1, c_2 are the true scattering sources.

We wish, in general, to replace the true sources c_1, c_2 with trial sources a_1, a_2 . It is required, then, to arrive at trial sources (or associated fields) which will give the same value of S_{21}^s . This implies that we replace, for instance, $(f_i^s)_1$ with a trial source $A(f_i^a)_1$. The resultant reaction S_{21}^a is required to remain unchanged, at least to first order in errors, as the distribution of the source within the obstacle is changed. Furthermore, as the relation of Eq. (21) is, in fact, normalized to unit exciting powers at transducers 1 and 2, respectively, the result should not be critical with respect to the chosen source amplitudes, f_i^a, h_{ij}^a although the amplitudes of $(f_i^a)_1, (h_{ij}^a)_1$ can be assumed to vary together as the amplitude of the excitation on transducer 1 is varied, because of the linear relations between fields.

Thus when we replace c_1, c_2 with trial sources or fields, we expect the variational theory to lead to the same result for

S_{21}^S . Hence to first order, the following condition must be satisfied:

$$S_{21}^a = K \langle A_1 a_1, A_2 a_2 \rangle = K \langle c_1, c_2 \rangle \quad (22)$$

where A_1, A_2 are amplitude factors.

Because the field-source relations are linear and Eqs. (20) and (21) are symmetric in c_1, c_2 , it follows that Eq. (22) can be written in the form

$$\langle c_1, c_2 \rangle = A_1 A_2 \langle a_1, a_2 \rangle = A_1 A_2 \langle a_2, a_1 \rangle \quad (23)$$

Now we would expect that if we replaced $A_1 a_1$ by the correct source c_1 we should obtain the same result, at least if the variational principle we are to use is a valid one. Thus we can also write

$$\langle c_1, c_2 \rangle = A_2 \langle c_1, a_2 \rangle = A_2 \langle a_2, c_1 \rangle \quad (24)$$

Similarly if we replace a source a_2 by c_2 we expect that

$$\langle c_1, c_2 \rangle = A_1 \langle a_1, c_2 \rangle = A_1 \langle c_2, a_1 \rangle \quad (25)$$

Solving for A_1 and A_2 from Eqs. (24) and (25) and substituting in Eq. (23) we find that

$$\langle c_1, c_2 \rangle = \frac{\langle a_1, c_2 \rangle \langle a_2, c_1 \rangle}{\langle a_1, a_2 \rangle} \quad (26)$$

So our variational solution takes the form

$$S_{21}^a = K \langle c_1, c_2 \rangle = \frac{K \langle a_1, c_2 \rangle K \langle a_2, c_1 \rangle}{K \langle a_1, a_2 \rangle} \quad (27)$$

We can write the numerator of Eq. (27) using trial functions for the sources in terms of Eqs. (12) and (13) and the denominator in terms of Eq. (20) replacing the sources with trial sources. Before doing this let us check the validity of Eq. (27) as a variational form. Suppose a_1, a_2 are in error by $\delta c_1, \delta c_2$ respectively, and we regard $\delta c_1, \delta c_2$ as the first order errors. Thus we regard the source distributions as having first order errors. Then this is a variational solution if a quantity R defined as

$$R = \frac{\langle a_1, c_2 \rangle \langle a_2, c_1 \rangle}{\langle a_1, a_2 \rangle} = \frac{(\langle c_1 + \delta c_1, c_2 \rangle \langle c_2 + \delta c_2, c_1 \rangle)}{\langle c_1 + \delta c_1, c_2 + \delta c_2 \rangle}$$

$$= \frac{(\langle c_1, c_2 \rangle + \langle \delta c_1, c_2 \rangle)(\langle c_2, c_1 \rangle + \langle \delta c_2, c_1 \rangle)}{\langle c_1, c_2 \rangle + \langle \delta c_1, c_2 \rangle + \langle c_1, \delta c_2 \rangle + \langle \delta c_1, \delta c_2 \rangle} \quad (28)$$

has no first-order error. Keeping only first-order terms we see that by using reciprocity and putting $\langle c_2, c_1 \rangle = \langle c_1, c_2 \rangle$ with $\langle \delta c_2, c_1 \rangle = \langle c_1, \delta c_2 \rangle$, then

$$R = \langle c_1, c_2 \rangle \frac{1 + \frac{\langle \delta c_1, c_2 \rangle}{\langle c_1, c_2 \rangle} + \frac{\langle c_1, \delta c_2 \rangle}{\langle c_1, c_2 \rangle}}{1 + \frac{\langle \delta c_1, c_2 \rangle}{\langle c_1, c_2 \rangle} + \frac{\langle c_1, \delta c_2 \rangle}{\langle c_1, c_2 \rangle}} \quad (29)$$

or

$$R = \langle c_1, c_2 \rangle \quad (30)$$

So there are no first-order errors in R and hence the statement of Eq. (27) is variational in form. First-order errors in the trial functions only give rise to second-order errors in the scattered fields.

We now substitute trial sources in Eqs. (12), (13) and (20) and substitute these into Eq. (27) to obtain the variational formula for scattering

$$S_{21}^2 = \frac{\int_{V_0} \left[(f_i^a)_1 (u_i^i)_2 + (h_{ij}^a)_1 (\epsilon_{ij}^i)_2 \right] dv \int_{V_0} \left[(f_i^a)_2 (u_i^i)_1 + (h_{ij}^i)_2 (\epsilon_{ij}^i)_1 \right] dv}{\int_{V_0} \left[-\frac{(f_i^a)_2 (f_i^a)_1}{\omega^2 (\delta \rho)} + (h_{ij}^a)_1 (\delta C_{ijkl})^{-1} (h_{ij}^a)_2 \right] dv - \int_{V_0} \left[(u_i^{as})_2 (f_i^a)_1 - (\epsilon_{ij}^{as})_2 (h_{ij}^a)_1 \right] dv} \quad (31)$$

This is a variational theory in which trial function for both stress and displacement can be used.

It is possible to use trial functions for only one of these quantities and derive the other. Thus if we use u_i^a as the trial function, we derive ϵ_{ij}^a from it by using Eq. (5) of paper I and write

$$\sigma_{ij}^a = C'_{ijkl} \epsilon_{kl}^a \quad (32)$$

If we do this, the variational theorem takes a simpler form; similarly if we use stress as the trial function and write

$$\sigma_{ij,j}^a = \omega^2 \rho' u_j \quad (33)$$

and derive the strain from the u_i by using Eq. (4) of paper I we can derive a variational principle based on trial stresses alone. In both cases, one term is eliminated from the denominator and the numerator and the numerator is somewhat simplified.

Alternatively, as we did earlier, in deriving variational eigenvalue theorems, we can write sources in terms of the fields, and thus put from Eqs. (3) and (5) of paper I

$$f_j^a = \sigma_{ij,j}^a + \omega^2 \rho u_j^a \quad (34)$$

$$h_{ij}^a = \sigma_{ij}^a - C_{ijkl} \epsilon_{kl}^a \quad (35)$$

It is understood, furthermore, that the trial strain is derived from the trial displacement by the use of the relation (with $g_{ij}^a = 0$),

$$\epsilon_{ij}^a = \frac{1}{2}(u_{i,j}^a + u_{j,i}^a) \quad (36)$$

It will be noted that these relations are written in terms of the total trial fields, not the scattered trial fields, although they would be valid in terms of either.

We also write the scattered trial field as

$$u_i^{as} = u_i^a - u_i^i \quad (37)$$

$$\sigma_{ij}^{as} = \sigma_{ij}^a - \sigma_{ij}^i \quad (38)$$

Substitution of Eqs. (32), (38) into Eq. (31) then yields, after some algebra, the variational theorem in the form of Eq. (39). It will be apparent that this is an extremely unwieldy and difficult form of variational theorem to use.

This variational formula can be used in the form given in Eq. (31), with a Green's function approach used to find $(u_i^{as})_2$ from $(f_i^a)_2$ and $(\epsilon_{ij}^{as})_2$ from $(h_{ij}^a)_2$, as is commonly done

$$S_{21}^s = \frac{\int_{V_0} \left[\sigma_{ij,j}^a + \omega^2 \rho u_j^a \right]_1 (u_j^i)_2 + (\sigma_{ij}^a - C_{ijk\ell} \varepsilon_{k\ell}^a)_1 (\varepsilon_{ij}^i)_2 \, dv}{\int_{V_0} \left[\frac{(\sigma_{ij,j}^a + \omega^2 \rho u_j^a)_1 (\sigma_{ij,j}^a + \omega^2 \rho u_j^a)_2}{\omega^2 \rho' - \rho} \right]_1 (u_j^i)_2 (\sigma_{ij,j}^a + \omega^2 \rho u_j^a)_1 \, dv} \quad (39)$$

when the Schwinger variational principle for scattering in quantum theory or waveguide is employed. An example of the direct use of this approach in antenna theory has been given by Tai.⁵ In this case the magnitudes of the f_i^a and h_{ij}^a could be adjusted by Rayleigh-Ritz procedures. But the mathematical complexities of such an approach also become very severe, because they involve the use of double integrals.

If the trial functions were exact, they would satisfy the relation

$$\sigma_{ij,i} = -\omega^2 \rho' u_i \quad . \quad (40)$$

However, the trial functions, in general, only satisfy this expression to a first-order error. Thus we can write

$$\sigma_{ij,i}^a = -\omega^2 \rho' u_i^a + \delta f_i \quad , \quad (41)$$

where δf_i is a first-order error term.

It then follows from Eqs. (40) and (41) that

$$f_i^a = \omega^2 (\delta \rho) u_i^a + \delta f_i \quad . \quad (42)$$

It follows similarly that

$$h_{ij}^a = -(\delta C_{ijkl}) \epsilon_{ij}^a + \delta h_{ij} \quad . \quad (43)$$

We note that as the source functions are defined only to a first order in error, it is appropriate to choose the ϵ_{ij}^a and u_i^a separately. But we can also choose ϵ_{ij}^a by writing

$$\epsilon_{ij}^a = \frac{1}{2} (u_{i,j}^a + u_{j,i}^a) \quad (44)$$

or choose σ_{ij}^a separately and write

$$\epsilon_{ij}^a = S'_{ijkl} \sigma_{kl}^a \quad (45)$$

where

$$S'_{ijkl} = (C'_{ijkl})^{-1} \quad (46)$$

We may now substitute Eqs. (42) and (43) in Eq. (31) and leave out the first-order error terms everywhere provided we use the Green's function to find u_i^{as} , ϵ_i^{as} . This is justified because as we have proved in Eqs. (28)-(30), first-order errors in the trial functions only give second-order errors in the scattered wave. Before writing down the variational principle, we will put it in a shorthand notation. We write

$$\int_{V_0} \left[(\rho - \rho') (u_i^x) (u_i^y)_\eta - (\epsilon_{ij}^x)_\xi (\delta C_{ijkl}) (\epsilon_{ij}^y)_\eta \right] dV = \{x_\xi, y_\eta\} \quad (47)$$

Then the variational principle can be written in the concise form

$$S_{21}^s = \frac{\{a_1, i_2\} \{a_2, i_1\}}{\{a_2, a_1\} - \{s_2, a_1\}} \quad (48)$$

The quantity s_2 can be written in terms of a_2 , by using the Green's function formalism of Gubernatis et al.⁶ From their work, it follows that

$$(u_i^{as})_2 = \omega^2 \int (\delta \rho) g_{im} (u_m^a)_2 dV' + \int (\delta C_{jklm}) g_{ij,k} (\epsilon_{lm}^a)_2 dV' \quad (49)$$

$$(\epsilon_{in}^{as})_2 = \omega^2 \int (\delta \rho) g_{im,n} (u_m^a)_2 dV' + \int (\delta C_{jklm}) g_{ij,kn} (\epsilon_{lm}^a)_2 dV' \quad (50)$$

where

$$g_{ij} = \frac{1}{4\pi\rho\omega^2} \left[\delta_{ij}\beta^2 - \frac{j\beta R}{R} - \frac{\partial}{\partial x_i} \frac{\partial}{\partial x_j} \left(\frac{e^{-j\alpha R}}{R} - \frac{e^{-j\beta R}}{R} \right) \right] \quad (51)$$

where β is the propagation constant for longitudinal waves and α that for shear waves in an isotropic medium. It is apparent that here too the use of the variational theorem is extremely unwieldy.

Surface Scattering

There is one case for which the variational technique is somewhat simplified, that of scattering from a vacancy. We know from Eq. (42) of paper I that the exact formula for scattering from a vacancy is

$$s_{21}^a = - \int_{S_0} (\sigma_{ij}^i)_2 (u_j)_1 n_i dS_0 \quad (52)$$

But we can write

$$(\sigma_{ij}^i)_2 n_i = (\sigma_{ij})_2 n_i - (\sigma_{ij}^s)_2 n_i \quad (53)$$

However, at the surface of a flaw $(\sigma_{ij})n_i = 0$. Hence

$$(\sigma_{ij}^i)_2 n_i = -(\sigma_{ij}^s)_2 n_i \quad (54)$$

It wherefore follows, using the same methods as before that the variational theorem for scattering from a vacancy becomes

$$s_{21}^s(\text{cavity}) = \frac{\int (\sigma_{ij}^i)_2 (u_j^a)_1 n_i dS \int (\sigma_{ij}^i)_1 (u_j^a)_2 n_i dS}{\int (\sigma_{ij}^{as})_2 (u_j^a)_1 n_i dS} \quad (55)$$

Thus we need the Green's function relating $(\sigma_{ij}^{as})_2$ to $(u_j^a)_2$ at the surface of the vacancy, with trial functions for the u_j^a . This is certainly a more tractable form of variational theorem.

A similar simplified variational formula can be derived for scattering from a rigid body. This is

$$S_{21}^s(\text{rigid body}) = - \frac{\int (\sigma_{ij}^a)_2 (u_j^i)_1 n_i dS \int (\sigma_{ij}^a)_1 (u_j^i)_2 n_i dS}{\int (\sigma_{ij}^a)_1 (u_j^{as})_2 n_i dS} \quad (56)$$

Again the quantity $(u_j^{as})_2$ may be derived from the value of $(\sigma_{ij}^a)_2$ at the surface by use of a Green's function formalism.

CONCLUSIONS

We observe that a wide variety of variational formulae for eigenvalue problems for scattering can be obtained by use of the reaction principle. Typically these formulae are, in the author's opinion, extremely unwieldy. It is doubtful whether the general scattering formulae will give enough additional physical information to be worth using. On the other hand, the variational formulae for scattering from a vacancy or rigid body might be worth adopting, as should those for determining the eigenvalues of propagating waves. Further work on simplification of these formulae and determining the best way to use them is obviously required.

We conclude that in the most complicated cases a direct use of numerical solutions of the wave equation is probably the best attack on the problem, although the variational method may

help in obtaining more rapidly convergent numerical solutions.

ACKNOWLEDGEMENTS

The author would like to thank W. Kohn for several illuminating discussions of variational principles. In addition, several discussions with J. Krumhansl, R. Thompson, S. Gubernatis and others in the group which met at the Materials Research Council Meetings of ARPA in 1975 were extremely stimulating. This research was initially supported by ARPA under Contract No. MDA903-76C-0250 with The University of Michigan and completed under Rockwell International Contract No. 74-20773 for the Advanced Research Projects Agency and the Air Force Materials Laboratory under Contract F33615-74-C-5180.

VARIATIONAL PRINCIPLE FOR SOUND SCATTERING
FROM A LOCALIZED DEFECT (ONE DIMENSION)

W. Kohn

The scattering of sound waves from defects is an important diagnostic tool for non-destructive testing of engineering components. Apart from an exact solution for homogeneous ellipsoidal defects, approximation methods must be used. In this paper we show how variational methods developed for potential scatterings in quantum mechanics can be adapted to the present problems. The theory is worked out in one dimension and a simple illustrative example is presented.

Variational methods have been extensively used in quantum mechanical and electromagnetic scattering problems. The present note, by means of a simple one-dimensional model system, indicates how one may also construct variational principles for ultrasonic scattering. This is not surprising since variational principles for other types of ultrasonic problems, e.g., dispersion relations in composite media, are known.^{1,2}

The Simplest Formulation

The one dimensional wave equation for a sound wave propagating in an inhomogeneous medium is

$$\frac{d}{dn} \left(\eta(x) \frac{du(x)}{dn} \right) + \rho(x) \omega^2 u(x) = 0 \quad (1)$$

where $u(x)$ is the displacement, $\eta(x)$ is the elastic constant, $\rho(x)$ is the density and ω is the frequency. We now consider a scattering problem, as indicated in Fig. 1. The medium is uniform ($\rho = \rho_0$, $\eta = \eta_0$) everywhere except in the interval $-a < x < a$, where ρ and η are x -dependent. For simplicity we take

$$\rho(-x) = \rho(x) \text{ and } \eta(-x) = \eta(x) \quad (2)$$

although these are not essential assumptions.

In view of (2) there exist symmetric and antisymmetric solutions of (1). The symmetric solution has, for $|x| \geq a$, the form

$$u(x) = \begin{cases} \cos kx - \tan \gamma \sin kx & x \geq a \\ \cos kx + \tan \gamma \sin kx & x \leq -a \end{cases} \quad (3)$$

where γ is the phase shift of the symmetric solution due to the defect.

Combining now the ideas of ref. 1 [Eqs. 14 ff] and of variational principles in potential scattering³ we define the quantity

$$I[u(x)] \equiv \int_{-\infty}^{\infty} u(x) \left[\frac{d}{dx} \left(\eta(x) \frac{du}{dx} \right) + \rho(x) \omega^2 u(x) \right] dx \quad (4)$$

In view of (1) the first variation of I is

$$\delta I[u(x)] = \int_{-\infty}^{\infty} u(x) \left[\frac{d}{dx} \eta(x) \frac{d\delta u(x)}{dx} + \rho(x) \omega^2 \delta u(x) \right] dx \quad (5)$$

By using the self-adjointness of the differential operator in

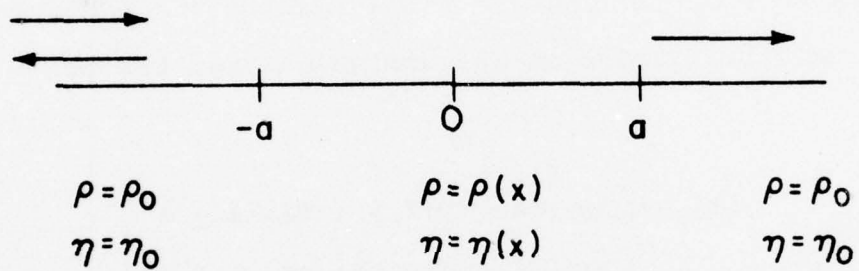


Figure 1. Scattering from a localized defect.

(1), we can write the identity

$$u \frac{d}{dx} \left(\eta \frac{d\delta u}{dx} \right) - \delta u \frac{d}{dx} \left(\eta \frac{du}{dx} \right) \equiv \frac{d}{dx} \left(u \eta \frac{d\delta u}{dx} - \delta u \eta \frac{du}{dx} \right) , \quad (6)$$

If we further restrict the variations of u to such functions which, for $|x| \rightarrow \infty$ have the form (3), so that

$$\delta u(x) = \begin{cases} -\delta(\tan \gamma) \sin kx & , \quad x \rightarrow +\infty \\ +\delta(\tan \gamma) \sin kx & , \quad x \rightarrow -\infty \end{cases} \quad (7)$$

we obtain

$$\begin{aligned} \delta I[u(x)] &= \int_{-\infty}^{\infty} \delta u \left[\frac{d}{dx} \left(\eta(x) \frac{du(x)}{dx} \right) + \rho(x) \omega^2 u(x) \right] dx \\ &+ \int_{-\infty}^{\infty} \frac{d}{dx} \left(u(x) \eta(x) \frac{d\delta u(x)}{dx} - \delta u(x) \eta(x) \frac{du}{dx} \right) dx \\ &= \eta_0 \left[u(x) \frac{d\delta u(x)}{dx} - \delta u(x) \frac{du(x)}{dx} \right]_{-a}^a \\ &= -2\eta_0 k(\tan \gamma) \end{aligned} \quad (8)$$

Therefore we see that the expression

$$J[u(x)] \equiv I[u(x)] + 2\eta_0 k \tan \gamma \quad (9)$$

is stationary near the correct solution $u(x)$,

$$\delta J[u(x)] = 0 , \quad (10)$$

and that the Stationary value of J is

$$J[u(x)]_{\text{stat}} = 2\eta_0 k \tan \gamma_{\text{exact}} \quad (\text{symm}) \quad (11)$$

Similarly we can establish a variational principle for the phase shift $\tilde{\gamma}$ of the antisymmetric solution of (1). Let us take it, for $(x) \geq a$, of the form

$$\tilde{u}(x) = \begin{cases} \sin kx + \tan \tilde{\gamma} \cos kx & x \geq a \\ \sin kx - \tan \tilde{\gamma} \cos kx & x \leq a \end{cases} \quad (12)$$

and

$$\delta \tilde{u}(x) = \begin{cases} \delta(\tan \tilde{\gamma}) \cos kx & x \rightarrow \infty \\ -\delta(\tan \tilde{\gamma}) \cos kx & x \rightarrow -\infty \end{cases} \quad (13)$$

Then defining $I[\tilde{u}(x)]$ by Eq. (4) as before, we find that the expression

$$J[\tilde{u}(x)] \equiv I[\tilde{u}(x)] + 2\eta_0 k \tan \tilde{\gamma} \quad (14)$$

is again stationary, relative to variations of the form (13) and that its stationary value is given by

$$J[\tilde{u}(x)]_{\text{stat}} = 2\eta_0 k \tan \tilde{\gamma}_{\text{exact}} \quad (\text{antisymm}) \quad (15)$$

From the symmetric and antisymmetric solutions we can form the linear combination representing a wave incident from the left which is partly reflected and partly transmitted. The reflection and transmission amplitudes are given, respectively, by

$$r = \frac{1}{2} \frac{i(\tan \gamma - \tan \tilde{\gamma}) + \tan \gamma \tan \tilde{\gamma} - (\tan \gamma)^2}{1 - i(\tan \gamma + \tan \tilde{\gamma}) - 2 \tan \gamma \tan \tilde{\gamma}} \quad (16)$$

$$t = \frac{1}{2} \frac{2 + i(\tan \gamma - \tan \tilde{\gamma}) + \tan \gamma \tan \tilde{\gamma} + (\tan \gamma)^2}{1 - i(\tan \gamma + \tan \tilde{\gamma}) - 2 \tan \gamma \tan \tilde{\gamma}} \quad (17)$$

Homogeneous formulation

As in the case of the Rayleigh Ritz method for eigenvalue problems it is usually convenient to use a variational function which is a linear combination of a well chosen set of functions, $u_\ell(x)$:

$$u(x) = \sum c_\ell u_\ell(x) \quad (18)$$

The functions u_ℓ are held fixed and the coefficients c_ℓ are the variational parameters. Let us again consider first the symmetric solution $u(x)$. Then naturally we take all $u_\ell(x)$ to be symmetric and require that,

$$u(x) = \begin{cases} a \cos kx - b \sin kx & x \rightarrow \infty \\ a \cos kx + b \sin kx & x \rightarrow -\infty \end{cases} \quad (19)$$

Then defining I as before (Eq. (4)), we obtain the result

$$\begin{aligned} \delta I &= -2\eta_0 k (a\delta b - b\delta a) \\ &= -2\eta_0 k \left(\delta(ab) - \frac{b}{a} \delta(a^2) \right) \end{aligned} \quad (20)$$

For the correct solution $b/a = \tan\gamma$. Hence, if we define

$$J \equiv I + 2\eta_0 k (ab - \tan\gamma a^2) \quad (21)$$

then, if γ is considered fixed at its correct value

$$\delta J = \delta I + 2\eta_0 k \left(\delta(ab) - \tan\gamma \delta(a^2) \right) = 0 \quad (22)$$

(cf. ref. 3). Furthermore, clearly

$$J_{\text{exact}} = 0$$

Therefore the expression

$$\tan \gamma = \frac{I(c_\ell) + 2\eta_0 k ab}{2\eta_0 k a^2} \quad (23)$$

represents a stationary homogeneous expression for $\tan \gamma$. As in the conventional Rayleigh Ritz method this leads to a scalar equation, involving $\tan \gamma$, from which an approximate value for the latter can be obtained. In general one does, however, not know if the approximate value is a lower or upper bound for the exact value.

Illustration

As a simple illustration consider the case where

$$\left. \begin{array}{lll} -1 < x < 1 & \eta(x) = 1.1 & \rho(x) = 1 \\ |x| > 1 & \eta(x) = 1 & \rho(x) = 1 \end{array} \right\} \quad (24)$$

The exact symmetric solution for $\omega = 1$, satisfying continuity of displacement u and stress $\eta \frac{du}{dx}$ is given by

$$u_{\text{exact}} = \begin{cases} 0.9686 \cos (0.9535 x) & 0 < x \leq 1 \\ \cos x + (0.02423) \sin x & 1 \leq x \end{cases} \quad (25)$$

corresponding to a value of

$$\tan \gamma_{\text{ex}} = -0.02423 \quad (26)$$

We now calculate $\tan \gamma$ approximately using as a trial function the unperturbed solution corresponding to $\eta(x) \equiv 1$,

$$u = \cos x \quad \text{all } x \quad (27)$$

This gives

$$J[u] = I[u] = 0.1[\frac{1}{2} \sin 2 - 1] = -0.05454 \quad (28)$$

where we have taken care to include the contribution to I from the points of discontinuity at $x = \pm 1$. Hence, from (9) and (11) we obtain the approximate value

$$\tan \gamma \approx \frac{J[u]}{2n_0 k} = \frac{J[u]}{2} = -0.02727 \quad (29)$$

which is to be compared to (27).

ACKNOWLEDGEMENT

It is a pleasure to thank Drs. J. E. Gubernatis, G. Kino and J. A. Krumhansl for stimulating discussions. This research was supported by the Advanced Research Projects Agency of the Department of Defense under Contract No. MDA903-76C-0250 with The University of Michigan.

References

1. W. Kohn, J. A. Krumhansl, E. H. Lee, "Variational Methods for Dispersion Relations and Elastic Properties of Composite Materials," J. Appl. Mech. 39, 327 (1972).
2. S. Nemat-Nasser, "General Variational Mechods for Waves in Elastic Composites," J. Elasticity 2, 73 (1972).
3. W. Kohn, "Variational Methods in Nuclear Collision Problems," Phys. Rev. 74, 1763 (1948).

EXPERIMENTAL CHARACTERIZATION OF DEFECTS
WITH ELASTIC WAVES

L. Adler, G. S. Kino, R. B. Thompson
and B. R. Tittman

INTRODUCTION

The details of the elastic fields scattered by flaws in solids contain much information about the geometrical shape of the defect. In the past, few serious attempts have been made to use much of this information. More recently, however, the principles of fracture mechanics have been incorporated in design procedures¹. In certain cases, it is now possible to predict the remaining lifetime of a part if the expected loading sequence, certain material parameters, and the size, shape, and orientation of flaws are known. Consequently, increased efforts are being made to determine quantitative geometric parameters of flaws from scattered elastic fields, and the discipline of quantitative nondestructive evaluation has emerged.² The economic and other benefits of such a capability are large^{3,4}.

This paper describes, from the experimental point of view, our present status and future needs in characterizing defects from scattered fields. The second section discusses the accessible "window" through which scattering information can be obtained, and summarizes a number of practical considerations which determine its bounds. The third section discusses the

present status of existing models to describe the measured fields when the defect shape is known and emphasizes the need for solution of the inverse problem, wherein defect characteristics are estimated from measured data.

EXPERIMENTALLY AVAILABLE INFORMATION

The defect information is contained in a pair of scattered elastic fields which combine to produce the far field displacement

$$u = \frac{\vec{S}_\ell e^{iK_\ell r}}{K_\ell r} + \frac{\vec{S}_t e^{iK_t r}}{K_t r} \quad (1)$$

where K_ℓ and K_t are the longitudinal and transverse wave vectors respectively, r is the distance from the defect, and \vec{S}_ℓ and \vec{S}_t are the scattering amplitudes. These have functional dependences on frequency, angle, and polarization of the incident wave from which the size, shape, and orientation of the defect can be estimated.

Measurement regimes are usefully classified according to the parameter, ka , where a is a characteristic dimension of the defect. Imaging approaches yield good resolution of defect structure when $ka \gg 1$, but other techniques for processing of the scattering fields can be quite useful when $ka \sim 1$.

A number of practical constraints exist which limit the regime available for measurement. Consider, for example, the configuration schematically shown in Fig. 1. Part geometry often precludes very low frequency observations, the regime

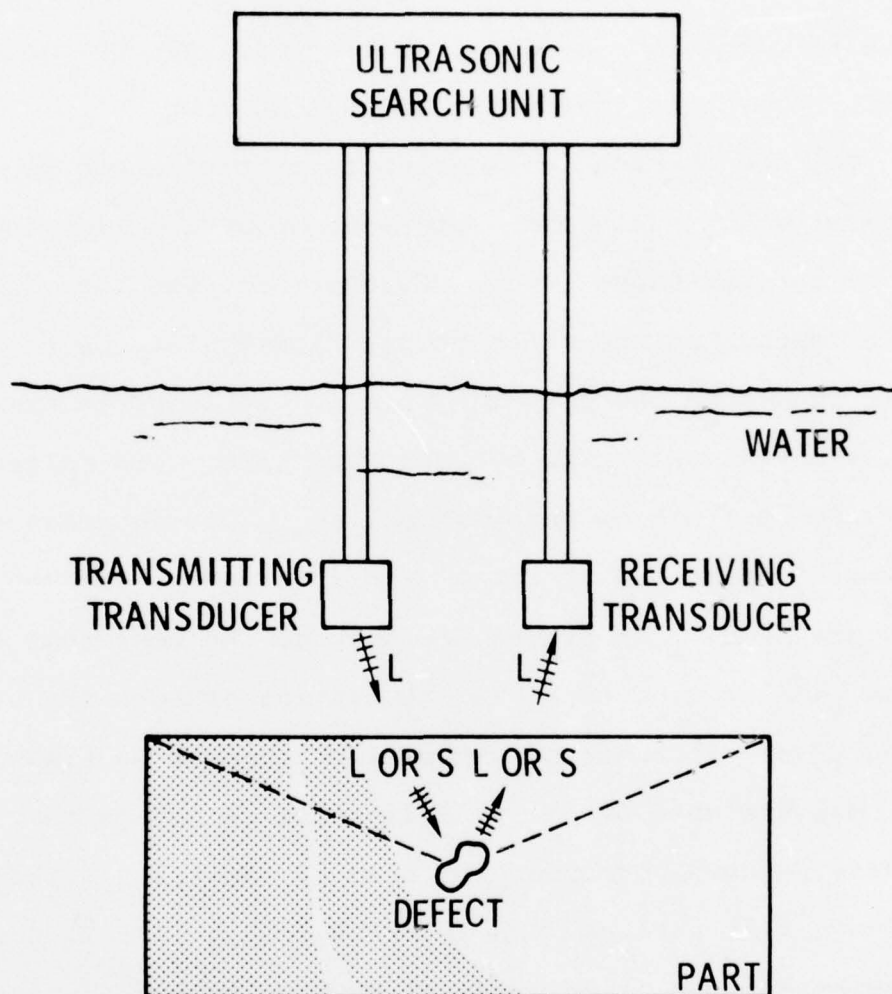


Figure 1. Schematic view of system for measuring scattered ultrasonic fields in immersion configuration. The polarizations, angles, and amplitudes of the waves in the solid are selected by the angular orientation of the transducer in accordance with Snell's law and the detailed boundary conditions.

$ka \ll 1$, since reflections from exterior surfaces or interfaces will interfere with those from defects. In addition, access is often possible from only a single surface, and the range of available angles within the material is limited, say, on the order of $\pm 60^\circ$ with respect to the surface normal at most.

The use of high frequencies is often limited by grain scattering, which adds both a propagation attenuation and a coherent background noise level. Furthermore, the flaw sizes of interest depends on the crack propagation resistance of the material, and from the data in Table I,² it is clear that there is a substantial variation between materials. The normalized high frequency limit of observation, ka_{\max} , is determined by the interplay of these two effects. For some cases, the $ka \gg 1$ regime is practical, for others one must do the best that is possible when $ka \ll 1$. Of course, the attenuation effects are also a function of the distance of material which must be traversed.

Measurements of all polarizations cannot be made with equal ease. Again, consider the case of immersion testing of a part with a flat surface such as shown in Fig. 1. If the part is illuminated with a longitudinal wave at oblique incidence in the fluid, mode conversion effects will generate both shear and longitudinal waves in the part at angles determined by Snell's law.⁵ However, the coexistence of these two types of waves can make interpretation of reflected signals difficult. Hence, one of two approaches is often adopted. When the longitudinal wave in water is at near normal incidence, the mode conversion is

TABLE I. Order of magnitude estimates of critical flaw sizes in some metal and ceramic systems.

| | Materials | Flaw Size (mm) | Frequency for $\lambda_c = 2a_c$ (MHz) |
|---------------------|-----------------------|----------------|---|
| Steels | 4340 | 1.5 | 2.0 |
| | D6AC | 1.0 | 3.0 |
| | Marage 250 | 5.0 | 0.59 |
| | 9N14Co 20C | 18.0 | 0.16 |
| Aluminum Alloys | 2014-T651 | 4.5 | 0.71 |
| | 2024-T3511 | 25.0 | 0.26 |
| Titanium Alloys | 6Al-4V | 2.5 | 1.2 |
| | 8Al-1Mo-IV(β) | 14.5 | 0.21 |
| Silicon Nitrides | Hot Pressed | 0.5 | 100 |
| | Reaction Sintered | 0.02 | 250 |
| Glasses | Soda Lime | 0.001 | 2,500 |
| | Silica | 0.003 | 830 |

quite small and primarily longitudinal waves are transmitted into the part. Shear waves can then be considered to be second order effects. On the other hand, if the longitudinal wave in water strikes the surface at an angle larger than the critical angle, then the longitudinal wave in the part will be evanescent, and only a shear wave will penetrate to the defect. Its angle can be varied from about 35° with respect to the normal to 90° with no longitudinal wave being generated. In special cases, clever approaches can be used to extend those limits. For example, time gating can be used in pulsed measurements to separate longitudinal and shear waves when both are strongly excited.

As noted in Eq. (1), the wave scattered from the defect can have either shear(S) or longitudinal(L) components. Present ultrasonic inspection techniques generally measure either the L+L or the S+S scattering. It is likely that future quantitative systems will make use of the L+S or S+L mode converted signals as well.

When the scattered waves return to the part surface, the efficiency of coupling to a wave in water must again be considered. Longitudinal waves striking the surface at near normal incidence after scattering from a defect will be most efficiently converted into longitudinal waves in the water, whereas shear waves must strike the surface at greater than about 35° in order to strongly couple to the water. Hence, the range of angles (referred to the interior of the part) over which the scattered signals can be readily measured is the same as the range of

angles over which an incident wave can be conveniently excited.

Figure 2 graphically summarizes the limitations on the available ultrasonic information that were discussed above.

DEFECT CHARACTERIZATION

The primary goal of quantitative NDE is to estimate the size, shape, and orientation of a defect from this experimentally accessible information. In the last two years, the cooperative efforts of several investigators have established a foundation for this by developing a firm understanding of the scattering of elastic waves from a defect of specified geometry.⁶⁻⁸ Particular emphasis has been placed on approximate models which can be applied to defects of complex shape. By direct comparison of theory and experiment, it has been established that for $ka \lesssim 1$, the Born approximation⁹ produces useful results for three-dimensional inclusions and cavities, particularly in the backward scattering directions.¹⁰ For $ka > 1$, a scalar version of the geometrical diffraction theory of Keller¹¹ has had considerable success in describing L+L scattering from two dimensional, crack-like defects.¹²

However, there are some major regimes in the experimental window of Fig. 2 in which further theoretical work is needed. Accurate models are presently not available for crack-like defects when $ka > 1$, or for extended objects when $ka > 1$ and perturbations are large. Furthermore, the geometrical diffraction theory¹¹ must be extended to include mode conversion effects. In the regime $ka \sim 1$, additional models are needed and variational techniques appear to hold considerable promise. Appropriate

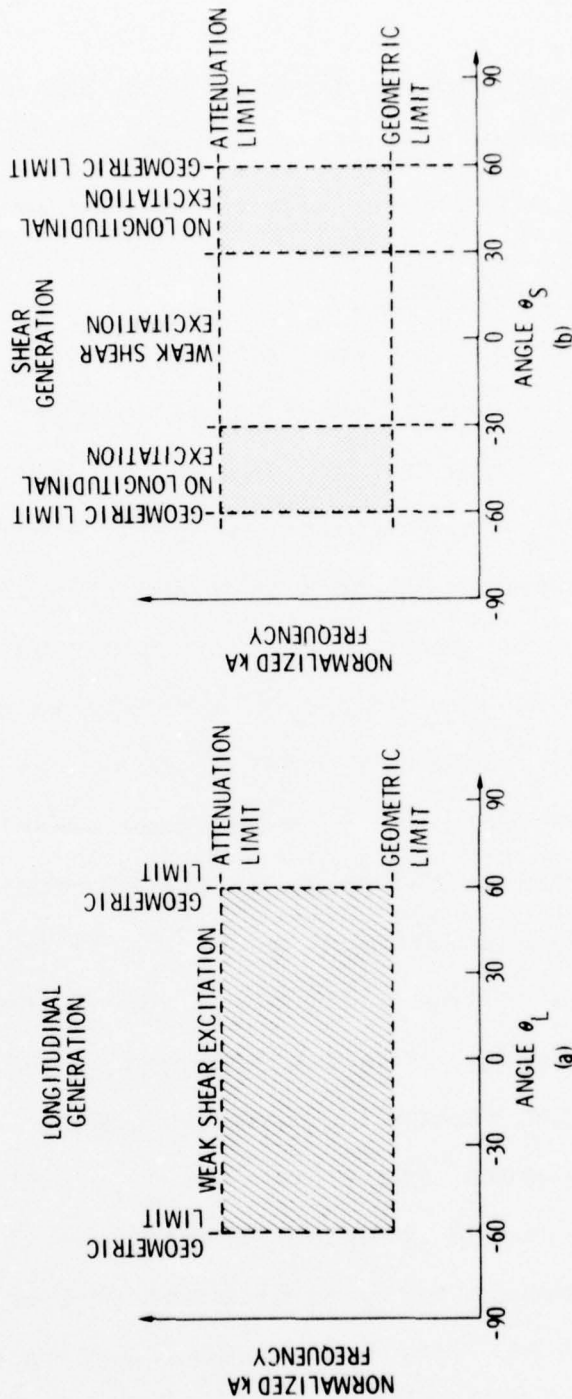
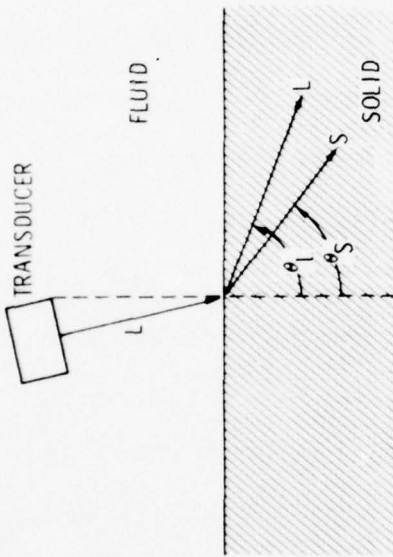


Figure 2. Summary of limits imposed by geometry, attenuation, and polarization effects on available ultrasonic scattering information. (a) Longitudinal generation as a function of angle of longitudinal wave in a solid. (b) Shear generation as a function of angle of shear wave in a solid. Note that for a given angle of incidence of wave fluid, $\theta_L > \theta_S$.

experimental samples should be fabricated to test the critical features of these models.

The basic experimental tools, transducers and signal processing techniques should also continue to be improved so the most accurate ultrasonic information can be obtained. For example, most transducer radiation pattern studies have been done in fluids, and this work should be extended more completely to the case of an elastic solid. The success of defect characterization schemes depends critically upon the availability of high quality experimental data.

A major area where emphasis must be placed in the next few years is in the development of inversion techniques for estimating unknown defect characteristics from experimental data. Imaging techniques represent a rapidly advancing technology that accomplishes this objective.¹³ Here, further attention needs to be paid to defining the precise characteristics of a defect in a solid that are measured by the imaging system. Use of scattering models should aid substantially in this process. Alternate approaches involve deducing geometrical properties of the defect directly from the scattered fields. One concept that has shown considerable recent promise is the use of adaptive learning techniques to define predictive nonlinear operators relating scattered fields to size information.¹⁴ This approach is limited, however, by its empirical nature, which requires that new operators be developed as new defect types are encountered. It may prove useful to combine the optimum features of the classi-

cal and adaptive approaches by using theoretical solutions in the training phase to avoid the difficulty of fabricating many parts with complex shaped defects. Estimation theory, which has been used successfully in inverting other types of ultrasonic data,¹⁵ also appears applicable to the inverse scattering problem.

SUMMARY

The scattering of elastic waves by flaws in solids provides much information about the geometrical shape of the defect. This has recently been identified as having considerable potential value in the area of quantitative nondestructive evaluation, wherein techniques for predetermining the in-service failure probabilities of structural components are sought. Our ability to measure this information is limited at low frequencies by part sizes and at high frequencies by attenuation. Longitudinal or shear waves can be used, depending on the angle of incidence or scattering. A number of approximate models have now been developed which describe the scattering in various regimes. The area where the greatest effort is now needed is in inversion, wherein defect characteristics are deduced from measured data. Both imaging and approaches based upon other operations on the scattered fields should be considered.

ACKNOWLEDGEMENT

Much of the information presented in this work was developed by the authors under the support of the Center for Advanced NDE, operated by the Science Center, Rockwell International,

for the Advanced Research Projects Agency and the Air Force Materials Laboratory under contract F33615-74-C-5180.

References

1. M. D. Coffin and C. F. Tiffany, "How the Air Force Assures Safe, Durable Air Frames," Metal Progress (March 1976).
2. R. B. Thompson and A. G. Evans, "Goals and Objectives of Quantitative Ultrasonics," IEEE Trans. on Sonics and Ultrasonics, SU-23, p. 292 (1976).
3. D. O. Thompson and M. J. Buckley, "New Opportunities and Challenges for NDE," in ASM Handbook, Vol. II (in press).
4. M. J. Buckley, "The Future Economic Role of NDE," IEEE Trans. on Sonics and Ultrasonics, SU-23, p. 287 (1976).
5. J. C. Couchman, J. R. Bell, B. G. W. Yee, "The Role of Boundary Value Problems in Improving NDE Technology." Research Report ERR-FW-1696, Research Engineering Dept., General Dynamics, Fort Worth Division (December, 1975).
6. R. B. Thompson, "Overview of Ultrasonic NDE Research," Nondestructive Characterization of Materials, Proceedings of the Sagamore Army Research Conference, 23 (in press).
7. Proceedings of the ARPA/AFML Review of Quantitative NDE, held July, 1976, in Thousand Oaks, California, Air Force Technical Report AFML-TR-75-212.
8. Proceedings of the ARPA/AFML Review of Progress in Quantitative NDE, held September, 1976, in Monterey, California, to be published as technical report by the Air Force Materials Laboratory.
9. J. E. Gubernatis, E. Domany, M. Hubernam, and J. A. Krumhansl, "Theory of the Scattering of Ultrasound by Flaws," 1975 Ultrasonics Symposium Proceedings (IEEE, N.Y., 1975), p. 107.
10. B. R. Tittmann, "Measurement of Scattering of Ultrasound by Elliptical Cavities," Ref. 7 (in press).
11. J. B. Keller, "Diffraction an an Aperture," J. Appl. Phys. 28, p. 426 (1957).
12. L. Adler and D. K. Lewis, "Models for the Frequency Dependence of Ultrasonic Scattering from Real Flaws," Ref. 7 (in press).

13. T. M. Waugh, G. S. Kino, C. S. Defilets, J. D. Fraser,
"Acoustic Imaging Techniques for Nondestructive Testing,"
IEEE Trans. on Sonics and Ultrasonics, SU-23, p. 313 (1976).
14. R. Shankar, A. M. Mucciardi, D. Cleveland, W. E. Lawrie,
and H. L. Reeves, "Adaptive Nonlinear Signal Processing for
Characterization of Ultrasonic NDE Waveforms, Task 2:
Measurement of Subsurface Fatigue Crack Size," Air Force
Report AFML-TR-76-44.
15. B. R. Tittmann and J. M. Richardson, "Estimation of Surface
Layer Structure from Rayleigh Wave Dispersion. III. Sparse
Data Case - Interpretation of Experimental Data," SC-PP-76-
167 (submitted for publication).

REPORT OF A MEETING ON FATIGUE CRACK GROWTH

B. Budiansky, D. C. Drucker,
J. W. Hutchinson and J. R. Rice

INTRODUCTION

A meeting was held to review the current status of the fatigue crack growth problem. The schedule for the meeting and a list of participants are attached as an Appendix.

Fatigue continues to be an area of great practical significance and the time seemed particularly suitable for a review of the area in terms of recent developments. Principal among these are refinements in the observation of crack surface closure effects, which have suggested a rational basis - not yet realized - for the prediction of crack growth rates under very general oscillating but non-cyclic loadings, including the thus-far paradoxical case of growth retardations by overloads. Experience has accumulated as a result of fractographic observations of fatigue crack propagation along with an enhanced understanding of the role of the environment and of the contributions to crack growth from static fracture mechanisms. The time seemed opportune to review these aspects of the problem also.

THE CRACK CLOSURE CONCEPT

Fatigue crack surfaces are not perfectly smooth but, instead show evidence of the plastic crack tip opening and separation processes which have generated them. Further, the material adjacent to the surfaces retains residual plastic strain from the time when it was part of the crack tip plastic zone. Hence, upon removal of external loadings from a fatigue cracked body, the crack surfaces need not fit perfectly together again, but rather they can be wedged open by these "misfit" effects so that compressive residual stresses develop across portions of the crack faces.

As shown first by Elber, there is experimental evidence for closure near the crack tip even when the load is not fully removed. Figure 1 shows the successive crack profiles, according to Elber's concept, in a body which is being subjected to a steady cyclic loading from L_{\min} to L_{\max} . The crack is closed near its tip until the opening load, L_{op} , is attained and thus Elber suggests that the variation in stress intensity factor K be taken as

$$\Delta K_{eff} = K_{\max} - K_{op} \quad . \quad (1)$$

Far from the range at which static fracture modes contribute to growth, it might be expected that there is little direct effect of K_{\max} . The crack growth per cycle should then depend on the cyclic opening and closing in each cycle (determined by ΔK_{eff}), and be represented in the form

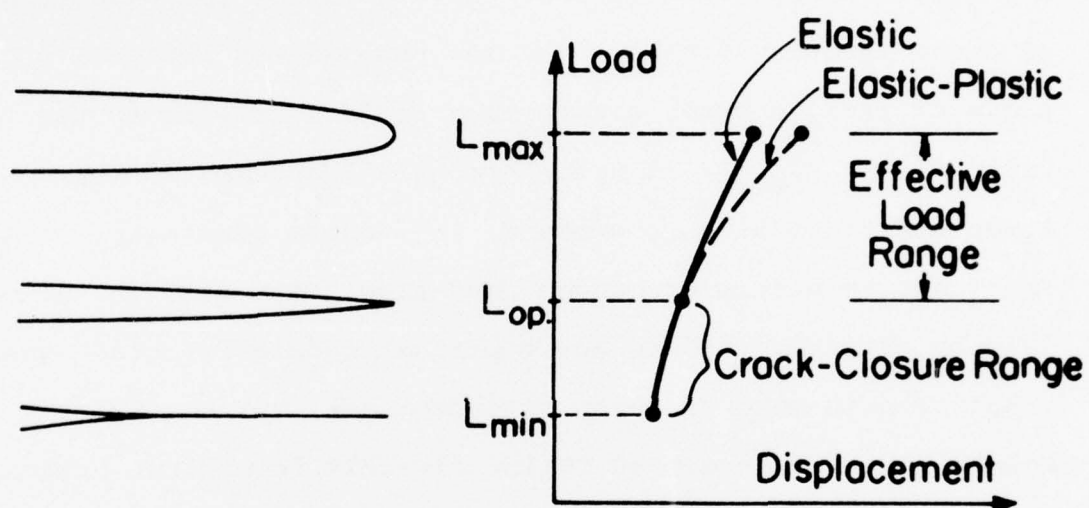


Figure 1. The Elber crack closure concept as applied to cyclic loading between L_{min} and L_{max} .

$$da/dn = f(\Delta K_{eff}) \quad (2)$$

where the function f will in general, be environment-dependent for a given material.

The limitations to validity of the closure concept and Eq. (2) for low K_{max}/K_c levels remain unclear. Indeed, there are many unanswered questions. Nevertheless, the phenomena is of great interest because it holds promise for rational predictions of fatigue crack growth that include effects of the load ratio $R(=K_{min}/K_{max})$, of near-threshold loadings, of peak overloads and retardation phenomena, and, quite generally, of arbitrary deterministic or random load-time histories. As summarized by Gallagher, there are empirical models for crack growth prediction in some of these circumstances, but none of the models thus far developed follow directly from first principles.

More generally, when there is an effect of K_{max} , Eq. (2) is assumed to take the form

$$da/dn = F(\Delta K_{eff}, K_{max}),$$

although it would perhaps be more logical not to use K_{max} , but rather to use some "effective" maximum K value, which is less than K_{max} by the intensity factor contribution from the residually stressed material in the plastic wake along the crack surfaces.

The meeting revealed, however, that there is little consensus on the closure concept, among specialists in fatigue.

Some suggest that the phenomenon is a surface effect, involving contact within shear-lip layers at the specimen surfaces. Others have reported a failure of closure observations to explain delays following peak overloads - although a presentation on this topic by P. C. Paris suggested that previous work had not focused on the proper measurement point (as explained below) and that the closure concept provided an experimentally self-consistent explanation of overload effects.

Little consistency was reported among different methods of measuring crack closure, in part, it seemed, due to lack of measurement accuracy but also in part because the different techniques measure different events which are nominally referred to as crack closure.

Elber summarized a series of experimental studies, intended to compare electric potential, ultrasonic, interferometric, and bridging strain gage techniques with his small displacement gage, called a COD gage, attached near the crack tip. Unfortunately, there was little consistency, in the tests and in the closure measurements. Objections to the experimental techniques were raised for some of the studies thus far carried out. Consequently, the full extent of the lack of consistency between the different measurement methods has not yet been well identified. A further technique developed by Paris is based on measurement of the load-point displacement (approximated as the crack surface displacement under the load point) in compact specimens. The relation of the displacement reading to the ex-

tent of closure is, as for the Elber gage, given by plane elasticity theory for a contacting crack surface. However, the Paris measurement should be less sensitive to closure non-uniformities at the lateral surfaces of the specimen.

For the future with regard to experimental techniques, it seems essential to resolve the extent to which observed closure effects are shear-lip dominated as opposed to a true plane strain effect. Study by ultrasonic methods as well as study of the thickness dependence of results from the other techniques at a given K level should be sufficient to clear-up this matter. The necessary information may well be at hand. Certainly, electric potential measurements of closure in any environment for which a non-conducting surface film forms cannot be considered reliable, and some of the work suggesting the shear-lip interpretation may have been based on this technique.

In this regard, it is important to resolve the questions of how thick a specimen must be, perhaps by comparison to K^2/Y^2 , where Y = yield strength, to show negligible shear-lip dependence, and of how closure measurements are to be interpreted if this condition cannot be met in available specimen sizes.

Given the potential relevance of closure to unraveling poorly understood load-sequence effects in fatigue, it is important that comparison of the different measurement techniques be continued. As a goal, it is important to determine precisely what aspect of the closure process is measured by a given tech-

nique, how this relates to the measurements made by other techniques, and what accuracy is needed for a reliable examination of different aspects of fatigue closure (e.g., the Paris explanation of overload effects requires considerably greater accuracy of measurement than is normally obtained).

It would seem also to be important that more fatigue crack growth data report closure effects, to provide a mechanistically more basic characterization of the load environment experienced at the crack tip and help to sort out various effects in fatigue. For example, Fig. 2 shows the opening load as a function of R level based on an empirical curve-fit by Elber and based on a simplified model by Paris. The ratio K_{op}/K_{max} at $R = 0$ is often near 0.5, but the ratio is not fixed in value for all materials and Paris showed an example in a 2024 Al alloy in which there was a transition, over a comparatively small range of K_{max} values, from a K_{op}/K_{max} ratio of 0.5 to 0.2, whereas Wei showed an opposite trend with K_{max} based on electric potential closure measurements in a Ti alloy.

There was some discussion at the meeting in terms of the role of closure role in near-threshold crack growth. Elber's position, over which some skepticism was expressed by Ritchie, was that the growth relation as reported in the form of Eq. (2) could be extended in a smooth fashion down to extremely small ΔK_{eff} values, say of order $1 \text{ ksi}\sqrt{\text{in}}$, and that apparent threshold conditions result because the ratio K_{op}/K_{max} acquires a larger than usual value at small K_{max} levels. Buck also sug-

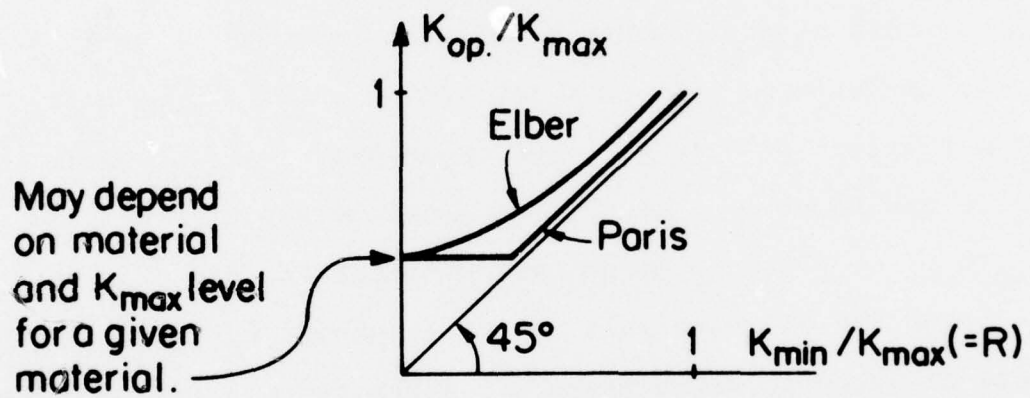


Figure 2. The stress intensity factor at crack opening, for states of steady cyclic growth corresponding to various ratios R .

gested near-threshold closure effects as a source of the "endurance limit" for small, grain-sized surface cracks. It is clear, however, that closure per se cannot explain the environmental effects on fatigue crack growth, which seem often to be dominant at near-threshold conditions. Indeed, the high-R results of Ritchie suggest environmental effects that are not explainable in terms of a closure model. Nevertheless, closure observations may provide an effective tool for sorting out those environmental interactions which affect the process of surface contact, and those which affect the more intrinsic fatigue rupture processes of the material. The environmental effect on the process of closure would in different circumstances range from: (i) partial re-welding at asperities (say, in vacuum) upon closure with their subsequent tensile extension upon reloading, to (ii) oxide film protection (say, in dry air) of asperities against closure re-welding or tensile extension, to (iii) partial dissolution of asperities (in a corrosive environment). It is reasonable to expect that the scale of the crack surface roughness and misfits would be greatest in case (i), next greatest in case (ii) and least in case (iii). The corresponding variations of ΔK_{eff} , for a given ΔK and K_{max} , would then be consistent with lower apparent threshold, ΔK levels in the more reactive environments, and this kind of closure-based environmental effect, as well as those effects which operate directly on intrinsic fatigue rupture processes, need to be more completely identified and isolated from one-another.

Further, there would seem much to be gained by combining the more macroscopic closure observations with direct fractographic studies of striation spacings, for example, in block loadings of variable amplitude as reported by Pelloux, and of some of the other microstructural features discussed by Pelloux, Ritchie, and Thompson.

INTERPRETATION OF RETARDATION FOLLOWING OVERLOADS

Part of the impetus for convening the fatigue meeting was provided by the recent studies of P. C. Paris on the explanation of overload retardation effects in terms of crack surface interference. Paris' concept of the crack configuration at the minimum load level of cycling after some crack growth from the site of a large, peak overload, is shown in Fig. 3a. He describes the crack surfaces as closed by the misfit layer at the tip and at distances from the tip that are well beyond the site of the overload. In his view, the extensive plane-strain deformation of the overload has left an interfering "bump" on the crack surfaces, which props the crack open over a distance in back of it, and causes the crack segment which has grown beyond the overload site to be tightly wedged shut.

Figs. 3a to d show the progressive opening of the crack tip according to this picture. Paris notes that there is a stage of crack opening for which the surfaces are open to the site of the overload but are closed beyond it, as shown in Fig. 3c. The load-displacement relation is linear in this stage, which corresponds to the load range from L_1 to L_2 in Fig. 4.

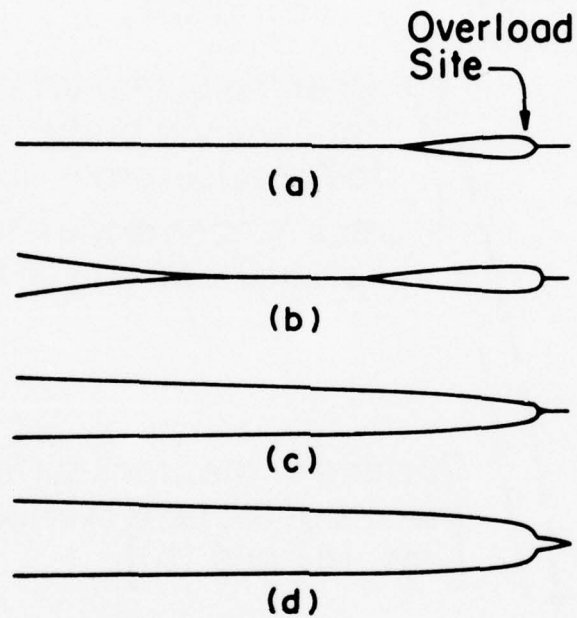


Figure 3. (a) to (d): The opening of a crack which contains misfitting material on its surfaces and which is also wedged open near its tip by the residual plastic strain field of a recently applied overload (model of P. C. Paris). The crack has grown slightly beyond the site of the overload.

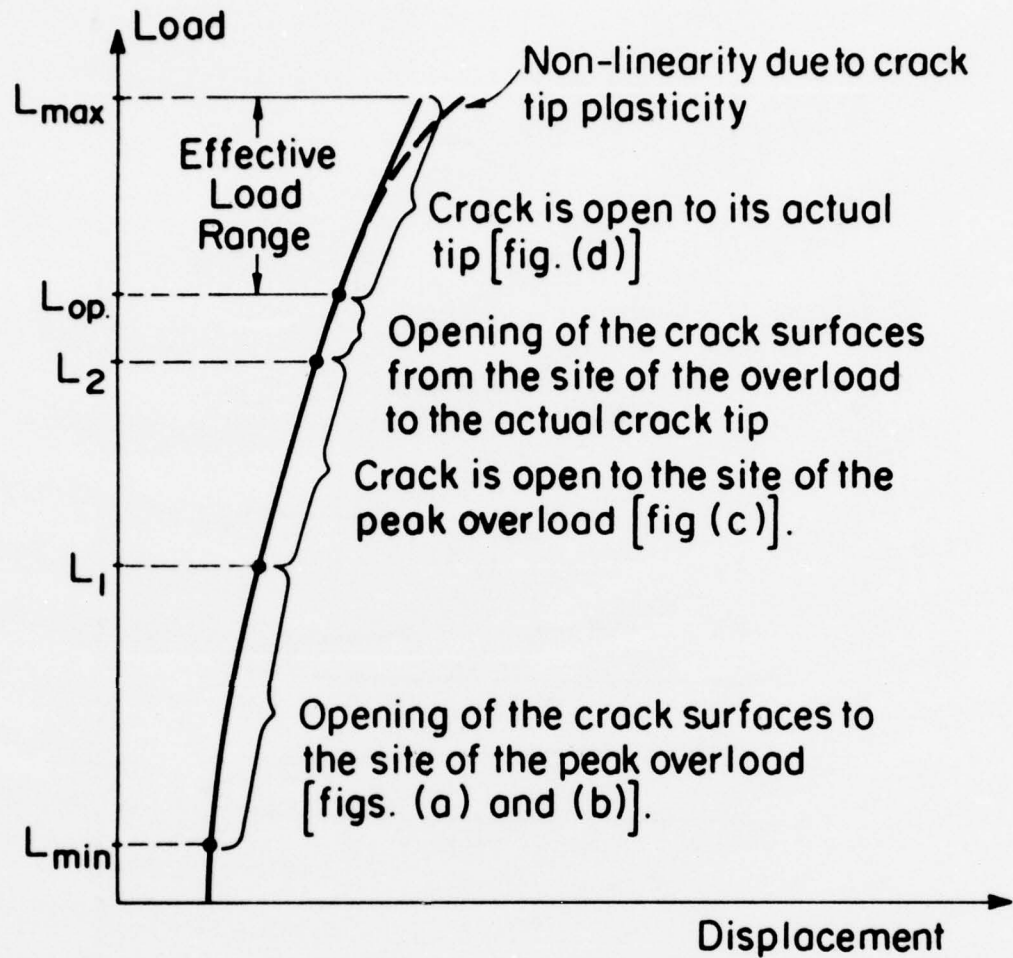


Figure 4. The load displacement diagram according to the overload and crack-closure model of Paris (Figs. (a) to (d)). The solid curve (with straight segments) represents elastic response in combination with crack surface opening; the dashed line represents actual elastic-plastic response.

In this kind of load-displacement plot, the load L_1 is liable to be interpreted as the opening load, although the crack is not, in fact, open to its tip until a considerably higher load (L_{op} in Fig. 4) is reached. Paris suggests that the nonlinearity shown between loads L_1 and L_{op} is small, and hence the second (or actual crack tip) opening can be detected only with very sensitive measurements. Previous investigations have discounted closure as an explanation of overload effects because the opening load was assumed to be L_1 and this is found to be smaller for cyclic loads applied after an overload than it is before.

Paris' measurements are intended to measure L_{op} in Fig. 4, and he reports that when ΔK_{eff} , based on $L_{max} - L_{op}$, is employed the crack growth rates in the retardation period following the overload are found to be consistent with the relation of da/dn to ΔK_{eff} for cyclic loading of the same material. It is clear that the accuracy of measurement in these experiments needs to be improved since one must be able to detect very small changes in crack length. Nevertheless, if the promising results reported by Paris are confirmed by subsequent experience, there is the strong implication that general load-sequence and load-spectrum effects on crack growth can be explained in terms of cyclic crack growth data and closure concepts. This has significant implications for the course of future work and points up the need for modeling methods which can reliably include closure effects in general loading histories.

MODELS

As suggested above, there is a level of modeling which can be divorced from any direct detailed prediction of fatigue crack growth based on microstructure. Instead the aim, as in models organized around the closure concept, is to predict crack growth in general oscillatory but non-cyclic loadings, typical of service load spectra, in terms of measured growth rates in cyclic loading. In this connection, Elber discussed a program of computer-based finite-element analysis now being carried on by Newman at NASA and demonstrated crack closure under a number of cyclic, overload, and block loading conditions. The calculations discussed were all for plane stress but Elber reports similar, if less extensive, closure results under plane strain conditions. Such analyses have a great potential for the modeling of fatigue closure processes, as well as many other fracture processes, and there would be much to be gained by a more organized analysis of specific cases in conjunction with experiments of the kind that Paris has reported.

Dill and Hutchinson discussed generalizations of the Dugdale/BCS model, wherein stretched ligaments as formed at the crack tip are left in place and can interfere in subsequent loadings. Also, Paris discussed a simple model in which the misfit zone is represented as an elastic dislocation wedge, of thickness related to the COD, centered within the plastic zone. Both of these approaches have potential for future development.

Cyclic plastic hardening or softening descriptions, and

also cycle dependent creep and relaxation of mean stress, as summarized by Dowling, have not yet been incorporated in fatigue crack plasticity models, and this area would seem to deserve greater attention. In addition, the distinction between effects of residual stresses, as opposed to effects of geometric interference between crack surfaces, are not generally well understood. Both arise, of course, from the permanent deformations experienced during previous crack growth, and they cannot be fully separated in the sense that crack surface interference generates compressive contact stresses. For an ideally plastic material model in which crack surface contact is neglected, the large residual compressive stress field generated by a peak overload is found by theoretical analysis to have no significant effect on the cyclic plastic response to a cyclic loading that follows the overload. In this sense, the often quoted "explanation" of overload retardation effects in terms of residual compressive stress, without consideration of associated crack closure effects (Fig. 3), would seem to be incomplete. Still, the residual stress problem has not yet been investigated for realistic cyclic constitutive descriptions and, indeed, these descriptions are not yet well formulated.

The modeling of the growth process per se has received little recent attention. Nevertheless, a general framework for understanding the growth mechanism has been evolving in recent years, and this received support from the presentations on micro-mechanisms by Pelloux and by Ritchie and, indirectly,

from the mode of data representation favored by McEvily. The concept is that fatigue crack growth is, essentially, a consequence of the plastic opening at the crack tip in each load cycle in a manner that, apparently, cannot fully be retraced upon reverse flow in unloading, so that some new material has been drawn onto the crack surface in each cycle. This basic process is, however, altered in important ways by the following considerations:

(i) When the size scale of the plasticity becomes too small in comparison with the relevant microstructural dimensions (i.e., at near-threshold conditions), there may be large alterations in the relation of the crack tip COD to ΔK_{eff} or in the reversibility of the plastic tip opening and closing process. Alternatively, there may be no change in either of these factors from the situation at higher K levels but, as Elber suggests, it may be the case that the ratio $\Delta K_{\text{eff}}/\Delta K$ becomes lower.

(ii) Modes of static fracture may be activated and contribute significantly to the rate of growth. This is likely at high K_{max} levels when the size of the plastic region is large on the microstructural scale so that, for example, significant strain and stress levels exist over distances comparable to the mean spacing of void-nucleating particles. Also, when a static fracture mechanism can be aided by the permeation of a species from the surrounding environment (e.g., H), there can be environmental effects on the static mode contribution to growth. Wei suggests that the rate limiting step may not always be

related to transport of the species through the solid but rather to its entry at the crack tip where there is a competition between fresh metal exposure by deformation and film formation by a reaction product. Additional static fracture effects can occur. For example, as emphasized by Pelloux, deep delaminations can occur on surfaces perpendicular to the crack plane, thus greatly changing the tip geometry, and hence its plastic tip opening response, from what might result without delaminations. These are, as McClintock emphasized, to some extent explainable in terms of the kinematics of crack tip closing.

(iii) Additional environmental effects, some of a rather subtle kind, may also play an important role. First, as observed earlier, the height of the misfit zone and hence the ratio of $\Delta K_{\text{eff}}/\Delta K$ may be affected by environment-based surface responses. These range from chemical dissolution of asperities, to their protective oxide filming against either reaction or re-welding, to the possibility (e.g., in vacuum) of significant re-welding at asperity contacts, with related effects on the load necessary to reopen the crack to its tip and on the heights of the asperities which are waiting to interfere with the crack surfaces on the next unloading. The second kind of environmental effect is an interaction with the process of crack tip opening and reclosing which may be significant in determining what fraction of the tip opening actually results in crack growth. For example, comparing air against a completely inert environment or vacuum, it is possible for some materials that essenti-

ally none of the crack tip opening is reversible for growth in air, whereas a large fraction may be reversible for growth in vacuum. A third type of environmental effect may entail direct dissolution of crack tip material, perhaps as made possible by progressive exposure of unfilmed material at the crack tip.

These considerations, together with the closure concept, seem broadly capable of rationalizing the many observations in fatigue. There are obviously very many uncertainties and very few of the ideas have been or can yet be carried through to a quantitative test. Whether the framework is capable of predicting even the very simple, if remarkable, result of a rather close correlation of growth rates among different materials in inert environments in terms of $\Delta K/E$ remains to be seen.

ACKNOWLEDGEMENT

This research was supported by the Advanced Research Projects Agency of the Department of Defense under Contract No. MDA903-76C-0250 with The University of Michigan.

MEETING ON FATIGUE CRACK GROWTH

July 7-9, 1976

AGENDA

P. C. Paris - Continuum mechanics aspects of fatigue crack propagation.

R. M. Pelloux - Relationships between Fractography and Microstructure.

J. P. Gallagher - Air Force crack propagation problems and needs.

W. Elber - Comparative discussion of methods of closure observation.

Discussion by D. M. Corbly and O. Buck (ultrasonics), W. Reimann (interferometric), G. R. Chanani and R. P. Wei (electric potential, bridging strain gauge), P. C. Paris (elastic unloading compliance), and others as appropriate on closure observations and relevance to mechanisms and/or models of fatigue.

R. O. Ritchie - Influence of superposed static fracture mechanisms on fatigue.

R. P. Wei - General environmental and temperature effects.

O. Buck - Environmental effects on closure and fracture mode.

Discussion by G. R. Chanani (fractographic features associated with overloads), A. W. Thompson (effect of microstructure in Ti alloys).

J. W. Hutchinson - Closure effects predicted from Dugdale/BCS crack models.

W. Elber - Summary of J. Newman finite-element predictions of crack surface closure effects.

H. Dill - Spectrum crack growth prediction.

A. J. McEvily - Modified COD model.

Discussion: Fatigue detection by NDE, modeling, crack growth prediction.

PARTICIPANTS AND GUESTS

W. J. Baxter
General Motors Res. Labs.
12 Mile & Mound Rds.
Warren, Michigan 48090

J. G. Bjeletich
Lockheed Missile & Space Co.
Bldg. 204
Palo Alto, California 94304

Otto Buck
Rockwell International
Science Center
1049 Camino Dos Rios
Thousand Oaks, California 91360

Govind R. Chanani
Northrop Corporation
ORG 3771/62
Hawthorne, California 90250

D. M. Corbly, Jr.
AFML/LLN
Wright-Patterson AFB
Dayton, Ohio 45433

H. D. Dill
McDonnell Douglas
Bldg. 32, P.O. Box 516
St. Louis, Missouri 63166

N. E. Dowling
Westinghouse Research
Beulah Road
Pittsburgh, Pennsylvania 15235

W. Elber
NASA, Langley
MS 188E
Hampton, Virginia 23665

J. P. Gallagher
AFFDL/FBE
Wright-Patterson AFB
Dayton, Ohio 45433

Harris Marcus
University of Texas
Austin, Texas 78759

A. J. McEvily
University of Connecticut
Metallurgy Department
Storrs, Connecticut 06268

P. C. Paris
Brown University
Providence, Rhode Island 02912

R. M. Pelloux
Room 8-237
Massachusetts Inst. of Tech.
Cambridge, Massachusetts 02139

W. Reimann
AFML
Wright-Patterson AFB
Dayton, Ohio 45433

R. O. Ritchie
University of California
Room 139, LBL bldg. 62
Berkeley, California 94720

Anthony Thompson
Rockwell International
Science Center
1049 Camino Dos Rios
Thousand Oaks, California 91360

Robert P. Wei
Lehigh University
327 Sinclair Lab., Bldg. 7
Bethlehem, Pennsylvania 18015

FATIGUE CRACK GROWTH

P. C. Paris

HISTORICAL INTRODUCTION

In the early 1960's it was found that fatigue crack growth rates could be correlated in terms of the crack tip stress field intensity factor, K . In particular it was suggested to plot $\text{LOG } da/dn$ (cycle growth rate) vs. (linear or) $\text{LOG } \Delta K$ (stress intensity factor range) to characterize a material's fatigue crack growth properties. Secondary mechanical variables were considered to be mean K (or load ratio, $R = K_{\text{MIN}}/K_{\text{MAX}}$), cyclic frequency, etc. The development of electro-hydraulic servo-controlled testing equipment in the 1960's finally made it possible to explore these fatigue crack growth properties conveniently.

In the mid-1960's it was found that atmosphere and other environments significantly affect rates of fatigue crack growth over wide portions of the range of growth (from 10^{-8} to 10^{-2} inches per cycle). Though mechanical aspects of fatigue crack growth were observed to be quite insensitive to material variables, e.g., alloying, thermal treatment, etc., conversely the environmental effects were found to be very sensitive to these material variables. Indeed, tests in inert environment showed that fatigue crack growth rate data, da/dn from a wide variety

of metal alloy systems (aluminum, titanium, iron, nickel, copper, beryllium, magnesium, etc., based alloys) are correlated into a reasonably single curve when using $\Delta K/E$, (stress intensity factor range over elastic modulus), within a factor of about 2 or 3 on crack growth rates for the mid-range of growth rates (i.e., 10^{-7} to 10^{-4} inches per cycle). This rather dramatic lack of influence, though seemingly very fundamental, has received (too) little attention to date. On the other hand, the influence of aggressive environment was observed to alter the purely mechanical growth rates by factors of 3 to over 1000, both above and below the thresholds for static stress corrosion crack growth. Moreover, though the mechanical component of fatigue crack growth seems only slightly affected by stress state (plane stress or plane strain at the crack tip) the environmental component was observed to be of decidedly more influence with plane strain at the crack tip. Also, it was noted that for fatigue stress intensities, K , above the threshold for static environmental cracking, the environmental component to be added to the mechanical component of fatigue crack growth is crudely equal to superimposing the appropriate static environmental growth effects expected.

In the late 1950's and early 1960's, there were reports of non-propagating cracks from several sources. The nature of the experiments reporting these non-propagating cracks did not make clear whether the non-propagation was induced by residual stresses due to prior local or general plasticity, or whether

the lack of propagation was non-propagation under steady state conditions. In the late 1960's more definitive experiments began to attempt to define the fatigue crack growth characteristics at and below the 10^{-8} inches per cycle decade and an apparent threshold ΔK_{TH} level was found below which cracks do not seem to grow (steady state). The threshold, ΔK_{TH} , is reportedly more strongly influenced by mean load (or load ratio, R) than the growth portion of behavior. Evidence on environmental influence of the threshold, ΔK_{TH} , remains contradictory, some researchers reporting no influence and others reporting rather large influences; it might best be regarded as unresolved to date.

The above results have within themselves been sufficient to examine and predict fatigue crack growth in structures subject to purely cyclic loads. Interest in mechanisms and micro-processes of crack growth are academic except for attempts to develop improved materials, etc. However, many structures which are fatigue crack growth critical, such as aircraft structures, are subject to complicated variable amplitude loading. Moreover, by the early 1960's it was recognized that load interaction, (history) effects in variable amplitude fatigue crack growth were significant. However, modest attempts did not lead to prediction models at that time.

Indeed, until the late 1960's detailed analysis of crack tip plasticity effects were not sufficiently described for purposes of modeling fatigue cracking load-interaction effects.

Moreover, it was not until 1968 that fatigue crack closure was noted which may be regarded as a physical feature which influences greatly any load interaction effects. But even with this knowledge, only crude load-interaction models have been developed to date and closure is usually not included as a feature of these models.

CURRENT RESEARCH AND FUTURE PROSPECTS

CRACK CLOSURE

Though crack closure was first observed and reported in 1968 for tension-tension fatigue crack growth under cyclic loading, very few definitive studies have been made to date. Experimentally, it is evident that very sensitive instrumentation is required to observe closure, thus of those studies done most, perhaps all have inadequate or misleading data. Of those measurements or closure made with adequate sensitivity, different instrumentation approaches used by different people seem to lead in some cases to opposing results. Thus it seems self-evident that for closure under cyclic loading additional carefully run tests are needed. And indeed in order to assure proper interpretation of results, it is suggested that dual or multiple instrumentation systems with differing sensing approaches (such as: load-displacement method vs. ultrasonic method vs. electrical potential method, etc.) be used simultaneously on some tests. Or if not simultaneously on a single test, then on tests with the same material-environment combination in independent labora-

atories using differing instrumentation approaches.

Summarizing the available data and observed trends under cyclic load, results are as follows:

(1) Tension-tension closure surely does occur and has been established by independent methods.

(2) Closure levels K_{open}/K_{MAX} , do depend on material (such as alloy, heat treatment, etc.).

(3) Closure levels appear to depend on absolute K-level (i.e., K_{MAX}). (And thus appear to change as crack length changes in test under constant cyclic load levels.)

(4) Steady state closure levels (K_{open}/K_{MAX}) seem to characterize portions of behavior within certain ranges of K_{MAX} levels.

(5) For such steady state closure level situations under cyclic loading, the closure level seems to be fairly independent of load ratio, R (unless the minimum load is high enough that the crack is open throughout the load cycle).

Mathematical - physical models of crack closure under cyclic loading are just now beginning to be the subject of some studies. One first order approach is to view closure as resulting from asperities left behind on the propagating crack surface which under steady state conditions form a "dislocation" of interference between crack surfaces. Analysis of this effect using first order fracture mechanics concepts, such as monotonic plastic zone, cyclic plastic zone, and crack opening stretch and crush lead to results implying substantial dependence on cyclic

flow properties vs. monotonic flow properties. However, such models inherently would imply such a dependence and thus until they are more fully developed and verified, the result should be viewed as inconclusive. Other modeling studies such as strip-yield models, and finite element models show promising trends but remain in an early stage of development.

CRACK GROWTH RATES UNDER CYCLIC LOADING INTERPRETED IN TERMS OF CRACK CLOSURE

Under the concept of crack closure it can be argued that crack growth should only be affected by excursions of the crack tip stress intensity, ΔK_{EFF} , while the crack is open. Observation of growth rates simultaneously with closure observations by several investigators fairly strongly support this hypothesis. However, it is acknowledged that contradictory data using electrical potential sensing of closure exists, which incidentally also disagrees with other aspects of the previous investigations. Therefore it is thought that this hypothesis works rather well with details remaining to be explored in the future.

CRACK CLOSURE FOLLOWING OVERLOADS

It is rather well documented with several investigations that following overloads, the cyclic loading rates of growth of cracks are slowed (or sometimes arrested) until the crack tip grows out of the region of overload influence and resumes normal steady state rates. It seems that these results show a strong influence which can only be explained by effects on closure.

Only one investigator has reported experimental studies of transient effects on closure loads following overloads. The results seem reasonably consistent with previous overload-retardation observations without closure load measurements. These new results also show crack growth rates during transient effects of retardation to be correlated rather well with steady state cyclic loading growth rates, when the instantaneous ΔK_{EFF} is used as the loading variable, as determined from closure load measurements in both the overload and steady state cyclic tests. Therefore these results are very promising but to date the observations are very limited.

CRACK CLOSURE EFFECTS AND RETARDATION FOR GENERAL VARIABLE AMPLITUDE LOADING

Though under single overloads there is a transient effect on growth under subsequent cycling, under more general variable amplitude loading, where higher loads occur sufficiently frequently, it may well be possible that closure will settle down to a more or less steady state level (or at least be reasonably approximated by a steady level in its effect on crack growth rate). At least two investigations have incorporated such prospects in predictions of local average crack growth rates for such applications as aircraft load spectrums (where the local average is computed over a representative flight or group of representative flights). Moreover, modeling of such a steady state level can perhaps be done in terms of the "Dislocation

Model" (previously discussed) in terms of averages of disparities left on the crack surface in the wake of the growing tip.

On the other hand, an analysis which lends itself to computing transient effects might be necessary for computing crack growth rates to a sufficient precision for other types of load spectrums with less frequent high loads, etc. For such cases the single overload transient effects analysis as discussed earlier may be sufficient for the basis of an analysis.

At this point it is self-evident that the prospects are good to predict variable amplitude fatigue cracking rates from such models, but the models remain undeveloped and test data are sparse if not non-existent on measuring closure for a variety on variable amplitude load spectra.

OTHER WORTHY TOPICS NOT DISCUSSED HEREIN (i.e., not fully discussed at these meetings.)

(1) Current knowledge of environmental influences on fatigue crack growth.

(2) Effects of mechanical variables and environment and closure on thresholds for fatigue crack growth.

(3) Metallurgical aspects and micromechanisms of fatigue crack growth.

(4) Crack growth under fully plastic conditions.

(5) Growth of micro cracks and relationships between fatigue cracking thresholds and endurance limits.

ACKNOWLEDGEMENT

This research was supported by the Advanced Research Projects Agency of the Department of Defense under Contract No. MDA903-76C-0250 with The University of Michigan.

SUMMARY OF THE MEETING ON EPITAXY

A. Yariv

Members of MRC and a group of experts from both the industrial and the university communities met to discuss the state of the art in epitaxial growth of crystalline layers and the variety of applications which depend on them. It was hoped that the meeting would be able to identify and pinpoint serious problem areas where additional work may be required.

The main topics discussed at the meeting were: (1) The various techniques used in epitaxial growth primarily liquid (LPE) and vapor phase (VPE) epitaxy and the recently developed technique molecular beam epitaxy (MBE). (2) The use of epitaxially grown films in the fabrication of a variety of electronic and electrooptic devices, especially CW injection lasers, light emitting diodes, photodetectors for near visible and infrared applications, impatt diodes and field effect transistors, integrated optics and magnetic bubbles for computer memories. (3) The intriguing possibility of crystal engineering by MBE which makes it possible to grow new crystals with controlled periodicities.

It became clear from the meeting that epitaxy is playing a key role in a great variety of new technologies of increasing importance to U.S. technology and to DoD. It was also evident

that in spite of the vigorous pursuit of this technology by industrial concerns there are a few problem areas that may become potential bottlenecks.

The use of GaAs-Ga_xAl_{1-x}As epitaxial technology to fabricate long life (>10,000 hrs) CW semiconductor injection lasers has been described by Panish (Bell). The dependence on the index of refraction and energy gap were used to confine the optical power as well as the injected electron and holes to a narrow (~3000Å) active region thus attaining low threshold current.

The main application projected for the injection lasers is as the power source for optical fiber communication systems. These fibers, however, display their lowest loss and material dispersion in the $1.2 < \lambda < 1.3 \mu\text{m}$ region. The emission wavelength of $\lambda \approx 0.85 \mu\text{m}$ of the GaAs-GaAlAs laser is thus not optimal for high data rates (≥ 1 G bit/sec) links.

A program aimed at producing reliable and long lived injection lasers for the $1.2 < \lambda < 1.3 \mu\text{m}$ region was described by A. Strauss (Lincoln). The laser uses epitaxial layers of Ga_xIn_{1-x}As_yP_{1-y} grown on InP substrates. The use of a quaternary compound makes it possible to, independently, match the lattice constant to that of the InP substrate while controlling the energy gap, thus the emission wavelength to the optimal region. This work which, potentially, is very important is a good illustration of the need for basic material information - phase diagrams, lattice constants, index, and energy gap vs. composition, etc., in designing sophisticated electrooptic devices.

The whole program, at the moment, is geared to the use of InP as a starting substrate material. The availability of ternary, or quaternary, crystals of good quality should greatly increase the flexibility and the number of possibilities open to the designer of specific electrooptic components. These materials are not presently available.

A critical review of the various techniques employed in epitaxial technology was offered by Stringfellow (Hewlett Packard). These include LPE, VPE and MBE. Some of the best optical devices (lasers, detectors) and microwave (Impatt diodes, mixers) are now grown by LPE. The technique, based on the use of small, limited volume multi-well carbon crucibles does not lend itself to large scale and/or large area fabrication. Vapor phase epitaxy (VPE) - a technique which is amenable to large scale production has extreme difficulty in handling reactive constituents such as Al which are used in these compounds. The technique of MBE in which atomic beams originating in effusion cells impinge on the target substrate is deemed too slow (growth rate at present $\sim 1 \mu\text{m/hr}$).

One potential solution to this problem is through the use of organometallic compounds such as $\text{Al}(\text{CH}_3)_3$, $\text{Al}(\text{C}_2\text{H}_5)_3$, $\text{Ga}(\text{C}_2\text{H}_5)_3$, $\text{In}(\text{C}_2\text{H}_5)_3$, etc. The basic chemical reaction in this case proceeds at much lower temperatures and the technique was used successfully mostly in Japan, to grow epitaxial GaAlAs layers. A key problem here is the lack of high purity organometallic reagents. This results in high impurity concentration in the grown layers which causes low carrier mobility and poor recombination efficiency.

The technique of molecular beam epitaxy was reviewed by both A. Cho and A. Gossard (Bell). The first described the application of MBE to the fabrication of a variety of electrooptic devices including GaAs-GaAlAs double heterostructure lasers, distributed feedback lasers, field effect transistors and microwave mixers. The characteristics of these devices fall somewhat short of their LPE grown counterparts. The reasons for the difference are not understood and deserve a serious study. The big advantage of MBE, however, is in its unique thickness control capability. This control, extending to a few angstroms was used by A. Gossard to grow artificial crystals of alternating GaAs and AlAs monolayers. This results in new electronic band structures and thus in modification of the optical and electronic properties of the material.

A theoretical analysis by Yeh and Yariv (Caltech) showed how the use of periodic stratified media can be used to fabricate new types of optical devices based on Bragg interference. One example was a dielectric waveguide in which the guiding layer possesses a lower index of refraction than the bounding media. This is the exact opposite to conventional dielectric waveguide. Laser waveguides composed of layered medium-air-layered medium were discussed. A more remote application is to X-ray lasers where the feedback is produced by internal Bragg reflection in artificially periodic crystals.

Selective epitaxial growth through oxide masks was described by Samid (Caltech). The technique results in the growth

of embedded layers which is of importance in optically confined laser structures. Low threshold lasers were fabricated.

The fabrication of photoemissive surfaces with a response up to $\lambda \sim 1.8 \mu\text{m}$ was described by Harris (Rockwell). These devices use multilayers of epitaxially grown GaAlSb. The long λ response is achieved by absorption in an n type GaSb layer. The electrons are then accelerated through a reverse biased punched-through junction with the higher energy gap GaAlSb n layer and are emitted into the vacuum through a Cs_2O monolayer which lowers the work function of the p-type GaAlSb emitter layer.

The problems of epitaxial growth of PbSnTe and HgCdTe for infrared detector and laser applications was considered by Vohl and Walpole (Lincoln Labs.) who described the growth problems and fabrication procedures using these materials.

The meeting convinced us that due to the combined incentive of commercial and military application and of government support, the epitaxial technology is pursued vigorously in the U.S. A few areas, however, were identified where additional effort could play an important role in advancing the technology. These are:

1. The development of U.S. sources for high grade InP crystals is recommended. This material is the starting point for growing epitaxial GaInAsP lasers oscillating near $1.25 \mu\text{m}$, a region where the dispersion and loss characteristics of silica based optical fibers are optimum.

2. Development of ternary crystals as substrate sources is recommended. All of today's epitaxial technology is based on starting from binary substrates (GaAs, InP, CdTe, etc.) which places a limit on the flexibility and choice of materials available to device designs.

3. Support of research on the use of organo-metallic compounds in vapor phase epitaxy (VPE) is recommended. VPE techniques will be important in large scale fabrication of epitaxial structures. Present VPE techniques cannot handle reactive elements such as Al and Sb. Preliminary work in the U.S. and in Japan indicates that VPE using organo-metallic compounds (such as $\text{Al}(\text{C}_2\text{H}_5)_3$), can overcome this problem. It will also be important to develop a supply of high purity organo-metallic reagents.

4. Studies in academic institutions on the detailed kinetics of epitaxial growth are recommended. While the thermodynamic properties are, in general, sufficiently well known, basic knowledge on diffusion rates growth habits, sticking coefficients and non-equilibrium growth is inadequate for the systems of III-V and II-VI compounds. The question whether ternary crystals could provide high grade crystals for use as substrates should be addressed.

5. Vapor phase and MBE techniques for InP based systems should be explored. Particular attention should be given to the causes of the generally poorer device performance resulting from these techniques, compared to LPE.

6. The garnet epitaxy technology for magnetic bubble

materials appears to be further developed than that of the compound semiconductors. It will be important to determine if this is an inherent property of the different material system, and if the techniques of a high degree of supercooling and liquid motion be successfully transferred to III-V and II-VI systems.

ACKNOWLEDGEMENT

This research was supported by the Advanced Research Projects Agency of the Department of Defense under Contract No. MDA903-76C-0250 with The University of Michigan.

A MECHANISM FOR LIQUID PHASE
EPITAXIAL GROWTH OF NONEQUILIBRIUM
COMPOSITIONS PRODUCING A COHERENT INTERFACE

J. P. Hirth and G. B. Stringfellow

In a study of growth of $\text{Ga}_x\text{In}_{1-x}\text{P}$ by LPE on a GaAs substrate, Stringfellow¹ observed that growth from liquids with a range of compositions produced the same solid composition. Liquids within about ± 10 percent of the zero lattice parameter composition yielded solid with $x=0.51$, the zero lattice parameter mismatch composition. Other reports have confirmed this effect in the Ga-In-P system^{2,3} and in the Ga-As-Sb and In-As-Sb systems⁴ as well as such dissimilar systems as magnetic garnet materials grown from a flux.⁵ However, in the quaternary system Ga-In-As-P, the effect is not observed.^{6,7}

Stringfellow¹ attempted to calculate the magnitude of the effect by computing the free energy of the nearly lattice matched overgrowth, determining the minimum free energy composition including strain energy terms and chemical terms. Reduction in the strain energy contribution was found to offset the increase in the chemical contribution in this model. The observed variation of nearly lattice-matching composition with liquid composition was found to agree very well with the model.

The ultimate breakdown to a dislocation interface was also rationalized by a free energy argument. For large enough

mismatch, the free energy of a dislocated overgrowth of equilibrium composition was computed to be less than the lattice matching overgrowth. Again, the computed transition composition agreed well with the computations. However, the dislocation energy was probably overestimated because of neglect of image stresses, so the latter part of the correlation is in question.

Here, we suggest a kinetic model for the ultimate breakdown, which nevertheless retains the thermodynamic portion of the correlation when lattice matching occurs.

In the deposition of a one-component epitaxial overgrowth on a substrate with near lattice matching, the initial nuclei are coherent because the attendant reduction in surface energy offsets the strain-energy in the nucleus.⁸⁻¹⁰ As the nuclei grow they can become semicoherent in several ways. For lateral growth, nucleation of an interface dislocation at the periphery of the nucleus becomes favorable for large particles and dislocations are injected, reducing the strain energy and creating lattice mismatch.^{8,9} For thick overgrowth, dislocations can also be injected from the free surface.¹¹ However, image forces prevent this injection below a critical thickness of the order of 1 to 2nm.¹²

For growth from a multicomponent system, such as Ga-In-P, an alternative model is possible. Again the nucleus should be coherent. Now as growth occurs, however, rather than accumulating elastic strain energy, the particle can initially grow with nearly the lattice-matching composition as suggested by

Stringfellow.¹ This form of growth greatly suppresses the probability of dislocation nucleation and permits growth of macroscopic, coherent, lattice matching overgrowths.

The ultimate breakdown in such coherent overgrowth is then supposed to be dislocation nucleation controlled in a ledge-type growth model.¹³ The observations reported by Strauss⁷ for growth of Ga-In-As-P, indicating more rapid growth of (100) surfaces than for (111) surfaces having the same temperature dependence of growth, strongly suggest such a ledge type model. As atoms attach at kink sites on ledges, the strain-chemical free energy model applies locally and atoms are selected to reduce local strain buildup of the type shown in Fig. 1. With sufficient chemical driving force, the nucleation of a dislocation loop, as shown in Fig. 2, will eventually lead to breakdown of the coherent interface.

Conventional nucleation theory¹⁰ indicates that the free energy of such a configuration is

$$\Delta G = (\ell/b) \Delta G + \mu b^2 \ell / 10 + \mu b^4 / \ell \quad (1)$$

where ΔG is the negative chemical free energy difference per atom between solid of equilibrium bulk composition and solid of lattice-matching composition ℓ , is defined in Fig. 2, b is the lattice spacing, $\mu b^2 / 10$ is the roughly core-type energy per unit length of such a dislocation, and $\mu b^4 / \ell$ is the interaction energy between the dislocation kinks at the ends of the length ℓ . Minimization of the free energy with respect to ℓ

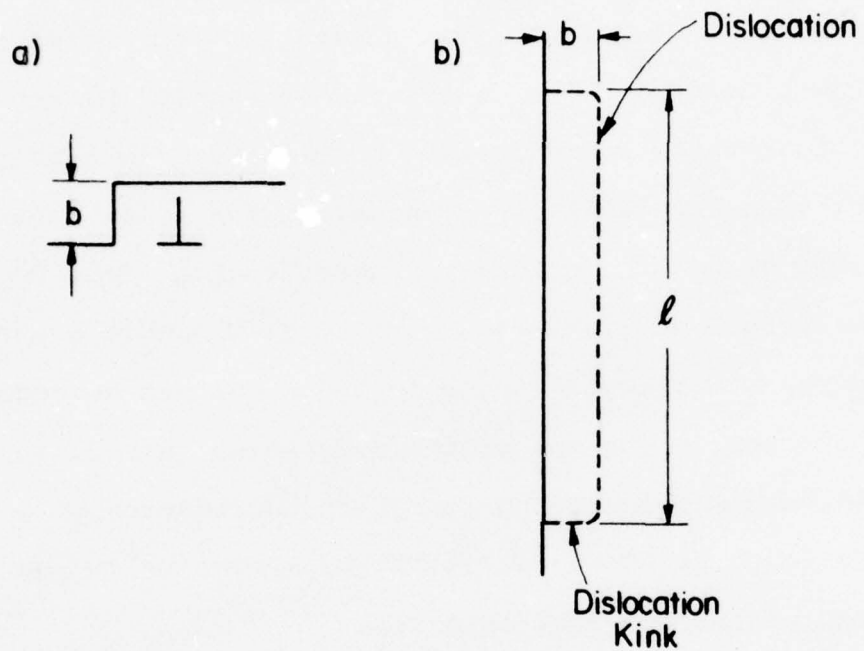


Figure 2. Dislocation being created at a ledge: (a) cross-sectional view, (b) view normal to solid-liquid interface.

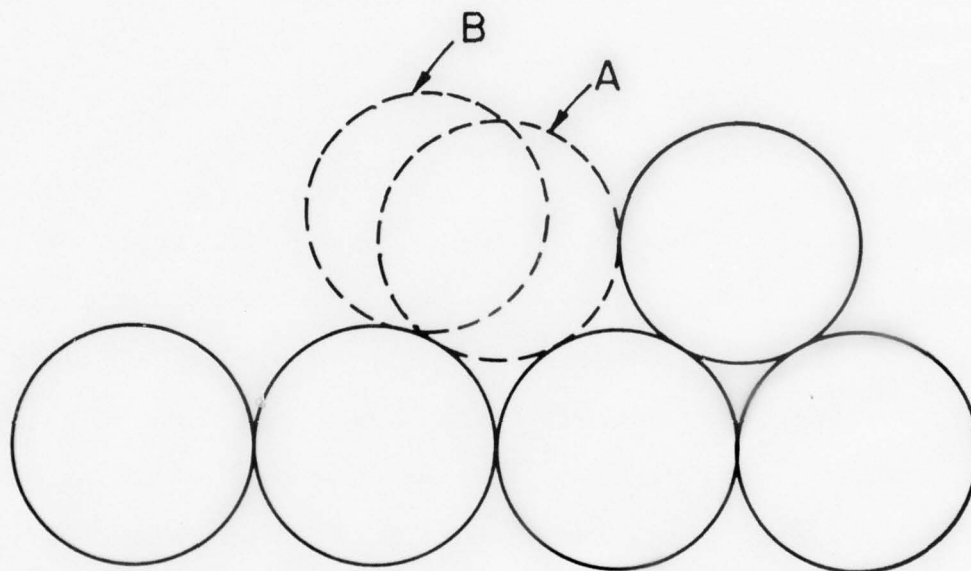


Figure 1. Atom being added at a ledge in air unstrained configuration A and a locally strained configuration B.

gives a critical length

$$\ell^* = \left[\frac{\mu b^5}{(\mu b^3/10 + \Delta G)} \right]^{\frac{1}{2}} \quad (2)$$

and a critical free energy

$$\Delta G^* = 2(\mu b^3)^{\frac{1}{2}} (\mu b^3/10 + \Delta G)^{\frac{1}{2}} \quad (3)$$

Theory predicts nucleation when

$$\Delta G^* = kT \ln (nv/J) \quad (4)$$

where $n = 2.5 \times 10^9 \text{ m}^{-1}$ is the number of sites per meter of ledge, $v = 10^{13} \text{ s}^{-1}$ is the atomic vibration frequency (the attempt frequency for nucleation of a loop) and $J \sim 10^2 \text{ m}^{-1} \text{ s}^{-1}$ is the critical, observable nucleation rate required for nucleation. Substituting Eq. (4) into Eq. (3) gives a prediction of ΔG required for nucleation as a function of known parameters. For Ga-As-P grown on Ga-As, with the use of the value of $\mu = 3.39 \times 10^{10} \text{ Pa}$ from the work of Hakki et al.¹⁴, $b = 0.4 \text{ nm}$ and $T = 1060 \text{ K}$ this procedure yields a value of ΔG of -97.9 kJ/mole . In terms of the computations of Stringfellow¹ for this system, this corresponds to the free energy difference between solids with $x=0.31$ or 0.71 and the lattice matching solid with $x=0.51$. These predicted values of $\Delta x = 0.20$ at which the epitaxial layer growing on a Ga-As substrate should become noncoherent compares with an experimentally observed value of $\Delta x = 0.11$.

Thus, there is only fair agreement between expectation and experience, but it is reasonable in view of the approxima-

mations in the above estimates. The dominant factor in the predicted values is the core energy: a value of $\mu b^3/27$ (much smaller because of the nonlinear relation between ΔG and Δx) would be required for this parameter to give perfect agreement. Core energies this small are possible, but to resolve the parameter more accurately than above, atomic calculations, including surface image effects, would be required for the nonlinear elastic core-type configuration shown in Fig. 2.

ACKNOWLEDGEMENT

This research was supported by the Advanced Research Projects Agency of the Department of Defense under Contract No. MDA903-76C-0250 with The University of Michigan.

REFERENCES

1. G. B. Stringfellow, J. Appl. Phys. 43, 3455(1972).
2. W. R. Hitchens, N. Holonyak, Jr., M. H. Lee and J. C. Campbell, J. Cryst. Growth 27, 174(1974).
3. H. Beneking, N. Grote, P. Mischel and G. Schul, in Ga As and Related Compounds, (Inst. Phys. and Phys. Soc., London, 1975), p. 113.
4. J. S. Harris, Report of the ARPA Materials Research Council (University of Michigan, Ann Arbor, Michigan, 1976).
5. D. C. Miller and R. Caruso, J. Cryst. Growth 27, 274(1974).
6. G. Antypas, Varian Associates, Palo Alto, Calif., private communication, Aug. 1976.
7. A. Strauss, Reprot of the ARPA Materials Research Council (University of Michigan, Ann Arbor, Michigan, 1976).
8. N. Cabrera, Surface Sci. 2, 230 (1964); Mem. Sci. Rev. Metall. 62, 205(1965).
9. W. A. Jesser and D. Kuhlmann-Wilsdorf, Phys. Stat. Sol. 19, 95(1967).
10. J. P. Hirth and G. M. Pound, Condensation and Evaporation, Pergamon, New York (1963).
11. J. W. Matthews and J. L. Crawford, Thin Solid Films 5, 187(1970).
12. K. Shinohara and J. P. Hirth, Phil. Mag. 18, 883(1973).
13. W. K. Burton, N. Cabrera and F. C. Frank, Phil. Trans. Roy. Soc. 243A, 299(1951).
14. B. L. Hakki, A. Jayaraman and C. K. Kim, J. Appl. Phys., 5291(1970).

SUMMARY OF MEETING ON RAPIDLY SOLIDIFIED
POWDERS AND RELATED TECHNOLOGY

E. E. Hucke, J. P. Hirth and M. Cohen

A two-day meeting on rapidly solidified powders (RSP) and technology relevant to subsequent consolidation into useful shapes was held as part of the 1976 MRC summer study. This meeting extended the activities begun at the 1975 meeting and had the threefold objectives to: 1) Disseminate the early findings of the newly initiated ARPA program on improved Ni base superalloys at Pratt-Whitney Florida, 2) Identify and discuss emerging scientific and technological problems requiring further attention in direct support of this program, and 3) Identify and discuss the relative merits and problems in extending rapid solidification technology to other materials systems.

Since considerable progress had been made on items 2 and 3 in 1975, the program was structured to fill in the gaps previously identified. The program is incorporated along with a list of invited participants. In addition, the Council members active in part or all of the sessions are also recorded. It should be noted that the meeting was in no way intended to completely review particulate technology or even powder metallurgy, but rather to focus on the range of exceptional structures and properties obtainable from rapid cooling and the special problems or opportunities of processing and consolidation.

SMALL-PARTICLE PHENOMENA AND TECHNOLOGIES MEETING

July 14-15, 1976

First Session - Morris Cohen, Chairman

- E. C. van Reuth - ARPA Program in Small-Particle Processing
- *Alan Lawley - Overview of Advanced Powder-Making Processes; Fundamentals of Droplet Formation
- *M. C. Flemings - Theory of Dendritic Solidification During Very Rapid Cooling
- **J. B. Moore and A. R. Cox - Progress in the P&W Rapid Solidification Program

Second Session - E. E. Hucke, Chairman

- *N. G. Grant - Special Methods of Achieving Rapid Solidification in Fine Particles
- E. J. Dulis - Inert Gas Atomization and Shape Consolidation of Commercial Alloys
- *O. D. Sherby - Fundamentals of Superplasticity; Extension to Refractory Metals
- *A. G. Evans - Prospects for Attaining Superplasticity in Intermetallic and Ceramic Materials

Third Session - J. P. Hirth, Chairman

- *Larry Kaufman - Calculation of Metastable Phase Relationships
- ****R. E. Maringer - Survey of Microcrystalline - and Amorphous - Metal Technologies
- ***Five-minute presentations on new ideas relative to processing, structural control, novel properties, and applications; preparation of brief memoranda

Fourth Session - Morris Cohen, Chairman

Identification of important research opportunities and potential applications

Recommendations to ARPA

- * A more complete written account is to be published in the final report of the Materials Research Council Meeting for 1976, ARPA Contract MDA903-76C-2050.
- ** Written reports are issued under ARPA Contract F33615-76-C-5136.
- *** Brief notes to be published in the final report of the Materials Research Council Meeting for 1976, ARPA Contract MDA903-76C-0250.
- **** Report entitled "Amorphous and Metastable Materials", Battelle Columbus Labs., Tactical Technology Center by R. E. Maringer may be obtained from NTIS #AD-A032 064/8WM.

PARTICIPANTS AND GUESTS

Attwell M. Adair
Wright-Patterson AFB
Ohio 45433

David Arnold
General Electric Company
Evendale, Ohio

Gordon A. Bruggeman
AMMRC
Watertown, Mass. 02172

Gilbert Y. Chin
Bell Telephone Laboratories
Murray Hill, New Jersey 07974

Arthur R. Cox
Pratt and Whitney Aircraft
West Palm Beach, Florida 33402

Edward J. Dulis
Crucible Materials Research Ctr.
Pittsburgh, Pa. 15230

Norbert B. Elsner
General Atomic
San Diego, Cal. 92138

James N. Fleck
Crucible Materials Research Ctr.
Pittsburgh, Pa. 15230

Merton C. Flemings
M.I.T.
Cambridge, Mass. 02139

Nicholas J. Grant
M.I.T.
Cambridge, Mass. 02139

Larry Kaufman
ManLabs, Inc.
Cambridge, Mass. 02139

Bernard H. Kear
Pratt & Whitney Aircraft
Middletown, Conn. 06457

Alan Lawley
Drexel University
Philadelphia, Pa.

Harry A. Lipsitt
Wright-Patterson AFB
Ohio 45433

Robert E. Maringer
Battelle Columbus Laboratories
Columbus, Ohio 43201

Robert Mehrabian
University of Illinois
Urbana, Illinois 61801

Joseph B. Moore
Pratt & Whitney Aircraft
West Palm Beach, Florida 33402

Oleg D. Sherby
Stanford University
Stanford, Cal. 94305

Jack H. Wernick
Bell Telephone Laboratories
Murray Hill, New Jersey 07974

Participating Council Members

R. L. Coble
M. Cohen
D. C. Drucker
P. E. Duwez
H. Ehrenreich
A. G. Evans
W. H. Flygare
J. J. Gilman
J. P. Hirth

E. E. Hucke
R. A. Huggins
G. S. Kino
J. L. Margrave
F. A. McClintock
H. Reiss
M. Tinkham
M. J. Sinnott
G. H. Vineyard

The motives for ARPA's initiation and possible extension of rapid-quenching technology were discussed by E. C. van Reuth. Since PM techniques in superalloys have recently been established in military engines and limited laboratory property data from finer-than-usual dendritic powders yielded encouraging results, it was decided to make a major effort to translate this behavior into actual engine components. Mechanical properties of various hot parts, including both rotors and glades, have long imposed well-known operating limitations on gas turbines. Increments in the various strength properties, particularly at high temperatures, can be directly translated into higher thrust-to-weight and/or improved fuel economy. Various estimates of these economies integrated over the lifetime of the applicable military fleet show cost savings in tens to hundreds of millions of dollars. In addition, the powder process is known to offer remarkable opportunities, because of the direct processing to near-final shapes, and large cost savings due to lower materials and machining costs. While the superalloy military application is obvious, other cases for exploitation of rapidly solidified materials should also be identified. These may involve metallic or non-metallic systems, of usual or exotic materials, where the unique benefits may be in chemical, electrical, physical, or mechanical properties.

Since a melt usually offers the most economical means of achieving the required homogeneity, Alan Lawley gave an extensive review of the various means available for breaking up

liquid into small particles suitable for rapid quenching. Broadly, he classified these atomization methods into gas, liquid (H_2O), centrifugal, and mechanical. Within each group, various examples of laboratory and/or pilot production processes were schematically presented. The models and equations relating material and process parameters to the output parameters of interest, such as particle size and distribution, were discussed in detail. In addition, the detailed stages of liquid instability leading to droplet formation were presented along with an appraisal of the opportunities available in each process for rapid quench of the droplets.

M. C. Flemings concentrated on heat transfer from small droplets and the effects of increased solidification rate on the structure of the particle. He emphasized that, in the cases of interest, the resistance to heat transfer exists essentially at the particle surface, with negligible temperature gradients within the particle. Thus, the unsteady heat flow problem is relatively simple (Newton's law of cooling) and the main opportunity for increasing cooling resides in producing finer particles (increased surface to volume). However, at constant small particle size, gains can be made in cooling rate if very large relative velocities are maintained between the particle and quenching medium. A high conductivity of the quenching gas also leads to improved rates. The usual solidification theory gives a good picture of the structure in terms of an increasingly small dendrite arm spacing (DAS) with increasing cooling rate over the

range of usual casting (10^{-2} - 10^2 °C/sec) to perhaps 10^4 °C/sec. This analysis leads to an inverse 1/3 power relation between log DAS and the log of cooling rate. Such a relation is well supported by "ripening theory" and has been verified for some alloys at low to modest cooling rates. Above perhaps 10^4 °C/sec the traditional assumptions may be in question particularly with respect to nucleation of either equilibrium or non-equilibrium phases. Such behavior results in much lower microsegregation and other morphological modifications. At still higher rates, interface kinetics are expected to be limiting, giving completely homogeneous microcrystalline or glassy structures.

The Pratt and Whitney Rapidly Solidified Superalloy program was introduced by J. B. Moore who amplified many of the points made by van Reuth, showing the specific parts and target property improvements expected through rapid quenching powder metallurgy (PM). He emphasized the need for success in the several parallel Pratt and Whitney programs for powder handling, consideration to near-final shapes, heat treatment, NDE, and coating technology that will allow full utilization of the anticipated rapid quench properties. In particular, the goal of increasing the turbine blade operating temperature by 100°F over the best current superalloy performance requires coating success as well as better mechanical properties.

The design rationale, description of equipment, and report of the first runs in the Pratt and Whitney rapid quench facility were discussed by A. R. Cox. He pointed out that Pratt

and Whitney has taken into consideration all of the factors for rapid quenching mentioned by Flemings, and in addition they were attempting to maintain a large instantaneous temperature difference between the metal particle and gas stream. The minimum goals for cooling rate, yield, and particle size have already been achieved in the IN100 alloy, but much room for improvement exists in the current equipment and with modifications now in progress. Early difficulties with stream stability, spinning disk skull formation, and the spinning apparatus itself have been overcome such that high speed motion pictures now show reproducible formation of fine particles. The rapid helium-gas quench (about 1/2 of full capacity) resulted in DAS refinement which indicated significant improvements of the cooling rate over ordinary argon-gas atomization at a given particle size. Turbine modifications to lower the particle size should enhance the effect. Using the available DAS-cooling rate correlations, conservative determinations of DAS indicate $6 \cdot 10^5$ °C/sec rates for 40 μ particles.

The structures showed complete suppression of γ prime precipitation and progressively finer carbide precipitates with increased cooling rate; in the most rapid quenches to date, no particles were resolvable at 10,000X. At the higher rates, the usual fine dendritic structure gives way to a uniform (using an electron beam probe) "cellular" structure with some Ti segregation at cell boundaries. This was presumed to be due to yet unresolved fine TiC particles in the boundaries.

N. J. Grant reviewed the range of cooling rates achievable in various particle making methods stressing the need for high yield and uniformity in size (and therefore cooling rate) as well as overall process economy. He emphasized that many interesting materials can be made from non-equiaxed particles. He also detailed a process in which the metal stream is broken up in a shock wave created by modified Hartmann shock tubes arrayed around the stream. Gas velocities of about Mach 2 with pressure variations of ultrasonic frequency form a narrow size distribution powder rapidly quenched. In tin, a 90% yield of 10 μ powder was obtained.

Commercial consolidation to near final shapes was discussed by E. J. Dulis who gave many examples of difficult and large shapes made by hot-isostatic pressing (HIP) both with and without ceramic molds for tool steels, superalloys, and titanium alloys. Limitations in quality (e.g., heavy metal contamination of rotating electrode powders) and cost of current powders as well as the requirements for control in powder processing were discussed.

Since rapid-quench PM can be expected to yield extremely fine structures, considerable thought has been given to means of exploiting this fact both in consolidation (superplastic HIP and/or regular HIP) and in consolidated structures. O. D. Sherby reviewed the requirements for two kinds of behavior, 1) internal stress superplasticity, and 2) fine structure superplasticity. Examples of the former occur while thermally cycling materials

under loading through certain solid phase changes, while the latter can occur when a very fine stable microstructure exists. As a practical guide toward obtaining maximum superplasticity, Sherby stressed the need to produce and maintain in a temperature range of .4-.7 of melting, ultrafine (1-5 μ) structure, preferably multiphased with approximately equal phase strengths, and mobile, strong boundaries. Such structures should yield strain rate coefficients of .4-.6 and would be formable at low strain rates ($\dot{\epsilon} = 10^{-6}$ to 10^{-4} sec $^{-1}$).

The possibilities for getting superplastic behavior in intermetallic or ceramic phases were discussed by A. G. Evans. After pointing out that ordinary silica glasses are superplastic, he expressed some pessimism about many other ceramic systems, even though many would appear to be candidates on the basis of small stable structural size and high strain-rate sensitivity. The basic problem seems to lie in the low grain boundary migration causing tensile stress buildup and fracture. Possibly the most promising systems will be the cermets or intermetallics, especially in those systems that might be quenched fast enough to retain some disorder.

The achievement of rapid cooling rates may be expected to suppress some stable phases and/or lead to new metastable phases. The computer methods now available and under development, which yield phase diagrams calculated from various thermodynamic and physical data, were reviewed and demonstrated by L. Kaufman. This method should prove useful in predicting composition ranges

where liquids are stable at relatively low temperatures (liquidus troughs) and also were potentially unwanted brittle phases, e.g., sigma, could be suppressed, allowing the extension of alloying ranges by rapid quenching.

Many ideas for application of rapidly solidified structures were introduced by R. E. Maringer. He reviewed the differences in the several processes for making continuous ribbons by melt spinning or melt extraction. Several applications (e.g., reinforcing of concrete) for elongated particles including some "dog bone" shapes are under development.

Participants were given an opportunity to make short presentations on any subjects bearing on rapid solidification technology or powder processing. These were aimed at forming a basis for the subsequent discussion session. R. Mehrabian gave evidence based on microsegregation in a maraging steel for significant melt undercooling at cooling rates as low as $\sim 10^2$ °C/sec. Controlled laser skin melting as a means for studying solidified structures under well calculable conditions in the range 10^5 - 10^8 °C/sec was discussed by B. Kear. Epitaxial layers on superalloys with very fine cellular structure and suppressed carbide precipitation were shown. M. Cohen discussed the potential for making steels (9Ni-4Co-0.4C) with exceptional combinations of strength and toughness by small particle processing. An ultra-fine structure inherited from this type of processing would exploit TRIP steels for improved toughness. R. A. Huggins described chemical and physical means other than rapid solidifi-

cation for achieving materials of exceptional homogeneity. R. L. Coble discussed condensation from chemical and plasma as systems for making ultrafine particles. Progress in making PM shapes with improved ductility from Ti_3Al and $TiAl$ was outlined by H. Lipsitt. A. Adair presented evidence in PM aluminum alloys for simultaneous improvement in strength, corrosion, and fatigue-crack propagation properties. E. E. Hucke and G. H. Vineyard presented a potential method for using nearly adiabatic cooling from shocked states in macroscopic samples to observe effects of measurable high cooling rates (10^8 - 10^{10} °C/sec) on solidified structures. Possible applications of rapid-quench PM to electrical and magnetic alloys and to Cu-Ni-Sn spinodal alloys was presented by G. Y. Chin. J. H. Wernick discussed possibilities in rare earth-cobalt magnetic materials as well as in superconductor and advanced hydrogen storage materials. P. Duwez speculated about the possibilities of consolidating true glassy powders and maintaining this state. H. Reiss presented a thermodynamic argument which cautions against some of the calculations of phase stability in unstable regions. F. A. McClintock discussed the possibilities of using very fine-grained structures, and even graded structures, for improved fatigue crack propagation resistance. The exploitation of much finer-grained PM materials, together with high frequency sonic NDE methods for improving the crack detection limit, was discussed by G. S. Kino.

In the final session of the program many of the foregoing ideas were given further group discussion. Some of the highlights

are listed in a subsequent section. Suggested new alloys with promise for small particle alloy development are listed, and several technical notes by Council members are also included.

ADVANCED POWDER-MAKING PROCESSES
- FUNDAMENTALS OF DROPLET FORMATION -

Alan Lawley

Over the past decade powder metallurgy (P/M) has emerged as a viable and competitive processing route. To the conventional semi-dense press and sinter part is now added fully-dense material suitable for use in load-bearing applications. This advance in P/M technology has been the result of basic and applied research primarily in the areas of powder production and subsequent consolidation. Thus, new lower cost higher quality powders are now available. Coupled with consolidation processes such as preform working and hot isostatic pressing, these have served as the stimulus for expanding market potential in both commercial and military applications.

This paper provides an overview of the area of powder making; it is restricted to metal powders and considers only atomization techniques. To enhance coherency, the methods examined are grouped into four categories: gas atomization, water atomization; centrifugal atomization; mechanical atomization. Along with the general features and details of each technique, associated relationships between atomization processing parameters and primary powder properties/characteristics will be considered.

The prediction and control of powder properties in atomization has been largely empirical. However, recent experimental

and analytic work on gas and water atomization has provided a much more detailed insight into the actual mechanism(s) of drop-let formation. This work is reviewed since it provides the basis for optimal design of the atomization process (e.g., selection of operation parameters) vis a vis the resultant powder in the future. Similarly, it will be shown that two of the techniques considered under the category mechanical atomization (viz. roller atomization and the melt drop technique) are amenable to modeling of the break up of the liquid.

It should be pointed out that the atomization techniques considered in this paper pertain to current commercial practice, pilot-scale operation and laboratory-scale exploration. As the last ten years have shown, metal powder atomization is a dynamic technology - the laboratory curiosities of today may well constitute industrial practice in as little as five years from now.

POWDER MAKING PROCESSES

Gas Atomization

Gas atomization is often termed two-fluid atomization and involves the production of liquid metal drops by the disintegration of a stream of metals with a subsonic or supersonic jet of gas. Atomization is produced by the kinetic energy of the atomizing medium, typically nitrogen, argon, or air. Usually two or more jets, or an annular ring are used, positioned around the axis of the metal stream. The axes of the gas jets are equally inclined to the metal stream axis and intersect this axis at the

geometrical impingement point. A representative configuration is shown in Figure 1. Detailed reviews of gas atomization have been published by Lubanska¹, Dixon², Klar and Shafer³ and Rao⁴.

The overall process of gas atomization is governed by several interrelated operating parameters. Controllable variables include: jet distance, jet pressure, nozzle geometry, velocity of gas and metal, metal superheat. In consequence, interpretation of experimental data is difficult. Several expressions have been proposed that relate particle size to atomization conditions. These do not provide quantitative insight into the mechanism(s) of droplet formation; examples are given in Appendix I.

In general it can be concluded that gas atomized powders tend to be smooth and spherical. Higher pressures and smaller jet distances produce finer powder^{4,5}. A power law relationship exists between mean particle size and gas pressure. Increasing the mass flow rate of the gas decreases the mass median particle diameter⁶.

Inert gas atomization is currently in use for the production of superalloy and other reactive metal powders. It suffers from a very low overall efficiency (~3%) and is expensive if inert gases other than nitrogen have to be used. A typical size distribution for superalloy powder is illustrated in Figure 2; mean particle diameter is ~150 μ m. Yields ~80% are obtained for -35 mesh powder⁹.

Water Atomization

Gas atomization is characterized by a continuous stream of fluid (gas) in contact with the metal stream. In contrast, in water atomization, a high pressure water stream is forced through nozzles to form a dispersed phase of droplets which impact the metal stream. The arrangement and type of fluid jets provides for an unlimited number of atomization geometries; Figure 3 will serve to illustrate water atomization. Water atomization has been reviewed by Watkinson¹⁰, Vorsa¹¹, Tamura and Takeda¹², Small and Bruce⁵, Grandzol¹³ and Gummeson¹⁴.

Water atomization requires large quantities of energy to supply the water at high pressures. It is estimated that the overall process efficiency is $\leq 4\%$. This notwithstanding, the method has had significant economic and technical impact in the production of low and high-alloy steels, including stainless. Water atomization is not likely to be used in the atomization of highly reactive metals such as titanium and the superalloys.

In general, water atomized powders are irregular in shape with rough oxidized surfaces. From the several experimental studies of gas atomization it is concluded that finer particle sizes are favored by:

- low metal viscosity
- low metal surface tension
- superheat
- low metal flow rate
- high atomizing pressure
- high water flow rate
- short metal stream
- short jet length

Particles less irregular in shape (i.e., more spherical) are favored by:

- a narrow melting range
- high metal superheat
- large apex angles

Some experimentally determined relationships between particle size and atomizing conditions are given in Appendix II.

Centrifugal Atomization

In centrifugal atomization, molten metal is ejected from a rapidly spinning container (e.g., dish, crucible, plate). Under the action of centrifugal force the melt moves up the walls of the container to the lip where it is ejected in the form of droplets.

Until recently, interest in this approach was limited to low melting point metals and alloys. Erosion, dissolution, oxidation and creep of the spinner material presented severe problems. With the advent of improved ceramics and advances in inert gas electrode melting, it became attractive to consider this mode of atomization for titanium alloy and nickel-base superalloys.

Details of a variety of centrifugal atomization units are given in Table I. Atomization configurations are illustrated schematically in Figure 4. The technique has the distinct advantage that energy requirements are very low. Particle shape can be varied from spherical to flake but usually the average particle size is large, $\geq 200\mu\text{m}$.

The rotating electrode process (REP) is a form of centrifugal atomization^{9,22}. A rod of the material to be atomized is rotated rapidly while being melted at one end by an electric arc. Molten metal spins off the bar and solidifies before hitting the walls of the inert gas filled outer container, Figure 5. The process was developed primarily for the atomization of high purity low oxygen content titanium alloys and superalloys. Powder particles are smooth and spherical with an average diameter $\sim 200\mu\text{m}$; the size range is $\sim 50\text{-}400\mu\text{m}$, Figure 6. Typically, yields run $\sim 75\%$ -35 mesh powder.

Tungsten contamination from the stationary electrode is a current limitation of REP powders. Two modifications are being evaluated to avoid the problem: replacement of the stationary tungsten cathode with titanium; rotation of the titanium cathode and titanium anode²².

The Durarc[®] process is a recent and novel form of centrifugal atomization²³. Key to the process is a water cooled electrode containing a cylindrical field coil at its tip. The coil generates a magnetic field having a large flux component parallel to the surface, Figure 7. On striking an arc between the tip and metal charge (contained in a water-cooled copper skull), the direction of the arc is towards the melt. With the flux field parallel to the tip surface, it is perpendicular to the arc current. Interaction between the magnetic field and the current in the arc causes the latter to rotate over the tip. Having established a molten pool, the arc is made to rotate

rotate rapidly. Electromagnetic forces also exist in the melt at the point of arc attachment and cause ejection of metal from the pool as droplets.

This method of powder fabrication has been utilized in the atomization of titanium alloys. The resulting powders are spherical. Advantages include: no limitation on the form of the starting material, a low production cost and a capability for producing high-quality powder from scrap or defective material. Clearly the absence of mechanically rotating components and/or seals is a further attraction. The complete operation is carried out in vacuum or an inert gas atmosphere.

Mechanical Atomization

Atomization techniques in this category do not involve rotation and/or impact of the melt by gas or water. Beyond this, there is no particular commonality.

Roller atomization

This novel process produces metal powder by atomization of a stream of molten metal that is fed between rapidly rotating (up to 12000 rpm) rolls²⁴. A schematic is given in Figure 8. Typically, the roll gap is $\sim 50\mu\text{m}$ and it is important that heat transfer to the roller surface be minimized. The effect of various process parameters (e.g., roll speed, flow rate and relative roller speed) has been examined for the atomization of copper, tin and lead.

For tin, a median particle size of $220\mu\text{m}$ was obtained with powder yields $\sim 70\%$. Median particle size was found to be

inversely proportional to rotational speed and to decrease with stream velocity. The method is capable of converting a wide range of metals into flake, acicular, irregular or spherical particles.

Vibrating Electrode

Unlike previous ultrasonic devices, this approach produces high-purity metal powders by the vibration of a consumable electrode²⁵. The electrode, forming a resonant rod with a fixed and free end, is continuously moved between rollers toward a slowly rotating copper disc, Figure 9. Atomization takes place in the arc struck between the water cooled disc and the vibrating end of the electrode. Spherical particles are formed; size and size distribution can be controlled by changing the length of the resonant rod.

Atomization results have been obtained for mild steel, a CrNi steel and cupronickel. The narrowest particle size distribution is obtained at the resonant frequency of the electrode. At a given frequency of oscillation, the mean particle diameter and particle size range decrease with decreasing wire diameter. It is interesting to note that tungsten could be atomized when the arc was struck under water. The powder was spherical and had a low oxygen content ($<0.1\%$).

Melt Drop Technique

In this method liquid metal flows through the nozzle at the bottom of a crucible²⁶. The metal stream expends into a vacuum or inert gas chamber as spherical particles. For small

diameter nozzles, a back up pressure of hydrogen is used over the melt, Figure 10.

The most important parameters in controlling particle size are nozzle diameter, melt stream velocity, specific gravity and surface tension of the liquid. Under normal conditions of droplet formation a wide particle size distribution is obtained. Imposing vibrations in the form of longitudinal oscillations (50-1000 Hz) to the melt resulted in narrow size distributions. The absolute particle size also decreased with increasing frequency of oscillation. In this mode, droplet size can be precisely controlled. To date the melt-drop technique has been applied to lead, Beryllium and astroloy.

Ultrasonic Atomization

This is the so-called Swedish Kohlswa process. High intensity pulses of gas at a characteristic frequency in the range 60,000 to 120,000 cps impinge on the liquid metal stream¹⁸. There is no contact between the ultrasonic die (generator) and the liquid metal. The multiple ducts that deliver the energy pulses to the metal stream function as Hartman shock wave tubes. Powders produced by ultrasonic atomization are spherical, exhibit a very narrow size range, and have a small mean diameter. As an example, average particle sizes $\sim 4\mu\text{m}$ and $10\mu\text{m}$ have been reported in 18-8 stainless steel and tin respectively.

Vacuum Atomization

This process is shown schematically in Figure 11. It is based on the principle that when a molten metal supersaturated

with gas under pressure (e.g., hydrogen) is suddenly exposed to vacuum, the gas expands and causes atomization of the metal^{9,27}. Clean high-purity spherical powders are formed. Alloy powders based on Ni, Co, Fe, Cu, and Al have been made successfully. A typical size distribution for superalloy powder is illustrated in Figure 2.

ATOMIZATION MECHANISMS

In terms of droplet formation, the geometries utilized in gas or water atomization are not amenable to simple modeling or analysis. However, from recent detailed experimental observations of each process it has been possible to delineate plausible mechanisms. Geometry and boundary conditions in roller atomization and the melt-drop technique are less complex; reasonable mechanisms describing the break up of the liquid metal have been proposed for each.

Gas atomization

Johnston and See²⁸ have recently made a detailed review of investigations describing the stability of bulk liquid and liquid drops moving at a relative velocity to a gas stream. While geometric conditions vary widely, the proposed mechanisms of disintegration always involve the initiation of a sinuous wave which rapidly increases in amplitude. These waves are detached from the bulk of the liquid producing ligaments whose dimensions depend on the wavelength at disintegration. It is not surprising to find diverse physical models for the actual process of droplet formation from such waves²⁹⁻³⁵. Stability

criteria all involve the Weber number of the liquid metal. Dombrowski and Johns³⁰ are credited with the first attempt to develop a physical model for the disintegration of a liquid sheet. The sequence of events is illustrated in Figure 12.

Bradley³⁶ has recently developed a mathematical model for gas atomization of liquids which predicts drop size in both the subsonic and sonic gas velocity ranges. The mechanism invoked is similar to that proposed by Castleman²⁹. In common with Dombrowski and Johns³⁰, the analysis is based on sound theoretical principles.

Detailed experimental studies of gas atomization* by Rao⁴ and Johnston and See^{6,28} have confirmed that the liquid metal stream breakup does involve the formation of ligaments; in turn, these break up into nearly spherical particles. Johnston and See^{6,28} propose a three step mechanism: primary disintegration or initiation; secondary disintegration; solidification. The three stages are shown schematically in Figure 13. Thus, lateral spreading of the metal stream occurs prior to disintegration. The point at which spreading occurs depends on the velocity distribution in the gas. The metal droplets are then formed from the periphery of a metal cone by a ligament-forming process. Application of the Dombrowski and Johns model³⁰ to experimental data for gas atomized lead gave reasonable agreement³⁷ - sufficient to warrant a more detailed analysis of fluid flow.

*In total, the experimental work involved high speed and Schlieren photography, a quantitative determination of velocity distribution in the gas and a complete characterization of metal flow conditions.

Water Atomization

Up to 1973 no mechanisms had been proposed for the atomization of liquid metals by water jets. Intuitively it might be expected that ligament-formation mechanisms similar to those confirmed in gas atomization would be operative.

From a detailed study of the water atomization of 4620 steel, Grandzol¹³ concluded that there was no evidence for the existence of ligaments as an intermediate step in particle formation. A simple functional relationship existed between measured metal particle median diameter and water droplet velocity, namely:

$$d_m = A/V_w$$

It is also possible to derive this relationship from a simple two-liquid atomization model based on conservation of momentum^{13,16}. In essence, Grandzol and Tallmadge proposed that metal droplets are formed as a result of the impact of the water droplets on the surface of the metal. From subsequent experimental observations it was further concluded that the normal velocity component of the water was the dominant factor¹⁷ in controlling particle diameter, i.e.,:

$$d_m = \frac{A}{V_w \sin \alpha}$$

where α is the angle between metal stream axis and water jet axis. This further reinforces the credibility of an impact rather than shear mechanism for water atomization. Conceptual descriptions of two mechanisms are given in Figures 14 and 15;

these are termed "splash" and "scrape", respectively. There are inherently fewer restrictions on the scrape than on the splash mechanism.

Roller Atomization

From photographic evidence of the metal emerging from the rollers, it is proposed that the mechanism of atomization is similar to that known as cavitation in oil lubricated bearings²⁴. Thus, the liquid metal cavitates a small distance downstream from the roll nip; this produces perforations and streamers. At high roller speeds the liquid is believed to flow around the points of cavitation and so form thin threads of liquid metal. The liquid threads or streamers subsequently break up due to propagation of liquid jet instabilities.

Mathematical modeling is in progress aimed at elucidating the fundamentals of primary break up of the liquid by cavitation, and the secondary break up and coalescence of liquid streamers and perforations. Analysis requires a solution to the Reynolds equation of lubrication theory and establishment of the cavitation boundary conditions.

Melt-Drop Atomization

For this mode of atomization, the theory of droplet formation is well-established³⁸. The stream of molten metal leaving the crucible is analogous to a jet formed from a capillary tube. The jet disrupts into a series of small droplets because of dynamic instability under the action of surface tension. Thus, if a capillary wave is applied to the jet,

disintegration occurs. The process can be described precisely in terms of Reynolds number and Weber number. Droplet size is directly related to metal velocity, jet diameter and frequency of vibration of the crucible.

REFERENCES

1. H. Lubanska, J. of Metals 22, 45(1970).
2. C. F. Dixon, Canadian Met. Quarterly 12, 809(1973).
3. E. Klar and W. M. Shafer, "Powder Metallurgy for High Performance Applications," eds. J. J. Burke and V. Weiss, Syracuse University Press, p. 57, 1972.
4. P. Rao, "Shape and Other Properties of Gas Atomized Powders," Ph.D. Thesis, Department of Chemical Engineering, Drexel University, Philadelphia, Pa., 1973.
5. S. Small and T. J. Bruce, International J. of Powder Met. 4, 7(1968).
6. G. H. Johnston and J. B. See, "Formation of Liquid Metal Droplets," paper presented at Symposium on Process Engineering of Pyrometallurgy, Imperial College, London, April 1974.
7. K. Y. Kim and W. R. Marshall, AIChE J. 17(3), 575(1971).
8. O. S. Nichiporenko, Soviet Powder Metallurgy and Metal Ceramics 60(112), 947(1967).
9. L. P. Clark, Advanced Manufacturing Methods and Their Economic Implications: Some pilot Papers on Powder Metallurgy and Joining, AGARD Reprot \$627, March 1975.
10. J. F. Watkinson, Powder Metallurgy 1(2), 13(1958).
11. O. Vorsa, Pokroky Praskove Metalurgie 1(1), 47 (Brutcher translation #6572) (1963).
12. K. Tamura and T. Takeda, Trans. Nat. Res. Inst. Metals 5(5), 252(1963).
13. R. J. Grandzol, "Water Atomization of 4620 Steel and Other Metals," Ph.D. Thesis, Department of Chemical Engineering, Drexel University, Philadelphia, Pa., June 1973.
14. P. U. Gummeson, p. 27, reference 3.
15. H. Kishidaka, Proc. Multidisciplinary Meeting on Sintered Metals and Magnetic Materials, Japon Soc. Powder and Powder Metallurgy, February 1972.
16. R. J. Grandzol and J. A. Tallmadge, AIChE. Journal 19(6), 1149(1973).

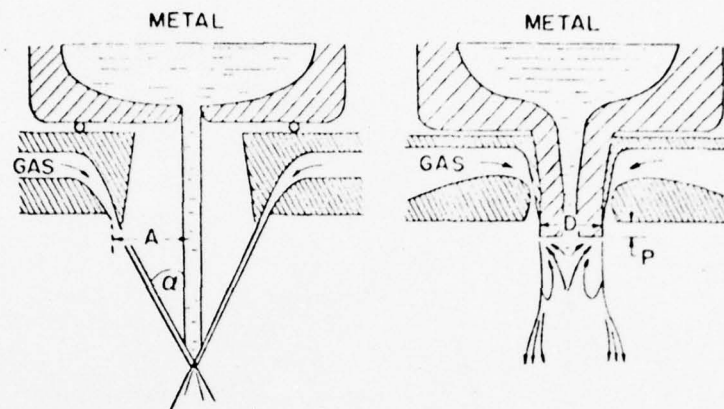
17. R. J. Grandzol and J. A. Tallmadge, Int. J. of Powder Metallurgy and Powder Technology 11(1), 103(1975).
18. N. Grant, p. 85 of reference 3.
19. H. Stephan, 42nd Meeting of the Structures and Materials Panel (AGARD) Advanced Fabrication Techniques in Powder Metallurgy and their Economic Implications, Ottawa, Canada, April 1976.
20. P. W. Sutcliffe and P. H. Morton, *ibid.* reference 19.
21. J. Decours, J. Devillard and G. Sainfort, *ibid.* ref. 19.
22. G. Friedman, *ibid.* ref. 19.
23. The Evaluation of Ti-6Al-6V-2Sn Pre-Alloyed Powder Processing, Westinghouse Electric Corporation, Technical Report AFML TR-76-65, July 1975.
24. A. R. E. Singer and A. D. Roche, Int. Powder Metallurgy Conference (P/M '76), MPIF Chicago, Illinois, June-July 1976.
25. G. Matei, E. Bucsak, W. Huppmann and N. Claussen, *ibid.* ref. 23.
26. F. Aldinger, E. Link, G. Petzow and N. Claussen, *ibid.* ref. 23.
27. J. M. Wentzell, see ref. 19.
28. G. H. Johnston and J. B. See, unpublished work, MIT, 1974.
29. R. A. Castleman, Phys. Rev. 35, 1014(1930).
30. N. Dombrowski and W. R. Johns, Chem. Eng. Sci. 18, 203(1963).
31. H. B. Squire, Brit. J. Appl. Phys. 4, 167(1953).
32. J. L. York, H. E. Stubbs and M. R. Tek, Trans. ASME, 1279 (1953).
33. W. W. Hagerty and J. F. Shea, J. Appl. Mech., 510(1955).
34. R. P. Fraser, N. Dombrowski and P. Eisenklam, Nature 4402, 945(1954).
35. R. P. Fraser, P. Eisenklam, N. Dombrowski and D. Hasson, AIChE Journal 8(5), 672(1962).

36. D. Bradley, J. Phys. D.: Appl. Phys. 6, 1724 and 2267(1973).
37. J. B. See, J. C. Runkle and T. B. King, Met. Trans. 4, 2669 (1973).
38. N. R. Lindblad and J. M. Schneider, J. Sci. Inst. 42, 635 (1965).

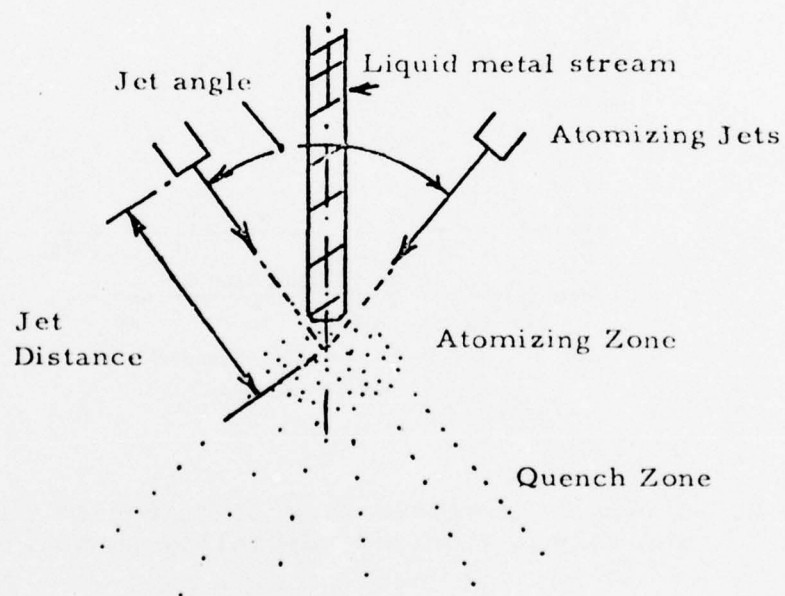
TABLE I

Centrifugal Atomization

| <u>Material</u> | <u>Facility</u> | <u>Powder</u> | <u>Reference</u> |
|-----------------|--|---|------------------|
| Al 2024 | rotating perforated steel drum spinner (3000 rpm) | acicular/tear drops ~1520 m x 5000µm; 95% yield | 18 |
| Ti, Ni-base | Combination vertical drip- melt with rotating disc. Electron beam - consumable electrode. Disc: 4000 - 14,000 rpm. Electrode: 10 - 40 rpm. Goal: 150 kg/hr melting. | Spherical 50-600µm dia. flake 20 - 400 mesh mix of flake and spheres high purity | 19 |
| Ti Alloys | Shot casting process rotating water-cooled crucible (3000-4000 rpm); arc melt in helium, argon (<1 atm) or vacuum 60mm dia. consumable electrode crucible dia. 75mm | Spherical 150-1000µm high purity | 20 |
| Ti Alloys | electron bombardment of rotating charge (4000 rpm) 30 kg/hr melting 50mm dia. electrode vacuum 10^{-4} torr | Spherical 100-1000µm | 21 |



(a)



(b)

Figure 1. Possible two-fluid atomization configurations.
(a) Ref. 3; (b) Ref. 4.

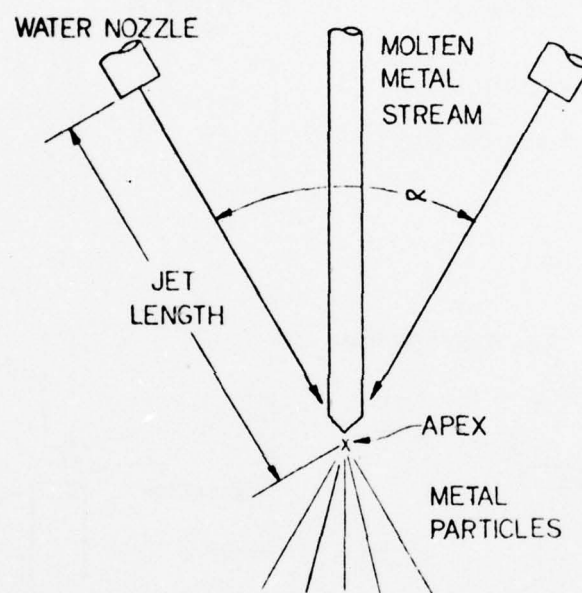


Figure 3. Water atomization, ref. 13.

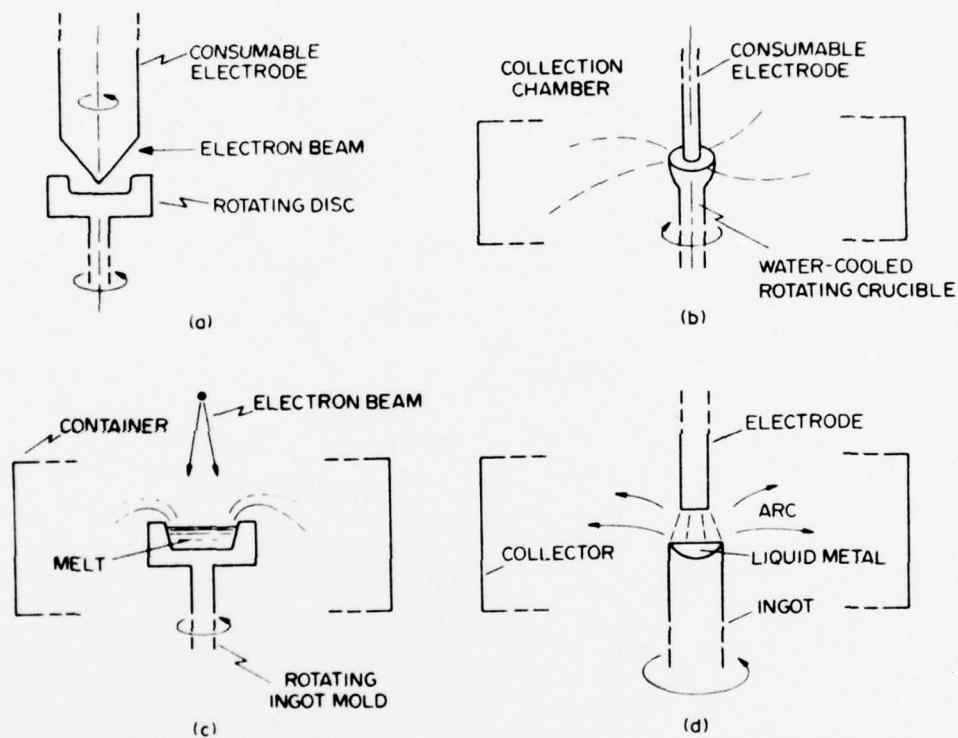


Figure 4. Centrifugal atomization configurations. (a) Ref. 19; (b) Ref. 20; (c) Ref. 21; (d) Rotating dish arrangement.

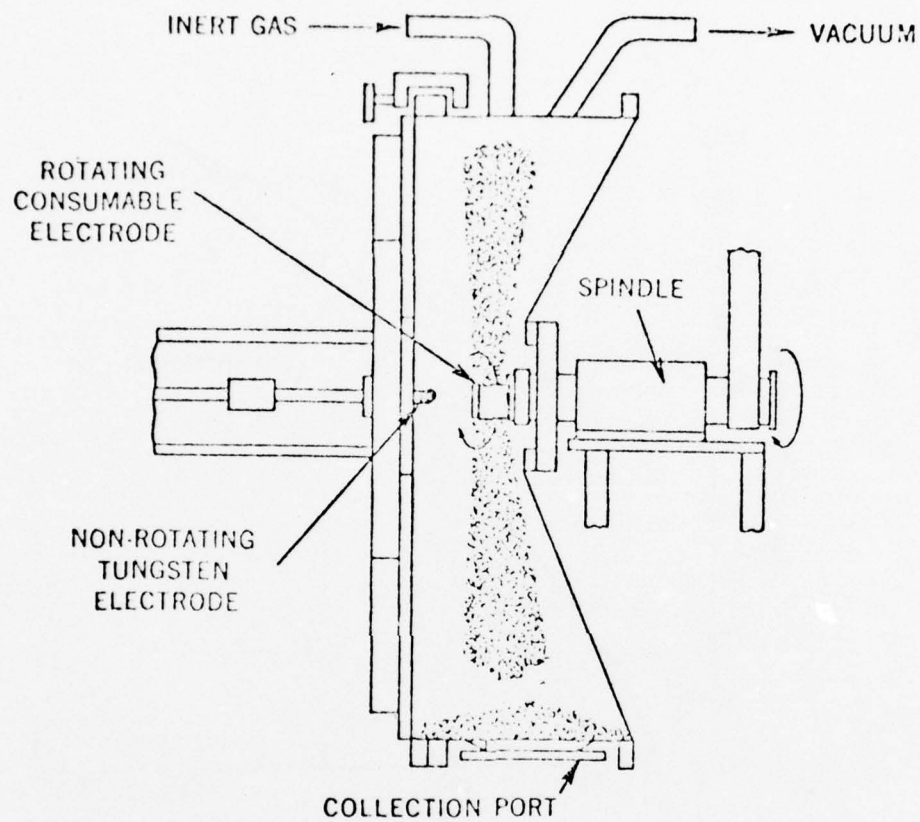
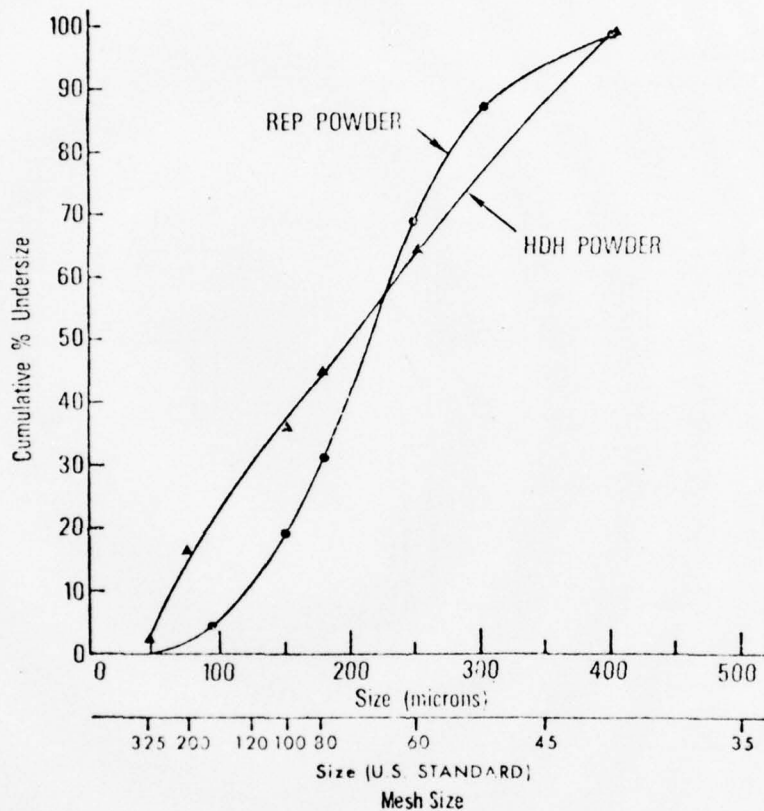


Figure 5. The rotating electrode process, Ref. 22.



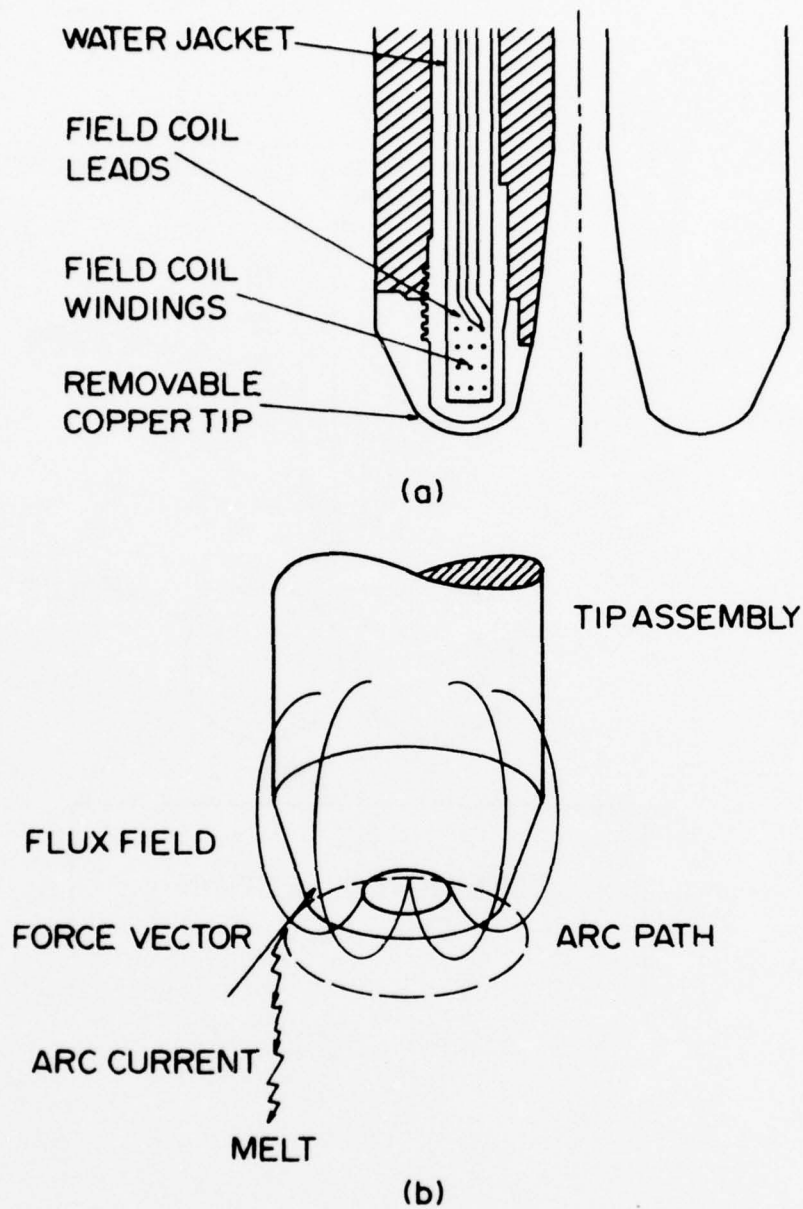


Figure 7. (a) The Durarc[®] electrode tip configuration; (b) Arc rotation in the Durarc[®] process, Ref. 23.

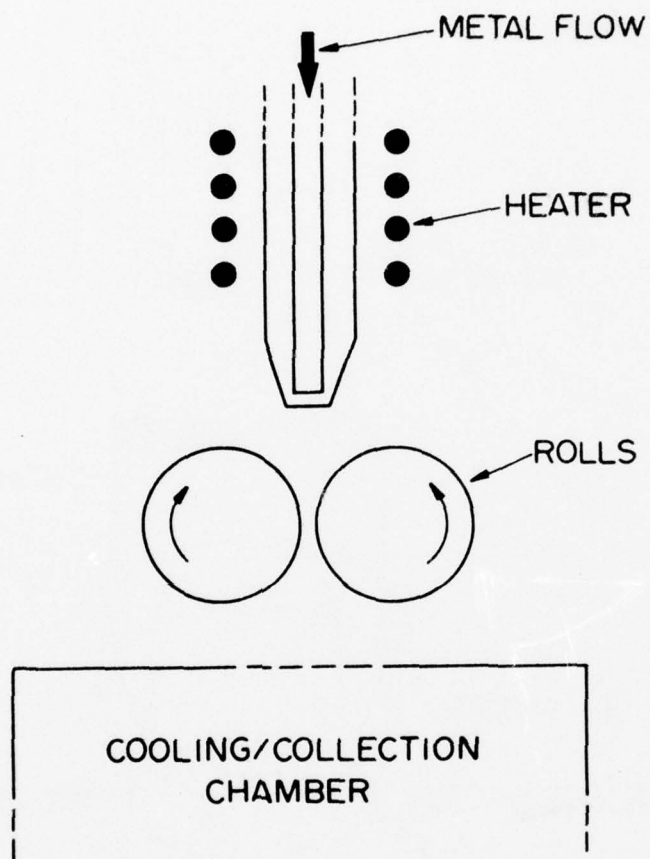


Figure 8. Roller atomization, Ref. 24.

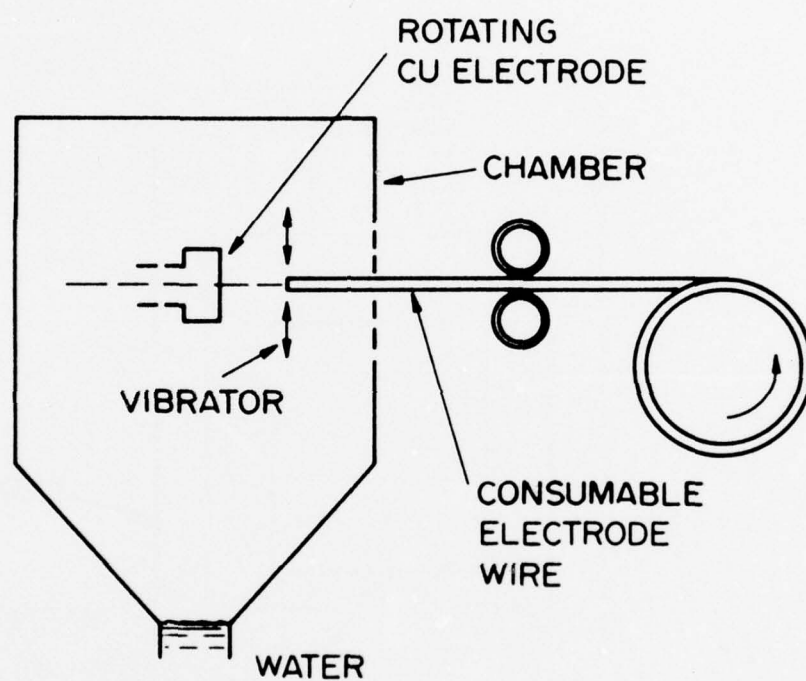


Figure 9. Vibrating electrode atomization, Ref. 25.

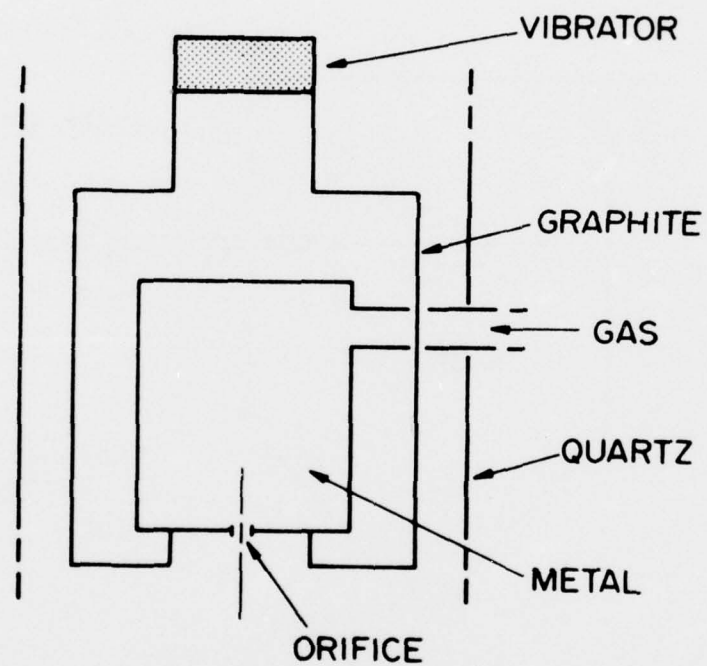


Figure 10. Atomization by the melt-drop technique, Ref. 26.

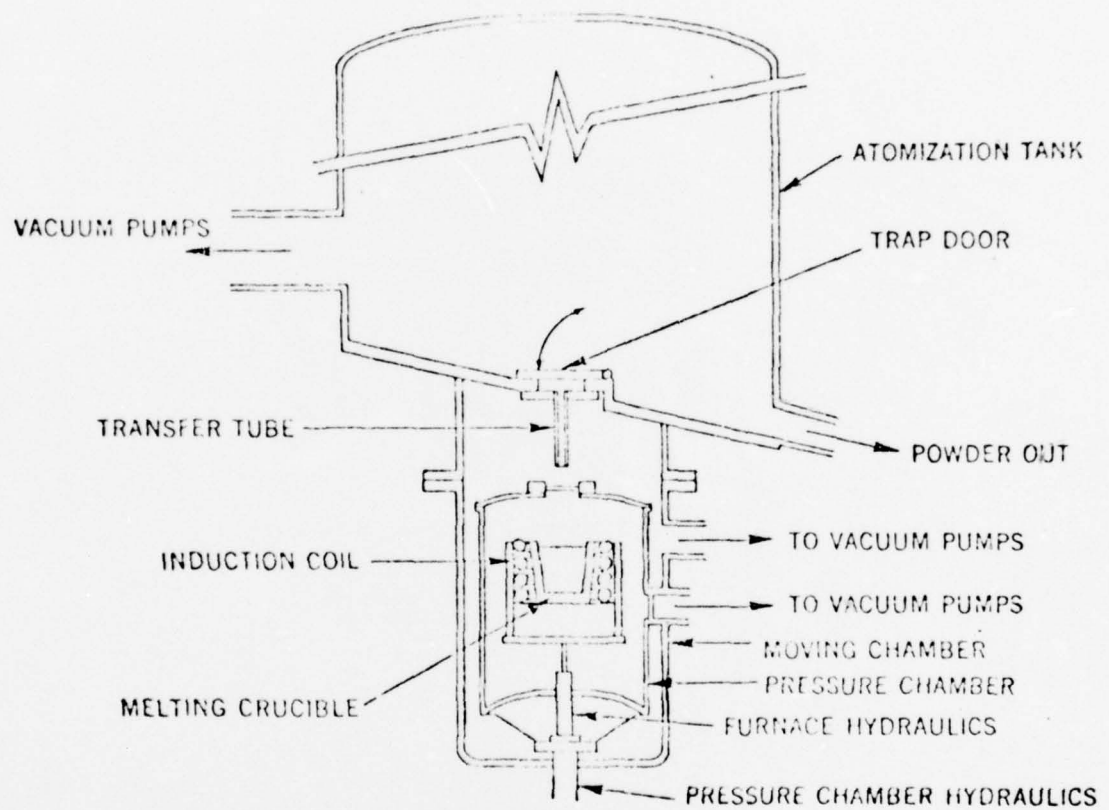


Figure 11. The vacuum atomization process, Ref. 27.

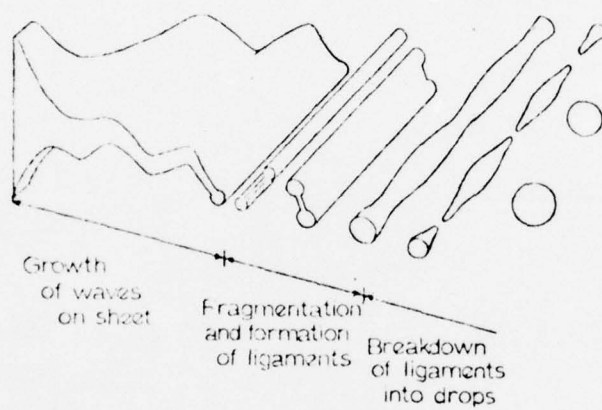


Figure 12. Model for the disintegration of a liquid sheet, Ref. 30.

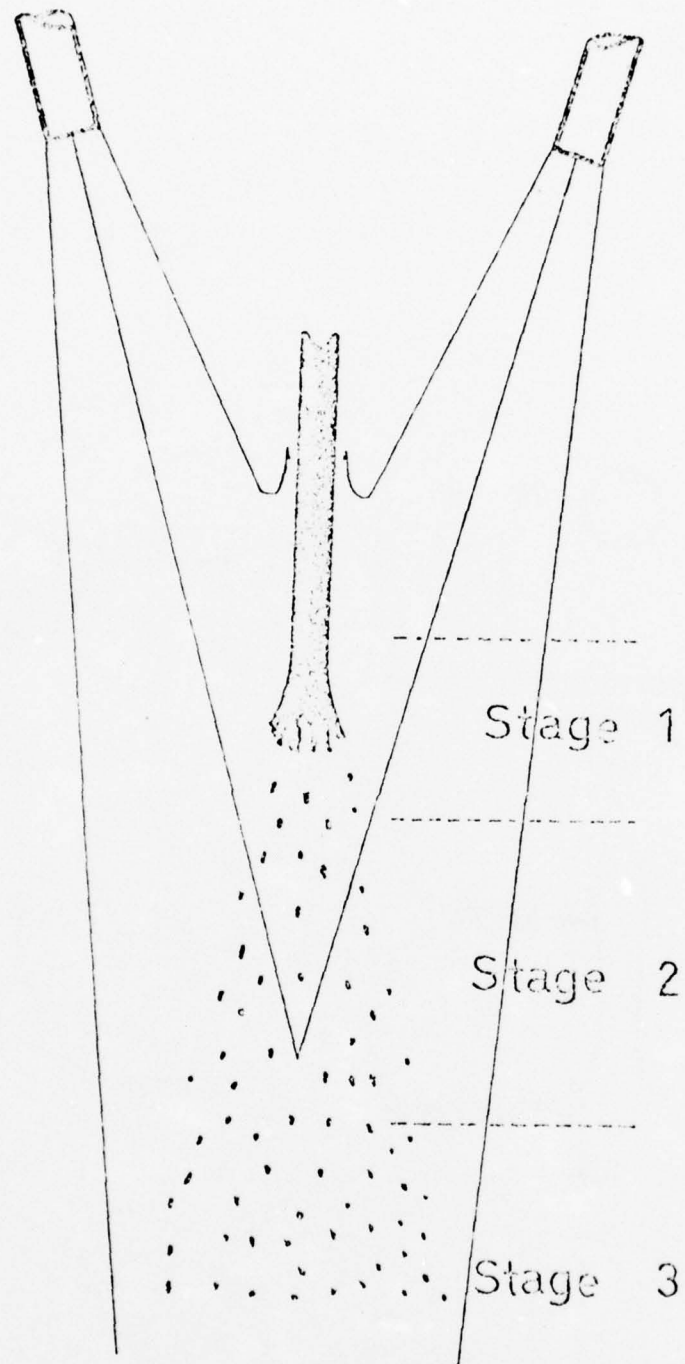


Figure 13. Schematic representation of the three stages of disintegration, Ref. 28.

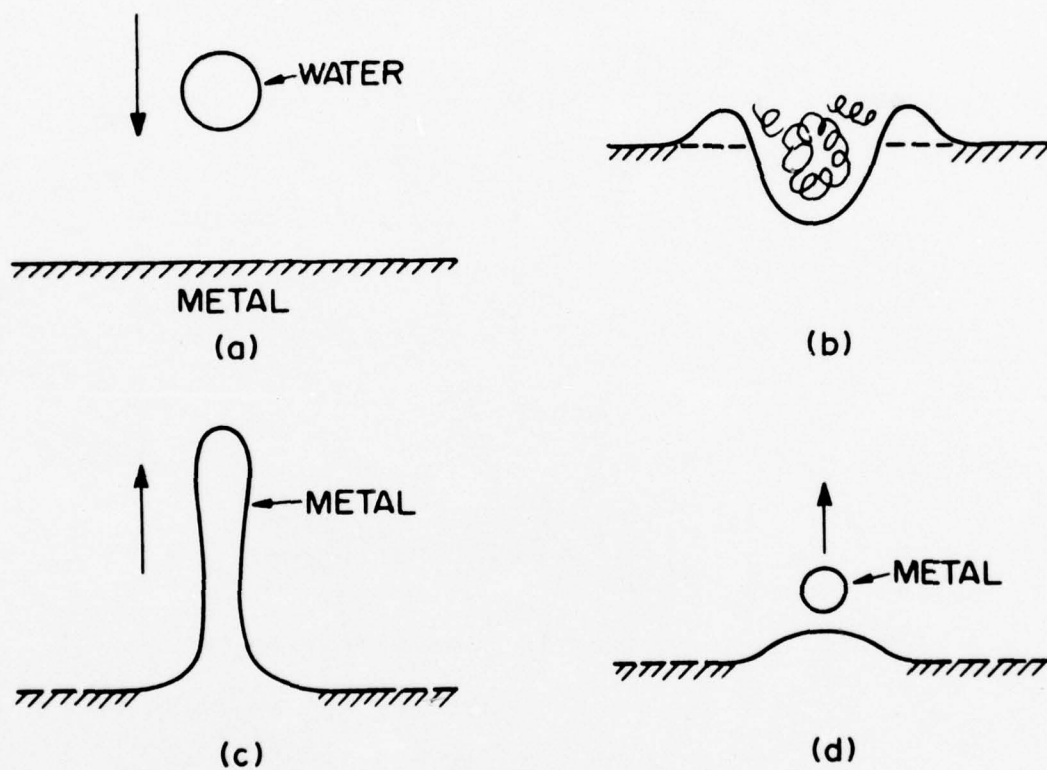


Figure 14. Splash mechanism of drop formation. Sequence is (a), (b), (c), (d), Ref. 13.

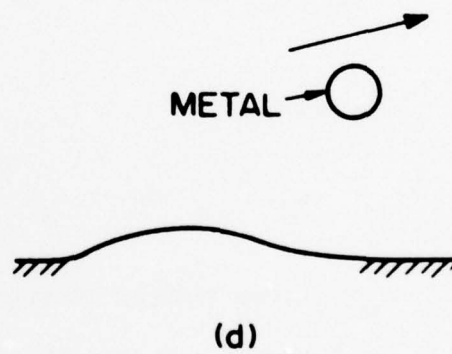
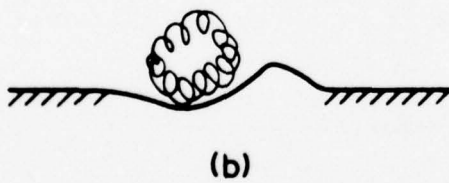
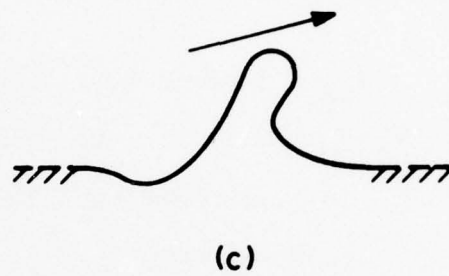
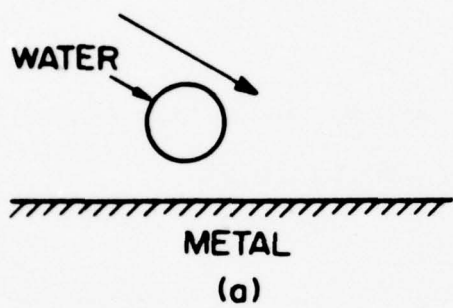


Figure 15. Scrape mechanism of drop formation. Sequence is (a), (b), (c), (d), Ref. 13.

APPENDIX I

The Size of Gas Atomized Powders - Empirical Relations

1. Kim and Marshall⁷:

$$d_{vs} = \frac{585}{V_g - V_m} \sqrt{\frac{\sigma}{\rho}} + 597 \left(\frac{\mu}{\sqrt{\rho \sigma}} \right)^{0.45} (1000 V_{ma})^{1.5}$$

d_{vs} = Sauter mean diameter or volume to surface mean diameter

$V_g - V_m$ = relative velocity of the gas to liquid

σ = surface tension

ρ = density

V_{ma} = volumetric ratio of liquid to gas flow rates

2. Lubanska¹:

$$d_m = d_t K \left[\frac{v_m}{v_g We} \left(1 + \frac{M}{A} \right) \right]^{0.5}$$

d_m = mass median diameter of powder

d_t = metal stream diameter

v_m = kinematic liquid metal viscosity

v_g = kinematic gas viscosity

We = Weber number

M/A = mass flow ratio of metal to gas

K = constant in range 40 to 50

3. Nichiporenko⁸:

$$d_{pr} = d_m (0.136 \cdot 10^{-5} Re_1 + 0.294)$$

$$182,000 < Re_1 < 238,000 \text{ at } We = 7.95$$

d_{pr} = diameter of predominant fraction of the powder

d_m = mean size of powder

Re = gas jet Reynolds number

We = metal stream Weber number

4. Small and Bruce⁵:

$$d_m = \ln \left(\frac{P}{C} \right)^n$$

d_m = mean particle diameter

P = atomization pressure

C, n are constants

APPENDIX II

The Size of Water Atomized Powders - Empirical Relations

1. Small and Bruce⁵:

$$d_m = \ln \left(\frac{P}{C} \right)^n$$

d_m = mean particle diameter

P = atomization pressure

C, n are constants

2. Kishidaka¹⁵:

$$d_m = KD \left(\frac{D \rho_L V_W}{\mu_m} \right)^{-0.57} \left(\frac{D \rho_L V_W^2}{\gamma_L} \right)^{-0.22} \left(\frac{W_m}{W_W} \right)^{-0.043}$$

d_m = mean particle diameter

K = constant

D = diameter of tundish

ρ_L = liquid metal density

V_W = water jet velocity

μ_m = liquid metal viscosity

γ_L = surface tension of liquid metal

W_m = metal flow rate

W_W = water flow rate

3. Grandzol and Tallmadge¹⁶:

$$d_m = A/V_W$$

d_m = metal particle median diameter

A = constant

V_W = water droplet velocity

4. Grandzol and Tallmadge¹⁷:

$$d_m = \frac{C}{V_W \sin \alpha}$$

d_m = metal particle median diameter

C = constant

V_W = water droplet velocity

α = angle between metal stream axis and water nozzle axis; two-jet system

THEORY OF DENDRITE SOLIDIFICATION
DURING VERY RAPID COOLING

M. C. Flemings

AIMS

The aim of small particle technologies discussed at the meeting is to achieve more homogeneous metals with finer structure. To achieve this all processes aim to:

1. achieve small liquid droplets, and
2. obtain a high heat transfer coefficient at the surface of the metal particle.

In addition, practical technologies must accomplish the foregoing economically in significant quantities, without contamination, and must produce the desired particle shape.

ATOMIZATION

Droplet formation has been discussed in the previous talk (Lawley). Many different methods are available, including those that form droplets by (a) achieving a high relative velocity between a liquid metal body and a gas phase, (b) mechanical means, (c) ultrasonics. Various analyses of droplet formation in liquids has been presented in the previous talk. For the most part, these are empirical and not well documented by data on liquid metals. However, these data do suggest that high velocity gases (or fast centrifuging) can break up coarse

globules or streams of metal into fine droplets ($<50\mu\text{m}$).

Figure 1 shows results of sample calculations for a Sn-10% Pb alloy atomized with helium, using the analyses of Kim and Marshall referred to by Lawley. Note for example that at 500 mph (a readily achievable gas speed), a particle size of $25\mu\text{m}$ is obtained. Thus, it appears that processes that achieve high relative velocity between liquid metal and a gas stream can achieve small ($<50\mu\text{m}$) liquid droplets.

HEAT FLOW

Cooling rate of metal particles is limited primarily by resistance to heat flow at the particle surface, as discussed further below. All processes for rapid solidification aim to achieve a maximum heat transfer coefficient, h . In gas atomization this is done by using gases of high conductivity moving at high velocity relative to the particle. The relevant heat transfer correlation is:

$$\frac{hD_o}{k_f} = 2.0 + 0.60 \left(\frac{D_o V' \rho_f}{\mu_f} \right)^{\frac{1}{2}} (P_r)^{\frac{1}{3}} \quad (1)$$

where h = heat transfer coefficient
 D_o = diameter of metal particle
 k_f = thermal conductivity of the gas
 V' = gas velocity relative to the particle
 ρ_f = density of the gas
 μ_f = kinematic viscosity of gas
 P_r = Prandlt number

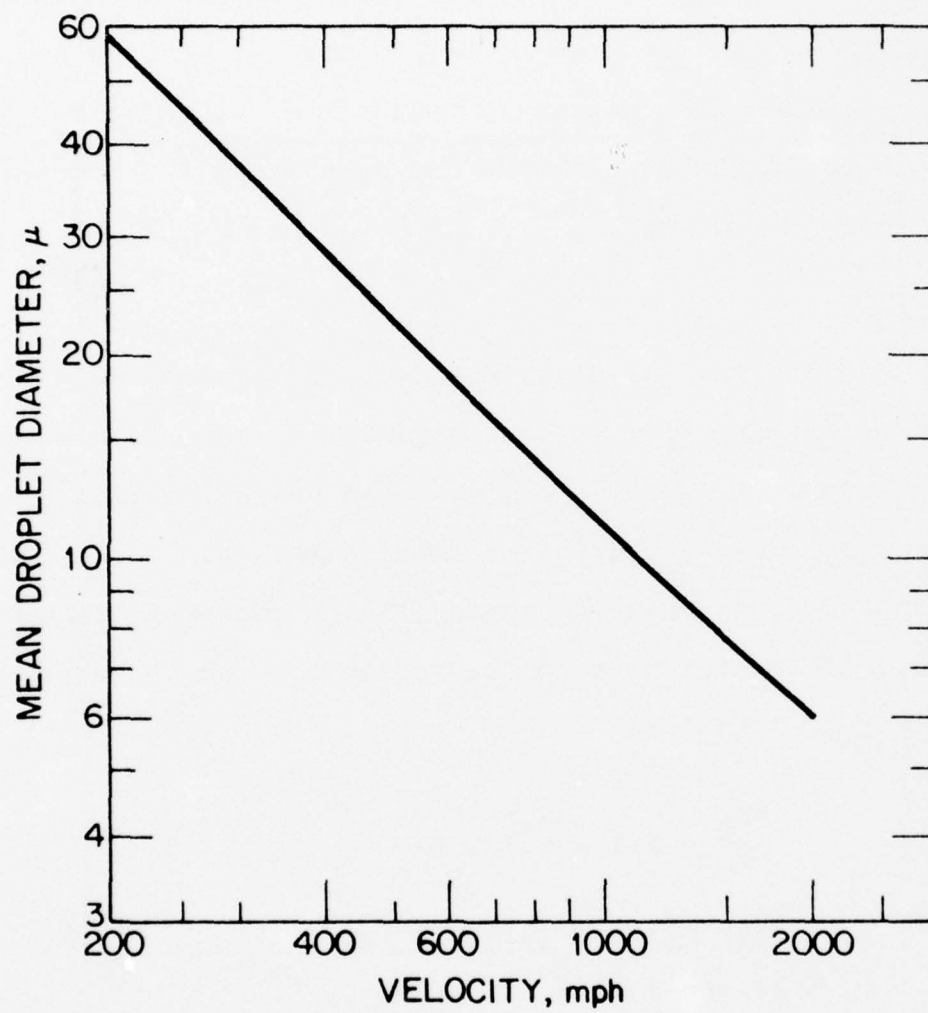


Figure 1. Mean droplet size as a function of gas velocity.

Figure 2 shows results of calculation for 25 μ m particles of Sn-Pb alloy assuming the gas to be helium. Note that for modest gas velocity of 500 mph, a heat transfer coefficient approaching unity is obtained - much higher than is obtained, for example, in conventional casting of metal into metal molds.

Generally, calculation of cooling rate in metal droplets is simplified because cooling is "Newtonian". Essentially all temperature drop during solidification is in the gas film at the surface of the particle (not within the particle) when:

$$\frac{hD_o}{k_m} \lesssim 0.1 \quad (2)$$

where k_m = thermal conductivity of the metal droplet. Inequality (2) can readily be shown to apply for most atomization processes. In these cases, the cooling rate of a liquid droplet is given by the simple expression:

$$\frac{dT}{dt} = \frac{6}{D_o} \frac{h}{\rho C_p} (T - T_g) \quad (3)$$

Figure 3 shows calculated results for the Sn-Pb alloy, 25 μ m dia., helium gas. Note that at the moderate gas velocity of 500 mph, a cooling rate of 10^5 °C/sec is obtained. Thus, gas quenching can clearly be used to obtain cooling rates above 10^5 °C/sec in molten metals.

SOLIDIFICATION

At least at moderate cooling rates (perhaps up to 10^5 °C/sec, solidification of metals can be described by the traditional Scheil equation, which assumes:

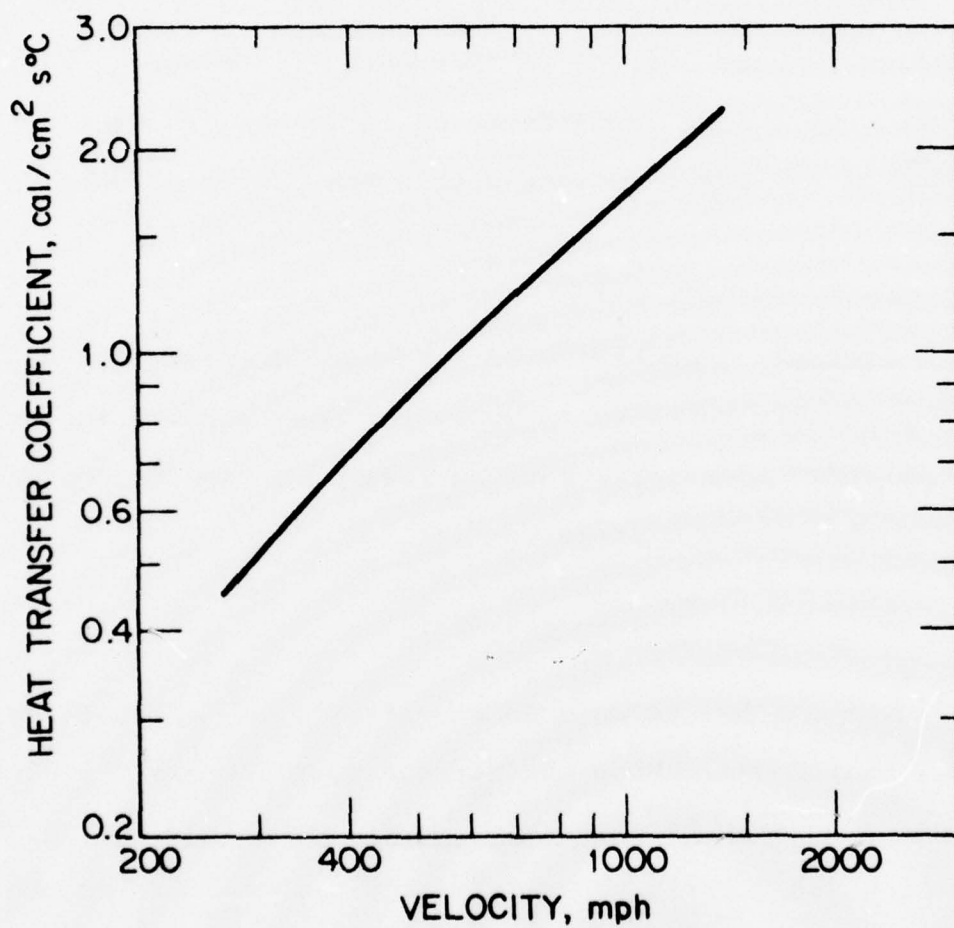


Figure 2. Heat transfer coefficients of droplets.

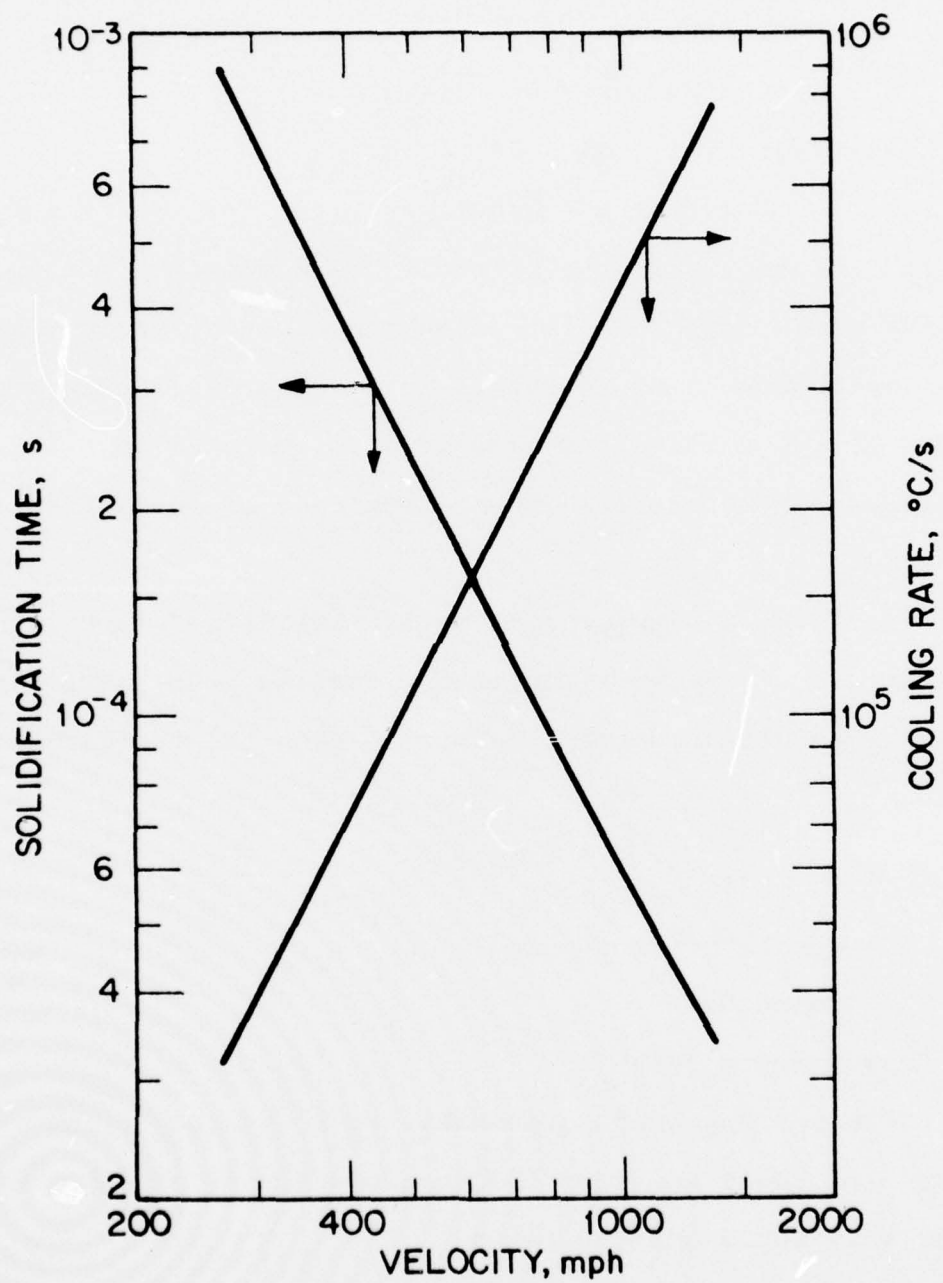


Figure 3. Solidification times and cooling rates of droplets produced with high velocity helium.

1. No significant barrier to nucleation
2. Equilibrium at all liquid-solid interfaces
3. Negligible concentration differences in the liquid between dendrite arms
4. Negligible solid diffusion

It follows from the above, and from the fact that temperature differences in the particle are negligible during solidification, that solidification takes place nearly simultaneously throughout the sample. That is, a solid skin does not form at the surface and grow inwards, but liquid exists at the surface of the particle throughout most of solidification (Figure 4).

Dendrite arm spacing in metals solidified in this way is known to decrease with increasing cooling rate. Empirical relations now obtained for many metals show the approximate relation:

$$d \approx A(\epsilon)^{-1/3} \quad (4)$$

where d = dendrite arm spacing

A = constant

ϵ = cooling rate

The $1/3$ exponential probably results from the fact that ripening ("Ostwald Ripening") controls dendrite arm spacing - even at very rapid cooling rates.

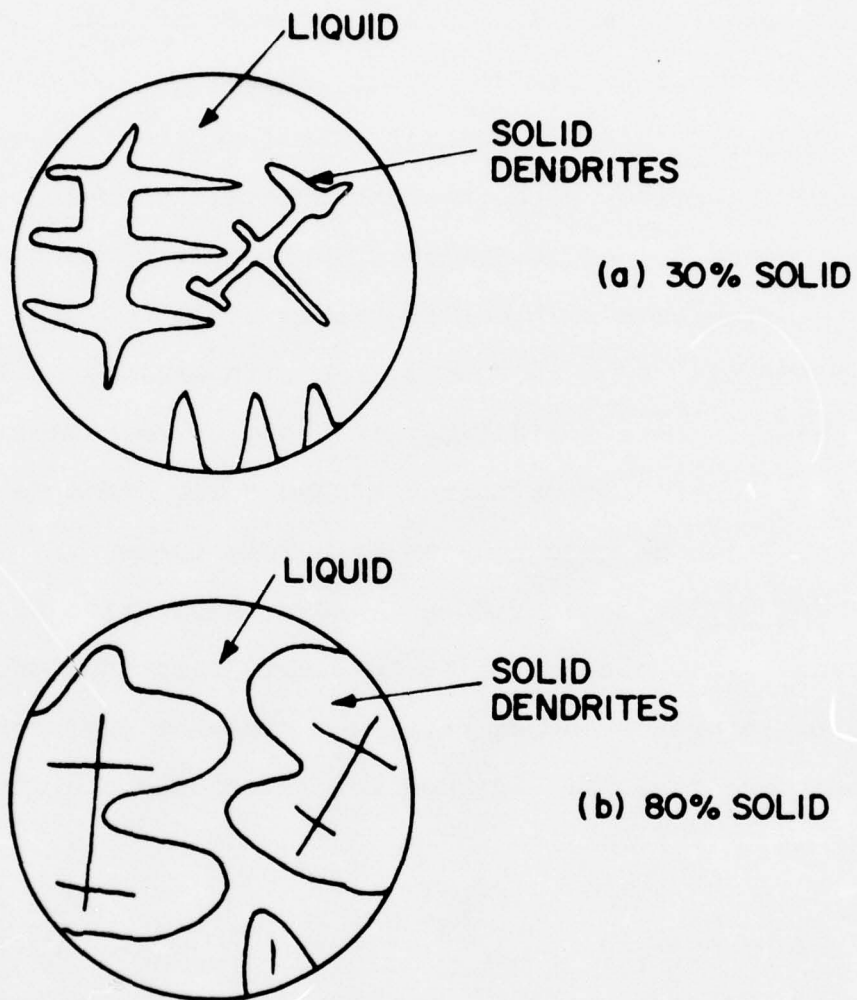


Figure 4. Sketch of solidification of a liquid alloy droplet.

MODIFICATION OF SOLIDIFICATION BEHAVIOR AT VERY RAPID COOLING
RATES

One can expect to be able to categorize 5 or more separate "cases" of solidification behavior of small particles depending on cooling rate and other process variables:

CASE I: "Classic Scheil". This is the case mentioned above which describes with reasonable accuracy most conventional casting processes, and is probably applicable to most atomized powders manufactured with cooling rates of 10^4 °C/sec or higher.

CASE II: Same as Case I, but with limited nucleation of 2nd phases. Here solidification behavior is similar in all respects to Case I except amount of 2nd solid phase (e.g., amount of eutectic) can be reduced - in principle to zero.

CASE III: Same as Case I except nucleation of all phases is limited. This case can also be simply treated quantitatively. It results in greater homogeneity and somewhat different structure than Case I or II. Segregation is reduced and structure altered, as

$$\frac{C_p \Delta T}{\Delta H} \rightarrow 1 \quad (5)$$

where C_p is specific heat of metal, ΔH is heat of fusion, and ΔT is the undercooling before nucleation.

CASE IV: Same as Case I except metastable phase or phases grow rather than stable phases.

CASE V: Growth is limited by kinetics at liquid-solid interface. At sufficiently high cooling rates growth can be

expected to be limited by interface kinetics, achieving (1) refined homogeneity, and/or (2) "glassy" structures.

ACKNOWLEDGEMENT

This research was supported by the Advanced Research Projects Agency of the Department of Defense under Contract No. MDA903-76C-0250 with The University of Michigan.

METHODS OF ACHIEVING RAPID SOLIDIFICATION
IN FINE PARTICLES

N. J. Grant

This presentation was concerned with the attainment of quench rates of 10^2 to about 10^9 °C/sec, although a more practical upper limit for now might be 10^7 .

While most processes will be looked at, there is every intention of pointing out the more practical, with commercial potential, capable of producing a useful particulate at economically attractive prices.

Emphasis will not be on "powdered metals" but on particulate material achieved through rapid quenching and including powders, flakes, fine foils, slivers, and even ribbons or strip provided that such high aspect ratio particulates (one dimension is much greater than the other two) can be chopped, crushed, or packed for consolidation or densification.

Equal emphasis is placed on both particulates and on the attainable quench rates.

Figure 1 remains the key reference plot, showing dendrite arm spacing (DAS) versus cooling rate in °C/sec, both plotted logarithmically. Changes that occur in the DAS are generally visited upon the final hot consolidated material in terms of grain size; there is a distinct proportionality.

Briefly large castings (including ingots) are cooled

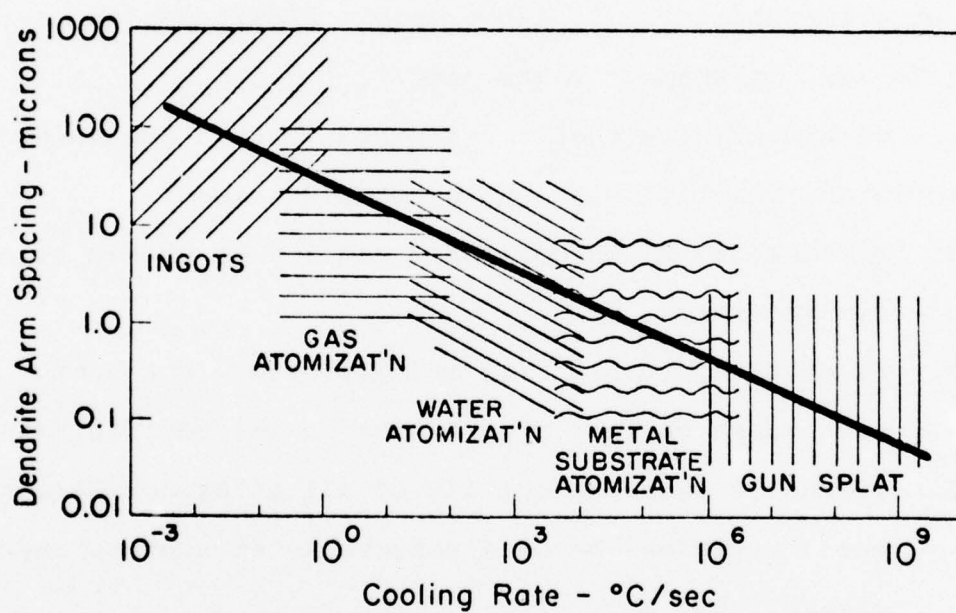


Fig. 1 Dendrite arm spacing as a function of cooling rate for aluminum and aluminum alloys.

at rates of about 10^{-3} to 10^0 °C/sec; gas atomized metals experience quench rates of about 10^0 to 10^2 ; liquid atomization (usually water, but including steam) are quenched at about 10^2 to 10^4 ; metal substrate quenching (one is now concerned with flattened shapes) reaches 10^4 to 10^6 °C/sec; and splat quenching (very fine particle flakes usually) attains rates of 10^6 to 10^9 °C/sec.

The quench rate bands are not sharply defined and depend on atomization and disintegration conditions, on particle sizes formed, on shape factors, etc.

Of the changes that are induced through quenching of particulates, the following serve as guide lines:

1. Refinement of DAS and grain size: progressive at all cooling rates.
2. Decreased particle size and improved distribution of all excess phases: progressive at all cooling rates.
3. Increased solid solubility of all alloying elements and impurities: becomes observable at quench rates greater than about 10^4 °C/sec.
4. Elimination of segregation phases: occurs at quench rates greater than about 10^2 to 10^4 °C/sec (AlCuFeMn in aluminum; Cr_7C_3 in superalloys, etc.).
5. Formation of new metastable phases, including intermetallics; observable at quench rates greater than about 10^2 or 10^3 (Cr_3S_2 in stainless steels).
6. Glassy metals; requires quench rates greater than about

10^6 °C/sec, although some can occur at 10^5 and in most alloys do not form even at quench rates of 10^9 °C/sec.

ATOMIZATION

If one includes all gas, steam and water systems, quench rates from 10^0 to 10^4 may be attained (without forced cooling). Gas pressures vary from about 200 to 600 psi; powder sizes vary from near micron to several mm. Because atomization is apparently a three-step process, the spread of powder sizes is large, resulting in usual powder yields that vary from 50 to 70 percent of the ladle melt. DAS values vary from perhaps 100 to 5 microns.

Atomization is today the practical source of most powders, however achieved. Prices are not low, but for high alloy materials are tolerable. Wherever an alloy can be processed by air or water atomization, perhaps including nitrogen, there is a potential for inexpensive powders with quench rates of 10^2 to 10^3 (maximum), at reasonable cost.

Argon is much more expensive as an atomization medium. To pay for argon use, one or more of the following should be possible; powder yields in excess of 80 percent, quench rates of 10^4 , unit atomization runs and powder production volume which make argon recycling attractive, or much narrower powder size yields than are now achieved.

The gas solubility (Homogeneous Metals) process, rotating electrode process, and plasma atomization do not appear attractive as economical, longer term processes.

Ultrasonic atomization

The Swedish Kohlsva process, utilizing a patented Hartman shock-wave tube device, accelerate gases to Mach 2 or greater and achieves frequencies of 80,000 c.p.s., gives high yields (over 80 percent) of a narrow powder size fraction (1 to 10 microns in many materials), and thereby achieves quench rates of 10^4 to 10^5 °C/sec. Thus far significant experimentation has confirmed the powder size and yields for tin, but not for aluminum (due to the refractory Al_2O_3 films). The aim is to move to copper alloys shortly and then to superalloys to check out yields and powder size numbers. At an indicated production rate of 0.3 to 0.4 pounds per second, the process shows commercial promise. The very fine powders quench and cool rapidly; thus only a small atomization chamber is necessary (versus towers which are 30 feet high and 6 to 8 feet in diameter for ordinary argon atomization). The argon cost per run is thus small, since purging and operating demands are small.

The ultrasonic atomization process is indicated to be a one step atomization method, which can account for the high yield of powder in a narrow size range.

Shear-lip atomization

The rotating dish principle of atomization, augmented by dynamic helium gas quenching, is being covered in the P&WA-Florida presentation and is not discussed here.

SUBSTRATE QUENCHING (METALLIC SUBSTRATES)

a) The gun technique, which achieves quench rates of 10^7 to 10^9 °C/sec, produces flakes which vary in thickness from about 0.1 to 1 micron, although thicker flakes are observed. The resultant DAS values vary from 0.01 to 0.5 micron. The process, in the foreseeable future, does not appear to offer commercial potential because the powders are far too reactive; a continuous process has not yet been proposed and looks remote.

b) The piston and anvil process, which quenches from two sides, can produce thicker foils (30 to 200 microns) at quench rates of 10^4 to 10^6 °C/sec, with DAS values from about 0.5 to 3 microns. Even with the latest developments, the process does not appear to offer continuous production capability and is therefore judged to be lacking in commercial potential for now.

c) Rotating disc - A vertical or horizontal copper disc (1500 to 2000 rpm) has liquid metal sprayed against the surface (by plasma gun, gas atomization, metallizing gun, etc.), and yields quench rates of 10^4 to 10^6 °C/sec. Quenching is from one side; splat flakes vary in thickness between about 30 and 200 microns. The flakes are removed from the disc by a series of doctor blades, not altogether a simple task.

The process has distinct commercial potential and can be quite continuous as long as flake removal off the disc works well. Results with 2024 Al (Lebo and Grant, MIT) showed sig-

nificant improvements in room temperature tensile values and fatigue, as well as improved creep resistance to high temperatures than those common for regular 2024.

d) Copper rolls - Heavy-walled copper rolls, which can be cooled internally, have been used successfully for a variety of alloys to produce foils and strip of 40 to 300 microns at quench rates of 10^4 to 10^7 °C/sec. Quenching of heavier thicknesses is enhanced because of quenching from two sides, with optimum contact between splot foil and substrate (unlike the rotating disc).

It is very easy to use liquid atomized particles as the feed to the rolls (or plasma gun, or a drip method, etc.) This gives a choice of methods to deliver liquid droplets to the rolls combined with two-sided substrate quenching.

This process has, perhaps, the greatest potential for commercialization since there are no basic limitations to continuous production; metal delivery is independent of the splot quenching apparatus and a holding tun-dish arrangement can be fed more or less continuously.

e) Melt spinning and melt extraction - Melt spinning involves delivery of liquid metal in a fine stream to a high speed rotating disc or dish; there is a short dwell time after rapid solidification, followed by release of long continuous ribbons (R. Pond of Johns Hopkins). Melt extraction delivers the spinning copper (or other metals) disc to an open crucible of molten metal; a shaped rim freezes on a thin layer of ribbon

or wire, followed by a short dwell time and release of the quenched ribbon (Battelle).

Quenching is from one side for each system; ribbons and wires (or elongated spikes or rods called L-D powders achieved by notching the disc in melt extraction) of 20 to 200 microns thickness are produced at quench rates estimated between 10^4 and somewhat better than 10^5 °C/sec.

A continuous or near continuous casting method can be visualized, more ideally by the melt extraction process wherein the molten alloy is continuously available in a crucible or holding furnace for extraction. If ribbon is produced, it is possible to continuously chop, crush or otherwise fragment the material into a suitable particulate size for consolidation. Rates of output vary between 2 and 40 meters/sec; metal delivery rates of 0.3 pounds/sec are indicated.

DETERMINATION OF QUENCH RATES

1. Direct measurements by thermocouple techniques. While very difficult, the method has been used and results are in agreement with those by indirect methods (described below). High speed measuring methodology is required.

2. DAS and eutectic phase spacing. Of these, due to broader alloy applicability, the DAS has yielded excellent results but must be calibrated against other methods (thermocouple measurements, for example).

3. Calibration: with thermocouple reference numbers. Now that there is evidence that a log-log plot of DAS vs. cooling

rate is a straight line relationship, direct measurements are made at quench rates up to 10^3 or 10^4 °C/sec (not too difficult) and the resultant curve (from 10^{-3} to 10^3) is extrapolated to much higher quench rates. This method has worked well both for aluminum and copper alloys.

4. Calculations. Once any of the above three methods has been shown to work for a particular set-up or alloy system, calculations have been made of the quench rate, based on a number of assumptions, with excellent agreement against experimental values.

In any event, the four above methods appear to offer agreement no worse than about one log cycle deviation from each other, which for now is adequate.

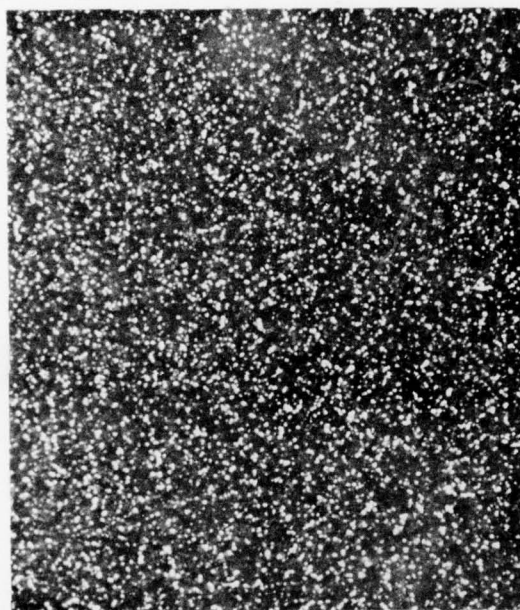
HIGH PERFORMANCE MATERIALS BY CRUCIBLE'S P/M PROCESSES

J. N. Fleck and E. J. Dulis

Advanced P/M processes have been developed by Crucible Materials Research Center of Colt Industries to make new and superior high performance products such as (1) high-speed tool steels, (2) superalloys for jet engines and (3) titanium alloy products for aircraft engines and airframes. Product forms include conventional billets and bars as well as preforms and near-finished shapes. The new process involves production of high quality powder, treatment and judicious powder handling, use of suitable containers of ceramic or metal, and application of hot-isostatic pressing (HIP) of powder filled containers.

After an R&D phase that started in 1965, a pilot operation was scaled up to a commercial operation to produce high-speed tool steel mill products at the Crucible Specialty Metals Division in Syracuse, New York in 1970. The steady growth of the market for Crucible Particle Metallurgy (CPM) high-speed steels is related to the superior performance of these steels over the steels made by conventional methods.

P/M high speed steels overcome the problem of carbide segregation related to the slow cooling during ingot solidification. The microstructure of P/M products show a homogeneous distribution of fine primary carbides, Figs. 1 and 2, that are



CPM Product



Conventional Product

250X

Figure 1. Typical primary carbide particles in Tl5; microstructure in longitudinal section at mid-radius of 2 inch (50 mm) diameter bar.

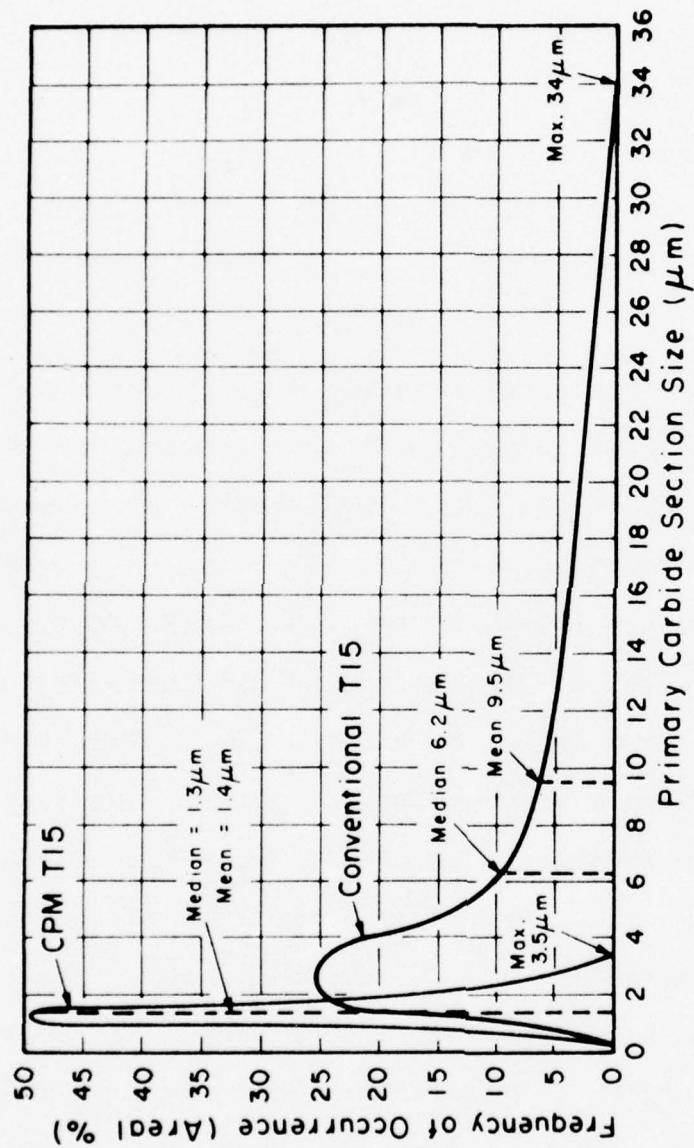


Figure 2. Primary carbide particle size distributions in T15.

related to significant advantages in tool manufacturing and tool performance. P/M steels have advantages in superior grindability, much improved size change uniformity after heat treatment, cross-sectional hardness uniformity, better hardening response, improved toughness, and significant increase in tool life under intermittent cutting conditions, Table I. Large sized high-speed steel products are made in Crucible's P/M plant, such as the hollow bar 14-inch O.D. by 3000 lbs shown in Fig. 3.

For the production of superalloy and titanium alloy products, a key Crucible development involved the use of ceramic mold process to produce fully dense as HIP's metal parts very near to net shape.

In one program funded by the U.S. Air Force (Contract F33615-73-C-5040), the as-HIP shaft plus disc assembly shown in Fig. 4 was produced in PA-101 alloy (hafnium modified IN-792). This P/M (powder metallurgy) shape weighs 33 pounds, whereas the conventional forging plus inertia-welded shaft weighs 103 pounds. Thus, P/M reduced input by 70 lbs, thereby conserving critical alloys and, of course, reduced dramatically the amount of machining required, thus effecting a savings in time, energy and dollars. Less apparent is the elimination of an intermediate manufacturing operation, viz. the inertia weld, and its associated quality control steps plus the total elimination of one item, the shaft, from inventory.

Under NASA sponsorship (NAS-3-200074) with General

Table 1. Typical commercial machining operations in which CPM super high speed steels have competed successfully against conventional super HSS, cast cobalt-base alloy and carbide tool materials.

| Machining Operation | | | Tool | | |
|---------------------|----------------------------|---|---|---|---------------------------|
| Type | Application | Material | Type | Material | Life |
| Form turning | Screw machine parts | Armco iron | $\frac{1}{2}$ in. (13mm) sq. tool bits and inserts | T15 W-Carbide Ti-Carbide CPM T15 | 30 min 50 80 180 |
| Turning | Tool shank weld flash | Alloy steel | $\frac{1}{2}$ in. (13mm) sq. tool bits | Cast Co alloy CPM T15 CPM Rex 76 | 3 hr 48 75 |
| End milling | Aircraft propeller barrels | AMS 6415 (4340) alloy steel at HRC 44 | $\frac{1}{2}$ in. (13mm) diameter 6-flute end mills | M42 Carbide CPM Rex 76 | 0 parts 4 22 |
| Thread milling | Jet engine parts | Nickel alloys | $4\frac{1}{2}$ in. (100mm) diameter multiple thread milling cutters | Carbide tip CPM Rex 76 | 5 parts 33 |
| Turning and shaping | QC test specimens | Ti alloys at 125 ksi (850 MPa) strength level | $\frac{1}{2}$ in. (13mm) sq. tool bits | M42 M46 Carbide CPM Rex 76 | 0 parts 0 0 10 |



Figure 3. Particle Metallurgy Hollow Bar of M2FM High Speed Steel (12-in OD by 518 ID by 2,946 lbs).

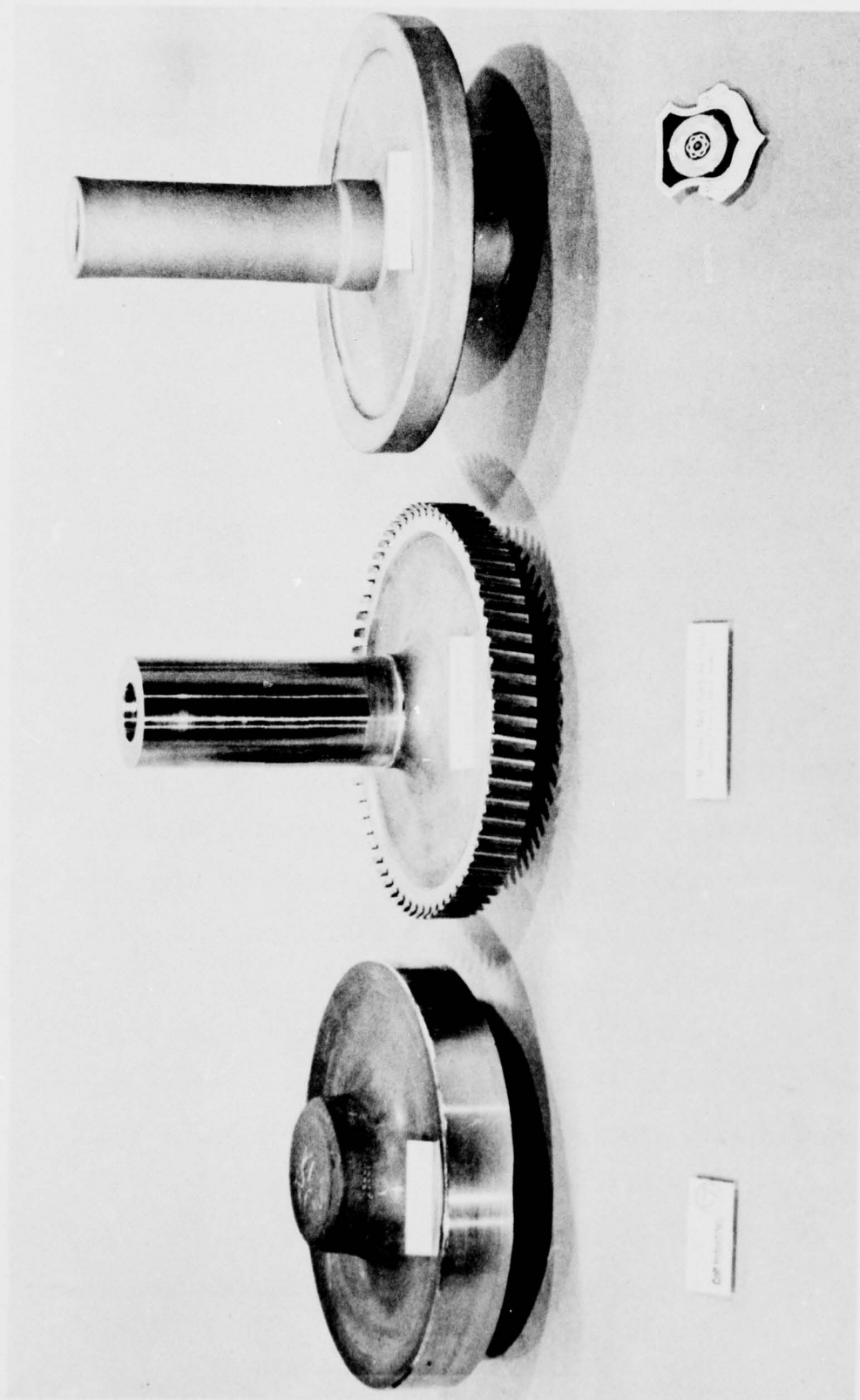


Figure 4. Stub Shaft of PA101

Electric, Crucible is attempting to produce a near-net shape (NNS) of the Rene 95 high pressure turbine rotor rear shaft for General Electric's CF6-50 engine. Our first attempt at this part is shown in Fig. 5. This is an ongoing program, and further shape optimization is planned. Also, General Electric will conduct engine tests on as-HIP parts.

We have also been active in the development of as-HIP titanium parts. For example, under U.S. Navy sponsorship we have produced a Ti-6-6-2 brace for the F-14 aircraft. A typical part is shown in Fig. 6. To date, mechanical property tests on this material have exhibited equivalence to cast and wrought. Under this continuing effort, Grumman is preparing to flight test this part.

A prime structural part, the Ti-6-4 keel splice former from the F-15 aircraft (shown in Fig. 7) has been produced and successfully component tested under an Air Force contract (F33615-74-C5114). In addition to a successful materials testing effort, the as-HIP parts were component tested and the data were compared directly with those for conventionally forged parts, Tables II and III.

It is especially noteworthy that these results were obtained using state-of-the-art REP (rotating electrode process) powder with its known shortcomings, most notably a significant number of small tungsten inclusions.

At this point in time, titanium powder cost and quality are the major obstacles to widespread application of

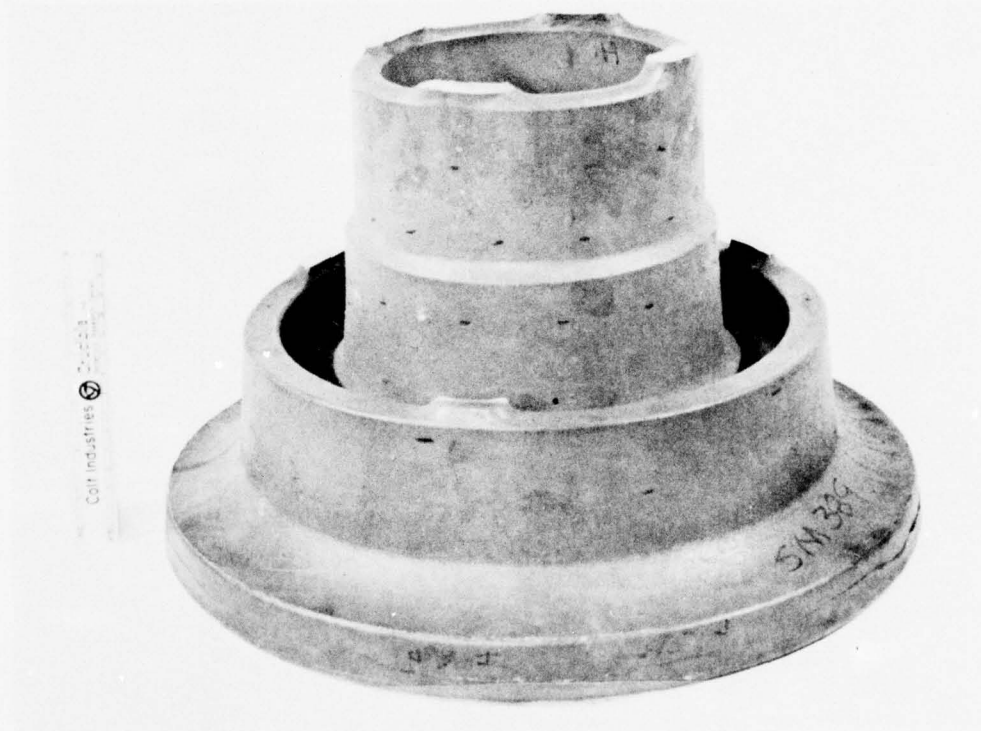


Figure 5. As-HIP's CF6 High Pressure Turbine Rotor Rear Shaft

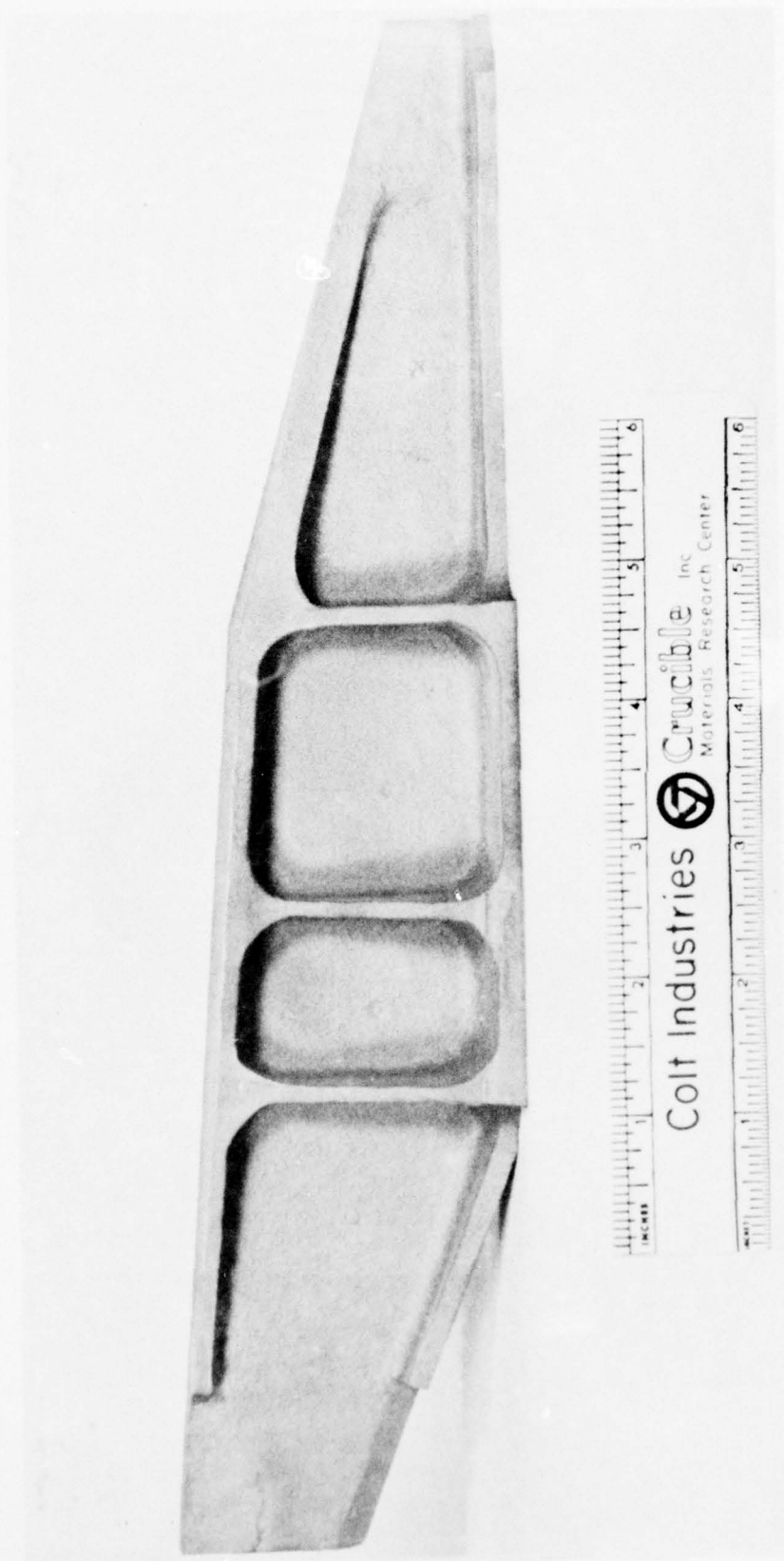


Figure 6. As-HIP'd Titanium Alloy Ti-6-6-2 Brace Fitting

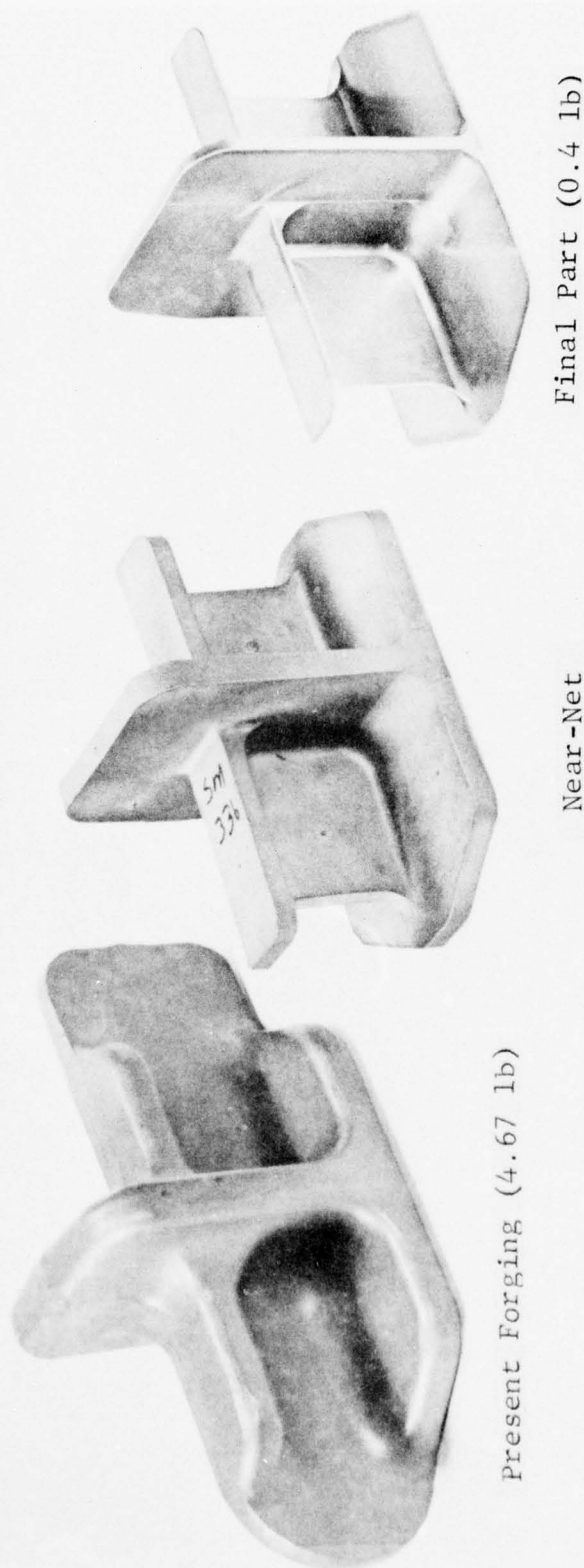


Figure 7. Titanium Alloy Ti-6-4 Keel Splice Fitting

Table 2. Static Test Results. Forged and "HIP"
Keel Splice Formers, 68A333019-2007

| <u>Specimen Number</u> | <u>Fabrication Method</u> | <u>Yield Load (lbs)</u> | <u>Failure Load (lbs)</u> |
|----------------------------|-------------------------------|---------------------------------|-----------------------------------|
| 1FS | Forged | 2,400 | 4,000 |
| 1HS | HIP | 2,600 | 4,140 |

Table 3. Spectrum Fatigue Data. R-4 Horizontal Tail
Spectrum (F-15) Keel Splice Formers, 68A333019-2007
Design Limit Load - 2,200 lbs

| <u>Specimen Number</u> | <u>Fabrication Method</u> | <u>Hours to Failure</u> | <u>Average</u> |
|----------------------------|-------------------------------|-----------------------------|----------------|
| 2FF | Forged | 11,255 | |
| 3FF | Forged | 10,400 | |
| 4FF | Forged | 6,960 | |
| 5FF | Forged | 5,760 | 8,594 |
| 3HF | HIP | 23,360 | |
| 5HF | HIP | 17,840 | |
| 6HF | HIP | 14,240 | 18,480 |

*Oversize hole and fasteners (.189" diameter in lieu of .169")

P/M near-net titanium shapes. There are a number of emerging processes which could impact quality of titanium powder, although until a suitable liquid-metal process for rapidly converting large quantities of metal to powder is established, conversion costs will remain higher than for superalloys where gas atomization is routinely used.

SUPERPLASTICITY IN METALS AND ALLOYS

O. D. Sherby

The term superplasticity has been used to describe extraordinary elongations (several hundred percent) obtained during tensile deformation of polycrystalline materials. Although superplasticity was first observed over 50 years ago (Rosenhain, Haughton, Bringham 1920), active research in this field began after Underwood's review paper on superplasticity in 1962. The term superplasticity originates from the Russian word "Sverhplastichnost" (ultra plasticity) first described by Bochvar when he studied the mechanical behavior of aluminum-zinc alloys.

Considerable effort has been devoted to studies of superplastic metals and alloys since 1962. This high research activity centers on attempts to understand this type of plastic behavior and on attempts to put such unusual characteristics to practical use in metal forming operations.

There are basically two different approaches to analyzing superplastic behavior of materials. One approach is through applied mechanics. This method emphasizes the importance of understanding nonuniform plastic flow and the factors influencing the progression of a neck during tensile deformation. Factors such as strain rate sensitivity and strain hardening rate are central to explaining the amount of ductility that can be attained

in a given material. This method points out clearly why superplastic materials are invariably highly strain-rate sensitive. The other approach to analyzing superplasticity is through materials science. Here, one attempts to understand the structural features that are needed to obtain high strain rate sensitivity. Two types of superplastic flow have been observed: internal stress superplasticity and fine structure superplasticity. Internal stress superplasticity refers to the extensive elongations that occur in certain metallic alloys under conditions where high internal stresses occur concurrent with deformation. Fine structure superplasticity refers to the extensive elongations that occur in metallic alloys in which a fine grain structure exists. Most of the investigations on the two types of superplasticity is described in recent reviews. (Chaudhari 1967, Sherby 1969, Burke and Weiss 1970, Johnson 1970, Davies, Edington, Cutler and Padmanabhan 1970, Nicholson 1972, Mukherjee 1975, Alden 1975, Shorshorov et al. 1973, Gittus, 1975).

In the following pages we outline the applied mechanics and materials science approach to studying superplasticity. Emphasis will be placed on fine structure superplasticity. The factors influencing this type of superplasticity are now fairly well documented. This knowledge, coupled with advances made in understanding normal plastic flow in crystalline solids (slip creep), permits us to outline methods for enhancing and optimizing superplasticity in materials.

APPLIED MECHANICS ASPECTS OF SUPERPLASTICITY

As implied earlier, all superplastic materials have one key characteristic in common - their resistance to plastic flow is a strong function of the strain rate. That is, they are highly strain rate sensitive. Phenomenologically, this can be seen in the following graph. Although high rate sensitivity is a necessary condition for superplasticity, it is not a sufficient one. Special structural changes occurring during plastic flow, such as internal cracking at interphase boundaries, cavitation or grain boundary separation can lead to premature failure.

Metals and alloys show high strain rate sensitivity at high temperatures. This rate sensitivity is usually measured by the exponent m in the phenomenological equation $\sigma = K\dot{\epsilon}^m$. Fig. 1 shows that the ductility (measured by elongation to fracture) increases as the strain rate sensitivity exponent increases. Superplastic metals and alloys generally exhibit strain rate sensitivity exponent (m) values in the range $m \approx 0.5$ (0.4 to 0.6).

The applied mechanics approach to explaining high plasticity can be best given by the following example. The true strain rate is given by $\dot{\epsilon} = \frac{dl}{l dt} = - \frac{dA}{A dt}$. Thus, $\frac{dA}{dt} = - \dot{\epsilon} A$. But $\dot{\epsilon} = K\sigma^{1/m} = K \left(\frac{F}{A} \right)^{1/m}$ where F is the applied force. Substituting this expression, one obtains $\frac{dA}{dt} = K' \left(\frac{1}{A^{1/m-1}} \right)$ where $K' = - KF^{1/m}$. This expression gives the rate change in area as a function of the area. For values of m less than unity, the magnitude of $\frac{dA}{dt}$ increases as A decreases (an expected result). However, as m approaches unity $\frac{dA}{dt}$ becomes a diminishing function of A and at

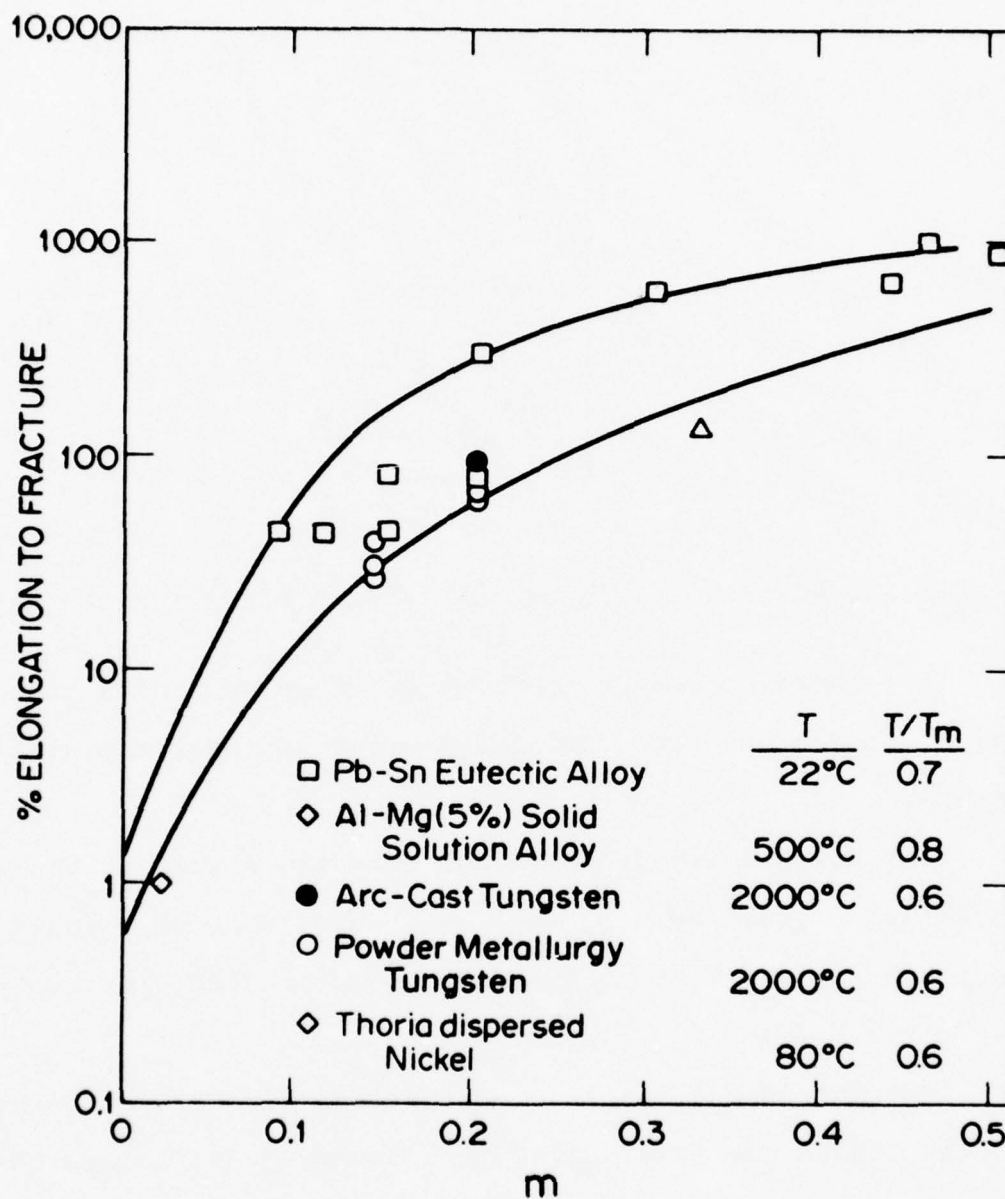
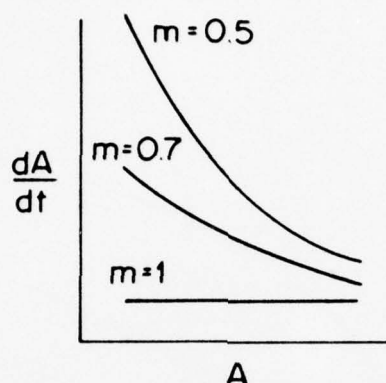


Figure 1. Data from Avery and Backofen, 1965, Mullendore and Grant, 1954, Conway and Flagalla, 1969, Green 1959, Wilcox and Clauer, 1966.

$m = 1$, $\frac{dA}{dt} \neq f(A)$. The later result explains why Newtonian fluids (such as glass, well masticated chewing gum, molasses, etc.) have such high plasticity.



Schematic showing the change of $\frac{dA}{dt}$ with A for various values of m .

There are other theories based on mechanics that have been developed to describe ductility. Four of these are outlined below:

(a) Rossard (1966) has shown that the strain at the start of necking is given by $\epsilon_{\text{neck}} = \frac{N}{1-2m}$, where N is the strain hardening exponent in $\sigma = K\epsilon^N$. His theory would predict infinity plasticity at $m = 0.5!!$

(b) Morrison (1968) showed that the dimensions of the sample will dictate the total elongation observed and showed that

$$\% \text{ elongation to fracture} = bm^2 \left(\frac{d_o}{L_o} \right) \times 100$$

where b is a material constant, and d_o and L_o are the diameter and length of sample respectively.

(c) Avery and Stuart (1968) took into account the possible tapered shape of the sample. Their equation is given as

$$\% \text{ elongation} = \left\{ \left[\frac{1-\beta^{1/m}}{1-\alpha^{1/m}} \right]^m - 1 \right\} \times 100$$

where α is the ratio of the minimum to maximum area at the start of the test and β is the same ratio at some arbitrary stage of the test at which the elongation is measured.

(d) Burke and Nix (1975), using a finite element approach, showed that the

$$\% \text{ elongation} = [\exp (\frac{2n}{1-m}) - 1] \times 100.$$

The predicted elongation to fracture (Fig. 2) is shown as a function of the strain rate sensitivity exponent, m , based on various analytical expressions (using applied mechanics arguments). The curves predicted by the Morrison relation were calculated using $b = 100$.

MATERIALS SCIENCE ASPECTS OF SUPERPLASTICITY

Internal Stress Superplasticity

Figure 3 illustrates internal stress superplasticity, through multiple phase transformations, in several steels. As can be seen, the influence of thermal cycling through the phase transformation temperature yields high elongations to fracture for several steels. The applied stress was 2500 psi.

Figure 4 illustrates that the strain obtained upon transformation can be written as

$$(\epsilon_{\text{transf.}}) = K \left(\frac{\Delta V}{V} \right) \frac{\sigma}{\text{Hardness}}$$

Thus the transformation strain is seen to be approximately a linear function of the applied stress. Furthermore, it is seen

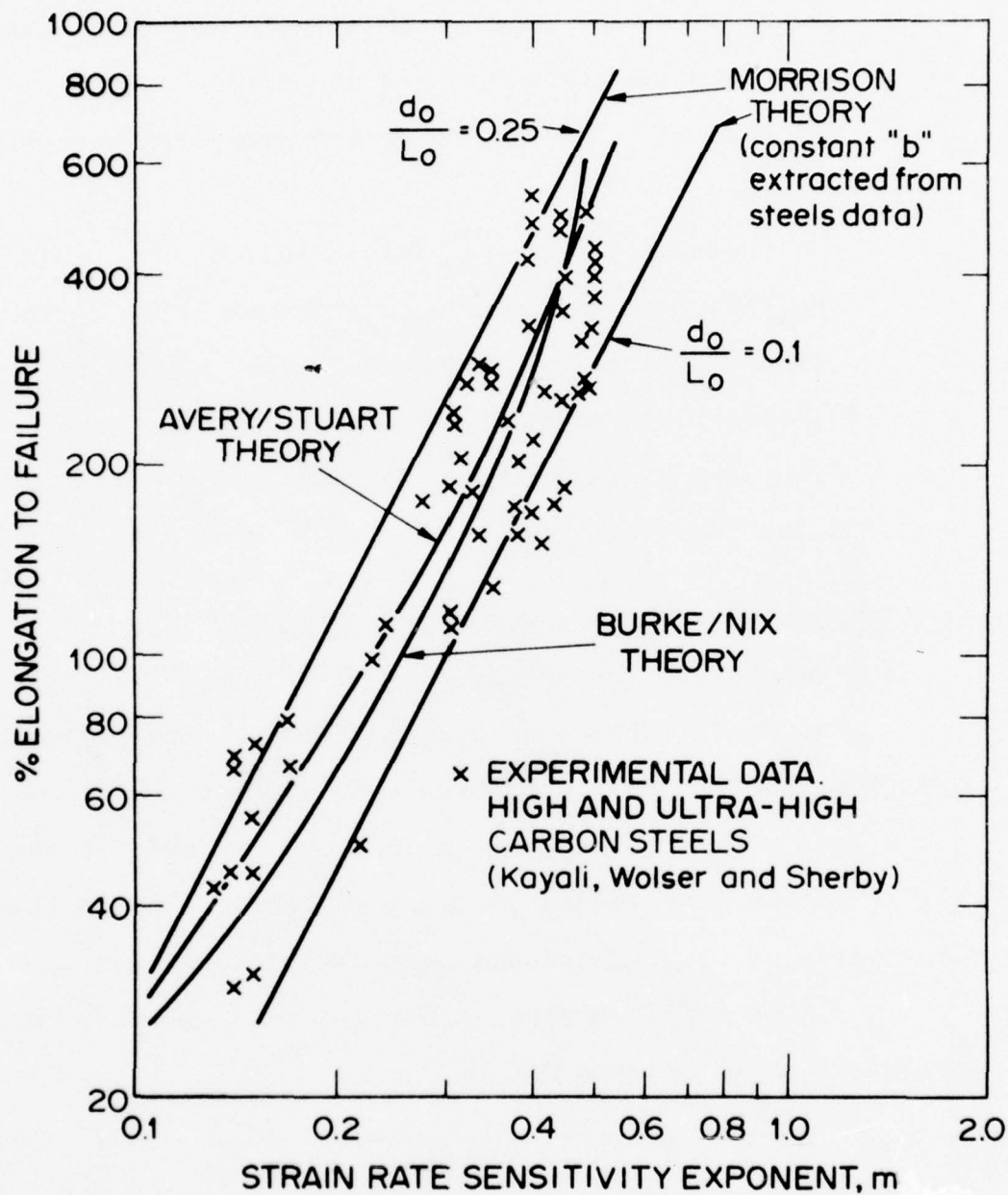


Figure 2. Data from Walser and Sherby, 1975 and Kayali, 1976.

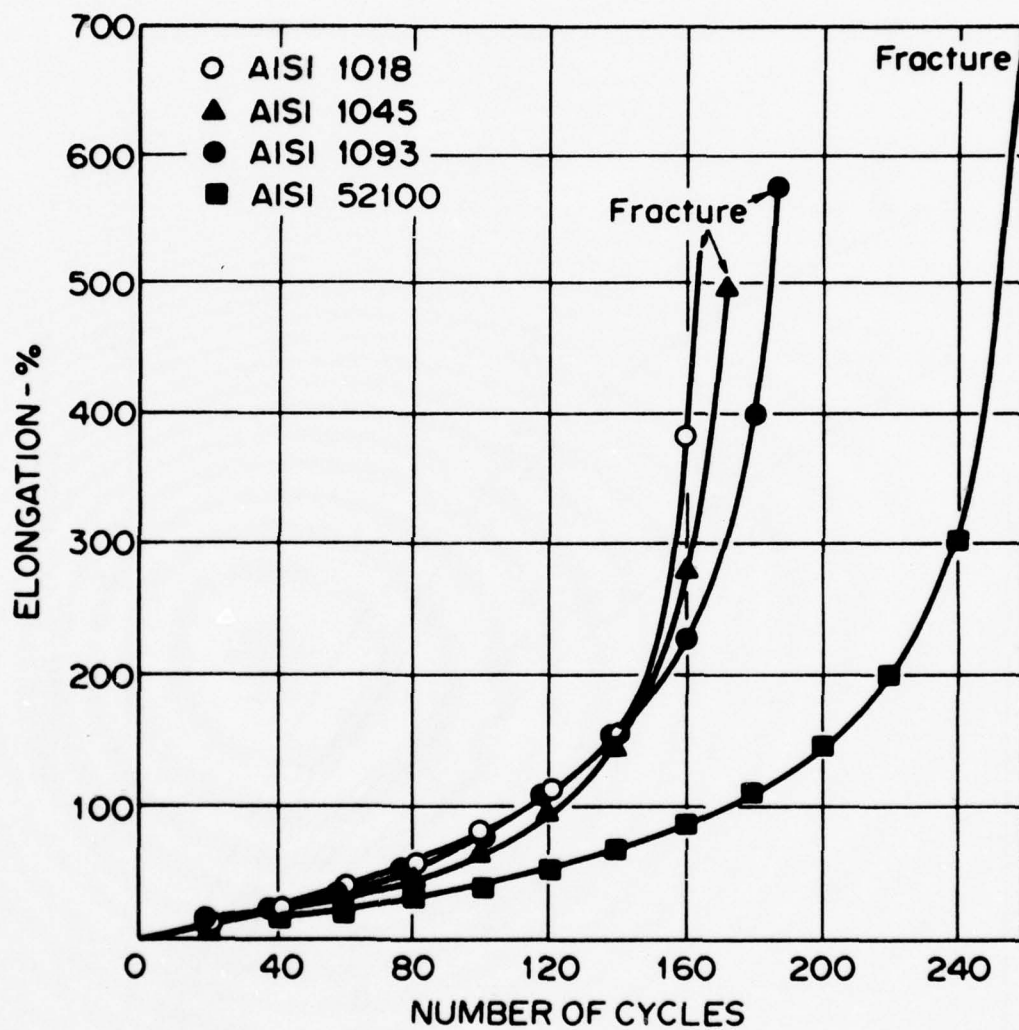


Figure 3. Data from Oelschlagel and Weiss, 1966.

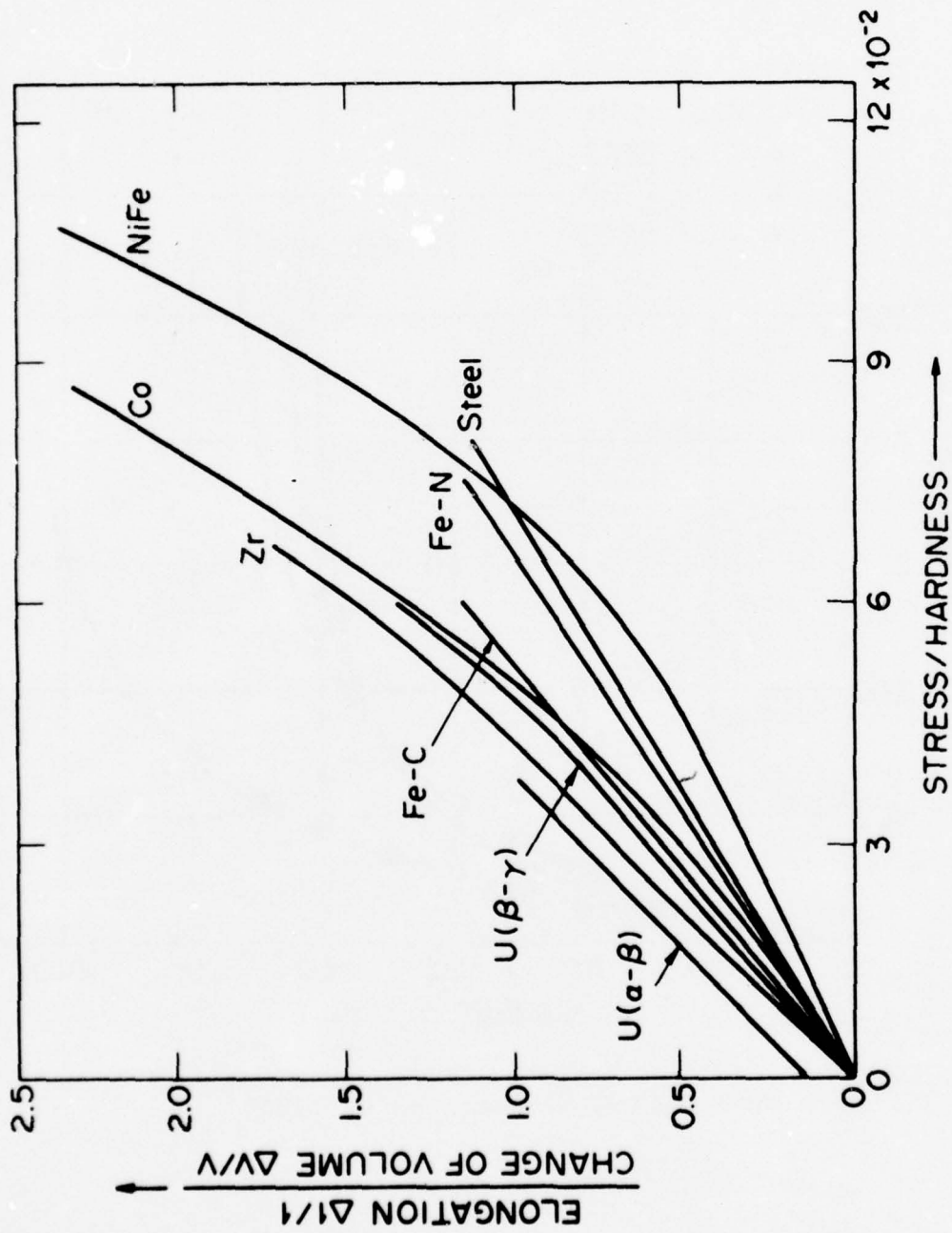


Figure 4. Data from de Jong and Rathenau, 1961, Johnson and Greenwood 1962, Greenwood and Johnson 1965, Chubb, 1955.

to be proportional to the volume change upon transformation (a measure of internal stress) and inversely proportional to the hardness (a measure of creep strength without internal stress).

Figure 5 illustrates internal stress superplasticity, through thermal cycling, in alpha uranium. The data are plotted as diffusion compensated creep rate versus modulus compensated flow stress. The high internal stress generated under thermal cycling leads to a high strain sensitive material ($m \approx 1$ as can be seen in the figure). If the diffusion compensated creep rate is replotted as a function of $(\frac{\sigma + \sigma_i}{E})$ where σ_i is the (proposed) internal stress then the data exhibits the normal power dependence observed in alpha uranium tested under isothermal conditions ($n = 5$ in the relation $\dot{\epsilon} = K\sigma^n$). [The high internal stress generated during thermal cycling arises from the high anisotropy of thermal expansion observed in alpha uranium; $\alpha_{[100]}$ is 60×10^{-6} per $^{\circ}\text{C}$ and $\alpha_{[100]}$ is -18×10^{-6} per $^{\circ}\text{C}$ at 500°C].

Thermal cycling of alpha uranium leads to a high strain rate sensitive material. This high strain rate sensitivity is manifested in high ductility as can be seen by the specimen at the bottom of Figure 6. Whereas creep deformation occurring under isothermal conditions leads to 50% elongation at 600°C , thermal cycling between 450°C - 600°C leads to creep elongations exceeding 500%.

Fine Structure Superplasticity

A dominating feature of materials that exhibit fine structure superplasticity is that they have a fine grain size.

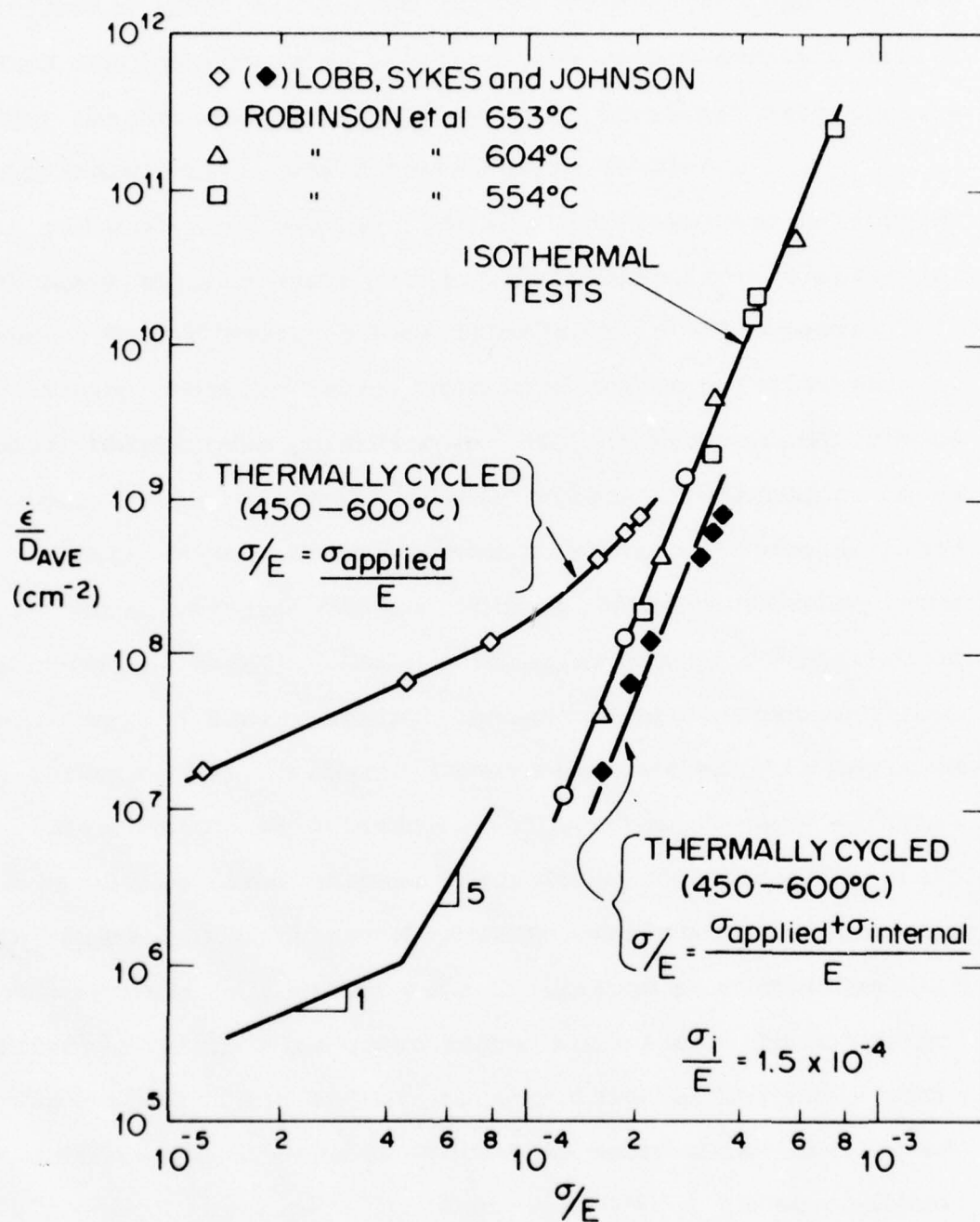
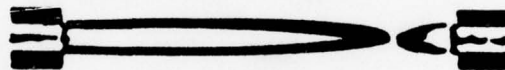


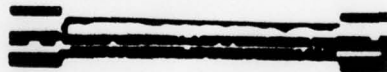
Figure 5. Data of Lobb, Sykes and Johnson, 1972, Robinson, Armstrong and Sherby, 1972, Adda and Kirianenko, 1962, Armstrong, Eash and Hockett, 1972.

α - URANIUM

ISOTHERMAL
TENSILE TEST, 600°C (50% elong.)



UNDEFORMED SAMPLE



THERMALLY CYCLED
(450 \rightleftharpoons 600°C) (>500% elong.)

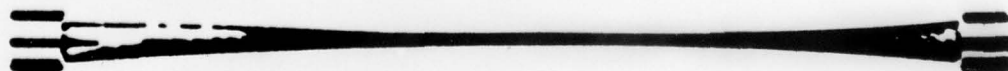


Figure 6. Data from Lobb, Sykes and Johnson, 1972.

Typically grains in the order of one to five microns are required in order to observe superplastic effects at reasonable strain rates. In contrast most technological materials have grain sizes in the order of 50 to 200 microns (.05 to .2mm).

Figure 7 shows the flow stress-strain rate relationships (log-log plot) for a two phase nickel-iron-chromium alloy at elevated temperatures (39%Cr-10%Fe-1.75%Ti-1%Al balance Ni). The strain rate sensitivity exponent is constant and high ($m \approx 0.5$) over a wide range of strain rate. Elongations exceeding 880% (extent of the machine travel elongation) were commonly observed.

Many superplastic materials exhibit an S shaped behavior when plotted as logarithm of the flow stress versus logarithm of strain rate (shown as A in Fig. 8). Each of the three regions (making up the S shaped curve) are often associated with specific mechanisms of plastic flow. Other materials exhibit only two regions, as shown in schematic diagram B; an example of this type of behavior is shown in Fig. 8 for the nickel-chromium-iron alloy.

The data of Figure 8 is sometimes plotted as logarithm of strain rate as a function of the logarithm of the flow stress. The slope of such a plot yields the stress exponent n in the equation $\dot{\epsilon} = K\sigma^n$. The value of n is equal to the reciprocal of m . Superplastic flow of fine grained materials, given as region 2 in Figure 9, is generally associated with a stress exponent of 2 (that is, $m = 0.5$).

Region 3, the high stress region, is generally associated with a slip creep (dislocation) mechanism. Some of the consider-

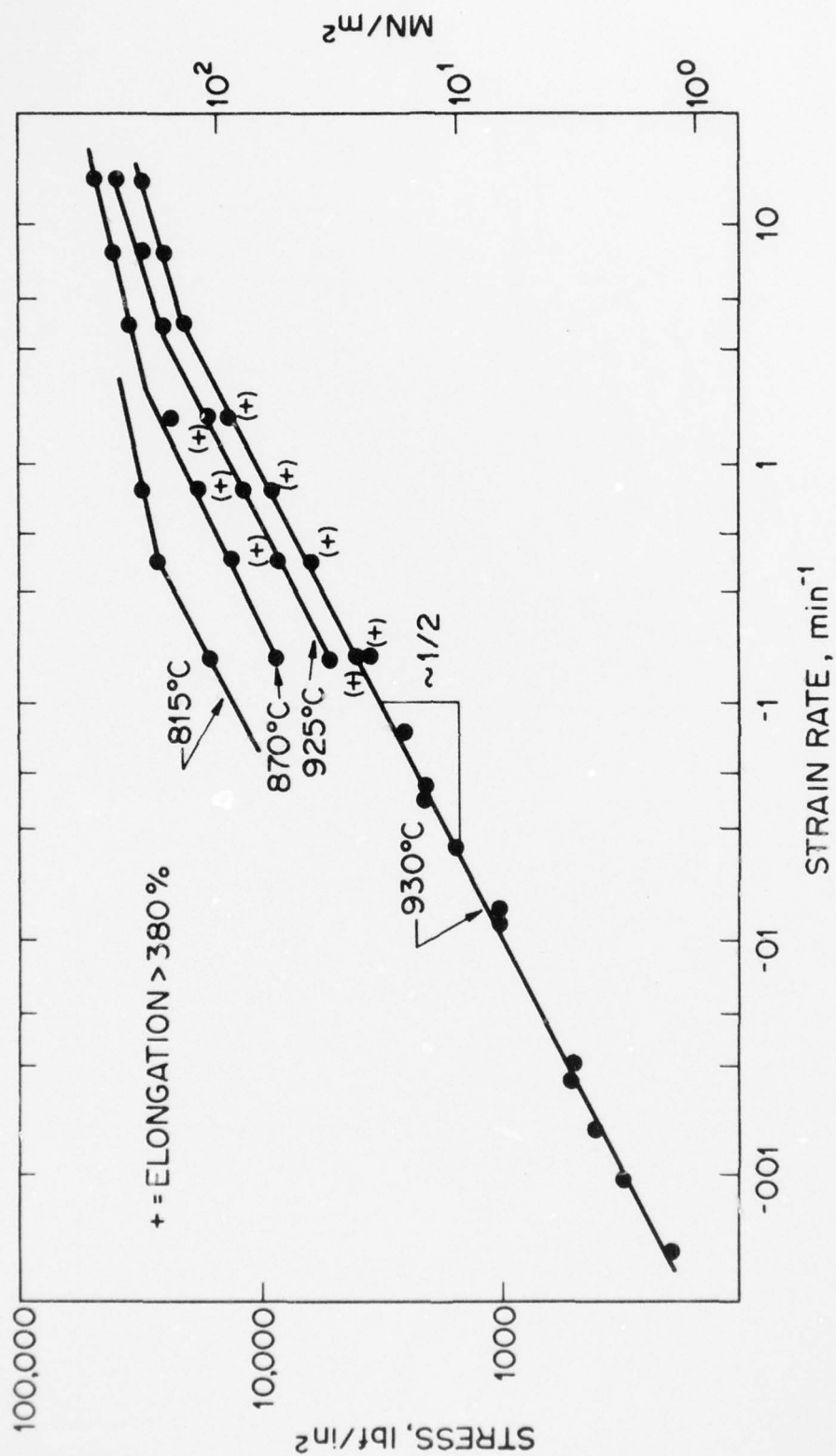


Figure 7. Data of Hayden, Gibson, Merrick and Brophy, 1967.

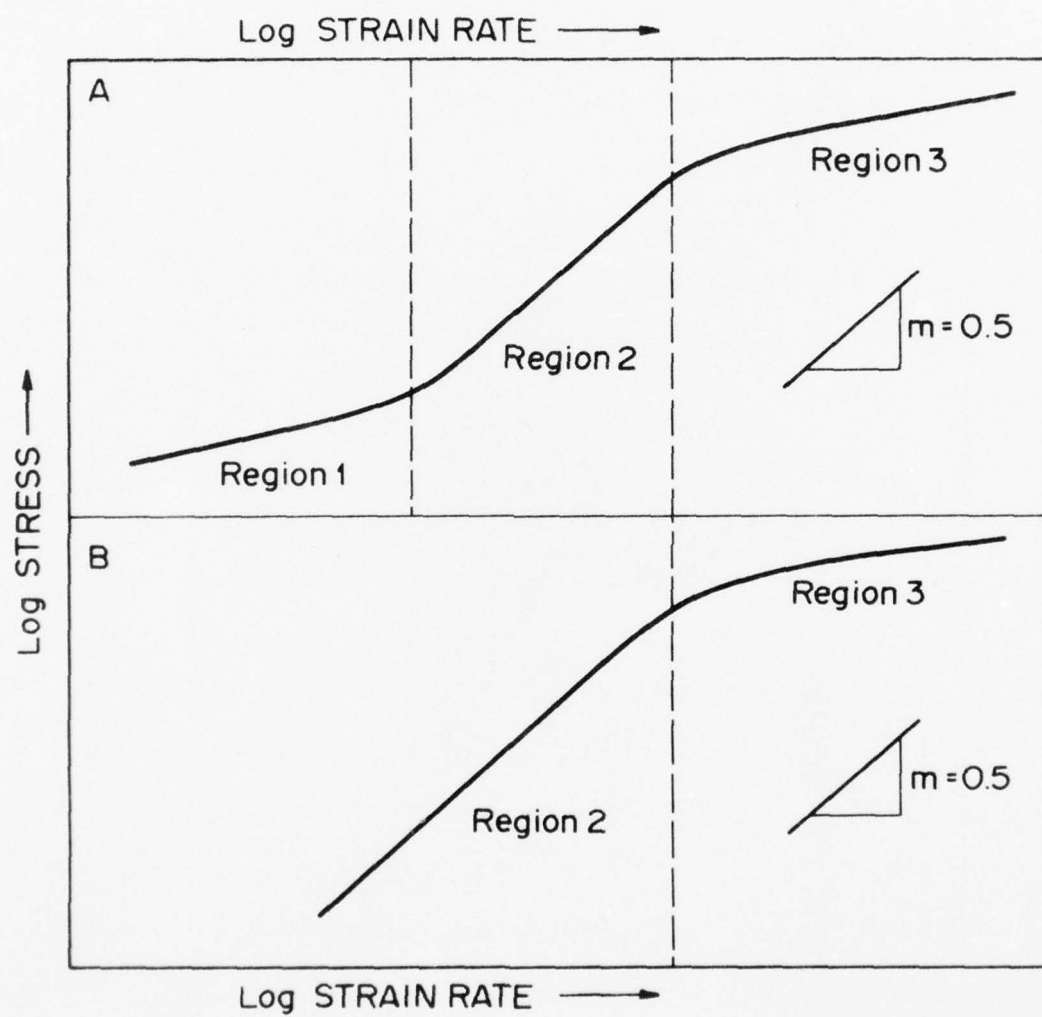


Figure 8.

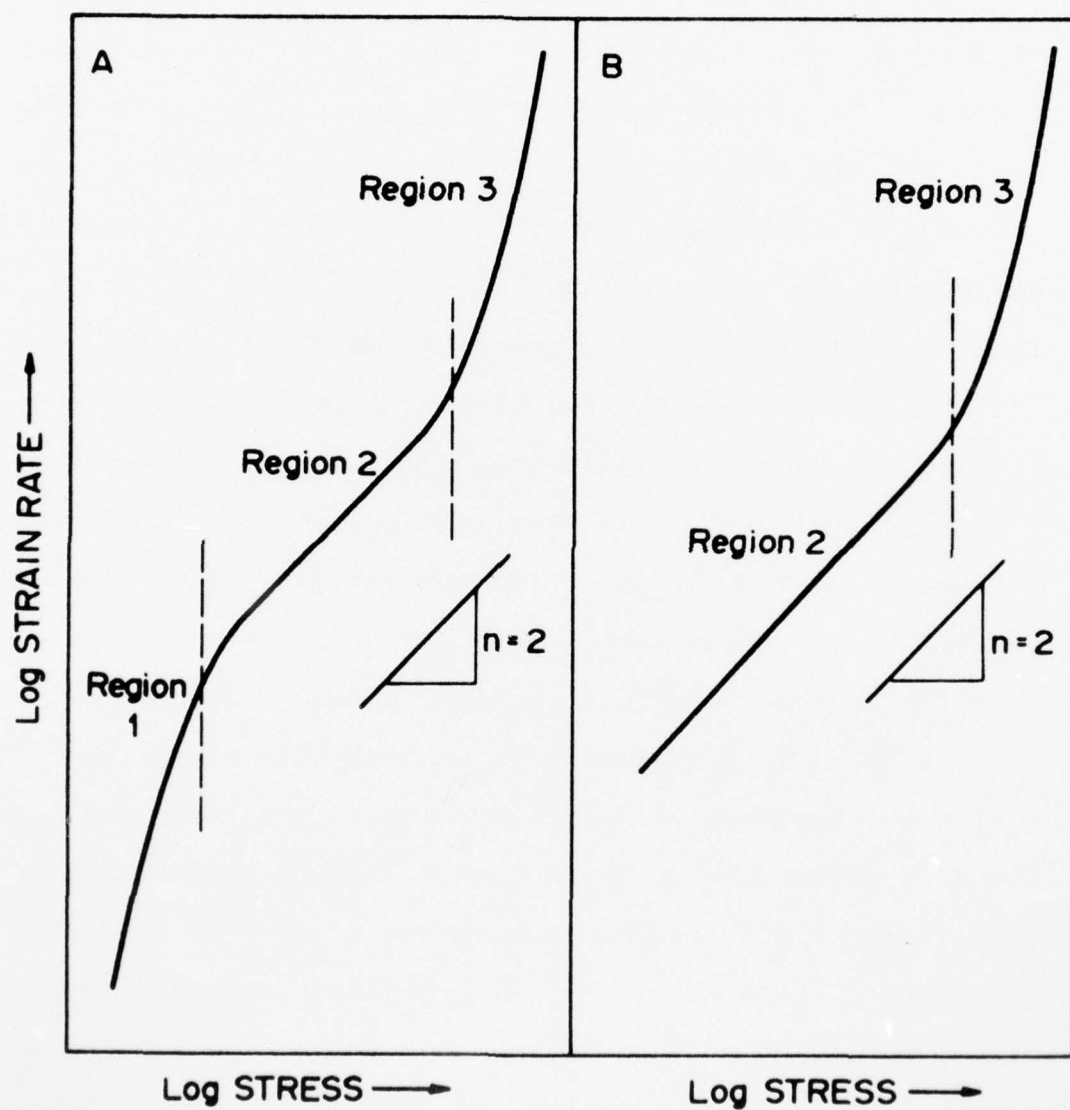


Figure 9.

ations given to region 2 and 1 are described below.

Microstructural Characteristics of Superplastic Deformation

Microstructural investigations on superplasticity revealed that the small grains associated with superplastic deformation (region 2) remain equiaxed and grain boundaries are smooth and curved. (Packer and Sherby 1976, Alden 1967, Alden and Schadler 1968, Dingley 1970). Few dislocations are observed in the grains and no subgrain boundaries are formed. (Hayden, Gibson, Merrick and Brophy 1967, Dunlop and Taplin 1971, Nicholson 1972). Slip lines are not seen on polished surfaces (Dingley 1970, and Geckinli 1973) and extensive grain boundary sliding and grain rotation are observed indirectly by displacements of surface scratches (Holt 1968, Lee 1969) and directly during deformation in the scanning electron microscope (Dingley 1970, Geckinli 1973). It is, therefore, generally believed that the deformation in region 2 is associated with grain boundary sliding.

There is very little experimental data available for region 1. However, it has been reported that there is less grain boundary sliding in region 1 than in region 2 (Holt 1968) and some evidence of grain elongation (Holt and Backofen 1966). In accord with observations of this type, Hart (1967a) and Alden (1969) suggested that dislocation climb may control the deformation rate in region 1. Ashby and Verrall (1973) consider that region 1 is associated with a threshold stress (involving grain boundary tension), developed a theory to explain the sigmoidal shape observed. Rai and Grant (1975) consider that grain growth

of the very fine grains during high temperature deformation will lead to an increase in strength and will result in region 1; thus, they conclude that it is a false region associated with grain growth. Conflicting data exist with respect to evidence for region 1 based on studies in the same system. For example, Hohamed and Langdon (1975) show sigmoidal behavior of the type depicted in Figure 8 for creep of monotectoid composition Al-Zn; on the other hand, Vaidya, Murty and Dorn (1973) and Misro and Mukherjee (1972) show no region 1, and in fact, show m increasing in region 1 approaching m values of unity which they attribute to Coble creep. Although there is controversy on the interpretation of region 1 we believe it is likely associated with a strengthening effect from grain growth and not with a grain boundary tension threshold stress effect.

Summary of Conditions, Including Microstructural Aspects,
for Fine Structure Superplasticity

In addition to the requirement that fine grains are needed for fine structure superplasticity, it appears that a number of other prerequisites usually need to be fulfilled. We list the following as a guide to obtaining maximum superplasticity.

1. ultrafine grain size (typically 1 to 5 μ m)
2. usually a two phase material is required. The purpose of the second phase is to prevent grain growth of the matrix phase.
3. second phase should have about the same strength as matrix phase. If the second phase is much stronger than matrix phase cracks may form at interphase boundary (e.g., alumina in copper).

4. $T \approx 0.4$ to $0.7T_m$. If above $0.7T_m$, grain growth can occur, minimizing superplastic effect. If below $0.4T_m$, dislocation mechanisms may dominate plastic flow leading to non-superplastic behavior.

5. $\dot{\epsilon}$ is typically low ($\dot{\epsilon} = 10^{-6}$ to 10^{-4} sec^{-1})

6. m should be high (0.4 to 0.6)

7. the grain boundaries should be high angle (disordered) boundaries. See example for eutectoid composition steel given in Fig. 10.

8. grain boundaries should be mobile (minimize stress concentration) and should not be prone to ready tensile separation (e.g., polycrystalline ceramics).

When a eutectoid composition steel is warm worked, a fine structure of ferrite grains and cementite particles is developed. (See Fig. 10.) The ferrite grain boundaries, however, consist of a mixture of high and low angle boundaries. Such a material is not superplastic; the m values are typically about 0.3 and only 100% elongation is obtained. If the steel is cold worked and recrystallized, high angle boundaries are obtained and the material is superplastic ($m = 0.5$ and elongations exceeding 400% are readily achieved).

The data given in Figure 11 illustrate that the activation energy for superplastic flow of many fine structure materials is equal to the activation energy for grain boundary diffusion. Some fine structure materials, however, exhibit a

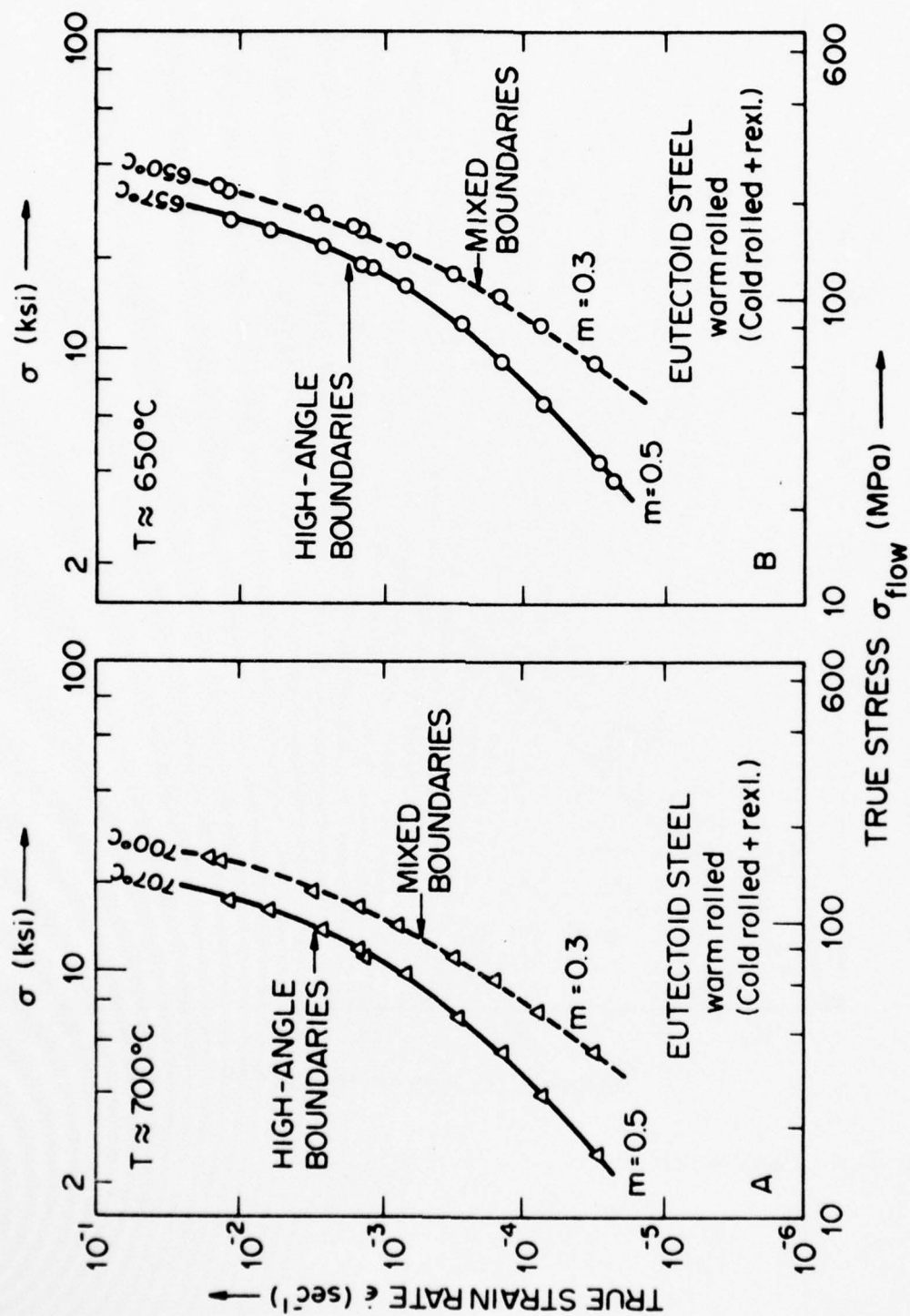


Figure 10. Data from Kayali, 1976.

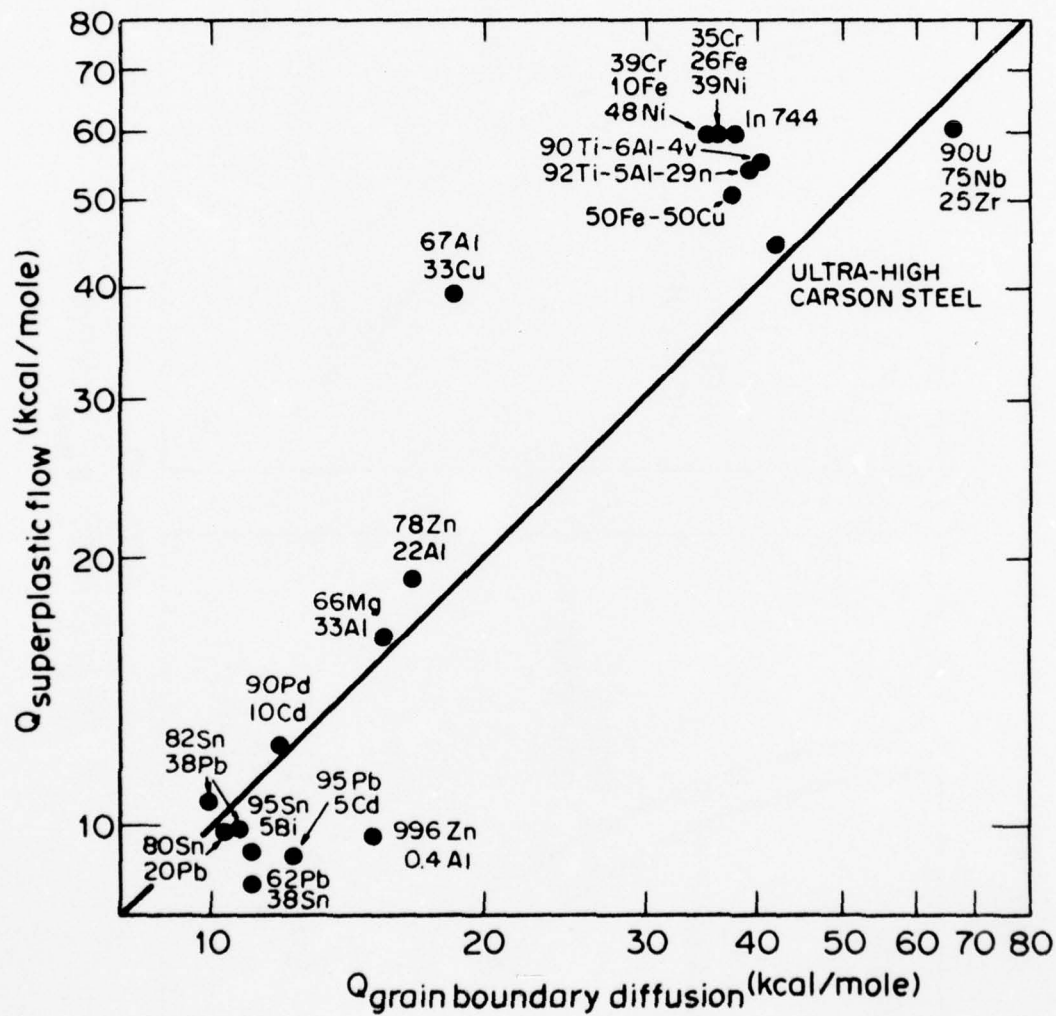


Figure 11. Data from White, 1976.

an activation energy for superplastic flow which is higher than that for grain boundary diffusion suggesting that lattice diffusion may be controlling the plastic flow process in these cases.

Phenomenological Equations for Superplastic Flow and for Slip Creep Flow

Data from various investigators suggest that the creep rate of many fine structure superplastic materials obey the following constitutive relation:

$$\dot{\epsilon} = 10^8 \frac{D_{gb} \cdot b}{L^3} \left(\frac{\sigma}{E} \right)^2 \quad (1)$$

Here D_{gb} is the grain boundary diffusion coefficient, b is burgers vector, L is the grain size, σ is the flow stress and E is the elastic modulus.

Since some superplastic materials exhibit activation energies for plastic flow that are nearly equal to those for lattice diffusion (see Figure 11 above), it is tempting to suggest that an effective diffusion coefficient should be used to correlate all the superplasticity data. Thus,

$$D_{eff} = D_L f_L + D_{gb} f_{gb} \quad (2a)$$

where f_L and f_{gb} are the fraction of atoms associated with the lattice and grain boundary respectively. f_L is about unity and f_{gb} is equal to $\frac{\pi w}{L}$ where w is the grain boundary width. Equation (2a) can thus be rewritten as

$$D_{eff} = D_L + D_{gb} \frac{\pi w}{L} \quad (2b)$$

If the concept of an effective diffusion coefficient is valid then equation (1) and (2) can be combined to yield

$$\dot{\epsilon} = \frac{10^8}{\pi} \frac{D_{\text{eff}}}{L^2} \left(\frac{b}{w} \right) \left(\frac{\sigma}{E} \right)^2 \quad (3)$$

We have found equation (3) to fit virtually all of the fine-structure superplasticity data provided the grain boundary width is assumed to be a function of the melting temperature of the material [namely $w \propto (T_m)^3$] which is not an unreasonable assumption.

The use of equation (1) with the known constitutive relation for plastic flow by slip creep permits us to determine the various factors that can be utilized to optimize the range of stress, strain rate and temperature over which superplastic mechanisms will dominate the plastic flow process.

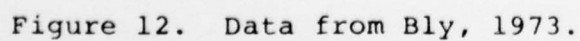
The constitutive equation for slip creep is given as

$$\dot{\epsilon} = \frac{K}{\alpha^5} \frac{D_L}{b^2} \left(\sinh \alpha \frac{\sigma}{E} \right)^5 \quad (4)$$

where α is a constant about equal to the reciprocal of the value of σ/E where power law breakdown occurs. K is a constant equal to 10^{11} for many bcc and fcc materials with high stacking fault energies; it is also a function of stacking fault energy and of texture (especially with hcp materials).

In the following we illustrate how we can use equation (1) and (4) to enhance the range where superplastic flow predominates.

The grain boundary diffusion coefficient for various metals is plotted as a function of the reciprocal homologous temperature. (See Figure 12.) It can be seen that D_{gb} is



uniquely a function of the absolute melting temperature, T_m , and can be described by the equation, $D_{gb} = 1 \exp - \frac{11T_m}{T}$ (in cm^2/sec). The lattice diffusion coefficient, D_L , on the other hand, is a function of crystal structure as well as of T_m .

Crystal structure can influence the extent of superplastic flow since $\dot{\epsilon}$ slip creep is a function of crystal structure (Eq. 4) whereas $\dot{\epsilon}$ superplastic is not for many materials (Eq. 1). The correlation shown in Fig. 13 was made at $T = 0.6T_m$ and for a grain size of $2\mu\text{m}$.

Grain size is the most important single factor influencing the range of superplastic flow since $\dot{\epsilon}$ superplastic is proportional to L^{-3} (equation 1) whereas $\dot{\epsilon}$ slip creep is not a function of grain size. Figure 14 illustrates the strain rate-flow stress relationship for a 1.6%C steel at 700°C . For a grain size of $L = 2\mu\text{m}$ superplastic flow is expected up to a strain rate of 10% per minute; if the grain size is decreased to $0.4\mu\text{m}$ superplastic flow can be expected to occur up to strain rates as high as 5000% per minute.

Tungsten enhances the creep resistance of nickel in the slip creep region by decreasing the stacking fault energy. On the other hand, $\dot{\epsilon}$ superplastic is unaffected by stacking fault energy. Thus, the extent of superplastic flow may be broadened by solute additions which decrease the stacking fault energy of the matrix. (See Figure 15.)

Texture can be an important variable in influencing the creep rate in the slip creep region. This is shown for textured

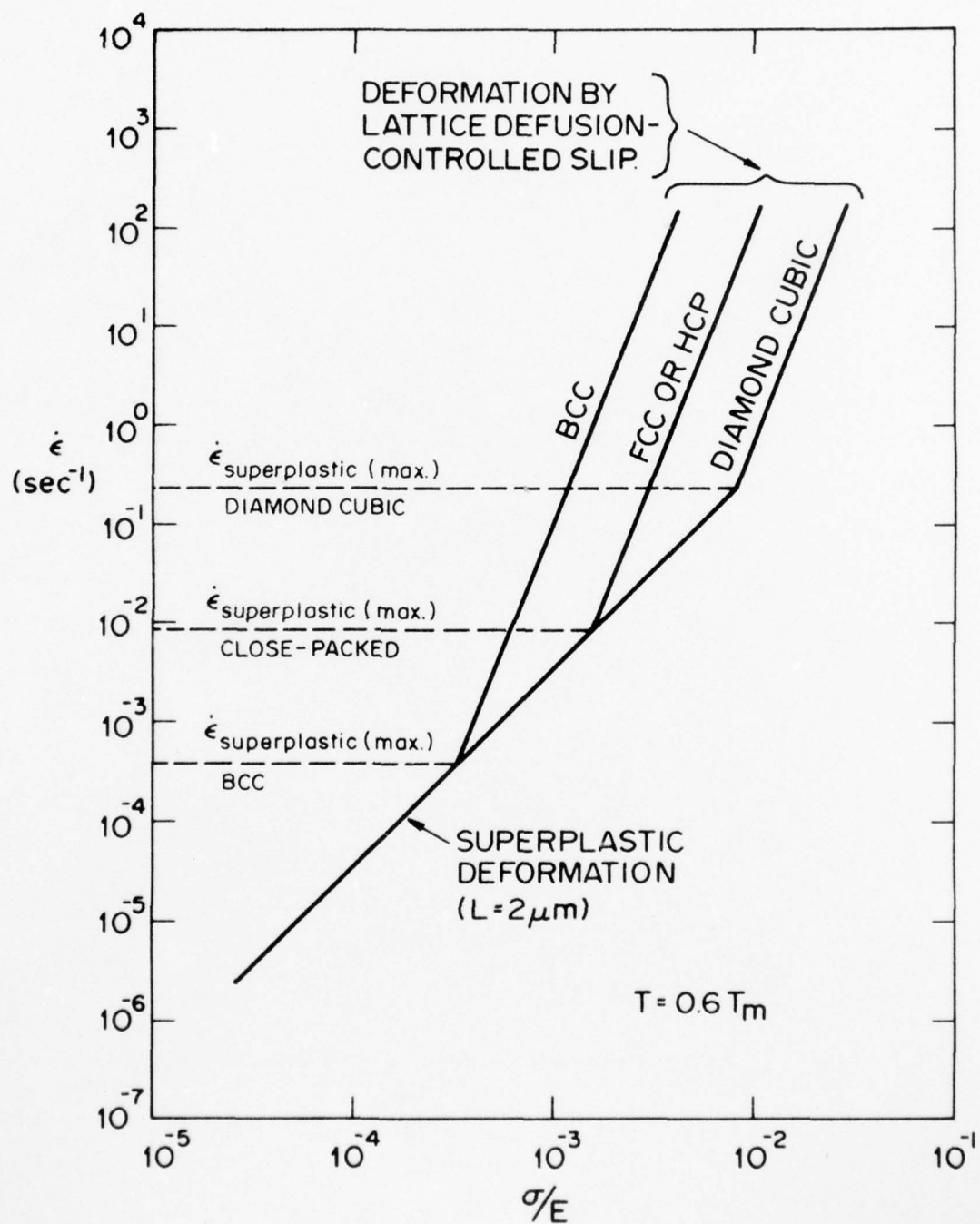


Figure 13.

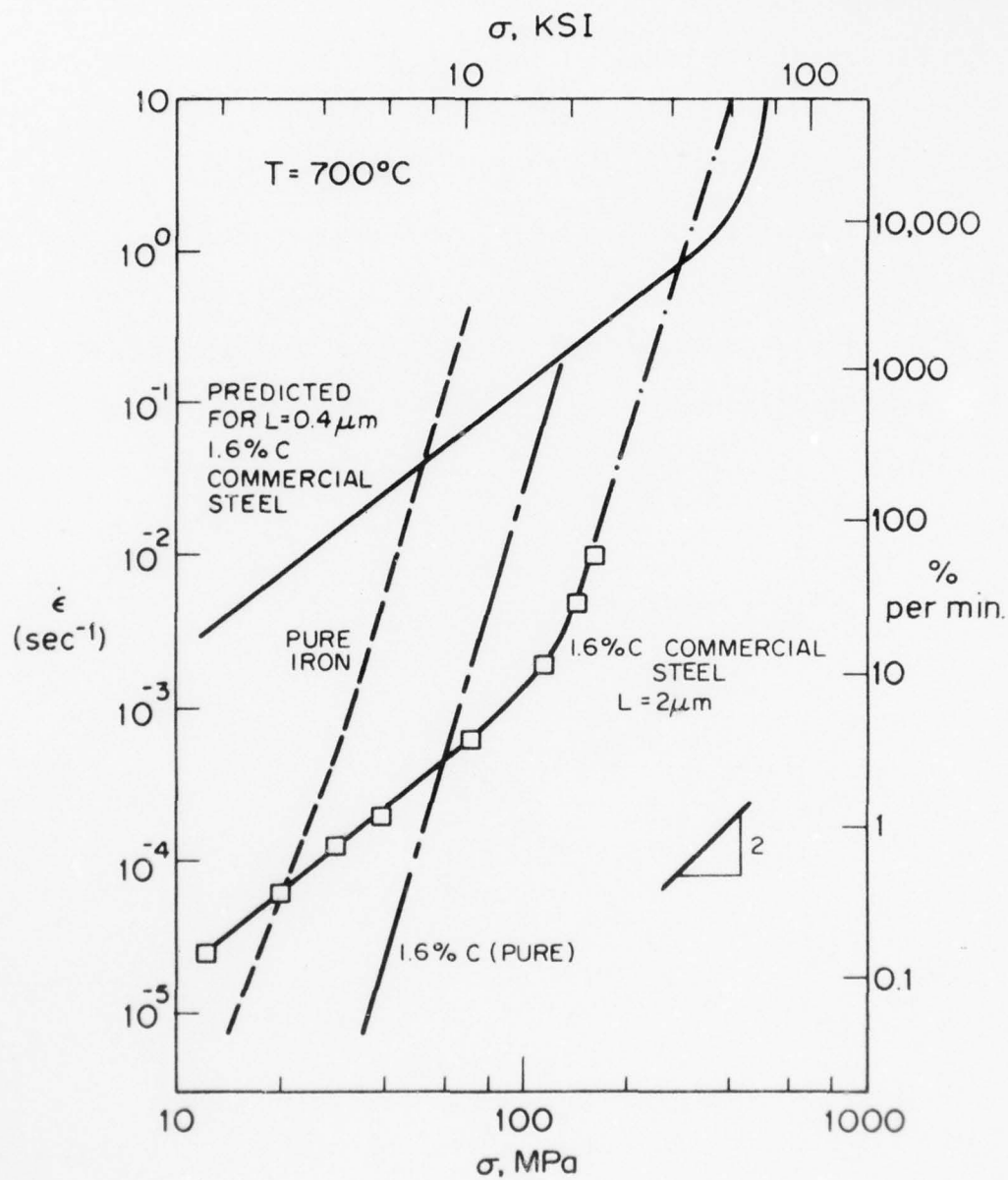


Figure 14. Data of Walser and Sherby, 1975.

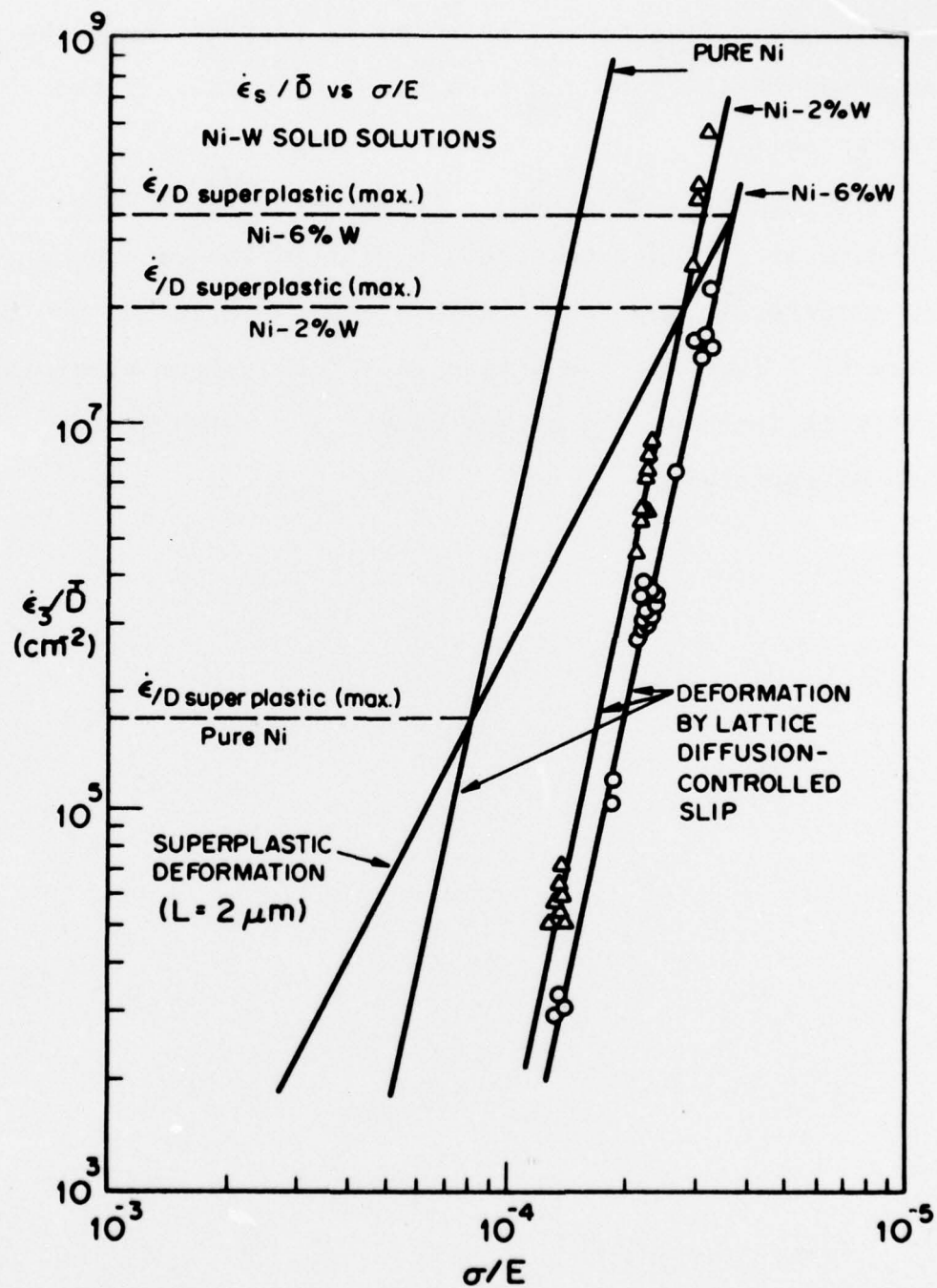


Figure 15. Data from Johnson, Barrett and Nix, 1972.

polycrystalline zinc which exhibits large differences in creep rates when tested in a longitudinal and transverse sense. If superplastic flow is not affected by texture, then the extent of superplastic flow can be altered by this variable. (See Figure 16.).

D_{gb} is less strongly influenced by temperature than D_L (Figure 17). Thus, temperature will influence $\dot{\epsilon}$ superplastic in a different way from $\dot{\epsilon}$ slip creep. Increasing the temperature will increase the strain rate for maximum superplastic flow but will decrease the stress range over which high plasticity can be expected.

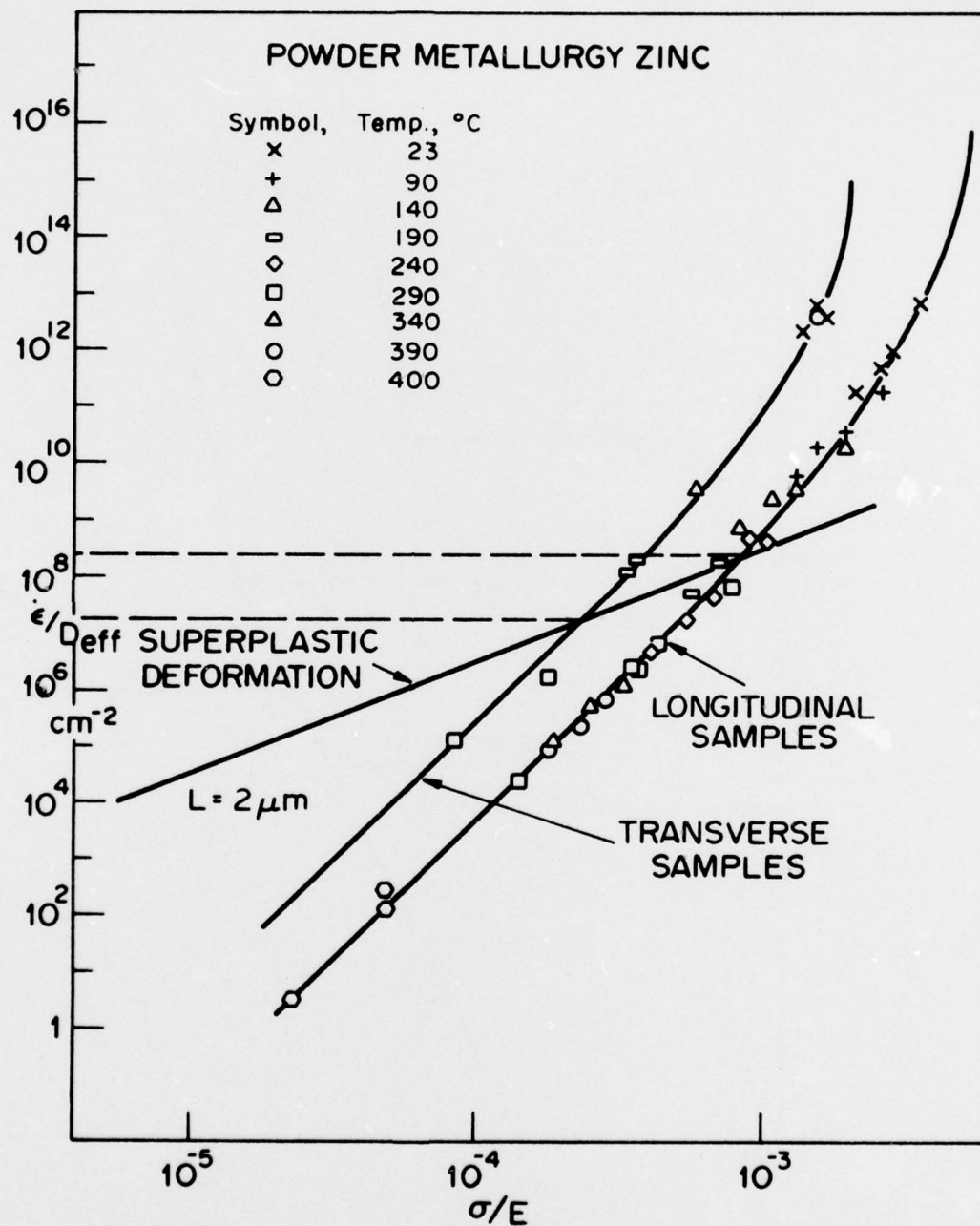


Figure 16. Data from Edwards, McNelley and Sherby, 1974.

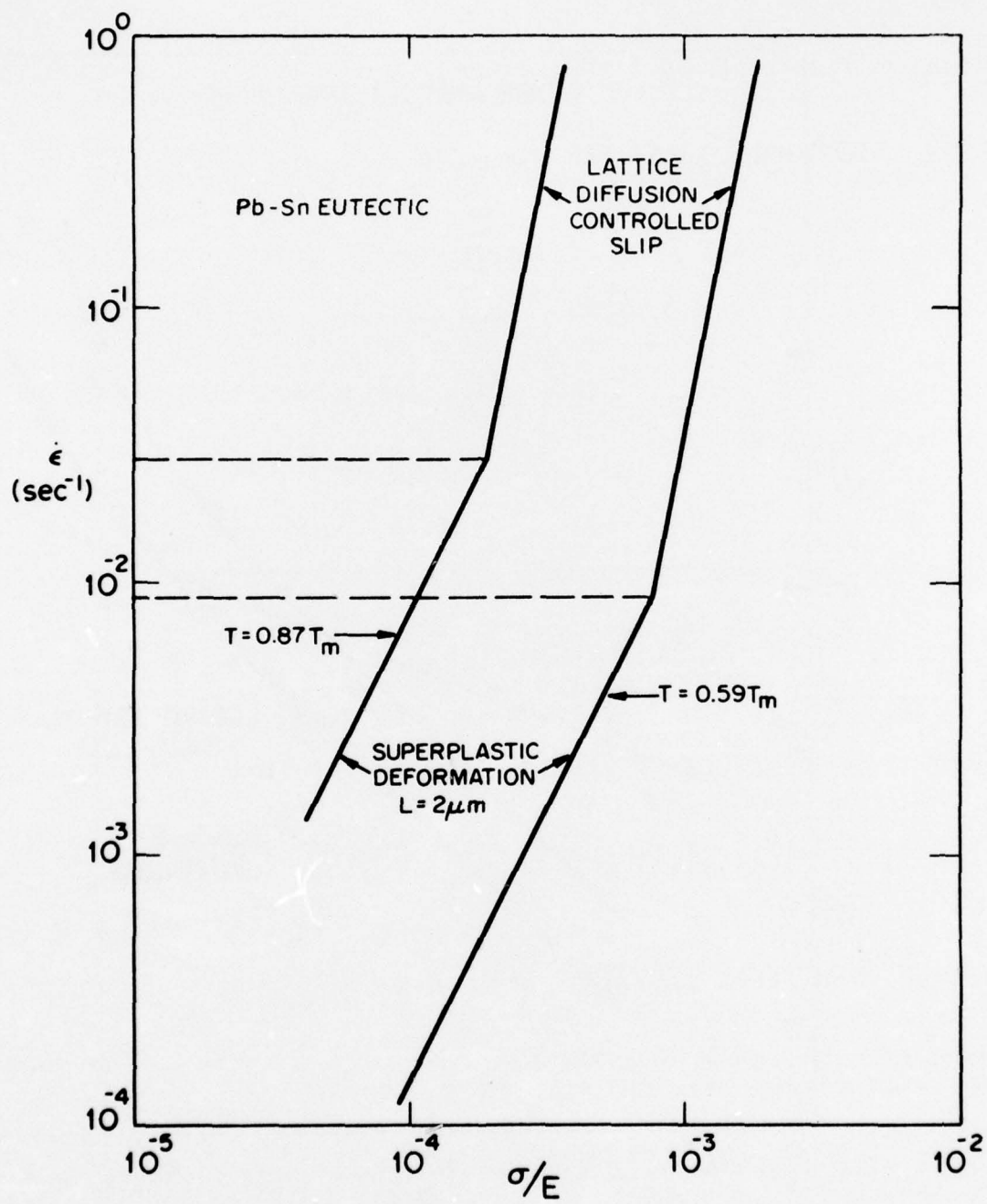


Figure 17.

REFERENCES

- Adda, and Kirianenko, A., 1962, J. Nuc. Mat., 6, 130
- Alden, T. H., 1976, Acta Met., 15, 469.
- Alden, T. H., 1968 ASM Trans. Quart., 61, 559.
- Alden, T. H., 1969, J. Aust. Inst. Metals, 14, 207.
- Alden, T. H., 1975, in Treatise on Materials Science and Technology, Vol. 6, ed. R. J. Arsenault, Academic Press, New York, p. 225.
- Armstrong, P. E., Eash, D. T. and Hockett, J. E., 1972, J. Nuc. Mat., 45, 211.
- Ashby, M. F., and Verrall, R. A., 1973, Acta Met., 21, 149.
- Avery, D. H., and Stuart, J. M. 1968, in Surfaces and Interfaces II, Physical and Mechanical Properties, ed. J. J. Burke, N. L. Reed and V. Weiss, Syracuse University Press, Syracuse, New York, p. 371.
- Bly, D., Ph.D. Dissertation, Department of Materials Science and Engineering, Stanford University, 1973.
- Bochvar, A. A. and Seiderskaya, Z. A., Izvestia Acad. Nauk, USSR, OTN, 1945, 9, 821.
- Burke, J. J., and Weiss, V., 1970, Ultrafine Grain Metals, Syracuse University Press, Syracuse, New York.
- Burke, M. A., and Nix, W. D., 1975, Acta Met., 23, 793.
- Chaudhari, P., 1967, Acta Met., 15, 1777.
- Chubb, W., 1955, Trans. AIME, 203, 189.
- Conway, J. B. and Flagella, P. N., 1969, Creep-Rupture Data for the Refractory Metals to High Temperatures, Nuclear Systems Programs Technical Report GEMP-685 [R-69-NSP-9], General Electric Company.
- Davies, G. J., Edington, J. W., Cutler, C. P., and Padmanabhan, K. A., 1970, J. Mater. Sci., 5, 1091.
- de Jong, M., and Rathenau, G. W., 1961, Acta Met., 9, 714.
- Dingley, D. J., 1970, in Proc. of the 3rd Annual Scanning Electron Microscope Symposium, Chicago, p. 329.

- Dunlop, G. L., and Taplin, D. M. R., 1972, J. Mater. Sci., 7, 84.
- Edwards, G. R., McNelley, T. R., and Sherby, O. D., 1974, Scripta Met., 8, 475.
- Geckinli, A. E., 1973, Ph.D. Thesis, Dept. of Materials Science, Stanford University, Stanford, California.
- Gittus, John, Creep, Viscoelasticity and Creep Fracture in Solids (Chapter II), Applied Science Publishers Ltd., London, 1975, 509.
- Green, W., 1959, Trans. AIME, 215, 1057.
- Greenwood, G. W. and Johnson, R. H., 1965, Proc. Roy. Soc., A283, 403.
- Hart, E. W., 1967a, Acta Met., 15, 1545.
- Hayden, G. W., Gibson, R. C., Merrick, H. F., and Brophy, J. H., 1967, Trans. ASM, 60, 3.
- Holt, D. L., 1968, Trans. AIME, 242, 25.
- Holt, D. L., and Backofen, W. A., 1966, ASM Trans. Quart., 59, 755.
- Johnson, R. H., 1970, Met. Rev., 15, 115.
- Johnson, R. H. and Greenwood, G. W., 1962, Nature, 195, 138.
- Johnson, W. R., Barrett, C. R., and Nix, W. D., 1972, Met. Trans. 3, 963.
- Kayali, E. S., Ph.D. Dissertation, Department of Materials Science and Engineering Stanford University, 1976.
- Lee, D., 1969, Acta Met., 17, 1057.
- Lobb, R. C., Sykes, E. C. and Johnson, R. H., 1972, Met. Sci. J., 6, 33.
- Misro, S. C., and Mukherjee, A. K., 1972, in Proc. of John Dorn Memorial Symposium. Amer. Soc. Metals, Metals Park, Ohio (to be published).
- Mohamed, F. A., and Langdon, T. G., 1975, Acta Met., 23, 117.
- Morrison, W. B., 1968, Trans. ASM, 61, 423.
- Mukherjee, A. K., 1975, in Treatise on Materials Science and Technology, Vol. 6, ed. R. J. Arsenault, Academic Press, New York, p. 163.

- Mullendore, A. W. and Grant, N. J., 1954, Trans. AIME, 200, 973.
- Nicholson, R. B., 1972, in Electron Microscopy and the Structure of Materials, ed. G. Thomas, R. M. Fulrath, and R. M. Fisher, Univ. of California Press, Berkeley, p. 689.
- Oelschlagel, D. and Weiss, V., 1966, Trans. ASM, 59, 143.
- Packer, C. M., and Sherby, O. D., 1967, Trans. ASM, 60, 21.
- Rai, G., and Grant, N. J., 1975, Met. Trans. 6A, 385.
- Robinson, S. L., Armstrong, P. E. and Sherby, O. D., 1972, J. Nuc. Mat., 46, 293.
- Rosenhain, W., Haughton, J. L., and Bingham, K. E., 1920, J. Inst. Metals, 23, 261.
- Rossard, C., 1966, Rev. Met., 63, 225.
- Sherby, O. D., 1969, Science Journal, 5, 75.
- Shorshorov, M. H., Tichonov, A. S., Bulat, C. I., Gurov, K. P., Nadirashvili, N. I. and Antipov, V. Z., Superplasticity in Metallic Materials, Uzdatelsvo, "Nauk", Moscow, 1973.
- Stewart, M. J., 1976, Met. Trans. 7A, 399.
- Underwood, E. E., 1962, J. Metals, 914, 919.
- Vaidya, M. L., Murty, L. K., and Dorn, J. E., 1973, Acta Met., 21, 1615.
- Walser, B., and Sherby, O. D., 1975, Second Annual Progress Report to Advanced Research Projects Agency, Center for Materials Research, Stanford University, Stanford, Ca.
- White, R., Ph.D. Dissertation, Department of Materials Science and Engineering, Stanford University, 1976.
- Wilcox, B. A., and Clauer, A. H., 1966, Trans. AIME, 236, 570.

PROSPECTS FOR SUPERPLASTICITY IN CERAMICS:
A PRELIMINARY APPRAISAL

A. G. Evans, R. L. Coble, R. M. Cannon

INTRODUCTION

The fabrication of ceramic parts with complex geometries is usually achieved by powder compaction (e.g., using injection moulding, slip casting, isostatic pressing) followed by sintering. However, the materials manufactured by this technique are generally inferior to those formed by hot pressing. It would thus be desirable to devise a procedure for forming complex parts that would generate microstructures comparable to those produced by hot pressing. Superplastic forming is such a possibility.

Superplastic deformation is achieved whenever plastic instabilities (necking) and elastic instabilities (fracture) are deferred to large strains. Herein these separate instabilities are examined for ceramic polycrystals, as needed to assess the potential for superplastic deformation in ceramic systems.

PLASTIC INSTABILITY

Plastic stability is related to the strain-rate, $\dot{\epsilon}$, sensitivity of the plastic flow stress, σ_y ; such that plastic stability is realized whenever the strain rate exponent, m , defined by;¹

$$m = \left(\frac{\partial \ln \dot{\epsilon}}{\partial \ln \sigma} \right) \quad (1)$$

attains a value approaching unity. Most ceramic systems exhibit major deformation anisotropy and it is usually impossible to achieve a general strain by dislocation motion at temperatures below that at which deformation by diffusion and grain boundary sliding begin to predominate. Hence, when significant deformation does occur, it tends to be diffusion controlled. Further, at fine grain sizes (Fig. 1), the diffusional deformation is usually manifested as Coble or Nabarro-Herring creep; these are processes that yield relatively large m values. In fact, plots of m derived from creep data for two fine-grained polycrystalline ceramics^{2,3} (Fig. 2a,b) show that m values in the range $0.5 < m < 1$ are obtained in these systems for significant regimes of temperature and stress. (Superplastic deformation has been achieved in many metal systems within this range of m .) It would thus appear that the occurrence of plastic instability is unlikely to produce a serious limitation to the superplastic deformation of ceramics.

ELASTIC INSTABILITY

When typical polycrystalline ceramics are subjected to large scale deformation, extensive grain boundary fracture (cavity formation) is generally observed" (Fig. 3). Since plastic instability does not appear to be a problem, this fracture process is clearly the major constraint affecting the attainment of superplasticity. It is crucial, therefore, that the

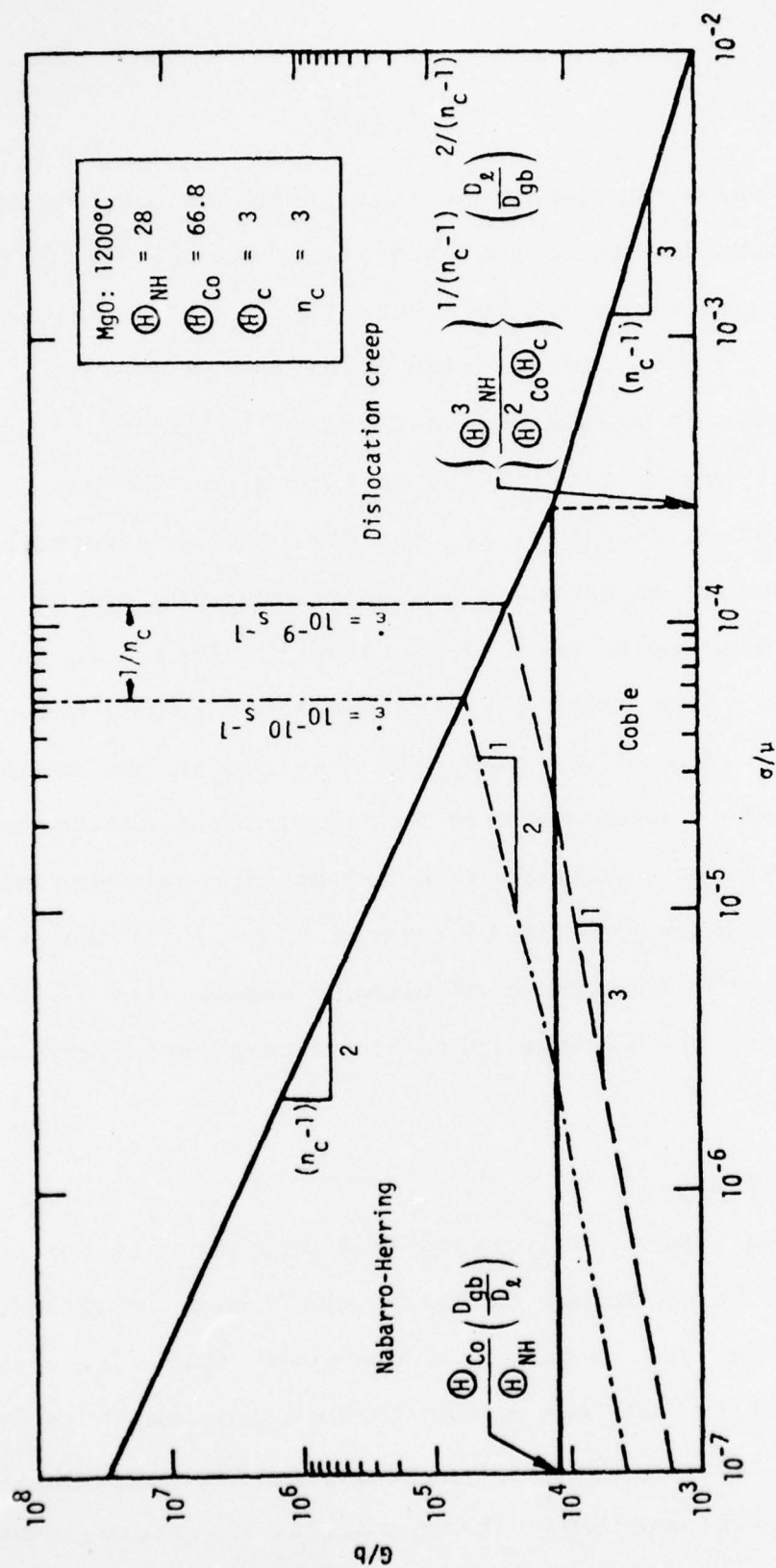
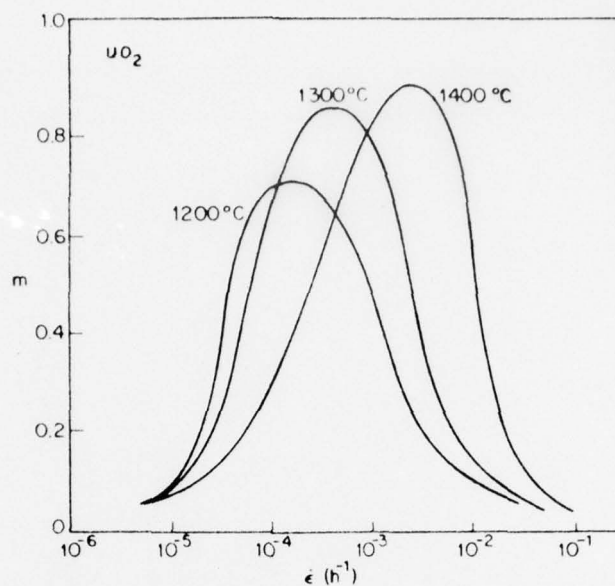


Figure 1. A deformation mechanism map for MgO at 1200°C, indicating the existence of Nabarro-Herring and Coble creep in the fine grain size regime.

(a)



(b)

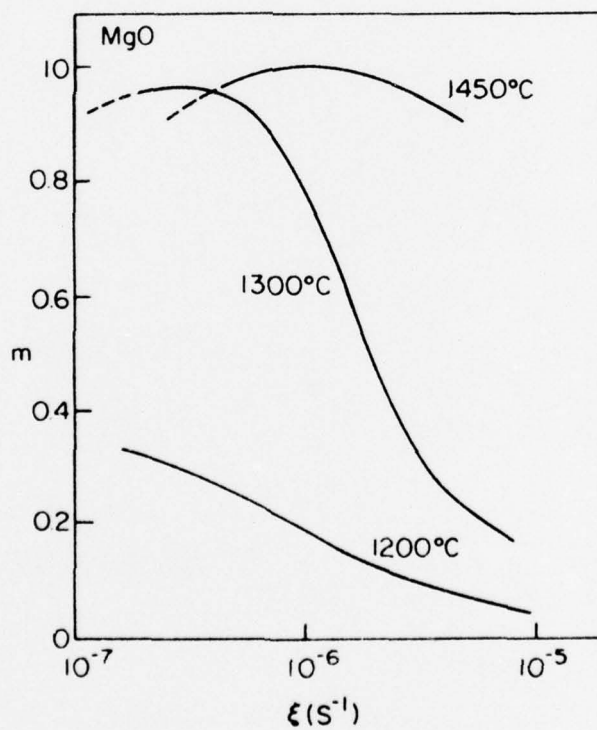


Figure 2. The strain rate dependence of m values for (a) UO_2 , (b) MgO .

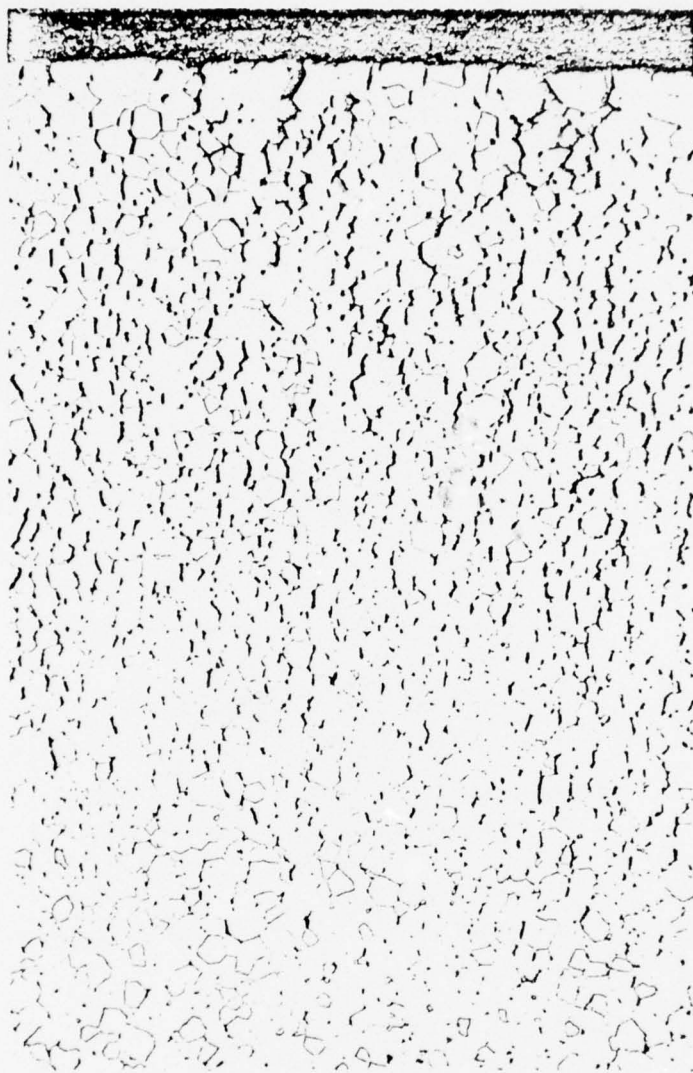


Figure 3. Cavities formed in Al_2O_3 during high temperature flexural creep (Coble⁴).

fracture be evaluated and the prospects for its prevention be assessed.

When a stress is applied to a ceramic polycrystal in the regime where deformation is diffusion controlled, the first relaxation that tends to occur is generally the sliding of those grain boundaries that lie along planes of principal shear stress (Fig. 4). However, sliding at the grain edges (A and B in Fig. 4a) is constrained by the adjacent grains and the sliding distance, δ , diminishes from a maximum at the grain boundary mid-plane to zero at the grain edges (Fig. 4b). The sliding is thus elastically accommodated by the adjacent grains and singularities develop as indicated in Fig. 4c. The singularities will inevitably lead to crack formation above a critical stress intensity factor (or crack opening) unless additional relaxation processes can occur. Four modes of relaxation are possible; (a) dislocation motion, (b) viscous flow (of a boundary phase), (c) diffusion (grain boundary and/or lattice), (d) solution/re-precipitation. Each of these relaxation processes tends to develop parabolic stress distributions along the grain boundaries (Fig. 4d). Hence, the tensile stress developed by sliding are partially relaxed and the resultant stress distribution is expected to exhibit the general form depicted in Fig. 4e, with a maximum (σ_m) at some distance (r_m) from the grain corners. Grain boundary fracture will now occur when the stress, σ_m , exceeds the stress $(\sigma_m)_c$ to extend grain boundary defects (inclusions, voids, etc.) located close to r_m , e.g., at²

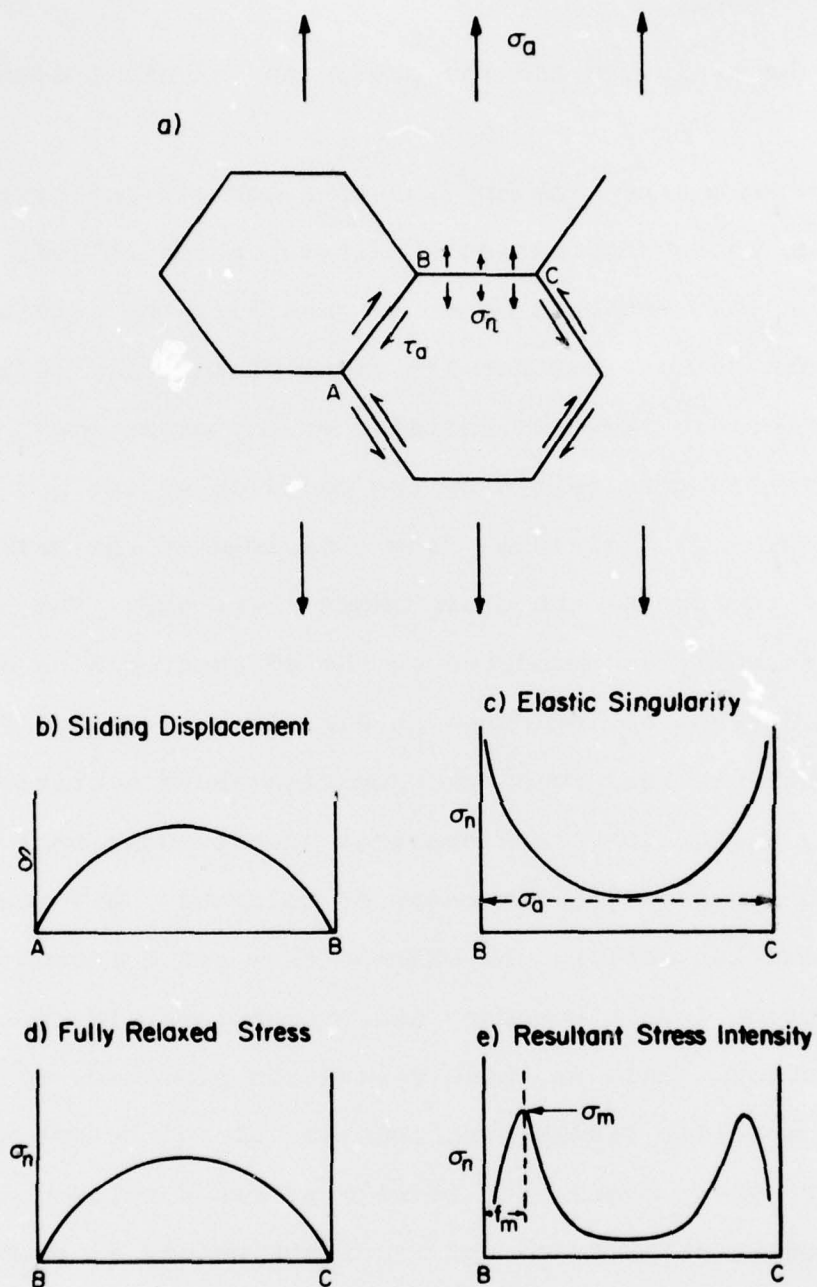


Figure 4. Grain boundary sliding and relaxation phenomena indicating (a) the sliding geometry, (b) the sliding distance, δ , along grain edges AB, (c) the singularity developed by elastic accommodation of the sliding, (d) the stress state in the fully relaxed condition, (e) the resultant stress field for simultaneous sliding and relaxation.

$$(\sigma_m)_c \approx \frac{K_B}{\sqrt{\pi a_D}} \quad (2)$$

where a_D is the defect radius and K_B is the grain boundary toughness. Alternately, when a viscous boundary phase is present, fracture might be controlled by cavity formation; whereupon the negative pressure $p (= \beta \sigma_m)$, where β lies between 0.33 and 1) would be the key parameter, requiring that a critical pressure (p_c) be exceeded, given by;⁵

$$p_c \equiv (\beta \sigma_m)_c \approx \sqrt{\frac{16\pi \gamma_\beta^3}{3kT \ln (NkT/h)}} \quad (3)$$

where γ_β is the surface energy of the boundary phase.

A quantitative model for cavity formation would thus require that the stress distributions that develop due to the simultaneous operation of the important deformation processes be evaluated and included into Eqs. (2) or (3). The complete analysis has not yet been performed; but preliminary estimates of the requirements for cavitation are obtained from a more detailed examination of the separate relaxation processes.

Grain Boundary Sliding

Grain boundary sliding rates, or the associated time constants (τ), have been evaluated for a number of grain boundary processes. The following are the most important for present purposes. Sliding in the presence of a boundary phase of thickness Δ and viscosity η_v is characterized by the time constant⁶;

$$\tau_v = 1.14 (1-v^2) \frac{d\eta_v}{E_\Delta} \quad (4)$$

where d is the grain diameter, and v is Poisson's ratio. Also, the viscosity is related to the diffusivity, D_v , by the Stokes-Einstein relation,

$$\eta_v = \frac{kT}{6\pi r D_v} \quad (5)$$

where r is the radius of the diffusing species.

For clean grain boundaries, the time constant has the same general form as Eq. (4), with Δ replaced by some multiple of the atomic dimension, a_o , or the Burger's vector, b . The equivalent boundary viscosity (η_b) is related to the boundary diffusivity, D_b ; in the extreme case of boundary diffusion between atomic asperities,

$$\eta_b = \frac{kT}{8bD_b} ; \quad (6)$$

while, for sliding limited by the climb of boundary dislocations;

$$\eta_b = \frac{kT}{8bD_b} (\rho\Lambda) \quad (7)$$

where ρ is the dislocation density at the boundary and $\Lambda \sim 3$ to $5b$.

The sliding represented by Eq. (4) is constrained by the adjacent grains (as noted above) and a singularity develops. The stress, time relation for first fracture caused by this singularity, in the absence of other relaxation phenomena, is

$$\sigma_a [1 - \exp(-\tau/t)] > \sigma_c \quad (8)$$

where σ_a is the applied stress, σ_c is the threshold fracture stress. Considering, for simplicity, that the singularity is similar to that for a mode II crack, σ_c is defined by;

$$\sigma_c \approx K_B / \sqrt{\pi L} \quad (9)$$

where $2L$ is the length of a grain edge.

Dislocation Deformation

The number of slip systems that can operate (at closely comparable stress levels) in typical structural ceramics is generally small. For example, in silicon nitride a c-axis Burger's vector pertains,⁷ which only supplies two independent systems. The accommodation of localized strains by intragranular dislocation motion is, thus, small and transient. The role of intragranular dislocation activity in the large scale deformation of structural ceramics is thus expected to be minimal.

Viscous Deformation

For a system of hexagonal grains (Fig. 5a) surrounded by a thin uniform dispersion of viscous phase (Fig. 5b) the deformation is controlled by the flow of liquid from the contracting boundaries into the expending boundaries (Fig. 5b). The deformation rate, $\dot{\epsilon}$, of such a system, when subjected to an applied tension or compression, is given at steady state by;⁶

$$\dot{\epsilon} = \frac{\sigma_a}{\sqrt{3}\eta_v} \left(\frac{\Delta}{L} \right)^3 \quad (10)$$

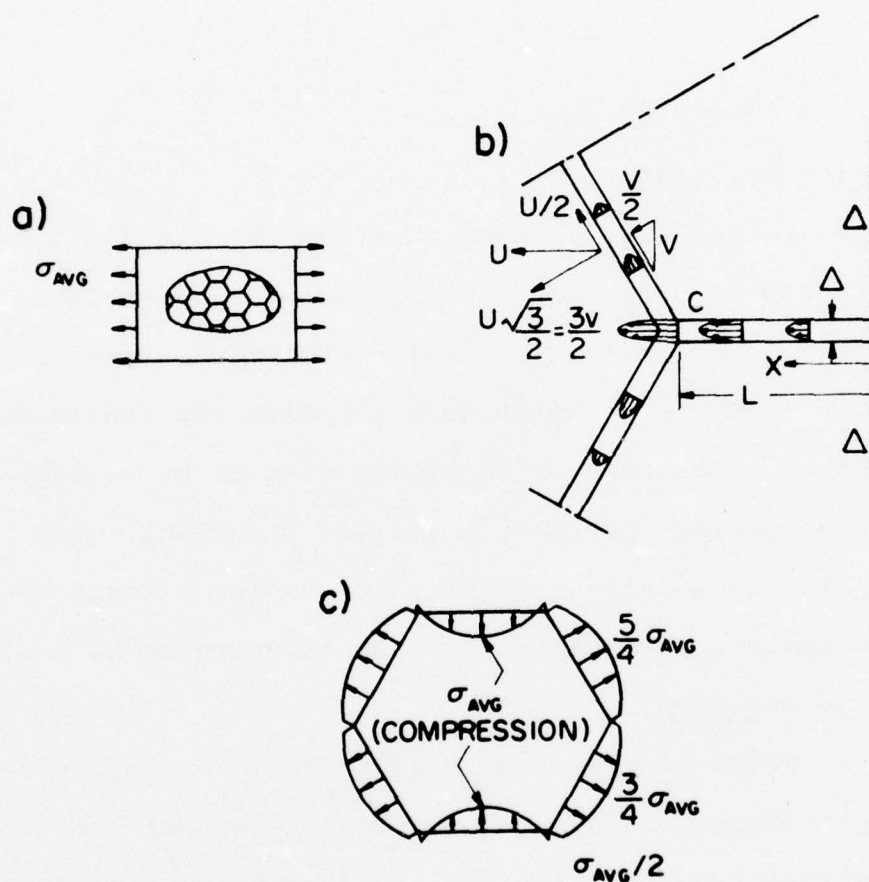


Figure 5. Viscous flow of a boundary phase (a) the hexagonal grain network and the stress state, (b) the movement of the liquid phase, (c) the stress distribution along the boundaries (Drucker⁸).

The stress distribution that results is shown in Fig. 5c. The equivalent expression for adjacent viscous layers of dissimilar thickness (Δ_1 and Δ_2) can be deduced using the same approach, to obtain;

$$\dot{\epsilon} = \frac{2\sigma_a \Delta_2^3}{\sqrt{3} L^3 [1 + (\Delta_2/\Delta_1)^3]} \quad (11)$$

Assuming that the volume is conserved, i.e., that the stress is low enough to prevent cavitation, and noting that

$$\begin{aligned} \Delta_1 &= \Delta_0 + \delta\Delta \\ \Delta_2 &= \Delta_0 - \delta\Delta \\ \epsilon &\approx \delta\Delta/L \end{aligned} \quad (12)$$

(where Δ_0 is the initial boundary width and $\delta\Delta$ is the change in boundary width), the strain dependence of the strain rate is obtained from Eqs. (11) and (12) as;

$$\dot{\epsilon} = \frac{\sigma_a \left(\frac{\Delta_0}{L}\right)^3}{\sqrt{3}} \left[\frac{1 - 3\xi^2 + 3\xi^4 - \xi^6}{1 + 3\xi^2} \right] \quad (13)$$

where $\xi = \epsilon(L/\Delta_0)$. The strain rate thus decreases rapidly with strain (Fig. 6) and approaches zero as ξ approaches unity. Also, significant strains are only realized if Δ_0 is a relatively large fraction of L (e.g., $\geq 30\%$).

Again, therefore, viscous flow of a boundary phase cannot lead to large scale deformation, unless the proportion of viscous phase is large enough to allow substantial grain rotation to occur.

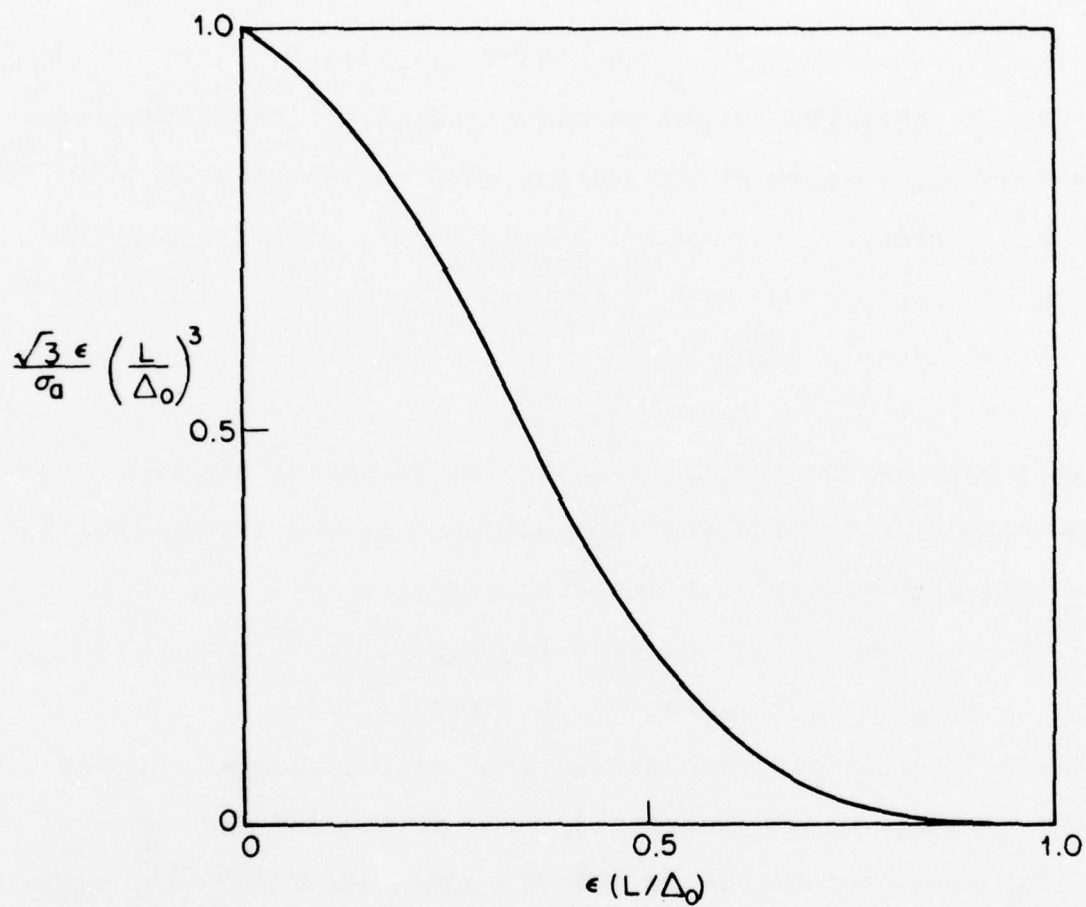


Figure 6. The strain dependence of the strain rate for viscous flow of a boundary phase without cavitation.

Diffusion

The diffusion of vacancies, either through the grains or along grain boundaries, from regions of localized compression to adjacent regions of localized tension can lead to a rapid relaxation of the stresses developed by grain boundary sliding. Also, the diffusional processes can proceed continuously, thereby allowing the large scale deformation required for superplasticity. There are a variety of diffusional processes that could occur, and a corresponding series of time constants, τ_D . For clean grain boundaries, and elastically deformable grains, the longest relaxation times have the general form^{9,10}

$$\tau_D = \frac{\kappa_1 d^2 kT}{D E \Omega C_0} \quad (14)$$

where Ω is the atomic volume, E is Young's modulus, C_0 is the stress free equilibrium concentration of vacancies, κ_1 is a geometric constant (≈ 1), and D is generally the grain boundary diffusivity: while for rigid grains;

$$\tau_D = \frac{\kappa_2 d^2}{D_b} \quad (15)$$

In the presence of a viscous boundary phase, the time constant has a different form¹¹;

$$\tau_D = \frac{32}{3} (1-\nu^2) L^3 \frac{kT}{D_v \Delta \Omega E} \quad (16)$$

PROSPECTS FOR SUPERPLASTICITY

Three possible approaches for achieving superplasticity

can be deduced from the preceding results: (a) the application of large hydrostatic compression to prevent the extension of cavities*, either by careful die design or by performing the operation in an autoclave; (b) the development of a multi-phase microstructure that generates a large fraction of viscous phase at the forming temperature, which can be devitrified when forming is complete (e.g., certain Sialon phases, Fig. 7);¹² (c) the design of a fine scale microstructure which would allow the diffusional relaxation rate to exceed the boundary sliding rate. The prospects for the first two are simple in concept, and might find several useful applications; although these would be limited to simple geometries or to components which do not require good high temperature creep properties. The prospects for the latter require a more detailed examination.

Initial estimates of the potential for superplasticity can be obtained by comparing the time constants for grain boundary sliding, τ_v , and diffusion, τ_D . For example, setting $\tau_D \leq \tau_v$ provides a conservative first order estimate of the superplasticity requirement. The solution of the coupled equations for sliding and diffusion, combined with the crack formation relations (Eqs. 2,3), affords a much superior estimate, although this too could be conservative, because the relaxations due to dislocation motion and/or viscous flow of a boundary phase could exert a limited influence on the peak stress.

*The nucleation of small triple point cavities will still occur.

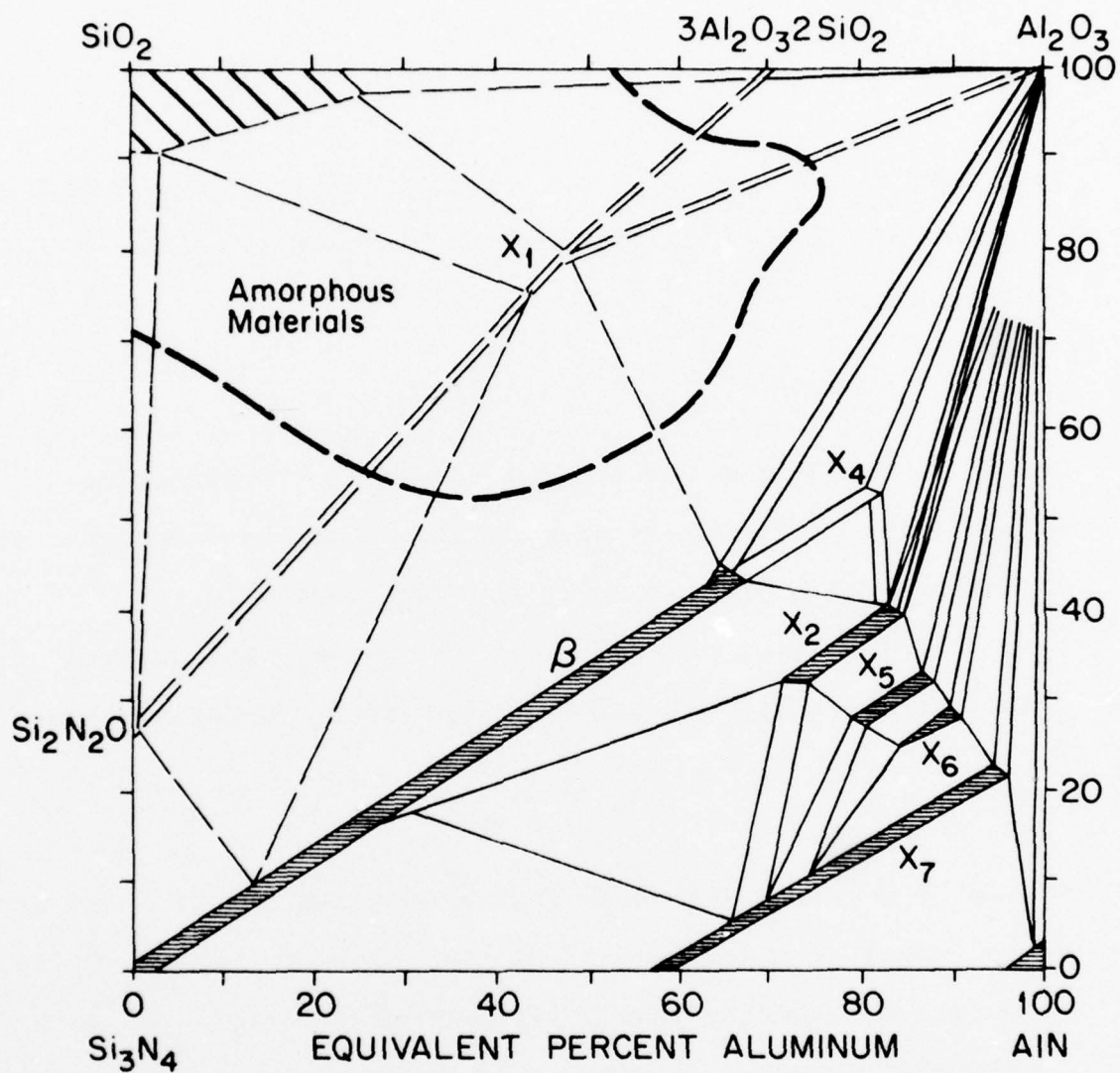


Figure 7. A phase diagram for a Sialon system (using the reciprocal salt solution notation) showing possible regions of extensive amorphous phase formation.

For a material containing a viscous boundary phase, setting the time constant for boundary sliding larger than that for diffusion gives;

$$\frac{\eta_v D_v \Omega}{kT} \gtrsim d^2 \quad (17)$$

Note that the thickness of the boundary layer does not influence the result. Introducing the Stokes-Einstein relation (Eq. 5) then gives;

$$d^2 \gtrsim \frac{\Omega}{6\pi r} \quad (18)$$

Hence, we obtain the impractical result (for crystalline materials) that the grain size should be of the same order as the atomic dimension, in order to avert cavitation.

For a material with clean boundaries, the equivalent result for boundary diffusion between atomic asperities is

$$d \gtrsim \frac{\Omega C_o}{8b^2} \quad (19)$$

The detailed significance of this result can not be fully appreciated until an understanding of the relations between C_o and temperature, impurity level, microstructure, etc., has been developed. However, it does imply that superplasticity should be possible at realistic grain sizes (0.1 to 1 μm) provided that the grain boundary chemistry can be controlled within specified limits.

ACKNOWLEDGEMENT

This research was supported by the Advanced Research Projects Agency of the Department of Defense under Contract No. MDA903-76C-0250 with The University of Michigan.

References

1. J. W. Edington, K. N. Melton and C. P. Cutler, Progress in Materials Science, 21 (1976) 61.
2. A. G. Evans and T. G. Langdon, Progress in Materials Science, 21 (1976) 171.
3. B. Burton and G. L. Reynolds, Acta Met., 21 (1973) 1073.
4. R. L. Coble, published in W. D. Kingery, Science of Ceramics (McGraw-Hill), 1960.
5. J. C. Fisher, J. Appl. Phys., 19 (1948) 1062.
6. E. Mosher and R. Raj, J. Mat. Sci., 49 (1976).
7. A. G. Evans and J. V. Sharp, J. Mat. Sci., 6 (1971) 1292.
8. D. C. Drucker, High Strength Materials (Ed. V. F. Zackay) Wiley, N.Y., 1967.
9. I. M. Lifshitz, Soviet Physics, JETP, 17 (1963) 909.
10. R. M. Cannon and R. L. Coble, Deformation of Ceramics (Ed. R. C. Bradt and R. E. Tressler) Plenum, N.Y. (1976).
11. R. Raj, Met. Trans. A (1975) 1499.
12. L. J. Gaukler, H. L. Lukas and T. Y. Tien, Mat. Res. Bull., 11 (1976) 503.

SYSTEMS FOR STORAGE AND RETRIEVAL OF THERMOCHEMICAL
DATA AND CALCULATION OF PHASE DIAGRAMS

L. Kaufman and H. Nesor

The systems developed by National Physical Laboratory and ManLabs have been coupled to provide a Metallurgical Thermochemical Data Bank for storage and retrieval of data and calculation of binary and ternary phase diagrams. Approximately two thousand data sets for pure elements and compounds are stored providing thermodynamic functions and differences for specific reactions in numerical form. Vapor pressure data for gaseous products and solubility data for gases in metals and dilute alloys covering the Henrian range can be retrieved. Similar data for dilute solutions of metals in pure metals and binary alloys is also accessible. The system can also be used to compute all of the forty-five binary systems composed of the metals iron, chromium, nickel, cobalt, aluminum, niobium, molybdenum, titanium, carbon, and tungsten. This facility is available through explicit descriptions of solution and compound phases generated in terms of lattice stability, solution and compound phase parameter which are employed to calculate the phase diagrams and thermochemical properties of the binary systems. The system can be used for calculation of the one hundred twenty possible ternary systems composed of these metals over a wide

range of temperature. A representative sample of thirty of these ternary systems covering many of the important superalloys has been computed and found to agree favorably with those cases where some phase diagram data are available. The level of agreement attained between calculated and observed diagrams shows that the method provides an important tool for prediction of sigma phase stability, eutectic formation and the location of melting point minima in complex systems. The system operates on data supplied by the user so that other inorganic, ceramic and metallic combinations can be considered. The ManLabs-NPL MATERIALS DATA-BANK is accessible via TSO (time sharing option) through standard teletype terminals which can be connected into the main computer by telephone anywhere in the U.S. and Canada. Users can employ almost any commercial terminal to gain access to the system and interact with the DATABANK.

UNDERCOOLING DURING ATOMIZATION OF
COMPLEX ALLOY POWDERS

R. Mehrabian

During atomization of alloy powders, such as gas atomization, a large number of the particles undercool substantially prior to nucleation of the solid. This is established by examining the microstructure and the distribution of solute within the as-solidified material.

Pre-alloyed coarse powders of maraging 300 steel produced by different techniques were studied using electron microprobe analysis. The solidification structure was so fine that concentration measurements were conducted only at specific points along paths chosen across dendrite arms. Elements analysed were nickel, cobalt and molybdenum. Their average concentrations in this steel were 18.5, 9.0 and 4.8 wt%, respectively. High solute dendrite arm cores were found which indicate that a substantial amount of undercooling occurred prior to nucleation of the droplets.

The microstructure of an undercooled droplet is shown in Figure 1. The light etching in the center of the dendrite arm is evidence of high solute cores signifying undercooled structures. The electron microprobe data taken in the middle of the "light" dendrite arm core (A), the middle of the "dark" dendrite arm shell (B), and at some point within the interdendrite

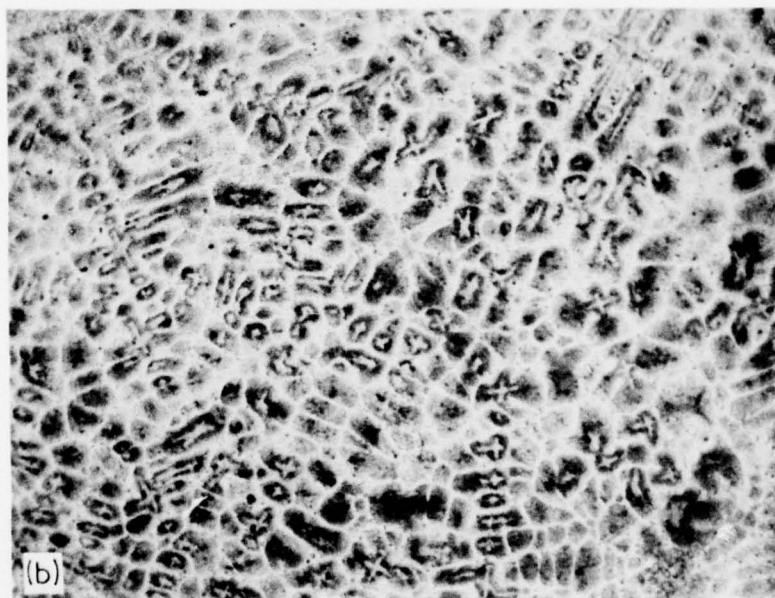
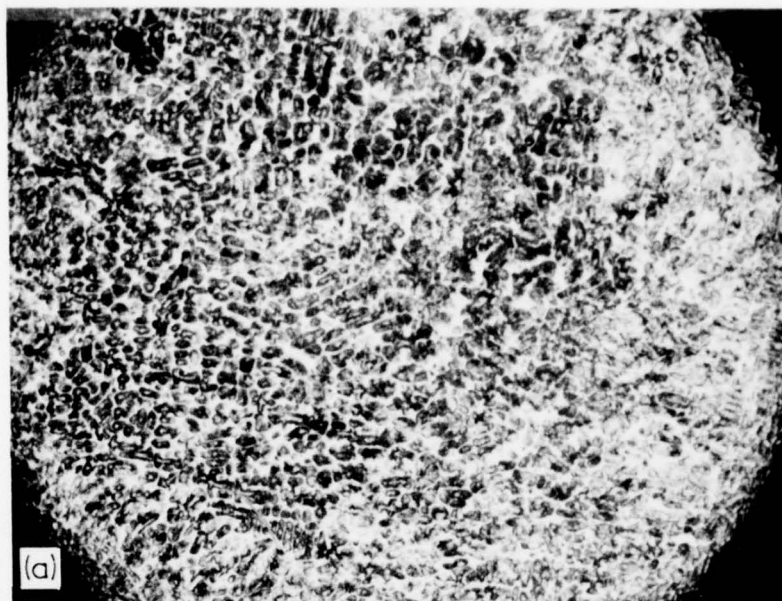


Figure 1. Photomicrographs of an undercooled powder particle of maraging 300 alloy exhibiting high solute cores (light etching) in the dendrite arms; (a) X200, (b) X500.

driftic region is shown in Figure 2. The solidification sequence resulting in the hump in the composition profiles of Figure 2 is as follows. Let an alloy of composition C_0 , Figure 3, be undercooled below the equilibrium solidus temperature, T_s , and nucleate at temperature T_N . The solid forming between T_N and T_s , during recalescence is of composition C_0 . The fraction of metal solidified during recalescence can be estimated from the following equation.

$$T_s = \frac{\bar{C}_p}{\Delta H} (T_s - T_N)$$

Where \bar{C}_p = average specific heat of (solid and liquid) T_s = fraction solid, and ΔH = latent heat of fusion.

The maximum recalescence temperature T_R , is in the liquid plus solid region. Solidification subsequent to recalescence proceeds according to the equilibrium phase diagram with little or no diffusion in the solid. The solid composition at the interface, C_s^* is given by the solidus line and the liquid composition at the interface C_L^* is given by the liquidus line. As noted in Figure 3, the first solid forming after recalescence to temperature T_R has a composition C_s^* , which is lower than C_0 . The remaining liquid then solidifies according to the Scheil equation, with the solid composition increasing continuously until the liquid composition reaches the eutectic.

Average cooling rates during solidification of the metal powders can be calculated using the following method. First, the variation of secondary dendrite arm spacing with cooling

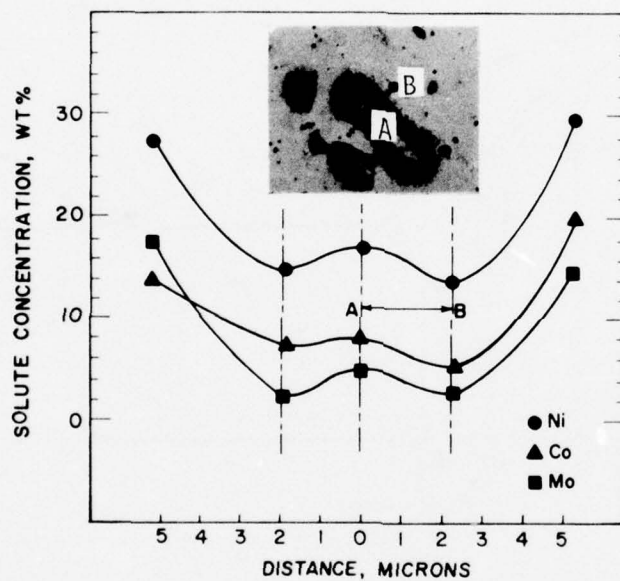


Figure 2. Distribution of Ni, Co, and Mo concentrations measured at various specific points along the chosen microprobe path across a dendrite in an undercooled powder particle of maraging 300 alloy.

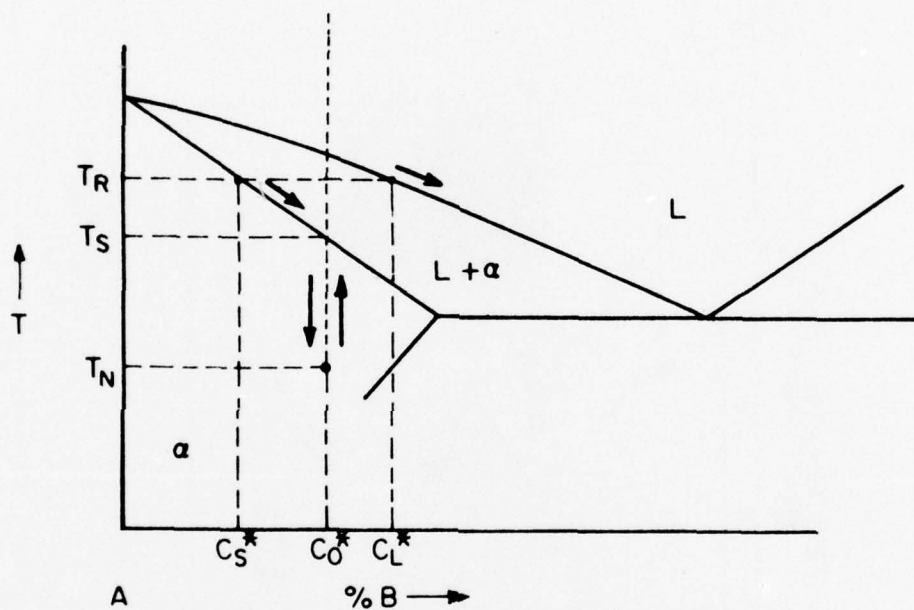


Figure 3. Schematic representation of the solidification sequence of an alloy of composition C_0 undercooled to a temperature T_N . Following nucleation at T_N the heat fusion released results in recalcrescence back up the temperature T_R in the liquid-solid range.

rate in the maraging 300 alloy is determined, Figure 4. Average cooling rate during solidification of the powders is then determined from this curve by measuring the secondary dendrite arm spacing in the powders. Calculated cooling rates for the undercooled coarse powders, ~500 μm diameter, are in the range of 10^2 to 10^3 $^{\circ}\text{C}/\text{sec}$.

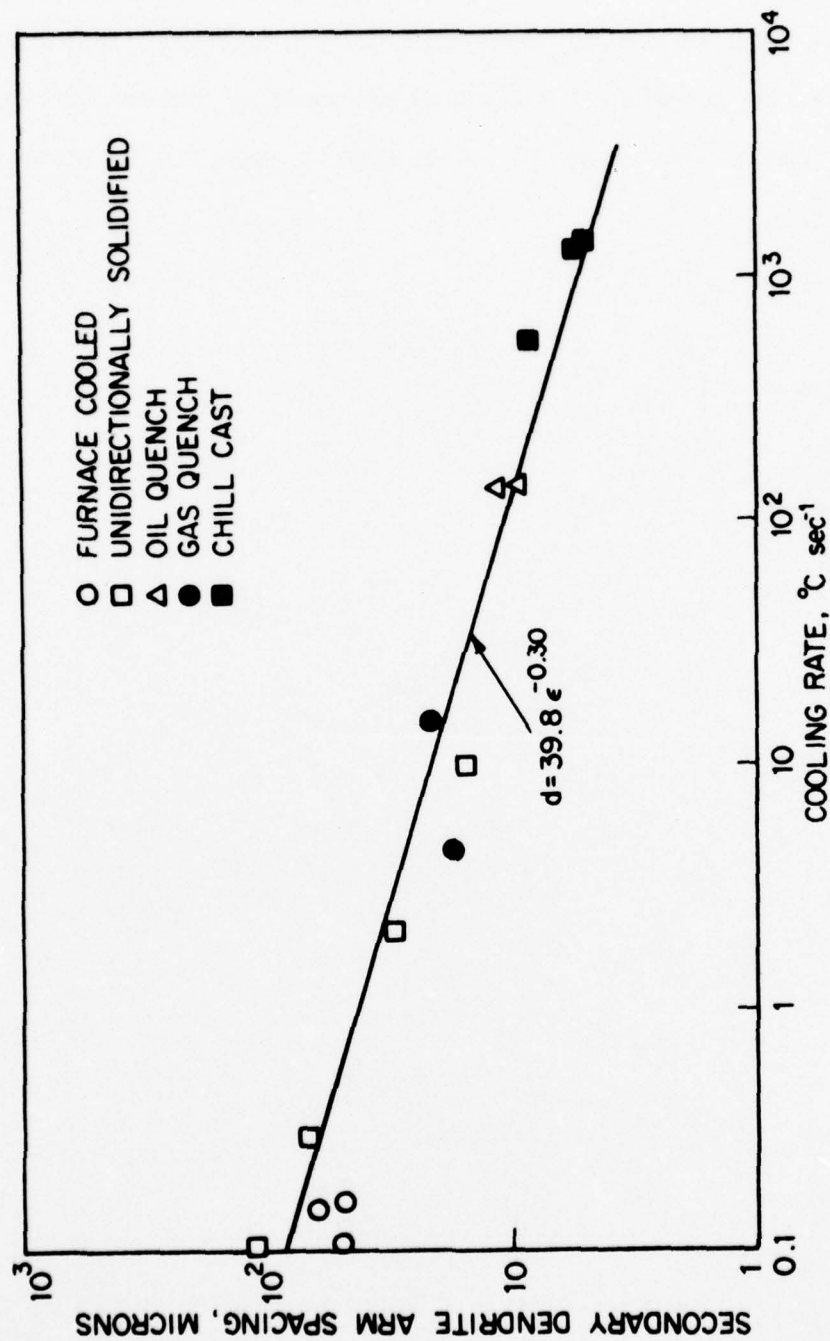


Figure 4. Secondary dendrite arm spacing versus cooling rate in maraging 300 alloy.

SURFACE TREATMENT OF SUPERALLOYS BY LASER SKIN MELTING

E. M. Breinan, B. H. Kear, C. M. Banas and L. E. Greenwald

A new process for the surface treatment of metals and alloys using lasers is described. Processing is accomplished by rapidly traversing a continuous, highly focused laser beam over the material surface. The high specific rate of energy delivery results in surface localized melting of a thin layer with high melting efficiency, i.e., a major fraction of the absorbed energy causes melting and a substantially smaller fraction goes into heating the substrate. This ability to melt a thin surface layer while maintaining a cold substrate results in rapid quenching of the molten layer by the bulk solid due to the intimate contact at the interface. It is calculated that cooling rates up to 5×10^8 °C/sec are possible in 2.5×10^{-3} mm thick melt layers in nickel-base alloys. For 2.5×10^{-2} mm thick layers, the cooling rates are up to 5×10^6 °C/sec.

A variety of metallurgical structures have been produced in nickel-base alloys by this process, some of which are unique. Several multi-component γ' precipitation hardened alloys, as well as eutectic superalloys, have been quenched to produce non-equilibrium structures, such as supersaturated solid solutions, which have the potential for being decomposed in the solid state into finely divided multiphase microstructures. Extremely fine

dendritic and filamentary eutectic structures have been obtained by skin melting of the superalloys. Moreover, in these alloys, oriented over-growth, or epitaxial growth, has been demonstrated for polycrystalline and monocrystalline substrates. Epitaxial growth is particularly favored on a cube oriented monocrystalline substrate.

Potential applications involving erosion, corrosion, wear and fatigue-resistant surface coatings for superalloys are briefly discussed. The process has been utilized as a reproducible screening technique for alloy design.

RAPID SOLIDIFICATION PROCESSING (RSP) OF THERMOELASTIC ALLOYS

M. Cohen

In some alloy systems, the strain energy accompanying the displacements of martensitic transformations on cooling can be accommodated elastically in the alloy, and this becomes available to help drive the reverse transformation on heating. Except for some hysteresis, a thermoelastic balance is set up between the chemical driving force and the stored elastic energy. These thermoelastic systems exhibit rubber-like behavior on loading and unloading because the applied stress shifts the thermoelastic balance; in other words, the operation of martensitic shears on loading and the reverse transformation shears on unloading result in extraordinary stress-strain characteristics for metallic systems.

One of these alloys is Cu-14Al-3Ni, which is relatively inexpensive and could be commercially feasible, but it suffers from undue brittleness arising from grain boundary precipitates occurring on cooling of the parent phase to room temperature. This undesirable precipitation cannot be inhibited in bulk materials, even by the most rapid quenching, but may well be suppressed or rendered innocuous by RSP methods. If the precipitation happens to take place during the consolidation step, it is not likely to be intergranular and hence should not cause

embrittlement. Another limitation of conventional Cu-Al-Ni alloys is that they are typically coarse grained and do not respond to grain refining treatments. In contrast, the RSP approach should lead to ultra-fine grain sizes with beneficial effects on the mechanical properties, and thus provide a superior base for the thermoelastic behavior.

ACKNOWLEDGEMENT

This research was supported by the Advanced Research Projects Agency of the Department of Defense under Contract No. MDA903-76C-0250 with The University of Michigan.

SMALL PARTICLE TECHNOLOGY

R. L. Coble

The atomization techniques discussed are operated such as to yield powder sizes and dendrite arm spacings which are much larger than the crystallites used for fabricating numerous modern ceramic products. ThO_2 , UO_2 and stabilized ZrO_2 ceramics have been made with powders containing 150\AA crystallites which are generally agglomerated into 500μ sized clumps, the latter being approximately 40-60% of theoretical density. Numerous other ceramics are made from powders with crystallites in the 0.1μ - 2μ size range, also generally agglomerated into larger assemblages, which facilitate fabrication (titanates, ferrites, aluminas). In general, sub-micron sized particles do not flow readily and the reproducibility required in die-filling depends on the use of larger agglomerates; the latter might be formed by spray drying a suspension of the desired crystallites in water containing lubricants and binders to permit compaction to high densities and rough handling, respectively. Thus, the inhibition to use very fine metallic powders because of fabrication difficulty can be overcome by the use of agglomerating techniques that are commonly practiced in the ceramics industry. The pyrophosphoricity will remain as a problem and require the appropriate handling precautions.

A central question not answered at this time is whether smaller sized particles with higher quench rates and smaller dendrite arm spacings are needed. Further improvements in mechanical properties are to be expected, if homogeneous super-alloys are made with finer grain sizes. Finer particle sizes of starting materials for HIP processing should give finer grain sizes (due to reduced grain growth) at shorter processing times (or lower temperatures) as has been found for ceramics (e.g., 2μ ZrO_2 sinters at 1800°C , 150\AA $0.18 \text{ Y}_2\text{O}_3$ 0.82 ZrO_2 sinters at 950°C). Also, the application of pressure permits reduction in sintering temperatures and will provide finer grain sizes at full density than the sintered counterparts.

Most of the processing techniques used for ceramics are not directly applicable to the production of super alloy materials. Coprecipitation of salts is commonly used in ceramics powder preparation to achieve homogeneity on a molecular scale, the size of the precipitated salt particles being controlled by accessible variables in precipitation. If direct reduction of those salts was possible using hydrogen, fine particle metallic alloys could be prepared following that technique. However, Cr and Al containing alloys are not susceptible to H_2 reduction. The prospect of using unstable metallo-organic compounds for these elements should not be overlooked, however, to be considered for use with carbonyl nickel and iron for growth of composite particles for subsequent fabrication. It is noteworthy that Fe and Ni carbonyl powders are recycled through

carbonyl growth furnaces in order to obtain 100 μ sized fabricable powder. Obviously, much finer powder could be produced with shorter growth times.

Alternate techniques to melt-atomization that could work with any alloy system involve vaporization and condensation at low temperatures to produce "snow" or bulk coatings with homogeneity on an atomic scale. Plasma-arc, flame-spraying, or electrical discharge explosion of wires are both attractive and available techniques to produce very fine metallic powder or coatings, and should be applied to push the HIP processing technology approach to the ultimate in order to determine what property improvements minimum sized homogeneous powder will provide.

Although the heat of vaporization is ten times the heat of fusion, the process should not be ruled out for possible use commercially, considering that the efficiencies reported for melt atomization are low (3% cited). After preparation of small sized homogeneous metal powders, spray drying using an organic carrier could be used to produce fabricable powder agglomerates.

Another vapor transport system for powder production could be based on a halide vapor transport and reaction scheme - hydrogen injected into a mixture of hot halides gases will yield metallic deposits, the form of which depends on the supersaturation, temperature level, and whether or not a substrate is available for deposition as well as the substrate temperature. Low temperatures and high supersaturations are required to produce "snow".

ACKNOWLEDGEMENT

This research was supported by the Advanced Research Projects Agency of the Department of Defense under Contract No. MDA903-76C-0250 with The University of Michigan.

PROGRESS IN MAKING PM SHAPES FROM Ti_3Al AND $TiAl$

H. A. Lipsitt and A. M. Adair

The titanium aluminides, Ti_3Al and $TiAl$, have considerable development potential as materials of construction for aircraft turbine engines. These ordered intermetallic compounds are lighter and stiffer than conventional titanium alloys. They do not have particularly high strength at room temperature, but because they are ordered they retain very high static strength, stiffness, and oxidation resistance to temperatures considerably in excess of those attainable by conventional titanium alloys. The aluminides, however, show only very limited ductility below 600°C. Our research program is a study of the physical metallurgy of the aluminides, of their alloying behavior, and of the properties that result. The goal, of course, is to learn to ameliorate the room temperature brittleness without sacrificing the elevated temperature properties.

A discussion was presented on the phase diagram, structure, and properties of the aluminides. Predicted and observed modes of deformation and fracture were compared. Data for the behavior in tension, creep, fatigue and oxidation was presented and some elements of the microstructure to property relationship were given.

SHOCK WAVES AS A MEANS OF PRODUCING
VERY RAPID COOLING

E. E. Hucke and G. H. Vineyard

A strong shock wave in a specimen produces very rapid heating followed by rapid cooling as the pulse passes along. Techniques exist for producing well controlled planar shocks with pressures ranging from hundreds of kilobars to megabars and associated heating in common metals of a few hundred to several thousand degrees centigrade. A number of workers have observed phase transformations and melting produced by such shocks. To our knowledge, the process has not been considered as a tool to cause very rapid cooling from the molten state for the purpose of investigating the microstructures and other phenomena that are produced in various substances by very rapid cooling. We suggest that it might be worthwhile to undertake such research, particularly with alloys in which interesting properties may be induced by rapid quenching.

Attainable strong shocks have velocities of propagation up to about 10^6 cm/sec, the actual value depending upon the material properties and the strength of the shock wave. If the trailing edge of the shock pulse has a thickness of the order of millimeters, the cooling then occurs in a microsecond to a tenth of a microsecond, and the cooling rates will typically

range from 10^8 °C/sec to 10^{10} °C/sec. Unlike the heating in the leading edge of a shock wave, the cooling in the trailing edge is approximately adiabatic.

It should be noted that the cooling in question is from a shocked state of elevated pressure, which may change the metallurgical behavior somewhat (or quite a lot) from the behavior at ambient pressure. There is also a rapid unloading of uniaxial strain (but with nearly hydrostatic pressure) during the cooling. On the other hand the specimens can be of ordinary size, thus convenient for examination and further experimentation.

Several possible embellishments of this idea suggest themselves. The specimen can be started at a state of elevated temperature, so that a less severe shock is required to melt it than when starting from room temperature. After passage of the shock the specimen is left at a temperature higher than its initial temperature (since irreversible work is done in the compressional phase), but in many cases the transformations of interest will have been completed relatively near the melting point, and therefore elevation of the initial temperature will do no harm.

Another stratagem for reducing the intensity of the shock required is to start with the specimen in an "expanded" state, such as a powder, a foam, or a specimen filled with pores. An expanded specimen shocked to a given pressure reaches a higher temperature than a specimen of normal density. With this method the melting point can be reached in many materials with quite modest pressures.

The shape of the trailing edge of a shock pulse has not been as extensively measured as the shape of the leading edge, which tends to be very steep. It may be that special measures can be found to sharpen the trailing edge in order to increase the cooling rate. In any event a long run of the shock pulse tends to smear out the trailing edge and thus the shortest possible run would appear to be preferred. The principle problem with the suggestion is that facilities for producing strong planar shocks are not widespread and experiments with the facilities are somewhat elaborate. However, facilities and research groups do exist in a number of places, and collaborations with metallurgists interested in rapid quenching could be arranged.

Acknowledgement

This research was supported by the Advanced Research Projects Agency of the Department of Defense under Contract No. MDA902-76C-0250 with The University of Michigan.

VERY RAPID QUENCHING WITH THERMAL SPIKES

G. H. Vineyard

When a heavily ionizing particle such as a fission fragment passes through matter the principle effect more than a few tens of Angstroms away from the track of the particle can be thought of as a very rapid heating of the material, followed by a very rapid cooling. This phenomenon is known as a thermal spike and has often been calculated by considering heat energy instantaneously introduced along a straight line in an isotropic continuum that is characterized by a coefficient of thermal conductivity and a specific heat, both assumed to be independent of temperature.¹ On this model, temperatures above the melting points of metals can be achieved and, because of the fact that the heated region is very small and completely surrounded by cool material, the quenching rate can be exceedingly high. Thermal spike pictures have been employed to interpret many observed effects of radiation on materials, including disordering and production of metastable phases.

Because of the current interest in very rapid quenching as a means of producing novel structures, fine particles, and metastable phases such as metallic glasses, it is worth inquiring whether thermal spikes offer any hope of being useful, either for producing rapidly quenched structures, or an an experimental

tool for studying ultra-rapid quenching phenomena in selected situations. It appears more likely that the usefulness, if any, will center around the latter purpose. Although the quench rates can be extraordinarily high, it should be made clear in the beginning that the effect occurs only in very small regions indeed, and that the temperature and cooling rate will be difficult to know with certainty since direct measurements can not be made and the theory is only approximate. There is the further consideration that the quench is from a temperature that has been reached only very briefly and that a pressure pulse of some magnitude, along with newly created point defects in the lattice always accompany it.

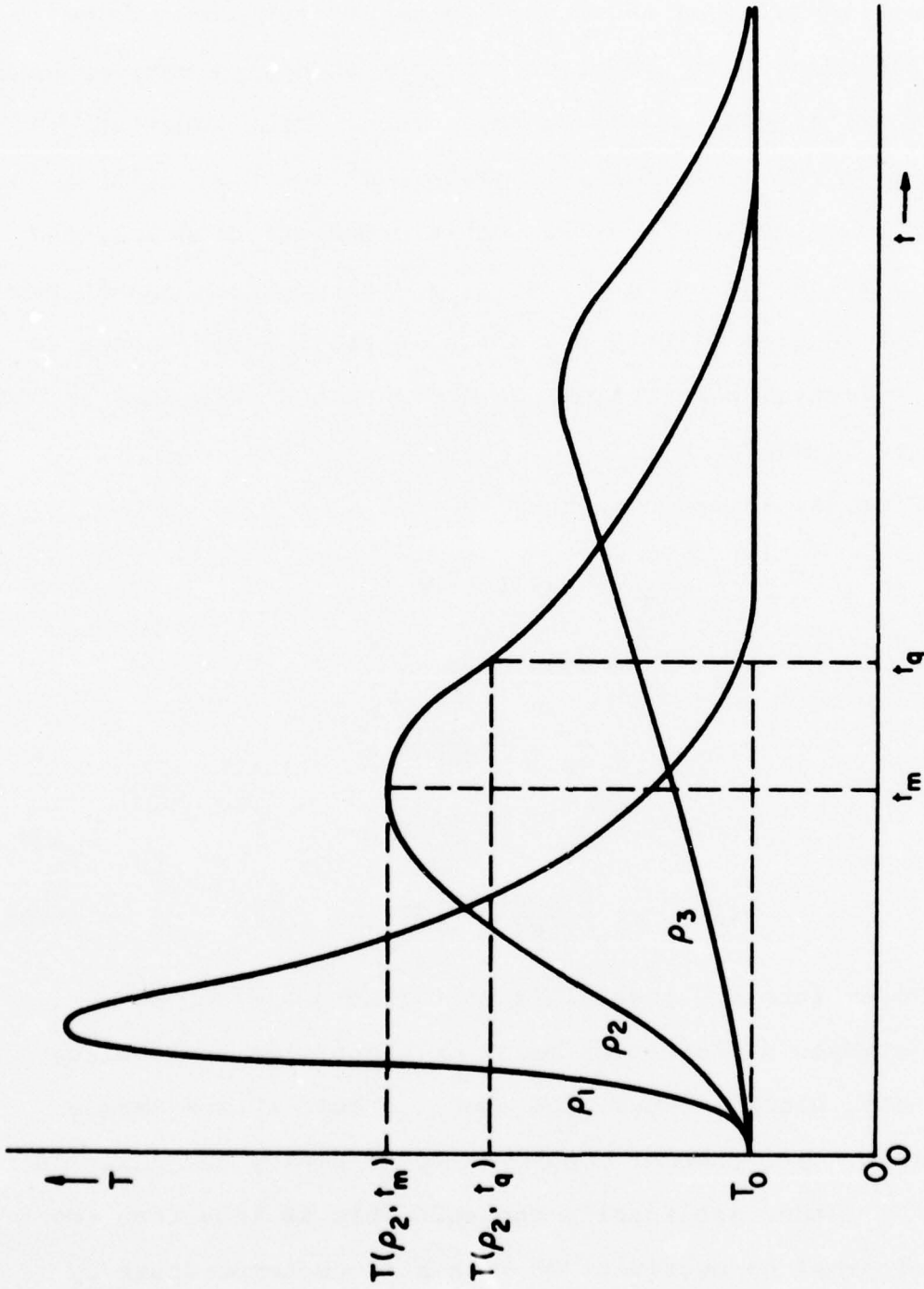
A MODEL CALCULATION

The familiar theory of thermal spikes² shows that if a bombarding particle releases energy into the lattice at the rate Q per unit length along its path, the temperature distribution is given by

$$T(\rho, t) = T_0 + \frac{Q}{4\pi cd} \frac{1}{\tau} e^{-\rho^2/4\tau} \quad (1)$$

In this equation ρ is the perpendicular distance of a point in the medium from the track of the particle, T_0 is the initial temperature, c is specific heat, and d is the density of the medium. Also $\tau = Dt$, where $D = \frac{\kappa}{cd}$, with κ the thermal conductivity of the medium.

Equation (1) shows that the temperature at a point ρ rises and falls with time as shown qualitatively in the graph below.



Temperature-time curves for three different distances $\rho_1 < \rho_2 < \rho_3$.

Curves are given for three different distances ρ_m , where $\rho_1 < \rho_2 < \rho_3$. The highest temperature and quench rates are achieved at the closest distances. On the other hand the theory becomes unreliable at very small distances and the region over which observations might be made becomes impossibly small. Thus the question to be answered is whether there exists an intermediate distance, say ρ_2 , at which the maximum temperature T_m , and the maximum quench rate \dot{T}_q have interesting values, but which is still large enough to allow experimental observations on the quenched structure in its vicinity to be made.

From (1) it is found that

$$t_q = 0.4268 \rho^2/D , \quad (2)$$

$$t_m = 0.25 \rho^2/D , \quad (3)$$

$$T(\rho, t_m) = T_o + \frac{0.1171Q}{cd} \rho^{-2} \quad (4)$$

$$T(\rho, t_q) = T_o + \frac{0.1028Q}{cd} \rho^{-2} \quad (5)$$

$$-\dot{T}(\rho, t_q) = \frac{0.1007QD}{cd} \rho^{-4} \quad (6)$$

To explore the possibilities further consider as a specific example a transition metal or transition metal alloy with density, atomic number, and specific heat approximately that of iron. For thermal conductivity we employ the value 10^{-2} watts/cm°K, rather arbitrarily chosen. This is less than the measured thermal conductivity of iron at room temperature by nearly two orders of magnitude, and is an estimated approximation

to the lattice part of the thermal conductivity only. The energy of the fission fragment that is imparted to the lattice will propagate first through the lattice and then communicate itself to the conduction electrons in a time characteristic of the electron-phonon coupling. This time is generally longer than the characteristic time for the central part of the spike to occur, and therefore the best simple estimate should be given by employing only the lattice part of the thermal conductivity. If a higher value of thermal conductivity is more appropriate, the characteristic times will be reduced proportionately and the cooling rate \dot{T} will be increased proportionately. (See Eqns. 1-6 and recall that D is proportional to thermal conductivity.)

Using a value of $Q = 10^{11}$ eV/cm which is characteristic of the heavier fission fragments, one finds the values given in the table below:

| ρ Angstroms | $-T(\rho, t_q)$ °C/sec | $T(\rho, t_m) - T_0$ °C | $T(\rho, t_q) - T_0$ °C | t_m sec | t_q sec |
|---------------------|---------------------------|----------------------------|----------------------------|-----------------------|-----------------------|
| 50 | 1.9×10^{13} | 2060 | 1820 | 2.3×10^{-11} | 3.9×10^{-11} |
| 100 | 1.2×10^{12} | 510 | 460 | 9.1×10^{-11} | 1.6×10^{-10} |
| 250 | 3.1×10^{10} | 80 | 70 | 5.7×10^{-10} | 9.7×10^{-10} |
| 500 | 1.9×10^9 | 21 | 18 | 2.3×10^{-9} | 3.9×10^{-9} |

DISCUSSION

It is seen that very high quenching rates indeed are predicted, ranging from 10^9 to 10^{13} °C/sec in the range of distance considered. The maximum temperature rise at 50\AA from the

center of the spike is calculated to be 2060°C , declining as the inverse square of the distance to only 21°C at 500\AA . If the specimen is initially at an elevated temperature, its melting point will be exceeded in the spike at quite respectable distances. Thus, if iron, for instance, is held at 1300°C it is predicted that its melting point would be exceeded to a distance of about 100\AA . A cylindrical region extending 100\AA from the core of the spike is a very small region in which to make observations, but it is not inaccessible, for example, to electron microscopy. Transitions that occur at lower temperatures could be studied in correspondingly larger regions.

If higher rates of deposition of energy were available, useful temperatures could be reached in a larger region. Higher deposition will be achieved with very heavy ions at higher energies that are achievable in a few accelerators. Without attempting to make a thorough catalog here, we note that simple range-energy theory indicates that a uranium ion of 8 GeV energy would deposit energy in intermediate-weight materials such as iron at the rate of about 4×10^{11} eV/cm, larger than the number assumed above for heavy fission fragments by a factor of 4. For such a spike the values of T and \dot{T} given in the table would be multiplied by 4, giving a 2000°C temperature rise at 100\AA and a 320°C rise at 250\AA , which would make observations easier and would reduce the very rapid variation of parameters with distance.

It is desired to bring about throughout a specimen a transformation that can only be achieved by very rapid quenching,

it could be done by irradiation with fission fragments or very heavy energetic ions if the following special conditions obtain:

1. The desired starting state can be produced in the very rapid heating inherent in the spike, from some starting temperature that is below the instability temperature of the quenched state.
2. The quenched state will be retained for all quenches from above a certain temperature that exceed a certain rate \dot{T} .
3. The pressure pulse and point defect production accompanying the spike do not prevent the desired transformation or disturb the transformed material unduly.
4. The transformation goes on as expected on the very small spatial scale of the spike.

If these assumptions are valid, then the transformed state will be produced throughout the interior of a cylindrical region around each spike, typically $10\mu\text{m}$ long and perhaps 200\AA in diameter. Sufficient radiation exposure to cause these regions to fill the sample will then transform all of the material.

ACKNOWLEDGEMENT

This research was supported by the Advanced Research Projects Agency of the Department of Defense under Contract No. MDA903-76C-0250 with The University of Michigan.

References

1. G. J. Dienes and G. H. Vineyard, Radiation Effects in Solids, Interscience Publishers, New York, 1957, Section 2.6. (A case of temperature-dependent coefficients is treated in the article, Thermal Spikes and Activated Processes by G. H. Vineyard. Radiation Effects 29, 245 (1976)).
2. Reference 1, Eq. 2-45.
3. American Institute of Physics Handbook, McGraw-Hill Book Co., New York, 1963, Section 8-c.

SOME RECENT DEVELOPMENTS OF POWDER PROCESSING
IN ELECTRONIC DEVICES

G. Y. Chin

Powder processing has traditionally been an important processing technique for components used in electronic devices. This is particularly true for ceramics such as magnetic ferrites and alumina substrates. It has also been important in shaping brittle alloys such as the permanent magnet Alnicos. Some examples of more recent developments are:

CONTROL OF COMPOSITION AND HOMOGENEITY

Magnetics

1. Twisting memory - used in telephone electronic systems. Consists of thin ribbon of molypermalloy (4Mo-79Ni-Fe). Close composition control needed for minimum strain sensitivity (magnetostriction) of the ribbon.

2. High permeability molypermalloy - requires zero crystalline anisotropy and magnetostriction. Close composition control needed.

Frequency Selectors

Some applications require a mechanical member to vibrate at precise frequencies and hence a near zero temperature coefficient of elastic modulus. In Vibralloy (41Ni-9Mo-Fe), dE/dT is very sensitive to Ni content.

SHAPING BRITTLE ALLOYS

Magnetics

1. New high performance permanent magnets such as Co_5Sm and $(\text{Co}, \text{Cu})_{17}\text{Sm}_2$ require powder processing. In this regard, direct calcium reduction of samarium oxide has resulted in dramatic decrease of materials cost. Also, segregation that normally comes from solidification of $(\text{Co}, \text{Cu})_{17}\text{Sm}_2$ could be alleviated by rapid freezing. Sendust is an Fe-Si-Al high permeability, physically hard alloy useful as recording head material, but brittle. Recent Japanese innovation involves plate-shaped particles which permit consolidation by rolling.

Connectors

1. Recent work at Bell Labs shows that Cu-Ni-Sn spinodal alloys have strength far exceeding Cu-Be, and quite ductile if segregation can be circumvented. Thin slab casting and powder metallurgy techniques are being pursued.

Magnetostrictive Transducers

1. Work at Naval Research Labs has shown Laves phases such as TbFe_2 exhibits extremely large magnetostriction suitable for transducers. Compounds are brittle and powder processing should be beneficial. Some lighter rare earths, e.g., PrFe_2 , do not exist under equilibrium cooling, but might be made metastable by rapid quenching.

NEW STRUCTURE AND PROPERTIES

Magnetics

1. Metallic glasses $(\text{Fe, Co, Ni})_{0.8} (\text{B, P, Al})_{0.2}$ pioneered by Allied Chemical are now well known. High permeability comes with absence of crystalline anisotropy and magnetostriction.

Other properties such as dielectric constants, piezoelectric coupling, etc., remain unexplored. Recent theory at Bell Labs indicates possibility of ferroelectric glasses.

CHEMICAL COPRECIPITATION

Chemical coprecipitation is an alternative technique to atomization in powder production. Particle size typically in the range of 100\AA to 1μ . Shape control possible. Technique is now used in preparing low loss MnZn ferrites of close composition control. Also needle-shaped Co-Fe powders suitable for high density recording. Also possibility of control of texture in plate-shaped particles.

ELECTRONIC MATERIALS APPLICATIONS SUGGESTIONS:
SMALL-PARTICLE PHENOMENA AND TECHNOLOGIES

J. H. Wernick

The new techniques now being developed to produce ultra-fine particles exhibiting different microstructures (and possibly new surface properties) and surface morphologies suggest several current areas of work that could benefit from these developments. They are:

1. Alteration of the fine particle magnetic properties of rare earth - Co intermetallic compounds, specifically YCo_5 and PrCo_5 through alteration of the surface morphology and microstructure.
2. Improvement and/or discovery of new hydrogen storage materials (ex: LaNi_5).
3. Alteration of catalytic behavior of metals and oxides (ex: perovskites) by alteration of surface properties via alteration of microstructure.
4. Production of particles of brittle high Tc superconductors, such as V_3Si , Nb_3Sn , and Nb_3Ge , such that, on compaction, bodies will result which could exhibit considerable ductility.

Regarding #1, the extremely good magnetic properties of SmCo_5 are not realized until it is ground to 10-20 μm powder before compacting by liquid phase sintering. YCo_5 and PrCo_5

with higher saturation magnetizations, do not behave in the same fashion and it is presently believed this is a result of the nature of the particle surface produced by grinding. The surface of SmCo_5 particles are such that reverse domains are either difficult to nucleate or existing domain walls are pinned by as yet unknown surface features.

The room temperature hydrogen absorption capabilities of materials being considered for hydrogen storage (such as LaNi_5) certainly must be influenced by the nature of the surface, which in turn is influenced by the microstructure. The decomposition of H_2 is surface catalyzed and H then diffuses into the material. Perhaps the pressures and temperatures required to have H enter the bulk can be influenced in a favorable manner.

The reasoning for item #3 follows from the above. The high T_c intermetallic compounds are brittle. Perhaps the new small-particle techniques can be investigated from the standpoint of producing compacts that will exhibit sufficient ductility to that they can be drawn into wire.

AMORPHOUS ALLOY POWDERS

P. E. Duwez

Various atomizing techniques are available to produce alloy powders less than 10 μ m in diameter with estimated rates of cooling of the order 10⁶°C/sec or higher. Under these conditions a number of alloys would be amorphous. The alloys based on Au, Pd and Ni would not be of practical interest, but might be considered for fundamental research. From the practical interest standpoint, studies should be made of alloys having the composition T₍₇₀₋₈₅₎G₍₃₀₋₁₅₎, T standing for the transition metals Ni, Co, Fe, Mn or Cr, G designating the semi-metals generally referred to as glass formers, namely B, C, Si and P, and the subscripts indicating the approximate limits in at.%. Many amorphous alloys of this type have been studied. They include ternary alloys such as Fe₇₅P₁₅C₁₀, Fe₇₆B₁₇C₇, Ni₇₅P₁₅B₁₀, Co₇₃P₁₇B₁₀ etc. More complex alloys such as Fe_{38.5}Ni_{38.5}P₁₄B₆Al_{1.5}Si_{1.5} and Co₇₂Fe₃P₁₆B₆Al₃ are typical magnetic alloys with very low coercive forces.

The majority of the alloys which have been rapidly cooled by atomization are super alloys whose composition is not favorable to glass formation, so the question of knowing whether or not glassy alloys can be obtained by atomization is still unanswered. It is almost certain however that if any of the alloy

compositions mentioned above were atomized at rates of cooling of 10^6 °C/sec or higher, the powder would be amorphous. The next question is to find out if such powder can be consolidated without inducing crystallization. As a general rule, glassy alloys will crystallize very rapidly at temperatures above about 400°C. At 300°C, the approximate time required for crystallization may be of the order of hours and it is conceivable that the HIP process could be used.

The alloy compositions suggested above have been obtained in the glassy state in the form of ribbons about 40µm thick and 3 to 5 mm wide. Depending on their compositions these alloys are of interest for their magnetic properties (coercive force as low as a few millioersted, very low hysteresis losses) strength properties (up to 350,000 lb. in²) and corrosion properties (comparable with some of the best stainless steels). At present, their usefulness is limited by the fact that they can be obtained only in ribbon form. The main justification for the powder approach is to remove the present limitations and develop a method by which large sheets of glassy alloys can be fabricated.

ACKNOWLEDGEMENT

This research was supported by the Advanced Research Projects Agency of the Department of Defense under Contract No. MDA903-76C-0250 with The University of Michigan.

CURVATURE EFFECTS IN THE THERMODYNAMICS OF MULTICOMPONENT SYSTEMS:
POSSIBLE EFFECT ON DENDRITE SPACING IN RAPIDLY
COOLED SMALL LIQUID METAL DROPS

H. Reiss

INTRODUCTION

One of the important factors in the behavior of rapidly quenched (10^5 deg/sec) liquid metal drops is the very fine grained dendritic structure which pervades the entire solidified drop. The spacing of these dendrites is supposedly controlled, in part, by curvature effects associated with surface tension. Thus, the process is not unlike the "Ostwald ripening" phenomenon in a more conventional chemical precipitate in which small crystals gradually dissolve and redeposit on larger ones. The increase in solution tension of a crystal, with increased curvature, is thought to be well understood as a result of increased pressure due to surface tension. However, it has been discovered recently¹ that for multicomponent systems the situation has not been so clear, due to the frequent omission of a necessary term in the chemical potential of a given component within a precipitate particle. This term was not discussed by Gibbs in his classic work, but Gibbs made no error; he simply didn't treat the matter.

In this paper we will call explicit attention to this term, and endeavor to assess its quantitative importance. However,

rather than discuss the "ripening" of dendrite systems, we will confine our attention to simple "spherical" crystals with an eye to elucidating the order of magnitude importance of the new term in determining the size and composition of the equilibrium crystal. The same order of magnitude influences ought to be at work in dendrite systems.

THE EXTRA TERM

We present here a not quite rigorous exposition of the extra term mentioned in the last section. For a fully rigorous treatment, however, in a rather different context the reader is referred to a paper submitted to the Journal of Chemical Physics¹. Our presentation will have the merits of brevity and the correct answer, even if it lacks somewhat in rigor.

As indicated in the last section, we will idealize a small crystal as a sphere possessing a surface tension, σ , independent of location on the surface of the sphere. Furthermore, we assume it to consist of a binary solution containing α molecules of component 1 and β molecules of component 2. If the partial molecular volumes of the two components are respectively v_1 and v_2 , then the radius of the crystal sphere will be

$$r = \left[\frac{3}{4\pi} (\alpha v_1 + \beta v_2) \right]^{1/3} \quad (1)$$

We also assume v_1 and v_2 to be constant and independent of pressure.

Under these circumstances the Gibbs free energy of the

crystal may be expressed as²

$$G_C = \alpha\mu_1 + \beta\mu_2 + 4\pi r^2 \sigma \quad (2)$$

where μ_1 and μ_2 are the chemical potentials which components 1 and 2 would have if they were present at the pressure, P_0 , outside of the crystal and at the prevailing temperature, T . The pressure, P_i , inside the crystal is determined by the well known Maxwell condition,

$$P_i = P_0 + \frac{2\sigma}{r} \quad (3)$$

and can exceed P_0 by an appreciable amount for small values of r .

Now the chemical potential, ϕ_1 , of component 1 in the crystal is specified by²

$$\phi_1 = \left(\frac{\partial G_C}{\partial \alpha} \right)_{T, P_0, \beta} = \mu_1 + 8\pi \sigma r \left(\frac{\partial r}{\partial \alpha} \right)_{T, P_0, \beta} + 4\pi r^2 \left(\frac{\partial \sigma}{\partial \alpha} \right)_{T, P_0, \beta} \quad (4)$$

Similarly, for the other component,

$$\phi_2 = \mu_2 + 8\pi \sigma r \left(\frac{\partial r}{\partial \beta} \right)_{T, P_0, \alpha} + 4\pi r^2 \left(\frac{\partial \sigma}{\partial \beta} \right)_{T, P_0, \alpha} \quad (5)$$

The second terms on the right of Eqs. (4) and (5) may be re-expressed with the aid of Eq. (1) so that we obtain

$$\begin{aligned} \phi_1 &= \mu_1 + \frac{2\sigma v_1}{r} + 4\pi r^2 \left(\frac{\partial \sigma}{\partial \alpha} \right)_{T, P_0, \beta} \\ \phi_2 &= \mu_2 + \frac{2\sigma v_2}{r} + 4\pi r^2 \left(\frac{\partial \sigma}{\partial \beta} \right)_{T, P_0, \alpha} \end{aligned} \quad (6)$$

We see from Eq. (3), that the second terms on the right of both of Eqs. (6) are

$$\frac{2\sigma v_1}{r} = (P_i - P_o) v_1 \quad (7)$$

$$\frac{2\sigma v_2}{r} = (P_i - P_o) v_2$$

respectively, and represent the increase of chemical potential due to the excess of pressure, $P_i - P_o$, in the crystal. In a one component system this is the only term additional to μ so that one writes

$$\phi = \mu + \frac{2\sigma v}{r} \quad , \quad (8)$$

a result which is intuitively pleasing since it seems that a molecule within a small crystal can only know that it is located there by the increase of pressure.

This result has been so intuitively pleasing that, for the two component system, the third terms on the right of Eqs. (6), involving the composition derivatives of the surface tension, have usually been neglected. This third term is the "extra" term we have been referring to. How important it is depends on its magnitude, relative to the second term. It is an expression of the fact that in a small enough crystal one cannot add or remove a molecule without changing the composition, and therefore, the surface tension when it depends on composition. Since the addition of a molecule does not change the composition, sensibly, in a large enough crystal, the term is of no importance there. On the other hand, the second term also vanishes as $r \rightarrow \infty$.

If one of the components, say the second, tends to concentrate in the surface, as is common with surfactants or with a low melting metal in a binary alloy, then the derivative term may become quite important at fairly macroscopic values of r , e.g., $r < 10^{-4}$ cm.

If the phase in equilibrium with the crystal has g_1 and g_2 as the chemical potentials of the respective components, then the condition of equilibrium may be expressed as

$$\begin{aligned} g_1 &= \mu_1 + \frac{2\sigma v_1}{r} + 4\pi r^2 \left(\frac{\partial \sigma}{\partial \alpha} \right)_{T, P_0, \beta} = \phi_1 \\ g_2 &= \mu_2 + \frac{2\sigma v_2}{r} + 4\pi r^2 \left(\frac{\partial \sigma}{\partial \beta} \right)_{T, P_0, \alpha} = \phi_2 \end{aligned} \quad (9)$$

These two equations determine the radius and composition of the crystal in unstable equilibrium with the surrounding phase.

In a binary nucleation problem¹ these same equations arise, and together they determine the size and composition of the nucleus. Most of the time the derivative terms are not included. For example, in a 1959 paper³ Cahn and Hilliard, using the "square gradient" theory of surface layers discuss the properties of a "diffuse" nucleus. Among other things, they contrast these properties with the so-called "classical" nucleus which corresponds to one determined by Eqs. (9) without the derivative terms. The qualitative properties of the classical nucleus, especially on the spinodal are vastly different from those of the diffuse one. On the other hand, it can be shown¹

that if the derivative terms are included in the specification of the classical nucleus, its properties become qualitatively very similar to those of the diffuse nucleus. This means that the "square gradient" theory treats the effects due to the derivative terms, implicitly.

MODEL SYSTEM

In order to perform a quantitative comparison of the conditions of equilibrium, Eqs. (9), with and without the derivative terms, it is necessary to introduce a model system with particular thermodynamic properties. Since we only wish to display the directions and orders of magnitude of various effects, it will be satisfactory to introduce the simplest model having reasonable physical characteristics. We therefore consider a model in which the second component is present in low concentration in both the small crystal and the surrounding phase (melt). If we were considering the problem of dendrites in rapidly quenched small drops, for example, the second component might be a trace additive or impurity in the original melt. In general, we shall be interested in second components present to the extent of not more than 5% in the melt.

Under these conditions we may write

$$\mu_2 = B_2(T, P_0) + kT \ln \frac{\beta}{\alpha + \beta} \quad (10)$$

$$\mu_1 = \mu_1^0(T, P_0) + kT \ln \frac{\alpha}{\alpha + \beta} \quad (11)$$

$$g_1 = g_1^0(T, P_0) + kT \ln \frac{x}{x+y} \quad (12)$$

$$g_2 = g_2^0(T, P_0) + kT \ln \frac{y}{x+y} \quad (13)$$

In these equations x is the number of molecules of component 1 in the melt, and y the number of molecules of component 2, while k is the Boltzmann constant. The quantities B_2 , μ_1^0 , g_1^0 and g_2^0 are chemical potentials in the standard states.⁴ The last three quantities are simply the chemical potentials of the pure components, but B_2 refers to a virtual standard state. This is because the crystal is considered dilute, but not perfect in component 2. However, because it is dilute in component 2, it is necessarily perfect in component 1.⁵ Hence, for component 1, we use μ_1^0 instead of B_1 . Note that we are considering the melt to be perfect in both components, hence the appearance of g_1^0 and g_2^0 , the chemical potentials of the pure components, in Eqs. (12) and (13). No essential loss in insight occurs in lieu of the melt being considered entirely ideal, but we gain a great deal of manipulative simplicity.

For equilibrium between the melt and a bulk crystal, we have $\mu_1 = g_1$, $\mu_2 = g_2$, which, upon use of Eqs. (10), (11), (12) and (13), translates into

$$\frac{\beta/(\alpha+\beta)}{y/(x+y)} = e^{(g_2^0 - B_2)/kT} = K_2 \quad (14)$$

$$\frac{\alpha/(\alpha+\beta)}{x/(x+y)} = e^{(g_1^0 - \mu_1^0)/kT} = K_1 \quad (15)$$

Note that Eq. (15) may be written as

$$\frac{1 - \frac{\beta}{\alpha+\beta}}{1 - \frac{Y}{x+y}} = \frac{1-K_2 \frac{Y}{x+y}}{1 - \frac{Y}{x+y}} = \frac{1 - \frac{K_2 \rho}{1+\rho}}{1 - \frac{\rho}{1+\rho}} = K_1 \quad (16)$$

where $\rho = y/x$. In arriving at Eq. (16) we have used Eq. (14).

Thus, once K_1 and K_2 are specified the composition, ρ , of the melt, in equilibrium with bulk crystal, is determined.

We elect to consider a system in which component 2 tends to remain in the melt so that we choose

$$K_2 = e^{-9} = 1.23 \times 10^{-4} \quad (17)$$

Then if for ρ we choose 0.05, we find from Eq. (16), that

$$K_1 = 1.05 \quad (18)$$

Furthermore, from Eqs. (14) and (15)

$$\begin{aligned} g_2^0 - B_2 &= kT \ln K_2 \\ g_1^0 - \mu_1^0 &= kT \ln K_1 \end{aligned} \quad (19)$$

We still have to deal with the surface tension σ and its dependence on composition. In order to model this we make use of the Gibbs adsorption equation⁶, namely (at constant temperature),

$$d\sigma = -\Gamma_1 d\mu_1 - \Gamma_2 d\mu_2 \quad (20)$$

where Γ_1 and Γ_2 are the superficial densities of matter at the interface. In view of the diluteness of the solution we assume that Γ_1 and Γ_2 are related to the volume concentrations,

$$\frac{\alpha}{\alpha v_1 + \beta v_2} = \gamma_1, \quad \frac{\beta}{\alpha v_1 + \beta v_2} = \gamma_2 \quad (21)$$

by equilibrium constant relations, namely,

$$\frac{\Gamma_1}{\alpha/(\alpha v_1 + \beta v_2)} = \gamma_1, \quad \frac{\Gamma_2}{\beta/(\alpha v_1 + \beta v_2)} = \gamma_2 \quad (22)$$

where γ_1 and γ_2 are the constants.

Using Eqs. (10) and (11) for μ_1 and μ_2 and Eq. (22) for Γ_1 and Γ_2 it is an easy matter to integrate Eq. (20) to show that

$$\sigma = \sigma_1 - \frac{kT(\gamma_2 - \gamma_1)\beta}{(\alpha v_1 + \beta v_2)} \quad (23)$$

where σ_1 is the surface tension of pure component 1.

Substitution of Eqs. (1), (10), (11), (12), (13) and (23) into Eqs. (9), and keeping terms only as far as β/α , yields for the conditions of equilibrium,

$$g_1^0 - \mu_1^0 = kT \left(\frac{y}{x} - \frac{\beta}{\alpha} \right) + 2\sigma_1 v_1 \left(\frac{4\pi}{3\alpha v_1} \right)^{1/3} \left(1 - \frac{1}{3} \frac{\beta v_2}{\alpha v_1} \right) + kT(\gamma_2 - \gamma_1) \left(\frac{4\pi}{3\alpha v_1} \right)^{1/3} \frac{\beta}{\alpha} \quad (24)$$

and

$$g_2^0 - B_2 = kT \ln \frac{\beta x}{\alpha y} + kT \left(\frac{x}{y} - \frac{\beta}{\alpha} \right) + 2\sigma_1 v_2 \left(\frac{4\pi}{3\alpha v_1} \right)^{1/3} \left(1 - \frac{1}{3} \frac{\beta v_2}{\alpha v_1} \right) - kT(\gamma_2 - \gamma_1) \left(\frac{4\pi}{3\alpha v_1} \right)^{1/3} \frac{\beta v_2}{\alpha v_1} - 3kT(\gamma_2 - \gamma_1) \left(\frac{4\pi}{3\alpha v_1} \right)^{1/3} \left(1 + \frac{\beta}{\alpha} \right) \quad (25)$$

For the left hand sides of these equations we can use Eqs. (19).

Eqs. (24) and (25) allow one to determine α and β when the composition, y/x , of the melt is given. If y/x is chosen equal to ρ (see Eq. 16) assuming K_1 and K_2 to have been given, the value of β/α will be given by Eq. (14) and $\alpha, \beta \rightarrow \infty$. In this case we simply deal with bulk stable equilibrium. On the other hand, if we choose $y/x < \rho$, the value of α becomes finite, and both β and α will correspond to the unstable equilibrium between the melt and a small crystal.

One of our goals is to contrast the values of α and β obtained under these conditions with the values which would be obtained if the "derivative" terms on the right of Eqs. (9) were neglected. To this end we derive the counterparts of Eq. (24) and (25) without these terms and get,

$$g_1^0 - \mu_1^0 = kT \left(\frac{y}{x} - \frac{\beta}{\alpha} \right) + 2\sigma_1 v_1 \left(\frac{4\pi}{3\alpha v_1} \right)^{1/3} \left(1 - \frac{1}{3} \frac{\beta v_2}{\alpha v_1} \right) - kT(\gamma_2 - \gamma_1) \left(\frac{4\pi}{3\alpha v_1} \right)^{1/3} \frac{\beta}{\alpha} \quad (26)$$

and

$$g_2^0 - B_2 = kT \ln \frac{\beta x}{\alpha y} + kT \left(\frac{y}{x} - \frac{\beta}{\alpha} \right) + 2\sigma_1 v_2 \left(\frac{4\pi}{3\alpha v_1} \right)^{1/3} \left(1 - \frac{1}{3} \frac{\beta v_2}{\alpha v_1} \right) - 2kT(\gamma_2 - \gamma_1) \left(\frac{4\pi}{3\alpha v_1} \right)^{1/3} \frac{\beta v_2}{\alpha v_1} \quad (27)$$

In the next section we establish reasonable values for the parameters in these equations and present solutions for discussion.

MODEL PARAMETERS AND SOLUTION

We set $\sigma_1 = 200 \text{ dynes cm}^{-1}$, a not unreasonable value for the interfacial tension between a metal crystal and its melt. Furthermore, we set

$$v_1 = v_2 = 5 \times 10^{-23} \text{ cm}^3$$

corresponding to a lattice parameter of about 3.5\AA . We set Γ_1 , and therefore γ_1 equal to zero corresponding to the so-called "equimolecular" dividing surface.⁷ We arrive at a choice for γ_2 as follows. Γ_2 is a two dimensional surface density. If we consider the effective thickness of the surface layer to be one lattice parameter we can convert Γ_2 to a volume density by dividing by $v_2^{1/3} = v_1^{1/3}$, (i.e., the surface volume density of component 2 inside the crystal is given by $\beta/(\alpha v_1 + \beta v_2)$). Since we want component 2 to concentrate at the surface we write

$$\frac{\Gamma_2/v_2^{1/3}}{\beta/(\alpha v_1 + \beta v_2)} = 1000 \quad , \quad (28)$$

i.e., we choose the ratio of surface to volume concentration to be 100. From Eq. (22) we see that γ_2 must then be

$$\gamma_2 = 1000 v_2^{1/3} = 3.68 \times 10^{-5} \text{ cm} \quad (29)$$

We also choose T to be 1000°K so that

$$kT = 1.38 \times 10^{-13} \text{ ergs}$$

Since values for K_2 and K_1 are already available from Eqs. (17) and (18), Eq. (19) can be used to obtain

$$g_1^0 - \mu_1^0 = 6.73 \times 10^{-15} \text{ ergs}$$

(30)

$$g_2^0 - B_2 = -1.24 \times 10^{-12} \text{ ergs}$$

The magnitudes of all the relevant parameters are then

$$\sigma_1 = 200 \text{ dyne cm}^{-1}$$

$$v_1 = v_2 = 5 \times 10^{-23} \text{ cm}^3$$

$$\gamma_1 = 0$$

$$\gamma_2 = 3.68 \times 10^{-5} \text{ cm}$$

$$kT = 1.38 \times 10^{-13} \text{ ergs}, \quad T = 1000^\circ\text{K}$$

$$g_1^0 - \mu_1^0 = 6.73 \times 10^{-15} \text{ ergs}$$

$$g_2^0 - B_2 = -1.24 \times 10^{-12} \text{ ergs}$$

$$\rho = 0.05$$

Using these parameters, the two sets of equations, Eqs. (24), (25) and Eqs. (26), (27), were solved numerically with the aid of a computer. The first set which we denote by I includes the derivative terms. The second set, denoted by II, does not. Several values of $y/x < \rho = 0.05$ were introduced, and the values α, β , corresponding to each y/x was determined for both sets of equations. The results appear in Table 1.

TABLE 1

| y/x | α_I | α_{II} | $(\beta/\alpha)_I$ | $(\beta/\alpha)_{II}$ | $r_I(\text{cm})$ | $r_{II}(\text{cm})$ |
|-------|--------------------|--------------------|-----------------------|-----------------------|-----------------------|-----------------------|
| 0.045 | 4.69×10^9 | 4.65×10^9 | 9.48×10^{-5} | 5.29×10^{-6} | 3.82×10^{-5} | 3.81×10^{-5} |
| 0.040 | 6.06×10^8 | 3.73×10^8 | 1.44×10^{-3} | 4.70×10^{-6} | 1.93×10^{-5} | 1.64×10^{-5} |
| 0.035 | 3.59×10^8 | 9.67×10^7 | 3.85×10^{-3} | 4.12×10^{-6} | 1.62×10^{-5} | 1.05×10^{-5} |
| 0.030 | 2.79×10^8 | | 6.21×10^{-3} | | 1.49×10^{-5} | |
| 0.025 | 2.34×10^8 | | 8.37×10^{-3} | | 3.82×10^{-5} | |

In Table 1 the subscripts I and II identify solutions which correspond to the respective sets of equations, I and II. The first column exhibits the five values of $y/x < \rho = 0.05$ for which solutions were sought. The α and β/α columns are self-evident. The last two columns list the radii (in centimeters) of the crystals in equilibrium with the melts having the various compositions y/x . Generally speaking, it may be seen that these crystals have diameters approximating 1/2 micron. For the larger crystals, the values of α do not differ much between set I (derivative terms ignored), but for the smaller crystals appreciable differences occur. For example, at $y/x = 0.035$, α_I is 3.5 as large as α_{II} .

When it comes to (β/α) , however, the differences are quite dramatic at all sizes.

Listings for set II do not appear for $y/x = 0.030, 0.025$, since solutions were apparently non-existent in this regime.

The indications of all of this are that reasonable situations can be found in which the overlooked derivative terms in Eqs. (9) can be quite important. They become even more important if either K_2 or γ_2 are increased. Thus, if we set $\gamma_2 = 3.68 \times 10^{-4}$ cm, the results in Table 2 are obtained.

TABLE 2

| y/x | α_I | α_{II} | $(\beta/\alpha)_I$ | $(\beta/\alpha)_{II}$ |
|-------|-----------------------|--------------------|-----------------------|-----------------------|
| 0.045 | 4.67×10^{11} | 4.32×10^9 | 2.76×10^{-3} | 5.29×10^{-6} |
| 0.040 | 3.21×10^{11} | 3.49×10^8 | 5.82×10^{-3} | 4.70×10^{-6} |
| 0.035 | 2.64×10^{11} | 9.13×10^7 | 8.49×10^{-3} | 4.11×10^{-6} |
| 0.030 | 2.29×10^{11} | | 1.09×10^{-2} | |
| 0.025 | 2.03×10^{11} | | 1.31×10^{-2} | |

Although, in Table 2 we do not show r_I and r_{II} , it is clear, from the values of α_I which are of the order of 10^{11} that we are dealing with particles several microns in diameter. Yet the differences between the two sets of solutions are quite considerable even in the α columns.

OSTWALD RIPENING AND DENDRITE SPACING

The results of the preceding sections have significance for the phenomenon of Ostwald ripening in which the distribution of crystal sizes in a precipitate changes with time under the influence of surface effects. It is clear that the overlooked derivative terms could play an important role. However, the same could be said of the fine structured dendrites observable in rapidly cooled small metal drops. These dendrites have curvatures of the order of a reciprocal micron, and the smaller dendrites are liable to "ripen" away in favor of the larger ones. The precise description of this phenomenon should include the effects of the derivative terms.

Because of the greater geometric complexity attending the direct treatment of the dendrite problem we have chosen to illustrate the effect by working with "spherical" crystals. However, in the future an attempt should be made to deal with dendrite geometry directly.

ACKNOWLEDGEMENT

The author expresses his appreciation to Dr. Brice Carnahan for the numerical solutions of equations (24) through (27). This

research was supported by the Advanced Research Projects Agency of the Department of Defense under Contract No. MDA903-76C-0250 with The University of Michigan.

REFERENCES

1. H. Reiss and M. Shugard, submitted to the Journal of Chemical Physics.
2. H. Reiss, "Methods of Thermodynamics," pp. 164-165 (Blaisdell, 1965).
3. J. W. Cahn and J. E. Hilliard, J. Chem. Phys. 31, 688(1959).
4. Reference 2, p. 144.
5. Ibid, Eq. (9.52), p. 145.
6. Ibid, p. 177.
7. Ibid, p. 167.

PROSPECTS FOR NDE OF POWDERED METALS

G. S. Kino

The problem of acoustic NDE of cast powdered metal structures has some similarity to that encountered in the NDE of the refractory ceramics used in turbine blades. It is desirable (1) to make transducer contact to curved surfaces in the as cast form, (2) detect surface cracks, (3) detect flaws of the order of 1 mm down to flaws of the order 10 μm comparable to the smallest grain sizes.

The contacting problems should be soluble by making a buffer with one flat surface made of a material with a comparable acoustic velocity and shaped to fit the part of interest. Gold foil, water, grease, or a material such as liquid indium or mercury could be used to make contact between the mating pieces, and a transducer moved along the flat surface. This would avoid refraction problems.

The scattering of acoustic waves of frequency f from flaws of a size a smaller than the acoustic wavelength varies as $f^4 a^6$ as does the back scattering from grains of this size. A pulsed acoustic beam of area A occupies a volume of the order of λA . Therefore scattering is obtained from all the grains occupying this volume.

The scattering from an individual grain depends on the

anisotropy of the material and may be reduced by an order of magnitude or more from that due to an inclusion or pore of the same size. Clearly, though, it is unlikely that a pulsed unfocused acoustic beam can be used to detect a flaw comparable to the grain size.

It is apparent that for optimum detection of a small flaw, it is desirable to work at as high a frequency as possible. Better still, by using focused beams, the volume occupied by the pulsed beam can be reduced to a volume $K\lambda^3$, where K is in the range 1-10. But the search procedures become correspondingly slower unless electronically focused and scanned beams are used; this would require a major step forward in the present technology of such systems for operation with flaw sizes in the 50-200 μm range.

Presently existing NDE systems could be used to detect flaw sizes of the order of 1 mm, for they are already employed with conventional materials. As the frequency is increased, the acoustic attenuation due to grain scattering increases as f^4 in the metal, while that due to thermal conduction increases as f^2 . So it is unlikely that flaws of the order of 50 μm in size could be detected at distances of more than a few millimeters from the surface using frequencies in the 50-100 MHz range with wavelengths of the order of 50-100 μm . But one could certainly envisage detecting flaws 10 cm or more from the surface, several times the grain size, using lower frequencies.

As far as surface cracks are concerned, it is con-

ceivable to use Rayleigh waves propagating along curved surfaces, and excited with shaped wedge transducers or through a liquid in which the part is dipped. Similar criteria as far as distance from the transducer from which flaws can be detected apply. But it would appear reasonable from measurements made by the author at 2.5 MHz in Al to use 10 MHz surface waves with a velocity of the order of 3×10^5 cm/sec and a wavelength λ of 0.3 mm to detect small voids and flaws $\lambda/4$ deep and of the order of λ in diameter.

The limits on these processes will basically depend on the acoustic losses at the frequencies used. As so little is known about the acoustic loss in these new materials, basic measurements of acoustic attenuation must first be carried out before more exact estimates of the ultimate resolution capabilities of NDE techniques can be made.

ACKNOWLEDGEMENT

This research was supported by the Advanced Research Projects Agency of the Department of Defense under Contract No. MDA903-76C-0250 with The University of Michigan.

NUCLEATION, UNDERCOOLING AND HOMOGENEOUS STRUCTURES IN RAPIDLY SOLIDIFIED POWDERS

J. P. Hirth

INTRODUCTION

Two classes of effects of cooling rate on the microstructure of rapidly solidified metal alloy powders have been discussed, see the notes in this volume by Flemings¹, Mehrabian², Kear³, and Cox and Moore⁴. One trend is the transition from dendritic to cellular to planar growth, in agreement with the standard theory of solidification, as the ratio G/R increases. Here, in accord with the solidification literature, G is the temperature gradient in the liquid adjacent to the interface and R is the mean growth rate normal to the interface.^{3,4} The other is the occasional appearance of a uniform composition region at the center of dendrites indicating nucleation and growth in conditions of undercooling at the interface.^{1,2} With respect to structures attainable with rapid solidification, both factors are important in striving for increased G values. In the following discussion, the dependence of both classes of behavior on G is considered and an index of merit is developed which identifies factors influencing the formation of uniform microstructures.

GROWTH-CONTROLLED STRUCTURES

In growth control, the solid-liquid interface is supposed to be advancing in a quasi-steady-state manner; and essentially equilibrium conditions, both for temperature and composition, are supposed to exist there. Implications with respect to microstructure for such growth are illustrated in Fig. 1 in regions on a $G-R_S$ plot. Here R_S designates growth, under the above near-equilibrium interface conditions, which invariably results in either macro- or microsegregation as opposed to growth R_U under conditions of undercooling which can occur without segregation. As shown in Fig. 1a, for large powder particles, large values of G/R_S lead to columnar grains growing from the surface to the interior and small values to equiaxed grains. For small particles there is not sufficient volume to develop columnar grains and nominally equiaxed grains form throughout the G/R_S region. The compositional substructure is indicated in Fig. 1b, where the columnar-type grains are shown to grow with a planar, cellular, or dendritic morphology while the equiaxed grains can also contain cellular or dendritic patterns. In any of the columnar models, the liquid is continually enriched in solute as solidification proceeds, producing macrosegregation which is most pronounced for the planar mode as shown in Fig. 1c. Figure 1d illustrates the microsegregation pattern which is absent for the planar growth mode, present as weak to moderate segregation to cell walls in the cellular mode, and present as moderate to strong segregation to

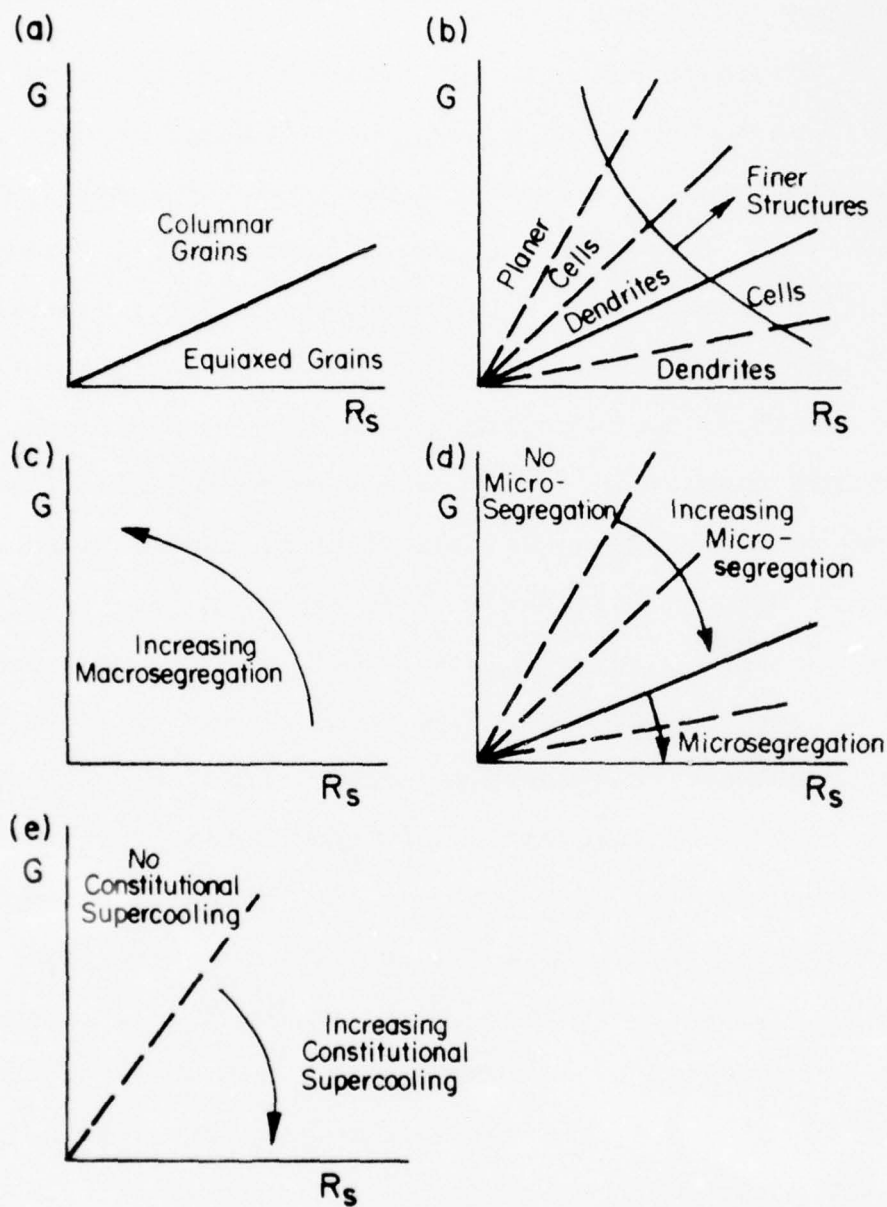


Figure 1. Features of structures produced in quasi-steady-state growth, illustrated on plots of growth rate R_s versus liquid temperature gradient G : (a) grain form, (b) substructure, (c) macrosegregation, (d) microsegregation and (e) constitutional supercooling.

interdendritic arm regions in the dendritic mode. Relevant to both the growth modes and the segregation pattern is the degree of constitutional undercooling in the various growth modes shown in Fig. 1e. Planar growth proceeds without such undercooling, whereas the other modes involve increasing undercooling with increasing values of the ratio R_S/G as illustrated.

The equiaxed grains can form in one of two ways. First⁵, a dendrite arm growing into an undercooled region can develop a cylindrical topology with length to diameter ratio greater than the critical value π for Rayleigh instability. Then, under surface energy driving force, the cylinder becomes unstable with respect to break up into shorter ellipsoidal to spherical shapes, the tip of the dendrite can break off, rotate under local convective forces and hence create a new grain. Second, with large undercooling, a new grain can nucleate in the region of maximum undercooling in the liquid near the interface. As these grains continue to grow, segregation patterns develop in either cellular or dendritic modes or in the macroscopic sense of solute enrichment in the last liquid to solidify at the grain boundaries.

Of major interest with respect to microstructural control^{3,4,6} is the trend to finer structure as also shown in Fig. 1b. The refinement of structure is again related to two phenomena. First⁵, the fine scale dendrite tips undergo an Ostwald ripening process under surface energy driving forces; this process at constant temperature varies as $t^{1/3}$ and hence

should give a dependence on cooling rate \dot{T} (which should be proportional to G) of an inverse power form. Second⁷, the wavelength of the initial interface instabilities, which develop as a competition between surface area increase and bulk driving force (related to undercooling), and which determine the initial dendrite spacings, decrease with increasing undercooling, or increasing R_S . To the extent that, in powder solidification, R_S itself increases with increasing G , to a limit, increases in G also result in finer structures by the latter mechanism. Hence, finer structures should develop with increasing values of the product GR_S . Indeed, the value of the dendritic arm spacing has been found^{1,6} to vary roughly proportional to $\dot{T}^{-0.3}$ for a number of materials for \dot{T} up to at least 10^4 - 10^5 K/s.

The decreasing dendritic spacings and the tendency to eliminate microsegregation patterns have provided the major motivation for the effort to achieve relatively larger \dot{T} values in powder solidification for subsequent microstructural control in alloy processing.^{4,6} However, because of problems in powder handling and contamination, effort to exceed the $\dot{T} \sim 10^5$ K/s value, particularly if it requires making powders with diameters ≤ 10 μm has been questioned. The next section suggests that still larger \dot{T} values can be beneficial and points to factors other than \dot{T} which can be important in achieving homogeneous microstructures.

NUCLEATION AND CONTROLLED STRUCTURES

As both Flemings¹ and Mehrabian² have noted, with sufficient undercooling, nucleation and growth to complete solidification can occur without the interface temperature ever reaching the solidus temperature of the alloy. The critical condition is^{1,2}

$$\bar{C}_p (T_S - T_N) = \bar{C}_p [\Delta T + (T_S - T_L)] \geq \Delta H \quad (1)$$

where \bar{C}_p is the average heat capacity of the solid and liquid, T_S , T_L and T_N are respectively the temperatures of the solidus, the liquidus, and nucleation; ΔH is the heat of fusion; and ΔT is the undercooling pertinent to nucleation. The only controllable variable in Eq. (1) is ΔT , which in turn is governed by the nucleation rate J of solid in liquid. Growth at a rate R_U under undercooled conditions can occur without segregation: the exception to this would be a case of interface-controlled growth where the atomic attachment process deposited one species selectively but even in this case no microsegregation would occur.

The propensity for nucleation and its consequences for microstructure are illustrated in Fig. 2 as a function of G and X . The number of nuclei formed per unit volume is given by

$$\int_{T_N}^{T_L} \left(\frac{\partial J}{\partial T} \right) \left(\frac{\partial T}{\partial t} \right) dt \propto Jt \quad (2)$$

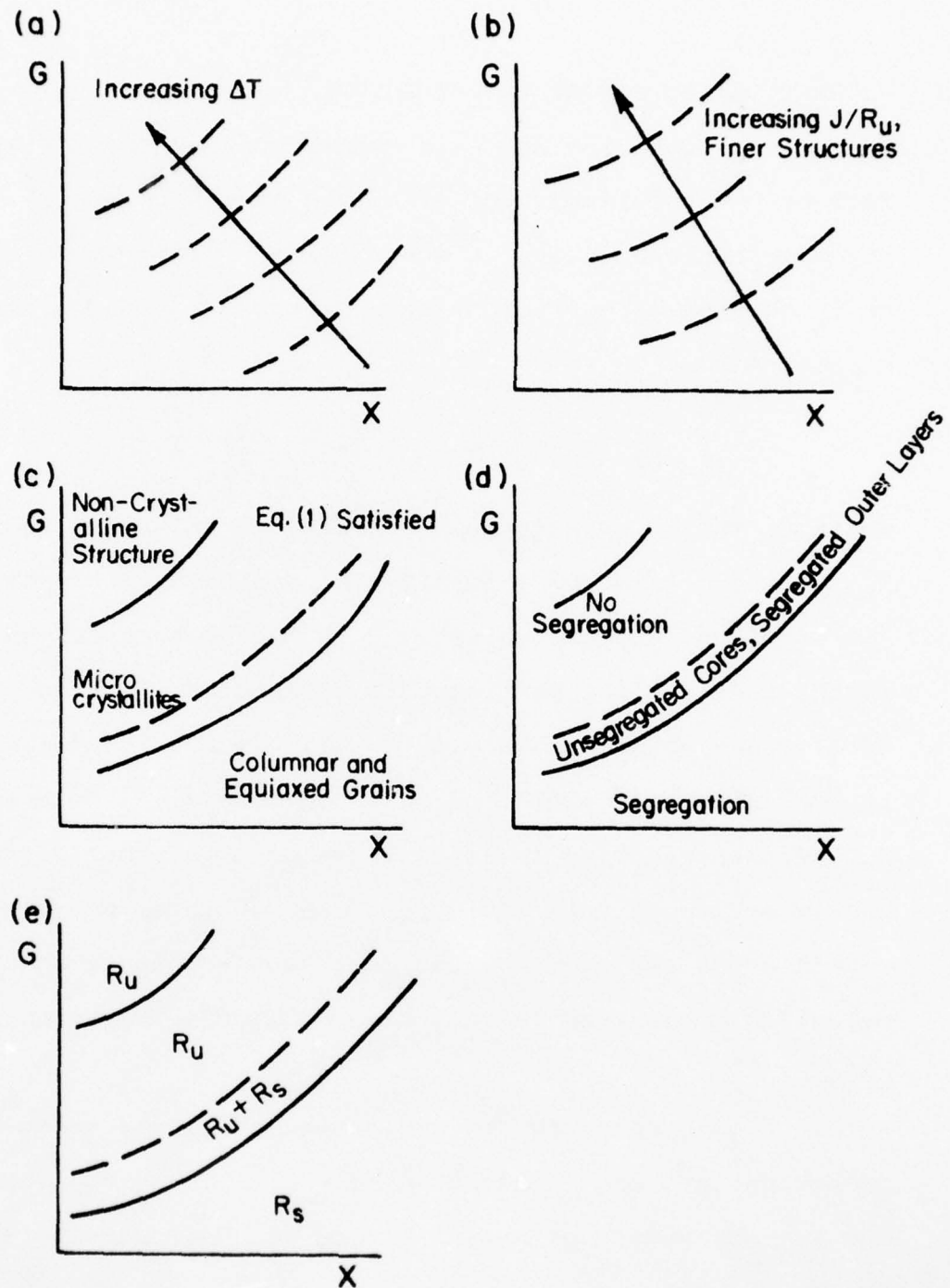


Figure 2. Features of structures in nucleation-controlled cases illustrated on plots of liquid temperature gradient G versus X , a term representing other factors which tend to enhance nucleation: (a) supercooling, (b) ratio of nucleation rate J to growth rate R_u , (c) grain form, (d) micro-segregation and (e) dominant growth mode.

However, the nucleation rate is essentially a delta function, zero for $T > T_N$, non-zero for $T = T_N$, so the number is proportional to Jt and thus to J/\dot{T} , i.e., to J/G . Therefore, the achievable ΔT before a nucleus can form is proportional to G/J . The factor X includes all other factors which influence nucleation. J decreases, or ΔT increases, with¹⁰ decreasing volume per particle (X) decreasing surface area per particle (X) when heterogeneous nucleation at the liquid-vapor interface is important, and with decreasing concentration of other heterogeneities (X) such as impurities, inclusions, and second phase particles.

Figure 2a demonstrates these variations for the undercooling ΔT . Increasing ΔT of course means decreasing T_N , decreasing average growth rate R_U over the growth range, and therefore an increasing ratio J/R_U at large ΔT , Fig. 2b. In turn a large J/R_U ratio results in a finer resulting microcrystallite size, also indicated. Figure 2c shows that somewhat above and below the critical value of ΔT , required to satisfy Eq. (1), equiaxed microcrystallites will supercede the growth structures of Fig. 1: for very large ΔT , such that T_N becomes less than T_g , the glass transition temperature, a non-crystalline powder will result. As depicted in Fig. 2d, there will be no micro- or macrosegregation (with the proviso noted earlier) for ΔT greater than the critical value to satisfy Eq. (1). Somewhat above this critical value, microcrystallites will form with homogeneous cores governed by R_U type growth

surrounded by a region where normal equilibrium growth occurs, with attendant segregation, as illustrated in Figs. 2d and e.

Hence, higher values of G and lower values of X can, in principle, produce even more homogeneous microstructures than the most uniform growth-controlled cases, and suggest further effort to control both variables. Qualitatively, the intercedance of nucleation control as opposed to growth control is illustrated in Fig. 3.

INDEX OF MERIT

The maximum attainable value of ΔT will be that for homogeneous nucleation. Of the parameters described by X , only the particle volume will influence J for this case. Each separate case of heterogeneous nucleation would require individual treatment, but with regard to parametric dependences, they would resemble the homogeneous nucleation case. Therefore the value of ΔT required to fit Eq. (1) for the homogeneous nucleation case is developed to give an index of merit for achievement of nucleation control. In the context of Eq. (2), the probability of forming one nucleus in a particle of volume V , taken to be the critical condition, is given by $J(T_N)V \delta t$ where δt is the time increment $\approx 0.01 \Delta T / \dot{T}$ to enter the regime of rapid nucleation behavior. Thus the critical condition is

$$\frac{0.01JV\Delta T}{\dot{T}} \approx 1 \quad (3)$$

The expression for the homogeneous nucleation rate¹⁰, rewritten

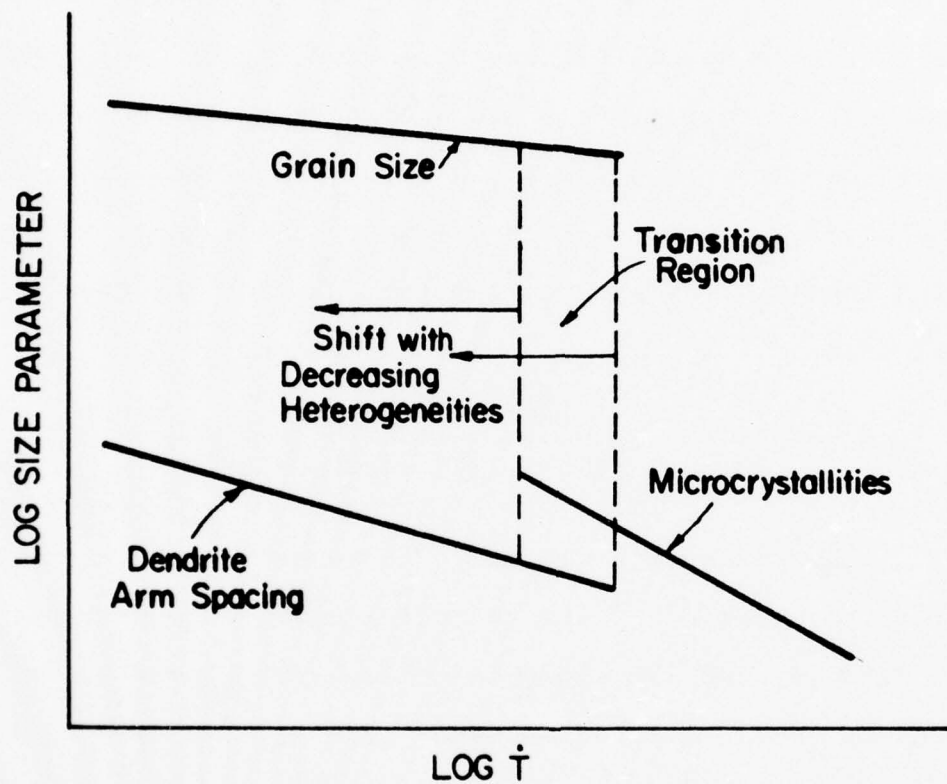


Figure 3. Plot of dendritic arm spacing, grain size, and microcrystallite size versus cooling rate dT/dt .

in terms of common metal properties for typical cases, is given by

$$J = 10^{-2} 4\pi (r/a)^2 (a/\Omega) D \exp - \left(\frac{16\pi\gamma^3 \Omega^2 T_L^2}{3kT_N \Delta H^2 \Delta T^2} \right) \quad (4)$$

where 10^{-2} is the so-called nonequilibrium factor, r is the critical nucleus radius, a is the atomic diameter, D is the liquid diffusivity, γ is the solid-liquid interfacial energy, Ω is the atomic volume and k is Boltzmann's constant. Substituting into Eq. (3) and rearranging, we find for the critical value

$$\Delta T^2 = \left(\frac{16\pi\gamma^3 \Omega^2 T_L^2}{3kT \Delta H^2 \ln(10^{-3} d^3 (r/a)^2 (a/\Omega) D \Delta T / \dot{T} J)} \right) \quad (5)$$

where d is the particle diameter. The variables which can be controlled to maximize ΔT are to increase \dot{T} and to decrease d .

Eqs. (4) and (5) apply in general for single or multi-component systems. Limited evidence to date^{8,9} indicates that supercoolings for homogeneous two-component liquids are about equivalent to those for the pure solvent. However, to the extent that added solute elements do not promote heterogeneous nucleation, they could influence (generally decrease) γ by interface adsorption. Evidently, in Eq. (5), such an effect would be more important than those produced by changes in d or \dot{T} and so would require control in attempting to attain large ΔT values.

As a demonstration that values given by Eq. (5) are attainable, we examine the case of homogeneous nucleation of mercury, where experimental results are available.¹¹ With $\bar{C}_p = 0.136$ J/g and $\Delta H = 11.6$ J/g, the value of ΔT required to satisfy Eq. (1), with $T_L = T_S$ for pure mercury, is 85 K. The experimentally observed value¹¹ was 79 K for a case where the logarithmic factor in Eq. (5) was 80.6 and where $d = 5\mu\text{m}$ and $\delta t \sim 10^2$ s. In order to attain $\Delta T = 85$ K, the logarithmic factor would have to equal 69.6. This could be achieved by decreasing the product $d^3\delta t$ by a factor of 6×10^4 . With constant d and with $\delta t = 0.01 \Delta T/\dot{T}$, the factor could be achieved with a cooling rate of 5×10^2 K/s. Alternatively for $d = 50 \mu\text{m}$, the factor could be achieved with a cooling rate of 5×10^5 K/s or for $d = 10^2 \mu\text{m}$ with a rate of 4×10^6 K/s. These rates are within the range of achievable rates with known powder making devices^{4,6} and demonstrate that the achievement of homogeneous powders is possible.

ACKNOWLEDGEMENTS

This research was supported by the Advanced Research Projects Agency of the Department of Defense under Contract No. MDA903-76C-0250 with The University of Michigan. Helpful discussions with M. Cohen, E. E. Hucke and B. H. Kear are gratefully acknowledged.

REFERENCES

1. M. C. Flemings, Report of the ARPA Materials Research Council, 1976.
2. R. Mehrabian, Report of the ARPA Materials Research Council, 1976.
3. B. H. Kear, Report of the ARPA Materials Research Council, 1976.
4. A. R. Cox and J. B. Moore, Report of the ARPA Materials Research Council, 1976.
5. M. C. Flemings, Solidification Processing, McGraw-Hill, New York, 1974.
6. N. J. Grant, Report of the ARPA Materials Research Council, 1976.
7. W. W. Mullins and R. F. Sekerka, J. Appl. Phys. 34, 323 (1963); 35, 444(1964).
8. D. H. Rasmussen and A. P. Mackenzie, in "Water Structure at the Water-Polymer Interface," ed. H. H. G. Jellinek, Plenum, New York (1975), p. 126; J. Chem. Phys. 59, 5003 (1973).
9. D. H. Rasmussen and C. R. Loper, Jr., Acta Met. 24, 117 (1976).
10. J. H. Holloman and D. Turnbull, Prog. Met. Phys. 4, 333 (1953).
11. D. Turnbull, J. Chem. Phys. 20, 441(1952).

SUGGESTED NEW ALLOYS WITH PROMISE FOR
SMALL-PARTICLE ALLOY DEVELOPMENT

E. E. Hucke, J. P. Hirth and M. Cohen

An exciting aspect of alloys produced from rapidly cooled small particles is the possibility of development of alloys with compositions which cannot be usefully achieved by other techniques. These alloys cannot be usefully achieved by other techniques. These alloys cannot be produced conventionally because of limitations of the solidification process in conventional casting, because phase-transformation kinetics exclude the relevant structure in conventional heat-treatment, and because the resulting structures are too brittle or reactive to process. A number of alloys which show promise in one of the above senses were suggested at the conference. Here these alloys are listed under general fields of application. Some detailed rationalizations for these suggestions are given in the MRC Conference Report to appear subsequently.

MECHANICAL PROPERTIES

1. Higher C-content stainless steels and superalloys.
2. β -stabilized Be.
3. High solute content Be for precipitation hardening.
4. Graded material with varied fine (10 μ m) to large (100 μ m) grain and particle sizes for resistance to fatigue crack growth.

5. Cu-Ni-Sn spinodal-decomposition alloys.
6. Precipitation hardening Al alloys for fatigue resistance, toughness and corrosion resistance.
7. TiAl and Ti_3Al with added solute elements (notably Nb).
8. Fe-9Ni-4Co-0.3C and TRIP steels for high toughness.
9. Cu-Al-Ni thermoelastic alloy.
10. High-P solution and precipitation hardened austenitic steel.
11. NiAl-Ni₂AlTi alloy.
12. Ni-Ti alloys.

MAGNETIC PROPERTIES

1. Co₅Sm, Co₅Re (Re = rare earth), Co₁₇Re₂ alloys for high B-H product hard magnets.
2. Co₅ (Y,Pr) in particular.
3. Co-Fe alloys.
4. Fe ~10Si ~6Al alloys for high permeability and low magnetostriction soft magnets.

SUPERCONDUCTING PROPERTIES

1. High critical-temperature V₃Si, Nb₃Sn, Nb₃Ce alloys.
2. Cu-Nb-Sn
3. β -W (but questionable).

MAGNETOSTRICTIVE TRANSDUCER

1. TbFe₂.
2. DyFe₂.
3. PrM₂ (M = transition metal).

HYDROGEN STORAGE

1. Transition metals.
2. LaNi_5 .

SONIC PROPERTIES

1. Fe-41Ni-9Mo (Vibralloy) for temperature-independent frequency response.

CATALYSIS

1. Cu-Ni-Cr alloys.

WEAR AND MACHINING

1. Co-WC.
2. Tribaloy (Co or Ni containing CoMoSi or $\text{Co}_3\text{Mo}_2\text{Si}$).

COMMENTS ON RSP

M. C. Flemings

Many different methods have been discussed at this meeting for atomizing and rapidly solidifying metal droplets. A number of these (and perhaps others not mentioned) have the potential (1) to produce modest quantities of rapidly solidified powder at ultra-fast cooling rates ($>10^6$ °C/sec or 10^7 °C/sec), and (2) to produce large quantities of powder at rapid solidification rates ($>10^5$ °C/sec) more economically than existing processes. Therefore, I make the following recommendation.

A number of small research projects should be started to develop promising new ideas for producing rapidly solidified small particles. Projects should be aimed at producing modest quantities of metal (e.g., $\frac{1}{4}$ lb. per run) and should have one or more of the following aims:

1. Develop (at modest cost) small scale equipment which could later be scaled up to commercial size to produce rapidly solidified powder ($>10^5$ °C/sec) at significantly lower cost than existing equipment.
2. Develop methods to produce ($\sim\frac{1}{4}$ lb.) quantities of ultra-rapidly solidified powder for research use. Powder should be solidified at $>10^6$ or 10^7 °C/sec.
3. Using laboratory equipment of item (1) and/or (2)

above, fundamental process variables should be studied and correlated with structure using heat flow, fluid flow, and solidification theories.

4. Quantities of powder produced ($\sim\frac{1}{4}$ lb. per run) should provide enough material for compaction and property testing. Work along these lines should be undertaken.

ACKNOWLEDGEMENT

This research was supported by the Advanced Research Projects Agency of the Department of Defense under Contract No. MDA903-76C-0250 with The University of Michigan.

A KEY BOTTLENECK IN THE EXPLOITATION OF
RAPID SOLIDIFICATION PROCESSING (RSP)

M. Cohen

A case is made for the implementation of flexible, small-scale RSP powder making facilities in order to extend and diversify research and development on many materials systems, particularly in the direction of structural control and structure/property relationships. The availability of such equipment, preferably adaptable to laboratory operation and not necessarily of a single design, is likely to do as much as anything else to expand the understanding and applicability of RSP materials. Moreover, the full benefit of RSP technology will inevitably require detailed studies of numerous parameters and their optimization, e.g., compositional variables, solidification rates, consolidation steps, and heat treatments. This type of development will likewise depend on ready access to small quantities of RSP powders.

Under these circumstances, it would be desirable for ARPA to elicit proposals for several types of small lot ($\frac{1}{4}$ -10 lbs.) RSP powder making machines with designated versatility for a range of materials. These proposals could be aimed at either the design and construction of the equipment in question or at the operation of central facilities for supplying the necessary RSP materials on request.

HIGHLIGHTS OF SESSIONS
ON RAPIDLY SOLIDIFIED POWDERS AND RELATED TECHNOLOGY

E. E. Hucke, J. P. Hirth and M. Cohen

The following highlights emerged from the presentations and discussions on "Rapidly Solidified Powders and Related Technology." A more explicit summary of these sessions will be given in the Final Report.

1. It is evident that scientific and technological ideas concerning rapidly solidified powders and their products are multiplying in excitement and potential.

2. Further reduction in droplet size appears to be the most effective way to achieve still faster solidification rates, ($>10^6$ °C/sec); the capability of forced convection in attaining even greater cooling rates requires more careful definition, particularly since the processing of fine powders becomes much more difficult with decreasing particle size.

3. There are new indications that the progressive decrease in dendritic-arm spacing with increasing solidification rate is interceded by spontaneous nucleation in the supercooled liquid. This is a very significant phenomenon because:

a. The microcrystallites or cells thus formed have a chance to grow just by atom-by-atom jumping across the liquid/

solid interface without compositional partitioning between the liquid and solid phases. Thus, in the limiting case, the microcrystallites will have exactly the same composition as the liquid, and the resulting grain boundaries can be unusually clean.

b. This prospect shows that it is important to strive for still faster cooling rates or, at least, solidification conditions in which the thermal gradients are large compared to the solid-front growth rate (i.e., without any long-range diffusion).

c. In this new regime, supercooling and nucleation phenomena will play a critical role in the size of the microcrystallites, possibly reaching down to 10-100Å.

d. In the light of these factors, the tolerance for impurities as well as for new alloy compositions can be sharply enhanced; indeed, it may well turn out that a quantum-step improvement in properties can be obtained in these highly-supercooled, nondendritic structures.

4. Skin-melting of bulk alloys by high-intensity laser-beam heating, together with conductive quenching by the metallic substrate, provides an excellent research tool for producing and studying the above-type of highly supercooled, nondendritic solidification and its competition with dendritic solidification. The inhibition of secondary-phase precipitation on solidification as well as the kinetics and morphology of the precipitation on reheating can also be investigated via this technique, comparing both dendritic and nondendritic structures in the skin-melted zone.

5. Consideration should be given to model alloy systems (such as Pd-Si and Pd-Si-Cu) which, even at conveniently accessible cooling rates applied to a given composition, will exhibit the complete range of processes from dendritic segregation to microcrystalline solidification to amorphous-glass formation.

6. It appears that an electrostatic field tends (a) to stabilize a stream of liquid metal against break-up into droplets, and (b) to damp out oscillations once the droplets are formed. These phenomena should be examined as to origin and possible application to atomization processes.

7. Particular attention should now be given to the powder-consolidation steps and their role in the resulting structure/property relationships. Very little systematic information is available on what happens to the grain size, dendritic structure, and secondary-phase morphology as a function of the processing and heat-treatment variables. These interactions also point up the need (and opportunity) to optimize compositions and treatments in order to take full advantage of the small-particle approach to materials technology.

8. The wide-scale exploitation of rapidly-solidified powder processing will require multi-faceted structure/property research programs on numerous alloy systems. To that end, there is urgent need for flexible, small-lot ($\frac{1}{4}$ to 10 lbs.) powder-making facilities which will permit the detailed study of compositional and structural variables. The availability of such equipment will probably do as much as anything to expand the understanding and

applicability of the resulting materials.

9. Although glassy-metal powders can be produced in some alloy systems, it is still not known whether these powders can be consolidated without degradation of the glassy state. Such experiments might be tried on the Pd-Si and Pd-Si-Cu prototype alloys mentioned in Item 5.

10. Results to date on the powder-processed intermetallics TiAl and Ti_3Al look encouraging; substantial progress has been made during the past year toward achieving some ductility and good fatigue strength along with noteworthy creep resistance.

11. There is increasing evidence that powder processed aluminum alloys exhibit improved resistance to stress-corrosion cracking and to corrosion fatigue, compared to the conventional wrought alloys. This finding has major implications from the standpoint of extending the mechanically-useful range of high-performance materials in typical environments.

12. A promising approach to the ultrasonic nondestructive testing of powder-processed bodies with curved surfaces has been described, based on the use of appropriately-shaped adapters between the transducer and the curved surface.

13. It appears that, in order to take advantage of the expected 100°F improvement in operating temperature for powder-processed jet-engine turbine blades, the development of a protective coating for the state-of-the-art superalloys will become mandatory.

14. Fe-Al-Si alloys look attractive for reasons of special

magnetic properties as well as oxidation and corrosion resistance, without requiring any potentially strategic metals. However, the development of such alloys has been blocked by brittleness problems, which may now be circumvented by powder processing. This means that the stable and metastable phase relationships in the ternary Fe-Al-Si system should now be roughed out by computational methods.

15. There are good prospects for substantial advances in titanium alloy formability and properties through the RSP approach. However, less expensive methods are needed for producing high quality titanium powders.

METALLIC GLASSES

H. Ehrenreich, J. Gilman, J. Hirth and G. Vineyard

INTRODUCTION

Glasses form a new class of metallic materials for two fundamental reasons. One is that previously inaccessible compositions can be obtained in useful forms by making them glassy; the second is that molecular structures which are distinct from polycrystalline structures can be obtained. These novel compositional and structural features lead to remarkable combinations of chemical and physical properties.

An absence of long-range-order at the molecular size scale characterizes metallic glasses. Short-range-order within molecular units may exist within a glass, but no long-range-order. Glasses are usually obtained by quenching a liquid rapidly into the solid-state so the long range structure of the liquid is retained in the solid form. The short-range-order may differ between the liquid and solid forms and in some cases it may increase during the quenching process. Metallic glasses may also be obtained by means of condensation from the vapor phase; by electro-deposition; by sputtering, or by disordering an ordered solid via particle bombardment.

Glasses can be made from combinations of two or more of a great variety of metallic elements. Thus the principle element

in a glass may be: titanium, iron, cobalt, nickel, zirconium, palladium, platinum, gold, samarium, or uranium; among others.

Useful shapes such as wires, ribbons, strips, and thin films can be made at high production rates using relatively simple equipment to continuously quench alloy liquids.

Exceptional mechanical, magnetic, electrical, and chemical properties have been observed for metallic glasses. These observations indicate that they have great promise for applications such as reinforcement of elastomers, corrosion resistant cables, transformers, magnetic filters, magneto-mechanical transducers.

Some of their exceptional properties are: high strength plus toughness, magnetic softness plus mechanical hardness, high biaxial strength, very low chloride corrosion rates, and low attenuation of acoustic waves. Also they may have good resistance to high energy radiation.

Because metallic glasses provide a novel state of matter that has not been available previously for scientific study, there is still much to be learned about their structures and behaviors. By looking through this new window, scientists can develop new insights and thereby make new predictions regarding solid-state behavior including novel systems of technological importance.

To review the present state of knowledge about metallic glasses, a brief conference that was organized by J. J. Gilman was held during the annual meeting of the Materials Research

Council. The agenda of the conference is attached. This conference had the purposes of informing interested members of the MRC about metallic glasses, and of identifying the research approaches toward the study of these materials that might be most fruitful in generating fresh understanding.

Some of the questions that arose during the conference are discussed in the following sections. The structures, the mechanical behavior, corrosion resistance, the electrical properties, and the magnetic properties are addressed in turn. Suggestions are also made for finding answers to several questions of importance.

STRUCTURAL QUESTIONS

Despite the attention bestowed upon metallic glasses, their structures are not very well understood. This is in sharp contrast with normal metals where the structure of almost every alloy is known from X-ray diffraction studies and is usually the starting point for discussions of properties. A model based on random dense-packing of spheres, sometimes called the Bernal Model, is much used. A competing model assumes that small irregular clusters of atoms are somehow packed together to build up a structure. Diffraction experiments give rather general information (total and partial radial distribution functions) which is related to the structure and which can be used to rule out some hypothetical structures, but which does not fully determine the structure. There are a number of indications that the short range order within metallic glasses is significantly

affected by deformation, heat treatment, and other processes, but the details are not known. It is desirable that further careful work be done with all available techniques. X-ray and neutron diffraction (particularly the combination of the two); neutron inelastic scattering; NMR; Mossbauer experiments; SAFS, ESCA; and field ion microscopy all appear to have promise for increasing the understanding of these structures. With their help the effects on structure of treatments such as annealing, irradiation, ion implantation, etc., can be studied.

Computer simulation of structures with models employing forces more realistic than hard spheres and with a variety of algorithms for generating the amorphous structure appears very much worthwhile. If a realistic model can be constructed other properties beside the structure itself can be looked at. The elastic moduli can be computed and the anomalously low shear modulus in the glassy state may become understood. Thermal properties can be investigated, including the entropy of the glassy state and the question of the balance between structural and dynamical contributions to the entropy. Diffusion and transport mechanisms could be investigated, and possibly also the mechanisms and kinetics of devitrification.

Raising the glass transformation temperature and reducing the rate of quenching needed to retain the glassy state are highly desirable goals. Better understanding of the nucleation and growth processes involved in devitrification might point the way to these goals. It also should be emphasized

that the range of compositions studied to date is surely only a small part of the range of possible glass-forming systems, and there is no clear reason for believing that systems with still better properties cannot be found. Rare earth elements have hardly begun to be tried as replacements for transition metals, and compositions with three, four and more components offer an immense range for study. Empirical rules uncovered to date for predicting the effects of various elements on glass properties are inadequate for guidance in this effort.

Radiation effects in metallic glasses have been studied relatively little. Since metallic glasses in general may have superior resistance to radiation damage, further work would be desirable. If the glassy state in these materials is, in some sense, the most random state possible, any amount of radiation which does not produce large thermal spike, implantation, or transmutation effects should not change its properties. Energetic electrons would be ideal for testing this question. If further randomization of the structure were found to alter the properties significantly, this would be evidence that short range order is important. On the other hand, irradiation that does produce large thermal spikes (i.e., fission fragments) would offer the possibility of producing devitrification. This could be the means of further studying the kinetics of devitrification. We note that a glass containing 70 atom per cent uranium has already been made.

In connection with the above suggestion it may be noted that in the case of quartz, heavy irradiation of either the crystalline or the vitreous form apparently produces a third state of substance, not crystalline but distinct from vitreous quartz, and of intermediate density. Although vitreous quartz has a network structure, whereas metallic glasses do not, it still would be of interest to know whether a similar phenomenon occurs in any glassy metals.

The stabilization by nitrogen of the glassy deposition of molybdenum from the vapor is not understood and deserves further study. Does the phenomenon occur in other systems, leading to other elemental glasses or new glassy alloys?

MECHANICAL BEHAVIOR

Whether plastic flow occurs via the motion of molecularly discrete dislocations or via viscous-type flow contained within shear bands remains an open question. One test of these ideas would be to compare (for self-consistency) the dilatational strain computed to fit flow stress data for the dislocation model with that required to explain the difference in flow stress under tension and compression or with superposed hydrostatic stress; the so-called strength differential effect. Another approach would be to perform low-temperature internal friction tests to probe for the kink-motion relaxation peaks characteristic of dislocation motion.

The limited work hardening and uniform structures of metallic glasses make them useful as model materials for

studying crack propagation from the mechanics viewpoint. Unlike most high strength bulk materials with their spectra of microstructural scale effects, inhomogeneous flow on a macroscale and uniform flow on a near crack-tip on a microscale are observed in metallic glasses. These simple structures suggest that glasses should be useful in determining mechanisms for crack closure and environmental effects in fatigue, hydrogen embrittlement during static loading, and the physics of cracking at the atomic level.

Research is needed to clarify the mechanism of the exceptionally low ultrasonic attenuation (particularly for longitudinal waves) found in metallic glasses.

One rough experimental result has been reported indicating phosphorous segregation on the normal-mode crack surface of a Fe-Ni-B-P metallic glass. This result appears questionable in the absence of a reason for such segregation and may therefore be spurious. However, the implications with respect to cracking are so important that the experiment should be carefully repeated using scanning Auger spectroscopy and other techniques.

CORROSION RESISTANCE

An important issue is whether the low corrosion rates and rapid formation of passive films for Cr-containing glasses is a consequence of the homogeneity of the surface or of an inhibition effect produced by phosphate ions derived from dissolved phosphorus. This question should be clarified by performing film growth studies in solutions already containing

phosphate additives.

Metallic glasses, relative to crystals of similar chemical compositions, show reduced dissolution rates in the active regions of potential-current plots. Studies should be performed to determine whether this effect is caused by enhanced film formation, shifting the passive region, or by an intrinsic resistance of the metallic glasses to dissolution. These studies have obvious implications with respect to alloy design.

While they generally show good corrosion resistance, several metallic glasses have exhibited hydrogen embrittlement. Extensive research is needed to determine how frequently this effect occurs for metallic glasses and whether it can be inhibited.

In many metal alloy systems with relatively small thermodynamic deviations from ideality, active dissolution rates follow a simple law-of-mixtures. Such rates should be measured as a fraction of metalloid content in metallic glasses to determine whether the rates are reduced relative to the law-of-mixtures because of the strong negative thermodynamic deviations from ideal solution behavior associated with the transition-metal-metalloid systems.

ELECTRICAL PROPERTIES

An understanding of the electronic energy-level structures of metallic glasses is prerequisite to a calculation of electrical transport coefficients such as the resistivity. Limited evidence is now available indicating that it may be

valid to regard a metallic glass as a frozen liquid alloy for such calculations. Further experiments should be performed on liquid alloys and glasses having the same composition to ascertain whether the transport coefficients and the magnetic susceptibilities are indeed usually the same for the two sets of materials. If so, theoretical calculations based on a liquid alloy model are entirely feasible because the theoretical techniques for performing such calculations are available. These also require knowledge of the partial structure functions as well as their temperature dependences. The latter have so far been obtained for only a limited number of systems.

The Faber-Ziman theory and its extensions have been successful in explaining the concentration dependence of the resistivity in several liquid-metal alloy systems. Experimental information of the sort just discussed will be helpful in establishing whether this theory, based on independent but positionally corrected scatterers embedded in a free electron gas, is generally applicable to metallic glasses. However, questions dealing with the number of electrons associated with metalloid atoms that are available for conduction, and the amount of charge transfer between metalloid and transition metal atoms require resolution before a definite viewpoint can be established.

A phenomenological theory due to Tauc and Nagel has suggested reasons for the origin of the metastability in metallic glasses. While it is probably not correct in detail, this

proposal is fruitful since it is closely linked to the liquid metal model. For example, it suggests why the temperature coefficient of the resistivity is negative or zero for many metal glass compositions. Its validity is currently being tested by detailed calculations. Measurements of the specific heat at very low temperatures would be desirable in providing information about the density of electronic states and the possible existence of soft vibrational modes associated with metalloid atoms located in cages formed by surrounding transition metal atoms.

Examination of the superconducting properties of several systems formed by quenching indicates that the transition temperature T_c is usually less than 10K. Incentives for further exploration of glasses in connection with the search for high T_c materials are therefore limited. By contrast, the formation of metastable alloys, whose constituents are immiscible by vapor deposition appears to hold more promise.

MAGNETIC PROPERTIES

Metallic glasses may be para, ferro, or ferri-magnetic. In certain cases they may also form spin-glasses, which are currently of great theoretical interest. The ferromagnetic Fe, Co, and Ni based alloys are characterized by lower magnetic moments and Curie temperatures than their transition metal counterparts. The Slater-Pauling curve for this portion of the 3d series is shifted downward towards lower magnetic moments by a constant amount. The fact that ferromagnetism persists,

except for Ni, in the presence of 20% metalloid is clearly inconsistent with the rigid-band model, which is invoked in the current transport theories. The Curie temperature appears to be extraordinarily sensitive to alloy composition and annealing. The explication of these effects will require a rather more sophisticated view of the electronic energy level structure of these alloys than anything currently available. In particular, one would expect the magnetic properties to be far more sensitive to details of the short range order than the transport properties.

The nature of the domain patterns and walls in systems such as the metal glasses that have no crystalline anisotropy is still imperfectly understood. Experimental investigations using more sophisticated techniques would be desirable. A comparison of the magnetic properties of vapor deposited, splattered, and rapidly quenched films would also be useful since the small thicknesses available with the first two techniques makes these materials useful as magnetic bubble memories.

RECOMMENDATIONS

Many military applications of these materials can be expected because superior bonded metal composites can be constructed from them with high strength, toughness, impact resistance, and perhaps radiation resistance. Also more efficient transformers can be designed which could reduce avionic weights. Another example, is strong cables that resist salt-water corrosion for use in control and force transmission systems. Other

applications can be cited at the present time and more will appear in the future.

The compositions available and the range of physical forms of metallic glasses are expanding rapidly along with scientific understanding of the structures and properties. As this expansion occurs, it is recommended that DARPA keep informed of the advances. The best way to do this is participate in the expansion by helping to maintain the scientific health of the field.

ACKNOWLEDGEMENT

This research was supported by the Advanced Research Projects Agency of the Department of Defense under Contract No. MDA903-76C-0250 with The University of Michigan.

METALLIC GLASSES

July 19, 20, 1976

AGENDA

J. Gilman - A Technological Overview
D. Turnbull - Genesis and Structure
R. Hasegawa - Electrical Properties
H. Ehrenreich - Round Table Discussion
L. David - Mechanical Behavior
R. Staehle - Corrosion Resistance
C. Graham - Magnetic Behavior
J. Hirth - Round Table Discussion

PARTICIPANTS AND GUESTS

T. W. Barbee, Jr.
Center for Materials Res.
Stanford University
Stanford, California 94305

L. A. Davis
Allied Chemical Corporation
Materials Research Center
Morristown, New Jersey 07960

C. D. Graham, Jr.
LRSM/K1
University of Pennsylvania
Philadelphia, Pennsylvania 19174

R. Hasegawa
Allied Chemical Corporation
Morristown, New Jersey 07960

R. W. Staehle
Metallurgical Engineering
Ohio State University
Columbus, Ohio 43201

David Turnbull
Harvard University
Pierce Hall
Cambridge, Massachusetts 02138

METALLIC GLASS STRUCTURES

J. J. Gilman

The most direct experimental approach to the determination of the structures of metallic glasses is the scattering of X-rays, neutrons, and other forms of radiation. After corrections for systematic errors, the resulting scattering data constitute a constraint on hypothetical glass structures. However, no unique connection exists between a proposed structural configuration and a set of scattering data. That is, many hypothesized configurations can be consistent with a given set of data.

Three types of model structures have been proposed by various authors. They are based on the ideas that the structure consists of: an aggregate of microcrystallites; a collection of densely random-packed individual spheres; or a collection of densely-packed clusters of spheres. These proposals compete for favor. There is a desire for a universal, but simple, model that is applicable to all glasses, but reality is probably too complex to allow this. Therefore, differing systems can probably be best described using differing models. Thus monatomic and simple molecular liquids might be best described in terms of dense random packing, but polyatomic systems containing atoms that interact relatively strongly with each other may be approxi-

mated best in terms of densely-packed clusters of unlike atoms.

The most stable metallic glasses (highest glass transition temperatures) are those composed of at least one transition metal and at least one metalloid (B, C, N, Si, P). These are also the glasses of most technical importance because they include ferrous glasses. Transition metal atoms and metalloid atoms interact strongly to form borides, carbides, nitrides, etc. Therefore, it is to be expected that the structures of glasses formed in these systems will be characterized by short range order that not only leads to dense packing of the atoms, but also to maximization of the proximity of metal-metalloid atoms relative to metal-metal and metalloid-metalloid pairs. In addition, transition metal-metalloid interactions tend to occur preferentially in particular bonding directions. This favors specific groupings of atoms (quasi-molecules).

As a result of the above considerations, it is proposed here that metallic glasses often consist of densely-packed non-periodic arrays of quasi-molecular groupings. Such a model appears to be consistent with such factors as: (a) the known structures of the adjacent crystalline phases; (b) the deep eutectics associated with glass-forming compositions; (c) the composition dependence of the liquid phase viscosity; (d) observed radial distribution functions; (e) the relatively high mass densities of metallic glasses; (f) properties of the glasses that are distinctly different from those of the equilibrium phases that lie adjacent to the glass-forming eutectics.

GLASSES AS MIXTURES OF QUASI-MOLECULES

Since there is no general structural model for liquids, special cases or groups of cases must be considered. The simple glasses of most engineering interest at present are those formed between Fe, Co, Ni and B, C, or P. The compositions are of the form $T_x M_{1-x}$ where T is the transition metal, M is the metalloid and x is typically 80 atomic percent. The discussion here will be limited to these cases.

The systems Fe-B, Co-B and Ni-B all have deep eutectics in their equilibrium diagrams at the atomic B concentrations: 17.0, 18.5 and 18.4 percent, respectively (Figure 1). These eutectics lie between the pure metals and the compounds TB_2 ; all of which have the same crystal structure. Fast quenching of the liquid alloys retains them as glasses which have unusually high glass transition temperatures.

In the case of Fe, similar equilibrium diagrams to those of Figure 1 exist for the Fe-C and Fe-P systems with eutectic compositions at 17.3 and 17.5 atomic percent, respectively. However, the compounds that participate in the eutectic are different; being Fe_3C and Fe_2P , respectively.

The liquids in all of these alloys are far from ideal or regular. This is indicated both by their equilibrium diagrams and by the properties of the liquids. Of the properties that can be readily measured for a liquid, the viscosity is most sensitive to the structure at the molecular level because it measures the amount of momentum that is transferred from

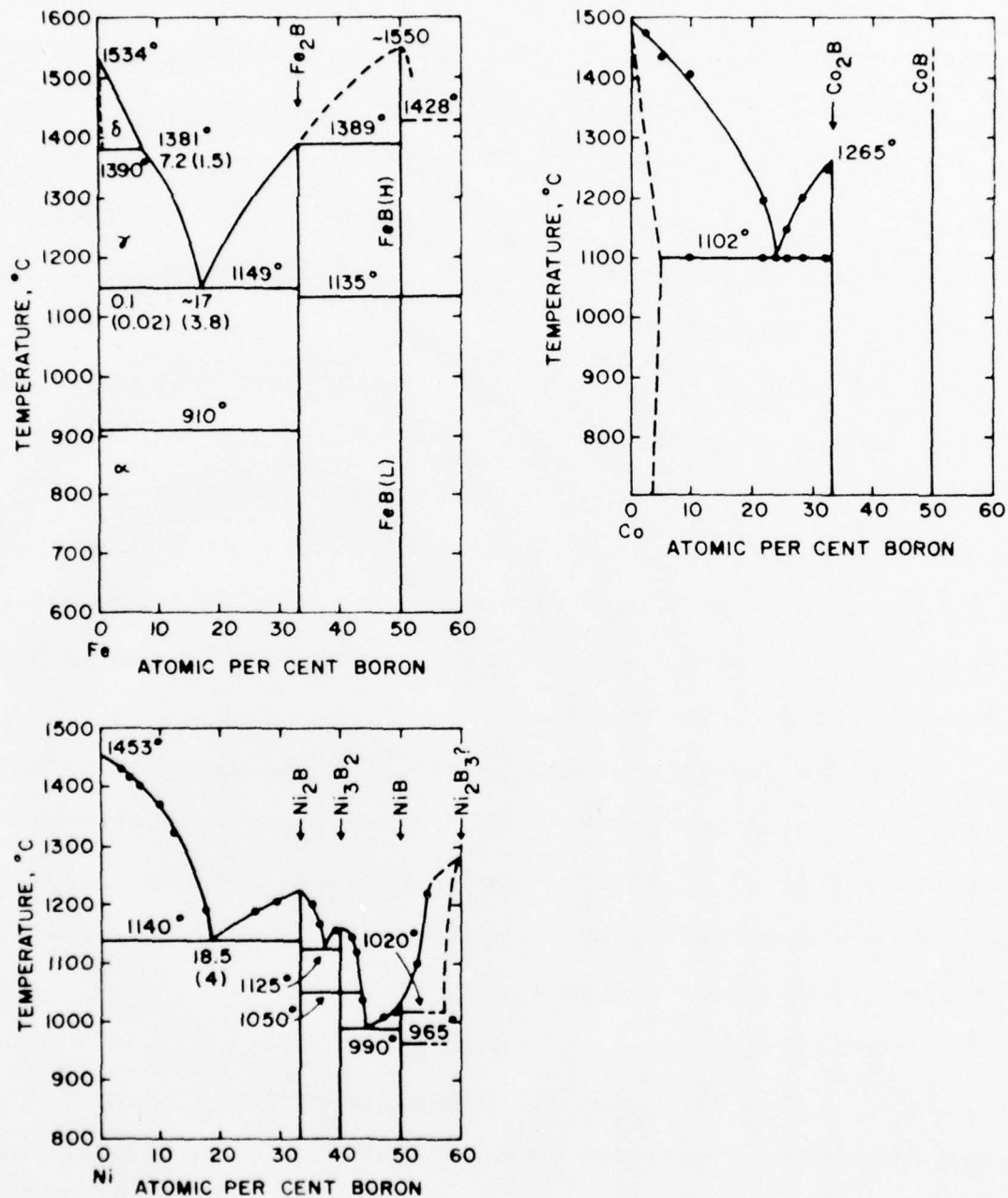


Figure 1. Fe-B, Co-B, Ni-B Equilibrium Diagrams.

one moving molecule or atom to another as they pass by one another. For an ideal liquid in which the constituent atoms are simply mixed together with little interaction between them, the viscosity is expected to interpolate linearly between the values for the liquids of the pure constituents. For the Fe-P and Fe-C systems (the only ones for which data are available) large deviations from this ideal behavior are observed (Figures 2 and 3).

In both sets of iron alloys the viscosity decreases as the solute concentration approaches the eutectic value. For the Fe-P case, it reaches a minimum at the eutectic composition and then increases to a maximum at the composition corresponding to the compound, Fe_2P . Note that the variation of the viscosity with composition pays little or no attention to the composition corresponding to Fe_3P . Thus the nature of this compound does not appear to play an important role in determining the structure of the liquid alloys.

The viscosity maximum at the Fe_2P composition reflects the influence of strong forces acting between the particles of the liquid. In the same way the minimum of the viscosity at the eutectic composition indicates weaker interactions. Thus one condition for a realistic liquid structure model is that it should be constructed from particles that interact relatively weakly; and yet reflect strongly interacting constituents. These two conditions are met if the Fe and B atoms interact to form molecular ions immersed in a sea of conduction electrons.

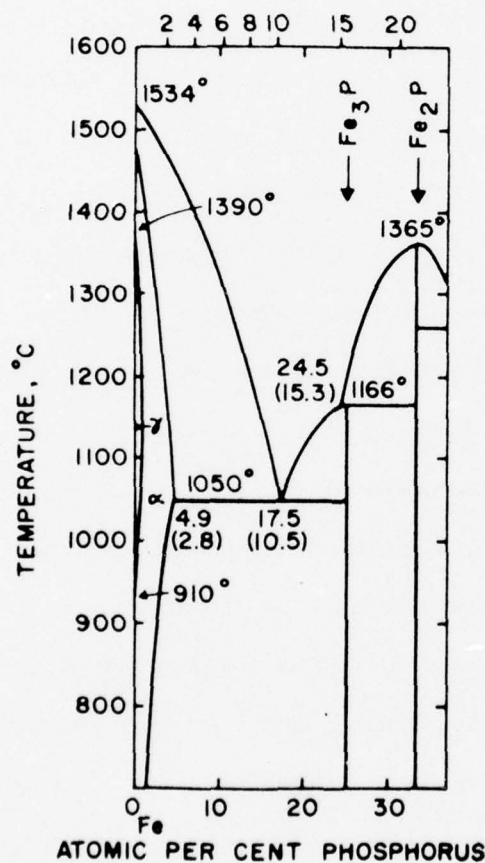
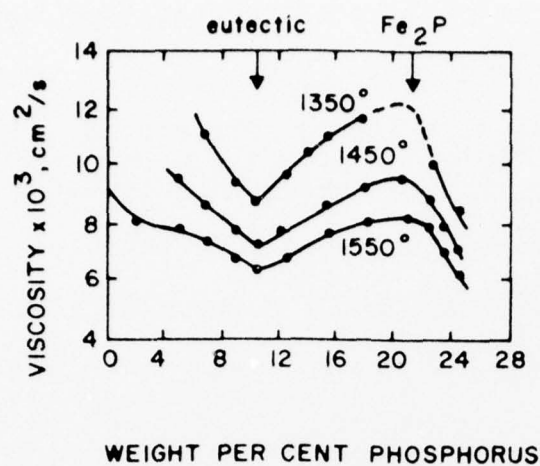


Figure 2. Viscosity vs Composition in the Fe-P System.

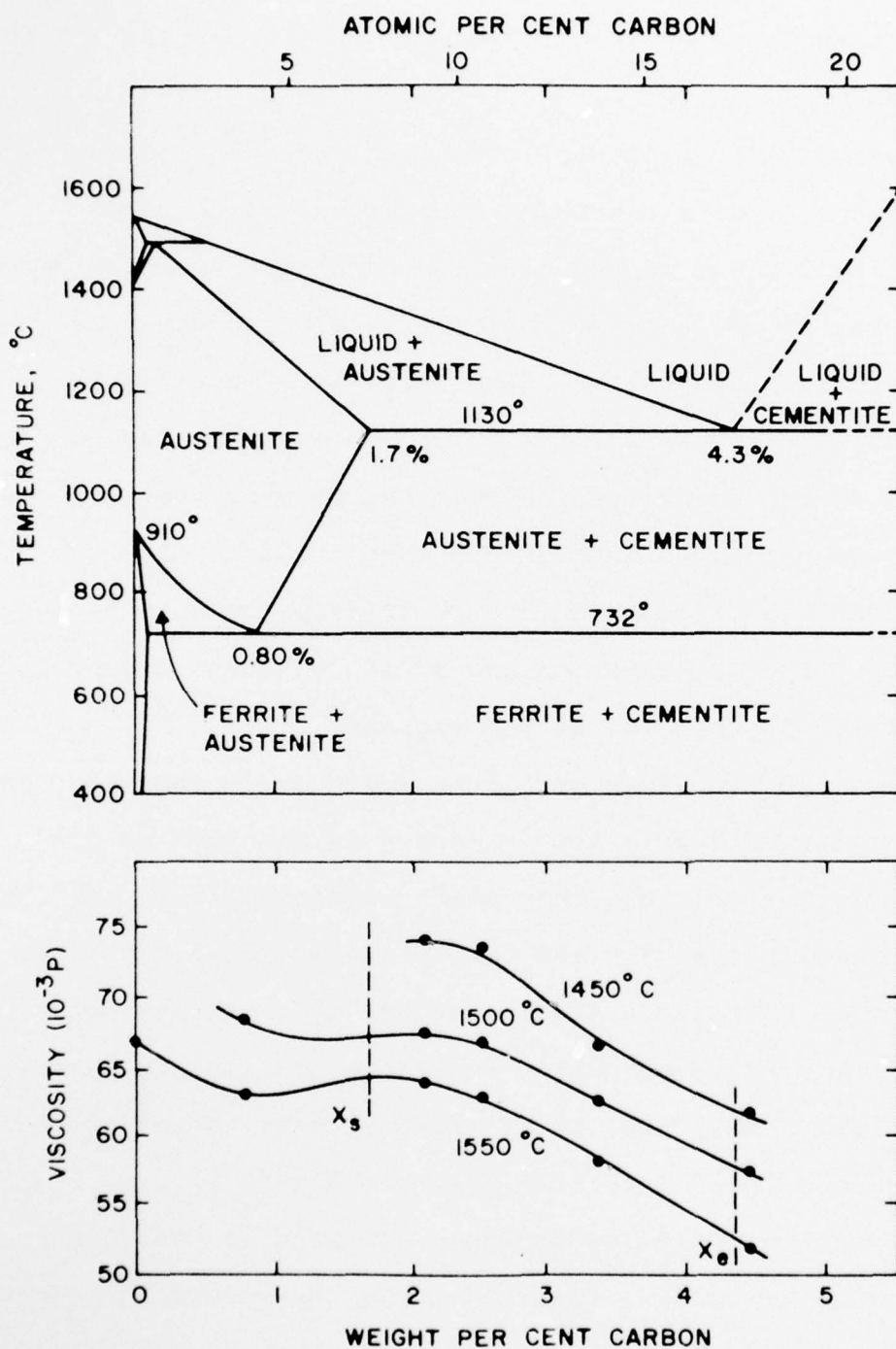


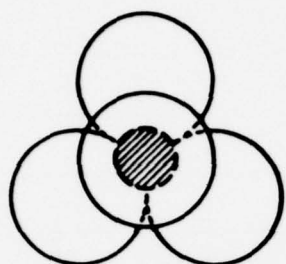
Figure 3. Viscosity vs Composition in the Fe-C System.

The positively charged ions are bound together by interactions of electrons in the d-orbitals of the transition metals and the metalloid atoms.

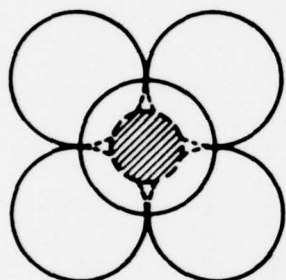
Possible molecular configurations that are consistent with the compositions and bonding symmetries are shown in Figure 4. The top two on the left (tetrahedron and octahedron) have the metal atoms in arrangements that are characteristic of the face-centered-cubic solid. The trigonal prism is a grouping characteristic of the Fe_2P crystal structure, while the two configurations on the right are found in the Fe_2B crystal structure. Although these groupings are derived from crystal structure groups, there is a difference because it is proposed that they do not share corners, edges, or faces with adjacent groups so they are nearly independent of one another.

Since the groupings of Figure 4 are self-contained, the metalloid concentration in each grouping is the same as the concentration of the liquid that might be formed from it. The numbers in parentheses give the percentage of metalloid in each grouping. The most stable liquids and/or glasses have metalloid concentrations of 17 ± 3 percent. No single grouping is consistent with this. Therefore, it is proposed that two or more of the groupings are needed to form a stable liquid.

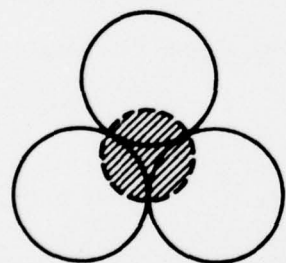
If a liquid consists of equal portions of two of the quasi-molecular groupings, Figure 5 shows the metalloid concentrations that result for all possible pairs of groups. The pairs that best match the characteristic eutectic composition



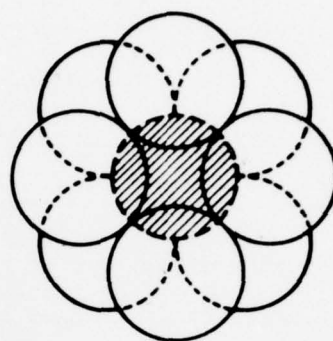
TETRAHEDRON (20)



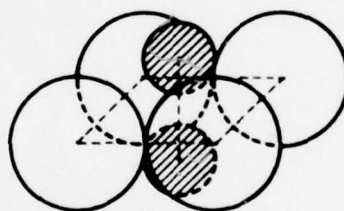
OCTAHEDRON (14)



TRIGONAL PRISM (14)



SQUARE ANTI-PRISM (11)



SQUARE PYRAMID (33)

Figure 4. Possible Transition Metal-Metalloid Clusters in Liquid Solutions.

| Tetrahedron | Octahedron | Trigonal Prism | Square Anti-Prism | Square Pyramid | Atomic % B |
|-------------|------------|-------------------|----------------------|-------------------|---------------|
| X | | | | X | 27 |
| | X | | | X | 23 |
| | | X | | X | 23 |
| | | | X | X | 20 |
| X | | | X | | 14 |
| | X | | X | | 13 |
| | | X | X | | 13 |
| X | | X | | | 17 |
| | X | X | | | 14 |
| X | X | | | | 17 |

Figure 5. Average Compositions Resulting from Various Pairs of Clusters.

(17 percent) are the tetrahedron/octahedron and the tetrahedron/trigonal-prism. A decision as to which pair might best describe the structure can be based on which pair can be packed most densely; this is the first pair because it allows close packing, whereas the second does not.

Although tetrahedral holes are rarely occupied by metalloid atoms in the solid-state, this is not necessarily true for liquids and is a question that needs investigation.

ACKNOWLEDGEMENT

This research was supported by the Advanced Research Projects Agency of the Department of Defense under Contract No MDA903-76C-0250 with The University of Michigan.

ELECTRICAL PROPERTIES AND METASTABILITY OF METALLIC GLASSES

H. Ehrenreich

It has recently been suggested that metallic glasses resemble liquid metals as far as many of the electrical and magnetic properties are concerned.¹ It is therefore of interest to examine the extent of this correspondence by regarding the metallic glass as a "frozen liquid" and to compare the calculated properties with experimental results. Unfortunately the amount of information concerning simple liquid metal alloys and the corresponding glasses having the same composition is still limited. As a beginning towards such a research program, it is necessary to resolve a number of puzzles in the application of the transport theory for liquid metals to systems of interest. These are:

1. Why should an approach based on potential scattering from single atoms in the Born Approximation in a liquid whose structure is characterized by the pair correlation function and neglects multiple scattering effects be valid for strong scatterers such as transition metal atoms? The scattering probability used to calculate the resistivity involves $|t(q)|^2 a(q)$, where $t(q)$ is the scattering matrix appropriate to a momentum transfer q and $a(q)$ is the structure factor. The scatterers are regarded as embedded in a free electron gas with effective

valence Z_{eff} , the charge contained in a Wigner-Sitz sphere having the same volume as the transition metal atom.

2. Why is the effective valence Z_{eff} associated with most transition metal liquid conduction electrons in the range $1 < Z_{\text{eff}} < 2$?

3. In transition metal-metalloid alloys, why, on the basis of existing calculations², do the polyvalent constituents appear to give up all of their valence electrons to the conduction band? This is consistent with the rigid band model, which, however, is known to be incorrect for substitutional alloys involving transition metal components. Furthermore, this model is known to be at variance with the results of magnetic moment measurements.

The first two of these questions can now be answered by utilizing recent results concerning the electronic energy levels in the 3d and 4d transition metals obtained by use of the "renormalized atom" approach³. It has been shown that the Fermi energy E_F can be determined to good accuracy by utilizing Lloyd's formula for the number of states per atom of a cluster of muffin tin potentials:

$$N(E) = N_0(E) + (2/\pi) \sum_{\ell} (2\ell+1) \delta_{\ell}(E) + N_m(E)$$

Here $N_0(E)$ is the integrated free electron density of states, proportional to $E^{3/2}$; the second term, which is also structure independent, depends only on the phase shifts, $\delta_{\ell}(E)$, of the single site potential, and $N_m(E)$ includes modification due to multiple scattering involving other sites. E_F is determined

by neglecting the structure dependent term $N_m(E)$, from the condition

$$Z = N(E_F) = N_0(E_F) + (2/\pi) \sum_{\ell} (2\ell+1) \delta_{\ell}(E_F),$$

where Z is the true valence of the atom. The fact that $N_m(E)$ is small for the 3d and 4d transition metals implies that this structure independent formula should also be applicable to liquids. In particular, in accord with the transport theory, a collection of atoms in a liquid can be pictured in terms of a single renormalized atom, characterized by its phase shifts $\delta_{\ell}(E)$, embedded in a free electron gas of effective valence $Z_{\text{eff}} = N_0(E_F)$. The result is just that to be expected on the basis of the Friedel sum rule. It is found that $Z_{\text{eff}} = 1.7, 1.2, 1.5, 1.3, 1.6$, respectively, for Ti, Ni, Cu, Pd, and Ag. Thus it appears to be valid;

1. to describe the scattering by scattering matrices $t(\{\delta_{\ell}\})$ which are a property of individual atoms arranged in a structure specified by $a(q)$, and

2. to associate Z_{eff} with effective conduction electron valences in the range $1 < Z_{\text{eff}} < 2$.

The resolution of the third points awaits further calculation, particularly in establishing the relative placement of transition metal and metalloid electronic energy levels.

As already noted, this approach has not yet been implemented for metallic glasses having the same composition as the corresponding liquid. The suggestion¹ concerning the metallic

glass-liquid alloy analogy is based on a comparison of Metglas 2826A ($\text{Fe}_{32}\text{Ni}_{36}\text{Cr}_{14}\text{P}_{12}\text{B}_6$) with $\text{Fe}_{80}\text{Ge}_{20}$. In effect, the metallic glass is viewed as a binary alloy (Transition Metal)₈₂ (Metalloid)₁₈ liquid, in which the transition metal and metalloid constituents, respectively, behave similarly.

This point of view is also supported by recent speculations concerning the metastability of metallic glasses by Tanc and Nagel⁴. They argue that in liquid metals the location of the first peak in the structure function $a(q)$ at wave number q_p occurs at an electron energy $E(q_p)$ at which the liquid has a minimum in the density of states which corresponds to a grain-gap. (In the case of an ordered crystal this gap would be real and q_p would correspond to a reciprocal lattice vector). They then invoke a Hume-Rothery type of argument to deduce that the Fermi wave number k_F is such that $k_F = q_p/2$. For the transition and noble metals $k_F < q_p/2$. The concentration of the metalloid must then be such that k_F is raised to the value $q_p/2$. For Ge or P, which are assumed to contribute 4 or 5 electrons per atom to the conduction band, the required concentration to fulfill the condition $k_F = q_p/2$ is about 20%, which is just the metalloid concentration at which most metallic glasses form. This view leads to an explanation of the negative temperature dependence observed in many metallic glasses, and, in particular, why this dependence occurs in glasses having large resistivity.

While these metastability considerations probably are not correct in detail, their consistency with the results of

electrical transport measurements is intriguing and suggests that further pursuit of the metallic glass-liquid alloy analogy in connection with both the electrical and magnetic properties of metallic glasses is likely to be fruitful.

ACKNOWLEDGEMENT

This research was supported by the Advanced Research Projects Agency of the Department of Defense under Contract No. MDA903-76C-0250 with The University of Michigan.

REFERENCES

1. M. Fischer, H-J. Güntherodt, E. Hauser, H. U. Künzi, M. Liard and R. Müller, Second International Conference on Rapidly Quenched Metals, Materials Science and Engineering (to be published).
2. O. Dreirach, R. Evans, H-J. Güntherodt, and H-U Künzi, J. Phys. F2, 709 (1972).
3. C. D. Gelatt, H. Ehrenreich and R. E. Watson (to be published in Phys. Rev.) H. Ehrenreich and L. M. Schwartz, Solid State Physics 31, 149 (1976).
4. J. Tanc and S. R. Nagel, Comments on Solid State Physics 7, 69 (1976).

ON THE MECHANISM OF SHEAR OF AN AMORPHOUS METAL

J. P. Hirth

For the shear deformation of a metallic glass, Gilman has suggested a model for the yield stress involving the glide motion of dislocations. These defects are supposed to have variable Burgers vectors along their lines, but to have a mean Burgers vector b equal to the mean atom spacing. The resistance to glide is assumed to be provided by the elastic resistance to a local dilatation, normal to the glide plane, which accompanies glide motion; somewhat of an analog to shear models in soil mechanics. By balancing the work done by the resolved shear stress τ per unit length of line per increment of advance b , τb^2 , with the work performed in creating the normal dilatation, he obtains an expression for σ_y . For the latter case, the work is assumed to be one-third of the work of formation of a spherical point defect as modeled by a ball in a hole.³⁻⁵ Thus, he obtains the expression for tension or compression, where the yield stress $\sigma = 2\tau$,

$$\sigma = 8\pi \epsilon^2 B / (1 + 3B/4\mu) \quad (1)$$

where ϵ is the strain normal to the glide plane, B is the bulk modulus and μ is the stress modulus.

Here, we consider several different cases, which give results for σ_l close to, but somewhat different from Eq. (1). If the dislocation moves as a line and creates a cylindrical dilatation field with strength $\delta A/A = 2\varepsilon$, where A is the area of the core region, then a two-dimensional analog of the three dimensional result of Eshelby³⁻⁵, including both the work done on the surroundings by the core and strain energy stored in the core, gives a work term

$$W_1 = A[2\varepsilon^2 B(1+4\mu/3B)+2\varepsilon P] \quad (2)$$

with a corresponding shear work term τA . Here, the work of interaction $2P\delta A$ of the defect and an external pressure P has been included. Alternatively, akin to the Gilman model, one can suppose that only strain normal to the glide plane is produced. Then the work term, again including strain energy stored in the core, is

$$W_2 = A[\varepsilon^2 B(1+4\mu/3B)+\varepsilon\sigma_N] \quad (3)$$

with σ_N the normal stress. Spaepen and Turnbull⁵ have suggested a model, not involving the dislocation concept, in which shear is accompanied by a local dilatation at the elastic-plastic boundary. This would lead to an expression such as Eq. (2), but with A' and ε' now referred to the new boundary rather than to the core and with an added term corresponding to the dissipated plastic work per unit volume, W_p ,

$$W_3 = A' [2\epsilon'^2 B(1+4\mu/3B) + 2\epsilon' P + W_p] \quad (4)$$

Another type of dislocation model would be to assume that motion occurs by lateral motion of kinks along a dislocation with work τb^3 now balanced by a local point-type strain field. If the local field is solely a strain normal to the glide plane, the work term would be $W = W_2 b$, which when balanced with the shear work would give the same result as Eq. (3); hence, this model need not be considered explicitly. Alternatively, the kink displacement could be a ball-in-hole type dilatation which would give

$$W_4 = V[6\epsilon^2 \mu(1+4\mu/3B) + 3\epsilon P] \quad (5)$$

Performing the appropriate work balances, the above expressions give corresponding predictions of the yield stress in tension or compression with or without superposed hydrostatic pressure. For this balance we assume core dimensions $A = b^2$ and $V = b^3$, giving:

$$\sigma_1 = 4\epsilon^2 B(1+4\mu/3B) + 2\epsilon P \quad (6)$$

$$\sigma_2 = 2\epsilon^2 B(1+4\mu/3B) - \epsilon \sigma_N \quad (7)$$

$$\sigma_3 = 4\epsilon'^2 B(1+4\mu/3B) + 2\epsilon' P + W_p \quad (8)$$

$$\sigma_4 = 6\epsilon^2 \mu(1+4\mu/3B) + 3\epsilon P \quad (9)$$

For purposes of correlation with experimentally observed yield strengths the interaction work terms are negligible, but for

the strength-differential (SD) effect, discussed next, they are important.

Models of the above type give specific predictions of the SD effect wherein the flow stress varies with the total applied stress tensor in general, or, in more limited cases, with superposed hydrostatic stress. The relevant SD expressions for the above forms are

$$(\partial\sigma/\partial P)_1 = 4\varepsilon^2(1+4\mu/3B)(\partial B/\partial P)+2\varepsilon \quad (10)$$

$$(\partial\sigma/\partial\sigma_N)_2 = 2\varepsilon^2(1+4\mu/3B)(\partial B/\partial\sigma_N)-\varepsilon \quad (11)$$

$$(\partial\sigma/\partial P)_3 = 4\varepsilon'^2(1+4\mu/3B)(\partial B/\partial P)+2\varepsilon' \quad (12)$$

$$(\partial\sigma/\partial P)_4 = 6\varepsilon^2(1+4\mu/3B)(\partial\mu/\partial P)+3\varepsilon \quad (13)$$

Pressure dependences of μ and B have not been measured for metallic glasses. However, on the basis of comparison with results for crystalline metals, they are assumed, as is evident from the above expressions, to have the same dependence on P or σ_N .⁶

Experimentally, the SD has been determined for $\text{Pd}_{78}\text{Si}_{16}\text{Cu}_6$ both by determining⁶ the variation of flow stress with superposed hydrostatic pressure of 6.9×10^8 Pa and by comparing^{6,7} the flow stress in compression, 1.54×10^9 Pa, and in tension, 1.44×10^9 Pa. The direct variation with P gives $(\partial\sigma/\partial P) = 0.08$. The variation in tension and compression gives $(\partial\sigma/\partial\sigma_N) = -0.07$, ref. 7, and -0.08 , ref. 6. If the variation

with σ_N were to reflect a true variation with P , since $\sigma_N = \sigma/2 = -3P/2$, the tension-compression tests would give $(\partial\sigma/\partial P) = 0.10$, ref. 7, and 0.11, ref. 8. On the other hand, if the variation with actual superposed P reflected a true variation with σ_N , the pressure experiments would give, since then $\sigma_N = -P$, $(\partial\sigma/\partial\sigma_N) = -0.08$. Thus, the results to date for the SD effect alone strongly support the σ_N dependent model dependence of Eq. (11) as opposed to the P dependent models. Nevertheless, for comparison of correlations between the SD results and the flow stress results, the value $(\partial\sigma/\partial\sigma_N) = -0.08$ is used for Eq. (11) and the mean value $(\partial\sigma/\partial P) = 0.09$ for Eqs. (10), (12) and (13). The use of $(\partial\sigma/\partial P) = 0.08$ instead in the latter case would give a decrease of about five percent in the values of ϵ computed from Eqs. (10), (12) or (13) to match the experimental SD results.

Values of ϵ computed from Eqs. (6)-(13) to fit the above experimental results are listed in Table 1. Data necessary for the correlation, in addition to those listed above, are^{6,8}:
 $B = 1.67 \times 10^{11}$ Pa, $\mu = 3.15 \times 10^{10}$ Pa, $(\partial B/\partial P) = (\partial \mu/\partial P) = -(\partial B/\partial \sigma_N) = -(\partial \mu/\partial \sigma_N) = 8.35$. The latter values are determined from the cited values of $(\partial \ln B/\partial P) = (\partial \ln \mu/\partial P) = 5 \times 10^{-11}$ Pa⁻¹.
 Again, the best correlation is with the normal-stress-type model of Eqs. (7) and (11). However, there is a factor of two difference in the results. The fit cannot be improved by changing the value of A since it affects both terms on the right sides of Eqs. (7) and (11) in the same way. Moreover, an attempt to modify Eq. (7) by adding a frictional term $\sigma\mu$ to the flow stress

TABLE 1. Values of normal strain ϵ required in Eqs. (6)-(13) to fit experimental data for σ and the SD effect.

| | ϵ to match σ | ϵ to match SD |
|------------------------------|---------------------------------|---------------------------|
| Eqs. (6), (8), (10) and (12) | 0.042 | 0.018 |
| Eqs. (7) and (11) | 0.059 | 0.030 |
| Eqs. (9) and (13) | 0.056 | 0.013 |

equation makes the fit worse. Nor can the fit of the ϵ values be reconciled by assuming a smaller dependence of the elastic constants on P or σ_N . The only plausible way to match the results is to suppose that the value $\epsilon = 0.030$ for Eq. (11) represents the true dilatational strain and that this strain, according to Eq. (7), contributes a fraction 0.26 of the flow resistance. The remainder of the flow resistance is then supposed to be contributed by a viscous or plastic dissipative term with minimal pressure dependence.*

In summary, the SD effect alone and a comparison of SD results and flow stress results favor a model of dilatation normal to the glide plane rather than one of hydrostatic pressure as a contribution to the flow resistance. This result is consistent with a dislocation-type flow mechanism in metallic glasses as suggested by Gilman.^{1,2} However, an exact fit to experimental results also requires a major contribution of a dissipative-type term to the flow resistance.

ACKNOWLEDGEMENT

This research was supported by the Advanced Research Projects Agency of the Department of Defense under Contract No. MDA903-76C-0250 with The University of Michigan.

*A model for a plastic-type term would be a local, bond-breaking, dislocation-core-like contribution to the flow resistance.

REFERENCES

1. J. J. Gilman, J. Appl. Phys. 46, 1625(1975).
2. J. J. Gilman, Physics Today 28, 46(1975).
3. J. D. Eshelby, Phil. Trans. Roy. Soc. 244, 87 (1951).
4. J. Friedel, Dislocations, Pergamon, Oxford, 1964, p. 360.
5. C. P. Flynn, Point Defects and Diffusion, Clarendon Press, Oxford, 1972.
6. L. A. Davis and S. Kavesh, J. Mater. Sci. 10, 453(1975).
7. L. A. Davis, P. Chou, L. E. Tanner, R. Ray and S. Kavesh, cited in L. A. Davis, Proc. 2nd Int. Conf. on Rapidly Quenched Metals, Mass. Inst. Tech. Cambridge, Mass. (1975).
8. M. Dutoit and H. S. Chen, Appl. Phys. Lett. 23, 357(1973).

STRUCTURAL RELIABILITY OF OPTICAL FIBERS

A. G. Evans and F. A. McClintock

ABSTRACT

When optical fibers are fabricated in very large lengths (~ 1 km), a significant proportion of failures are commonly encountered at relatively low stress levels. It is important that these failures either be statistically predictable or be eliminated by proof testing.

Methods for characterizing strength distributions in optical fibers, from tensile tests on relatively short fiber lengths, are described; and the use of such distributions for predicting failure on long lengths of fiber, subjected to axial strains and localized bending moments, is discussed. Also, the role of strength distributions in the isolation of defect origins is indicated.

The proof testing of optical fibers to truncate the strength distribution at an appropriate strength level is an attractive possibility. However, proof testing in environments that cause significant slow crack growth does not necessarily produce the desired truncation. The key relationships between the proof test cycle and the resultant strength distribution are thus described, to provide a rationale for devising effective

proof cycles. Alternatively, proof testing might be conducted at temperatures, $<-100^{\circ}\text{C}$, where slow crack growth does not occur. Heat transfer through coated optical fibers has been evaluated to demonstrate the feasibility of proof testing at such temperatures.

STRUCTURAL RELIABILITY OF OPTICAL FIBERS

A. G. Evans and F. A. McClintock

INTRODUCTION

There is an increasing requirement for optical fibers in applications that demand very long (up to 1 km) lengths of fiber. One of the key problems in the utilization of optical fibers in such large lengths is the relatively large proportions of fibers that fracture at moderate stress levels. This difficulty might be counteracted in three ways: (a) the most deleterious flaws might be eliminated or made ineffective by using stringent fabrication controls (and perhaps by utilizing surface compressive stressing techniques), thereby virtually eliminating service failures; (b) the statistics of fracture might be carefully analyzed such that, for designs that permit a certain proportion of 'redundant' fibers to fail during service, the predicted number of fiber failures can become a design allowable; (c) all fibers can be proof tested to enable all deficient fibers to be eliminated prior to service. Each of these approaches should not be viewed as mutually exclusive.

FIBER STRENGTHENING

The proportion of fibers that fail at the service stress level can be substantially reduced if the most deleterious flaws

in the long fibers can be identified and then virtually eliminated by exerting careful controls at the pertinent stage of fabrication. These deleterious flaws can be identified by fractographic studies of flaw origins¹ combined with the statistical analysis of strength data at the low strength extreme (see below). Once the type of flaw has been identified, it is required to determine the fabrication state that is the dominant source of these flaws. Then, the potential for eliminating the flaws by suitable modifications to the fabrication process can be assessed.

An alternate or additional method for enhancing the strength of fibers is to develop surface compressive stresses. However, this approach is only suitable for enhancing the long term strength* of the fibers if the most serious flaws occur at the surface of the fibers, i.e., internal flaws must be eliminated as a source of premature short term failures before surface compression strengthening should be contemplated.* A recently developed approach for surface compression strengthening that might be applied with good effect to the optical fibers problem is the 'molecular stuffing' process.² This process produces a layer of uniform compression - the most desirable profile for

*The strength of fibers containing quite large internal flaws can be enhanced by surface compression strengthening at intermediate times, because failure might still be controlled by the slow growth of smaller surface flaws. However, at long times, the hydroxyl ions that induce slow crack growth can easily diffuse into the interior of the small diameter fibers, and the slow growth of the internal flaws can occur at a rate similar to that for the surface flaws; surface compressive stresses are thus of little value.

enhancing the slow crack growth resistance³ - at levels up to $\sim 400 \text{ MNm}^{-2}$. This level of surface compression can be regarded as a minimum possible long term strength (provided that internal flaws are absent).

STATISTICS OF FRACTURE

The fracture of optical fibers can be statistically characterized by adopting a method recently proposed by Matthews et al.⁴ If the number of elements, δV , per unit volume with a uniaxial 'tensile strength' between S and $S+dS$ is defined as $g(S)dS$, then the probability, $1-\delta\phi$, that an element subjected to a tensile stress, S_1 , will survive, is given by;

$$1-\delta\phi = 1-\delta V \int_0^{S_1} g(S)dS \quad (1)$$

The probability of survival of a body containing elements subjected to a range of stress levels is the product of the survival probability of each element. For a one-dimensional stress distribution of the form

$$S = S_m (1-z/\ell)^k \quad (2)$$

where S_m is the peak stress, ℓ is a length dimension, z is the distance from the plane of peak stress and k is a constant, Matthews et al.⁴ have shown that the strength distribution function can be related to the overall failure probability ϕ (equal to the product of the failure probabilities, ϕ of each

element) by;

$$g(S) = \frac{kS}{2b\ell} \left[\frac{\phi''(1-\phi) + (\phi')^2}{(1-\phi)^2} + \frac{(1+1/k)\phi'}{S(1-\phi)} \right] \quad (3)$$

where b is dimension. The equivalent result for a two-dimensional stress distribution is given in Appendix I.

For a cylindrical body of radius r and length ℓ subjected to uniform tension, Eq. (3) simplifies to

$$g(S) = \phi' / 2\pi(1-\phi)r\ell \quad (4a)$$

for surface flaws; and to

$$g(S) = \phi' / \pi(1-\phi)r^2\ell \quad (4b)$$

for volumetric flaws. Hence, by ordering the strength data obtained in uniaxial tension tests* - the usual test mode for optical fibers - to obtain ϕ , the distribution function can be obtained with minimal ambiguity from Eqs. (4a) and (4b) (the only assumption is that the flaws are non-interacting). Then, by obtaining data on another sample with a substantially different gage length, and comparing the consistency of $g(S)$ derived from Eqs. (4a) and (4b), the parts of the distribution that are controlled by surface flaws and by internal flaws can be ascertained, as shown schematically in Fig. 1.

Once the distributions have been obtained over the

*The tests must be conducted in an inert environment, or at a stress rate that eliminates significant slow crack growth, otherwise the data analysis becomes highly complex (see section 4).

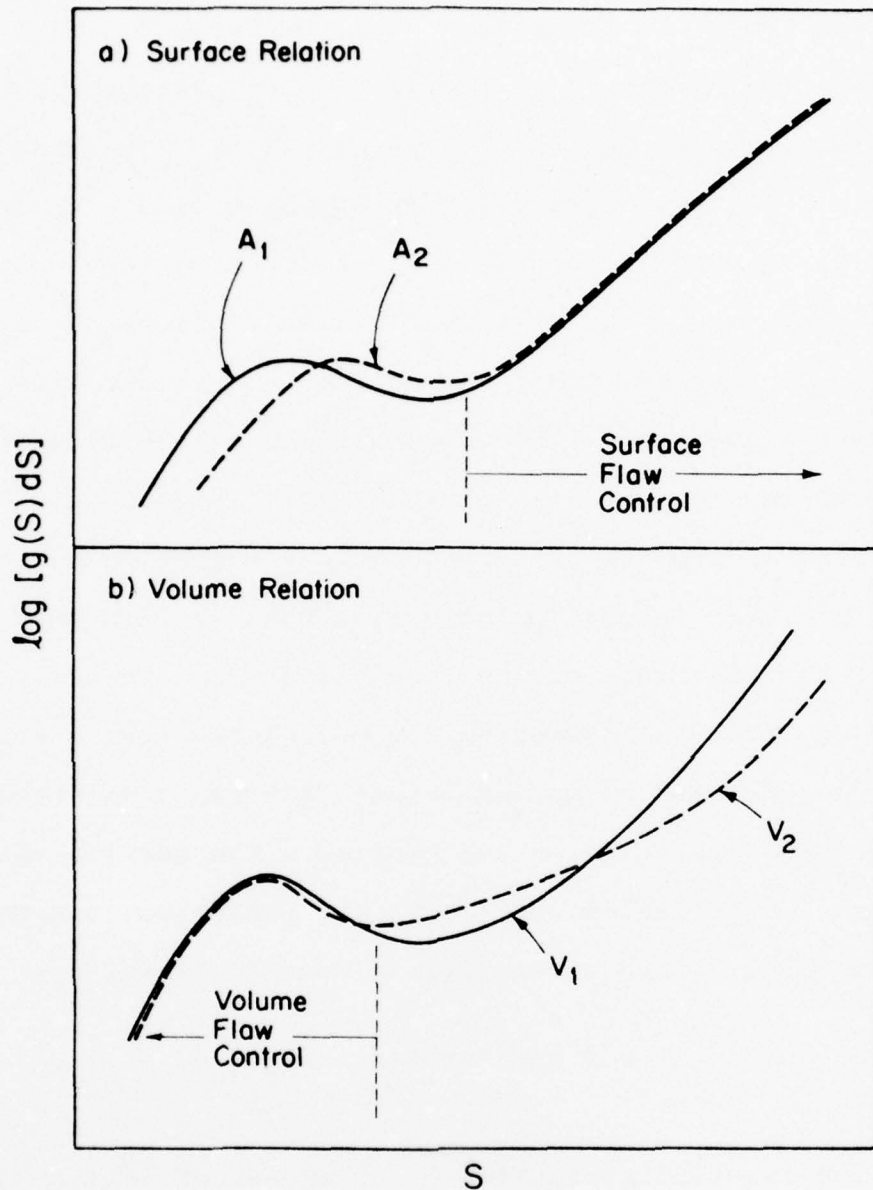


Figure 1. A hypothetical bimodal distribution showing $g(S)$ obtained from tensile tests on two sample sizes, analyzed using; (a) a surface flow assumption, and (b) a volume flow assumption. The coincidence of the two sets of data within the lower mode for the volumetric relation indicates that the lower strengths are volume flow controlled; whereas the data coincidence within the upper mode for the surface relation indicates that the larger strengths are surface flow controlled.

appropriate range of stress (i.e., at the service stress level and above), the confidence limits on the distribution can be established, within the measured stress range, using the recently developed analysis summarized in Appendix II. A typical example, using the data of Kurkjian et al⁵ is presented in Fig. 2. Thereafter, the distribution functions can be used for two purposes. Firstly, they may be used to estimate the source of the most deleterious flaws, by correlating the distribution function at the low strength extreme with fractographic studies of flaw origins from this regime. This information might then be used for fiber strengthening evaluation, as discussed above. Secondly, the distribution function can be used to predict the strength of fibers subjected to a range of in-service stress states. In the case of optical fibers the expected stress states are uniaxial tension and bending. The survival probabilities ($1-\phi$) of zones, of length ℓ_1 , subjected to a uniaxial tensile stress, S , are given (for volumetric flaws) by;

$$1-\phi = \exp \left[-\pi r^2 \ell_1 \int_0^S g(S) dS \right] \quad (5)$$

whereas the survival probabilities of zones, of length ℓ_2 , subjected to pure bending, radius of curvature R , are given (for volumetric flaws) by;

$$1-\phi = \exp \left[-r \ell_2 \int_0^{Er/R} \left(1 - \frac{SR}{Er} \right) g(S) dS \right] \quad (6)$$

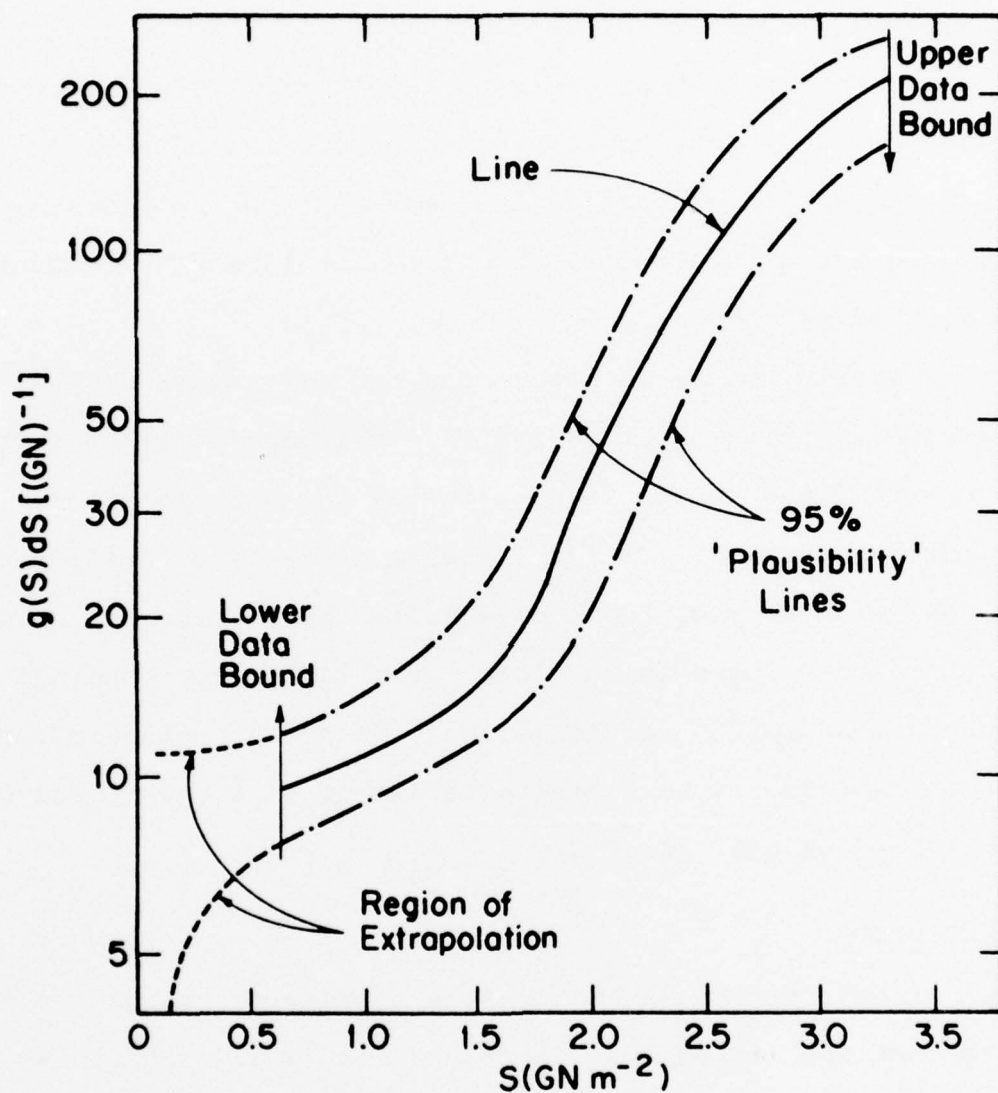


Figure 2. A flaw strength distribution and plausibility limits for optical fibers derived from the tensile data of Kurkjian et al.⁵ Also indicated is the large decrease in confidence that occurs in the extrapolated range.

where E is the Young's modulus of the fiber. The total survival probability of the fiber is then obtained from the product of the survival probabilities of each zone, $\prod(1-\phi)$. In this way the number of fibers that are expected to fail under a range of varying service conditions can be deduced. This number of failures could be allowed for (at the design stage) in systems that do not require a full complement of intact fibers throughout the lifetime of the system.

Finally, we re-emphasize one crucial aspect of the statistical prediction of strength. It is essential that the data are obtained at stresses as low as the service stress. This would require a very large number of tests on small samples or a smaller number of tests on samples approaching the size of the fibers to be used in service. If data are not obtained at stresses close to the service stress, data extrapolation introduces an uncertainty that manifests itself as a very broad confidence band on $g(S)$ (Fig. 2).

PROOF TESTING

Proof testing is the least ambiguous technique for ensuring that the fibers that enter service (i.e., those that pass the proof test) will survive for the required lifetime.* The proof test theory is now well established^{6,7} and shows quite clearly that certain proof ratios (proof stress, σ_p , to

*This assurance assumes that extraneous service stresses (such as impacts or unexpected overloads) can usually be eliminated.

service stress, σ_a) should provide specific lifetime, stress guarantees (as shown in Fig. 3 for silica fibers⁸) provided that no slow crack growth occurs while unloading from the proof stress.⁷ Slow crack growth in silica occurs in the presence of hydroxyl ions at temperatures $\geq -100^\circ\text{C}$. Hence, proof tests conducted in a standard ambience - room temperature in air - are subject to slow crack growth. A guaranteed minimum lifetime can only be realized for such a proof test if the unloading from the proof stress is conducted in a time less than t_o , where;⁷

$$t_o = 2K_c^2 / \pi \sigma_p^2 V_p \quad (7)$$

where K_c is the critical stress intensity factor and V_p is the maximum crack velocity in the slow crack growth regime. The time, t_o , for silica fibers at typical proof stress levels is < 0.1 s; it may be impractical to realize such short times in continuous proof test procedures. However, if the proof testing were conducted below -100°C , slow crack growth would be eliminated and the unloading rate would be irrelevant. Heat transfer estimates (Appendix III) indicate that it might be entirely possible to perform proof tests at these temperatures for the small diameter ($\sim 100\mu\text{m}$) fibers, because the fibers attain the requisite temperature in a time less than 1 s after immersion in liquid nitrogen. If this approach is adopted, it must of course be ensured that the proof stress is only applied to the segment of fiber that is at a temperature below -100°C .

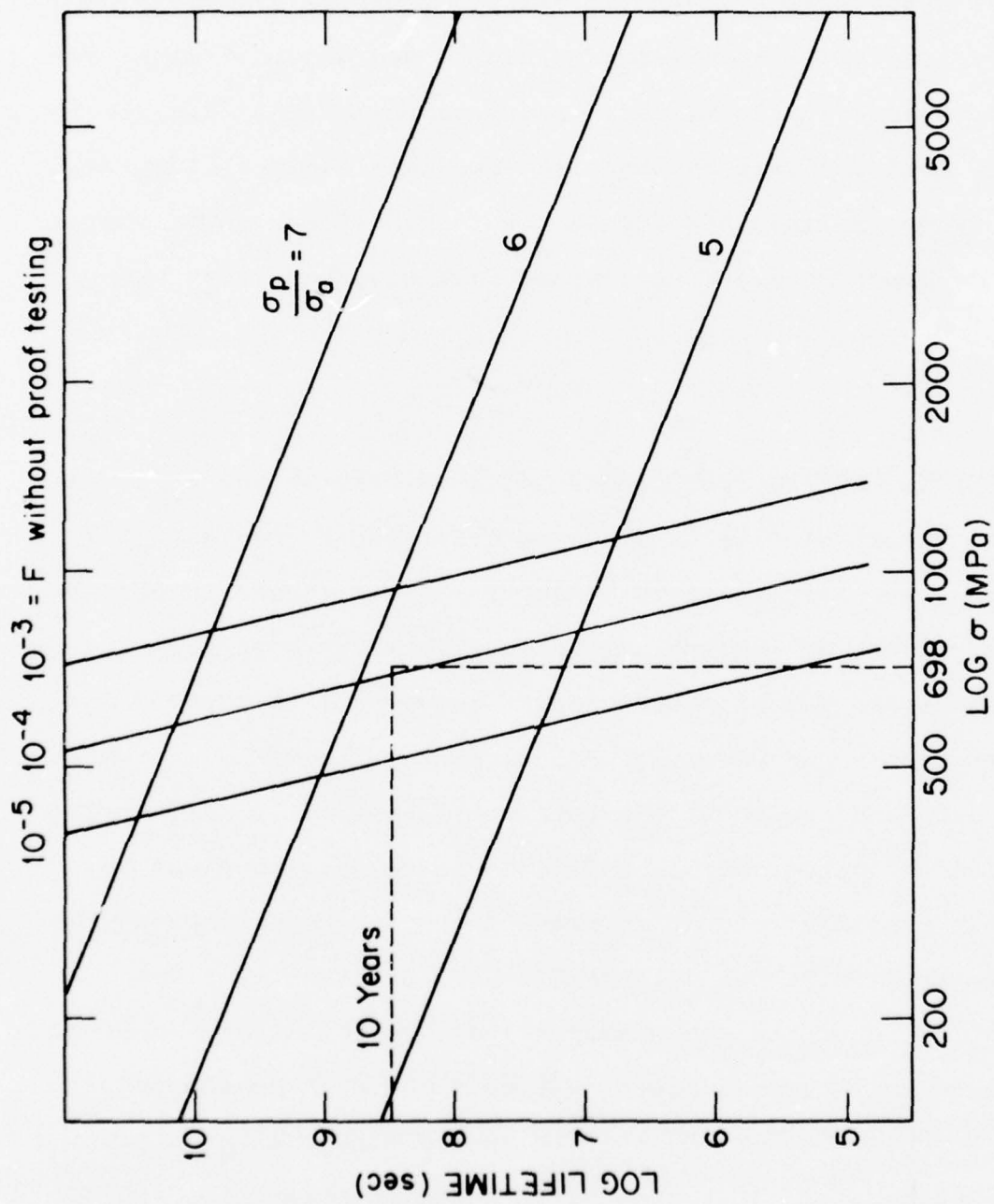


Figure 3. A failure diagram for silica fibers derived from dynamic fatigue data.⁸

Should the latter approach also prove to be impractical, the only recourse is to design the proof test to ensure a minimum possible failure probability at the service stress.⁸ The test design would be predicated on the results of a series of simulation tests (performed in the laboratory) which would determine the failure probabilities before and after proof testing, for a range of proof test cycles suggested by the available theory (Appendix IV).

Finally, it should be noted that the final proof test conditions selected depend quite sensitively on the function that is used to describe the rate of slow crack growth. The function that has been most commonly used to describe the data is a logarithmic function.^{6,7} This function does fit much slow crack growth rate data, and its analytic tractability makes it attractive. However, it should be recognized that this may not be the best function over a wide range of time (or crack velocity). An alternate function has thus been postulated,⁹ that might offer a superior description of the slow crack growth over time scales approaching 1 yr. This function is a reciprocal exponential;

$$V = V_{\infty} \exp(\beta/K) \quad (8)$$

where V is the crack velocity, K is the stress intensity factor and V_{∞} and β are constants. It is suggested that this function be considered as a possible descriptor of the slow crack growth in optical fibers.

SUMMARY

Three principal aspects of the fracture of optical fibers have been discussed, namely; fiber strengthening, the statistics of fracture and proof testing. Although all three aspects of the fracture behavior should be explored, it is apparent that fiber strengthening, by eliminating the most serious fabrication flaws in kilometer length fibers, should be a priority. Thereafter, proof test procedures based on small scale laboratory test data should be devised, with low temperature proof testing, perhaps exhibiting the most promise.

ACKNOWLEDGEMENT

This research was supported by the Advanced Research Projects Agency of the Department of Defense under Contract No. MDA903-76C-0250 with The University of Michigan.

APPENDIX I

RELATIONS BETWEEN THE FAILURE PROBABILITY AND DISTRIBUTION FUNCTION FOR LINEARLY VARYING TWO-DIMENSIONAL STRESS FIELDS

For a stress field defined by

$$S = S_m(1-z/\ell)(1-y/h) \quad (A1)$$

where ℓ and h are sample dimensions in orthogonal directions and z and y are distances in these directions taken from the point of peak stress, S_m . The failure probability for this stress state is given by;

$$\Phi = 1 - \exp \left[-b \int_0^\ell \int_0^h \int_0^{S_m(1-y/h)(1-z/\ell)} g(S) dS dy dz \right] \quad (A2)$$

where b is the third dimension of the sample. Changing the order of integration, enables (A2) to be reduced to;

$$\Phi = 1 - \exp \left[-b\ell d \int_0^{S_m} \left(1 - \frac{S}{S_m} - \frac{S}{S_m} \ln \frac{S}{S_m} \right) g(S) dS \right] \quad (A3)$$

Differentiating three times in the manner suggested by Matthews et al⁴ gives the derivatives

$$G' = \frac{2b\ell d}{S_m} \left[\int_0^{S_m} \left(\frac{S}{S_m} \ln \frac{S}{S_m} \right) g(S) dS \right] \quad (A4a)$$

$$G'' = \frac{2b\ell d}{S_m^2} \left[\int_0^{S_m} \left(\frac{S}{S_m} - \frac{2S}{S_m} \ln \frac{S}{S_m} \right) g(S) dS \right] \quad (A4b)$$

$$G''' = 2b\ell d \left[g(S_m) - \frac{1}{S_m^3} \int_0^{S_m} \left(5 \frac{S}{S_m} - 6 \frac{S}{S_m} \ln \frac{S}{S_m} \right) g(S) dS \right] \quad (A4c)$$

where $G = -\ln(1-\phi)$. Solving Eqs. (4) simultaneously enables $g(S_m)$ to be deduced, giving;

$$g(S_m) = \frac{1}{2b\ell d} \left[G''' S_m^2 + 5G'' S_m + 4G' \right] \quad (A5)$$

TABLE 1

Cooling Times for Various Filaments in Liquid Nitrogen

For $K/(Rh) > 6$, neglect internal resistance:

$$t = (\rho C_p R / 2h) \ln (T_o - T_f) / (T - T_f)$$

$$h = 30 \text{ Btu/hr ft}^2 \text{ F}$$

$$R = 0.05 \text{ mm} = .00017 \text{ ft}$$

$$(T_o - T_f) / (T - T_f) = 3$$

| | ρ | C_p | k | $k/(Rh)$ | t |
|-------------|-----------------------------------|------------------------------------|---|----------|-----|
| Units | $\frac{\text{lb m}}{\text{ft}^3}$ | $\frac{\text{Btu}}{\text{lb m F}}$ | $\frac{\text{Btu}}{\text{hr ft}^2 \text{ F}}$ | ---- | sec |
| Material | | | | | |
| Bakelite | 79.5 | .38 | .134 | 27 | .33 |
| Glass | 162 | .16 | .51 | 103 | .28 |
| Hard rubber | 74.8 | .48 | .087 | 18 | .39 |

APPENDIX II

LOW TEMPERATURE PROOF TESTING OF OPTICAL FIBERS

In proof testing, testing at low temperature may be important to prevent time-dependent growth of damage. Here we consider cooling rates attainable by quenching fibers 0.1 mm in diameter into liquid nitrogen. A typical value of the surface heat transfer coefficient h for such conditions is 30 Btu/hr ft² F¹⁰. More accurate estimates could be obtained by using the correlations reviewed by Hesse, et al.¹¹ in connection with their work on film boiling in carbon dioxide. Since the fibers may be either bare or coated with a polymer, consider the results for some related materials for which properties are readily available (e.g., Rohsenow and Choi,¹²) shown in Table 1. The ratio of surface to internal resistance is shown in terms of the ratio k/Rh . From the Gurney-Lurie chart for a long cylinder (e.g., McAdams,¹³), the internal resistance may be neglected when k/Rh is greater than 6, which is the case for all three materials of Table 1. The cooling curve of the fiber can then be derived directly by equating the heat flow rate from the surroundings to the rate of enthalpy rise of the fiber. In terms of original and final temperatures T_o and T_f , the time to reach T is

$$t = \frac{\rho C_p R}{2h} \ln \frac{T_o - T_f}{T - T_f} \quad (A6)$$

Taking $T_o = 300$ K, $T_f = 150$ K, and assuming a drop to 250 K to

be sufficient to suppress the damage rate gives the times shown in the last column of Table 1. Evidently cooling times of a fraction of a second appear to pertain. Higher pressures would give higher surface coefficients if needed.

APPENDIX III

APPROXIMATE CONFIDENCE LIMITS FOR EMPIRICAL DISTRIBUTION FUNCTIONS

In interpreting statistical data, it is frequently desirable to estimate what characteristics of empirical distribution functions are real and what are due to random sampling. Such estimates are particularly important in estimating the "tails" of distribution functions that are of interest in predicting rare fractures in generally reliable structures. When the shape of the distribution function of the population is known, such estimates can often be made theoretically by presenting confidence limits for various statistics of the population, such as mean standard deviation, various percentiles (tolerance limits), or individual further observations (prediction limits). These are well known for the normal distribution. Some progress has also been made for the extreme-value distribution of the first kind.¹⁴ Unfortunately, they are rather involved. More important is the fact that in practice the rare fractures in a part may arise from unusual events in the production process, so that the population is multi-modal, or at least does not conform to any one theoretical distribution function. Non-parametric tests will be presented below, but first consider an empirical approach.

Empirical Sampling

With modern computers, it is relatively easy to obtain approximate confidence bands by repeatedly sampling from the

test sample, regarded as a population. For example, it seems plausible that taking 20 test samples would give a band roughly corresponding to 95% limits for the population distribution function. A stronger statement would require further statistical analysis. Here we simply outline the procedure, which is summarized in Table 2. As shown in Fig. 4, arrange the original sample in order of increasing variate x and assign order numbers i_o . Assign a probability $P = i_o / (i_{o\max} + 1)$ to each variate $x(i_o)$, and plot the cumulative distribution of the sample. Complete the distribution by assigning arbitrary but plausible variates x_ϕ and x_1 to zero and unit probabilities.

Next choose test samples by random sampling uniformly over the interval 0 to 1, and assign variates according to the cumulative distribution you have constructed from the test sample. Order these test samples and plot their cumulative distributions as you did the original sample. Call the band of $i_{s\max}$ test samples the $(1 - 1/i_{s\max})$ "plausibility" band for the population from which the original sample was drawn.

The vague term "plausibility" is used because it is not backed up by a rigorous statistical analysis. For instance, suppose the underlying population had just two discrete values, x_1 and x_2 , with probabilities P and $1-P$. The band constructed by the above procedure would be much broader than the confidence limits for the fraction P of the population, which will be discussed below. The band would in fact be the $(i_{s\max} - 1) / (i_{s\max} + 1)$ prediction limits for one more sample drawn from the population.

TABLE 2

Computer generation of statistical samples from an assumed population with cumulative probability distribution $0 \leq P(x) \leq 1$

Input

Desired test sample size i_{tmax}
 Number of test samples i_{smax}
 Parameters of assumed population, $P(x)$, or original sample, $X(i_o)$, $i_o = 1, i_{omax}$ and extrapolated values x_ϕ, x_1

Preliminary Processing

If original sample is used, determine x_{i_o} as a function of order number i_o such that

$$x_{i_o}(i_o) \leq x_{i_o}(i_o+1)$$

Loop over test samples: $i_s = 1, i_{smax}$

Loop over test items: $i_t = 1, i_{tmax}$

Choose a random number: $\phi < P_{it} < 1$

Find the corresponding variate x , either from the assumed population, $x_{it}(P_{it})$, or from the original sample by interpolation:

Choose $i_o =$ largest integer in $P_{it}(i_{omax}+1)$

If $i_o = 0$, $x_L = x_\phi$, $P_L = \phi$

otherwise $x_L = x_{i_o}(i_o)$, $P_L = i_o/(i_{omax}+1)$

If $i_o+1 = i_{omax}$, $x_U = x_1$, $P_U = 1$

otherwise $x_U = x_{i_o}(i_o+1)$, $P_U = (i_o+1)/(i_{omax}+1)$

$$\text{Then } x_{it}(it) = x_L + \left(\frac{P_{it} - P_L}{P_U - P_L} \right) (x_U - x_L)$$

End loop over test items i_t

TABLE 2 (Continued)

Order the test sample such that

$$x_{it}(i_{to}) \leq x_{ito}(i_{to} + 1)$$

Printer-plot the test sample (superimposing plots for each test sample)

$$\frac{i_{to}}{i_{tmax} + 1} \text{ vs } x_{it}(i_{to})$$

End of loop over test samples i_s and of program.

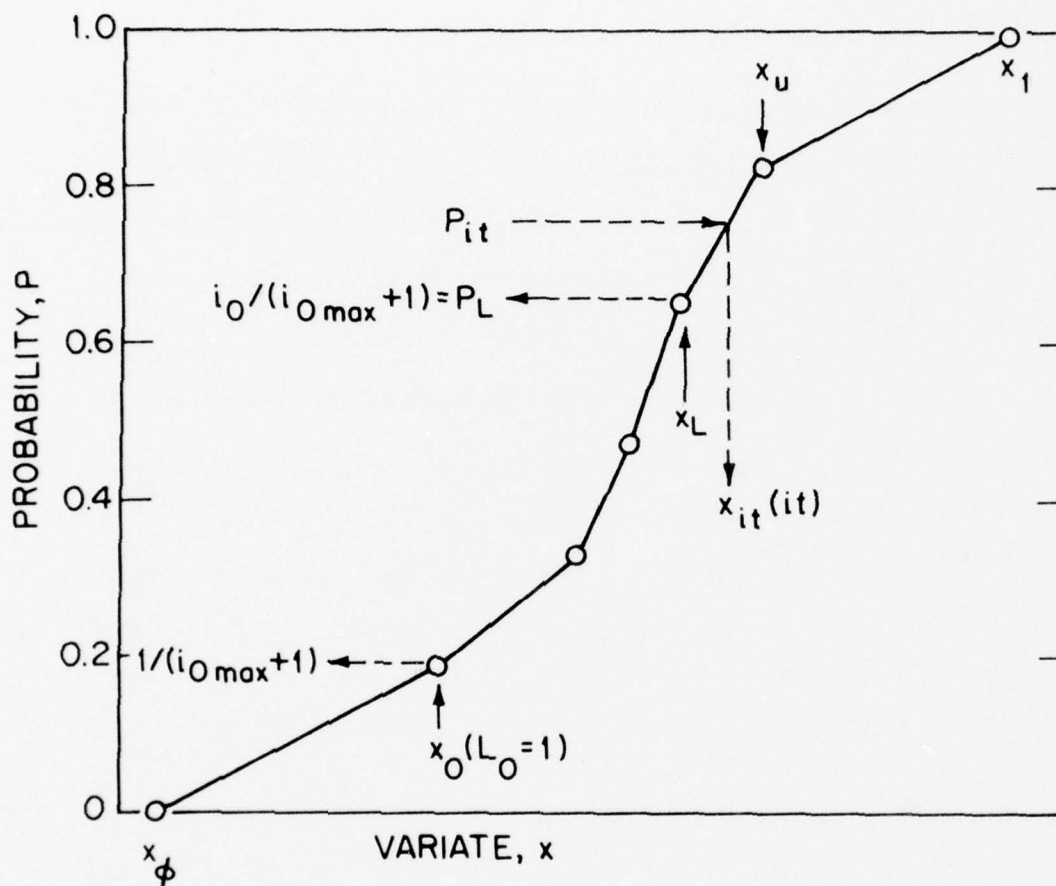


Figure 4. A schematic showing the technique used to obtain 'plausibility' limits based on a set of (5) test data; x_ϕ and x_1 are the selected limits at $P = 0$ and 1, respectively.

What we are concerned about in quality control and production, however, is a more or less continuous distribution function with possibly multiple modes, giving "bumps" in the frequency distribution. These bumps are somewhat correlated by the ordering process performed on the sample, so linear regression analysis is not applicable. Not knowing any better, we therefore use the intentionally vague term "plausibility band". Repeated sampling of the entire procedure would give more insight.

Non-parametric Confidence Limits for the Median of the Population

If one only wished to estimate the median of the population, not its probability $P(x)$ at each x , confidence limits could be obtained without making any assumption about the shape of the distribution by the following procedure. Later the methods will be given for any value of P , not only $1/2$.

Note that the probability of drawing a sample of N , all below the median of the population, is $\frac{1}{2}^N$. Similarly, the probability of drawing the sample with all above the median is $\frac{1}{2}^N$. These possibilities are mutually exclusive. The only other possibility is that the sample brackets the median. If one asserts that the median does in fact lie between the extremes of a sample of N , he will make correct statements $1-2(\frac{1}{2})^N$ of the time. Such estimates are called the $1-2(\frac{1}{2})^N$ confidence limits for the median of the population. With large samples this rule may give broad limits and a very high degree of confidence. Narrower limits and a lower degree of confidence can be obtained from the i^{th} members inward from the extremes of the sample, as

presented in Table 3, taken from Remington and Schork.¹⁵

Confidence Limits for the Probability Corresponding to a Given Variate

Suppose one wishes to take a given value x of the variate, such as a working strain level, and estimate the population fraction defective (failing to reach the variate x). Let \hat{P} be the fraction defective in the sample of size N . Then confidence limits for the population fraction defective P are obtained from the binomial distribution. Very large samples are required for high confidence for small fractions of the population. Charts are found in a number of places.^{15,16,17}

Standard Deviation of the Binomial Distribution

Again assume that the probability P is to be estimated for a single value of the variate x . The standard deviation of the fraction p of a sample of size N is

$$\sigma_p = \sqrt{P(1-P)/N} \quad (A7)$$

For large NP the binomial distribution is approximately normal, so if one desires, for example, the 95% (2σ) confidence limits for P to be ± 0.0001 with $P = 0.001$, the sample size would have to be enormous:

$$N = P(1-P)/\sigma_p^2 = 0.001/(0.0001/2)^2 = 400,000. \quad (A8)$$

Decision Analysis

The extreme sample sizes indicated by the preceding example make one question the need for such confidence, the

TABLE 3

Order Numbers i for Distribution-free Confidence Limits
for the Median of a Continuous Distribution

| N | <u>Confidence Coefficient</u> | |
|-----|-------------------------------|-------|
| | .95 | .99 |
| 6 | 1-6 | ----- |
| 10 | 2-9 | 1-10 |
| 15 | 4-12 | 3-13 |
| 20 | 6-15 | 4-17 |
| 30 | 10-21 | 8-23 |
| 40 | 14-27 | 12-29 |
| 50 | 18-33 | 16-35 |
| 60 | 22-39 | 20-41 |
| 70 | 27-44 | 24-47 |
| 80 | 31-50 | 29-52 |
| 90 | 36-55 | 32-58 |
| 100 | 40-61 | 37-64 |

cost of testing, the cost of failure, the need for research, and possibilities for redundant design. Decision analysis may be of help in balancing such factors.^{18,19}

APPENDIX IV

EFFECTIVENESS OF PROOF TESTING

J. E. Ritter

The minimum lifetime predictions after proof testing are only valid when no crack growth occurs on unloading during proof test. Crack growth during loading and at the proof stress presents no problem since we can still characterize the maximum flaw size. However, if flaw growth occurs on unloading, then the maximum flaw size cannot be defined and no assurance of a minimum service life can be given. Before proof testing can be used as a means for assuring a minimum lifetime, the effectiveness of the proof test in truncating the inert strength at one proof stress (σ_p) should be experimentally determined.

Evans and Wiederhorn⁶ have shown that the inert strength after proof testing (S'_i), considering crack growth during loading but not unloading, is related to the initial inert strength (S_i) by:

$$\left(\frac{S'_i}{S_i}\right)^{N_p-2} = 1 - \left(\frac{\sigma_p^*}{S_i}\right)^{N_p-2} \quad (A9)$$

where N_p is the crack propagation parameter appropriate for the proof test conditions and σ_p^* is the equivalent proof stress under inert conditions (i.e., where no crack growth occurs during proof).

Using the Weibull[†] inert strength distribution, σ_p^* is

[†]The strength distributions are fitted to the Weibull form for mathematical convenience.

determined from:

$$\ln \ln \left(\frac{1}{1-F_p} \right) = m \ln \left(\frac{\sigma_p^*}{S_o} \right) \quad (A10)$$

where F_p = failure probability during proof testing and m and S_o = initial Weibull inert strength constants. The failure probability after proof testing (F_a) is related to the initial failure probability before proof testing by:

$$F_a = \frac{F - F_p}{1 - F_p} \quad (A11)$$

Eq. (A9) can now be rewritten to give:

$$\left(\frac{S'_i}{S_o} \right)^{N_p - 2} = \left(\ln \frac{1}{1-F_a} + \ln \frac{1}{1-F_p} \right) \frac{N_p - 2}{m} - \left(\ln \frac{1}{1-F_p} \right) \frac{N_p - 2}{m} + \left(\frac{\sigma_p}{S_o} \right)^{N_p - 2} \quad (A12)$$

Thus, from Eq. (A12) it is seen that the inert strength distribution after proof testing depends upon the initial inert strength distribution parameters m and S_o , the crack propagation parameter N_p , and the failure probability during proof F_p . It is also significant to note that the S'_i distribution is truncated at σ_p and that the inert strength after proof testing will be greater than the initial inert strength at all levels of probability if $m < N_p - 2$.

To demonstrate the applicability of Eq. (A12), hence demonstrating the effectiveness of proof testing, Fig. 5 compares the inert strength of soda-lime microscope slides before proof testing to that after proof testing, obtained using a rapid

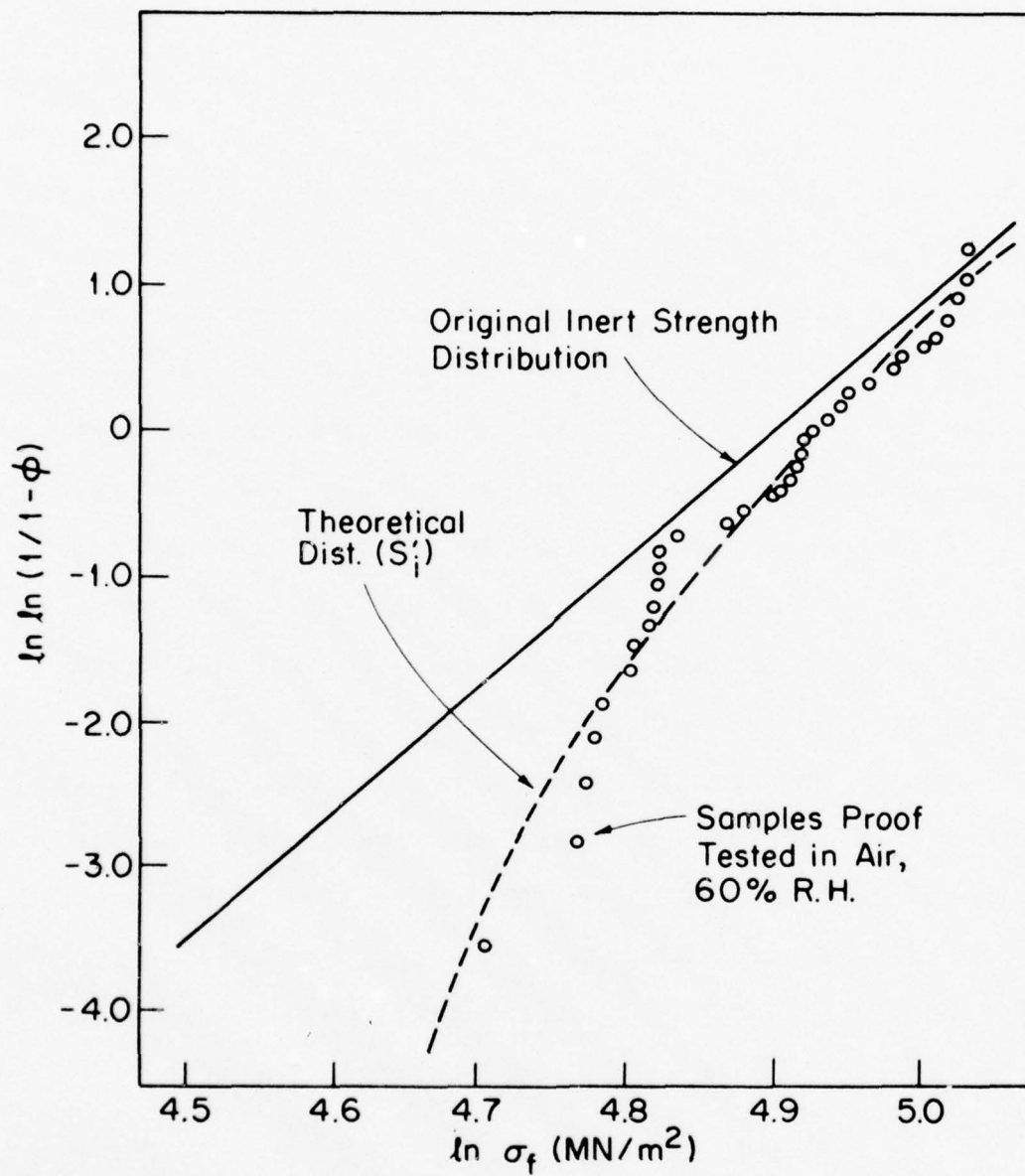


Figure 5. The probability of fracture before and after proof testing, shown with theoretical after proof curve.

unloading cycle (see section 4). The proof test environment was ambient air and the loading rate during the proof test was $5.18 \text{ MN/m}^2 \cdot \text{s}$ and the unloading rate $130 \text{ MN/m}^2 \cdot \text{s}$. The time at the proof stress of 79.3 MN/m^2 was $<0.5 \text{ s}$ and 33% of the samples broke during the proof test. Taking 17.34 as the value of N_p^\dagger in Eq. (A12), the predicted inert strength distribution after proof testing is also given in Fig. 5. On comparing the initial inert strength distribution to that after, it is quite apparent that the proof test was effective in eliminating the weaker samples and that the inert strength distribution after proof testing does follow that predicted from Eq. (A12). Thus, it is believed that on the basis of these results, no crack growth occurred on unloading and the proof test was effective in truncating the inert strength at σ_p ; hence, a minimum lifetime after proof testing could be assured.

It is important to realize that if crack growth had occurred on unloading, the inert strength distribution after proof would not have followed Eq. (A12) and not be truncated at σ_p . In this case, as assurance of a t_{\min} cannot usually be given; however, the proof test can still be helpful if $S_i' > S_i$. In this case, the time to failure after proof testing (t_f') is given by

$$t_f' = B S_i'^{N-2} \sigma_a^{-N} \quad (\text{A13})$$

[†]It should be noted that this value is consistent with that determined from crack velocity, static fatigue, and dynamic fatigue measurements.

If $S'_i > S_i$, then from Eq. (A13) it can be shown that for a given lifetime and applied stress in service the failure probability after proof testing will be less than that before.

References

1. R. W. Rice, work performed at NRL.
2. P. Macedo, work performed at Catholic University.
3. B. R. Lawn and G. Marshall, J. Amer. Ceram. Soc., in press.
4. J. R. Matthews, F. A. McClintock and W. J. Shack, J. Amer. Ceram. Soc. 59, 304 (1976).
5. C. R. Kurkjian, R. V. Albaino, J. T. Krause, H. N. Vazirani, F. V. Dimarcello, S. Torza and H. Schemahorn, Appl. Phys. Lett. 28, 588 (1976).
6. A. G. Evans and S. M. Wiederhorn, Intl. J. Frac. 10, 379 (1974).
7. A. G. Evans and E. R. Fuller, Mat. Sci. Eng. 19, 69 (1975).
8. J. Ritter, work performed at Univ. Mass. Amherst.
9. R. Doremus, work performed at R.P.I.
10. P. A. Griffith, personal communication, 1976.
11. G. Hesse, E. M. Sparrow and R. J. Goldstein, "Influence of Pressure on Film Boiling Heat Transfer," J. of Heat Transfer, Trans. A.S.M.E., vol. 98C, 166-172 (1976).
12. W. M. Rohsenow and H. Y. Choi, Heat, Mass, and Momentum Transfer, Prentice-Hall, Englewood Cliffs, New Jersey, 1961.
13. W. H. McAdams, Heat Transmission, McGraw-Hill, New York, 1954.
14. J. Lieblein, "A New Method of Analyzing Extreme-Value Data," NACA Technical Note 3053, Nat. Advisory Comm. for Aero., Washington, 1954.
15. R. D. Remington and M. A. Schork, Statistics with Applications to the Biological and Health Sciences, Prentice-Hall, Englewood Cliffs, New Jersey, 1970.
16. M. G. Natrella, Experimental Statistics, National Bureau of Standards Handbook 91, Washington, D.C. 1963.
17. J. A. Greenwood and H. O. Hartley, Guide to Tables in Mathematical Statistics, Princeton University Press, pp. 193-195, 1962.

18. W. L. Hays and R. L. Winkler, Statistics: Probability, Inference, and Decision, Holt, Rinehart and Winston, Inc., New York, 1971.
19. F. A. McClintock, R. L. Coble and R. M. Thomson, "Decision Analysis Applied to Penetrant Inspection of Ceramic Turbine Blades," Preliminary Reports of the Materials Research Council Summer Conference, v. 1, Advanced Research Projects Agency Order 2341, Dept. Materials and Metallurgical Engineering, University of Michigan, Ann Arbor, 357-371, 1973.

CHLOROFLUOROCARBON UPDATE, 1976

J. L. Margrave

THE PROBLEM--DO ANTHROPOGENIC SOURCES OF CHLORINE APPRECIABLY THREATEN THE EARTH'S OZONE LAYER?

In a series of reports over the past five years¹⁻³⁵ sampling data, calculations and extrapolations have been presented which suggest that current levels of anthropogenic introduction of chlorine compounds into the atmosphere (especially of CCl_2F_2 and CCl_3F) could provide sufficient reactant species for one of the ozone-destruction cycles to cause a significant decrease in the ozone layer and a serious reduction in the uv-protection it provides for man by 1985-2000²³.

For example, as shown by Cicerone, Stolarski and Walters¹¹ the extrapolated ozone destruction rates, based on available thermodynamic and kinetic data for three time-dependent cases of CF_xCl_y production and insertion into the atmosphere, are detectably sensitive to current levels of anthropogenic Cl-species in the stratosphere, (Model 3), even if the further production of fluorocarbons had been stopped in 1975. The calculations suggest, further, that the effect could be of major significance ($\sim 10\%$ or more ozone depletion) if the production of $\text{CCl}_2\text{F}_2/\text{CCl}_3\text{F}$ continues to increase at current rates, i.e., with a doubling time of 3.5 years, (Model 1) or somewhat less if production simply continues at the 1975-rate, (Model 2).

Actually, the experimental atmospheric sampling data are limited; there appear to be extensive and unexplained natural sources of CCl_4 and related chloro-species in the atmosphere; and, further, there are several simple reactions of atoms, molecules and ions which could be important but have not been definitively evaluated. The 1976 rate of introduction of chlorocarbons into the atmosphere by man is detectably less than the 1975 rate.

It is the purpose of this report to summarize the available information and speculations through July, 1976; to review the known reactions of Cl-containing species in the upper atmosphere and to suggest some further possibilities for research. In particular, it will be important to establish the relative importance of natural and anthropogenic chlorine sources if man is to know how to regulate and limit the anthropogenic sources as required to maintain the ozone layer.

NATURAL SOURCES OF CHLORINE-CONTAINING MOLECULES

Ground-level sources of chlorine include fumaroles, which emit gaseous HCl and volcanic explosions which can inject chlorine or chlorides into the atmosphere in association with ash particles and also with sea water which might intrude into the volcano pit and be flash-vaporized⁸⁻³⁴. One would anticipate the production of HCl , or metal chlorides and oxychlorides and of CCl_4 formed by carbon reduction of metal chlorides in these high-temperature processes. Cadle³⁴ estimates volcanic emissions of HCl and HF to be less significant than anthropogenic emissions except for short periods following intense volcanic activity.

Biological production of halogen compounds is rare but not unknown. Lovelock^{1-2,12}, for example, has reported certain marine algae to produce CH_3I in extensive amounts, ~40 Megaton/year and has also pointed out that the typical CCl_4 concentration is much greater than anticipated from known industrial production coupled with the fact that the soil, the sea and the stratosphere all appear to be CCl_4 sinks. To justify the existence of a natural CCl_4 source, possibly biological but more likely atmospheric, Lovelock¹² has noted (1) the abundance of CCl_4 is essentially the same in the Northern and Southern hemispheres; (2) a lack of correlation between CCl_4 concentrations and winds from industrial areas; and (3) the known synthesis of CCl_4 by chlorination of CH_4 . In a cryptic paragraph, Stolaski and Cicerone⁸ observed that there is a need to consider the interaction of Cl-containing molecules with CO/CO_2 in order to evaluate all possible chlorine sources/sinks.

ANTHROPOGENIC SOURCES OF CHLORINE-CONTAINING MOLECULES

Industrial Chemicals

The major industrial tonages of chlorine-containing compounds involve NaCl , HCl , and Cl_2 with the latter two gases making major contributions to lower atmospheric concentrations and even to stratospheric concentrations, although rain-out removes most of these species. In addition, there is significant production of SiCl_4 , SiCl_3H , BCl_3 , AlCl_3 , and other metal halides which are used in production of semi-conductors, for electrochemical and

vapor-decomposition processes, etc. Hypochlorite bleaches, chlorates and perchlorates are also significant industrial products.

Halogenated hydrocarbon production for 1972 and a chronological survey of world production of CF_2Cl_2 and CFCl_3 have been discussed by Rowland and Molina¹⁹. Most of the chlorinated ethanes and ethylenes are used in the production of polyvinyl and polyvinylidene chlorides. Large amounts of chloroethylenes are used in dry cleaning and CH_3Cl , CH_2Cl_2 , CHCl_3 , etc., are used in syntheses and as solvents. The fluorochlorocarbons are new in terms of historical production but are now manufactured in at least 20 countries. The major use for CFCl_3 is in aerosol sprays (85%) with another use (8%) involving the foaming of polyurethanes. The major use of CF_2Cl_2 is in refrigeration units. Approximately half of the world production of fluorochlorocarbons is from the United States.

Waste Disposal/Pyrolysis of PVC

Because world-production of chlorine-based polymers is in the range of 5,000,000 tons/year, it is clear that these materials will make up a significant portion of urban trash. Although the materials are relatively inert, the incineration of trash or the slow pyrolysis/deterioration in land-fill can lead to HCl and $\text{CH}_x\text{Cl}_{4-x}$ including the long-lived, slowly degraded CCl_4 molecule.^{36, 37}

Chlorination of Water Supplies

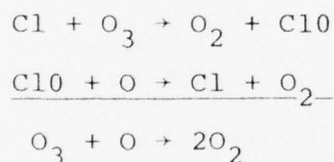
Millions of tons of elemental chlorine are used for water purification throughout the world. HCl and chloro-organics from

this process are released to the atmosphere in currently unknown concentrations. Recent reports claim significant concentrations of chloro-species, possibly carcinogens, in the water of major rivers being used to supply drinking water.³⁸ Hypochlorites are widely used for swimming pool water treatment.

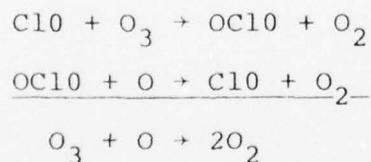
CHLORINE REACTIONS IN THE STRATOSPHERE

Reactions of importance in upper-atmospheric chemistry are given by Crutzen⁶ and by Rowland and Molina¹⁹.

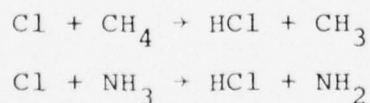
From these references, the major ozone-destroying catalytic cycle is described by the set of reactions:



Another set of reactions which catalytically destroys ozone is



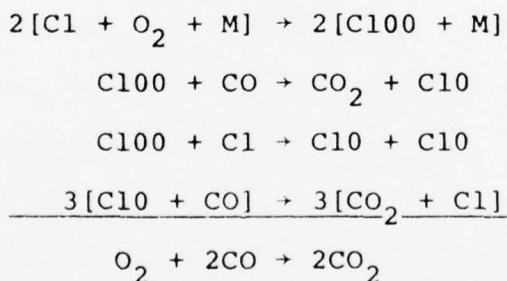
Among the other reactions of Cl-atoms are



which help maintain the atmospheric chlorine balance and represent significant chlorine sinks. A newly discovered molecule, HCOCl ,³⁹ can serve as a sink for HCl in the atmosphere.

Chlorine atoms in the upper atmosphere arise from the photolysis of CCl_4 , HCl , or perhaps from COCl_2 originating from natural sources along with Cl-atoms formed by photolysis of CCl_2F_2 and CCl_3F being inserted from anthropogenic sources. UV-radiation is sufficient to break the C-Cl or H-Cl bonds and provide atoms or radicals capable of further reactions. There are several likely reaction systems which have not been well studied, as listed in Table I. Of special interest and currently unexplored as to real importance are reactions leading to COCl , COCl_2 and to the long-lived halocarbenes: CF_2 , CCl_2 and CClF .

Interestingly, Prinn⁴⁰ has suggested a Cl-atom cycle which, instead of destroying ozone, catalyses the oxidation of CO to CO_2 :



It is surprising that none of the usually proposed Cl-reactions involve electron attachment processes. Rowland and Molina¹⁹ report that electron-trapping processes are important in the ionized layers (E and F) of the stratosphere:

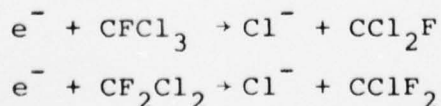
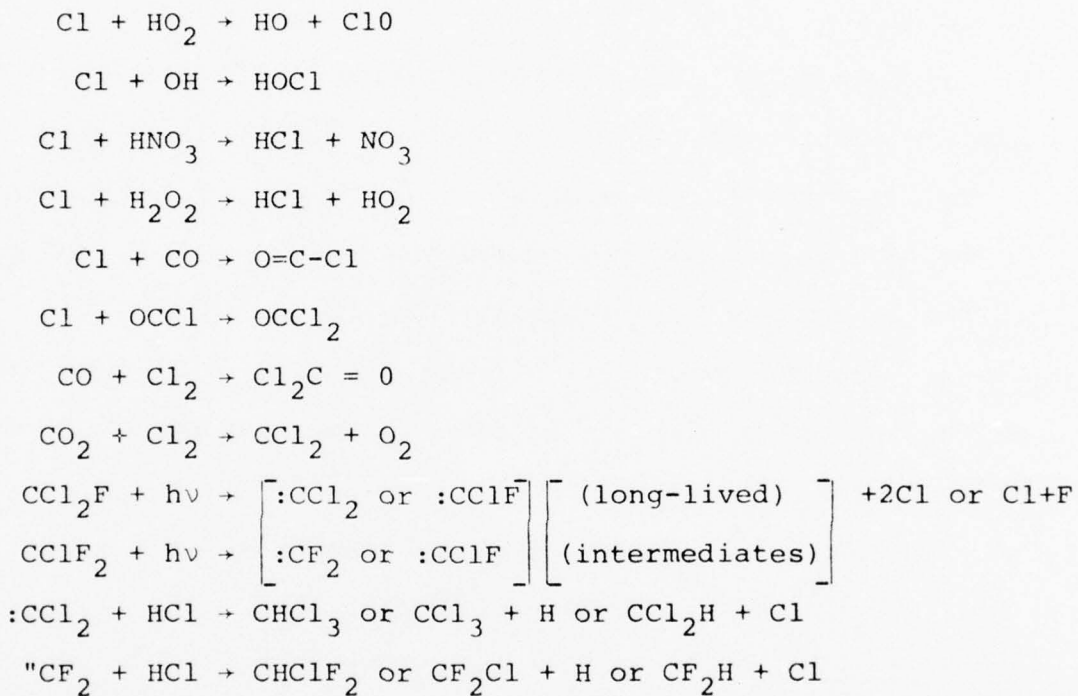
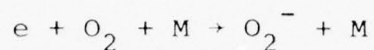


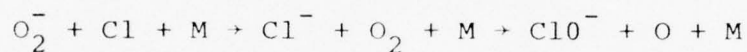
TABLE I



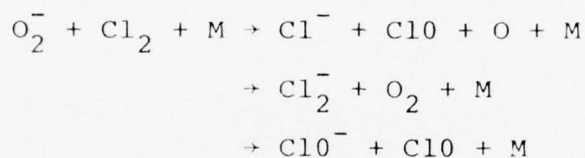
but they conclude that the concentration of electrons is kept low in the troposphere and lower stratosphere by the trapping reactions:



It is not clear why further charge exchange reactions like

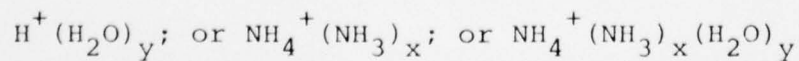


are ignored. Also consider these reactions:



Recent studies of chlorine oxides have yielded electron affinities for ClO and Cl₂O of 1.6 and 2.4 eV, respectively.⁴¹ Since the electron affinities of Cl or Cl₂ are in the 2.5-3.5 eV range, these are energetically acceptable, and spontaneous processes. In essence, the entire list of possible chlorine, chlorine monoxide and other cycles can be rewritten with ionic species involved since the electron affinities of chlorinated species will provide thermodynamic driving forces.

Positive ions are less likely since the ionization potentials to form them are in the 10-15 eV range. Nonetheless, positive ion clusters



are well-established atmospheric species which can interact with Cl or HCl to form NH_4Cl or NH_4ClO_x and, thus, to terminate chains which might involve Cl-atoms.²¹

SUMMARY AND SUGGESTIONS FOR RESEARCH

From the available sampling reports, one can compile inventories of Cl-containing species in the lower atmosphere and in the stratosphere, but there is still a need for more extensive sampling over the geographic grid as well as over a range of altitudes up to at least 50 km in order to provide a complete chlorine balance. Besides gross sampling and subsequent analyses to identify stable molecular compounds, there is a need for further mass-spectrometric sampling of the atmosphere with identification of neutrals, positive ions, negative ions, and radicals/fragments.

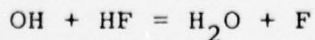
There is a long, but not complete list of relevant atomic and molecular interactions for which thermodynamic and rate data are available. There is also a long list of potentially interesting reactions involving ions--both positive and negative--as well as some neutral species which have been currently ignored in the various atmospheric modeling calculations. The available extrapolations regarding the ozone layer for the period 1985-2000 are based on "best estimates" for certain parameters and on the NO_x^{42} and ClO_x cycles for ozone destruction. As suggested in various places, if the Cl-atom catalyses of the CO/CO_2 oxidation is a competitive process and/or if reactions of ion clusters to

remove Cl as NH_4Cl and/or if $\text{Cl} + \text{NO}_2/\text{NO}$ interactions are appreciable and/or if CCl_2 species are involved in the CCl_4 -production and decomposition cycles, etc., the calculations published so far could be greatly in error.

Another important question which should be raised has to do with the long-term effects of introducing fluorine in significant concentrations into the stratosphere. The current problem under discussion concerns chlorine and not fluorine.⁴³ Several other fluorine compounds are also being added to the stratospheric mix, HF , SF_6 , etc.⁴⁴, although observers seem not to attribute any harmful effects to SF_6 yet. SF_6 is highly stable and easily survives hydrolysis or rain-out while making its way to the stratosphere. CF_4 is a by-product of some syntheses for tetrafluoroethylene and a decomposition product when polytetrafluoroethylene and other fluoro-polymers are burned. The major combustion products of rockets which use N_2F_4 or NF_3 oxidizers with hydrocarbon fuels will be CF_4 and HF . It is important that a careful look at fluorine compounds as well as chlorine compounds be part of the current research programs/sampling studies as one evaluates the importance of the ClO_x -cycle and other ozone-destruction processes.

There are some unique properties of fluorine compounds which cannot be overlooked:

- (a) fluorine bonds are stronger than for other halogens
- (b) HF will not react spontaneously with OH , i.e.,



is endothermic

(c) HF, CF₄ and F₂ are transparent throughout most of the ultraviolet and even the vacuum ultraviolet, with strongest absorptions in the range of 800-1000 Å.

(d) the F⁻ ion is stable by ~3.5 eV with respect to F + e

(e) the HF molecule has a high affinity for F⁻ to form the HF₂⁻ ion with a tremendously strong "hydrogen bond".

(f) Oxygenated species like O₂F₃, O₃F₂ and O₄F₂ are well known even at room temperature

(g) NF₂ molecules like CF₂ and SiF₂ have long lifetimes in their ground states--many minutes, perhaps hours at high altitudes and low pressures.

To summarize, one can pose the question: "Is it safe and/or necessary for man to contaminate the stratosphere with chlorine or fluorine?" Apparently, this challenging question of global importance has been asked in time. Usually, men have blundered irreversibly into the consequences before a problem is recognized. A rational evaluation of the question, the scientific facts, and the proper societal answers will require a previously unknown unanimity and spirit of international cooperation among the scientific, the industrial and the political communities of the world. Considerable progress has been made in 1976 toward understanding this inadvertant interaction between man and his environment.³⁰⁻³²

ACKNOWLEDGEMENT

This research was supported by the Advanced Research Projects Agency of the Department of Defense under Contract No. MDA903-76C-0250 with The University of Michigan.

References

1. J. E. Lovelock, *Nature* 230, 379 (1971).
2. J. E. Lovelock, *Atm. Env.* 6, 917 (1972).
3. J. E. Lovelock, R. J. Maggs and R. J. Wade, *Nature* 241, 194 (1973).
4. C-W Su and E. D. Goldberg, *Nature* 245, 27 (1973).
5. P. Wilkniss, R. Lamontagne, R. Larson, J. Swinnerton, C. Dickson and T. Thompson, *Nature* 245, 45 (1973).
6. P. Crutzen, *Can. J. Chem.* 52, 1569 (1974).
7. S. Wofsy and M. McElroy, *Can. J. Chem.* 52, 1582 (1974).
8. R. S. Stolarski and R. J. Cicerone, *Can. J. Chem.* 52, 1610 (1974).
9. M. J. Molina and F. S. Rowland, *Nature* 249, 810 (1974).
10. M. McElroy, S. Wofsy, J. Penner, J. McConnell, *J. Atm. Sci.* 31, 287 (1974).
11. R. J. Cicerone, R. S. Stolaski and S. Walters, *Science* 185, 1165 (1974).
12. J. E. Lovelock, *Nature* 252, 292 (1974).
13. P. J. Crutzen, *Geophys. Res. Lett.* 1, 205 (1974).
14. N. E. Hester, E. R. Stephens, and O. C. Taylor, *J. Air Poll. Control Assn.* 24, 591 (1974).
15. S. Wofsy, M. McElroy and N. Sze, *Science* 187, 535 (1975).
16. M. J. Molina and F. S. Rowland, *Geophys. Res. Lett.* 1, 309 (1974).
17. M. J. Molina and F. S. Rowland, *J. Phys. Chem.* 79, 667 (1975).
18. *ibid*; 79, 669 (1975).
19. F. S. Rowland and M. J. Molina, *Rev. Geophys. and Space Phys.* 13, 1 (1975).
20. F. S. Rowland, *New Scientist* 67, 717 (1974).

21. V. A. Mohnen, Private Communication, June 1975.
22. Anon., Chem. Engr. News, pp. 8-9, August 18, 1975.
23. H. U. Dütsch, Can. J. Chem. 52, 1491 (1974).
24. Anon., Contest, Vol. 2, 1975, p. 25, (E. I. DuPont, Wilmington, Delaware).
25. Petition, Consumer Product Safety Commission, Federal Register 40, No. 162, pp. 26419-21, August 20, 1975).
26. S. Rowland, New Scientist 68, 8 (1975).
27. Anon., Research & Development, February 1975, p. 14.
28. P. H. Howard and A. Hanchett, Science 189, 217 (1975).
29. J. P. Jesson, Science Update 2, 1 (1976). (E. I. DuPont, Wilmington, Delaware).
30. "The Possible Input of Fluorocarbons and Halocarbons on Ozone," Report of Interdepartmental Committee for Atmospheric Sciences, (ICAS 18a-FY75), May 1975.
31. "Fluorocarbons and the Environment," Report of Federal Task Force on Inadvertant Modification of the Stratosphere (IMOS), Federal Council for Science and Technology, June 1975.
32. "Further Information on the Fluorocarbon Industry and on Potential Economic Impacts of Restriction of Fluorocarbon Production," Report of Task Force on Inadvertant Modification of the Stratosphere (IMOS), Federal Council for Science and Technology, June 1975).
33. P. L. Hanst, L. L. Spiller, D. M. Watts, J. W. Spence and M. F. Miller, J. Air Poll. Control Assn. 25, 1220 (1975).
34. R. D. Cadle, J. Geophys. Res. 80, 1650 (1975).
35. D. Stedman, Research & Development, pp. 22-26, January 1976.
36. S. Madorsky, "Thermal Degradation of Organic Polymers," Wiley/Interscience, New York, 1964.
37. P. Kamarchik, R. Hauge and J. L. Margrave, unpublished work, 1976, Rice University.
38. Chem. Engr. News ___, p. (1975).
- 39.

40. R. G. Prinn, J. Atm. Sci. 28, 1058 (1971).
41. R. Pabst, M. Garrett, J. L. Franklin and J. L. Margrave, unpublished work, Rice University, 1976.
42. Harold Johnston, Science 173, 517 (1971).

THERMAL DECOMPOSITION OF CFX IN FLUORINE
AND IN OTHER ATMOSPHERES¹

Peter Kamarchik and J. L. Margrave

INTRODUCTION

Poly(carbon monofluoride), CFX^2 , is a nonstoichiometric solid fluorocarbon whose formula can vary from $\text{CF}_{x \sim 0}$ to $\text{CF}_{x=1.24}$. The color varies with fluorine content and is black for fluorine/carbon ratios up to about 0.9, gray from 0.9 to 1.0, and white above 1.0. CFX was first discovered by Ruff and Bretschneider in 1933.³ By heating graphite in a stream of F_2 to 420-460°C a gray product was formed with a composition $\text{CF}_{0.92}$. Later Palin and Wadsworth⁴ prepared under conditions similar to those of Ruff a compound analyzed as $\text{CF}_{1.04}$. The Rudorffs then took up the work and were able to prepare compounds which ranged in stoichiometry from $\text{CF}_{0.68}$ to $\text{CF}_{0.99}$.⁵

The highest fluorine content one can attain, by a high-temperature reaction between gaseous fluorine at 1 atmosphere and graphite, is quite reproducible and corresponds to a stoichiometry of $\text{CF}_{1.12}$.⁶ The conditions for preparing this composition of CFX are a temperature of 627°C and at least $1\frac{1}{2}$ times as many moles of F_2 and moles C. Slightly higher fluorine contents have been obtained by the use of a chlorine/fluorine mixture.

There has recently been a great deal of interest in CFX

both of a theoretical and practical nature. It has been shown to be a superior lubricant¹²⁻¹⁴ under the extreme conditions of high temperature and high vacuum. It has also been used quite successfully as a cathodic depolarizer in high energy density batteries¹⁰⁻¹⁴ and has been used as a gas chromatographic stationary phase.¹⁵ Nevertheless, few chemical properties have been described for this compound. Since CFX is inert to most kinds of chemical attack at room temperature, this study was undertaken to determine its reactivity at elevated temperatures, and to see if CFX can survive at high enough temperatures to have use as a protective coating on graphite objects.

EFFECTS OF VARIOUS ATMOSPHERES ON CFX DECOMPOSITION

Decompositions of CFX samples of various stoichiometries were carried out under 1 atm. pressures of various gases and gaseous mixtures to determine their effect on the decomposition rate and to check for reactions between CFX and these gases. In these experiments, from 10-30 mg. of the sample were heated in a nickel reaction boat in a stream of the desired gas. Percent weight loss versus temperature data were obtained, at constant reaction time, simply by weighing the sample before and after heating. Experiments were done in the temperature range 200°-800°C.

For reaction times of about 11 hours, it was found that in both N₂ and O₂ at 1 atm. pressure, detectable decomposition is initiated in the range 435°-450°C. These data are presented

in Table I and graphically in Figure 1. The percentage weight losses less than 100% for O_2 and less than about 80% for N_2 listed for any given temperature are time limited rather than temperature limited. It was shown, in further experiments, that as long as the temperature is maintained above approximately $435^\circ C$, if given enough time, the reaction would go to completion. These percentages listed are most closely related to the rate of decomposition at that temperature. It was also observed that up to about $600^\circ C$, the decomposition in N_2 stops at about 80% weight loss. The residue has been shown to contain a small percentage of fluorine.

The experiments done with $CF_{1.12}$ in fluorine and in fluorine/nitrogen mixtures indicate that fluorine will inhibit the decomposition. The results are given in Table II. In fluorine/nitrogen mixtures as dilute as 1% fluorine, no decomposition was observed after 12 hours at $795^\circ C$. A series of experiments all conducted at about $584^\circ C$ give 0.1% as the lower limit of fluorine concentration that inhibits decomposition. This pseudo-equilibrium pressure is about 0.5% F_2 at $714^\circ C$ and about 0.9% for $795^\circ C$. The total gas pressure in all these experiments is 1 atm. The existence of this pseudo-equilibrium condition suggests that the initial step in the decomposition is the breaking of C-F bonds, but a comparison of the C-F bond energy (115 kcal) with the C-C bond energy, (~ 90 kcal) and the fact that no elemental fluorine has been observed in the evolved gases makes this suggestion unlikely. Another scheme which could

TABLE I. Decomposition of $\text{CF}_{1.12}$ in Nitrogen and Oxygen
Atmospheres

| <u>O₂</u> | <u>11 hrs</u> | <u>N₂</u> | <u>11 hrs</u> |
|----------------------|---------------|----------------------|---------------|
| 453 °C | 3.9% | 463 °C | 2.0% |
| 476 °C | 13.0% | 485 °C | 7.4% |
| 500 °C | 47.1% | 520 °C | 37.9% |
| 516 °C | 85.3% | 534 °C | 68.3% |
| 545 °C | 100.0% | 567 °C | 81.1%* |
| 601 °C | 100.0% | 604 °C | 77.9% |

*25 hours

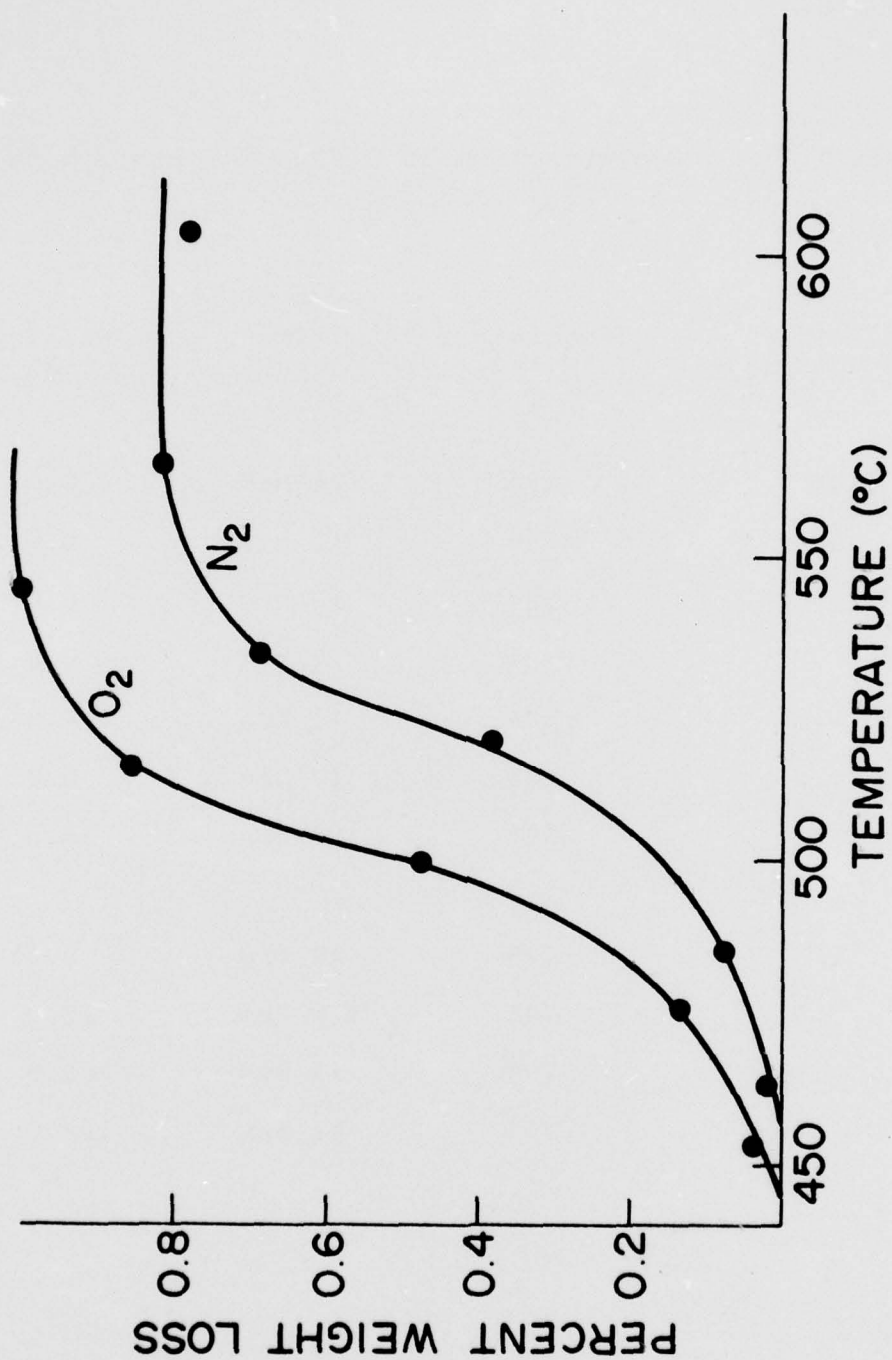


Figure 1. Decomposition of $CF_{1.12}$ in Nitrogen and Oxygen Atmospheres.

TABLE II. $\text{CF}_{1.12}$ Decomposition in a Fluorine Atmosphere

| <u>Fluorine Concentration</u> | <u>Temperature °C \pm 3</u> | <u>Time</u> | <u>% wt. loss \pm 2%</u> |
|-----------------------------------|--|-------------|---|
| 10% | 584 | 24 hrs | 0.0% |
| 5 | 584 | 12 hrs | 0.0 |
| 1 | 584 | 12 hrs | 0.0 |
| .5 | 584 | 12 hrs | 0.0 |
| .5 | 584 | 11 hrs | 0.0 |
| .2 | 584 | 12 hrs | 0.9 |
| .1 | 584 | 24 hrs | 15.0 |
| 1 | 795 | 12 hrs | 0.0% |
| .9 | 795 | 9.5 hrs | 17.8 |
| .5 | 795 | 11 hrs | 100.0 |
| .05 | 795 | 11 hrs | 100.0 |

account for the fluorine inhibiting effect would involve fluorine as a radical scavenger. This scheme assumes that the initial bond breakage is much slower than subsequent breakage at adjacent sites and thus, it is the presence of the initially formed radicals that leads to the further reaction. A much higher rate of growth of product phase than of initiation has been observed in many other cases and would not be unreasonable here. As the initial radicals are formed by C-C bond breakage they would be scavenged by F atoms present, and would not be available to accelerate the reaction. This has been observed by Wall and Michaelson^{16,17} for polytetrafluoroethylene where F₂, Cl₂, H₂ and toluene vapors were found to inhibit the decomposition. If the initial reaction is slow enough, no weight change would be observable in the experiments done.

A series of experiments, like those performed with CF_{1.12} in the N₂ atmosphere, was done with CF_{0.61}. The data are presented in Table III and in Figure 2. The onset temperature is about 360°C, which is considerably lower than for CF_{1.12}. Another difference is that the slope of the line, i.e., the rate of change in the rate of decomposition as a function of temperature, is considerably less for CF_{0.61} implying a lower activation energy. It is also noted that "complete" reaction for CF_{0.61}, at least up to 630°C, appears to be about a 47% weight loss. Samples of two of the partially fluorinated CFX compounds, CF_{0.61} and CF_{0.96}, were heated in the presence of fluorine and fluorine/nitrogen mixtures. CF_{0.61} was heated at four different tempera-

TABLE III. Decomposition of $\text{CF}_{0.61}$ in a Nitrogen Atmosphere

| <u>N₂</u> | <u>12 hrs</u> |
|----------------------|---------------|
| 361 °C | 0.0% |
| 407 °C | 10.7% |
| 452 °C | 23.7% |
| 456 °C | 19.0% |
| 484 °C | 28.0% |
| 557 °C | 43.7% |
| 583 °C | 48.0% |
| 627 °C | 46.0% |

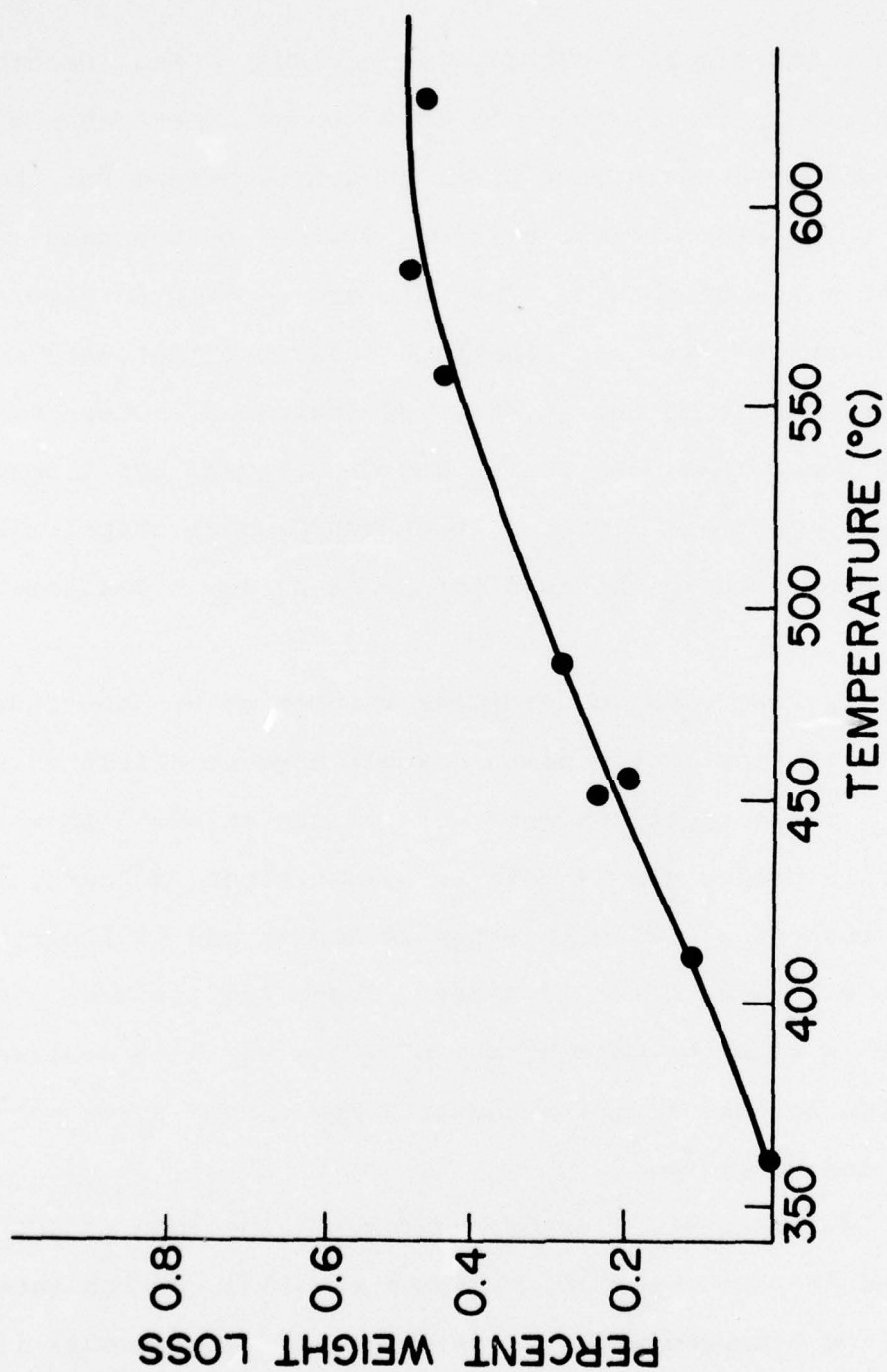


Figure 2. Decomposition of $\text{CF}_{0.61}$ in a Nitrogen Atmosphere.

tures in a mixture with a 33% fluorine content. The reaction times were all in the range of 17 to 23 hours. Without any information about the existence of an induction period for this reaction, the percent weight gain was divided by the reaction time to get a reaction rate. The data are plotted in Figure 3 as \ln rate versus $1/T$. The linearity indicates that this reaction has an activation energy, $E_a = 32$ kcal/mole. Other experiments have shown that both $CF_{0.61}$ and $CF_{0.96}$ will add fluorine to a lower temperature limit of about $400^\circ C$; pure graphite begins to gain appreciable weight in fluorine at as low a temperature as $240^\circ C$.

$CF_{0.96}$ was used to determine whether or not the concentration of fluorine in the mixture would have an effect on the reactions. Three reactions were carried out at $540^\circ C$ in which pure fluorine produced a 2% gain in weight after 13 hours, 10% fluorine produced a 0.2% gain after 27 hours, and 1% fluorine produced a 0.5% loss after 23 hours. These results show a strong dependence on fluorine concentration. This was also observed in the reaction between fluorine and graphite in the study done by Kuriakose and Margrave.¹⁸

A few exploratory experiments were also done on $CF_{1.12}$ when heated in pure chlorine, hydrogen fluoride, carbon tetrafluoride, and hydrogen atmospheres which all gave results like those of the decomposition in nitrogen. Especially the "inertness" of hydrogen argues against a decomposition mechanism which yields F_2 or F-atoms.

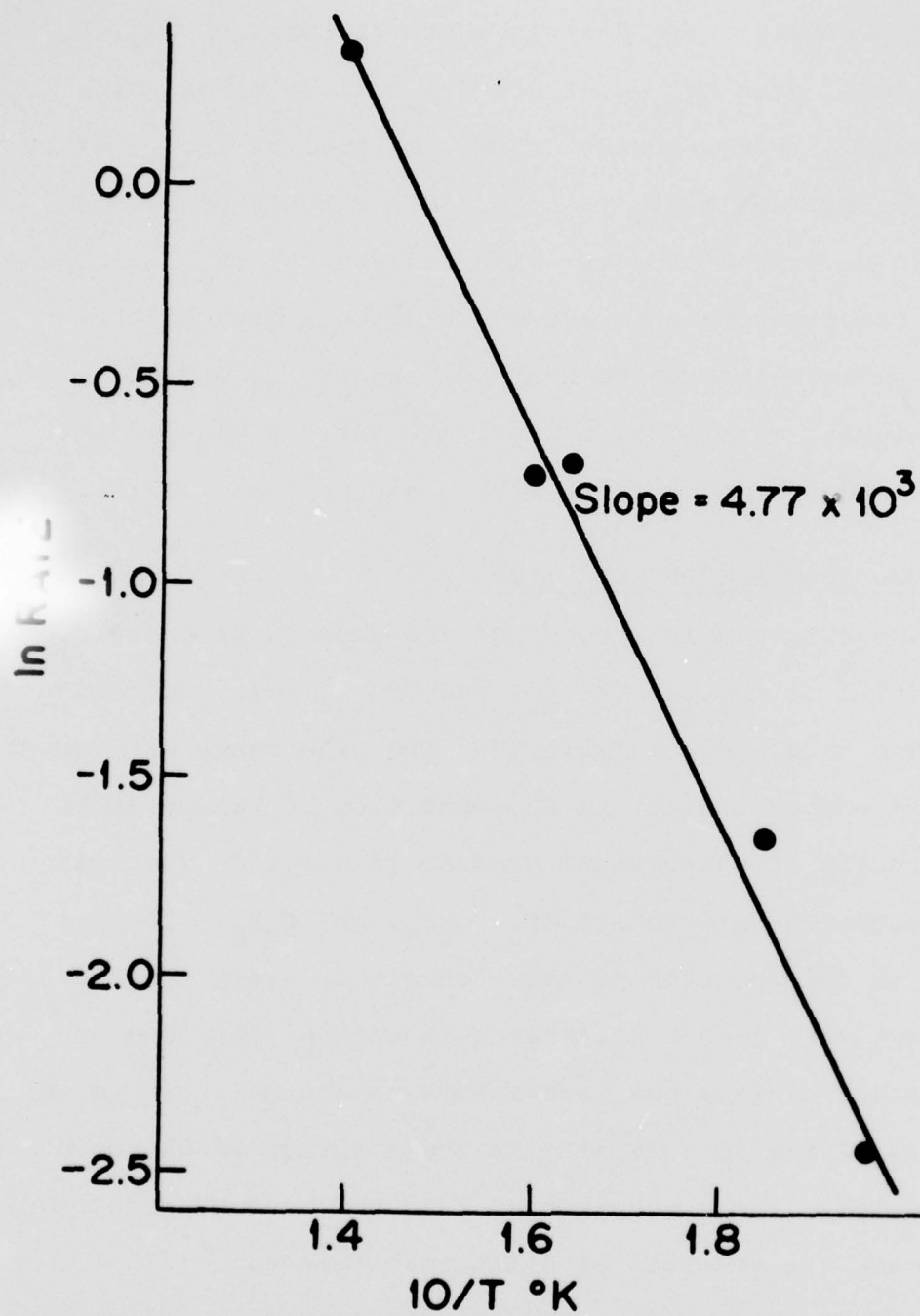


Figure 3. Arrhenius Plot for the Fluorination of $\text{CF}_{0.61}$.

Two experiments were done in which mixtures of Cl_2 , F_2 , and N_2 were used. With $\text{CF}_{1.08}$ at 638°C a mixture of 38% Cl_2 , 10% F_2 , and 52% N_2 left a product which analyzed as $\text{CF}_{1.24}$ after a 12 hour reaction. With $\text{CF}_{1.12}$ at 638°C a mixture of 23% Cl_2 , 38% F_2 and 38% N_2 left a product which analyzed as $\text{CF}_{1.17}$. These are the only reactions which produced CFX with x greater than 1.12. Other experiments showed that heating $\text{CF}_{1.08}$ and $\text{CF}_{1.12}$ to 638°C or higher, in a F_2/N_2 mixture without the Cl_2 did not result in the production of a CFX with x higher than 1.12.

MATRIX INFRARED SPECTROSCOPY RESULTS

The argon matrix IR spectra of the gaseous products from the decomposition of $\text{CF}_{1.12}$, $\text{CF}_{1.08}$, and $\text{CF}_{0.96}$ were recorded and the absorptions tabulated in Table IV. The wide range of products observed is in contrast with the decomposition of Teflon above 425°C in which 95% of the gaseous product is C_2F_4 .¹⁹ The most prominent absorptions are due to CF_4 , C_2F_4 , and C_2F_6 . The products appear in the spectrum of every sample at every temperature tried. In fact very little difference is seen either from one sample to another or from one temperature to another. There were only two peaks of medium intensity in the spectrum which could not be identified. These occurred at 1087 cm^{-1} and at 1103 cm^{-1} , and may indicate the presence of difluoroacetylene.

Some small but possibly significant dependence of gaseous composition on temperature was observed for $\text{CF}_{1.12}$. Higher temperatures seem to favor the formation of smaller molecules (CF_4 , C_2F_6) over the larger (C_3F_8 , C_5F_{10} , etc.). This dependence was

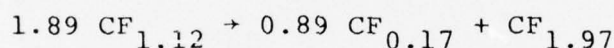
TABLE IV. Infrared Absorption Bands Observed for the Gaseous Products of CFX Decomposition

| $\nu(\text{cm}^{-1})$ | identity | intensity | $\nu(\text{cm}^{-1})$ | identity | intensity |
|-----------------------|--|-----------|-----------------------|--|-----------|
| 406 | C_2F_4 | VW | 1140 | $\text{n-C}_5\text{F}_{12}$ | M |
| 415 | ? | W | 1149 | $\text{n-C}_5\text{F}_{12}$ | M |
| 511 | ? | W | 1182 | $\text{C}_2\text{F}_4, \text{C}_3\text{F}_6$ | VS |
| 524 | C_2F_6 | M | 1209 | C_3F_8 | S |
| 558 | C_2F_4 | W | 1213 | C_3F_6 | W |
| 631 | CF_4 | W | 1220 | $\text{n-C}_5\text{F}_{12}$ | VW |
| 663 | C_3F_8 | M | 1242 | $^\circ(\text{C}_4\text{F}_8)$ | S |
| 705 | ? | M | 1244 | $^\circ(\text{C}_4\text{F}_8)$ | VS |
| 713 | C_2F_6 | S | 1251 | C_2F_6 | VS |
| 729 | C_3F_8 | W | 1257 | $\text{n-C}_5\text{F}_{12}$ | W |
| 767 | C_3F_6 | VW | 1261 | C_3F_8 | M |
| 975 | $^\circ(\text{C}_4\text{F}_8)$ | VW | 1274 | CF_4 | VS |
| 977 | ? | W | 1293 | $^\circ(\text{C}_4\text{F}_8)$ | VVW |
| 985 | ? | W | 1329 | C_2F_4 | S |
| 1005 | C_3F_8 | M | 1339 | $^\circ(\text{C}_4\text{F}_8)$ | VW |
| 1034 | $\text{C}_3\text{F}_8, \text{C}_3\text{F}_6$ | M | 1355 | C_3F_8 | VVW |
| 1087 | ? | M | 1399 | C_3F_6 | W |
| 1103 | ? | M | 1796 | C_3F_6 | W |
| 1112 | $\text{C}_2\text{F}_6, \text{C}_3\text{F}_8$ | VS | | | |

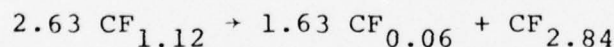
not observed when $CF_{1.08}$ and $CF_{0.96}$ were being decomposed. In going from $CF_{1.12}$ to $CF_{1.08}$ at about the same temperature the proportion of CF_4 decreased while the proportion of saturated compounds to unsaturated compounds increased. On the other hand, $CF_{0.96}$ shows a larger proportion of CF_4 than $CF_{1.12}$, and the saturated to unsaturated ratio is about the same as for $CF_{1.12}$.

SUGGESTED DECOMPOSITION MECHANISM

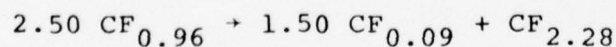
One can combine the various experimental data to deduce a decomposition mechanism. First, consider the percent weight loss at completion of decomposition and the F/C ratio of the decomposition residue. These data make it possible to write balanced equations for these reactions. For example 553°C under vacuum:



The $CF_{1.97}$ represents either the average empirical formula of all the gaseous products or the empirical formula for a single gaseous product if only one is formed. Another example, for a decomposition at 593°C is:



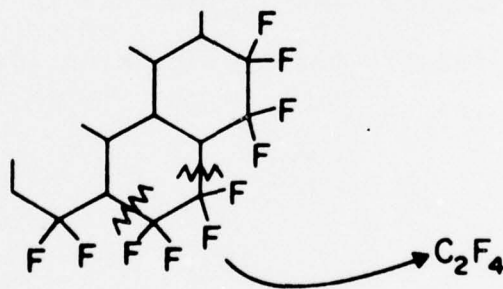
For $CF_{1.12}$ the F/C ratio of the gaseous products increases from ~2.0 to ~2.8 with increasing temperature; however, for $CF_{0.96}$ the equation



is approximately obeyed at every temperature tried.

If the gaseous product of the decomposition is the mixture of CF_4 , C_2F_4 and C_2F_6 observed in the matrix IR, then an average F/C ratio for all the product gases of about 2.0 is difficult to explain since little, if any, C_2F_2 was observed in the IR. We avoid this difficulty by suggesting that the only abundant gaseous product is C_2F_4 , as in the decomposition of Teflon,¹⁹ and that the other gases arise from pyrolysis of the C_2F_4 on the hot walls of the furnace. This pyrolysis would produce the carbon deposits which have been observed on the hot zone of the glass jacket.

If it is correct that C_2F_4 is the only product of the decomposition, it may be suggested that the final step is occurring at the edges of the CFX crystallites, where the carbon atoms are already bonded to two fluorine atoms and the only requirement for the production of C_2F_4 is that two C-C bonds be broken. See the sketch below.



As C-C bonds are broken, additional F atoms migrate from the interior of the crystallite to the edge, filling the vacant bonding positions on the carbon radicals, and resulting in a return to graphite-like C-C multiple bonds in the interior. This is consistent with the kinetic data which favor a contracting plane model and with X-ray powder diffraction results for the residues

which show the presence of graphite. Using 95 kcal/mole²⁰ for the strength of a C-C single bond and 176 kcal/mole as the strength of the $F_2C=CF_2$ bond, a ΔH of +89 kcal/mole can be calculated for loss of C_2F_4 . Because of the large spread in calculated activation energies, it is impossible to conclusively identify this process as the rate controlling one. In fact, because of the greater energy of the C-F bond, fluorine migration may be rate controlling.

The last step of the proposed mechanism is similar to the decomposition mechanism of Teflon²¹, i.e., formation of a radical site in the chain by C-C bond breakage followed by a second C-C bond breakage forming a new radical end site and tetrafluoroethylene monomer. This process of "unzipping" continues until the radical is quenched. However, this reaction follows a much simpler kinetic law than the decomposition of CFX follows, i.e., ordinary first order kinetics with an activation energy of 76 kcal²².

References

1. Extracted in part from the Ph.D. Thesis of Peter Kamarchik, Rice University, May 1976.
2. "CFX," Registered U.S. Trademark No. 931,639, issued April 4, 1972.
3. O. Ruff and O. Bretschneider with F. Ebert, Z. Anorg. u. Allg. Chem. 217, 1 (1934).
4. D. E. Palin and K. D. Wadsworth, Nature 162, 925 (1948).
- 5a. W. Rudorff and G. Rudorff, Z. anorg. allgem. Chem. 253, 281 (1947).
- b. W. Rudorff and G. Rudorff, Chem. Ber. 80, 413 (1947).
- c. W. Rudorff, in Handbook of Preparative Inorganic Chemistry, Vol. 1, (G. Brauer, ed.), Academic Press, New York, 1963, p. 635.
- d. W. Rudorff, Adv. Inorg. Chem and Radiochem. 1, 223 (1959).
6. R. J. Lagow, R. B. Badachhape, J. L. Wood and J. L. Margrave, J.C.S. Dalton, 1974, 1268 (1974).
7. R. L. Fusaro and H. E. Sliney, Graphite Fluoride: A New Solid Lubricant, NASA Technical Memorandum, NASA TMX-52624, 1969.
8. R. L. Fusaro and H. E. Sliney, Graphite as a Solid Lubricant in a Polyimide Binder, Lewis Research Center Technical Report, 1971.
9. H. Gisser, M. Petronio and A. Shapiro, J. Amer. Soc. of Lub. Eng. 28, 161 (1972).
- 10a. N. Watanabe and M. Takashima, Proceedings of the 7th International Symposium on Fluorine Chem., Santa Cruz, California, July 1973.
- b. N. Watanabe, et. al., J. Electrochem. Soc., Japan, 32, 17 (1964).
- 11a. K. Braeuer, Abstract No. 210, p. 495, Electrochem. Soc. Extended Abstracts, Spring Meeting, Boston, Mass., May 5-9, 1968.
- b. K. Braeuer, Abstract No. 64, p. 401, Electrochem. Soc. Extended Abstracts, Spring Meeting, New York, N.Y., May 4-9, 1969.

- 11c. K. Fraeuer, "Feasibility Study of the Lithium/C_xF Primary Cell," R & D Technical Report ECOM-3322, August 1970.
- d. K. Braeuer and K. R. Moyes, U.S. Patent No. 3,514,337, May 1970.
- 12a. N. Watanabe and M. Fukuda, Chem. Abstracts 72, No. 8, February 23, 1970, p. 549, No. 38270n.
- b. M. Fukuda and T. Iijima, Abstract No. 41, p. 100, Electrochem. Soc. Extended Abstracts, Fall Meeting, Cleveland, Ohio, October 3-7, 1971.
13. I. Takashi and T. Yoshinori, Japan, Patent No. 75,50,631, May 7, 1975.
14. H. F. Hunger and G. J. Heymach, J. Electrochem. Soc. 120, 1161 (1973).
15. L. C. Swope and E. A. Smith, U.S. Patent No. 3,877,894, April 15, 1975.
16. L. A. Wall and J. D. Michaelson, J. Res. Nat. Bur. Stds. 56, 27 (1956).
17. J. D. Michaelson and L. A. Wall, J. Res. Nat. Bur. Stds. 58, 327 (1957).
18. A. K. Kuriakose and J. L. Margrave, J. Phys. Chem. 69, 2272 (1965).
19. D. I. McCane, "Tetrafluorethylene Polymers," in Vol. 13 of Encyclopedia of Polymer Science and Technology, ed. E. H. Mark, 1970.
20. F. P. Lossing, private communication to V. H. Dibeler of the Mass. Spec. Section. Nat. Bur. Stds., Washington, D.C.
21. S. L. Madorsky, V. E. Hart, S. Straus, and V. A. Sedlak, J. Res. Nat. Bur. Stds. 51, 327 (1953).
22. J. M. Cox, B. A. Wrigy and W. W. Wright, J. Appl. Polymer Sci. 8, 2935 (1964).

TIGHT BINDING THEORY OF METALLIC ADHESION

W. Kohn and R. Gomer

INTRODUCTION

Interfacial energies between two metals play an important role in many materials problems. As examples we mention: grain-boundary energies, energies stored near crack-tips; adhesion between two different metals; interphase energies.

Recently there have appeared some interesting calculations of interface energies using the density functional theory of electronic structure¹. This method is most appropriate for so-called "simple" metals in which the conduction electrons have preponderantly s- and p-character, such as for example the alkali metals and Al.

For transition metals another approach, the tight binding method, has been used to describe bulk cohesive energies and surface energies.^{2,3,4} This method highlights the atomic character of the d-electrons. In the present note we develop this method for the problem of interfacial energies with special attention to electrostatic self-consistency. Exchange and correlation effects are not yet included in this treatment

The case of simple cubic metals with no lattice mismatch is considered in the present work. Extension to fcc and bcc lattices, and inclusion of mismatch should be feasible.

THE MODEL

In what follows we shall first be dealing with two reference systems, the bulk-metal and the metal-vacuum interface, and finally the metal-metal interface. For all these systems we make the following assumptions.

1. The atoms of each metal are arranged in a simple cubic lattice, R_{ℓ} , with lattice spacing d .

2. There is one valence electron per atom; the ionic potential energy due to atom ℓ is denoted by $v_{\ell}(\underline{r})$ which has the asymptotic behavior

$$v_{\ell}(\underline{r}) \rightarrow - \frac{1}{|\underline{r}-\underline{R}_{\ell}|} \quad (1)$$

(Here and in what follows we use atomic units)

3. We assume that all eigenfunctions can be written as linear combinations of the normalized Wannier functions $\psi_{\ell}(\underline{r})$ of the self-consistent bulk metal systems. Changes of these functions due to the vicinity of an interface are neglected and all orthogonality integrals are set equal to zero. Only diagonal and nearest-neighbor terms are retained.

4. We are limiting ourselves to the Hartree approximation. The effective single particle Hamiltonian is given by

$$H = - \frac{1}{2} \nabla^2 + v^{\text{tot}}(\underline{r}) \quad (2)$$

with

$$V(\underline{r}) = \sum_{\ell} v_{\ell}(\underline{r}) = \sum_{\ell} (v_{\ell}(\underline{r}) + n_{\ell} u_{\ell}(\underline{r})) \quad , \quad (3)$$

where $u_\ell(\underline{r})$ is the electrostatic potential energy due to the electronic density $g_\ell(\underline{r})$ associated with the Wannier function $\psi_\ell(\underline{r})$,

$$g_\ell(\underline{r}) = |\psi_\ell(\underline{r})|^2, \quad (4)$$

and n_ℓ is the occupation number of site ℓ .

5. The total Hartree energy is given by

$$E = E_s - \frac{1}{2} \sum_{\ell, \ell'} \int \frac{(n_\ell g_\ell(\underline{r}))(n_{\ell'} g_{\ell'}(\underline{r}'))}{|\underline{R}_\ell - \underline{R}_{\ell'}|} d\underline{r} d\underline{r}' + \frac{1}{2} \sum_{\ell \neq \ell'} \frac{1}{|\underline{R}_\ell - \underline{R}_{\ell'}|}, \quad (5)$$

where E_s is the sum of the single particle energies of the occupied eigenstates of the Hartree Hamiltonian (Eq. 2). If, in the second term, we neglect the overlap of the charge distributions $g_\ell(\underline{r})$ and $g_{\ell'}(\underline{r})$, for $\ell' \neq \ell$ we can write

$$E \approx E_s - \epsilon_{es} \sum_{\ell} n_\ell^2 + \frac{1}{2} \sum_{\ell \neq \ell'} \frac{1}{|\underline{R}_\ell - \underline{R}_{\ell'}|} (1 - n_\ell n_{\ell'}) \quad (6)$$

where ϵ_{es} is the electrostatic self energy

$$\epsilon_{es} \equiv \frac{1}{2} \int \frac{g_\ell(\underline{r}) g_\ell(\underline{r}')}{|\underline{r} - \underline{r}'|} d\underline{r} d\underline{r}' \quad (7)$$

6. From the matrix elements $(\ell_x \ell_y \ell_x | H | \ell'_x \ell'_y \ell'_z)$ in the Wannier representation, the single particle energy E_s and the occupation number n_ℓ can be calculated by the methods of Refs. 2-4.

Definition of Interface Energy

It is important to note that two interfacial energies can be defined. The first is the decrease in energy, per unit interface area, when two phases with unit surface areas and are joined into an interface. If the surface energies are denoted by σ_a and σ_b for the phases a and b respectively, the interfacial energy σ_{ab} so defined becomes

$$\sigma_{ab} = E_{ab}^{tot} - E_a - E_b - (\sigma_a + \sigma_b) \quad (8)$$

where E_{ab}^{tot} is the total energy of the combined system and E_a and E_b are the bulk energies of phases a and b.

On the other hand we may also define a quantity σ'_{ab}

$$\sigma'_{ab} = E_{ab}^{tot} - E_a - E_b \quad (9)$$

which represents the energy change when two infinite blocks of a and b, of 1/2 unit area cross section are cut and rejoined to form two composite blocks with total interfacial area of unity. The quantity σ'_{ab} is a measure of an interface's tendency to form from full phases and is obviously easier to calculate than σ_{ab} .

REFERENCE SYSTEMS

Single Bulk Metal

Here all occupation numbers, n_ℓ , are unity and the Hartree potential is periodic

$$V = \sum_{\ell} V_{\ell}(r) = \sum_{\ell} V(r - R_{\ell}) \quad (10)$$

Hence the eigenfunctions are of the Bloch form. Writing for the Wannier functions

$$\psi_{\ell}(\underline{r}) = \psi(\underline{r}-\underline{R}_{\ell}) \quad (11)$$

the eigenfunctions are given by

$$\psi_{\underline{k}}(\underline{r}) = \frac{1}{N^{1/2}} \sum_{\ell} e^{i\underline{k} \cdot \underline{R}_{\ell}} \psi(\underline{r}-\underline{R}_{\ell}) \quad (12)$$

where N is the number of atoms, and the single particle eigenvalue by

$$\epsilon_{\underline{k}} = \sum_{\ell} e^{i\underline{k} \cdot \underline{R}_{\ell}} (\psi(\underline{r}), H\psi(\underline{r}-\underline{R}_{\ell})) \quad (13)$$

We regard $\psi(\underline{r})$ as so localized that Eq. (13) needs to be summarized only up to nearest neighbors. If we denote by \underline{t}_1 one of the nearest neighbor lattice sites relative to the origin, we obtain

$$\epsilon_{\underline{k}} = \bar{\epsilon} + 2t(\cos k_x d + \cos k_y d + \cos k_z d) \quad (14)$$

where

$$\bar{\epsilon} = (\psi(\underline{r}), H\psi(\underline{r})) \quad (15)$$

and

$$t = (\psi(\underline{r}), H\psi(\underline{r}-\underline{t}_1)) \quad (16)$$

Now using the short range of the partial Hartree potentials $V(\underline{r}-\underline{R}_{\ell})$ we can further write

$$\bar{\epsilon} = \epsilon_0 + \alpha \quad (17)$$

where

$$\epsilon_0 = (\psi(\underline{r}), (-\frac{1}{2} \nabla^2 + V(\underline{r}))\psi(\underline{r})) \quad (18)$$

$$\alpha = 6(\psi(\underline{r}), V(\underline{r}-\underline{t}_1)\psi(\underline{r}))$$

Total and cohesive energies:

In the expression (Eq. 6) for the total energy we write

$$E_s = N \int^{\epsilon_F} n(\epsilon) \epsilon d\epsilon \quad (19)$$

where $n(\epsilon)$ is the normalized density of states associated with the single particle spectrum (Eq. 13). The last sum in Eq. (6) vanishes so that the total Hartree energy per atom becomes

$$E/N = \int^{\epsilon_F} n(\epsilon) \epsilon d\epsilon - \epsilon_{es} \quad (20)$$

where ϵ_F is the Fermi energy and ϵ_{es} is defined in Eq. (7).

To obtain the cohesive energy we must subtract the energy of an isolated atom, given by

$$\epsilon_{at} = (\psi_{at}, [-\frac{1}{2} \nabla^2 + v(\underline{r})] \psi_{at}) \quad (21)$$

Combining this with Eq. (20) gives

$$E_{coh}/N \approx \int^{\epsilon_F} n(\epsilon) (\epsilon - \epsilon_{at}) d\epsilon - \epsilon_{es} \quad (22)$$

If we neglect the difference between $\psi_{at}(\underline{r})$ and the Wannier function $\psi(\underline{r})$ we can write

$$\begin{aligned} \epsilon_{at} &= (\psi(\underline{r}), [-\frac{1}{2} \nabla^2 + v(\underline{r}) + u(\underline{r})] \psi(\underline{r})) \\ &\quad - (\psi(\underline{r}), u(\underline{r}) \psi(\underline{r})) \\ &= \epsilon_0 - 2\epsilon_{es} = \bar{\epsilon} - \alpha - 2\epsilon_{es} \end{aligned} \quad (23)$$

$$E_{coh}/N \approx \int^{\epsilon_F} n(\epsilon) (\epsilon - \bar{\epsilon}) d\epsilon + \alpha + \epsilon_{es} \quad (24)$$

The first term is due to the spreading of the atomic level into a band, the second is the change of the center of mass of the band due to the neighboring atoms and the third is the electrostatic self-energy which is present in the solid but absent in the atom. (Of course, exchange and correlation effects will greatly reduce this term.)

Metal-Vacuum Interface

Our model system is shown in Fig. 1.

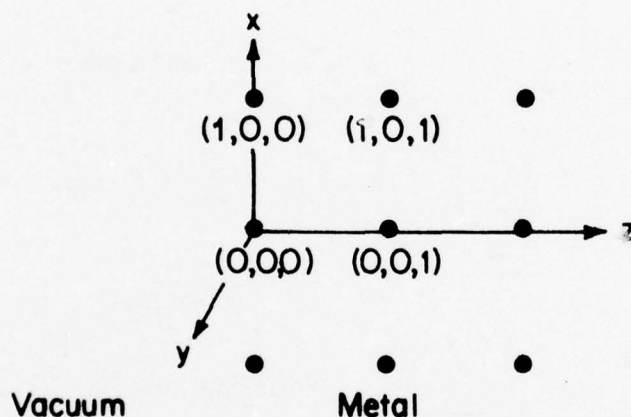


Figure 1. Metal vacuum interface for a simple cubic metal.

We shall assume that the occupation numbers n_{ℓ} differ from 1 only in the first two layers

$$n_{\ell} = \left\{ \begin{array}{ll} 1 + \delta n & \ell_z = 0 \\ 1 - \delta n & \ell_z = 1 \\ 1 & \ell_z \geq 2 \end{array} \right\} \quad (25)$$

Then the Hartree Hamiltonian H' of this system has the potential

energy

$$V' = \sum_{\ell} V_{\ell}(\underline{r}) + \delta n \left[\sum_{\ell, z=0} u_{\ell}(\underline{r}) - \sum_{\ell, z=1} u_{\ell}(\underline{r}) \right] \quad (26)$$

The term proportional to δn represents a dipole barrier due to the presence of an excess electron occupation ($+\delta n$) on the surface atoms and a deficit electron occupation ($-\delta n$) on the next layer. We replace it by the following averaged barrier potential energy

$$\delta n \left[+ \sum_{\ell, z=0} u_{\ell}(\underline{r}) - \sum_{\ell, z=1} u_{\ell}(\underline{r}) \right] \rightarrow V_B(\underline{r})$$

$$= \begin{cases} \delta n \left(+ \frac{2\pi}{d} \right) & z \leq 0 \text{ (in vacuum)} \\ \delta n \left(+ \frac{2\pi}{d} - \frac{4\pi}{d^2} z \right) & 0 < z < d \text{ (between top two layers)} \\ \delta n \left(- \frac{2\pi}{d} \right) & d \leq z \text{ (in metal)} \end{cases} \quad (27)$$

(See Fig. 2) Note that the potential energy in the vacuum is now not zero but $\delta n(+2\pi/d)$.

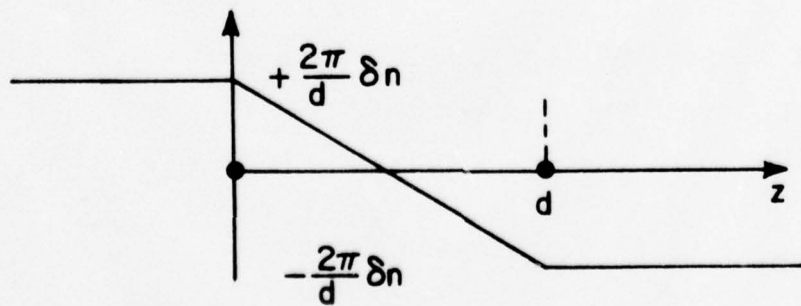


Figure 2. Barrier potential energy due to charge transfer δn between first two layers.

With this replacement we obtain the following matrix elements

$$(000|H|000) = \bar{\epsilon} - \frac{\alpha}{6} + \frac{2\pi}{d} \delta n \quad (28)$$

$$(00\ell_z|H|00\ell_z) = \bar{\epsilon} - \frac{2\pi}{d} \delta n \quad \ell_z \geq 1 \quad (29)$$

All off-diagonal matrix elements are 1 for nearest neighbors and 0 otherwise. From these matrix elements the single particle density of states and energy can be obtained by the methods of Refs. 2-4.

Total and surface energies:

From Eq. (6) we obtain for the total Hartree energy of this system

$$E' = E'_S - (N + 2N_S \delta n^2) \epsilon_{es} + \frac{1}{2} \sum_{\ell \neq \ell'} \frac{1}{|R_{\ell} - R_{\ell'}|} (1 - n_{\ell} n_{\ell'}) \quad (30)$$

Here E'_S is the single particle energy corresponding to the Hamiltonian H' and N_S is the total number of surface atoms. The last term is approximately evaluated in the appendix and leads to the following final result

$$E' = E'_S - (N + 2N_S \delta n^2) \epsilon_{es} + N \delta n \frac{2\pi}{d} + N_S (-2\delta n - 0.44 \delta n^2) \frac{2\pi}{d} \quad (31)$$

To obtain the surface energy we subtract from E' the energy of a bulk system with the same number N of atoms, which

is given by Eq. (20). Note that because of the additive potential energy $-\delta n(2\pi/d)$ which exists inside the system with a surface (see Eq. 26), $E'_S = E_S - N\delta n(2\pi/d)$ plus surface terms. Also, the Fermi level in the surface system is given by $\epsilon'_F = \epsilon_F - \delta n(2\pi/d)$. Therefore it is convenient to combine E'_S and $-N\delta n(2\pi/d)$ in Eq. (31) and write the sum of these two terms as

$$\begin{aligned} E'_S + N\delta n \frac{2\pi}{d} &= N \left\{ \int^{\epsilon'_F} n'(\epsilon) \epsilon d\epsilon + \int^{\epsilon'_F} n'(\epsilon) \left(\delta n \frac{2\pi}{d} \right) d\epsilon \right\} \\ &= N \int^{\epsilon'_F} n'(\epsilon) \left(\epsilon + \delta n \frac{2\pi}{d} \right) d\epsilon = N \int^{\epsilon_F} n' \left(\epsilon - \delta n \frac{2\pi}{d} \right) \epsilon d\epsilon, \end{aligned} \quad (32)$$

where $n'(\epsilon)$ is the normalized density of states of the surface system. Therefore, denoting the surface energy per surface atom by η_s , we have

$$\begin{aligned} N_s \eta_s = E'_S - E &= N \int^{\epsilon_F} \left[n' \left(\epsilon - \delta n \frac{2\pi}{d} \right) - n(\epsilon) \right] \epsilon d\epsilon \\ &\quad + N_s \left[-2\delta n \frac{2\pi}{d} - \delta n^2 \left(2\epsilon_s + 0.44 \frac{2\pi}{d} \right) \right] \end{aligned} \quad (33)$$

Now we define the incremental surface density of states, $\Delta n'(\epsilon)$, by

$$N_s \Delta n'(\epsilon) = N \left[n' \left(\epsilon - \delta n \frac{2\pi}{d} \right) - n(\epsilon) \right] \quad (34)$$

Then Eq. (33) becomes

$$\begin{aligned} \eta_s &= \int^{\epsilon_F} \Delta n'(\epsilon) \epsilon d\epsilon - \delta n \frac{4\pi}{d} \\ &\quad - \delta n^2 \left(2\epsilon_s + 0.44 \frac{2\pi}{d} \right) \end{aligned} \quad (35)$$

Since in general one expects δn to be small (say <0.1) the last term in Eq. (35) is a minor contribution to η_s .

Work function:

The work function, ϕ , in general is given by

$$\phi = \Delta\phi - \mu \quad (36)$$

where $\Delta\phi$ is the electrostatic lower energy and μ is the chemical potential relative to the average interior electrostatic potential. In the present model this becomes

$$\phi = + \frac{4\pi}{d} \delta n - \epsilon_F \quad (37)$$

In addition there is also a dipole barrier due to the uncompensated spillover of the electronic charge density of the surface layer of atoms. Its contribution is found to be

$$\Delta\phi' = \frac{8\pi}{d^2} \int_{d/2}^{\infty} \left(z - \frac{d}{2} \right) g(r) dr \quad . \quad (1+\delta n) \quad (38)$$

which is to be added to ϕ .

One final remark: In the cubic tight binding limit there is a special symmetry about the center of the band as a result of which $\delta n = 0$ for a half-filled band. In general, however, δn does not vanish.

Metal-Metal Interface - Formalism

We now consider the system illustrated in Figure 3, representing two cubic metals contacting one another in perfect register

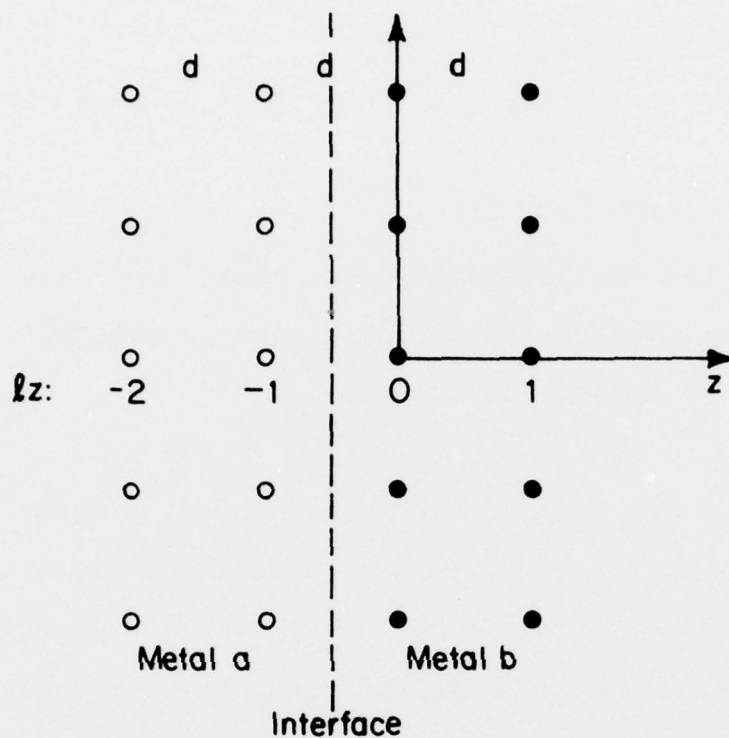


Figure 3. Interface between two cubic metals, a and b.

We shall make the following assumptions for the occupation numbers (c.f. Eq. 25).

$$n_{\ell} = \begin{cases} 1 + \delta n_{\ell} & \ell = -2, -1, 0, 1 \\ 1 & \ell \leq -3, \ell \geq 2 \end{cases} \quad (39)$$

Charge neutrality of the surface region requires

$$\sum \delta n_{\ell} = 0 \quad (40)$$

The potential energy of the Hartree Hamiltonian H'' is given by

$$\begin{aligned}
 V'' = & \sum_{\ell \leq -1} v_{\ell}^a(\underline{r}) + \sum_{\ell \geq 0} v_{\ell}^b(\underline{r}) \\
 & + \sum_{-2 \leq \ell \leq -1} \delta n_{\ell} u_{\ell}^a(\underline{r}) + \sum_{0 \leq \ell \leq 1} \delta n_{\ell} u_{\ell}^b(\underline{r})
 \end{aligned} \quad (41)$$

where

$$v_{\ell}^{a,b}(\underline{r}) \equiv v_{\ell}^{a,b}(\underline{r}) + u_{\ell}^{a,b}(\underline{r}) \quad (42)$$

Due to the charge displacements (Eq. 39) there is an electrostatic potential energy at the various layers given by the following expressions

$$V_B = \left\{ \begin{array}{ll} \frac{2\pi}{d} (\delta n_{-1} + 2\delta n_0 + 3\delta n_1) & \ell_z \leq -2 \\ \frac{2\pi}{d} (-\delta n_{-1} + \delta n_1) & \ell_z = -1 \\ \frac{2\pi}{d} (-\delta n_{-1} - 2\delta n_0 - \delta n_1) & \ell_z = 0 \\ \frac{2\pi}{d} (-\delta n_{-1} - 2\delta n_0 - 3\delta n_1) & \ell_z \geq 1 \end{array} \right\} \quad (43)$$

(We have arbitrarily expressed these electrostatic barrier potentials in terms of δn_{-1} , δn_0 and δn_1 ; the fourth quantity is given in terms of these three by the charge neutrality condition, Eq. (40)).

We can now write down the required matrix elements:

$$\left. \begin{aligned}
(000|H''|000) &= \epsilon_o^a + \tilde{\alpha}^a + \frac{2\pi}{d} (-\delta n_1 - 2\delta n_0 - \delta n_1) \\
(00\ell_z|H''|00\ell_z) &= \epsilon_o^a + \alpha^a + \frac{2\pi}{d} (-\delta n_{-1} - 2\delta n_0 - 3\delta n_1), \ell_z \geq 1 \\
(00-1|H''|00-1) &= \epsilon_o^b + \tilde{\alpha}^b + \frac{2\pi}{d} (-\delta n_{-1} + \delta n_1) \\
(00\ell_z|H''|00\ell_z) &= \epsilon_o^b + \alpha^b + \frac{2\pi}{d} (\delta n_{-1} + 2\delta n_0 + 3\delta n_1), \ell_z \leq -2
\end{aligned} \right\} (44)$$

Here

$$\begin{aligned}
\tilde{\alpha}^a &= 5(\psi^a(\underline{r}), V^a(\underline{r}-\underline{t})\psi^a(\underline{r})) \\
&+ (\psi^a(\underline{r}), V^b(\underline{r}+\underline{t})\psi^a(\underline{r})) \\
&= \alpha^a + (\psi^a(\underline{r}), [V^b(\underline{r}+\underline{t}) - V^a(\underline{r}+\underline{t})]\psi^a(\underline{r})) \\
&= \alpha^a + \delta\alpha^a
\end{aligned} \tag{45}$$

For some applications we expect that $\delta\alpha^a$, the difference between $\tilde{\alpha}^a$ and α^a can be neglected. $\tilde{\alpha}^b$ is similarly defined.

All off-diagonal matrix elements involving only a-atoms are equal and written as t^a , those involving only b-atoms are written as t^b . The off-diagonal elements connecting a- and b-atoms are important interface characteristics and are written as

$$(00-1|H''|000) \equiv t \tag{46}$$

Interface energy:

The total energy of the system is

$$E'' = E''_s - (N^a \epsilon_{es}^a + N^b \epsilon_{es}^b) - \sum_{\ell_z=-2,-1} [(1+\delta n_{\ell})^2 - 1] \epsilon_{es}^a$$

$$\begin{aligned}
& - \sum_{\ell_z=0,1} [(1+\delta n_{\ell})^2 - 1] \epsilon_{es}^b \\
& + \frac{1}{2} \sum_{\ell_z=-2}^1 \sum_{\substack{\ell \neq \ell' \\ \ell_z' = -2}} \frac{1}{|R_{\ell} - R_{\ell'}|} (1 - (1+\delta n_{\ell})(1+\delta n_{\ell'})) \quad (47)
\end{aligned}$$

The last sum in Eq. (47) can be carried out in exactly the same manner as was done in the appendix.

Dipole barrier:

By Eq. (43), the difference in electrostatic potential energy between the bulk of b and the bulk of a is

$$\begin{aligned}
\Delta V_B &= \frac{2\pi}{d} (-2\delta n_{-1} - 4\delta n_0 - 6\delta n_1) \\
&= \frac{2\pi}{d} (3\delta n_{-2} + \delta n_{-1} - \delta n_0 - 3\delta n_1) \quad (48)
\end{aligned}$$

where the last step (taken to give a left-right symmetrical expression) has utilized the neutrality condition, Eq. (40).

Clearly this barrier potential energy, will in a self-consistent calculation, bring the two Fermi levels into coincidence.

Therefore, if we denote the bulk Fermi levels (relative to the bulk electrostatic potentials) by ϵ_F^a and ϵ_F^b , we must have

$$\Delta V_B = \epsilon_F^a - \epsilon_F^b \quad (49)$$

Metal-Metal Interface - Simple Application

The preceding discussion has attempted to treat electrostatic self-consistency with some care. The dominant effect, of course, is the creation of a dipole layer with a potential energy

difference exactly equal to and opposite in sign to the difference in the Fermi levels of the separated metals. This insures equality of ϵ_F on both sides of the junction after contact. The principal contributions to σ_{ab} arising from the requirement of a common Fermi level can be estimated as follows. For specificity let us assume $\epsilon_F^a > \epsilon_F^b$. Then the energy gain per atom-pair of interface when δn electrons per atom pair are transferred from a to b [to equalize ϵ_F when the metals are brought into (electrical) contact] is

$$\frac{1}{2} (\epsilon_F^a - \epsilon_F^b) \delta n \quad (50)$$

The electrostatic potential difference across the resulting dipole layer is

$$\epsilon_F^b - \epsilon_F^a = 4\pi \left(\frac{\delta n}{d^2} \right) x \quad (51)$$

when x is the dipole layer length. Substituting the value of n obtained from (2) in (1) we find

$$\Delta E = \frac{1}{2} \frac{(\epsilon_F^a - \epsilon_F^b)^2 d^2}{4\pi x} \quad (52)$$

For a numerical estimate of ΔE , let us assume $\epsilon_F^a - \epsilon_F^b = 2\text{eV}$, $d \sim 2\text{\AA}$, $x \approx d$. We find $\Delta E = .02\text{eV}$. If $\epsilon_F^a - \epsilon_F^b$ were as high as 5eV which seems quite unlikely, ΔE would only be $.13\text{eV}$ or $\sim 5\%$ of typical transition metal surface energies per atom pair. We are therefore justified, in first approximation, in neglecting energy contributions arising from the self consistency requirement except for the equality of Fermi levels.

We now estimate very crudely the contribution of the single particle energy E_s to the interface energy. As was just explained, the dipole barrier will line up the Fermi levels of metals a and b. For a cubic half-filled band the Fermi level is exactly at $\bar{\epsilon}$, the center of the band.

The single particle Hamiltonian matrix elements are then

$$(\ell|H|\ell) = \left. \begin{array}{ll} \bar{\epsilon} & \ell_z \leq -3, \ell_z \geq 2 \\ \bar{\epsilon} + \delta\alpha^a & \ell_z = 0 \\ \bar{\epsilon} + \delta\alpha^b & \ell_z = -1 \end{array} \right\} \quad (53)$$

where

$$\bar{\epsilon} = \frac{\epsilon^a + \epsilon^b}{2} \quad (54)$$

and $\delta\alpha^a$, $\delta\alpha^b$ have been defined in Eq. (45).

All nearest neighbor matrix elements connecting two a-sites and t^a , those connecting an a- and a b-site are t^b and, the matrix elements connecting an a site with a b-site are written as

$$(00-1|H|000) \equiv t \quad (55)$$

The total density of states, $n(\epsilon)$ can be written as

$$n(\epsilon) = \sum_{\ell} n_{\ell}(\epsilon) \quad (56)$$

where the $n_{\ell}(\epsilon)$ are normalized local densities of states:

$$n_{\ell}(\epsilon) = \frac{1}{\pi} \sin \left(\psi_{\ell}, \frac{1}{H - \epsilon - i\delta} \psi_{\ell} \right) \quad (57)$$

(see ref. 3). The total single particle energy is then

$$E''_S = \int_{-\infty}^{\bar{\epsilon}} n(\epsilon) \epsilon d\epsilon = \sum_{\ell} \int_{-\infty}^{\bar{\epsilon}} n_{\ell}(\epsilon) \epsilon d\epsilon \quad (58)$$

The integrals, occurring in Eq. (58) can be estimated from the moments

$$\mu_{\ell}^P \equiv \int_{-\infty}^{\infty} n_{\ell}(\epsilon) \epsilon^P d\epsilon \quad (59)$$

These moments are given by

$$\mu_{\ell}^P = \sum_{\ell_1, \ell_2, \dots} (\ell | H | \ell_1) (\ell_1 | H | \ell_2) \dots (\ell_{P-1} | H | \ell) \quad (60)$$

In the present case, where all states with $\epsilon < 0$ are filled, clearly

$$\int_{-\infty}^{\bar{\epsilon}} \epsilon n_{\ell}(\epsilon) d\epsilon = \mu_{\ell}^{(1)} - \gamma [\mu_{\ell}^{(2)}]^{\frac{1}{2}} \quad (61)$$

since $[\mu_{\ell}^{(2)}]^{\frac{1}{2}}$ is a measure of the width of $n_{\ell}(\epsilon)$. The constant γ will depend on the shape of $n_{\ell}(\epsilon)$. It has the following values for some simple shapes

| Form of $n_{\ell}(\epsilon)$ | γ |
|--|----------|
| $[n_{\ell}(\epsilon)]_{\text{simple cubic}}^{(3)}$ | 0.39 |
| Triangular | 0.41 |
| Parabolic | 0.42 |
| Gaussian | 0.56 |

We shall take $\gamma = 0.30$ even though, for $\ell_z = -1$ and 0 , the density of states is not quite simple cubic.

Using the matrix elements of the present Hamiltonian we find

$$\mu^{(1)} = \left\{ \begin{array}{l} \bar{\epsilon} \\ \bar{\epsilon} + \delta\alpha^a \\ \bar{\epsilon} + \delta\alpha^b \end{array} \quad \begin{array}{l} l_z \leq -2, \quad l_z \geq 1 \\ l_z = -1 \\ l_z = 0 \end{array} \right\} \quad (62)$$

$$\mu^{(2)} = \left\{ \begin{array}{l} 6(t^a)^2 \\ 6(t^a)^2 \\ 6(t^a)^2 + t^2 - (t^a)^2 \\ 6(t^b)^2 + t^2 - (t^b)^2 \end{array} \quad \begin{array}{l} l_z \leq -2 \\ l_z \geq 1 \\ l_z = -1 \\ l_z = 0 \end{array} \right\} \quad (63)$$

Therefore, using Eq. (58) and Eq. (61) we find for the total single particle energy

$$\begin{aligned} N'' &= (N^a + N^b) \bar{\epsilon} + N_s [(\delta\alpha^a + \delta\alpha^b)] \\ &\quad - \gamma \left\{ [6(t^a)^2 + t^2 - (t^a)^2]^{\frac{1}{2}} - [6(t^a)^2]^{\frac{1}{2}} \right. \\ &\quad \left. + [6(t^b)^2 + t^2 - (t^b)^2]^{\frac{1}{2}} - [6(t^b)^2]^{\frac{1}{2}} \right\} \end{aligned} \quad (64)$$

where N_s is the number of atoms on the a- or b-surface.

From their definitions, Eq. (56), we expect $\delta\alpha^a$ and $\delta\alpha^b$ to largely cancel and we shall therefore neglect the term involving them in Eq. (64). Also, treating $t^2 - (t^{a,b})^2$ much smaller than $6(t^a)^2$ or $6(t^b)^2$ we expand the square-roots and thus obtain for the interface energy relative to the bulk phases,

$$\Delta E'' = -N_s \gamma \frac{\sqrt{6}}{12} \left(\frac{t^2}{t^a} + \frac{t^2}{t^b} - t^a - t^b \right)$$

$$= -N_s 0.08 \left\{ t^a \left[\left(\frac{t}{t^a} \right)^2 - 1 \right] + t^b \left[\left(\frac{t}{t^b} \right)^2 - 1 \right] \right\} \quad (65)$$

A simple interpolative approximation for t is⁵

$$t = \frac{1}{2} \left[\frac{t^a}{(00-2|00-1)} + \frac{t^b}{(000|001)} \right] (00-1|000) . \quad (66)$$

t^a and t^b can be estimated from the widths of the bulk bands of a and b respectively since

$$\left. \begin{aligned} \mu^{a,(2)} &= \int n_{\ell}^a(\epsilon) \epsilon^2 d\epsilon = 6(t^a)^2 \\ \mu^{b,(2)} &= \int n_{\ell}^b(\epsilon) \epsilon^2 d\epsilon = 6(t^b)^2 \end{aligned} \right\} \quad (67)$$

An estimate of t then requires, in addition, only some knowledge of the relative values of the overlap integrals between a - a , b - b , and a - b atom pairs.⁵

CONCLUSION

In this note we have attempted to lay down the conceptual and mathematical framework for a treatment, in a tight-binding spirit, of the electronic structure of metallic interfaces. We hope to apply this approach to concrete interface systems in the future.

ACKNOWLEDGEMENT

This research was supported by the Advanced Research Projects Agency of the Department of Defense under Contract No. MDA903-76C-0250 with The University of Michigan.

APPENDIX

Evaluation of the Lattice Sum in Eq. (30)

We wish to evaluate approximately the lattice sum in Eq. (30) with

$$\left. \begin{array}{ll} n_{\ell} = 1 + \delta n & , \quad \ell_z = 0 \\ 1 - \delta n & , \quad \ell_z = 1 \\ 1 & , \quad \ell_z \geq 2 \end{array} \right\} \quad (\text{A.1})$$

We break the sum into two terms

$$S = S_1 + S_2 \quad (\text{A.2})$$

where

$$S_1 = + \frac{1}{2} \sum_{\substack{\ell_z, \ell'_z \leq 1 \\ \ell \neq \ell'}} \frac{1 - n_{\ell} n_{\ell'}}{|\tilde{R}_{\ell} - \tilde{R}_{\ell'}|} \quad (\text{A.3})$$

$$S_2 = + \sum_{\ell_z \leq 1, \ell'_z \geq 2} \frac{1 - n_{\ell}}{|\tilde{R}_{\ell} - \tilde{R}_{\ell'}|} \quad (\text{A.4})$$

The second sum is easy to evaluate, since, for fixed ℓ' , the sum over ℓ represents a dipole potential energy

$$\sum_{\ell_z \leq 1} \frac{1 - n_{\ell}}{|\tilde{R}_{\ell} - \tilde{R}_{\ell'}|} \approx + \frac{2\pi}{d} \delta n \quad \ell_z' \geq 2 \quad (\text{A.5})$$

so that

$$S_2 \approx \frac{2\pi}{d} (+N - 2N_s) \delta n \quad (\text{A.6})$$

Using the notation $\tilde{t}_1 = (0, 0, d)$, S_1 can be written as

$$\begin{aligned}
S_1 = & + \frac{1}{2} N_s \left\{ [(1-\delta n)^2 - 1] \sum_{\substack{\ell'_z=0 \\ \ell' \neq (0,0,0)}} \frac{1}{|R_{\ell'}|} \right. \\
& + [(1-\delta n)(1+\delta n) - 1] \sum_{\ell'_z=1} \frac{1}{|R_{\ell'}|} \\
& + [(1+\delta n)^2 - 1] \sum_{\substack{\ell'_z=1 \\ \ell' \neq (0,0,1)}} \frac{1}{|R_{\ell'} - t_1|} \\
& \left. + [(1+\delta n)(1-\delta n) - 1] \sum_{\ell'_z=0} \frac{1}{|R_{\ell'} - t_1|} \right\} \\
= & + N_s \delta n^2 \left\{ \sum_{\substack{\ell'_z=0 \\ \ell' \neq (0,0,0)}} \frac{1}{|R_{\ell'}|} - \sum_{\ell'_z=1} \frac{1}{|R_{\ell'}|} \right\} \quad (A.7)
\end{aligned}$$

We now replace the summations by appropriate integrations, omitting in the first sum a circular area of magnitude d^2 . This gives

$$\begin{aligned}
S_1 = & + N_s \delta n^2 \frac{1}{d^2} \lim_{R \rightarrow \infty} \left[\int_{d/\sqrt{\pi}}^R \frac{1}{\rho} 2\pi \rho d\rho - \int_0^R \frac{1}{(\rho^2 + d^2)^{\frac{1}{2}}} 2\pi \rho d\rho \right] \\
= & + N_s \delta n^2 \left(1 - \frac{1}{\sqrt{\pi}} \right) \frac{2\pi}{d} \\
= & + \frac{2\pi}{d} N_s \delta n^2 (0.44) \quad (A.8)
\end{aligned}$$

Combining (A.6) and (A.7) gives

$$S = [N\delta n - N_s(2\delta n - 0.44 \delta n^2)] \frac{2\pi}{d} \quad (A.9)$$

This has been used in going from Eq. (30) to Eq. (31).

REFERENCES

1. J. Ferrante and J. R. Smith, Surface Science 38, 77 (1973); Sol. St. Communications (in press).
2. F. Cyrst-Lockman, J. Phys. Chem. of Solids 29, 1235 (1968).
3. R. Haydock et.al., J. Phys. Chem. 5, 2845 (1972).
4. R. Haydock and M. J. Kelly, Surf. Sc. 38, 139 (1973).
5. See S. P. McAlyum et.al., Introduction to Applied Quantum Chemistry, Holt, Rinehart and Winston, Inc., New York (1972).

THE USE OF BUBBLE DOMAIN MATERIALS FOR
SUBMILLIMETER WAVE MAGNETIC DEVICES

P. L. Richards

INTRODUCTION

The submillimeter or far infrared wavelength region of the electromagnetic spectrum remains largely undeveloped. Measurements of a sort which would be easy in other wavelength ranges are often arduous, or impossible, in the submillimeter band. There is a wide variety of scientific problems which require measurements in this spectral range, which correspond roughly to the temperature range from 10-200°K. In solids the list includes superconducting energy gaps, phonons, magnons in ordered magnetic systems, crystal field splittings in paramagnets, plasma effects, cyclotron resonance, and many other phenomena.

The submillimeter wave spectrum of many molecules is very rich. A very important potential astrophysical application of submillimeter spectroscopy is the investigation of interstellar molecular clouds. Many of these radiate a large fraction of their energy in the submillimeter band. The primitive state of development of submillimeter narrow line receivers is a serious hinderance to this extremely promising field of spectroscopy.

In the microwave frequency range, ferromagnetic resonance in an insulating material such as YIG is used as the basis of a number of signal processing devices. These include circulators, isolators, filters, modulators, etc. In principle, most of these devices can be simply scaled to operate at submillimeter wavelengths. In practice, however, the magnetic fields required are higher than can be achieved conveniently, even with superconducting magnets. The dimensional tolerances and attenuation in enclosed structures favor the use of quasi-optical techniques. It appears, therefore that new materials and device designs are desirable for optimum performance in this wavelength range.

The material properties required are rather easily specified. A narrow magnetic resonance is needed which is intense enough to dominate the optical properties of the material, and which can be adjusted to the proper frequency relative to the operating frequency of the device. Room temperature operation is very desirable for the usual reactive devices. For cases in which a superconductive magnet is required to adjust the resonant frequency, low temperature operation and resistive devices can also be considered. The materials should be available with large enough dimensions to make the quasi-optical approach practical.

The requirements of frequency adjustability and narrow linewidths are difficult to meet simultaneously at submillimeter wavelengths. Large g -factors and large anisotropy fields are often correlated with wide resonance lines. Two classes of

magnetic materials which appear to provide specific exceptions to this general trend are the yttrium and rare earth orthoferrites, and garnets. Because of the wide range of magnetic properties of the chemically similar yttrium-rare earth series, these insulating ferromagnets have a wide range of detailed magnetic properties. Although the submillimeter resonance behavior of these materials has been studied in only a few simple cases, many of their other magnetic properties are well known. Potential applications of both classes of material to bubble-domain memory structures have made available large area single crystal plates of high quality in a variety of compositions. Techniques for epitaxial growth are highly developed in the case of the garnets.

In this paper I will describe several candidate materials for submillimeter device applications and describe some ways in which they can be used to solve pressing problems of submillimeter spectroscopy.

YFeO₃

Yttrium orthoferrite is essentially a two sublattice antiferromagnet, except for a small canting angle introduced by an antisymmetric exchange interaction. The zero-field resonance frequencies are $\omega_1 = 10 \text{ cm}^{-1}$ and $\omega_2 = 18.16 \text{ cm}^{-1}$ and the line widths are $\Delta\omega_1 < 0.02 \text{ cm}^{-1}$ and $\Delta\omega_2 \approx 0.02 \text{ cm}^{-1}$ at 300°K .¹ The field dependence of these resonances² is shown in Fig. 1 for an applied field parallel to the ferromagnetic moment $\vec{M}_1 + \vec{M}_2$ and parallel to the antiferromagnetic axis, $\vec{M}_1 - \vec{M}_2$. If a NbTi

super-conductive magnet is used for field tuning, it should be possible to reach any frequency up to $\sim 22 \text{ cm}^{-1}$. Essentially nothing is known about the linewidth at low temperature and finite field, but the available numbers appear promising.

Rare earth orthoferrites such as SmFeO_3 as well as rare earth substituted YFeO_3 have been grown for use in bubble domain studies. Nothing is known about the submillimeter resonance properties of these materials. Since some susceptibility measurements are available, it should be relatively straightforward to interpret any resonance measurements that are made. It is probably safe to guess that the addition of rare earths to YFeO_3 will shift the zero field resonance frequencies, strengthen the field dependence, and (unfortunately) broaden the resonances. It will also introduce single ion resonances of the rare earth ions. It may thus be possible to obtain a desired resonant frequency with a lower bias field than is needed for YFeO_3 . Since the physical processes involved are simple, this possibility can clearly be explored most efficiently by an experimental investigation of existing materials.

Ga Substituted EuIG

For the present discussion, a rare earth iron garnet, $\text{R}_3\text{Fe}_5\text{O}_{12}$ can be thought of in terms of three co-linear sublattices: The octahedral and tetrahedral Fe sublattices are coupled by a strong antiferromagnetic exchange interaction. The rare earth sublattice, which orders at low temperatures, is more weakly coupled to the net iron moment. Consequently, both

a high frequency iron-iron exchange resonance and a lower frequency iron-rare earth exchange resonance³ are to be expected in addition to the ferromagnetic (FMR) mode of the net moment and any single ion resonances. In EuIG, the Eu^{+3} ion is in a $J=0$ state, so the rare earth sublattice has no angular momentum. The moment induced by exchange coupling to the tetrahedral iron sites can thus be lumped together with the tetrahedral iron moment into a two sublattice model, with a single exchange resonance mode and the usual FMR. In $\text{Eu}_3\text{Ga}_x\text{Fe}_{5-x}\text{O}_{12}$, the Ga is known to enter the tetrahedral iron sites for $x \leq 1.5$. This reduces the moment on the larger sublattice leading to a magnetic moment compensation point ($M=0$) at $x = 0.75$ and an angular momentum compensation point ($S=0$) at $x = 1.2$.

The magnetic resonance behavior of this system has been explored.^{4,5} The exchange resonance can be compositionally tuned from 200 cm^{-1} to $<10 \text{ cm}^{-1}$ as x increases from 0 to 1.2. The measured line widths at 4.2K were unfortunately very broad ($Q \approx 4$). The ferromagnetic resonance linewidths at 20 GHz, on the other hand, were quite narrow, except near the magnetic moment compensation point. For $x = 1.6$, $\Delta H \leq 10 \text{ Oe}$ for $T < 50\text{K}$ and $\sim 350 \text{ Oe}$ at 200K. This resonance is of considerable interest since there is a singularity in g_{eff} at the angular momentum compensation point. It has the value $g_{\text{eff}} = 5$ at $x = 1.6$ where the narrow low temperature lines were observed. This FMR would be an ideal candidate for submillimeter wave devices, except that the large g_{eff} and narrow line do not persist for frequencies beyond $\sim 10 \text{ cm}^{-1}$.

For small x , the line is broad. For large x , the FMR mixes with the nearby exchange resonance.

Although this system does not appear to produce resonance lines with the required behavior, it has sufficiently interesting properties that it seems worthwhile to explore the related substituted garnets produced for bubble domains.⁵ Epitaxial layers of high quality have been grown of rare earth substituted YIG in which the magnetic moment has been partially compensated by replacing part of the Fe with Ga^{3+} or with Ge^{4+} and Ca^{2+} . No submillimeter measurements have been made on any of these materials. There will be compositionally tuned submillimeter resonance lines in many of these systems, but the possibility of very narrow line widths seems problematical.

MnF₂

Although not a bubble domain material, mention should be made of the properties of the classic antiferromagnetic material manganese fluoride. The well known splitting of the degenerate uniaxial AFMR mode in a field parallel to the moments is shown in Fig. 1. The linewidth at low frequencies⁷ is known to be narrow (≤ 1 Oe), presumably because the Mn^{2+} ion is in an S-state. There is some evidence, however, that the linewidth increases rapidly with frequency.⁸

Reactive Devices

The usual practice in microwave signal processing is to use magnetic devices in a reactive mode. If a plane polarized electromagnetic wave at a frequency close to resonance propagates

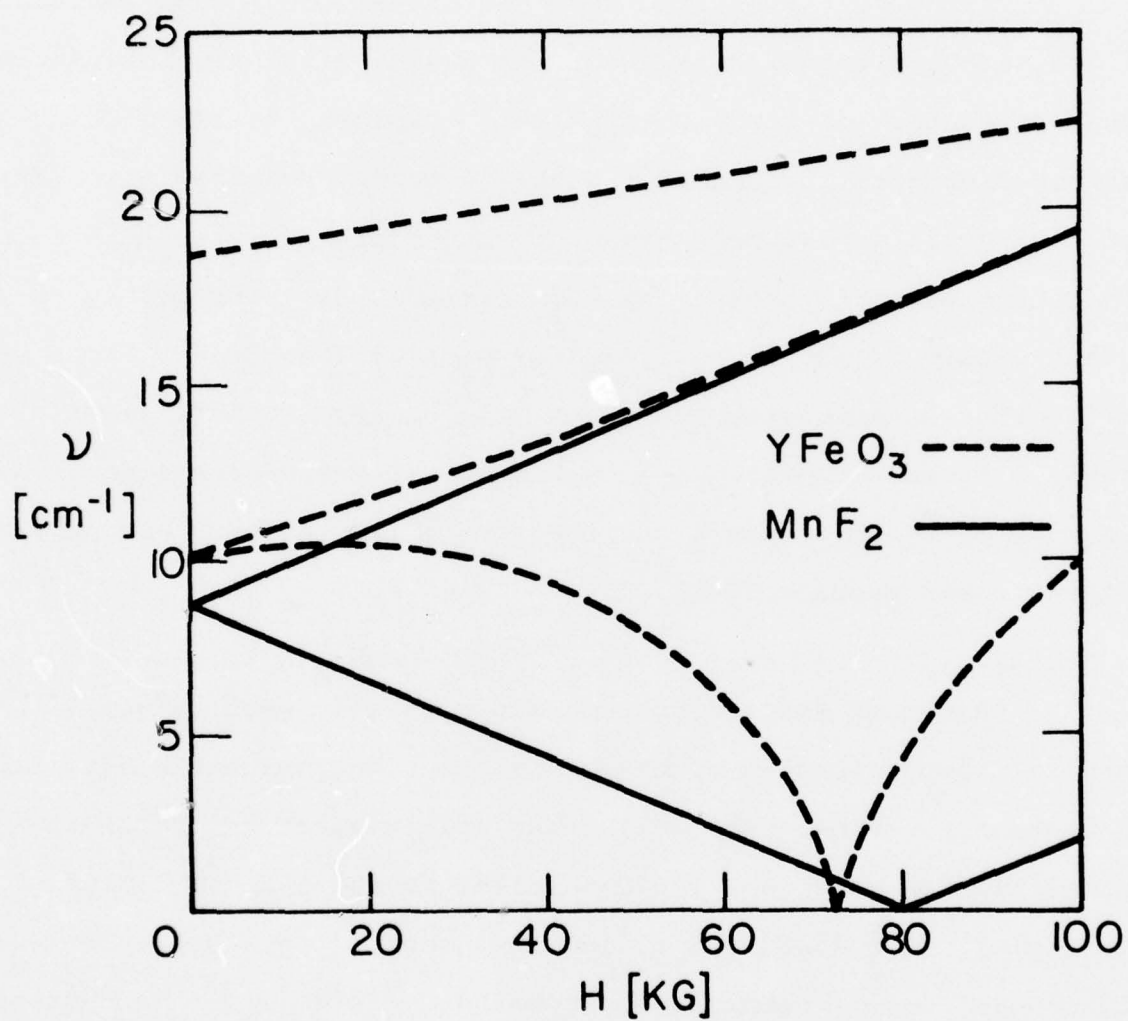


Figure 1. Magnetic resonance frequency as a function of magnetic field for YFeO_3 and MnF_2 .

along the field in a material with a circularly polarized FMR mode, the plane of polarization is rotated because of the dispersion is different for the two circularly polarized components of the wave. When coupled with input and output polarizers, such an active medium can be made to serve as a filter, an isolator or a circulator, whether in a waveguide or in a quasi optical geometry.⁹ If the line is narrow enough that it can be field modulated by a significant fraction of its width, then such a structure can also serve as a modulator. Losses in the device arise from the wings of the resonance line, so narrow line widths are important for high efficiency.

All of the resonance modes described above are circularly polarized, except for those in YFeO_3 which are elliptically polarized. Such modes will retain some residual rotary power.

The angle of rotation of the plane of polarization $\theta(\omega)$ at the frequency ω can be obtained for an absorption line of arbitrary shape and strength from the dispersion relation¹⁰

$$\theta(\omega) = \frac{\omega^2}{2\pi} P \int_0^{\infty} \frac{\Delta\alpha(\omega') d\omega'}{\omega'(\omega^2 - \omega'^2)}$$

where $\Delta\alpha(\omega')$ is the difference in absorption coefficient for right and left circularly polarized waves at frequency ω' .

Resistive Devices

Because the tools available to the submillimeter wave spectroscopist are so primitive, types of devices may be useful which would not be competitive in the microwave frequency range.

One promising example is to use a resonant absorption which is field swept over more than its line width to amplitude modulate the spectral range over which the resonance is swept. For example, a slice of YFeO_3 or MnF_2 which is several extinction lengths thick on resonance could be used with a broad band detector to measure a simple line spectrum such as that of a submillimeter laser. The resolution of such a spectrometer could be considerably narrower, and the optical efficiency higher, than the conventional Fourier spectrometers in use today.

The most sensitive broad band submillimeter wave detectors available are composite He temperature bolometers with metal-film absorbing elements. If the absorbing surface were replaced by a magnetic insulator which was transparent, except on resonance, the resulting bolometer could serve as spectrometer and detector combined. A small heat capacity is required for good bolometric sensitivity. This can be achieved by using a magnetic material with high Debye and magnetic ordering temperatures, and by operating at pumped ^4He or ^3He temperatures. A superconductive magnet would be used to tune the spectrometer. An arc lamp could be used as a source for measuring transmittance spectra.

The best bolometer technology available today¹¹ should be able to provide an optical noise equivalent power (NEP) of $\sim 10^{-15} \text{ W}/\sqrt{\text{Hz}}$ at ^4He temperatures and $\sim 10^{-16} \text{ W}/\sqrt{\text{Hz}}$ at ^3He temperatures. Since the power per mode from an unpolarized $T = 10^3 \text{ K}$ source is $2kT \approx 3 \times 10^{-20} \text{ W/Hz}$, a single mode receiver could have a bandwidth as small as 10^4 - 10^5 Hz . In some experiments it should

be possible to use as many as 10-100 modes, thus further decreasing the noise limit to the spectrometer bandwidth.

Such a spectrometer could have higher throughput, higher optical efficiency (transmittance) and higher resolution than the Fourier spectrometer-He temperature bolometer combination in use today. It would also be simpler and less expensive. It would be most useful for measuring spectral lines whose width is comparable to the resonance width. This width can be adjusted somewhat by the use of inhomogeneous fields or magnetostatic effects. There is a limit to the improvement that can be obtained in the sensitivity with which broad spectral features are observed, since broadening the line will increase the extinction length and so require a thicker slice of magnetic material with higher heat capacity.

The best available materials for this purpose appear to be YFeO_3 and MnF_2 . The available information on line widths and strengths appears promising, but further measurements and detailed calculations will be necessary to design a device.

If the line width of the magnetic resonance is not sufficiently narrow, either the modulator or the selective absorbing bolometer described above can be used as the order sorter of a confocal Fabry Perot interferometer. Because the magnetic device can provide efficient order sorting it is possible to operate the interferometer in high order and thus obtain very high resolution. Such an interferometer could also be used to provide frequency markers for the tuned magnetic spectrometer.

The most immediate scientific applications of the tune-able narrow band submillimeter spectrometer described here are to the measurement of narrow magnetic resonances in solids, and the measurement of gaseous molecular spectra. The latter can be either in the laboratory, or in the form of interstellar molecular clouds. In this latter application, the multimode nature of the receiver makes it useful with large incoherent "light bucket" telescopes.¹²

ACKNOWLEDGEMENT

This research was supported by the Advanced Research Projects Agency of the Department of Defense under Contract No. MDA903-76C-0250 with The University of Michigan.

References

1. P. L. Richards, unpublished.
2. Deduced from an analysis given in V. I. Ozhogin et al., Soviet Physics JETP 35, 1162 (1972).
3. J. Kaplan and C. Kittle, J. Chem. Phys. 21, 760 (1953).
4. L. C. LeCraw et al., J. Appl. Phys. 36, 901 (1965).
5. P. L. Richards and J. P. Remeika, J. Appl. Phys. 37, 1310 (1966).
6. R. Burmeister, Talk at 1976 Materials Research Council Meeting.
7. J. P. Kotthaus and V. Jaccarino, Phys. Rev. Letters 28, 1649 (1972).
8. F. M. Johnson and A. H. Nethercot, Jr., Phys. Rev. 114, 705 (1959).
9. See for example, P. L. Richards and G. E. Smith, Rev. Sci. Inst. 35, 1535 (1964).
10. W. P. Healy and E. A. Power, Am. J. Phys. 42, 1070 (1974).
11. J. Clarke, G. I. Hoffer, P. L. Richards and N-H. Yeh, Low Temperature Physics - LT14, M. Krusius and M. Vuorio eds. (North Holland, Amsterdam/American Elsevier, New York (1975) pp. 226-229.
12. Telescope and Detector Systems for Submillimeter Line Spectroscopy, P. L. Richards, Lawrence Berkeley Laboratory Report LBL-3983, 1976, Infrared Physics (to be published).

MECHANISTIC LIMITATIONS ON THE SPEED
OF RESPONSE OF ELECTROCHROMIC OPTICAL DEVICES

R. A. Huggins

INTRODUCTION

Development efforts are currently underway in several laboratories on the production of so-called "electrochromic" devices for information display and related applications. Most of the present work is aimed at systems for visual presentation of alphanumeric symbols by electrically-controlled changes in optical reflectance or absorption. Thus they compete with light emitting diodes (LED's) and liquid crystal displays (LCD's) for certain types of applications.

Light emitting diodes and liquid crystal systems both have important practical limitations. LED's require appreciable power for operation, while LCD's have only moderate optical contrast, and a limited viewing angle. Both are volatile.

On the other hand, the amount of contrast is controllable and can be quite high in electrochromic systems. Various colors are possible. They can be observed over a large viewing angle, can probably be utilized in transmission, as well as reflection modes, and are not volatile. Present electrochromic systems involve the use of a liquid (acid) electrolyte. In principle, this type could be replaced by all-solid systems.

While light emitting diodes act very rapidly, one of the features that may limit the application of liquid crystal devices is the speed of response ($\sim 10^{-2} + 10^{-1}$ sec), which is determined by the time necessary for the rotational reorientation of the optically-active polymeric species. Current electrochromic systems are also relatively slow. It is the purpose of this paper to discuss the physical mechanisms involved in their operation and to examine the factors which control the speed of response of an electrochromic device and their fundamental limitations.

GENERAL DESCRIPTION OF ELECTROCHROMIC SYSTEMS

While there is some confusion in the literature about terminology and labels, as well as the mechanism of operation, for present purposes an electrochromic system is one in which the application of electric potential difference causes changes in optical reflectance or absorption of a bulk solid. Such a system is illustrated schematically in Fig. 1.

The active electrochromic material changes its optical reflectance, or color, when the value of the applied voltage V across the three-phase system is changed. Such materials are typically transition metal compounds, e.g., oxides, and always have a range of solubility for some species M , typically hydrogen or an alkali metal. The oxidation state of the transition-metal N and the optical properties of the compound, nominally M_xNO_y , vary with the M concentration. Typical examples are the

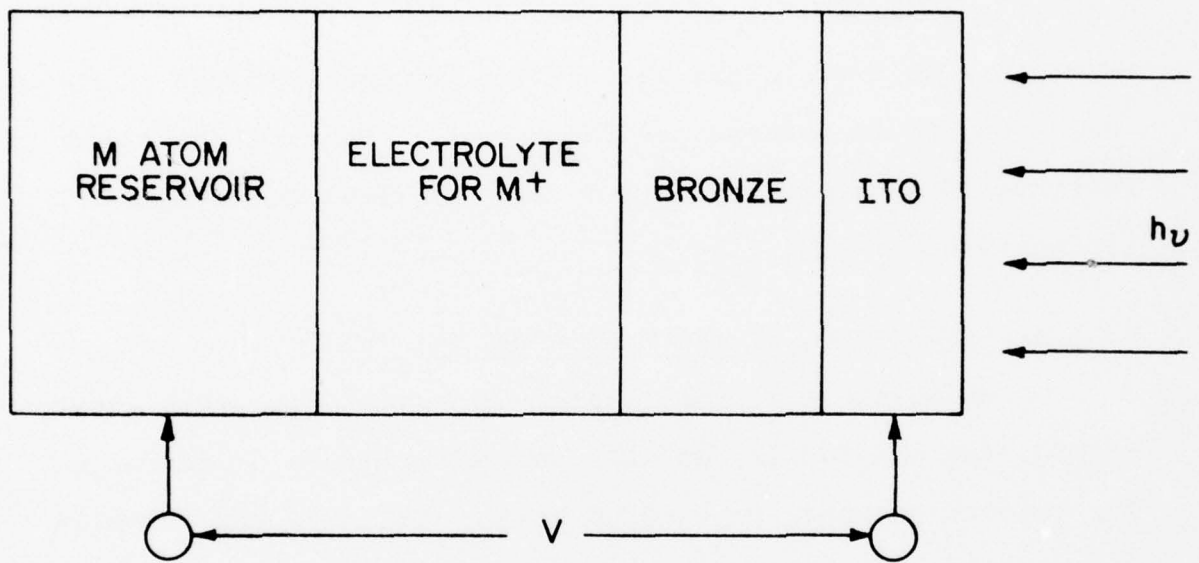


Figure 1. Schematic Illustration of Electrochromic System.

tungsten bronze family, which can be represented as M_xWO_3 , with x denoting the mole fraction of M present. While such materials are often oxides, their metallic appearance in certain ranges of x caused them to be called "bronzes" more than a century ago. Some of them exhibit a wide range of intense colors. In the case of sodium tungsten bronzes, Na_xWO_3 , the range of colors runs from pale green for WO_3 , through dark grey, royal blue, purple, brick red, orange, to golden yellow as the value of x increased.

This is an electrochemical system, so that the applied voltage tends to cause a difference in the activity of the species M across the electrolyte according to the Nernst equation

$$V = \left(\frac{RT}{nF} \right) \ln \left(\frac{a_M^I}{a_M^{II}} \right)$$

where I and II represent the phases on the two sides of the electrolyte. If the M activity is maintained at a fixed value on the left hand side of the cell, a change in V causes a change in the M activity - and therefore the M concentration - at the interface between the electrolyte and the bronze electrochromic material on the right hand side. The species M diffuses into the M_xWO_3 in the form of M^+ ions and electrons. Every M atom that is incorporated donates an electron to the band structure of the bronze. Changes in V across the cell thus cause M species (ions and electrons) to be transported across the electrolyte and move into and out of the bronze, M_xWO_3 , thereby changing its optical properties.

While the tungsten oxides were the first bronzes known, having been discovered in 1824 by Wöhler¹, analogous compounds of titanium^{2,3}, niobium⁴, vanadium⁵ and molybdenum⁶ have become recognized in recent years. Reviews of these materials and their properties can be found in several places⁷⁻¹³.

Although amorphous H_xWO_3 films are used in present devices, they are related to the crystalline hydrogen tungsten bronzes, which were first prepared by Glemser and Naumann¹⁴, and whose electronic properties were investigated by Dickens and Hurditch¹⁵. In parallel with the sodium tungsten bronzes, three distinct phases are found:

| | |
|--------------|-----------------------------|
| Tetragonal B | $x = 0.15 \rightarrow 0.23$ |
| Tetragonal A | $x = 0.33 \rightarrow 0.5$ |
| Cubic | $x = 0.5 \rightarrow 0.6$ |

These phases are stable in vacuum to 400°K, but are unstable in air with respect to oxidation.

Thermochemical measurements¹⁶ have shown that the binding energy of hydrogen is not significantly different in the two tetragonal phases. Available data are shown in Table I.

TABLE I. THERMOCHEMICAL DATA FOR CRYSTALLINE HYDROGEN TUNGSTEN BRONZES

| Value of x | Structure | ΔH (formation) | ΔH_f per mole H_2 |
|--------------|--------------|------------------------|-----------------------------|
| 0.18 | Tetragonal B | -4.8 ± 0.6 kJ | -26.7 ± 3.3 kJ |
| 0.35 | Tetragonal A | -9.6 ± 0.8 kJ | -27.4 ± 2.3 kJ |

OPERATING CHARACTERISTICS OF PRESENT ELECTROCHROMIC SYSTEMS

Electrochromic systems are being developed in several laboratories. Present efforts center around the use of thin ($\sim 1 \mu\text{m}$) layers of amorphous WO_3 as the electrochromic material, with hydrogen as the solute. An acid liquid electrolyte is used to introduce protons into the WO_3 , forming colored H_xWO_3 .

Voltages of about 1 volt are applied across these cells, and protons pass through the electrolyte and enter the bronze, causing the formation of an optical absorption band centered in the infrared. A typical absorption spectrum is shown in Fig. 2. As the value of x changes, the spectral distribution of the absorption changes in a relatively minor way, the major influence being in the magnitude of the absorption. Absorption data, expressed in terms of the resultant optical density (OD), where

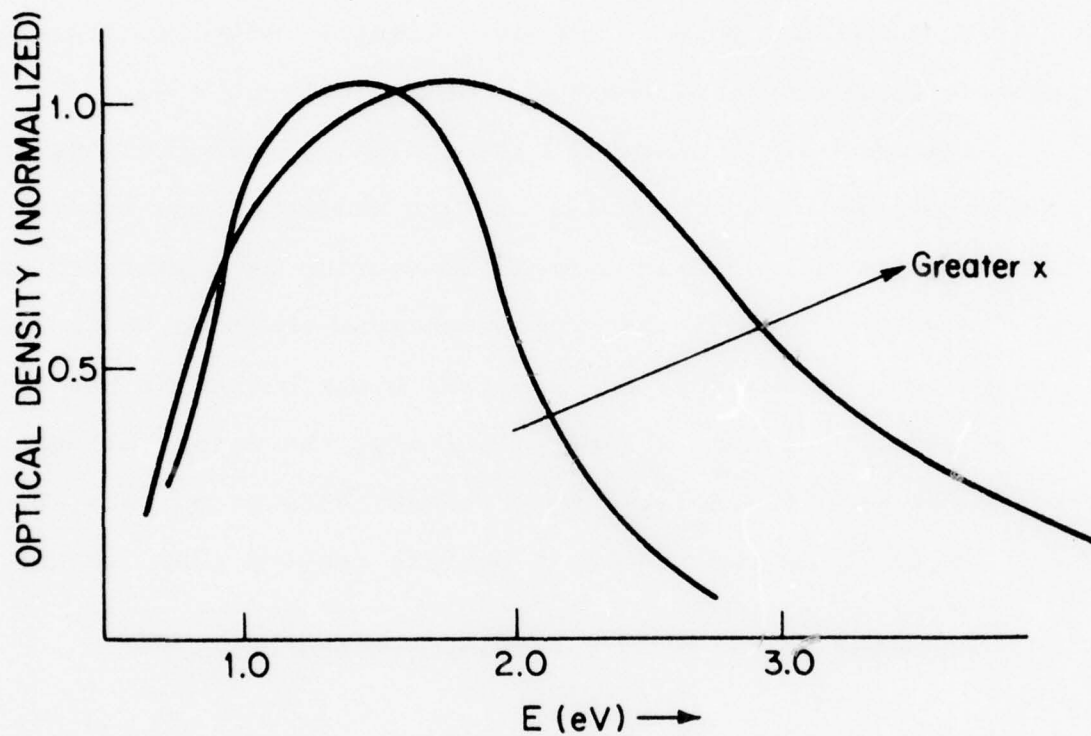
$$\text{OD} = \log t^{-1} \quad (t = \text{transmittance} = I/I_0)$$

versus the value of x are shown in Fig. 3.

For alphanumeric display systems, optical density changes of about 0.5 are typically required. This means that a total of about 6 millicoulombs/cm² charge is transferred across the cell. Thus, if a cell operates at 1 volt, the energy consumed per color-bleach cycle is 12 millijoules/cm². Response times of a fraction of a second have been reported. Such displays are non-volatile under open circuit conditions.

Comparison with Field Effect Liquid Crystal Displays

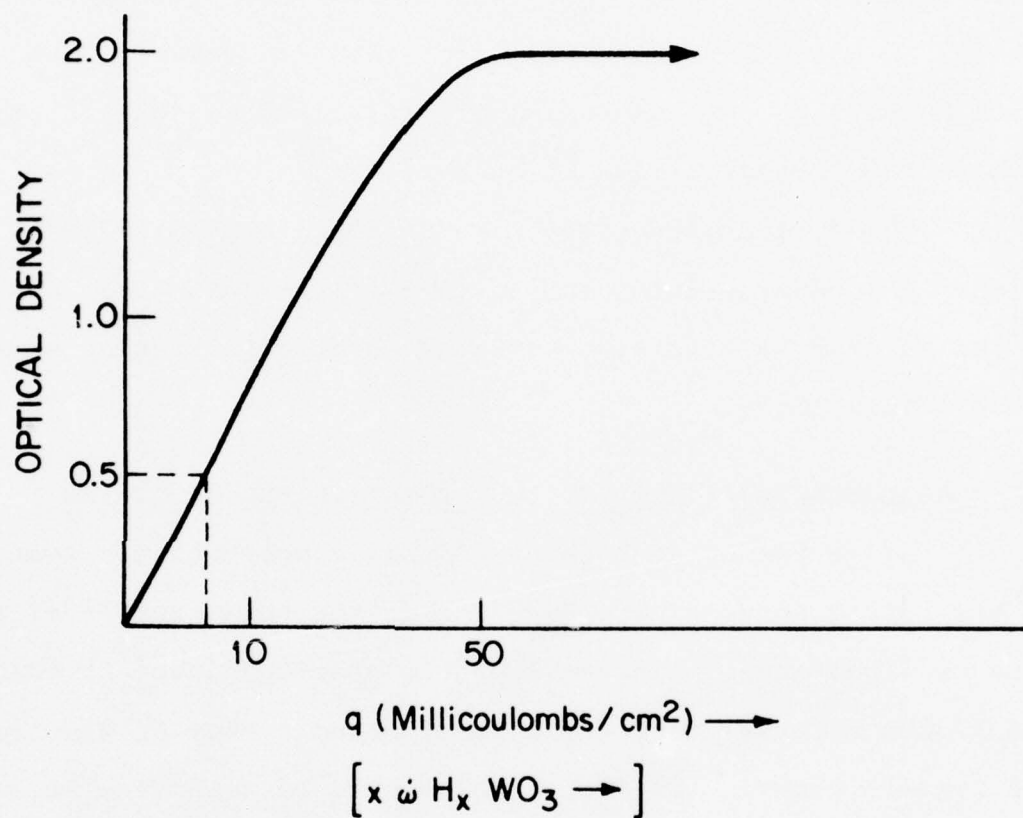
One of the alternative methods that can be used to dis-



Typical Values

| <u>Bronze</u> | <u>Abs. Peak (eV)</u> | <u>$\frac{1}{2}$ Height Width (eV)</u> |
|---------------|-----------------------|---|
| H_xWO_3 | 1.4 | 1.28 |
| H_xMoO_3 | 1.53 | 0.86 |
| 12% MoO_3 | 2.0 | 1.58 |

Figure 2. Typical absorption spectrum for electrochromic bronzes.



Typical Values (O.D. \approx 0.5)

$$q = 6 \text{ millicoulombs/cm}^2$$

$$n = 3.7 \times 10^{16} \text{ ions/cm}^2$$

Figure 3. Variation of optical density with composition in H_xWO_3 .

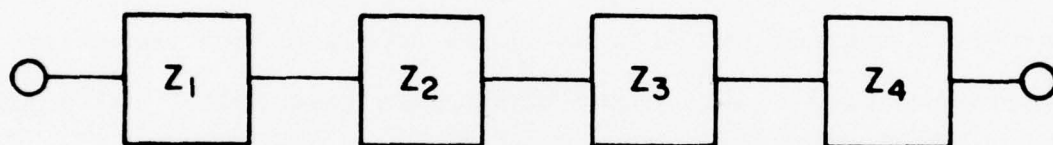
play digital information optically is by the use of Field Effect Liquid Crystal Displays (FELCD's). In this approach, polymeric species adopt a preferred orientation under the application of an internal field. When the field is removed, thermal energy causes the molecular orientation to again randomize. Thus devices based upon this mechanism are volatile, in contrast to the electrochromic systems described here.

The active materials in FELCD's are typically 10-15 μm thick. A potential difference of 3-5 volts is applied, and 90% of the maximum polarization is attained after a time of some 20-50 milliseconds.

PHYSICAL MECHANISMS INVOLVED IN COLORATION AND BLEACHING

Since the optical properties of electrochromic systems of the type discussed here depend upon the total number of protons or alkali metal ions that become absorbed into the bulk of the bronze material (and the corresponding number of electrons), the dynamic behavior of such systems will be dependent upon the rate at which one can deliver the required number of M^+ ions and electrons to the bronze and disperse them sufficiently throughout that phase.

This process involves the transport of charge through the system under the influence of the applied potential difference V . One can model this process in terms of the simple equivalent circuit model shown in Fig. 4. Since they are the important species controlling the process, the various im-



Z_1 = Impedance at reservoir/electrolyte interface

Z_2 = Electrolyte impedance

Z_3 = Impedance at electrolyte/bronze interface

Z_4 = Diffusion impedance within bronze

Figure 4. Simple equivalent circuit model for electrochromic system.

pedances involved are those relating to the transport of the M^+ species.

There is no evidence that the process of transferring atoms from the M reservoir as M^+ ions to the electrolyte, represented by Z_1 , is ever rate-limiting in processes of this type.

Experiments on the H_xWO_3 system involving the use of dilute acid electrolytes have been interpreted¹⁷ as indicating that the rate-limiting step is proton transfer across the aqueous electrolyte-bronze interface, Z_3 . While this may be characteristic of aqueous electrolyte systems, experience in solid electrolyte systems, as well as those involving the insertion of cationic species into mixed conductors from molten salts at elevated temperatures or non-aqueous electrolytes at room temperature lead to the conclusion that this may not generally be the case.

Therefore, for present purposes we shall neglect Z_1 and Z_3 , and consider only cases involving Z_2 and Z_4 .

The impedance within the electrolyte, Z_2 , is due to the resistance of the electrolyte to the transport of the M^+ species. Under the application of a stepped dc voltage across the whole system, this part of the device will act as a simple resistor if the M^+ species dominates the ionic conductivity. If it has a transference number t_M^+ appreciably less than unity, the electrolyte will act as a "supported electrolyte", and there will be an additional initial transient current due to the establishment of new equilibria for the species which have

the largest t 's. For practical purposes one can neglect this initial transient, and treat the electrolyte as a pure resistor.

In the next two sections, the time necessary to achieve an optical density of 0.5 by introducing an ionic charge of 6 millicoulombs/cm² will be calculated for two limiting cases, when ionic transport through the electrolyte to the electrolyte-bronze interface is rate-controlling, and when concentration-driven diffusion of the M^+ ions into the bronze is rate-controlling.

Following these, the case in which both electrolyte resistance and diffusion in the bronze are involved in the total process kinetics will be discussed.

Case I: Kinetics Limited by Ionic Transport in the Electrolyte,
 Z_2

If transport of M^+ ions through the electrolyte is appreciably slower than ionic diffusion into the bronze, we can assume that the speed of response of the system is controlled by Z_2 . In this case, we can simply calculate the time necessary to transport the required charge q across the electrolyte. Since

$$q = i t = \frac{V}{R} t$$

for an area of 1 cm²,

$$t = \frac{Rq}{V} = \frac{\rho \ell q}{V}$$

where ℓ is the electrolyte thickness.

If we assume that

$$q = 6 \text{ millicoulombs/cm}^2$$

$$V = 1.0 \text{ volt}$$

$$l = 0.1 \mu\text{m} = 10^{-5} \text{ cm}$$

then

$$t = (6 \times 10^{-8}) (\rho) \text{ seconds}$$

and, for example, if

$$\rho < 10^6 \text{ ohm cm}$$

$$t < 6 \times 10^{-2} \text{ seconds} = 60 \text{ milliseconds}$$

Case II: Kinetics Limited by Ionic Diffusion in the Bronze

On the other hand, if transport of the ionic species through the electrolyte is fast, we can consider another limiting case in which Z_4 , the diffusion of the M^+ ions into the bronze controls the overall speed of response.

Since the electrical conductivity of the bronze is much greater than the ionic conductivity, and they typically exhibit metallic properties, we can assume that the imposition of a step voltage across the total system is equivalent to suddenly stepping the potential at the electrolyte-bronze interface. If the electrolyte serves as a ready source of M^+ ions, this means that there will be a sudden jump in the concentration of M^+ ions just inside the surface of the bronze to a new value C_s , from an initially uniform concentration throughout, C_i . This step in the surface concentration causes diffusion of M^+ into the interior in response to the concentration gradient.

This is a standard one-dimensional diffusion problem if the bronze is thick relative to the diffusion distance, with initial conditions at $t = 0$;

$$C = C_s \quad \text{for } x = 0$$

$$C = C_i \quad \text{for } x \geq 0$$

and when $t > 0$;

$$C = C_s \quad \text{for } x = 0$$

$$C_s > C > C_i \quad \text{for } x \geq 0$$

If we assume that the diffusion coefficient D is independent of concentration, that there is no volume change, and that the interface ($x = 0$) is stationary, Fick's second law

$$\frac{\partial C}{\partial t} = D \frac{\partial^2 C}{\partial x^2}$$

can be solved to give the time dependence of the M^+ concentration profile in the bronze as

$$\frac{C - C_i}{C_s - C_i} = 1 - \operatorname{erf}\left(\frac{x}{2\sqrt{Dt}}\right) = \operatorname{erfc}\left(\frac{x}{2\sqrt{Dt}}\right)$$

where $\operatorname{erf}(P)$ is the error function of the argument P . Concentration profiles for several values of time are shown schematically in Fig. 5.

Since the optical properties depend upon the total number of M^+ ions (and corresponding electrons) that have entered the bronze, n , where

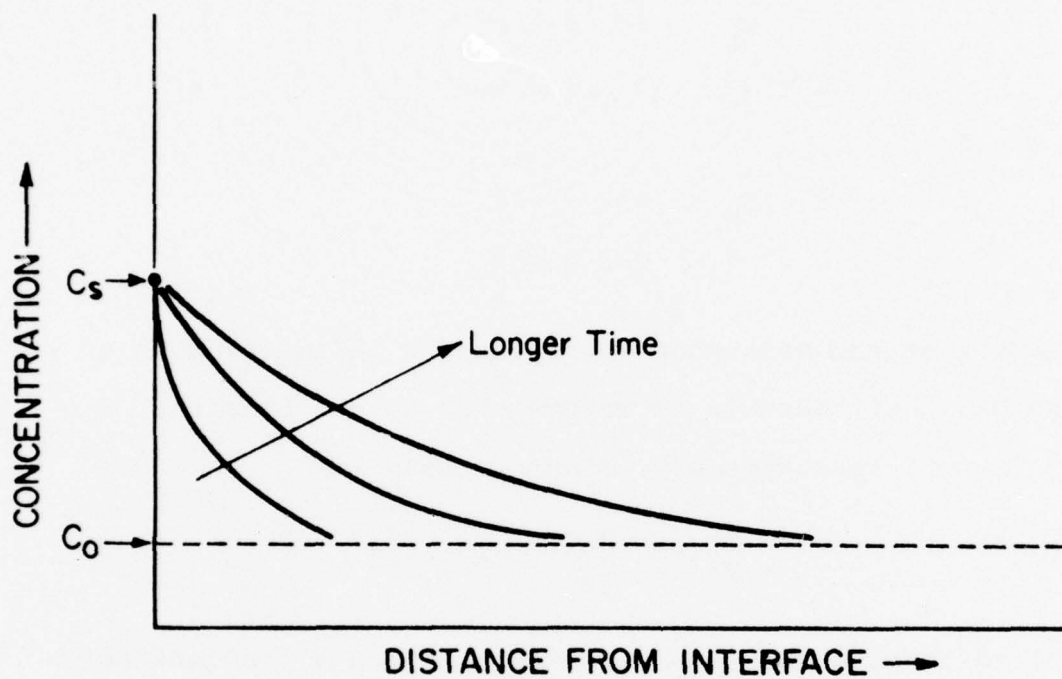


Figure 5. Schematic concentration profiles as a function of time.

$$n = \int_0^{\infty} (C - C_i) dx$$

Integration yields the result that

$$n = \left(\frac{2}{\sqrt{\pi}} \right) (C_s - C_i) (Dt)^{\frac{1}{2}} \quad \text{ions/cm}^2$$

and since

$$q = n \left(\frac{F}{N} \right)$$

where F is the Faraday constant and N Avogadro's number, we have

$$q = \left(\frac{2F}{\sqrt{\pi} N} \right) (C_s - C_i) (Dt)^{\frac{1}{2}}$$

This can be rearranged to give

$$t = \left[\left(\frac{\sqrt{\pi} N}{2 F} \right) \frac{q}{(C_s - C_i) (D^{\frac{1}{2}})} \right]^2$$

$$t = \frac{(3.07 \times 10^{37}) q^2}{(C_s - C_i)^2 D}$$

If we assume that

$$q = 6 \times 10^{-3} \text{ Coulombs/cm}^2$$

$$C_i = 0$$

$$C_s = 10^{22} \text{ ions/cm}^3 \quad (x \approx 0.5)$$

then

$$t = 1.1 \times 10^{-11} (D)^{-1} \text{ sec.}$$

and if, for example,

$$D > 10^{-9} \text{ cm}^2/\text{sec}$$

$$t < 10^{-2} \text{ sec}$$

It can readily be shown that under these conditions the concentration profiles remain quite steep and penetrate only a short distance into the bronze. Even a layer as thin as 0.1 μm can be treated as a semi-infinite solid.

Case III. Kinetics Limited by Both Ionic Transport Through Electrolyte and Diffusion Into Bronze

We can also have the case in which the ionic transport through the electrolyte is sufficiently slow that it cannot provide and maintain ionic species at the electrolyte-bronze interface to meet the initial and boundary conditions for the purely diffusion-controlled case. Then Z_2 and Z_4 act in series. This can be represented as an equivalent circuit of the type shown in Fig. 6, where the symbol -W- represents a so-called Warburg impedance, which has the electrical characteristics of an infinite transmission line and is kinetically analogous to one-dimensional concentration-driven diffusion into a solid, with D independent of concentration. The impedance of the Warburg (diffusional) component can be written as

$$Z_W = \frac{A}{\sqrt{S}}$$

Its current response to a step voltage is

$$i_W = \left(\frac{V_W}{A} \right) \frac{t^{-1/2}}{\sqrt{\pi}}$$

We saw earlier that the number of ions entering the bronze per cm^2 of the interface can be written as

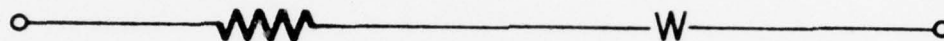


Figure 6. Simple equivalent circuit for case in which kinetics are limited by both electrolyte conductivity and diffusion in the bronze.

$$n = \left(\frac{2}{\sqrt{\pi}} \right) (C_s - C_i) (Dt)^{\frac{1}{2}}$$

This can be differentiated with respect to time to give the instantaneous ionic flux density m :

$$m = \frac{dn}{dt} = \left(\frac{C_s - C_i}{\sqrt{\pi}} \right) \left(\frac{D}{t} \right)^{\frac{1}{2}}$$

and since

$$i = z \left(\frac{F}{N} \right) m$$

where z is the charge number of the ions, we see that

$$\left(\frac{V_W}{A} \right) = z \left(\frac{F}{N} \right) (C_s - C_i) D^{\frac{1}{2}}$$

Because Z_2 and Z_4 act in series, the applied voltage V is distributed over both of them, being primarily across Z_2 at small times, and Z_4 at longer times.

The current response to a step voltage applied across the circuit in Fig. 6 is given by

$$i = \left(\frac{V}{R} \right) \exp(P^2) \operatorname{erfc}(P)$$

where

$$P = \left(\frac{At}{R} \right)^{\frac{1}{2}} = \frac{V_W N t^{\frac{1}{2}}}{R z F (C_s - C_i) D^{\frac{1}{2}}}$$

and R is the ionic resistance of the electrolyte (Z_2).

This can be simplified when the parameter p has extreme values. When p is very small,

$$\exp(p) \rightarrow 1$$

$$\operatorname{erfc}(p) \rightarrow 1 - \left(\frac{2}{\sqrt{\pi}} \right) p \rightarrow 1$$

and thus

$$i \approx \left(\frac{V}{R} \right)$$

and the ionic resistance dominates.

On the other hand, when p is very large,

$$\operatorname{erfc}(P) \rightarrow \left(\frac{\exp(-P^2)}{\sqrt{\pi} P} \right)$$

and thus

$$i \approx \frac{\left(\frac{V}{R} \right) \exp(P^2) \exp(-P^2)}{\sqrt{\pi} P} \approx \frac{Vt^{-1/2}}{A\sqrt{\pi}}$$

as expected for pure diffusion control.

For intermediate values of p , the full equation must be evaluated.

DISCUSSION AND CONCLUSIONS

The rate at which changes in the optical properties of bronzes can be accomplished in electrochromic systems is determined by the rate at which ions are introduced into the bronze phase. To achieve an optical density of 0.5, a total charge of about 6 millicoulombs/cm² (equivalent to 3.7×10^{16} ions/cm²) must be transported through the system.

Aqueous electrolyte systems are evidently limited by the relatively small values of exchange current density at the electrolyte-solid interface, and will thus be relatively slow

unless that limitation can be overcome. There is as yet almost no quantitative information available for any system except amorphous H_xWO_3 .

The development of thin film all-solid systems that have relatively fast response times (e.g., $<10^{-2}$ seconds) will require both a solid electrolyte with a conductivity of about $10^{-6} (\text{ohm cm})^{-1}$ and a bronze with a diffusion coefficient of $10^{-9} \text{ cm}^2/\text{sec}$ or greater.

Unfortunately, there are no presently known solid electrolytes that are fast proton conductors, so regardless of the existence of bronzes with high diffusion coefficients for protons, the speed of response of proton-conducting all-solid electrochromic systems will be less than that of aqueous electrolyte systems. The discovery of good proton-conducting electrolytes could, of course, make such solid state systems practical.

The situation is different for lithium-conducting, sodium-conducting and silver-conducting systems. In these cases, solid electrolytes are either already known or seem to be attainable that meet the kinetic requirements of electrochromic systems. Data on some of these solid electrolytes are given in Table II.

On the other hand, very little information is yet available concerning the alkali metal diffusion coefficients in appropriate bronzes. This does not seem to be a serious problem, as there are indirect indications that satisfactory bronzes exist, at least for lithium systems.

TABLE II

| Material | Mobile Ion | Conductivity at 25°C (ohm-cm) ⁻¹ | Reference |
|---|-----------------|--|-----------|
| RbAg ₄ I ₅ | Ag ⁺ | 2.7×10^{-1} | 18 |
| Ag Beta Alumina | Ag ⁺ | 6.3×10^{-3} | 19 |
| Na Beta Alumina | Na ⁺ | 7.4×10^{-2} | 20 |
| Na ₃ Zr ₂ PSi ₂ O ₁₂ | Na ⁺ | 1.8×10^{-3} | 21 |
| Li ₄ SO ₄ + 40 mole % Li ₃ PO ₄ | Li ⁺ | 1.7×10^{-6} | 22 |
| Li ₃ PO ₄ + 40 mole % Li ₄ SO ₄ | Li ⁺ | 3.7×10^{-6} | 23 |
| LiAlCl ₄ | Li ⁺ | 1.2×10^{-6} | 24 |

ACKNOWLEDGEMENT

This research was supported by the Advanced Research Projects Agency of the Department of Defense under Contract No. MDA903-76C-0250 with The University of Michigan.

References

1. R. Wöhler, *Ann. Physik* 2, 350 (1824).
2. M. Kestigian and R. Ward, *J. Am. Chem. Soc.* 77, 6199 (1955).
3. S. Andersson and A. D. Wadsley, *Acta Cryst.* 15, 201 (1962).
4. D. Ridgley and R. Ward, *J. Am. Chem. Soc.* 77, 6132 (1955).
5. R. P. Ozerov, *Russian J. Inorg. Chem.* 4, 476 (1959).
6. A. Wold, W. Kunmann, R. J. Arnott and A. Ferretti, *Inorg. Chem.* 3, 545 (1964).
7. P. G. Dickens and M. S. Whittingham, "The Tungsten Bronzes and Related Compounds," *Quart. Rev.* 22, 30 (1968).
8. P. Hagenmuller, "Les Bronzes Oxygénés," in *Prog. in Solid State Chem.* 5, 71 (1971).
9. J. B. Goodenough, "Metallic Oxides," in *Prog. in Solid State Chem.* 5, 145 (1971).
10. P. Hagenmuller, "Tungsten Bronzes, Vanadium Bronzes and Related Compounds," in *Comprehensive Inorganic Chemistry*, 4, ed. by J. C. Bailar et al., Pergamon (1973) p. 541.
11. D. J. M. Bevan, "Non-Stoichiometric Compounds: An Introductory Essay," in *Comprehensive Inorganic Chemistry*, 4, ed. by J. C. Bailar et al., Pergamon (1973) p. 453.
12. P. Hagenmuller, "Structures and Chemical Bonds in Vanadium Bronzes," in *Crystal Structure and Chemical Bonding in Inorganic Chemistry*, ed. by C. J. M. Rooymans and A. Rabenau, North Holland Pub. Co. (1975) p. 69.
13. P. G. Dickens and P. J. Wiseman, in *MTP International Review of Science, Series Two, Vol. 10, Inorganic Chem.*, ed. by L. E. J. Roberts, Butterworths (1975) p. 211.
14. O. Glemser and C. Naumann, *Z. Anorg. Allg. Chem.* 265, 289 (1951).
15. P. G. Dickens and R. J. Hurditch, in *The Chemistry of Extended Defects in Non-metallic Solids*, ed. by L. Eyring and M. O'Keefe, North Holland (1970), p. 555.
16. P. G. Dickens, J. H. Moore and D. J. Neild, *J. Solid State Chem.* 7, 241 (1973).

17. R. S. Crandall and B. W. Faughnan, Appl. Phys. Letters 28, 95 (1976).
18. D. O. Raleigh, J. Appl. Phys. 41, 1876 (1970).
19. M. S. Whittingham and R. A. Huggins, J. Electrochem. Soc. 118, 1 (1971).
20. M. S. Whittingham and R. A. Huggins, J. Chem. Phys. 54, 414 (1971).
21. J. B. Goodenough, H. Y-P Hong and J. A. Kafalas, Mat. Res. Bull. 11, 203 (1976).
22. Y-W. Hu, I. D. Raistrick and R. A. Huggins, Mat. Res. Bull. 11, 1227 (1976).
23. Y-W. Hu, I. D. Raistrick and R. A. Huggins, to be published.
24. W. Weppner and R. A. Huggins, Phys. Letters, A58, 245 (1976).

ALUMINUM-CARBON COMPOSITES
DEVELOPED FOR SLIDING SEAL MEMBERS

E. E. Hucke

During the period when the rotary engine was under intense development in the U.S. many seal materials were investigated. Among them were aluminum alloy infiltrated-carbon composites. Various carbons, including fibers, particulate, and skeletal structures were tried. While the major property desired was wear resistance in high velocity, high temperature sliding, additional requirements on corrosion resistance, (resistance to disintegration from Al_4C_3), elastic modulus, strength, and fatigue resistance were needed.

One class of such material made by infiltration of controlled particle and pore size glassy carbon skeletons resulted in isotropic properties which in many respects compare favorably to those now being produced in Al-graphite fibrous systems. A typical microstructure is shown together with some mechanical properties. Since in the case shown the carbon used was not high modulus, the composite Young's modulus is low compared to the stiff fiber composites. However, skeletons incorporating chopped, or woven fibers can easily be used. The strength properties are isotropic.

TYPICAL PROPERTIES

| | |
|-----------------------------|---------------------|
| Density, gm/cm ³ | 1.96 |
| Approx. Vol.% Carbon | 50 |
| Coefficient of expansion/°F | $5.5 \cdot 10^{-6}$ |
| Sonic Modulus, psi | $8.5 \cdot 10^6$ |
| Strength, 4 pt. M.O.R., psi | |
| R.T. | 70,000 |
| 700°F | 46,000 |
| 900°F | 30,200 |
| 1000°F | 19,700 |
| 1100°F | 15,200 |
| 1200°F | 15,800 |
| Wear Resistance, inches | .0018 |
| in 100 hrs. engine test | |
| Fatigue resistance, 100 | No pitting |
| engine test | |

A FLUID THERMAL SWITCH

H. Reiss

INTRODUCTION

In this paper we analyze the thermal transport properties of a plane parallel system without edge effects, such as is displayed in Fig. 1.

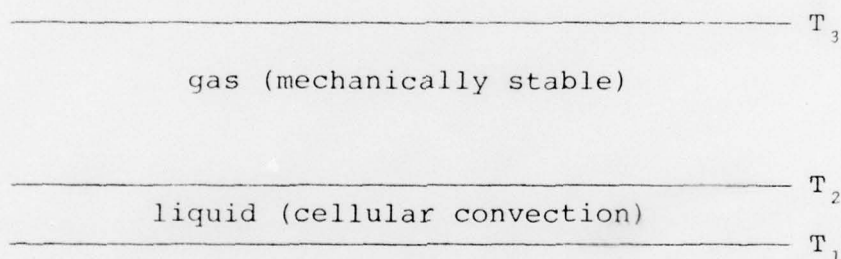


Figure 1.

The lowest horizontal line represents a flat plate at temperature T_1 . Between the plate and the next horizontal line is a film of liquid (several millimeters thick) whose upper surface is at temperature, T_2 . The third horizontal line indicates another plate maintained at temperature, T_3 . Between this plate and the surface of the liquid is a gas (usually a mixture). Generally $T_3 < T_2 < T_1$.

This particular arrangement is a schematic representation of the configuration of a diffusion cloud chamber within which

one can perform experiments on the phenomenon of vapor phase nucleation. Used as a cloud chamber, the device might contain liquid water as the film of liquid. The gas might consist of helium plus water vapor, evaporated and transported by steady state diffusion to the upper plate where it condenses and spreads, as a thin film, to the sides of the chamber to be returned to the lower film. Even though the lower regions of the gas are hotter than the upper regions the gas remains mechanically stable because of the relatively large mass loading of the lower regions with H_2O vapor, the heavier component (compared to He). However, the film of liquid may (and undoubtedly does) support cellular convection.

It is easy to show¹ that the relative humidity, as a function of elevation in the chamber, passes (in the steady state) through a maximum far from either T_2 or T_3 . Indeed, at this maximum the relative humidity might be several hundred percent, and if it exceeds the level required to induce nucleation liquid drops are formed and subsequently fall to the film at the bottom.

The rate of nucleation, which depends upon the level of supersaturation is therefore a reflection of the steady state of transport attained in the chamber.

In very recent work with a cloud chamber, such as the one described, the present author and his collaborators were able to switch the chamber repeatedly between two rates of nucleation while maintaining T_1 and T_3 constant. We have not measured the heat flux in the system, but from the statement of the last

paragraph, it is implied that there exist two different states of transport, locally stable, and consistent with the same values of T_1 and T_3 . The chamber is therefore bistable and offers the possibility of serving as a thermal switch. Fluid dynamic switches (based on mechanics) have been known and even used for some time, but to the author's knowledge this is the first example of a thermal fluid switch (if in fact it is). The purpose of this paper is to explore the conditions under which such a phenomenon would occur, and to inquire into whether these conditions could possibly be met in the arrangement of Fig. 1. Before doing this, however, we might mention the conditions under which the system was apparently switched.

Switching occurred upon pumping the helium pressure down to a point such that the liquid film boiled. Then when the helium pressure was restored, and the T_1 and T_3 maintained at their previous values, the rate of nucleation was indefinitely changed. However, if the chamber was shut down (overnight) and reactivated again with T_1 and T_3 maintaining their values, the original rate of nucleation was restored. The apparent switching could be performed repetitively, and reproducibly.

CONDITIONS FOR BISTABLE BEHAVIOR

In order to investigate how the bistable behavior could originate, we consider a very simple model. Introduce the following definitions.

$$T_1 - T_3 = \Delta T > 0 \quad (1)$$

$$T_1 - T_2 = \tau > 0 \quad (2)$$

From these we discover

$$T_2 - T_3 = \Delta T - \tau \quad (3)$$

Although we know that convective heat transfer is liable to occur in the film, we nevertheless characterize it by an effective thermal conductivity $\kappa(\tau)$ which will depend upon τ in some way. For the thermal conductivity of the gas we use the symbol κ_g , and assume it relatively independent of temperature. Then the thermal flux in the liquid layer will be (at steady state),

$$\phi = \kappa(\tau) \frac{\tau}{t} \quad (4)$$

where t is the thickness of the layer. At the same time, the thermal flux in the gas will be

$$\phi_g = \kappa_g \frac{(\Delta T - \tau)}{t_g} \quad (5)$$

where t_g is the vertical thickness of the gas.

Under steady state conditions, $\phi = \phi_g$, and we have the requirement

$$\phi = \kappa(\tau) \frac{\tau}{t} = \kappa_g \frac{(\Delta T - \tau)}{t_g} = \phi_g \quad (6)$$

Now suppose

$$\begin{aligned} \kappa(\tau) &= \kappa_1, & \tau < \tau^* \\ &= \kappa_2, & \tau > \tau^* \end{aligned} \quad (7)$$

$$\kappa_1 > \kappa_2$$

Figure 2 contains schematic plots of both $\phi(\tau)$ and $\phi_g(\tau)$ versus τ , based on Eqs. (4), (5) and (7).

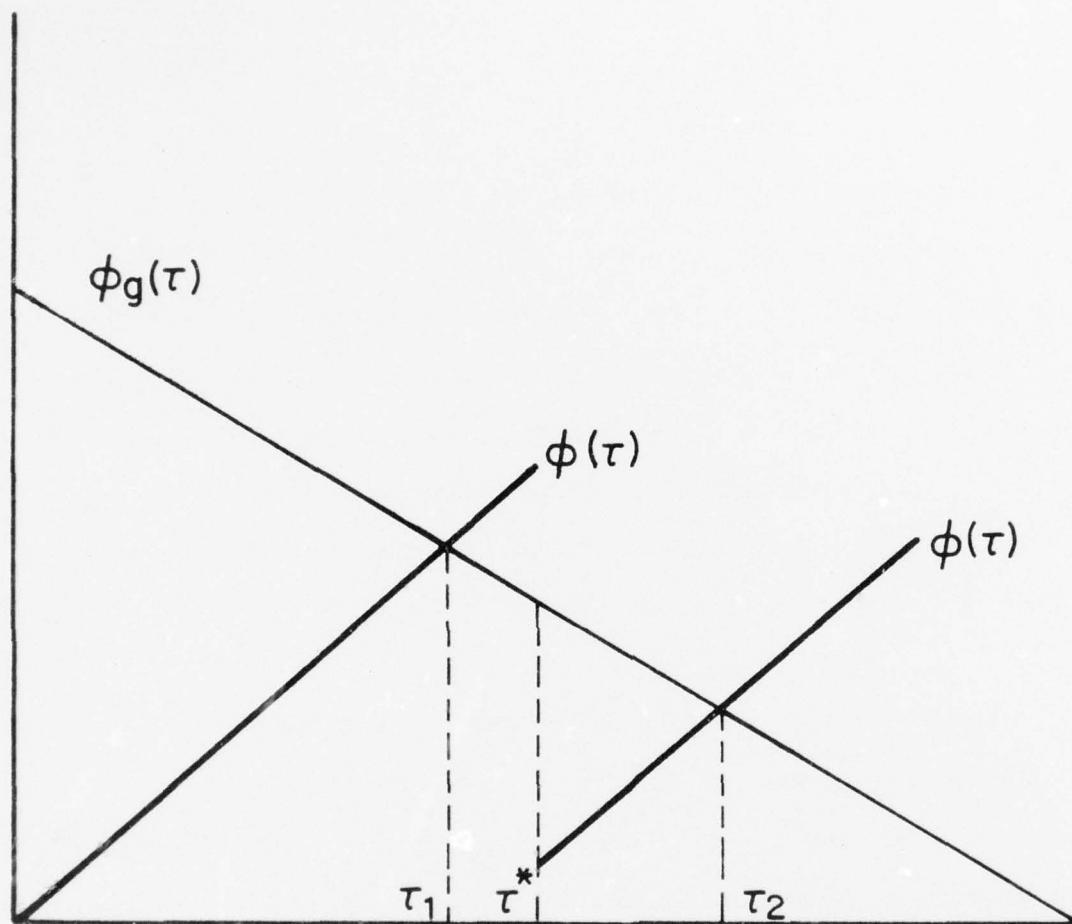


Figure 2.

The break in $\phi(\tau)$ at $\tau = \tau^*$ occurs because of Eq. (7). As is obvious, it leads to two solutions of Eq. (6) at τ_1 and τ_2 (see Fig. 2), respectively. These two solutions characterize the states between which switching occurs. They are both locally stable, i.e., any fluctuation from τ_1 towards τ_2 is met by a restoring influence, and vice versa.

This may be easily demonstrated as follows. Suppose the system is steady at τ_1 . Now suppose the system is displaced to higher values of τ , moving toward τ^* and τ_2 . Since such a displacement increases the temperature gradient across the liquid layer more heat is delivered to the interface at T_2 . This increment of heat flux will tend to raise T_2 , and therefore decrease τ , since T_1 is fixed. Thus τ tends to be restored to its original value.

Next consider steady operation at τ_2 , and suppose we have a displacement towards τ^* and τ_1 . Since this represents a reduction of τ it implies an increase in T_2 , T_1 being fixed. Thus the temperature gradient across the liquid layer is reduced and the same is true of the corresponding heat flux with the result that T_2 will be reduced. Thus the temperature of the interface is again forced towards its original value, indicating local stability.

A more reasonable choice for $\kappa(\tau)$, instead of Eq. (7) would contain a finite negative slope instead of a discontinuity in the neighborhood of τ^* (see next section). Thus Fig. 3 would be more realistic than Fig. 2.

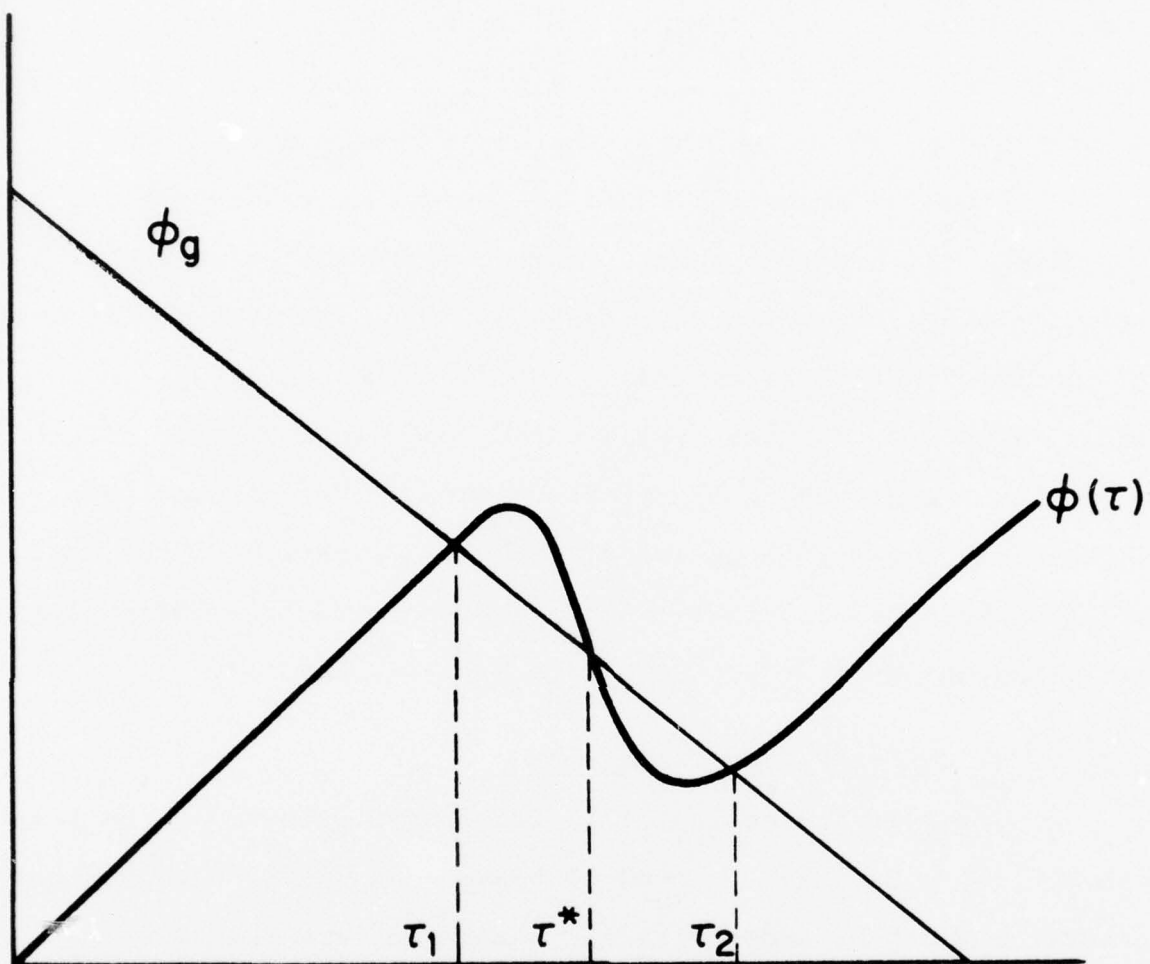


Figure 3.

According to Fig. 3, another solution, i.e., $\tau = \tau^*$ now presents itself. However, by arguments similar to those demonstrating the stabilities at τ_1 and τ_2 , it may easily be shown that $\tau = \tau^*$ is an unstable solution, and will therefore never be realized.

From the above it should be obvious that the critical ingredient for bistable thermal switching is the existence of a negative slope region for the function $\kappa(\tau)$. Whether or not this is possible in the system under consideration still remains to be seen. However, it is not ruled out by any broad generic scientific laws (e.g., thermodynamics) because it has already been observed in some systems. We discuss this question in the next section where we also inquire into how the switching observed in our cloud chamber may actually have been facilitated.

EFFECTS OF CELLULAR CONVECTION MODES

Cellular convection,^{2,3,4} frequently referred to as Bénard convection, was first observed by Bénard⁵ in 1901. Although the general principles underlying the phenomenon are fairly well understood, it remains true, seventy-five years later, that the details in any one experimental situation are unclear, due to the difficulty of non-numerical mathematical analysis.

The general characteristics, however, are the following. In a fluid film of thickness d , bridged by temperature gradient τ , quiescent conductive heat transfer occurs until the so-called first critical Raleigh number is exceeded, whereupon cellular convection becomes a factor. The Raleigh number is given by

$$R = \frac{\alpha g \tau d^3}{\nu \kappa_0} \quad (8)$$

where α is the thermal volume expansivity, g is the acceleration of gravity, ν the kinematic viscosity, and κ_0 the thermal conductivity. The quantities τ and d have already been defined. The critical value R_c of the Raleigh number varies with the boundary conditions. We shall use the notation (free-free), (rigid-free), and (rigid-rigid) to denote situations in which the lower and upper boundaries of the liquid film are free or rigid, respectively. We then have the following

$$\begin{aligned} R_c &= 6.57.5, & a_c &= 2.22 \text{ (free-free)} \\ R_c &= 1100.6, & a_c &= 2.68 \text{ (rigid-free)} \\ R_c &= 1707.7, & a_c &= 3.117 \text{ (rigid-rigid)} \end{aligned} \quad (9)$$

Here a_c is the wave number $2\pi/\lambda_c$, where λ is the wavelength of the critical cellular mode.

It is generally observed, as the Raleigh number is extended above the critical value that λ increases, and the effective thermal conductivity $\kappa(\tau)$ increases. For example, it has been computed⁶ in a crude manner (roughly confirmed by experiment) that the heat flux ϕ will go as

$$\phi = 0.068 \kappa_0 \left(\frac{\alpha g}{\nu^2} \right)^{1/2} \tau^{4/3} \quad (10)$$

The actual conductive flux would be

$$\phi_0 = \frac{\kappa_0}{d} \tau \quad (11)$$

and the Nusselt number, ϕ/ϕ_0 , is

$$\text{Nu} = 0.068 d \left(\frac{\alpha g}{\nu^2} \right)^{1/2} \tau^{1/3} \quad (12)$$

increases as $\tau^{1/3}$. In fact this implies that

$$\kappa(\tau) = 0.068 \kappa_0 d \left(\frac{\alpha g}{\nu^2} \right)^{1/2} \tau^{1/3} \quad (13)$$

This shows $\kappa(\tau)$ to have a positive slope with respect to τ . This positive slope has generally been confirmed⁷ (as has been the discontinuity $\kappa_0 \rightarrow \kappa(\tau)$ with $\kappa(\tau) > \kappa_0$) at the critical Raleigh number for the rigid-rigid case.

On the other hand, cases of negative slope have been observed. The most prominent examples occur in two component fluids, but, possibly, also in one component fluids confined by an upper plate which is slightly sloped.⁸ The latter example is clouded by the fact that oscillations are observed to occur in the transfer of heat. However, such oscillations are generally connected with such negative slopes. It should be mentioned that sustained oscillations have also been observed in our cloud chamber nucleation rates under certain conditions.

It is now known that many poorly understood factors (including surface tension - very prominently) are involved in cellular convection. These and others could be producing negative slope regions in our cloud chamber.

The switching which we observed is probably connected to the transition from one (positive slope) convective mode to another (positive slope) mode separated by a negative slope mode.

Both modes are stable. The transition is probably induced by the fairly violent perturbation caused by the boiling described in section 1.

POSSIBLE APPLICATIONS

The possibility of applying the thermal switch phenomenon must await further exploration. It might even be possible to provide amplifying action. The phenomenon may have a place in atmospheric physics where extensive thin layers of water may be found on the earth's surface. However, at the moment it remains an interesting curiosity.

ACKNOWLEDGEMENT

This research was supported by the Advanced Research Projects Agency of the Department of Defense under Contract No. MDA903-76C-0250 with The University of Michigan.

REFERENCES

1. J. L. Katz, J. Chem. Phys. 52, 4733(1970).
2. S. Chandrasekhar, "Hydrodynamic and Hydromagnetic Stability" (Oxford, 1961).
3. E. L. Koschmieder, in "Advances in Chemical Physics," Vol. XXVI, p. 177, edited by I. Prigogine and S. A. Rice (John Wiley & Sons, 1974).
4. Ibid, R. S. Schechter, M. G. Velarde and J. K. Platten, p. 265.
5. Reference 3, p. 180.
6. M. Jakob, "Heat Transfer, I", p. 536, (John Wiley, New York, 1949).
7. Reference 2, p. 63.
8. Reference 4, pp. 291-293.